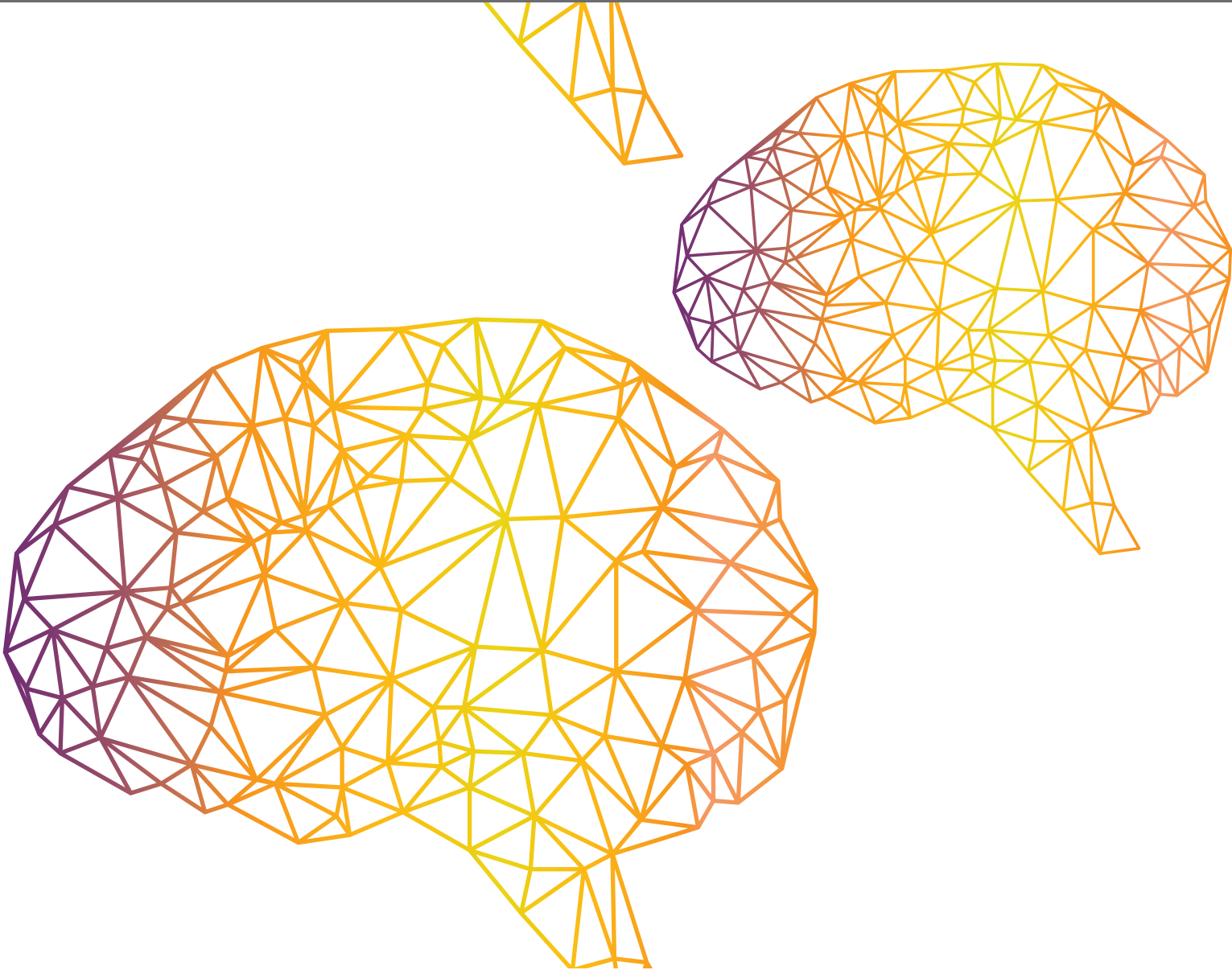


# **REHABILITATION ROBOTICS: CHALLENGES IN DESIGN, CONTROL, AND REAL APPLICATIONS**

EDITED BY: Francisco Romero Sánchez, Luciano Luporini Menegaldo,  
Josep M. Font-Llagunes and Massimo Sartori  
PUBLISHED IN: Frontiers in Neurorobotics





# frontiers

## Frontiers eBook Copyright Statement

The copyright in the text of individual articles in this eBook is the property of their respective authors or their respective institutions or funders. The copyright in graphics and images within each article may be subject to copyright of other parties. In both cases this is subject to a license granted to Frontiers.

The compilation of articles constituting this eBook is the property of Frontiers.

Each article within this eBook, and the eBook itself, are published under the most recent version of the Creative Commons CC-BY licence.

The version current at the date of publication of this eBook is CC-BY 4.0. If the CC-BY licence is updated, the licence granted by Frontiers is automatically updated to the new version.

When exercising any right under the CC-BY licence, Frontiers must be attributed as the original publisher of the article or eBook, as applicable.

Authors have the responsibility of ensuring that any graphics or other materials which are the property of others may be included in the CC-BY licence, but this should be checked before relying on the CC-BY licence to reproduce those materials. Any copyright notices relating to those materials must be complied with.

Copyright and source acknowledgement notices may not be removed and must be displayed in any copy, derivative work or partial copy which includes the elements in question.

All copyright, and all rights therein, are protected by national and international copyright laws. The above represents a summary only. For further information please read Frontiers' Conditions for Website Use and Copyright Statement, and the applicable CC-BY licence.

ISSN 1664-8714

ISBN 978-2-88976-881-3

DOI 10.3389/978-2-88976-881-3

## About Frontiers

Frontiers is more than just an open-access publisher of scholarly articles: it is a pioneering approach to the world of academia, radically improving the way scholarly research is managed. The grand vision of Frontiers is a world where all people have an equal opportunity to seek, share and generate knowledge. Frontiers provides immediate and permanent online open access to all its publications, but this alone is not enough to realize our grand goals.

## Frontiers Journal Series

The Frontiers Journal Series is a multi-tier and interdisciplinary set of open-access, online journals, promising a paradigm shift from the current review, selection and dissemination processes in academic publishing. All Frontiers journals are driven by researchers for researchers; therefore, they constitute a service to the scholarly community. At the same time, the Frontiers Journal Series operates on a revolutionary invention, the tiered publishing system, initially addressing specific communities of scholars, and gradually climbing up to broader public understanding, thus serving the interests of the lay society, too.

## Dedication to Quality

Each Frontiers article is a landmark of the highest quality, thanks to genuinely collaborative interactions between authors and review editors, who include some of the world's best academicians. Research must be certified by peers before entering a stream of knowledge that may eventually reach the public - and shape society; therefore, Frontiers only applies the most rigorous and unbiased reviews. Frontiers revolutionizes research publishing by freely delivering the most outstanding research, evaluated with no bias from both the academic and social point of view. By applying the most advanced information technologies, Frontiers is catapulting scholarly publishing into a new generation.

## What are Frontiers Research Topics?

Frontiers Research Topics are very popular trademarks of the Frontiers Journals Series: they are collections of at least ten articles, all centered on a particular subject. With their unique mix of varied contributions from Original Research to Review Articles, Frontiers Research Topics unify the most influential researchers, the latest key findings and historical advances in a hot research area! Find out more on how to host your own Frontiers Research Topic or contribute to one as an author by contacting the Frontiers Editorial Office: [frontiersin.org/about/contact](http://frontiersin.org/about/contact)



# REHABILITATION ROBOTICS: CHALLENGES IN DESIGN, CONTROL, AND REAL APPLICATIONS

Topic Editors:

**Francisco Romero Sánchez**, University of Extremadura, Spain

**Luciano Luporini Menegaldo**, Federal University of Rio de Janeiro, Brazil

**Josep M. Font-Llagunes**, Universitat Politècnica de Catalunya, Spain

**Massimo Sartori**, University of Twente, Netherlands

**Citation:** Sánchez, F. R., Menegaldo, L. L., Font-Llagunes, J. M., Sartori, M., eds. (2022). Rehabilitation Robotics: Challenges in Design, Control, and Real Applications. Lausanne: Frontiers Media SA. doi: 10.3389/978-2-88976-881-3

# Table of Contents

- 05 Editorial: Rehabilitation robotics: Challenges in design, control, and real applications**  
Francisco Romero-Sánchez, Luciano Luperini Menegaldo, Josep M. Font-Llagunes and Massimo Sartori
- 09 A Cable-Driven Three-DOF Wrist Rehabilitation Exoskeleton With Improved Performance**  
Ke Shi, Aiguo Song, Ye Li, Huijun Li, Dapeng Chen and Lifeng Zhu
- 25 Using a Robot to Treat Non-specific Low Back Pain: Results From a Two-Arm, Single-Blinded, Randomized Controlled Trial**  
Honorio Marín-Méndez, Patricia Marín-Novoa, Silvia Jiménez-Marín, Itziar Isidoro-Garijo, Mercedes Ramos-Martínez, Miriam Bobadilla, Eduardo Mirpuri and Alfredo Martínez
- 33 User-Centered Design and Development of the Modular TWIN Lower Limb Exoskeleton**  
Matteo Laffranchi, Stefano D'Angella, Christian Vassallo, Chiara Piezzo, Michele Canepa, Samuele De Giuseppe, Mirco Di Salvo, Antonio Succi, Samuele Cappa, Giulio Cerruti, Silvia Scarpetta, Lorenzo Cavallaro, Nicolò Boccardo, Marialaura D'Angelo, Claudia Marchese, Jody A. Saglia, Eleonora Guanziroli, Giacinto Barresi, Marianna Semprini, Simone Traverso, Stefano Maludrottu, Franco Molteni, Rinaldo Sacchetti, Emanuele Gruppioni and Lorenzo De Michieli
- 50 Wearable Robots: An Original Mechatronic Design of a Hand Exoskeleton for Assistive and Rehabilitative Purposes**  
Nicola Secciani, Chiara Brogi, Marco Pagliai, Francesco Buonamici, Filippo Gerli, Federica Vannetti, Massimo Bianchini, Yary Volpe and Alessandro Ridolfi
- 65 Usability Assessment of Body Controlled Electric Hand Prostheses: A Pilot Study**  
Sasha B. Godfrey, Cristina Piazza, Federica Felici, Giorgio Grioli, Antonio Bicchi and Manuel G. Catalano
- 81 Assessment of a Robotic Walker in Older Adults With Parkinson's Disease in Daily Living Activities**  
Sergio D. Sierra M., Daniel E. Garcia A., Sophia Otálora, María Camila Arias-Castro, Alejandro Gómez-Rodas, Marcela Múnera and Carlos A. Cifuentes
- 95 Adaptation Strategies for Personalized Gait Neuroprosthetics**  
Anne D. Koelewijn, Musa Audu, Antonio J. del-Ama, Annalisa Colucci, Josep M. Font-Llagunes, Antonio Gogeoascoechea, Sandra K. Hnat, Nathan Makowski, Juan C. Moreno, Mark Nandor, Roger Quinn, Marc Reichenbach, Ryan-David Reyes, Massimo Sartori, Surjo Soekadar, Ronald J. Triolo, Mareike Vermehren, Christian Wenger, Utku S. Yavuz, Dietmar Fey and Philipp Beckerle

- 103** *A Novel Clinical-Driven Design for Robotic Hand Rehabilitation: Combining Sensory Training, Effortless Setup, and Large Range of Motion in a Palmar Device*  
Raphael Rätz, François Conti, René M. Müri and Laura Marchal-Crespo
- 125** *Development and Electromyographic Validation of a Compliant Human-Robot Interaction Controller for Cooperative and Personalized Neurorehabilitation*  
Stefano Dalla Gasperina, Valeria Longatelli, Francesco Braghin, Alessandra Pedrocchi and Marta Gandolla
- 146** *Evaluation of Optimal Control Approaches for Predicting Active Knee-Ankle-Foot-Orthosis Motion for Individuals With Spinal Cord Injury*  
Míriam Febrer-Nafria, Benjamin J. Fregly and Josep M. Font-Llagunes
- 160** *A Hybrid 3D Printed Hand Prosthesis Prototype Based on sEMG and a Fully Embedded Computer Vision System*  
Maria Claudia F. Castro, Wellington C. Pinheiro and Glauco Rigolin
- 171** *Wearable Power-Assist Locomotor for Gait Reconstruction in Patients With Spinal Cord Injury: A Retrospective Study*  
Soichiro Koyama, Shigeo Tanabe, Takeshi Gotoh, Yuta Taguchi, Masaki Katoh, Eiichi Saitoh, Yohei Otaka and Satoshi Hirano
- 183** *Performance of Impedance Control-Based Strategies in Power-Assisted Wheelchairs: A Predictive Simulation Study*  
Vinicius Ishimoto Cuerva, Marko Ackermann and Fabrizio Leonardi
- 198** *Safety and Feasibility of a Novel Exoskeleton for Locomotor Rehabilitation of Subjects With Spinal Cord Injury: A Prospective, Multi-Center, and Cross-Over Clinical Trial*  
Sijing Chen, Zhanbin Wang, Yongqiang Li, Jiashuai Tang, Xue Wang, Liping Huang, Zhuangwei Fang, Tao Xu, Jiang Xu, Feng Guo, Yizhao Wang, Jianjun Long, Xiaodong Wang, Fang Liu, Jianfeng Luo, Yulong Wang, Xiaolin Huang, Zishan Jia, Mei Shuai and Jianan Li
- 213** *sEMG-Based Gesture Classifier for a Rehabilitation Glove*  
Dorin Copaci, Janeth Arias, Marcos Gómez-Tomé, Luis Moreno and Dolores Blanco



## OPEN ACCESS

EDITED AND REVIEWED BY  
Florian Röhrbein,  
Technische Universität Chemnitz,  
Germany

\*CORRESPONDENCE  
Francisco Romero-Sánchez  
fromsan@unex.es

RECEIVED 31 May 2022  
ACCEPTED 13 June 2022  
PUBLISHED 27 July 2022

CITATION  
Romero-Sánchez F, Loporini  
Menegaldo L, Font-Llagunes JM and  
Sartori M (2022) Editorial:  
Rehabilitation robotics: Challenges in  
design, control, and real applications.  
*Front. Neurobot.* 16:957905.  
doi: 10.3389/fnbot.2022.957905

COPYRIGHT  
© 2022 Romero-Sánchez, Loporini  
Menegaldo, Font-Llagunes and Sartori.  
This is an open-access article  
distributed under the terms of the  
[Creative Commons Attribution License](#)  
(CC BY). The use, distribution or  
reproduction in other forums is  
permitted, provided the original  
author(s) and the copyright owner(s)  
are credited and that the original  
publication in this journal is cited, in  
accordance with accepted academic  
practice. No use, distribution or  
reproduction is permitted which does  
not comply with these terms.

# Editorial: Rehabilitation robotics: Challenges in design, control, and real applications

Francisco Romero-Sánchez<sup>1\*</sup>, Luciano Loporini Menegaldo<sup>2</sup>,  
Josep M. Font-Llagunes<sup>3,4</sup> and Massimo Sartori<sup>5</sup>

<sup>1</sup>Departamento de Ingeniería Mecánica, Energética y de los Materiales, Escuela de Ingenierías Industriales, Universidad de Extremadura, Badajoz, Spain, <sup>2</sup>Programa de Engenharia Biomédica, COPPE, Universidade Federal do Rio de Janeiro, Rio de Janeiro, Brazil, <sup>3</sup>Biomechanical Engineering Lab, Department of Mechanical Engineering, Research Centre for Biomedical Engineering, Universitat Politècnica de Catalunya, Barcelona, Spain, <sup>4</sup>Health Technologies and Innovation, Institut de Recerca Sant Joan de Déu, Esplugues de Llobregat, Spain, <sup>5</sup>Department of Biomechanical Engineering, University of Twente, Enschede, Netherlands

## KEYWORDS

wearable robots, exoskeletons, exosuits, rehabilitation, human augmentation, neuromusculoskeletal modeling, assistive devices

## Editorial on the Research Topic

**Rehabilitation robotics: Challenges in design, control, and real applications**

## Introduction

In the last decade, research focused on rehabilitation robotics has progressed from proposing restricted or rigid solutions in a clinical setting to portable devices compliant with the user and also adapted to their requirements, based on their disability and the rehabilitation training program. Novel techniques have inspired the evolution of rehabilitation devices from hard and bulky to soft, lightweight, and fully wearable. For example, biologically inspired actuators have relaxed the constraint of having to rely on rigid supports, as the skeletal system can be used to that end. Furthermore, the use of synergies has led to a reduction in the number of actuators and improved their control. Moreover, the latest advances in modeling and simulation have allowed for assessing and compensating for fatigue, as well as simulating the use of assistive devices out of a clinical environment. All these research achievements have enabled a new generation of portable rehabilitation devices. In the present Frontiers Research Topic, novel techniques for the design, simulation, sensing, and control of rehabilitation devices are presented for rehabilitation devices such as powered exoskeletons, neuroprostheses, and equipment for moving the rehabilitation environment out of the clinical setting.

## Challenges in design, control, and real applications

A key challenge in rehabilitation robotics is to create devices that facilitate positive neuroplasticity in the intact moving human *in vivo*. That is, robots that provide as-least-as-needed assistance to neuromuscular targets while promoting voluntary execution of functional movements. In this context, the robot must be transparent and intuitive to prevent an increase of cognitive loads during the rehabilitation process. This objective is not easy to accomplish, as there are many challenges to overcome and many approaches to tackle. Examples of that, among others, are include the simulation of the human-machine interaction, the design and control of the rehabilitation device, the validation in a clinical environment, or the adaptation of the neuromusculoskeletal system to the rehabilitation process. Based on them, we present the contributions to this Research Topic according to the aforementioned challenges, although they are usually found intertwined in this research field.

### Simulation

Simulation-based studies in rehabilitation robotics provide a time- and cost-effective approach to preview real world scenarios. In this sense, [Febrer-Nafría et al.](#) simulate crutch-orthosis-assisted walking to choose the optimal active orthosis controller parameters for a specific subject. Their findings improve the traditional trial-and-error approach to select the best maximum knee flexion angle. The simulation provides optimal values to achieve a more balanced assisted gait pattern, making the process fully personalized to the patients' needs and less time-consuming. [Cuerva et al.](#) show a predictive simulation study to improve control in power-assisted wheelchairs. Their work investigates the advantages and disadvantages of an impedance control strategy, which that is more natural and effective than other alternatives. They employed predictive simulations of locomotion with power-assisted wheelchairs in different scenarios by using a realistic physiological model of the user's musculoskeletal system and its interaction with the wheelchair. Their results confirm this control strategy as the most useful, but their simulations also found a waste of energy during the propulsion cycle.

### Design

The personalised/personalized design of rehabilitation devices has been a challenge for researchers worldwide. Design requirements are different depending on the body segment part to be treated. In addition, these design specifications may change depending on the neuromuscular impairment. For

example, assisting a patient with spinal cord injury (SCI) is not the same as helping a patient who has suffered a stroke. In addition, the designed device must be focused on the user's needs. It also must consider the evolution of the rehabilitation process, which may imply adaptations in the structure of the device or its control. In this Research Topic, [Laffranchi et al.](#) present the TWIN, a modular exoskeleton for SCI subjects. In their work, users' needs drove an iterative process to improve the system's design and construction. Sensing and control approaches are also presented. Supervised tests in a clinical setting demonstrated a stable gait pattern for rehabilitation, improving cost effectiveness. Regarding the upper limbs, [Secciani et al.](#) propose an original mechatronic design of a hand exoskeleton for both home assistance and telerehabilitation. It uses a real-time intention detection algorithm, but can also perform exercises preset by therapists in remotely supervised or unsupervised rehabilitation sessions. Surface electromyography (sEMG) signals are used to detect the user's intention, leading to a customizable, compliant, and comfortable design. In the opposite direction, [Rätz et al.](#) establish their design of a robotic hand by a set of clinical, anatomical, and mechanical requirements established before the development of the device. This novel clinical-driven robotic hand rehabilitation device is capable of fine haptic rendering, offering an effortless setup that supports physiological full flexion/extension of the fingers while providing high mechanical transparency. Lastly, [Shi et al.](#) develop a cable-driven three-degree-of-freedom wrist rehabilitation exoskeleton actuated by the distributed active semi-active (DASA) system. The proposed design has a larger workspace than current wrist rehabilitation training robots, able to cover a broader range of the activities of daily living, with an improved cable-driven design able to increase the effective torque and reduce the parasitic force.

### Control

Control strategies are quite significant to achieve important in achieving proper rehabilitation. In some cases, the rehabilitation routine imposes a pre-defined trajectory to be followed and, therefore, the control strategy must account for it. In others, the primary purpose is to regain neuroplasticity, and, thus, the patient's intention imposes control actions, and establishes how the system acts to achieve a proper trajectory. In this sense, [Dalla Gasperina et al.](#) present a cooperative control framework that promotes compliant motion and implements a variety of high-level rehabilitation modalities, including six actuation modes: passive, corrective, weight counterbalance, resistive, transparent, and hypergravity. The purpose is to change the haptic behavior perceived by a human when interacting with the rehabilitation robot by tuning different impedance control parameters. That variety of physical human-robot interactions helps the user to accomplish the task



while exploiting physiological muscular activation patterns. Moving on to the work presented by [Copaci et al.](#), a new classifier for sEMG signals is presented. The algorithm is based on a Bayesian Neural Network in parallel with an Artificial Neural Network, which the results of which are connected in series with a Layer Recurrent Network. By doing so, the accuracy of the hand gesture recognition based on sEMG signals is improved. The authors' main purpose is to prove that the device control algorithm fits the patient's features and needs. The authors demonstrate that the proposed classifier could achieve high accuracy in hand gesture recognition. Last in this section, [Castro et al.](#) present a new approach for a 3D-printed hand prosthesis commanded by a simple sEMG system aided by a fully embedded computer vision system. The results show high percentages of accuracy, sensitivity, and specificity for grasping objects from neutral and pronated palmar grasp, tripod pinch, key grasp, and index finger extension gesture. This study shows that using a vision system is a promising alternative to traditional methods, as the pattern of grasping and manipulating objects is better defined.

## Validation

The assessment or validation of the designed prototype is a valuable step in developing rehabilitation devices before clinical testing. It allows the implementation of possible improvements before evaluating their actual effect on the target population. In this sense, [Godfrey et al.](#) present the first poly-articulated, electrically-actuated, and body-controlled artificial hand, called SoftHand Pro-Hybrid, and compared its performance against the Hand Pro-Hybrid benchmark. Their results on a limited number of subjects to assess prototype's functionality, with and without limb loss, confirm the possibility of using hybrid solutions as a valid alternative to myoelectric control, especially in situations requiring high versatility of the device. Finally, the work by [Sierra et al.](#) present the assessment of the AGoRA Smart Walker in daily living scenarios with older adults with Parkinson's disease. This kind of device represents a valuable tool for assisting people with gait motor deficits. The actuators of the AGoRA Smart Walker adapt their assistance level to the subject's demands, improving the rehabilitation process. The authors also compared the performance of using their device by between two groups of older adults with different physical and cognitive characteristics (Parkinson's disease vs. other conditions).

## Clinical testing

A final step in assessing rehabilitation devices is their evaluation in a clinical setting. In this way, it is possible to evaluate the effects of the assistive device on a suitable target population. In this Research Topic, [Chen et al.](#) present a

prospective, multi-center, and cross-over trial to evaluate the Ali-robot's safety, walking efficiency, donning and doffing time cost, and user satisfaction. They conclude that subjects with paraplegia below T6 level could ambulate safely and efficiently with that device, although its use should be learned under the guidance of experienced medical personnel. [Marín-Méndez et al.](#) present data from a two-arm, single-blinded, randomized, and controlled clinical trial. The objective was to evaluate the efficiency of a therapeutic massage robot (ADAMO) in reducing non-specific low back pain. Their main finding is that the ADAMO robot is at least as efficient as a regular treatment in reducing low back pain. However, it may be more beneficial for specific patients, such as those with who are overweight. Lastly, [Koyama et al.](#) present a prospective study for the Wearable Power-Assist Locomotor (WPAL). This device has been updated seven times, from the first validated prototype in 2005 to the latest in 2020. This study includes updated results from previous reports from July 2007 to December 2020 for 1785 different subjects. These results confirm that the WPAL improves walking independence for a wide range of spinal cord injury levels, and that further refinement of the WPAL will enable its long-term use at home.

## Adaptation strategies for future research in gait neuroprosthetics

To close this Research Topic, [Koelewijn et al.](#) expose an overview of research directions regarding interfaces with the peripheral and central nervous systems, and the requirements of interface- computing architectures. Their work guides the research on modular and adaptable interfaces that can assist as needed and process all data recorded in real-time while accounting for signal variations among subjects. Furthermore, biomechanical models and simulation techniques are pointed out to predict motion and interactions between the human and the rehabilitation device. This work summarizes the main challenges in designing and using neuroprosthetic devices.

## Conclusions and future perspective

The design of rehabilitation devices results from tight cooperation between engineers, industrial designers, physical therapists, physiatrists, and patients. Therefore, a lot of effort is required to achieve transparent and clinically efficient neuroprostheses and rehabilitation robots that assist neurological patients as needed. From the publications in this Research Topic, we foresee that biomechanical modeling and simulation will be increasingly used to optimize the design of such devices and study human-device interaction, as it allows virtual testing in different scenarios. Moreover, the design of efficient control strategies, and the development of data

acquisition and processing techniques will lead to adequate and timed actuation to improve rehabilitation routines. The reduction in the dimensions and energy requirements of the actuation units will also lead to portable devices and increase the rehabilitation process at home. Lastly, the information gathered from biosignals or the possibility to interact with the neuromusculoskeletal system, such as in functional electrical stimulation or spinal cord stimulation, will make possible a new generation of rehabilitation devices able to overcome the current challenges faced in the rehabilitation of subjects with motor disabilities.

## Author contributions

FR-S wrote the first draft of the manuscript. All authors have made substantial and iterative contribution to the work and approved its final version for publication.

## Funding

The authors, in order of appearance, wish to thank the following support given by: the Ministry of Science and Innovation—Spanish Agency of Research (MCIN/AEI/10.13039/501100011033) through project PID2019-107491RB-I00 (FR-S), the National Council for Scientific and Technological Development (CNPq) through the Productivity Grant No. 311715/2021-4 (LL), the Ministry of Science and Innovation—Spanish Agency of Research (MCIN/AEI/10.13039/501100011033) and ERDF A way of

making Europe through project RTI2018-097290-B-C33 (JF-L), and the European Union's Horizon 2020 Research and Innovation Programme as part of the European Research Council (ERC) Starting Grant INTERACT (803035) (MS).

## Acknowledgments

The guest editors gratefully acknowledge the contributions to this Research Topic. It is also acknowledged the support of more than 50 referees who reviewed the manuscripts submitted for possible publication in this Research Topic.

## Conflict of interest

The authors declare that the research was conducted in the absence of any commercial or financial relationships that could be construed as a potential conflict of interest.

## Publisher's note

All claims expressed in this article are solely those of the authors and do not necessarily represent those of their affiliated organizations, or those of the publisher, the editors and the reviewers. Any product that may be evaluated in this article, or claim that may be made by its manufacturer, is not guaranteed or endorsed by the publisher.



# A Cable-Driven Three-DOF Wrist Rehabilitation Exoskeleton With Improved Performance

Ke Shi, Aiguo Song\*, Ye Li, Huijun Li, Dapeng Chen and Lifeng Zhu

School of Instrument Science and Engineering, Southeast University, Nanjing, China

## OPEN ACCESS

### Edited by:

Francisco Romero Sánchez,  
University of Extremadura, Spain

### Reviewed by:

Wenbin Chen,  
Huazhong University of Science and  
Technology, China

Dong Hyun Kim,  
Korea Advanced Institute of Science  
and Technology, South Korea

### \*Correspondence:

Aiguo Song  
a.g.song@seu.edu.cn

**Received:** 04 February 2021

**Accepted:** 15 March 2021

**Published:** 08 April 2021

### Citation:

Shi K, Song A, Li Y, Li H, Chen D and  
Zhu L (2021) A Cable-Driven  
Three-DOF Wrist Rehabilitation  
Exoskeleton With Improved  
Performance.  
Front. Neurobot. 15:664062.  
doi: 10.3389/fnbot.2021.664062

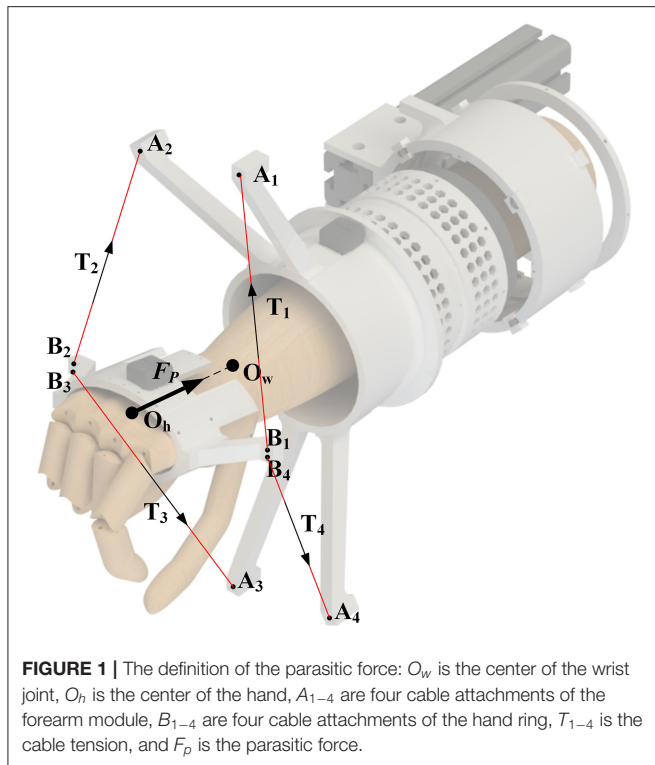
This paper developed a cable-driven three-degree-of-freedom (DOF) wrist rehabilitation exoskeleton actuated by the distributed active semi-active (DASA) system. Compared with the conventional cable-driven robots, the workspace of this robot is increased greatly by adding the rotating compensation mechanism and by optimizing the distribution of the cable attachment points. In the meanwhile, the efficiency of the cable tension is improved, and the parasitic force (the force acting on the joint along the limb) is reduced. Besides, in order to reduce the effects of compliant elements (e.g., cables or Bowden cables) between the actuators and output, and to improve the force bandwidth, we designed the DASA system composed of one geared DC motor and four magnetorheological (MR) clutches, which has low output inertia. A fast unbinding strategy is presented to ensure safety in abnormal conditions. A passive training algorithm and an assist-as-needed (AAN) algorithm were implemented to control the exoskeleton. Several experiments were conducted on both healthy and impaired subjects to test the performance and effectiveness of the proposed system for rehabilitation. The results show that the system can meet the needs of rehabilitation training for workspace and force-feedback, and provide efficient active and passive training.

**Keywords:** cable-driven robot, rehabilitation robot, mechanism design, distributed drive system, human-robot interaction

## INTRODUCTION

Many people suffer from movement disorders and reduced muscle strength, which are resulted in neural diseases (Stroke Center). They have difficulties in performing activities of daily living (ADLs). Studies have shown that rehabilitation training can promote brain damage or redundant nerves to re-learn and restore function (Bayona et al., 2005; Donatelli, 2012; Hatem et al., 2016). In recent years, researchers have developed a variety of different types of robots for post-stroke rehabilitation training. Many related clinical trials based on these robots have been carried out, and the results verified the effectiveness of robot-assisted rehabilitation (Reinkensmeyer et al., 2000; Lum et al., 2002; Kwakkel et al., 2008). The robot is very suitable for repetitive stroke rehabilitation training and has the advantages of high precision.

The flexible movement of the wrist is indispensable for daily life, especially some delicate movements like drinking and eating. The size of the wrist is much smaller than the shoulder and elbow joint. However, it still has a large workspace, including three DOFs of flexion/extension (FE), radial/ulnar deviation (RU), and pronation/supination (PS). In this paper, the forearm PS is considered as one DOF of the wrist. The required range of motion and torque range of ADLs



are shown in **Table 3** (Perry et al., 2007; Gupta et al., 2008). To meet the workspace and output force/torque requirements of rehabilitation training in a small space, some robots use a parallel mechanism to achieve weight reduction while maintaining structural rigidity (French et al., 2014; Bian et al., 2017). However, to avoid interference with the movement of the forearm, the workspace of the wrist robot is limited. Some robots use a series spherical mechanism to reduce interference with the arm, which increases the workspace and has sound effects, such as Pehlivan et al. (2014) and Buongiorno et al. (2018). But its structure is relatively complicated. In particular, wrist motion is not just a simple spherical joint motion, but with a certain wrist center shift (Schiele and van der Helm, 2006; Rijnveld and Krebs, 2007). Moreover, some errors are inevitable in the process of wearing the robot. These reasons may lead to misalignment between the center of the human joint and the robot joint during training, resulting in potential physical injury and low recovery training efficiency (Cempini et al., 2013). Existing robots often adapt to changes in the joint center through complex mechanisms, which increases the complexity of the mechanism to a certain extent and reduces stability (Omarkulov et al., 2016; Su et al., 2019). Also, for the rigid robots discussed above, the negative influence of the inertia on the force-feedback performance cannot be ignored, especially in PS.

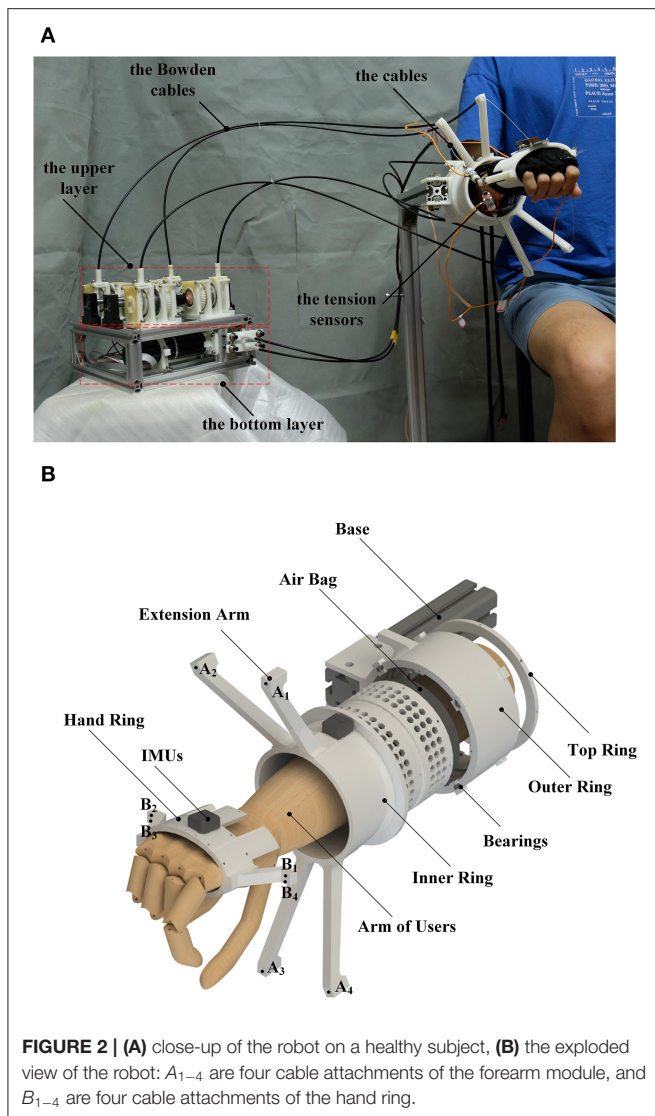
The cable-driven rehabilitation training robot has attracted extensive research due to its lightweight, simple structure, low inertia, high flexibility, and excellent adaptability. It should be noted that the cable-driven robot is divided into cable-transmitted like (Veneman et al., 2005; Alamdari and Krovi,

2015), cable-driven like (Mustafa et al., 2006; Mao and Agrawal, 2012), but only the cable-driven robot was discussed in this paper because the cable-transmitted robots are similar to the rigid exoskeletons, which have a rigid structure to interact with the users. Although many different cable-driven exoskeletons have been proposed (Mustafa et al., 2006; Chen et al., 2015; Cui et al., 2017), their performances are still not good enough to support flexible wrist rehabilitation. Because of the inherent characteristic that the cable only generates tension along its direction, existing cable-driven exoskeletons cannot efficiently match the wrist motion in any rehabilitation training. By analyzing the engineering requirements, we aim to improve the cable-driven design in terms of the following three points:

- Larger workspace. The sufficient joint movement range and DOFs are essential design criteria for the rehabilitation exoskeleton (Riener, 2007). Limited by cable-driven form, the workspace of typical cable-driven design is relatively small so that it cannot match the workspace of the complete ADLs training. Moreover, unlike rigid robots, cable-driven robots will be uncontrollable when it is out of the feasible workspace. This disadvantage causes potential danger, especially for patients with weak motor capacity, so the trajectory out of the feasible workspace must be avoided. The large workspace can ensure that the tension is always controllable.
- Higher cable tension efficiency. The inherent characteristics of the cable may exert a parasitic force on the limb. As shown in **Figure 1**, the parasitic force is the force generated by the robot along the limb, which is challenging to eliminate in existing cable-driven exoskeletons. The cable tension efficiency is defined as the magnitude of the torque acting on the wrist joint generated by the same tension. The greater the torque, the higher the tension efficiency. At the same time, the smaller parasitic force acting on the joint, the training is more comfortable.
- Higher bandwidth. The previous research has confirmed the importance of the force bandwidth to the rehabilitation robot (Manna and Dubey, 2018). However, because the application of traditional electromechanical actuators introduces high intrinsic inertia, the compliant element (cables or Bowden cables) between the actuators and the output component of the robot lowers the natural frequency of the system, thus limiting its dynamic performance (Viau et al., 2017).

Therefore, this paper proposed a cable-driven three-DOF wrist rehabilitation exoskeleton with optimized performance, the SEU-WRE. As shown in **Figure 2A**, the cable-driven system is adopted, and the overall structure is straightforward. The main structure is made of nylon material by 3D printing, and the weight except the driven system is 350 g (the grip portion is only 50 g). The inertia is pretty low in all three DOFs. To improve the first two disadvantages, the rotating compensation mechanism on the forearm module is designed, and the distribution of the cable attachments can be adaptively changed, optimizing the workspace of the cable-driven robot and the tension efficiency of the cable. The workspace meets the training requirements of ADLs completely, and the cable can generate sufficient torque





output during training within limited tension. At the same time, the parasitic force is reduced.

Routing the cables via the Bowden cable reduces the structural complexity and size worn by the users. For optimizing the force performance and reducing the influence of the elastic elements of the cable-drive system, the DASA system based on MRs is adopted. Viau et al. (2017) applied this kind of drive system on a cable-driven manipulator, and it exhibits excellent force-feedback performance. In this paper, the structure of this drive system is optimized for the rehabilitation exoskeleton to improve the force bandwidth and the tension control.

Regarding safety, the advantage of rigid robots is that their joints can be mechanically limited, but they usually have to be tightly fixed to the limb, which cannot unbind quickly in abnormal conditions. For SEU-WRE, two safety modes have been set up to improve safety. One is used for the protection during the training process when it exceeds the pre-set movement range, or the cable tension is abnormal. The other is used to achieve

fast unbinding, based on the DASA drive system with high back-drivability and the nature of the cable-driven system, which is difficult for rigid robots. The performance comparison of several typical robots is shown in **Table 1**.

Section System Concept introduces the structural design of SEU-WRE; section System Analysis and Optimization carries out the robot dynamics analysis, workspace optimization and tension efficiency analysis; section Control Algorithm presented the passive and active training algorithms to test the performance and effectiveness of the proposed system for rehabilitation; section Experiments and Analysis carries out the related experiments including one healthy and two impaired subjects, and analyzes the experimental results; finally, section Conclusion summarizes and discusses this paper.

## SYSTEM CONCEPT

### Mechanical Design of the Robot

The cable-driven robot is typical to use at least  $n+1$  up to  $2n$  cables to drive  $n$  DOFs, or to act as a cable by external forces such as gravity (Mustafa and Agrawal, 2012). Since the cable can only provide a pulling force in the direction of the cable, even if the redundant cables are used, the workspace of the robot is usually quite limited. In particular, when the cable pulls the limb to move, the relative position of each cable attachment changes, and the cable configuration changes, affecting the tension efficiency, further limiting its workspace and increasing the parasitic force. For instance, in FE and RU DOFs of the wrist joint, the cable attachment distribution can be optimized to satisfy the ADLs space as much as possible and provide enough torque applied to the wrist for rehabilitation. But no matter what kind of cable configuration, without prejudice to the compactness requirements of the overall structure, it is challenging to meet the motion space requirements for the forearm PS. In particular, when the cable-driven wrist robot drives the wrist to rotate in PS, the configuration of the cables changes, and the tension efficiency of the cable in this DOF gradually decreases until a singularity occurs and no torque is supplied. Moreover, for the PS, interference between the cables and between the cable and the limb is not easy to avoid, so how to deal with the PS movement is an essential problem for the three-DOF joint exoskeleton. Based on this consideration, this paper proposed a dynamic change strategy of the cable configuration, that is, by adding a rotating compensation mechanism, the inner and outer rings of the forearm module can be relatively rotated, and the fixed cable attachments can be dynamically adjusted according to the current wrist posture. Thereby the cable configuration can be changed in real-time, increasing the workspace and improving the cable tension efficiency.

As shown in **Figure 2B**, it is an exploded view of this robot without cables and Bowden cables. The outer ring is fixed with a bracket or any other upper limb rehabilitation robot, which can be combined with the wrist robot. And the inner ring can be driven by a cable wound on it to rotate relative to the outer ring. The inner side of the outer ring is provided with a plurality of miniature bearings for keeping the rotation of the inner ring stable. When the inner and outer rings rotate relative to each



**TABLE 1** | The performance comparison of several typical exoskeleton.

	Rigid parallel	Rigid serial	Existing cable-driven	SEU-WRE
Typical Example	MAHI EXO-II (French et al., 2014)	RiceWrist-S (Pehlivan et al., 2014)	CDWRR (Chen et al., 2015)	/
Workspace	Low	High	Low	High
Torque	Medium	High	Low	Medium
Inertia	Medium	Low	High	High
Joint alignment	Low	Medium	High	High
Force-feedback performance	Medium	Medium	Medium	High
Safety	Medium	Medium	Low	Medium

Rough comparison and classification are shown in the table. "Low" indicates poor performance, and "High" indicates relatively good performance. The force-feedback performance is determined by the inertia and drive performance (back-drivability and system friction, etc.). The safety analysis is presented in section Introduction and Safety Modes.

other, the cable attachments on the four extension arms of the inner ring also rotate at the same time to complete dynamic adaptation. The inner ring rotation is controlled by position-based mode and always follows the Z-axis rotation of the hand ring, so the cables configuration never changes due to the forearm PS movement. The four cables are respectively connected to the four cable attachments  $B_{1-4}$  on the hand ring through  $A_{1-4}$  on the four extension arms, generating different tensions, and the hand ring is controlled to drive the limb movement or provide the force-feedback. The relationship between the output of the MR clutch and the input current can be fitted. However, there is still the hysteresis of the MR and many other disturbances (e.g., the unmodeled friction of the Bowden cables) in the system that cannot be accurately predicted, so a tension sensor is added to each cable to establish the tension close-loop. Inside the inner ring, there is a non-slip silicone inside the airbag to assist the forearm to be located on the central axis of the inner ring as much as possible, and to provide certain axial friction during movement to reduce the axial displacement of the arm due to parasitic force. At the same time, the hand posture and the rotation angle of the inner rings are collected by two inertial measurement units (IMU). The robot forearm module is connected to the hand ring through four cables, and there is no rigid connecting device. For the rotating compensation mechanism, although the connection between the inner ring and the outer ring is rigid, and the position control is adopted, the PS rotation is controlled directly by four cables. So three DOFs of the wrist are still driven by the flexible cable. This is crucial because the flexibility of the cable, the inertia of PS and the human-robot interaction through the tension control play an important role in the safety and comfort of rehabilitation training. Moreover, the force-feedback bandwidth generated by this motor is far from satisfactory. Only by directly applying the force to the wrist through the cable can the better dynamic performance be ensured. The motor-driven rotating compensation mechanism is only used to ensure sufficient speed tracking, adapt to the hand posture so that the cable configuration can be adjusted in real-time to meet the requirement of cable-driven strategy.

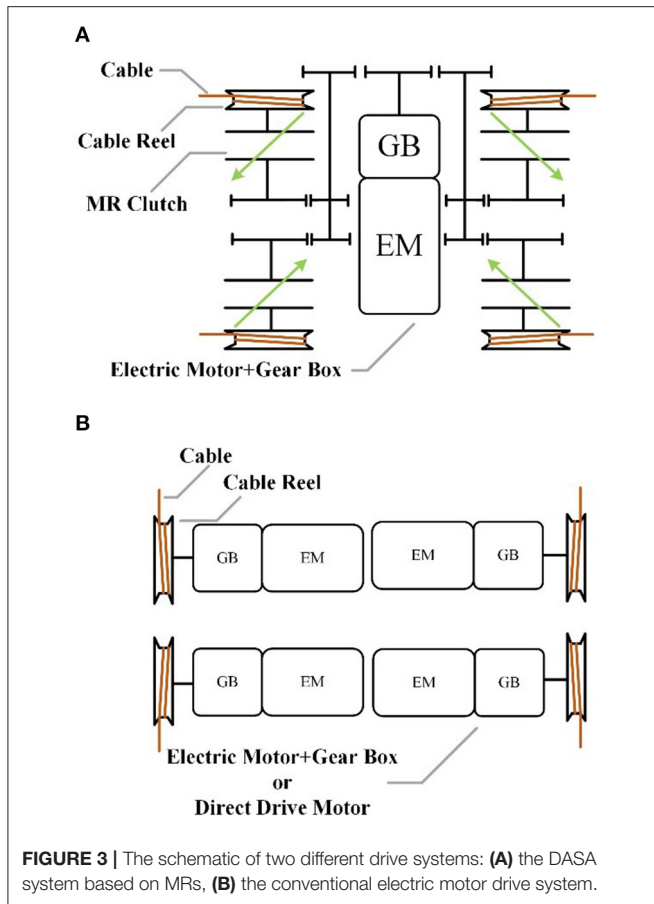
The structure is simple and easy to wear. Before training, if the patient's ability is poor, the forearm module can be taken off the base and put on the arm, and the inner diameter is large enough

to pass through easily. The hand only needs to wear the hand ring, and the tension cables will firmly fix it on the hand.

## MR-DASA Drive System

As mentioned in section Introduction, cable-driven robots have many advantages. However, much like SEA (series elastic actuator), the compliant elements between the actuators having high inherent inertia and the output lowers the natural frequency of the system, the dynamic performance is limited. Compared to the conventional motor, the use of an MR clutch can weaken this effect, since its low output inertia. Therefore, the MR is used for this cable-driven robot, which can improve the force-feedback performance and is very suitable for human-robot interaction, including the rehabilitation robot (Viau et al., 2017). MR is a passive clutch that only provides damping and cannot provide active output. Therefore, the DASA system is utilized to actuate the cable-driven robot, and the geared DC motor with high power-density is used as the power source of the DASA system, which is shown in **Figure 3A**. The conventional electric drive system is shown in **Figure 3B**, the direct-drive or geared motor are usually used as the tension generators, which has poor dynamic performance due to the high output inertia.

As shown in **Figure 4**, the lower layer includes the actuator system for the rotating compensation mechanism, composed of the Z-axis motor (MAXON RE40) and the tensioning module. After transmission through the cables, the maximum speed of the rotating compensation mechanism is 80 rpm. The other side of the lower layer is composed of the main power module (24V/60W), data acquisition card (NI6060), and switching circuit. The control program of this system runs on the PC. The upper layer is the DASA system, including the power motor and four MR-Cable units, which are placed in parallel. When the system works, the power source motor keeps rotating to drive MRs to rotate in slippage. The MR distributes the mechanical power provided by the motor and generates the required torque to the cable reel. The MR clutch pulls the cable through the cable reel, and the cables drive the hand ring and the outer ring through the Bowden cable. When in slippage, the MR clutch decouples the dynamic behavior of the power source motor from the output, resulting in actuators with high force resolution as actuator has low reflected inertia and negligible non-linear effects. The MR



clutch is made in our laboratory. The performance of the MR clutch and the DC motor is shown in **Table 2**.

## SYSTEM ANALYSIS AND OPTIMIZATION

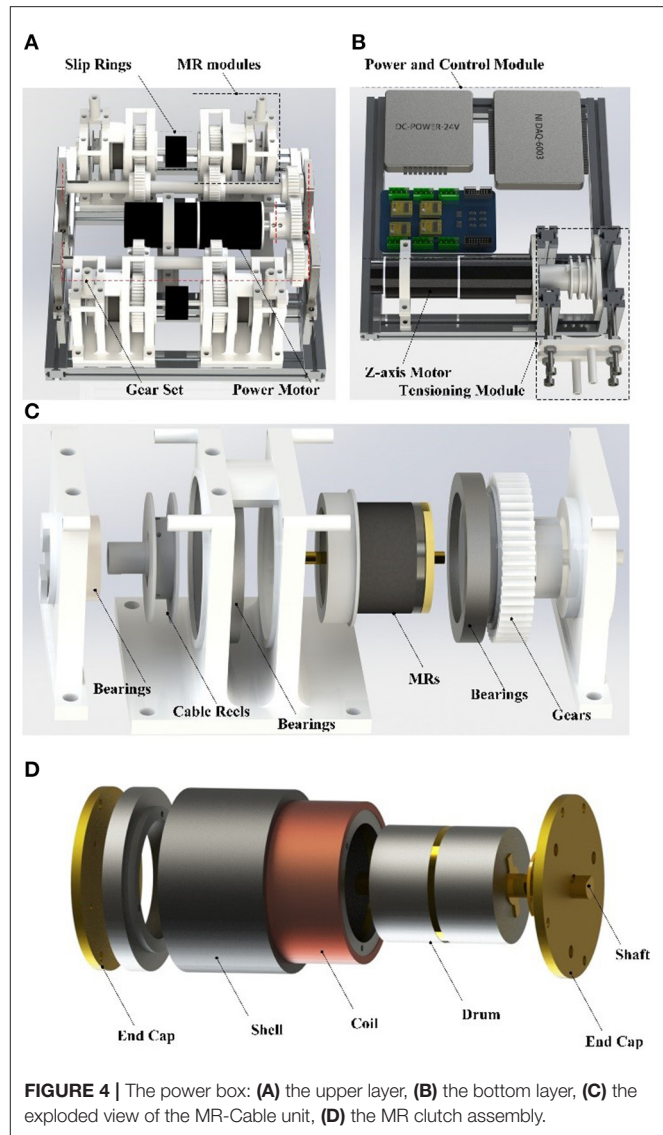
### System Dynamics Analysis

The dynamic equations of motion for this wrist exoskeleton are derived using the Lagrangian method. The generalized coordinates  $q_1$ ,  $q_2$ , and  $q_3$  represent wrist FE, RU, and PS, respectively. The dynamic modeling for this three-DOF robot is presented as follows:

$$D(q)\ddot{q} + C(q, \dot{q})\dot{q} + g(q) = J(q)^T T(t) \quad (1)$$

where  $D$  denotes the inertia matrix,  $C$  denotes Coriolis and centrifugal term, and  $G$  denotes the gravity term of both device and the human limb,  $q$  represents the joint angle, and  $J(q)$  is the Jacobian matrix relating cable tensions to joint moments, and  $T(t)$  is the vector of cable tensions. Due to the characteristic of cables, the tension must be kept for system control. The cable tension planner has been proposed in many related researches. Usually, the tension planner can be expressed as:

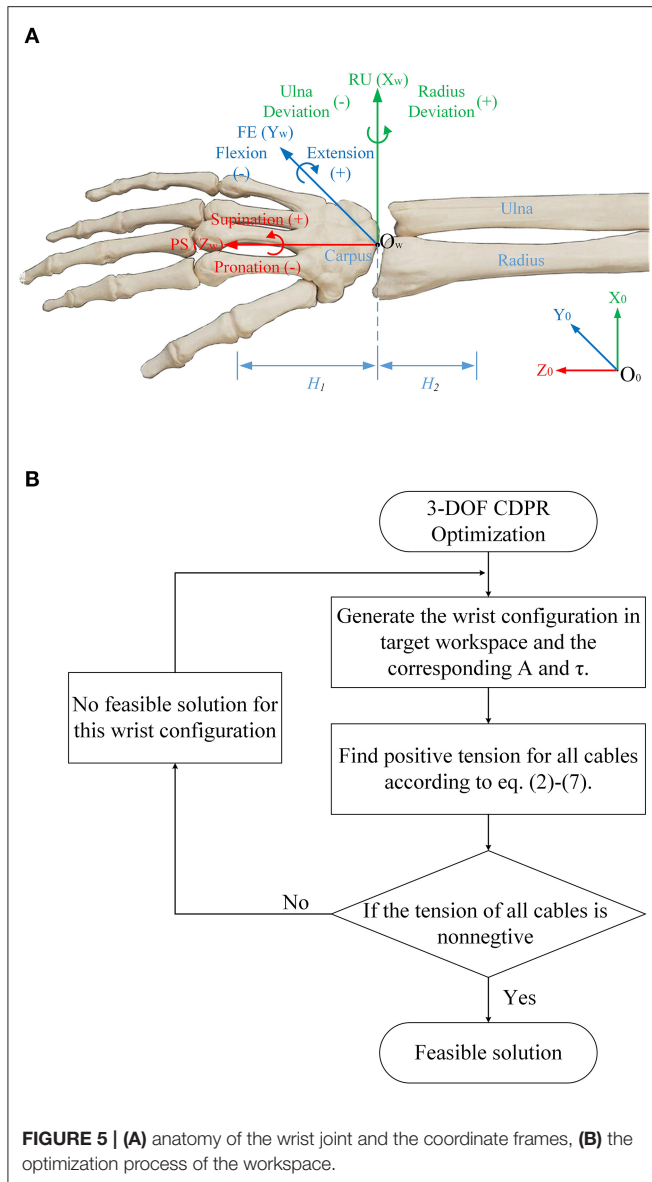
$$AT = \tau \quad (2)$$



**TABLE 2 |** Performance of the drive system.

Parameter	Value
MR maximal torque	1.2 nm
MR maximal current	1 A
MR outer diameter	42 mm
MR Width	38 mm
Power motor max speed	700 rpm
Power motor max torque	4 Nm
Z-axis motor max speed	180 rpm
Z-axis motor max power	48 W

where  $A = J(q)^T$  in (1),  $\tau$  is the torque that is required at the joints to drive the arm. Because the number of cables is more than the number of DOFs, the solution of (2) can be written as:



**FIGURE 5 | (A)** anatomy of the wrist joint and the coordinate frames, **(B)** the optimization process of the workspace.

$$T = \bar{T} + N(A)m \quad (3)$$

where  $\bar{T} = [t_1; t_2; t_3; t_4]$  is the minimum norm solution of (2) which is given by:

$$\bar{T} = A^T(AA^T)^{-1}\tau \quad (4)$$

$N(A) = [n_1; n_2; n_3; n_4]$  is a null space matrix of  $A$  and  $m$  is an arbitrary value, assuming  $A$  is full rank. Considering constraints of the tension, the planner can be expressed as:

$$\begin{bmatrix} N(A) \\ -N(A) \end{bmatrix} m \geq \begin{bmatrix} T_{\min} - \bar{T} \\ -T_{\max} + \bar{T} \end{bmatrix} \quad (5)$$

Finally, the optimal solution of cable tensions can be found as the following:

$$\begin{aligned} \min \sum_{i=1}^4 (t_i + n_i m) \\ \text{s.t. } T_{\min} \leq \bar{T} + N(A)m \leq T_{\max} \end{aligned} \quad (6)$$

$T_{\max}$  is the upper bound of tension, which is set as 42N in this paper, and  $T_{\min}$  is the lower bound, which is 1.5N.

To calculate the cable tension efficiency and solve the cable tension in unknown conditions for robot control, maximum torque in assigned direction within the limitation of cable tension can be given by (6), that is, in the cable tension range, if there is no solution for the given torque, the maximum torque that can be generated in the same direction is generated.

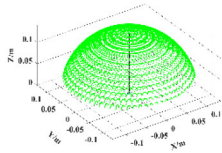
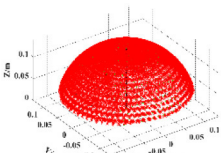
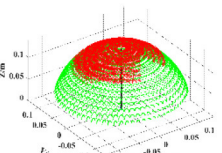
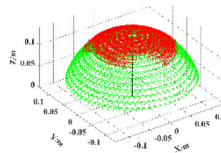
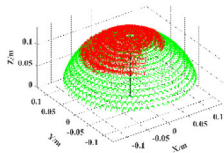
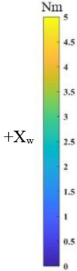
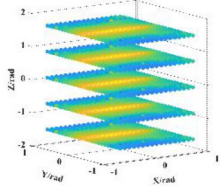
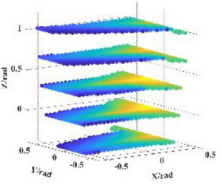
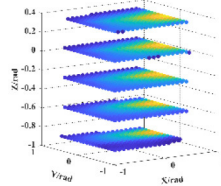
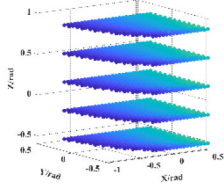
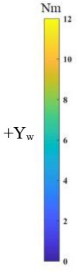
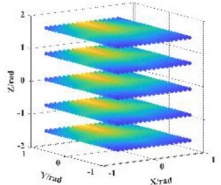
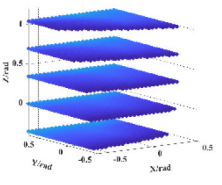
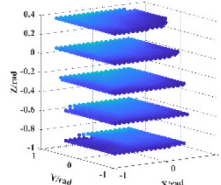
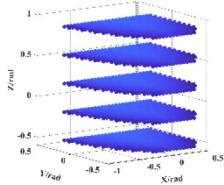
$$\begin{aligned} \begin{bmatrix} N(A) \\ -N(A) \end{bmatrix} m_2 \geq \begin{bmatrix} T_{\min} \\ -T_{\max} \end{bmatrix} + \begin{bmatrix} -\bar{T} \\ \bar{T} \end{bmatrix} m_1 \\ \max \sum_{i=1}^4 t_i \\ \text{s.t. } T_{\min} \leq \bar{T}m_1 + N(A)m_2 \leq T_{\max} \end{aligned} \quad (7)$$

## Workspace Optimization and Analysis

Research on the cable-driven exoskeleton robot shows that the distribution of the cable attachments, the diameter of each component, and the angle of inclination of the fixed brackets have a significant impact on the workspace (Mustafa et al., 2006; Mustafa and Agrawal, 2012; Shao et al., 2014). Regarding the optimization of the distribution of the cable attachments, many researchers have done related research, including particle swarm algorithms (Bryson et al., 2016), which are used to explore the optimal solution. Cable-driven robot workspace optimization is a complex problem with many variables. Therefore, to simplify the optimization process, some parameter ranges are usually constrained. **Figure 5A** shows the anatomy of the wrist joint and the coordinate frames. Considering the actual situation, the following constraints are imposed:

- 1) When optimizing the workspace, we neglect PS and the wrist joint is regarded as a spherical joint. The range of human joint is show in **Table 3**. Considering the approximate symmetry of its motion, we assume that the forearm cable attachment plane is perpendicular to the forearm;
- 2) The diameter of each component of the wrist rehabilitation training robot also has a significant influence on the optimization, mainly  $R_1$  (the radius of the hand ring) and  $R_2$  (the radius of the inner ring extension arm). Through the preliminary the study of Shao et al. (2014), the excessive  $R_1/R_2$  value, will lead to lower tension efficiency, that is, increased parasitic force. In order to ensure that the cable does not interfere with the hand during the movement, the  $R_1$  value is 38 mm, to avoid the interference between the trunk and the inner ring, to ensure compact, the  $R_2$  value is 75 mm, and the cable attachments are distributed on the ring;

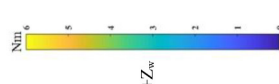
**TABLE 3 |** The workspace and tension efficiency comparison of four cable-driven robot.

Workspace											
	Human	SEU-WRE	CDWRR	NTU	CAREX-7						
Orientation workspace											
X <sub>W</sub>	Max [−33, +19]	ADLs [−33, +19]	[−40, +40]	[−35, +19]	[−40, +40]						
Y <sub>W</sub>	Max [−73, +71]	ADLs [−60, +54]	[−75, +75]	[−38, +38]	[−35, +40]						
Z <sub>W</sub>	Max [−86, +71]	ADLs [−85, +70]	[−90, +90]	[−18, +60]	[−50, +20]						
Tension efficiency in the joint angle range of ADLs											
	Human	SEU-WRE	CDWRR	NTU	CAREX-7						
+X <sub>w</sub>											
	X(°)	X+/(Nm)	Y(°)	Y+/(Nm)	Z(°)	Z+/(Nm)					
	35	5.2/4	−70	3.9/3.9	−90	6.2/4.4					
	20	5.6/4.4	−35	5.2/4.5	−45	6.1/4.8					
	0	5.7/4.7	0	6.2/4.7	0	6/5.1					
	15	5.3/4.6	35	6.3/4.7	45	6.2/4.7					
25	4.9/4.5	70	4.5/4.5	90	6.5/4.2						
	ADLs: 0.35Nm	Avg = 2.9408	Avg-A = 3.0247	Avg = 2.8226	Avg-B = 3.5331	Avg = 1.7285	Avg-N = 3.4142	Avg = 1.3775	Avg-C = 3.5043		
	Max: 19.8Nm	Max = 4.9538	Max-A = 4.9538	Max = 7.1970	Max-B = 4.9538	Max = 4.8606	Max-N = 4.9538	Max = 2.9111	Max-C = 4.9538		
		Min = 1.4020	Min-A = 1.5689	Min = 0.0148	Min-B = 1.8204	Min = 0.0035	Min-N = 2.4569	Min = 0.0024	Min-C = 2.8804		
+Y <sub>w</sub>											
	X(°)	Y+/(Nm)	Y(°)	Y+/(Nm)	Z(°)	Z+/(Nm)					
	−35	8.3/5	−70	6.8/3.4	−90	10.2/5.5					
	−20	8.7/5.1	−35	7.5/5.4	−45	10/5.8					
	0	9/5.2	0	9/5.9	0	9.5/6.3					
	15	8.6/5.1	35	11.4/5	45	9/6.4					
25	8.2/5	70	7/4.1	90	8.5/5.9						
	ADLs: 0.35Nm	Avg = 5.7219	Avg-A = 6.5226	Avg = 1.8461	Avg-B = 6.7920	Avg = 2.3310	Avg-N = 6.5510	Avg = 1.4961	Avg-C = 6.4604		
	Max: 20.8Nm	Max = 11.4369	Max-A = 11.4369	Max = 4.5151	Max-B = 10.5180	Max = 6.3025	Max-N = 10.6207	Max = 2.6033	Max-C = 10.0733		
		Min = 1.2776	Min-A = 1.8204	Min = 0.0043	Min-B = 3.0704	Min = 0.0011	Min-N = 3.2893	Min = 0.0049	Min-C = 2.6518		

(Continued)



TABLE 3 | Continued

Tension efficiency in the joint angle range of ADLs						
Human		SEU-WRE	CDWRR	NTU	CAREX-7	
	<b>Z(°)</b>					
	-60	15.3/11.8				
	-24	14.9/11.6				
	0	14.8/12.6				
	24	12.7/11.7				
60	10.7/11.4					
ADLs: 0.06Nm		Avg = 3.7551	Avg-A = 3.5543	Avg-B = 3.8317	Avg-N = 4.0220	
		Max = 5.9374	Max-A = 5.1836	Max = 3.0191	Max = 2.5223	
		Min = 2.4284	Min-A = 2.4284	Min = 0.0089	Min = 0.0018	

X-A/B/C represents the torque generated by SEU-WRE/NTU/CDWRR in ADLs, and X represents Avg/Max/Min. The human data refer to Gupta et al. (2008), Perry et al. (2007), and La Delfa and Potvin (2017).

- 3) The rotating compensation mechanism is adopted, so that the distribution of the cable attachments can be dynamically changed. Hence, it is not necessary to set the PS movement range as  $\pm 90^\circ$  in the calculation. The motor that drives the rotating compensation mechanism can quickly respond to the movement of the wrist PS and compensate the rotating angle. So the PS range is set in  $\pm 20^\circ$  as an optimization condition to cope with the motor response delay;
- 4) During the optimization process, point  $A_{1-4}$  is calculated by  $2.5^\circ$  step along the radius of 75 mm, and point  $B_{1-4}$  is calculated by  $2.5^\circ$  step along the radius of 38 mm. Each point is constrained to a certain range to avoid repeated combinations;
- 5) Regarding the wearing error and individual differences, the  $H_2$  length (the wrist joint center to the forearm cable attachment plane) and the  $H_1$  length (the wrist joint center to the hand ring cable attachment plane) are set as  $1 \pm 1$  cm and  $14 \pm 2$  cm, respectively. It allows the error within the range to be generated while training and still can ensure that the workspace is effective.

The optimization process is shown in **Figure 5B**. Finally, 128 sets of feasible solutions can be obtained after optimization, and the final cable attachment distribution will be selected according to the cable tension efficiency introduced in the next section.

As shown in **Table 3**, the top part is a comparison of the workspace of four cable-driven robots, which are SEU-WRE, CDWRR (Chen et al., 2015), NTU (Mustafa et al., 2006), and CAREX-7 (Cui et al., 2017). The hand is approximately equivalent to a 14-cm-long rod. One end is fixed at the center of the wrist joint, and the three-DOF rotation axis coincides with the rotation axis of the wrist joint. When calculating, the spatial position of the other end of the rod corresponding to the feasible joint angle is printed as a visual display of the feasible workspace. The red point is the feasible workspace for each robot, and the green point is the human joint workspace for the corresponding. It can be seen that SEU-WRE can completely cover the human wrist joint workspace. In contrast, the other three robots have a great gap in the workspace and the human joint space, and there is also a certain gap with the ADLs space. Insufficient workspace makes it necessary to pre-calculate the trajectory during the rehabilitation training. Otherwise, it will cause unpredictable errors and danger in the movement beyond the workspace.

## Tension Efficiency Analysis

In this paper, the cable tension efficiency is defined as the magnitude of the torque acting on the wrist generated by the same tension conditions. The greater the torque, the higher the tension efficiency. At the same time, the smaller the parasitic force acting on the joint, the higher the comfort of training. The workspace priority strategy is adopted. Under the premise of satisfying the workspace of the human joint, the tension efficiency of each cable attachment distribution is analyzed, and the set with the highest tension efficiency is selected as the final solution.

As shown in the bottom part of **Table 3**, the tension efficiency analysis is performed for each robot. CDWRR, NTU, and SEU-WRE are independent wrist rehabilitation robots or upper-limb



robots with detachable design. The wrist joints can be analyzed independently. But, the cables are routed from the proximal cuffs to the distal cuffs in CAREX. It is difficult to analyze directly, so the wrist structure of CAREX is equivalent to an independent structure, and the tension efficiency analysis is performed.

Based on the maximum torque in the assigned direction algorithm, as expressed in (7), the maximum joint torque that can be generated in the workspace is analyzed. **Table 3** lists the torque in the positive direction of three DOFs to compare cable tension efficiency. For the column of human joint torque, the research shows that the joint torque is different under different joint angles (La Delfa and Potvin, 2017; Su et al., 2019). Therefore, the wrist joint torque of several discrete joint angles is selected as the human joint value. Among them, the torque of FE and RU is affected by the angle of three DOFs, and the PS joint moment is only affected by the PS angle. Moreover, studies have shown that there is a big difference between the daily joint torque and the maximum joint torque of the human body. This is a concern when developing the force-feedback function of the wrist joint robot (mainly for healthy people), that is, the force-feedback needs to have a broad range of stiffness variation. In SEU-WRE, CDWRR, NTU, and CAREX-7 columns, the maximum positive torque of each DOF is shown when the cable tension is limited to a specific range. To ensure the consistency of the comparison, the minimum tension of each robot is limited at 5 N. But the maximum depends on the number of cables, that is, the maximum cable tension of the 4-cable-driven robots is 45 N, and the 6-cable-driven robots is 30 N. **Table 3** shows the maximum, minimum, and average joint torque output of the four robots in their workspace, and the joint torque output of the SEU-WRE in the human ADLs, CDWRR, NTU, CAREX workspace to ensure the comprehensiveness of the comparison. In the visual processing of the joint torque, for the clear display, five Z-axis joint angle values are selected, and 100 X/Y-axis joint angle values are chosen in the range. But in the actual numerical calculation, 500 values of each joint are chosen to ensure the accuracy of the calculation. As can be seen from **Table 3**, SEU-WRE has a significant advantage in the generation of any joint torque, that is, it has exceptionally high cable tension efficiency, which means that the parasitic force generated during the rehabilitation process is smaller and the training is more comfortable and safe. The maximum torque generated is still different from the maximum output of the human joint torque, because the cable tension necessarily needs to be limited based on safety and comfort.

It is not difficult to find that SEU-WRE has significant advantages in both aspects. It is due to that the rotating compensation mechanism is used, dynamically changing the cable attachments distribution and greatly increasing the workspace and tension efficiency. This is very important for rehabilitation training.

## CONTROL ALGORITHM

### MR-Cable Tension Control Algorithm

The system uses the Bowden cable as a transmission to reduce overly complex cable routing. Many studies on the Bowden cable

transmission have shown that the Bowden cable inner sleeve and the passing cable can cause friction, including coulomb friction, viscous friction stiction, and stick-slip (Letier et al., 2006; Palli and Melchiorri, 2006). In order to reduce the influence of friction, according to the previous research, this paper chooses a 1\*7 multi-strand steel cable with a diameter of 1 mm. Both the cable shell and the Bowden cable inner sleeve are made of PTFE material to minimize the viscous friction. The Bowden cable inner sleeve is selected from the longitudinal construction of flat-band steel to reduce the effect of its elasticity on the system. The diameter of the Bowden cable is 5 mm.

Even if the above material is used, the stiction can be eliminated, but Coulomb friction still exists. According to the model proposed in (Palli and Melchiorri, 2006), the feedforward compensation of the friction is achieved. Although the current-to-torque relationship of the MR clutches can be fitted by the model, when the cable tension control is performed, the open-loop control is not directly adopted, but the cable tension sensor is used. A closed-loop tension control model was established to compensate for the effects of the unmodeled friction and the MR hysteresis. The control block diagram is shown in **Figure 6**, in which the reel velocity is used to distinguish the direction of the friction force. Through experimental measurement, even if the dynamic adaptive structure rotates between  $\pm 90^\circ$ , the Bowden cable friction efficiency does not change significantly, so the friction coefficient  $\mu$  is set as a constant.

### Passive and Active Training Algorithm

The passive training can help patients to move their weak limb in the desired trajectory, which incorporates the stretching of muscles and connective tissues to regain their movement ability by provoking the motor plasticity (Alamdari and Krovi, 2015). The existing cable-driven exoskeleton robots do not mention related training methods. In this paper, the projected PID control algorithm proposed in the literature (Viau et al., 2015) is used to design a mirror training algorithm that can be applied in the three-DOF rehabilitation training robot. In order to perform the force control with friction compensation and enhance safety in rehabilitation training, the open-loop tension control in this algorithm is replaced with the closed-loop control described in section MR-Cable Tension Control Algorithm. Although the force control bandwidth will be reduced, it fully meets the needs of rehabilitation training. The experiment shown in section MR Performance Experiment confirmed this.

The active training is an important part of the rehabilitation training process, including resistive training and assistive training (Proietti et al., 2016). Through the set training strategy, the patient is assisted by the robot to complete the training and strengthen the motor function. The AAN algorithm is used on this robot to verify its active training function:

$$\mathbf{r} = \dot{\mathbf{q}} - \dot{\mathbf{q}}^d + \Lambda(\mathbf{q} - \mathbf{q}^d) \quad (8)$$

where  $\Lambda$  is a positive-definite matrix that determines the weight of position errors relative to velocity errors. Because the weight of the hand ring is only 50 g, the inertia and Coriolis terms are

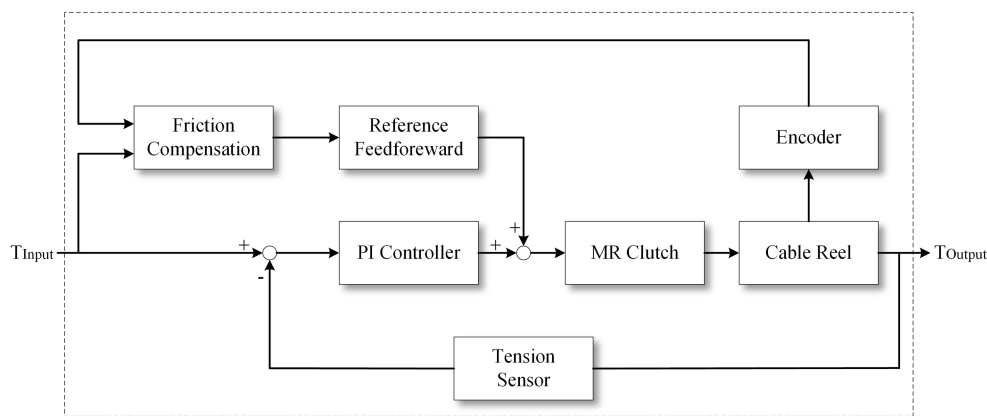


FIGURE 6 | The MR-Cable tension control block diagram.

ignored. The controller can then be written:

$$\tau_r = g(q) - K_D \dot{r} \quad (9)$$

where  $K_D$  is a positive-definite gain matrix. The controller functions as a PD controller, where  $K_D$  and  $K_D \Delta$  serve as the derivative and proportional gains, respectively.

In order to provide appropriate challenges to the subjects and strengthen the rehabilitation training,  $K_D$  is updated according to  $r$ , which represents the patient's performance.

$$K_{D,i+1} = (1 + \alpha_i) K_{D,i} \quad (10)$$

$$\alpha_{i+1} = \alpha_{norm} \frac{\bar{r}_i - r^*}{r^*} \quad (11)$$

$\alpha_{norm}$  is a constant nominal change rate,  $\bar{r}_i$  is the current task's error, and  $r^*$  is the maximum allowable average trajectory error. If  $\bar{r}_i$  is bigger than  $r^*$ , the algorithm dictates that the subject cannot provide enough error performance, and hence, the feedback gain increases for the next task.

## Safety Modes

Safety is an essential requirement in rehabilitation training. As shown in Figure 7, there are three work modes of SEU-WRE to avoid injury when abnormal conditions occur:

1. Normal Work Mode: The tension of each cable can be controlled, and the required torque is provided according to the rehabilitation training algorithm.
2. Safe Mode I: When the patient exceeds the set training area or the interaction force is abnormal, the MRs of the DASA system can be powered off by software or hardware switches, and the rotation speed of the power motor is reduced. At this time, although the power motor continues to rotate, because the MRs have no current input, the tension is the minimal value which is generated by the inherent damping of the MRs. The measured minimum tension is about 1.2 N. When the condition becomes normal, the robot can return to Normal Work Mode directly.

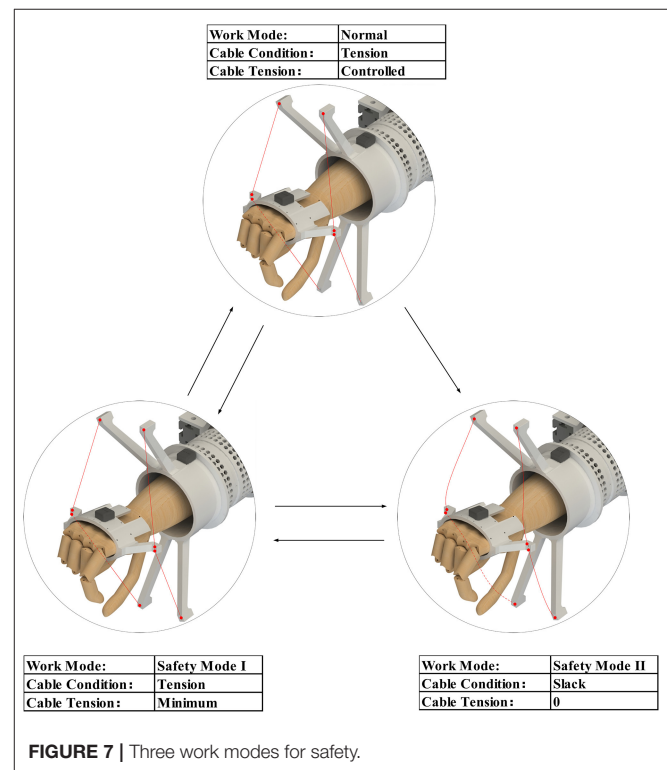


FIGURE 7 | Three work modes for safety.

3. Safety Mode II: When an emergency situation occurs, and the training needs to be stopped, the whole DASA system can be powered off through the emergency switch. At this time, the power motor stops rotating, the cable will not be tensioned any more, and can be pulled arbitrarily. At this time, the patient does not interact with the robot, and the hand ring can also be quickly taken off, avoiding the potential damage caused by the robot system friction and inertia.

Safety Mode II is similar to the wearing state before starting training, and it can be switched to Safety Mode I, then to Normal

Work Mode. Both Safe Mode I and Normal Work Mode can be directly switched to Safe Mode II. These safety work modes, especially Safety Mode II are difficult to be achieved in the rigid robots, even the OpenWrist, which is convenient to wear (Pezent et al., 2017).

## EXPERIMENTS AND ANALYSIS

### MR Performance Experiment

To demonstrate the performance of the MR clutches and MR-Cable system, the following sets of experiments were carried out. The MR performance test platform is shown in **Figure 8A**. The motor drives the MR clutch to rotate by the coupling, and the force gauge at the end of the linkage measures and records the output of MR with a given current or step signal input. The MR-Cable system test platform is presented in **Figure 8B**, the end of one cable is connected to the fixed base and the tension is measured and recorded by the tension sensor.

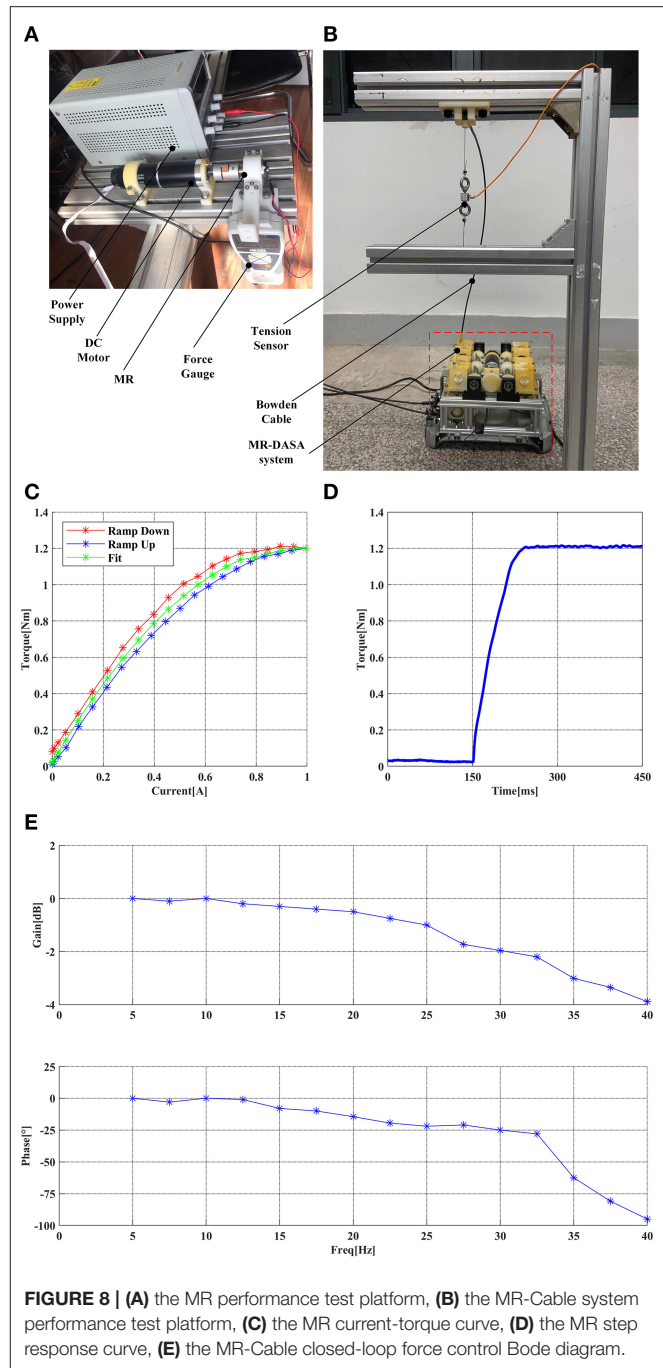
**Figure 8C** shows the MR current-torque curve. It can be seen that there is a certain hysteresis between the ramp up and down. In this paper, a second-order polynomial function was used to fit the current-to-torque relationship, and only 50% of its maximum output was used to provide sufficient tension in the DASA system. **Figure 8D** shows the MR step response curve. It can be seen that the MR clutch has a high step response speed. Combined with the low output inertia of the MR clutch, the MR-Cable system has a high dynamic performance.

As shown in **Figure 8E**, for the MR-Cable closed-loop force control Bode diagram, the input was a sinusoidal signal with amplitude  $30\text{ N}$ , the frequency growth step is  $2.5\text{ Hz}$ , the gain and phase of each point were recorded. To explore the effect of different bending conditions on the force-feedback bandwidth, the robot system was placed in the normal work state, and the *Cable-1* ( $A_1-B_1$ ) was selected as the test sample (the remaining three cables have the same characteristics). The Z-axis was kept at  $0^\circ$ . The bandwidth of this system is about  $35\text{ Hz}$  at  $-3\text{ dB}$  and is fully superior to the human force bandwidth that is between  $5$  and  $10\text{ Hz}$  (Shimoga, 1992).

### Passive Training Experiment

Because the patient has limited ability in speed and range of movement, in order to fully verify the passive training functions, including tracking speed, accuracy, workspace, and parasitic force, one healthy subject S1 (26 years old, male) was selected to participate in the experiment. The subject wore the motion capture glove in the left hand and the wrist rehabilitation robot in the right hand. The right hand was in a relaxed state as the affected hand and provided some impedance, simulating the patient's muscle stiffness. The subject's left hand moved at a comfortable speed within the maximum reachable range as much as possible. The right hand followed the left hand movement driven by the exoskeleton. The joint angles were recorded, and the equivalent end position error of the  $14\text{ cm}$  rod was also calculated. The simultaneous angle tracking performance of all three DOF and position error is shown in **Figure 9**.

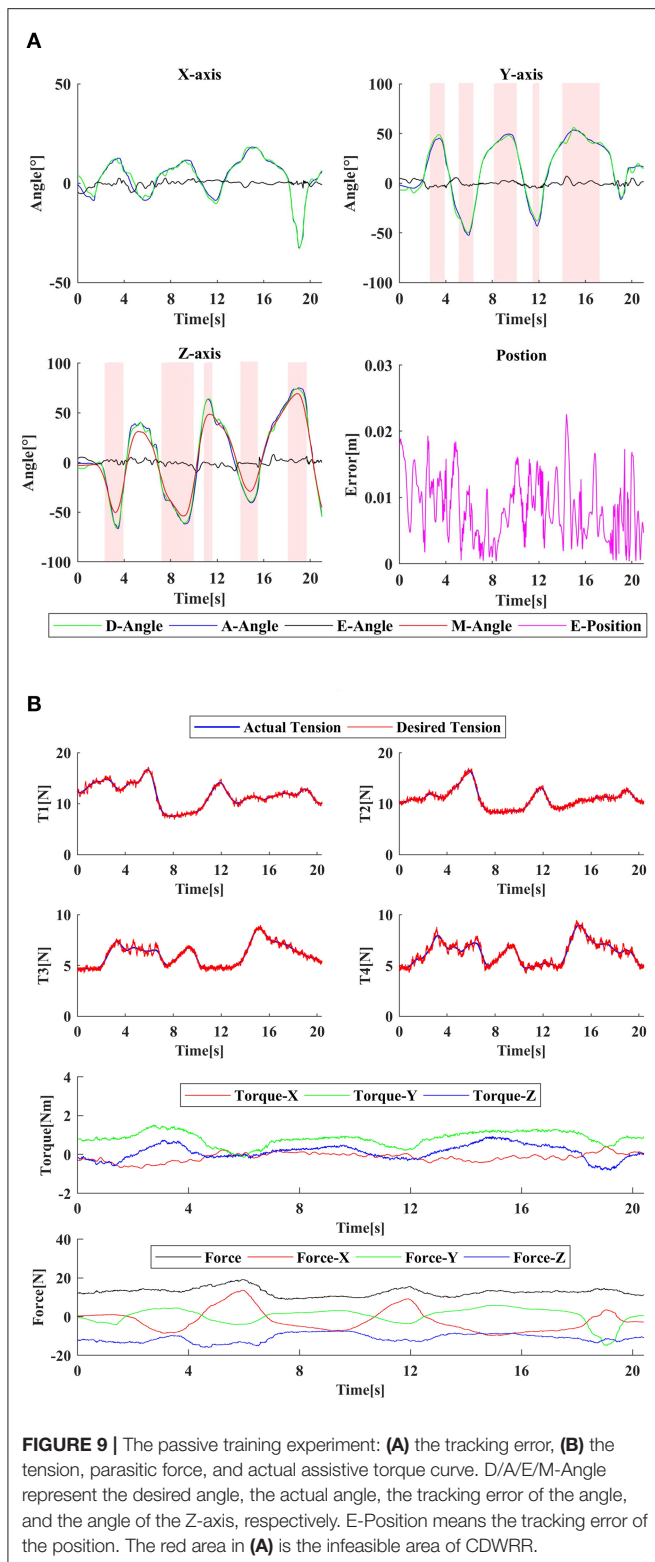
It can be seen that the right hand can follow the left hand well, even if there was impedance interference. The Z-axis



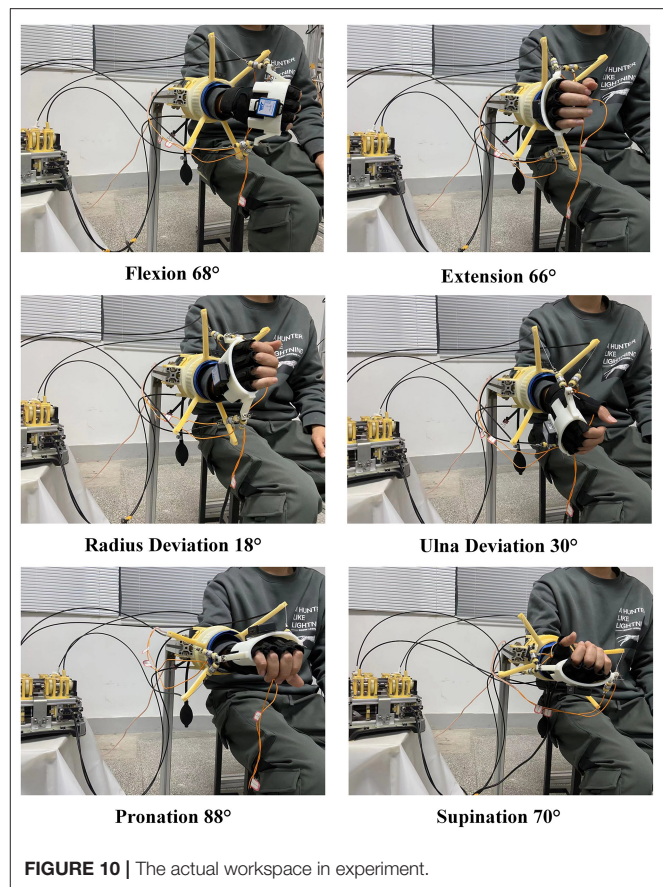
**FIGURE 8 | (A)** the MR performance test platform, **(B)** the MR-Cable system performance test platform, **(C)** the MR current-torque curve, **(D)** the MR step response curve, **(E)** the MR-Cable closed-loop force control Bode diagram.

curve (M-Angle) demonstrates that the adaptive structure can follow the hand movement well, to change the cable attachment distribution in real-time and ensure cable tension. The passive training control algorithm can be implemented well. The cable tension curve and the parasitic force curve during the training were also recorded. It can be seen that for passive training, the required cable tension was small, and the parasitic force did not exceed  $20\text{ N}$ , which can fully meet the safety and comfort training requirements. During the experiment, the cable





tension controller performs well. But due to the characteristics of the MR and the friction characteristics of the Bowden cable, the actual cable tension curve had a certain continuous small

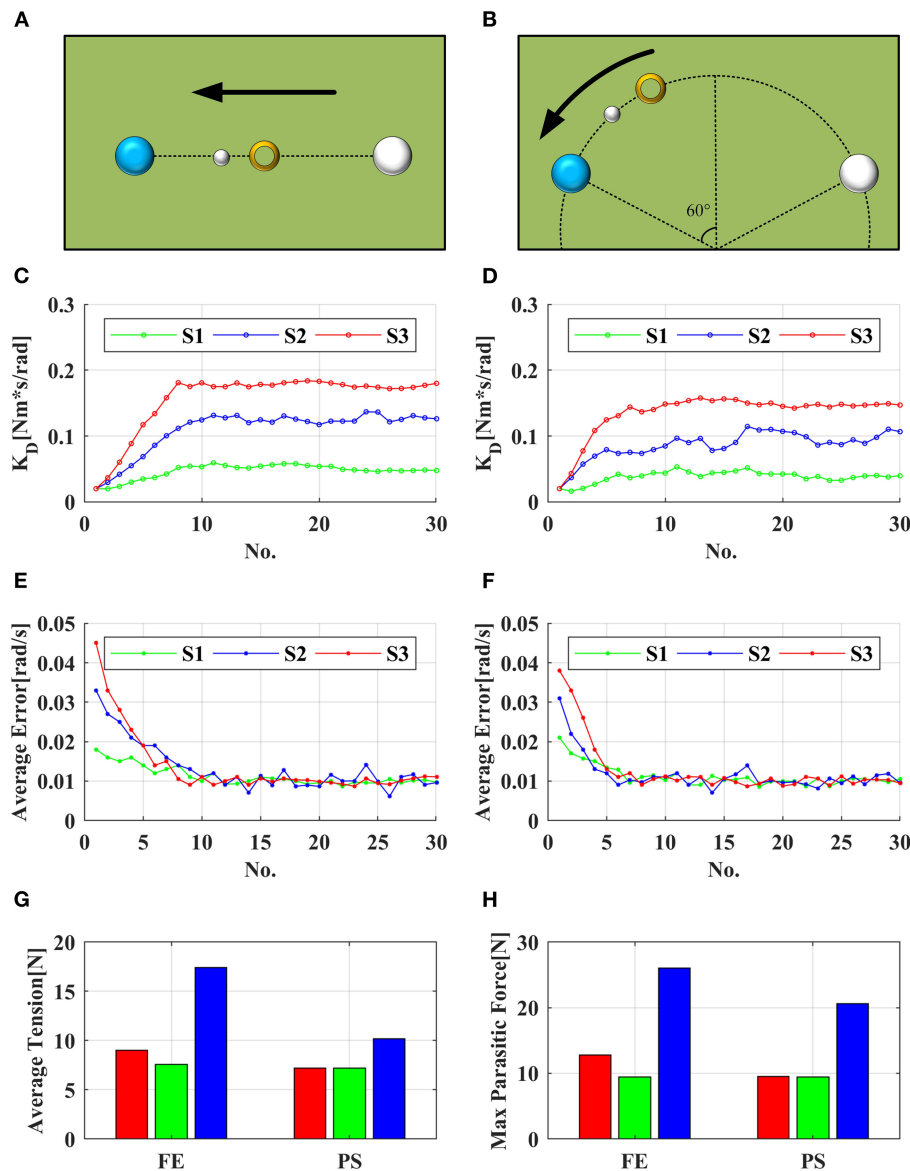


jitter with the amplitude  $\pm 0.4$  N, but did not affect tracking of tension command. In the meanwhile, CDWRR with the highest performance of the existing cable-driven robots was selected for workspace comparison. It can be seen that CDWRR cannot cover the normal wrist joint space, which will have a limitation on the setting of clinical rehabilitation tasks.

In passive training mode, the subject S1 was driven by the robot and the reachable range is demonstrated in **Figure 10**. The actual workspace is similar to the simulated results.

## Active Training Experiment

A healthy subject S1 (26 years old, male) and two stroke patients S2 (45 years old, male, Fugl-Meyer Arm score = 52) and S3 (51 years old, male, Fugl-Meyer Arm score = 20) participated in the experiment to verify the performance of the active training. In the experiment, the subject wore the robot on the affected side, and performed FE ( $-50^\circ \sim +50^\circ$ ) movement for the first experiment and PS ( $-60^\circ \sim +60^\circ$ ) movement for the second experiment according to the visual indication of the display. As shown in **Figures 11A,B**, the blue circle is the target, the small white circle is the guide cursor, and the yellow ring is the current position. When one DOF training was performed, the feedback gain  $K_D$  of the other two DOFs was set high ( $0.5$   $Nm^*/s/rad$ ) to constrain their movement. The subjects conducted pre-experiments before the formal experiment to familiarize

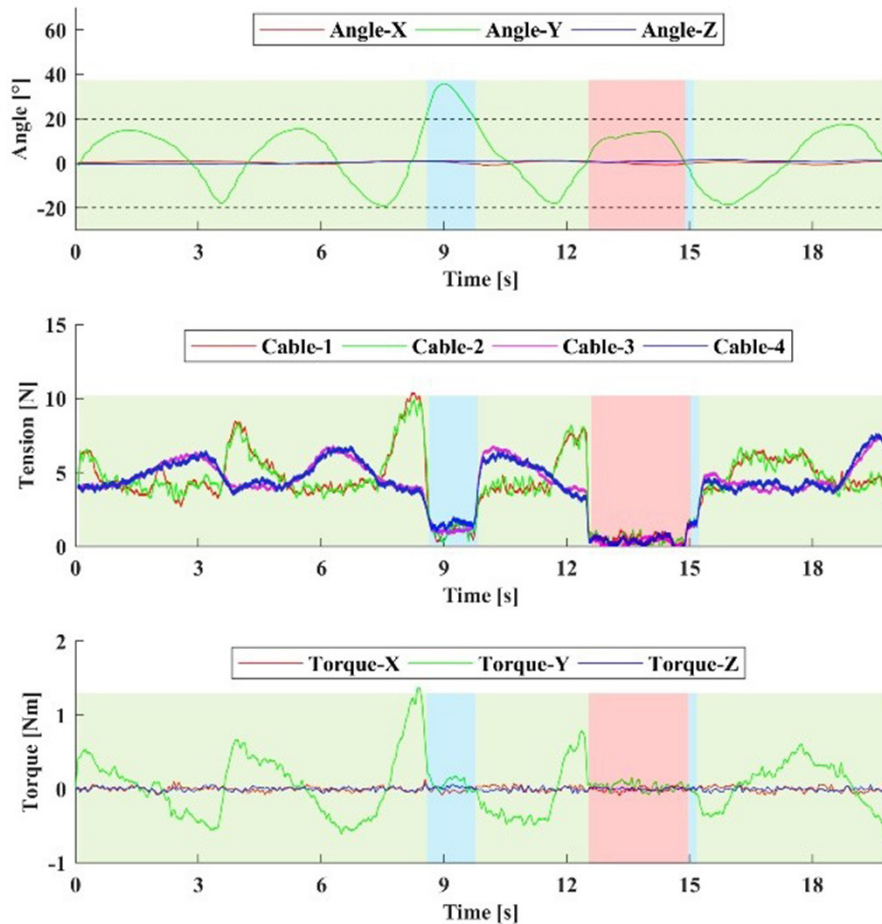


**FIGURE 11 |** (A,C,E) show the visual interface, adaptive  $K_D$  and average error for FE experiment, respectively; (B,D,F) show the visual interface, adaptive  $K_D$  and average error for PS experiment, respectively; (G,H) demonstrate the average tension and max parasitic force in task no. 15–30 of S3, respectively. The red bar is the average value of SER-WRE in the large range, the green bar is its average value in the small range, and the blue bar is the average value of CDWRR in the small range.

themselves with the operation of the system. Each task was about 5 s, and one experiment consisted of 30 tasks.  $r$  and  $K_D$  of each task were recorded, and the target error was set as 0.01 rad/s. CDWRR was selected to compare the tension efficiency with SEU-WRE. FE ( $-30^\circ \sim +30^\circ$ ) and PS ( $-10^\circ \sim +50^\circ$ ) were defined as the small range, and FE ( $-50^\circ \sim +50^\circ$ ) and PS ( $-60^\circ \sim +60^\circ$ ) were defined as the large range. Due to the large movement range exceeded its maximum range, the average cable tension and parasitic force of CDWRR in small range were calculated for comparison. In the meanwhile, the data of SEU-WRE in small and large range were calculated, respectively.

It can be seen from the results that with the assistance of this robot, no matter the health or the patient reached the set error target after several tasks, and the error fluctuated around the target value.  $K_D$  was continuously adjusted according to the subjects' performance. Since the set error target was pretty small, even healthy subjects must be assisted to reach the target. It can be seen from **Figure 11** that three subjects showed similar fluctuations in the FE and PS experiments. The assistance for S2 was smaller than for S3, but the assistance fluctuation was larger. It was because that S2 had good movement ability but it was unstable. Especially, S2 had poor movement accuracy, so that





**FIGURE 12 |** The healthy subject performs a safety mode test. The damping coefficient  $B_D$  is 1 Nm·s/rad. The subject actively exceeds the safe range near the 9th s, and then returns to the safe range. Near the 12th s, the drive system is powered off and the robot enters Safety Mode II. Then, the drive system is powered on near the 15th s, the robot returns to Normal Work Mode. The blue and red regions are Safe Mode I and Safe Mode II, respectively.

the robot needed to provide more assistance to help him correct the wrong movement. The ability of S3 was weak, so the required assistance was high, but the overall change was stable.

For comparison of the tension efficiency, in the experiment of S3, the average value of  $r$ , cable tension, and parasitic force in the small range and large range of tasks 15–30 were recorded, respectively. In these 16 tasks, the average assistive torque provided by the robot did not show the significant difference in both large and small range. In FE, the average tension was lower in the small range than in the large range, that was, in the small movement range, the tension efficiency was higher. Comparing with CDWRR, it was obvious that SEU-WRE can provide higher tension efficiency and lower parasitic force. In PS, the average cable tension was similar in the small and large range. Because of the rotating compensation mechanism, PS movement did not change the configuration of the cables, and SEU-WRE also provided higher efficiency compared with CDWRR. In the experiment, all subjects indicated that they did not feel the abnormal effect of the parasitic force. The therapist believed that this robot is simple to operate without adjustment for individual

differences and it has enough DOFs and workspace to meet the requirements of a variety of rehabilitation training tasks.

## Safety and Comfort Experiment

To verify the safety mode proposed in this paper, one healthy subject were selected for the experiment. The FE safety range was set in  $(-20^\circ \sim +20^\circ)$ , and the resistive training was performed in this range. The controller can then be written:

$$\tau_r = g(q) - B_D \dot{q} \quad (12)$$

$B_D$  is the damping coefficient. As shown in **Figure 12**, when the subject exceeded the boundary, the cable tension dropped to a minimum, but the cables still remained tense. At this time, the subject's hand can move freely without obvious interference. Even if the tension sensor or IMU fails, this mode is also effective. Then the subject actively moved to the safe range, and the robot quickly changed to the Normal Work Mode to provide the required assistance. When it is controlled by the software, the tension switch is not hard. Then the drive system was powered off, and

the robot entered Safe Mode II. After the cables were pulled out with a very small force, the tension of all cables became zero. The cables slacked, and the subject can move freely without any interaction with the robot. The hand ring was easy to be taken off. After powering on the drive system, the system returned to Safe Mode I and to Normal Work Mode.

## CONCLUSION

This paper proposed a cable-driven three-DOF wrist rehabilitation training robot with high-bandwidth force-feedback function. The addition of the Z-axis rotation adaptive mechanism increases the robot workspace and tension efficiency, which is critical to the safety and comfort of rehabilitation and force-feedback. By combining the MR clutches with the geared motor, the decoupling of the output characteristics of the motor can be realized. The power system has the advantages of good safety and high force bandwidth compared to the conventional actuator. Several experiments were carried out to verify that this robot system can provide high-bandwidth force-feedback, accurate tracking performance, and safe human-robot interaction. Compared with the previous cable-driven robots, the proposed design has the larger workspace that can cover the ADLs range, and has higher tension efficiency, which can increase the effective torque and reduce the parasitic force. At the same time, it still has the characteristic of the flexibility, low inertia, free alignment.

However, due to the unidirectional tension characteristic of the cable, although the parasitic force is reduced, it cannot be eliminated completely. If this device is used for the patient with high muscle tone, the parasitic force could be large. In addition, the initial length of the cable and the length of the limb are

measured manually, and it is not convenient in the clinic. In the next work, these parameters including the wrist joint center shift can be self-identified using the length of the redundant cables. The clinical experiments are also in progress.

## DATA AVAILABILITY STATEMENT

The original contributions presented in the study are included in the article/supplementary material, further inquiries can be directed to the corresponding author.

## ETHICS STATEMENT

The studies involving human participants were reviewed and approved by Zhongda Hospital Southeast University. The patients/participants provided their written informed consent to participate in this study.

## AUTHOR CONTRIBUTIONS

KS, AS, and HL proposed and designed the robot system including the exoskeleton and the DASA system. KS and YL developed the controller and DC designed the MR clutches. KS wrote the manuscript with the help of AS and LZ. All authors contributed to the article and approved the submitted version.

## FUNDING

This work was supported by the National Key Research and Development Program of China (No. 2017YFB1303201), and the Key Research and Development Program of Jiangsu Province (No. BE2018004-4).

## REFERENCES

- Alamdari, A., and Krovi, V. (2015). "Modeling and control of a novel home-based cable-driven parallel platform robot: PACER," in *2015 IEEE/RSJ International Conference on Intelligent Robots and Systems (IROS)* (Hamburg: IEEE), 6330–6335. doi: 10.1109/IROS.2015.7354281
- Bayona, N. A., Bitensky, J., Salter, K., and Teasell, R. (2005). The role of task-specific training in rehabilitation therapies. *Topics Stroke Rehabil.* 12, 58–65. doi: 10.1310/BQM5-6YGB-MVJ5-WVCR
- Bian, H., Chen, Z., Wang, H., and Zhao, T. (2017). Mechanical design of EFW Exo II: a hybrid exoskeleton for elbow-forearm-wrist rehabilitation. *IEEE Int. Conf. Rehabil. Robot.* 2017, 689–694. doi: 10.1109/ICORR.2017.8009328
- Bryson, J. T., Jin, X., and Agrawal, S. K. (2016). Optimal design of cable-driven manipulators using particle swarm optimization. *J. Mech. Robot.* 8, 0410031–0410038. doi: 10.1115/1.4032103
- Buongiorno, D., Sotgiu, E., Leonardis, D., Marcheschi, S., Solazzi, M., and Frisoli, A. (2018). WRES: a novel 3 DoF wrist exoskeleton with tendon-driven differential transmission for neuro-rehabilitation and teleoperation. *IEEE Robot. Autom. Lett.* 3, 2152–2159. doi: 10.1109/LRA.2018.2810943
- Cempini, M., De Rossi, S. M., Lenzi, T., Vitiello, N., and Carrozza, M. C. (2013). Self-alignment mechanisms for assistive wearable robots: a kinetostatic compatibility method. *IEEE Trans. Robot.* 29, 236–250. doi: 10.1109/TRO.2012.2226381
- Chen, W., Cui, X., Zhang, J., and Wang, J. (2015). A cable-driven wrist robotic rehabilitator using a novel torque-field controller for human motion training. *Rev. Sci. Instrum.* 86:65109. doi: 10.1063/1.4923089
- Cui, X., Chen, W., Jin, X., and Agrawal, S. K. (2017). Design of a 7-DOF cable-driven arm exoskeleton (CAREX-7) and a controller for dexterous motion training or assistance. *IEEE/ASME Trans. Mechatron.* 22, 161–172. doi: 10.1109/TMECH.2016.2618888
- Donatelli, R. A. (2012). *Physical Therapy of the Shoulder*. St. Louis, Mo: Elsevier.
- French, J. A., Rose, C. G., and O'Malley, M. K. (2014). System characterization of MAHI EXO-II: a robotic exoskeleton for upper extremity rehabilitation. *Proc. ASME Dyn. Syst. Control Conf.* 2014:V003T43A006. doi: 10.1115/DSCC2014-6267
- Gupta, A., O'Malley, M. K., Patoglu, V., and Bugar, C. (2008). Design, control and performance of RiceWrist: a force feedback wrist exoskeleton for rehabilitation and training. *Int. J. Robot. Res.* 27, 233–251. doi: 10.1177/0278364907084261
- Hatem, S. M., Saussez, G., Della Faille, M., Prist, V., Zhang, X., and Dispa, D., et al. (2016). Rehabilitation of motor function after stroke: a multiple systematic review focused on techniques to stimulate upper extremity recovery. *Front. Hum. Neurosci.* 10:442. doi: 10.3389/fnhum.2016.00442
- Kwakkel, G., Kollen, B. J., and Krebs, H. I. (2008). Effects of robot-assisted therapy on upper limb recovery after stroke: a systematic review. *Neurorehabil. Neural Repair.* 22, 111–121. doi: 10.1177/1545968307305457
- La Delfa, N. J., and Potvin, J. R. (2017). A musculoskeletal model to estimate the relative changes in wrist strength due to interacting wrist and forearm postures. *Comput. Method. Biomed.* 20, 1403–1411. doi: 10.1080/10255842.2017.1366994
- Letier, P., Schiele, A., Avraam, M., Horodincă, M., and Preumont, A. (2006). "Bowden cable actuator for torque-feedback in haptic applications," in *Proceedings of Eurohaptics 2006* (Paris).

- Lum, P. S., Burgar, C. G., Shor, P. C., Majmundar, M., and Van der Loos, M. (2002). Robot-assisted movement training compared with conventional therapy techniques for the rehabilitation of upper-limb motor function after stroke. *Arch. Phys. Med. Rehabil.* 83, 952–959. doi: 10.1053/apmr.2001.33101
- Manna, S. K., and Dubey, V. N. (2018). Comparative study of actuation systems for portable upper limb exoskeletons. *Med. Eng. Phys.* 60, 1–13. doi: 10.1016/j.medengphy.2018.07.017
- Mao, Y., and Agrawal, S. K. (2012). Design of a cable-driven arm exoskeleton (CAREX) for neural rehabilitation. *IEEE Trans. Robot.* 28, 922–931. doi: 10.1109/TRO.2012.2189496
- Mustafa, S. K., and Agrawal, S. K. (2012). On the force-closure analysis of n-DOF cable-driven open chains based on reciprocal screw theory. *IEEE Trans. Robot.* 28, 22–31. doi: 10.1109/TRO.2011.2168170
- Mustafa, S. K., Yang, G., Yeo, S. H., and Lin, W. (2006). Optimal design of a bio-inspired anthropocentric shoulder rehabilitator. *Appl. Bionics Biomech.* 3, 199–208. doi: 10.1155/2006/891953
- Omarkulov, N., Telegenov, K., Zeinullin, M., Tursynbek, I., and Shintemirov, A. (2016). “Preliminary mechanical design of NU-Wrist: a 3-DOF self-aligning wrist rehabilitation robot,” in *2016 6th IEEE International Conference on Biomedical Robotics and Biomechanics (BioRob)* (Singapore: IEEE), 962–967. doi: 10.1109/BIROB.2016.7523753
- Palli, G., and Melchiorri, C. (2006). “Model and control of tendon-sheath transmission system,” in *Proceedings 2006 IEEE International Conference on Robotics and Automation*, 2006. ICRA 2006 (Orlando, FL: IEEE), 988–993.
- Pehlivan, A. U., Sergi, F., Erwin, A., Yozbatiran, N., Francisco, G. E., and O'Malley, M. K. (2014). Design and validation of the RiceWrist-S exoskeleton for robotic rehabilitation after incomplete spinal cord injury. *Robotica* 32, 1415–1431. doi: 10.1017/S0263574714001490
- Perry, J. C., Rosen, J., and Burns, S. (2007). Upper-limb powered exoskeleton design. *IEEE/ASME Trans. Mechatron.* 12, 408–417. doi: 10.1109/TMECH.2007.901934
- Pezent, E., Rose, C. G., Deshpande, A. D., and O'Malley, M. K. (2017). Design and characterization of the OpenWrist: a robotic wrist exoskeleton for coordinated hand-wrist rehabilitation. *IEEE/RSJ Int. Conf. Intell. Robots Syst.* 2017, 720–725. doi: 10.1109/ICORR.2017.8009333
- Proietti, T., Crocher, V., Roby-Brami, A., and Jarrasse, N. (2016). Upper-limb robotic exoskeletons for neurorhabilitation: a review on control strategies. *IEEE Rev. Biomed. Eng.* 9, 4–14. doi: 10.1109/RBME.2016.2552201
- Reinkensmeyer, D. J., Kahn, L. E., Averbuch, M., McKenna-Cole, A., Schmit, B. D., and Rymer, W. Z. (2000). Understanding and treating arm movement impairment after chronic brain injury: progress with the ARM guide. *J. Rehabil. Res. Dev.* 37, 653–662. doi: 10.1067/mmt.2000.110940
- Riener, R. (2007). Robot-aided rehabilitation of neural function in the upper extremities. *Acta Neurochir. Suppl.* 97, 465–471. doi: 10.1007/978-3-211-33079-1\_61
- Rijnveld, N., and Krebs, H. I. (2007). Passive wrist joint impedance in flexion-extension and abduction-adduction, in *2007 IEEE 10th International Conference on Rehabilitation Robotics* (Noordwijk: IEEE), 43–47. doi: 10.1109/ICORR.2007.4428404
- Schiele, A., and van der Helm, F. C. T. (2006). Kinematic design to improve ergonomics in human machine interaction. *IEEE Trans. Neural Syst. Rehabil. Eng.* 14, 456–469. doi: 10.1109/TNSRE.2006.881565
- Shao, Z. F., Tang, X. Q., and Yi, W. M. (2014). Optimal design of a 3-DOF cable-driven upper arm exoskeleton. *Adv. Mech. Eng.* doi: 10.1155/2014/157096
- Shimoga, K. B. (1992). “Finger force and touch feedback issues in dexterous telemanipulation,” in *NASA-CIRSE International Conference Intelligent Robotic Systems for Space Exploration* (Troy, NY: IEEE).
- Stroke Center. (2002). Available online at: <http://www.strokecenter.org/patients/about-stroke/stroke-statistics/reference> (accessed October 22, 2019).
- Su, Y.-Y., Yu, Y.-L., Lin, C.-H., and Lan, C.-C. (2019). A compact wrist rehabilitation robot with accurate force/stiffness control and misalignment adaptation. *Int. J. Intell. Robot. Appl.* 3, 45–58. doi: 10.1007/s41315-019-00083-6
- Veneman, J. F., Ekkelenkamp, R., Kruidhof, R., van der Helm, F. C. T., and van der Kooij, H. (2005). “Design of a series elastic and bowdencable-based actuation system for use as torque-actuator in exoskeleton-type training robots,” in *IEEE International Conference Rehabilitation Robotics* (Chicago, IL: IEEE), 496–499.
- Viau, J., Chouinard, P., Lucking Bigué, J.-P., Julió, G., Michaud, F., and lante, J.-S. (2017). Tendon-driven manipulator actuated by magnetorheological clutches exhibiting both high-power and soft motion capabilities. *IEEE/ASME Trans. Mechatron.* 22, 561–571. doi: 10.1109/TMECH.2016.2605379
- Viau, J., Chouinard, P., Lucking Bigué, J.-P., Julió, G., Michaud, F., Shimoda, S., et al. (2015). “Projected PID controller for tendon-driven manipulators actuated by magneto-rheological clutches,” in *IEEE/RSJ International Conference Intelligent Robotic System* (Hamburg: IEEE), 5954–5959. doi: 10.1109/IROS.2015.7354224

**Conflict of Interest:** The authors declare that the research was conducted in the absence of any commercial or financial relationships that could be construed as a potential conflict of interest.

Copyright © 2021 Shi, Song, Li, Li, Chen and Zhu. This is an open-access article distributed under the terms of the Creative Commons Attribution License (CC BY). The use, distribution or reproduction in other forums is permitted, provided the original author(s) and the copyright owner(s) are credited and that the original publication in this journal is cited, in accordance with accepted academic practice. No use, distribution or reproduction is permitted which does not comply with these terms.



# Using a Robot to Treat Non-specific Low Back Pain: Results From a Two-Arm, Single-Blinded, Randomized Controlled Trial

Honorio Marín-Méndez<sup>1</sup>, Patricia Marín-Novoa<sup>1</sup>, Silvia Jiménez-Marín<sup>1</sup>, Itziar Isidoro-Garijo<sup>1</sup>, Mercedes Ramos-Martínez<sup>1</sup>, Miriam Bobadilla<sup>2</sup>, Eduardo Mirpuri<sup>2</sup> and Alfredo Martínez<sup>2\*</sup>

<sup>1</sup> Rehabilitation Service, High Resolution Center San Millán, Servicio Riojano de Salud, Logroño, Spain, <sup>2</sup> Oncology Area, Center for Biomedical Research of La Rioja (CIBIR), Logroño, Spain

## OPEN ACCESS

### Edited by:

Luciano Luperini Menegaldo,  
Federal University of Rio de  
Janeiro, Brazil

### Reviewed by:

Elisangela Manfra,  
Pontifical Catholic University of  
Parana, Brazil  
Ye Ma,  
Ningbo University, China

### \*Correspondence:

Alfredo Martínez  
amartinezr@riojasalud.es

**Received:** 27 May 2021

**Accepted:** 19 August 2021

**Published:** 14 September 2021

### Citation:

Marín-Méndez H, Marín-Novoa P, Jiménez-Marín S, Isidoro-Garijo I, Ramos-Martínez M, Bobadilla M, Mirpuri E and Martínez A (2021) Using a Robot to Treat Non-specific Low Back Pain: Results From a Two-Arm, Single-Blinded, Randomized Controlled Trial. *Front. Neurobot.* 15:715632. doi: 10.3389/fnbot.2021.715632

Non-specific low back pain (NSLBP) affects many people and represents a high cost for health care. Manual pressure release of myofascial trigger points is used to treat NSLBP and is very effective but difficult to standardize since it is provided by different therapists, which also suffer musculoskeletal complications from this highly repetitive activity. A robot designed for this purpose may help in reducing these problems. Here, we present data from a two-arm, single-blinded, randomized controlled clinical trial evaluating the efficiency of a therapeutic massage robot (ADAMO) in reducing NSLBP (clinicaltrials.gov, registration number: NCT04882748). Forty-four patients were randomly distributed into the two arms of the study (robot vs. control). A physician filled the Oswestry disability index (ODI) before starting the treatment and at the end of it, in a blind fashion. In addition, patients filled a visual analogue scale (VAS) after each of the 10 treatment sessions. The ODI and the VAS were analyzed as the primary and secondary outcome measures. Both treatments (robot and control) resulted in a significantly lower ODI ( $p < 0.05$ ). On the other hand, robot-treated patients significantly reduced their VAS levels ( $p = 0.0001$ ) whereas control treatment did not reach statistical significance. Patients of both sexes obtained similar benefits from either treatment. Overweight patients (body mass index  $\geq 25\text{kg/m}^2$ ) in the robot arm benefited more from the treatment ( $p = 0.008$ ) than patients with normal weight. In conclusion, the ADAMO robot is, at least, as efficient as regular treatment in reducing low back pain, and may be more beneficial for specific patients, such as those with excessive weight.

**Keywords:** low back pain, robot, therapeutic massage, body mass index, overweight, perceived pain

## INTRODUCTION

Low back pain is defined as a musculoskeletal syndrome, or group of symptoms, whose main characteristic is the pain, which is focalized in the lumbar area of the spine. The diagnosis is rather easy since symptoms are very evident. When this pain cannot be attributed to a known cause (traumatism, systemic diseases, nerve root compression, etc), it is called non-specific low back pain (NSLBP) (Maher et al., 2017), which may represent 90–95% of all cases of back pain (Bardin et al., 2017).



NSLBP cannot be considered a benign pathology. On the contrary, it is responsible for a high index of work absenteeism and early retirement (Ekman et al., 2005; Hoy et al., 2014). This syndrome affects 70–80% of the population of developed countries at some stage during their lifetime, representing the main cause of motility restriction, long-term incapacity, and reduction in the quality of life. In Europe, it has an associated cost of between 1.7 and 2.1% of the gross domestic product (Lambeek et al., 2011), while in the US it costs about \$ 100 billion a year (Dieleman et al., 2016).

The treatment for this pathology has been collected in several clinical practice guidelines, with little differences among them (Oliveira et al., 2018). All of them recommend: (i) maintaining physical activity as far as the pain allows; (ii) pharmacological treatment (analgesics, non-steroidal anti-inflammatories, muscle relaxants); and (iii) non-pharmacological measures (local heat, cognitive-behavior therapy, spinal manipulation, rehabilitation programs). Rehabilitation therapy, including different exercises, such as stretches, back workshops, and aquatic exercises, among others, provides excellent results in managing chronic back pain (Searle et al., 2015). In addition, manual pressure release of myofascial trigger points constitutes the most common practice to treat back pain and is very effective in the short term, although it may not address the underlying causes (Dayanir et al., 2020). These trigger points are hyperirritable zones located in a taut band of skeletal muscle that generate pain with compression, distension, overload, or contraction of the tissue, which usually responds with a referred pain (Moraska et al., 2017).

Pain evaluation is a fundamental requisite in the outcome assessment of any pain intervention. It is well-known that psychological and psychosocial factors may substantially influence pain perception, so different scales have been developed to measure the intensity of perceived pain in patients. The most extended ones are the visual analogue scale (VAS) and the Oswestry disability index (ODI) (Haefeli and Elfering, 2006; Mehra et al., 2008).

The main problem in measuring and reporting manual massage practices is that the massage is applied by different therapists, with different strength and intensity, which may vary from session to session (Farber and Wieland, 2016). The use of massaging robotic devices should solve all these problems and several prototypes have been proposed (Wang et al., 2018; Li et al., 2020).

In this study, we will test the efficiency of the new ADAMO robot system (<https://adamorobot.com/>), produced and distributed by Future Sense, Inc (Spain). ADAMO bases its operation on a computer program that controls the manipulator robot, which, by means of cameras installed at the end of its arm, must find in each session the points of treatment in the patient previously defined by the health professional and apply the necessary pressure. This pressure is generated by means of a compressed air nozzle integrated in a handpiece installed at the end of the robot arm (Figure 1).

The objective of our study was to measure the efficiency of adding the ADAMO robot to the current protocol of non-pharmacological measures in reducing NSLBP.

## MATERIALS AND METHODS

This was a two-arm, single-blinded, randomized controlled trial. The study was approved by the local ethics committee (Comité de Ética de Investigación con Medicamentos de La Rioja, CEImLAR, protocol P.S 7) and registered at [clinicaltrials.gov](https://clinicaltrials.gov) (registration number: NCT04882748). The study follows all tenets of the Declaration of Helsinki and was conducted at the Rehabilitation Service, High Resolution Center San Millán, in Logroño (Spain) between October 2020 and February 2021.

### Subjects

Patients of both sexes that arrived to the Rehabilitation Service seeking treatment for NSLBP were included in the trial if they were suffering from NSLBP, had between 18 and 60 years of age, and they signed the informed consent form. Participants were excluded if they fulfilled any of the following criteria: pregnancy, impossibility of staying in a prone position, previous pathologies (spinal surgery, cancer, rheumatic diseases, cardiopathies, respiratory compromise, etc), allergies and/or skin afflictions.

Sample size was calculated based on data published by Patti et al. (2016). In that study, the pain of patients suffering from NSLBP was measured with the ODI. On their first visit, patients exhibited a pain rate of  $13.7 \pm 5.0$ , which after several sessions of Pilates exercises became  $6.5 \pm 4.0$ . Power was set as 80% for an alpha of 5% and attrition of 20%, resulting in 22 patients per study arm, in order to reach a significant relief at the end of treatment.

### Intervention

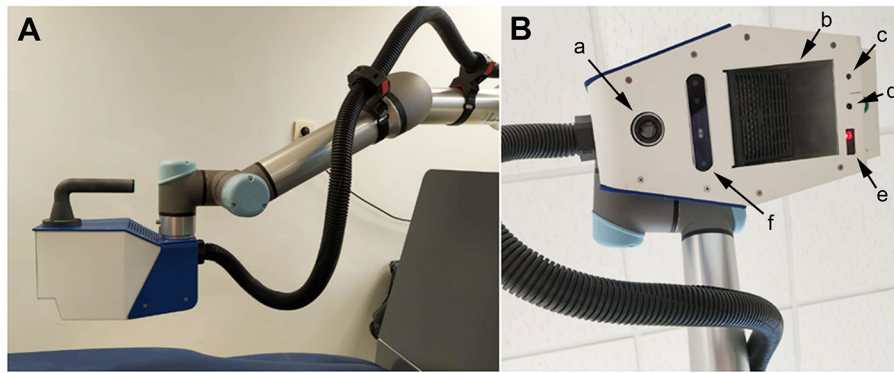
For each patient, the intervention period lasted for five weeks, with one-h exercise sessions twice a week (10 sessions). Before starting treatment, clinical characteristics of the patient were collected (age, sex, body mass index, previous treatments, etc). Then, patients were assessed with an ODI questionnaire and were randomly allocated to one of the two arms of the study: robot and control (Figure 2). Allocation was achieved with the help of an online resource that provides randomized lists (<https://pinetools.com/es/aleatorizar-lista>).

In the robot arm, a physiotherapist with more than 15 years of experience identified the trigger points in the patient, programmed the robot, and applied robot-controlled air pressure massage for 10 min. The ADAMO robot applies an air current to the trigger points on the back of the patient, guided by cameras and computer programs (<https://adamorobot.com/>) (Figure 1). Then, thermotherapy and rehabilitation exercises were provided, as is the standard treatment for NSLBP at the Rehabilitation Service (High Resolution Center San Millán).

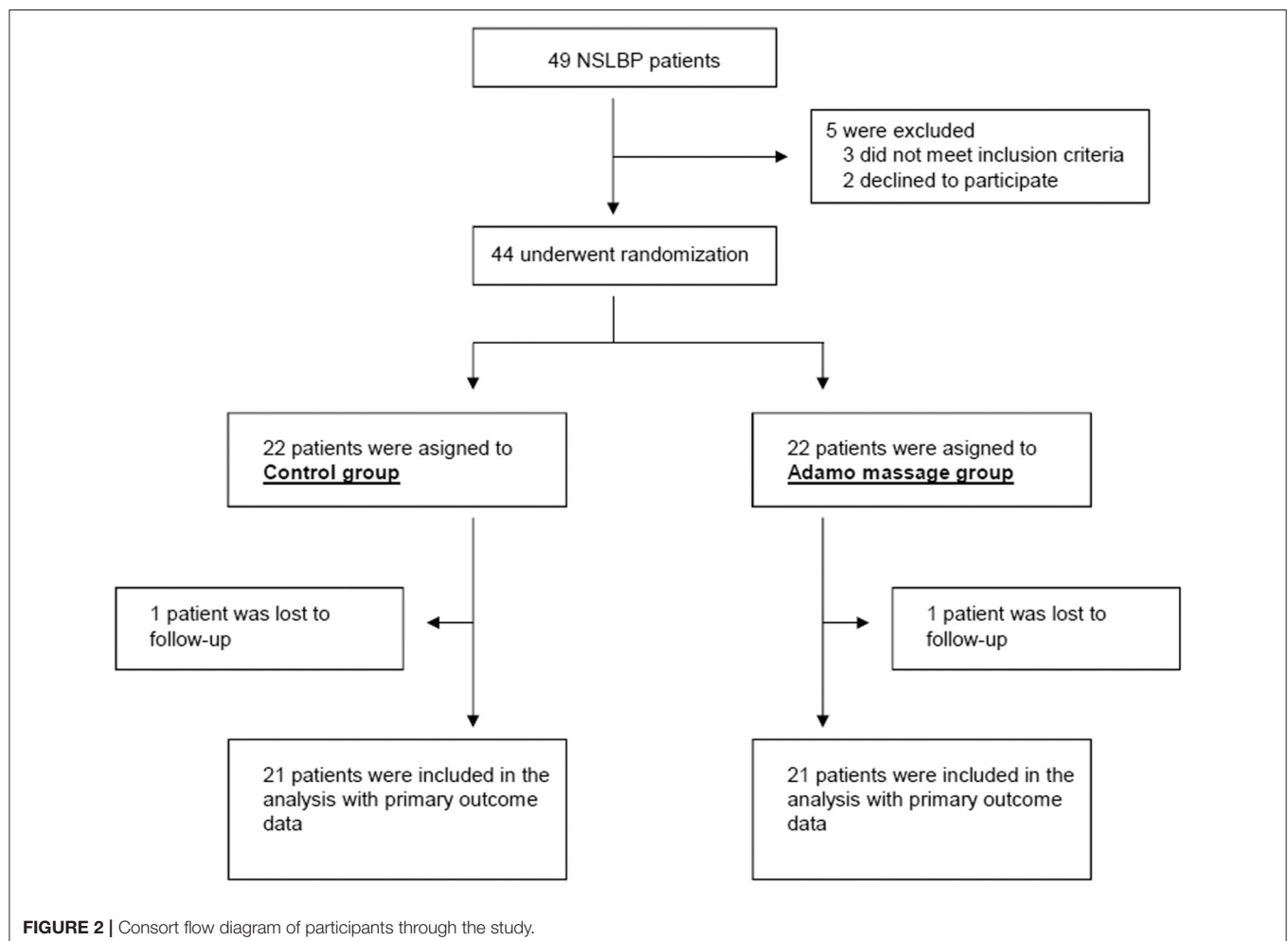
In the control arm, patients were laid down on the robot platform. Physiotherapists identified the trigger points and the robot was connected, providing the expected background noise and vibration, but the air pressure was not applied. Thermotherapy and rehabilitation exercises were also applied.

At the end of each session, the physiotherapist applied the VAS questionnaire (not blinded). At the





**FIGURE 1** | Representative photographs of the ADAMO device showing the robotic arm with the terminal handpiece (A), and detail of the handpiece (B) indicating the location of the thermal camera (a), the air heater (b), the cross selection laser (c), the air nozzle (d), the distance sensor (e), and the 3D camera (f). The black tube carries compressed air.



**FIGURE 2** | Consort flow diagram of participants through the study.

end of the 10 sessions, the patient went back to the physician's office to complete the second and final ODI questionnaire (the physician was blinded to the treatment).

## Outcome Measures

The primary outcome for this study was pain-related disability as tested by the Oswestry disability index (ODI). This is a questionnaire which gives a subjective percentage score of level

of function (disability) in activities of daily living in those rehabilitating from low back pain. Possible scores go from 0 to 50, being 0 no pain and 50 the highest possible pain (Mehra et al., 2008). The secondary outcome was perceived pain as assessed by the visual analogue scale (VAS), which is a unidimensional measure of pain intensity. The patients are presented with a horizontal line of face pictograms. The patients mark on the line the point that they feel represents their perception of their current state, which may rank from 0 (best, no pain) to 10 (worst pain) (Haefeli and Elfering, 2006).

## Data Analysis

Categorical variables were compared using chi-square test. Normal distribution of all datasets was determined by the Shapiro-Wilk test. Since none of the datasets followed a normal distribution, only non-parametric tests were used. The temporal variation in VAS was analyzed with the Kruskal-Wallis test, followed by the Dunns *post-hoc* test. The variation on ODI and VAS questionnaires was compared between the two experimental groups with the Mann-Whitney's *U* test. *p* values lower than 0.05 were considered statistically significant. All these analyses were carried out with SPSS 17.0.

## RESULTS

Forty-nine potential participants were approached and asked to participate in the study. Of these, three were excluded for not meeting inclusion criteria (age > 60) and two other candidates declined to participate. At the end, 44 patients were randomized into the two arms of the study, and one patient from each arm was lost during the trial. Finally, we obtained complete data from 21 patients in each arm (Figure 2).

Of the 42 patients, 14 were men and 28 women with a median age of 52 years and a median body mass index (BMI) of 27 kg/m<sup>2</sup>. At the beginning of the trial, they presented a median score of 15 in the ODI and 6 in the VAS. After allocation into the two arms of the study, the baseline characteristics of both populations were similar (Table 1).

After 10 sessions, patients filled out another ODI questionnaire. All patients experienced a significant relief in the disability index in both arms of the trial (Figure 3A). In the control treatment, patients went from 15 (9–19) to 10 (6–15) (*p* = 0.009). In the robot treatment group, patients went from 15 (11–20.5) to 11 (5.5–15.5) (*p* = 0.036). No significant differences were found between the groups in their final ODI (*p* = 0.58). When analyzing pain perception through the VAS questionnaire, patients in the control treatment arm did not express a significant relief of their symptoms (*p* = 0.13). On the other hand, patients treated by the robot experienced a significant relief after their 10th session (*p* = 0.0001), going from an initial VAS of 6 (6–7.5) to 3.6 (2–4). There was no significant difference in VAS final values between both treatments (*p* = 0.94) (Figure 3B).

Then, we investigated whether the sex of the patients had any influence in their treatment. For the ODI values, both women and men experienced a significant amelioration of their symptoms due to the treatment (Figure 4A). Regarding the VAS, women reported a significant relief for their symptoms both in the

control (*p* = 0.038) and in the robot (*p* = 0.005) arms. Among men, the control treatment did not reach statistical significance (*p* = 0.36) but men treated with the robot experienced a very significant relief (*p* = 0.008), going from 6 (6–8) to 2 (1–4) (Figure 4B).

Another variable we wanted to measure was the influence of the patient's body composition, as measured by the body mass index (BMI). According to metabolic guidelines (Kahan and Manson, 2019), patients with BMI ≥ 25 kg/m<sup>2</sup> are considered overweight. Clinical characteristics of these patients are summarized in Table 2. Interestingly, the best results were obtained among overweight people, both with the ODI (Figure 5A) and the VAS (Figure 5B) indexes. When analyzing the VAS data, only overweight patients treated with the robot experienced a significant relief of their symptoms (*p* = 0.001), going from 6 (6–8) to 4 (2–5).

All individual participant data are available in Supplementary Material.

## DISCUSSION

The aim of this randomized controlled trial was to evaluate the effectiveness of adding a robot-mediated massage to the usual treatment to alleviate NSLBP, consisting of thermotherapy and rehabilitation exercises. Both treatments were significantly beneficial for the patients and had similar effects for the primary outcome (ODI), reducing disability symptoms. On the other hand, only the robot was able to reduce perceived pain, as measured by the VAS. Interestingly, overweight patients experienced more significant relief than patients of normal weight, and this difference was more striking in the patients treated by the robot.

Obesity is a leading preventable cause of death and disease worldwide. The prevalence of obesity was 42.4% in the US in 2018. Obesity-related conditions include heart disease, stroke, type 2 diabetes, and certain types of cancer (CDC, 2021). The medical costs for people who have obesity was US\$ 1,429 higher than those of normal weight (Finkelstein et al., 2009). In addition, the excessive weight generates undue stress to the joints and musculoskeletal system (Viester et al., 2013), making these people more prone to seek physical therapy treatments. Furthermore, overweight patients pose additional problems to physiotherapists that may not reach properly their trigger points during manual treatment. Our finding that robotic massage is more efficient than control treatment for overweight patients may indicate that the constant air pressure provided by the robot adds more relief to these patients.

The use of robotic devices to perform therapeutic massages has been previously reported (Wang et al., 2018; Li et al., 2020). The main difference of the ADAMO robot with other versions is that the massage is produced by a directed current of compressed air with constant intensity. This avoids direct contact with the skin, which reduces potential cross-contamination among patients and simplifies decontamination procedures. Another difference is that previous devices are based in multipurpose robotic arms that have been programmed to perform massages,

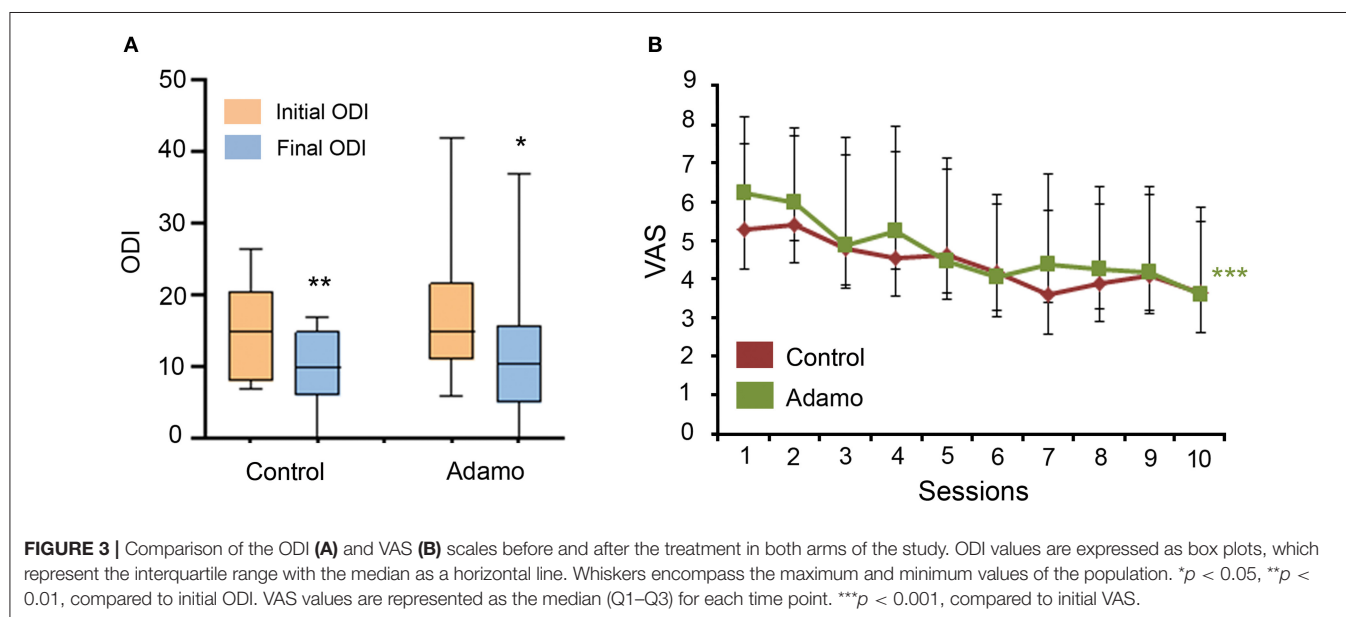
**TABLE 1** | Clinical characteristics of patients.

	Total	Control arm	Robot arm	<i>p</i> value*
n	42	21	21	1.0 <sup>x</sup>
Sex, female (%)	28 (66.6%)	12 (57.1%)	16 (76.2%)	0.29 <sup>x</sup>
Age (years)	52 (46.75;57)	48.5 (46;57)	54 (51;58.25)	0.063 <sup>†</sup>
BMI (kg/m <sup>2</sup> )	27.0 (23.7–29.5)	27.3 (24.5–32.3)	26.1 (22.7–28.1)	0.14 <sup>†</sup>
ODI baseline	15 (10–20)	15 (9–19)	15 (11–20.5)	0.34 <sup>†</sup>
ODI post-treatment	10 (6–15)	10 (6–15)	11 (5.5–15.5)	0.58 <sup>†</sup>
VAS baseline	6 (4–6.5)	5 (4–6)	6 (6–7.5)	0.15 <sup>†</sup>
VAS post-treatment	4 (2–6)	3.6 (2–6)	3.6 (2–4)	0.94 <sup>†</sup>

BMI, body mass index; ODI, oswestry disability index; VAS, visual analogue scale.

Continuous variables are presented as median and interquartile interval.

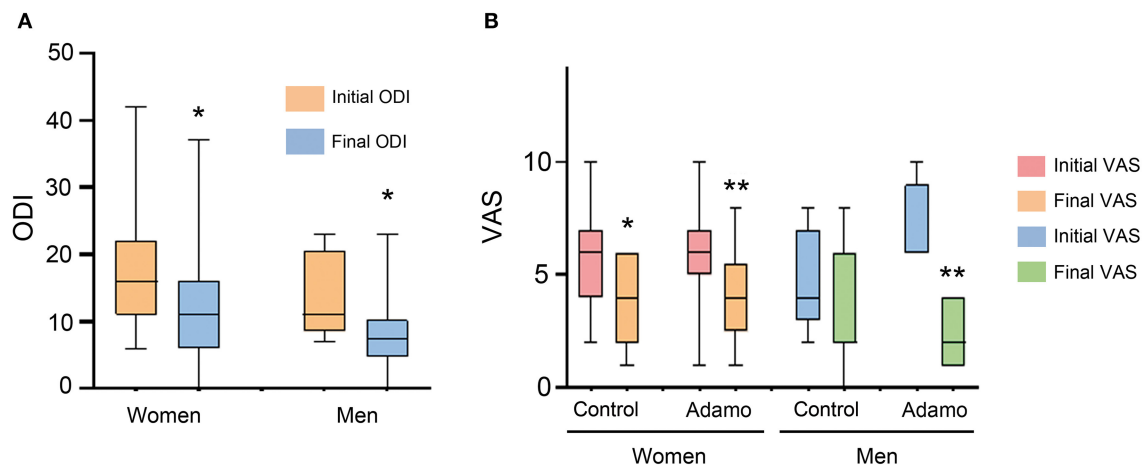
\*Tests used in each case: <sup>x</sup>Chi square; <sup>†</sup>Mann-Whitney's U test.



whereas the ADAMO robot has been specifically designed for this single purpose.

The mechanism by which pressure and massage can diminish pain has been described. Cutaneous pressure receptors are located in the deep layers of the skin and are, mainly, the Ruffini and Pacini corpuscles (Munger and Ide, 1988). Both are connected to thick A $\beta$  nerve fibers, which are those with the highest conduction velocity. These nerve fibers, for the most part, do not establish synapses in the posterior horn of the spinal cord but continue to higher structures. Nevertheless, these fibers emit collateral branches toward the posterior horn where they contact pain inhibitory interneurons. Taking into account the different conduction velocity of the pain-carrying fibers (fibers C and A $\delta$ , very slow) and of the fibers activated by pressure (A $\beta$ , very fast), the latter produce an activation of the inhibitory interneurons and block the transmission of the nociceptive stimulus to the higher nervous centers (Garcia et al., 2021). This is in agreement with the gate control theory, which proposes that the nociceptive sensory information transmitted

to the brain relies on an interplay between the inputs from nociceptive and non-nociceptive primary afferent fibers. Both inputs are normally under strong inhibitory control in the spinal cord. Under healthy conditions, pre-synaptic inhibition activated by non-nociceptive fibers modulates the afferent input from nociceptive fibers onto spinal cord neurons, while postsynaptic inhibition controls the excitability of dorsal horn neurons, and silences the non-nociceptive information flow to nociceptive-specific projection neurons (Guo and Hu, 2014). However, in addition to this mechanism, it is likely that pressure on the skin may block the release of algogenic substances (substance P, bradykinin, histamine) through resident skin cells (Schmelz, 2011). On the other hand, it cannot be ruled out that the pressure stimulus acts on the release of neurotransmitters related to pain in the posterior horn of the spinal cord (Yam et al., 2018) and on blocking the activation of the microglia responsible for central algetic sensitization and neuropathic pain (Chen et al., 2018). The pressure elicited by the robot seems to be very efficient in activating cutaneous receptors and fast fibers. Future studies

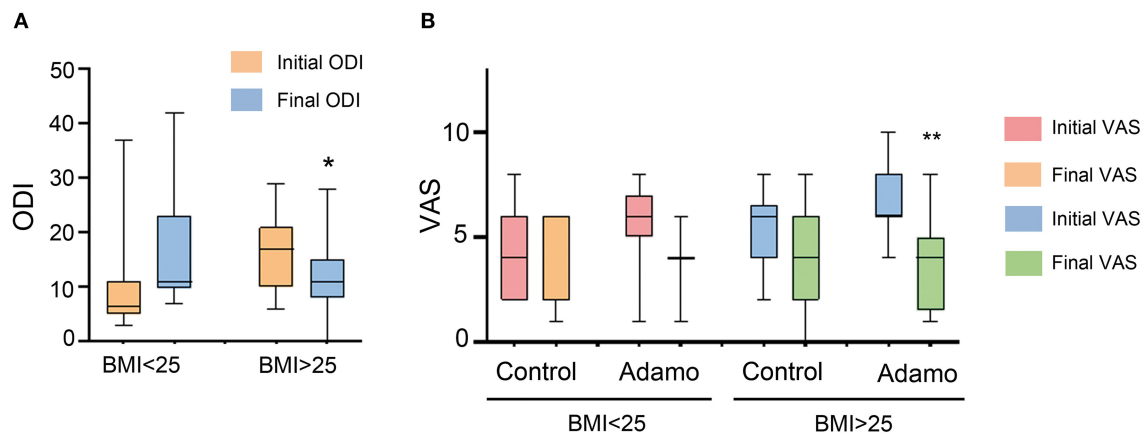


**FIGURE 4 |** Comparison of the ODI (A) and VAS (B) scales, before and after the treatment in both arms of the study, taking into consideration the sex of the patients. Values are expressed as box plots, which represent the interquartile range with the median as a horizontal line. Whiskers encompass the maximum and minimum values of the population. \* $p < 0.05$ , \*\* $p < 0.01$ , compared to initial test.

**TABLE 2 |** Clinical characteristics of patients divided by BMI.

	BMI < 25			BMI ≥ 25		
	Total	Control arm	Robot arm	Total	Control arm	Robot arm
n	15	7	8	27	14	13
Sex, female (%)	10 (66%)	3 (42.8%)	7 (87.5%)	18 (66.6%)	9 (64.2%)	9 (69.2%)
Age (years)	51 (47–58)	51 (48–53.7)	50 (43.7–53.7)	54 (47–57)	48.5 (46–57)	54.5 (50–59.5)
ODI baseline	11 (10–25)	10 (8–25)	11 (11–21.6)	17 (10.5–20.5)	16.5 (10.5–18.7)	20 (13–21)
ODI post-treatment	6.5 (5–10.75)	7 (5–8.5)	5 (5–13.5)	11 (8–15)	12 (8–15)	11 (9–15.5)
VAS baseline	6 (4–6.5)	4 (2–6)	6 (5–7)	6 (4–7)	6 (4–6.5)	6 (6–7.5)
VAS post-treatment	4 (2–6)	2 (2–6)	4 (4–4)	4 (2–6)	4 (2.5–6)	4 (2–5)

BMI, body mass index; ODI, oswestry disability index; VAS, visual analogue scale.



**FIGURE 5 |** Comparison of the ODI (A) and VAS (B) scales, before and after the treatment in both arms of the study, taking into consideration the BMI of the patients. Values are expressed as box plots, which represent the interquartile range with the median as a horizontal line. Whiskers encompass the maximum and minimum values of the population. \* $p < 0.05$ , \*\* $p < 0.01$ , compared to initial test.

must demonstrate whether the use of the robot influences the release of algogenic substances.

Addition of robot massage has shown a significant improvement in the treatment of specific patients, as well as a broader feeling of well-being (VAS score) in all patients. Nevertheless, larger effects could be expected from this technology. First, in this study, the air pressure that was applied by the robot arm was always constant. Perhaps patients would benefit from different pressures depending on their specific pathology or body type. Also, a single patient may receive different pressures in specific trigger points, depending on their thickness. Second, in this study, a trained therapist identified the trigger points. We are working on a routine that would allow the robot to identify the trigger points by itself, thus liberating a lot of extra time for the therapist. Of course, the efficiency of the robot in locating the trigger points will need to be validated with a clinical trial.

There is evidence that, despite receiving proper training in therapy postures and self-care, a high proportion of massage therapists suffer from upper extremity pain and discomfort as a result of delivering therapy treatments. The most affected areas are the wrist and the thumb, followed by the low back, neck, and shoulders (Albert et al., 2008). As expected, the intensity of the pain and discomfort experienced by the therapist is directly related with the number of patients per day and the intensity of the massage (Vieira et al., 2016). Therapeutic robots may be very useful in reducing the most damaging aspects of physical therapy, since they may substitute the therapist in performing the actual massage. Furthermore, a single therapist may coordinate several robots simultaneously, thus increasing the number of treated patients and reducing physical therapy waiting lists.

In conclusion, we have shown that the addition of massage performed by the ADAMO robot to regular non-pharmacological therapeutic protocols is at least as efficient as the control treatment, while demonstrating more efficiency in the treatment of specific patients, such as those with excessive weight. The use of massaging robots may increase the reporting and

reproducibility of physical therapy protocols among different hospitals.

## DATA AVAILABILITY STATEMENT

The original contributions presented in the study are included in the article/**Supplementary Material**, further inquiries can be directed to the corresponding author.

## ETHICS STATEMENT

The studies involving human participants were reviewed and approved by Comité de Ética de Investigación con Medicamentos de La Rioja. The patients/participants provided their written informed consent to participate in this study.

## AUTHOR CONTRIBUTIONS

HM-M, EM, and AM: design of the study. HM-M, PM-N, SJ-M, II-G, and MR-M: patient treatment and data gathering. MB, EM, and AM: data analysis. EM and AM: funding. AM: manuscript writing. All authors approved the final version of the manuscript.

## FUNDING

This study was supported by a grant from Agencia de Desarrollo Económico de La Rioja (ADER), grant number: 2018-I-IDD-00039.

## ACKNOWLEDGMENTS

We gratefully acknowledge Future Sense, Inc. for generously providing an ADAMO robot for the duration of this study.

## SUPPLEMENTARY MATERIAL

The Supplementary Material for this article can be found online at: <https://www.frontiersin.org/articles/10.3389/fnbot.2021.715632/full#supplementary-material>

## REFERENCES

- Albert, W. J., Currie-Jackson, N., and Duncan, C. A. (2008). A survey of musculoskeletal injuries amongst Canadian massage therapists. *J. Bodyw. Mov. Ther.* 12, 86–93. doi: 10.1016/j.jbmt.2007.03.003
- Bardin, L. D., King, P., and Maher, C. G. (2017). Diagnostic triage for low back pain: a practical approach for primary care. *Med. J. Aust.* 206, 268–273. doi: 10.5694/mja16.00828
- CDC (2021). *Adult Obesity Facts*. Available online at: [https://www.cdc.gov/obesity/data/adult.html#:\\$sim\\$:text=Obesity](https://www.cdc.gov/obesity/data/adult.html#:$sim$:text=Obesity) (accessed August 27, 2021).
- Chen, G., Zhang, Y. Q., Qadri, Y. J., Serhan, C. N., and Ji, R. R. (2018). Microglia in pain: detrimental and protective roles in pathogenesis and resolution of pain. *Neuron* 100, 1292–1311. doi: 10.1016/j.neuron.2018.11.009
- Dayanir, I. O., Birinci, T., Kaya, M. E., Akcetin, M. A., and Akdemir, A. O. (2020). Comparison of three manual therapy techniques as trigger point therapy for chronic nonspecific low back pain: a randomized controlled pilot trial. *J. Altern. Complement Med.* 26, 291–299. doi: 10.1089/acm.2019.0435
- Dieleman, J. L., Baral, R., Birger, M., Bui, A. L., Bulchis, A., Chapin, A., et al. (2016). US spending on personal health care and public health, 1996–2013. *JAMA* 316, 2627–2646. doi: 10.1001/jama.2016.16885
- Ekman, M., Johnell, O., and Lidgren, L. (2005). The economic cost of low back pain in Sweden in 2001. *Acta Orthop.* 76, 275–284. doi: 10.1080/00016470510030698
- Farber, K., and Wieland, L. S. (2016). Massage for low-back pain. *Explore (NY)* 12, 215–217. doi: 10.1016/j.explore.2016.02.014
- Finkelstein, E. A., Trogon, J. G., Cohen, J. W., and Dietz, W. (2009). Annual medical spending attributable to obesity: payer- and service-specific estimates. *Health Aff. (Millwood)* 28, w822–w831. doi: 10.1377/hlthaff.28.5.w822
- Garcia, K., Wray, J. K., and Kumar, S. (2021). *Spinal Cord Stimulation*. Treasure Island (FL): StatPearls Publishing. Available online at: <https://www.ncbi.nlm.nih.gov/books/NBK553154/> (accessed April 7, 2021).
- Guo, D., and Hu, J. (2014). Spinal presynaptic inhibition in pain control. *Neuroscience* 283, 95–106. doi: 10.1016/j.neuroscience.2014.09.032
- Haefeli, M., and Elfering, A. (2006). Pain assessment. *Eur. Spine J.* 15, S17–S24. doi: 10.1007/s00586-005-1044-x



- Hoy, D., March, L., Brooks, P., Blyth, F., Woolf, A., Bain, C., et al. (2014). The global burden of low back pain: estimates from the global burden of disease 2010 study. *Ann. Rheum. Dis.* 73, 968–974. doi: 10.1136/annrheumdis-2013-204428
- Kahan, S., and Manson, J. E. (2019). Obesity treatment, beyond the guidelines: practical suggestions for clinical practice. *JAMA* 321, 1349–1350. doi: 10.1001/jama.2019.2352
- Lambeek, L. C., van Tulder, M. W., Swinkels, I. C., Koppes, L. L., and Anema, J. R., van, M. W. (2011). The trend in total cost of back pain in The Netherlands in the period 2002 to 2007. *Spine (Phila Pa 1976)* 36, 1050–1058. doi: 10.1097/BRS.0b013e3181e70488
- Li, C., Fahmy, A., Li, S., and Sienz, J. (2020). An enhanced robot massage system in smart homes using force sensing and a dynamic movement primitive. *Front. Neurobot.* 14:30. doi: 10.3389/fnbot.2020.00030
- Maher, C., Underwood, M., and Buchbinder, R. (2017). Non-specific low back pain. *Lancet* 389, 736–747. doi: 10.1016/S0140-6736(16)30970-9
- Mehra, A., Baker, D., Disney, S., and Pynsent, P. B. (2008). Oswestry disability index scoring made easy. *Ann. R. Coll. Surg. Engl.* 90, 497–499. doi: 10.1308/003588408X300984
- Moraska, A. F., Schmiede, S. J., Mann, J. D., Butryn, N., and Kruttsch, J. P. (2017). Responsiveness of myofascial trigger points to single and multiple trigger point release massages: a randomized, placebo controlled trial. *Am. J. Phys. Med. Rehabil.* 96, 639–645. doi: 10.1097/PHM.0000000000000728
- Munger, B. L., and Ide, C. (1988). The structure and function of cutaneous sensory receptors. *Arch. Histol. Cytol.* 51, 1–34. doi: 10.1679/aohc.51.1
- Oliveira, C. B., Maher, C. G., Pinto, R. Z., Traeger, A. C., Lin, C. C., Chenot, J. F., et al. (2018). Clinical practice guidelines for the management of non-specific low back pain in primary care: an updated overview. *Eur. Spine J.* 27, 2791–2803. doi: 10.1007/s00586-018-5673-2
- Patti, A., Bianco, A., Paoli, A., Messina, G., Montalto, M. A., Bellafiore, M., et al. (2016). Pain perception and stabilometric parameters in people with chronic low back pain after a pilates exercise program: a randomized controlled trial. *Medicine (Baltimore)* 95:e2414. doi: 10.1097/MD.0000000000002414
- Schmelz, M. (2011). Neuronal sensitivity of the skin. *Eur. J. Dermatol.* 21, 43–47. doi: 10.1684/ejd.2011.1265
- Searle, A., Spink, M., Ho, A., and Chuter, V. (2015). Exercise interventions for the treatment of chronic low back pain: a systematic review and meta-analysis of randomised controlled trials. *Clin. Rehabil.* 29, 1155–1167. doi: 10.1177/0269215515570379
- Vieira, E. R., Schneider, P., Guidera, C., Gadotti, I. C., and Brunt, D. (2016). Work-related musculoskeletal disorders among physical therapists: a systematic review. *J. Back Musculoskelet. Rehabil.* 29, 417–428. doi: 10.3233/BMR-150649
- Viesters, L., Verhagen, E. A., Oude Hengel, K. M., Koppes, L. L., van der Beek, A. J., and Bongers, P. M. (2013). The relation between body mass index and musculoskeletal symptoms in the working population. *BMC Musculoskelet. Disord.* 14:238. doi: 10.1186/1471-2474-14-238
- Wang, W., Zhang, P., Liang, C., and Shi, Y. (2018). A portable back massage robot based on traditional Chinese medicine. *Technol. Health Care* 26, 709–713. doi: 10.3233/THC-181300
- Yam, M. F., Loh, Y. C., Tan, C. S., Khadijah, A. S., Abdul, M. N., and Basir, R. (2018). General pathways of pain sensation and the major neurotransmitters involved in pain regulation. *Int. J. Mol. Sci.* 19:2164. doi: 10.3390/ijms19082164

**Conflict of Interest:** The authors declare that the research was conducted in the absence of any commercial or financial relationships that could be construed as a potential conflict of interest.

**Publisher's Note:** All claims expressed in this article are solely those of the authors and do not necessarily represent those of their affiliated organizations, or those of the publisher, the editors and the reviewers. Any product that may be evaluated in this article, or claim that may be made by its manufacturer, is not guaranteed or endorsed by the publisher.

Copyright © 2021 Marín-Méndez, Marín-Novoa, Jiménez-Marín, Isidoro-Garijo, Ramos-Martínez, Bobadilla, Mirpuri and Martínez. This is an open-access article distributed under the terms of the Creative Commons Attribution License (CC BY). The use, distribution or reproduction in other forums is permitted, provided the original author(s) and the copyright owner(s) are credited and that the original publication in this journal is cited, in accordance with accepted academic practice. No use, distribution or reproduction is permitted which does not comply with these terms.



# User-Centered Design and Development of the Modular TWIN Lower Limb Exoskeleton

Matteo Laffranchi<sup>1\*</sup>, Stefano D'Angella<sup>1</sup>, Christian Vassallo<sup>1</sup>, Chiara Piezzo<sup>1</sup>, Michele Canepa<sup>1</sup>, Samuele De Giuseppe<sup>1</sup>, Mirco Di Salvo<sup>1</sup>, Antonio Succi<sup>1</sup>, Samuele Cappa<sup>1</sup>, Giulio Cerruti<sup>1</sup>, Silvia Scarpetta<sup>1</sup>, Lorenzo Cavallaro<sup>1</sup>, Nicolò Boccardo<sup>1</sup>, Marialaura D'Angelo<sup>1</sup>, Claudia Marchese<sup>2</sup>, Jody A. Saglia<sup>1</sup>, Eleonora Guanziroli<sup>3</sup>, Giacinto Barresi<sup>1</sup>, Marianna Semprini<sup>1</sup>, Simone Traverso<sup>1</sup>, Stefano Maludrottu<sup>1</sup>, Franco Molteni<sup>3</sup>, Rinaldo Sacchetti<sup>2</sup>, Emanuele Gruppioni<sup>2</sup> and Lorenzo De Michieli<sup>1</sup>

<sup>1</sup> Rehab Technologies Lab, Istituto Italiano di Tecnologia, Genova, Italy, <sup>2</sup> Centro Protesi INAIL, Istituto Italiano per l'Assicurazione contro gli Infortuni sul Lavoro, Vigorso di Budrio, Italy, <sup>3</sup> Villa Beretta Rehabilitation Centre, Valduce Hospital, Costa Masnaga, Italy

## OPEN ACCESS

### Edited by:

Massimo Sartori,  
University of Twente, Netherlands

### Reviewed by:

Yu Cao,  
Huazhong University of Science and  
Technology, China  
Janez Podobnik,  
University of Ljubljana, Slovenia

### \*Correspondence:

Matteo Laffranchi  
matteo.laffranchi@iit.it

**Received:** 14 May 2021

**Accepted:** 31 August 2021

**Published:** 07 October 2021

### Citation:

Laffranchi M, D'Angella S, Vassallo C, Piezzo C, Canepa M, De Giuseppe S, Di Salvo M, Succi A, Cappa S, Cerruti G, Scarpetta S, Cavallaro L, Boccardo N, D'Angelo M, Marchese C, Saglia JA, Guanziroli E, Barresi G, Semprini M, Traverso S, Maludrottu S, Molteni F, Sacchetti R, Gruppioni E and De Michieli L (2021) User-Centered Design and Development of the Modular TWIN Lower Limb Exoskeleton. *Front. Neurobot.* 15:709731. doi: 10.3389/fnbot.2021.709731

For decades, powered exoskeletons have been considered for possible employment in rehabilitation and personal use. Yet, these devices are still far from addressing the needs of users. Here, we introduce TWIN, a novel modular lower limb exoskeleton for personal use of spinal-cord injury (SCI) subjects. This system was designed according to a set of user requirements (lightweight and autonomous portability, quick and autonomous donning and setup, stability when standing/walking, cost effectiveness, long battery life, comfort, safety) which emerged during participatory investigations that organically involved patients, engineers, designers, physiatrists, and physical therapists from two major rehabilitation centers in Italy. As a result of this user-centered process, TWIN's design is based on a variety of small mechatronic modules which are meant to be easily assembled and donned on or off by the user in full autonomy. This paper presents the development of TWIN, an exoskeleton for personal use of SCI users, and the application of user-centered design methods that are typically adopted in medical device industry, for its development. We can state that this approach revealed to be extremely effective and insightful to direct and continuously adapt design goals and activities toward the addressment of user needs, which led to the development of an exoskeleton with modular mechatronics and novel lateral quick release systems. Additionally, this work includes the preliminary assessment of this exoskeleton, which involved healthy volunteers and a complete SCI patient. Tests validated the mechatronics of TWIN and emphasized its high potential in terms of system usability for its intended use. These tests followed procedures defined in existing standards in usability engineering and were part of the formative evaluation of TWIN as a premise to the summative evaluation of its usability as medical device.

**Keywords:** exoskeleton, mechatronics, healthcare robotics, user-centered design, wearable robotics

## INTRODUCTION

Spinal cord injury (SCI) is a particularly critical condition which often leads to permanent disability, use of wheelchair, and several secondary clinical complications. These complications inevitably impact on physical, mental, social and economic conditions of SCI patients (WHO, 2013). As a consequence, traditional therapy based on manually assisted mobilization of the patients has been introduced to prevent, or even cure, many complications. Nevertheless, this approach presents a series of difficulties: the therapist has often to perform the treatment in awkward positions, experiencing early fatigue, which may result in poor therapeutic outcome (Foulds et al., 2014). Furthermore, traditional assisted gait retraining of incomplete subjects is often critical, given the large number of joints to be simultaneously managed and to the consequent poor repeatability and reproducibility (Foulds et al., 2014).

In this scenario, exoskeletons are a valid tool that can easily overcome the mentioned limitations: they can intensify the training, allow the patient to autonomously walk over ground, for longer duration, and reproduce rhythmically correct movement patterns. Motivated by this, researchers have been developing a vast range of robotic exoskeletons for SCI patients. The current leading products are Rewalk (Esquenazi et al., 2012), Ekso (Milia et al., 2016), and Indego (Farris et al., 2014), which have demonstrated their effectiveness in the prevention of secondary complications, patient's health and improvement of the quality of life in several clinical studies.

However, these devices are typically adopted in the clinical context. Others, such as the MINDWALKER (Wang et al., 2015) and the Symbitron (Meijneke et al., 2021), are examples of striking research devices, which are however far from effectively and autonomously being used for independent training. Unfortunately, as the health benefits resulting from exercising largely depend on its frequency of execution, duration, and continuity (Foulds et al., 2014), SCI patients should be able to autonomously use the exoskeleton as a personal device to keep the training frequency high and hence fully benefit from the efficacy of exoskeleton-based therapy.

Nevertheless, current exoskeletons suffer from poor usability (Lajeunesse et al., 2016), which is the main cause that prevents them from being exploited to solve problems of everyday life. Poor usability is the consequence of the lack of several crucial points which are common in most current devices: they are frequently indicated as difficult to be worn autonomously (Gorgey, 2018), mainly due to the considerable weight, size, and “monolithic” structure, which creates difficulties in donning-doffing, transportation and general device handling (Fritz et al., 2019). Moreover, even among the most prominent commercial exoskeletons, surprisingly only the Parker Indego exoskeleton has made an attempt to solve these issues by improving usability contextualized into personal use. Indeed, it is the only available device that can be disassembled without the need of tools for ease of transportation, and which claims wheelchair compatibility. The latter point is essential as the vast majority of SCI patients use the wheelchair as primary mobility aid (Berkowitz et al., 1998). As high usability is an essential prerequisite to increase the

effective adoption of exoskeletons as personal devices in everyday life, their design approach should be completely revised, from traditional technology-centered engineering design processes, to user-centered methods which guarantee the direct addressment of user needs (Masia and Vitiello, 2020).

In this work, we present a novel lower limb exoskeleton named TWIN, for personal utilization of SCI patients, that was developed to address SCI patients' needs directly by means of user-centered design. This process initially involved the final users, which indeed confirmed autonomous usage, that is strictly correlated to usability, as top priority among a set of critical features. This information was then employed for drafting the general architecture layout of the exoskeleton and the requirements of the device to guide its development. Following these procedures (based on medical device design practices), the TWIN exoskeleton was hence conceived to maximize usability, by facilitating donning, transportation, and general device handling. We indeed believe that enabling autonomous usage of these devices can increase the frequency of exoskeleton-based training which is necessary for the successful outcome of the training program (Foulds et al., 2014). Moreover, its structural elements come in different sizes to accommodate the anatomy of the specific patient and are compatible with wheelchair use. Preliminary evaluation was carried out on healthy subjects and an SCI patient to validate the mechatronic viability of the device alongside its ergonomics, considering safety, comfort, and other aspects of usability that must be assessed far before the clinical trials.

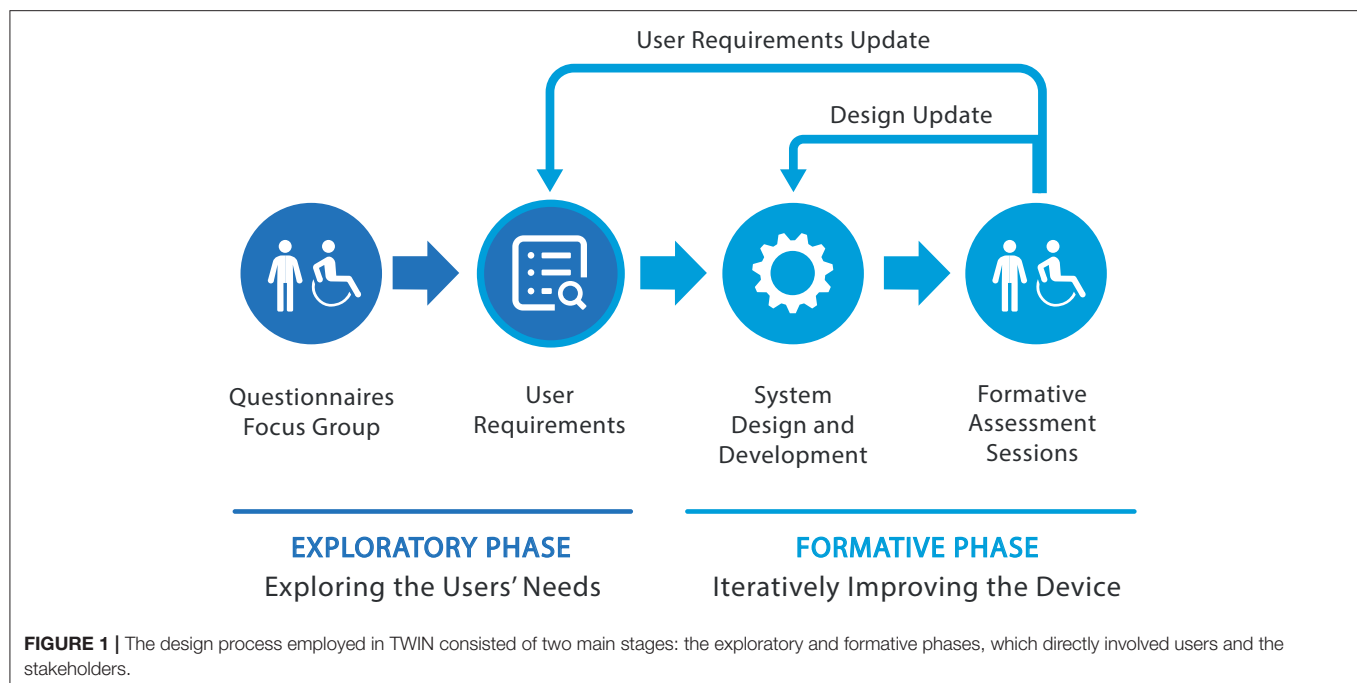
## USER NEEDS AND DESIGN REQUIREMENTS

The design process that enabled the user-centered development of TWIN followed two consecutive phases as listed below:

1. An “exploratory phase” was characterized by the investigation of the user needs to establish a set of user-centered design requirements (Martin et al., 2006; Chandran et al., 2020).
2. A “formative phase” which was designed based on the international standard IEC 62366-1:2015 on the application of usability engineering to medical devices (Scherer and Gouveia Filho, 2019). This phase sustained the participatory evaluation processes adopted to progressively improve the system usability, iteration by iteration (Simonsen and Hertzum, 2010).

This process can be summarized in the conceptual scheme shown in **Figure 1**. After completion of the exploratory phase, the formative phase which follows includes iterations where the design of the device and its subsystems are continuously assessed and updated to comply with the set user requirements. The formative phase may also update the design requirements of the device to comply with possible additional request emerged during the above-mentioned participatory evaluation.

Considering the literature in wearable robotics, the most characteristic trait of our approach is the adoption of methodologies typically exploited in industrial contexts which



**TABLE 1 |** Occurrence of lesion based on type and level.

Type			Level			
Complete	Incomplete	Not specified	Cervical	Dorsal	Lumbar	Not specified
69%	27%	4%	22%	68%	6%	2%

target at achieving the development of systems with high technology readiness level (TRL), and according to users' needs. Indeed, the TWIN exoskeleton was considered a medical device in all its development phases. Consequently, we adopted the perspective of user research and the international standards of usability engineering for medical devices (Privitera et al., 2017; Bitkina et al., 2020). This choice constitutes one of the original contributions provided by this manuscript to the domain of wearable robotics research.

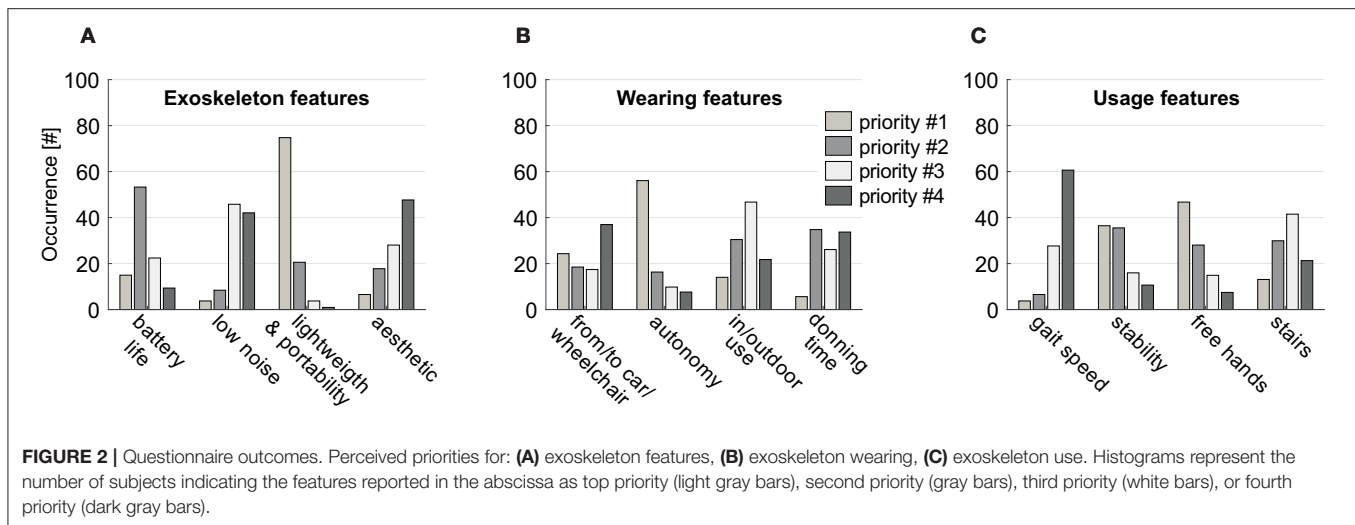
### Exploratory Phase: Analysis of User Needs

As part of the exploratory phase, we first conducted a preliminary series of studies based on questionnaires and focus groups involving patients, aimed at understanding their primary needs and requirements (Shah and Robinson, 2008). This information was then translated into requirements for new device concepts and control strategies that were taken into account for the implementation of the TWIN exoskeleton.

This investigation was conducted in collaboration with the Centro Protesi INAIL (i.e., the Italian National Institute for Insurance against Accidents at Work) in Vigorso di Budrio (Italy) and with the ISTUD foundation. The study comprised a questionnaire and three focus groups that took place in three SCI centers assisting SCI patients. Data collection was performed between June and October 2014 and inclusion criteria were: age >18 years; at least 6 months from spinal unit hospitalization;

no related psychopathological comorbidity. Included subjects granted the authorization to treat personal data, in accord with national laws (D.Lvo. 196/2003) and GDPR regulation. The questionnaire was made available electronically on different platforms and web resources that are usually accessed by spinal patients and was advertised in many hospitals and spinal units. Questions regarded: (1) *socio-demographic information*; (2) *SCI information*; (3) *domestic life*; (4) *work/school*; (5) *free time, hobby, and sport*; (6) *health condition and quality of life*; (7) *autonomy in everyday life and transfers* (autonomy in domestic and non-domestic duties, and autonomy with respect to different ways of travelling); (8) *standing* (habits, perception of standing benefits, opinions related to strength, and limits of available orthoses); (9) *exoskeleton* (impressions of available devices, of their utility and utilization, preferences, and interest for a possible new device). We collected 107 questionnaires. The interviewed population was composed by 79% males with average age of 44 years, confirming the results of a previous study on the Italian population (Pagliacci et al., 2003). **Table 1** summarizes the type and level of lesions of the interviewed patients.

We also performed focus groups, in which a moderator stimulated the discussion between a group of selected patients and collected their response, impressions, and feelings toward the covered topics. A co-creation session followed, where subjects were asked to brainstorm and provide potential use case scenarios and design inputs. Focus groups were organized in three Italian spinal cord centers: Montecatone Rehabilitation Institute (Imola,



17 people—14 males); Unità Spinale Unipolare of Careggi hospital (Florence, 7 people—6 males); Unità Spinale Unipolare of Alesini hospital (Rome, 8 male people).

The data analysis that followed focused on the aspects that were significant to the development of the exoskeleton device, to draft conclusions which could in turn be useful for the following design phases. Therefore, we aimed at understanding: (1) main adversities encountered during daily life, (2) opinion and perception of SCI subjects on the benefits obtained by adopting a standing posture, and (3) opinion on the use of exoskeletons.

Regarding adversities encountered in personal life, collected data reported shared difficulties in traveling and commuting, mostly related to architectonic barriers, both during travel and at destination. Indeed, many people complained about the lack of autonomy during commuting, which is often by car and affected by the difficulties of transferring from wheelchair to car and vice versa. Only 58% of the interviewed people found this transfer easy to perform, while others rely on external help. It must also be noted that traveling and visiting friends were indicated as the free time activities mostly affected by the injury.

We observed the attitude toward the standing posture and found that 58% of the interviewed subjects used devices for standing that are not orthoses, on average 3 days per week for around 90 min per session. Only 8% used a knee-ankle-foot orthosis (KAFO) and they all judged the device very useful. Around 29% of the participants declared that they did use KAFO for some time but then they abandoned the device for diverse reasons, such as fatigue, time issue, difficulty of use, etc. However, almost the totality of the sample (93%) believed in the beneficial effects of standing on rehabilitation and for improving health condition and thus demonstrated a positive attitude toward the development of a device truly designed around their needs. Addressing issues related to the features of exoskeleton, 92% of people with incomplete lesion and 74% of subjects with complete lesions demonstrated interest in them, and they indicated lightweight and portability as the top priority, followed

by battery life (>2 h), low noise, and aesthetics (Figure 2A). With respect to battery life, given that a typical exoskeleton session performed by an expert user lasts about 1 h, we decided to set 2 h as the lower bound, so as to allow the use of the device for 1–2 training sessions.

Regarding device wearing features, the highest priority was represented by the possibility of being worn and removed quickly and autonomously, also from/to the wheelchair or the car, and to be used both indoor and outdoor (Figure 2B). Finally, on usage features, the interviewed sample stated that standing without arm support and stability, are more important than speed or the possibility of access stairs (Figure 2C). Overall, what emerged were specific suggestions for an effective application of robotics to people with SCI. Their feedback could be summarized in two main key needs, i.e., the device should be used autonomously and should be practical to facilitate its employment during its daily usage. Based on the results reported in Figure 2 and on the feedback given during the focus groups, the main user-driven requirements for the development of the TWIN exoskeleton were drafted.

As expected, the first two requirements are directly linked to autonomy and have therefore been prioritized. Stability during use is directly linked to the safety of the device, whereas cost effectiveness, although not reported in Figure 2, has been added because all the subjects verbally complained about the current cost of these machines during focus groups. Finally, from the focus groups, we had insight that long battery life is required to make the subjects feel safe and autonomous during the session. These requirements were then employed to draft conceptual layouts of the machine in cooperation with industrial designers, so as to co-develop the device to address usability as well as technical issues. These aspects were all taken into account for the design of the TWIN exoskeleton. Another priority that is not listed in the requirements was represented by the possibility of reaching a standing posture with free hands, but the practical implementation of this point required solutions that were in contrast with most of the other priorities and was thus left for future developments.



This preliminary study triggered the development of TWIN and its formative assessment.

## Formative Phase: Iterative Improvements of the Device

The international standard IEC 62366-1:2015 and its related technical report IEC 62366-2:2016 (Kendler and Strohlic, 2015) indicate methods to be used for the formative evaluation phase to assess the usability of medical devices. This evaluation must be carried out starting from the most preliminary design iterations throughout to the final prototype so as to guarantee that usability is considered during the whole design process. Accordingly, the role of the formative evaluation is to guide the iterative and participatory design and development of the system for progressively resolving its most critical usability issues. The standard IEC 62366-1:2015 defines how formative evaluation can exploit a heterogeneous set of techniques to collect individual feedback, including qualitative observations expressed (spontaneously or partially guided by a user researcher) by a limited number of subjects for checking major usability problems of each preliminary prototype. These subjects can include both final users and stakeholders—e.g., caregivers and orthopedic technicians who, according to their own expertise, heuristically predict critical flaws in systems usability (Bitkina et al., 2020).

The standard IEC 62366-1:2015 also establishes that, after completion of the formative evaluation, the design process will be concluded with a summative assessment, which is defined as the validation of the system on usability and safety aspects before its certification and release. Differently from the formative assessment, the summative assessment typically requires a comprehensive (especially quantitative and objective) test of the ultimate iteration of the system, possibly with the involvement of numerous users. Before proceeding with the summative assessment, clinical trials are currently performed on the device for the advanced stages of the formative phase.

In order to improve the methodological rigor of our formative assessment, its advanced sub-phases will focus on the correlation of subjective and objective indices to obtain consistent measures of exoskeleton usability. First of all, the protocol will include standardized questionnaires on perceived (subjective) usability: the System Usability Scale (Brooke, 1996) to investigate the caregivers' (which will manage the GUI of the TWIN software) perspective; the NASA-TLX (Hart and Staveland, 1988) for deepening our understanding of the patients' cognitive load in using the device. The questionnaire scores of the users will be analyzed according to (objective) motor and physiological data collected during the exoskeleton usage (and exploited to assess the user's effort, for instance) (Kozłowski et al., 2015). We plan to analyse observable patients' behaviors during autonomous donning/doffing and in the execution of training. Such a multimodal approach is just a demonstration of our plans in matching the subjective and the objective measures for showing a final, and comprehensive, estimation of system usability which will be carried out in the near future.

This paper focuses on the first 36 months of exploratory and formative phases of TWIN. Initially, 10 healthy volunteers

**TABLE 2 |** Requirements of the TWIN exoskeleton.

#	Requirement
1	Lightweight and autonomous portability
2	Quick and autonomous donning and setup
3	Stability when standing/walking
4	Cost effectiveness
5	Long battery life (>2 h)
6	Comfort
7	Safety

participated to the tests. They had no neurological or muscular diseases. Once the TWIN device underwent a first series of iterative improvements and was assessed to be ready for user trials, a second stage involved one 31-year-old SCI patient with a complete D5 lesion and experience in the use of lower limb exoskeletons. All the participants gave written and informed consent before their inclusion in the study. The tests respected the standards of the Declaration of Helsinki (rev. 2013) and were formally approved by the ethics evaluation committee Comitato Etico Interaziendale Bologna-Imola of the Pharmaceutical Department U.O.C. Farmacia Ospedale Maggiore, Bologna, Italy (Protocol number: CP-POR1-01 ver.01).

During the sessions of the formative phase, the evaluation was carried out in empty areas, under the supervision of qualified personnel to ensure the safety of the subjects. Both subjects and supervisors were instructed on how to use the exoskeleton. During exoskeleton sessions, which consisted in walking tasks, the users were invited to freely express their opinions on the experience, following semi-structured interviews too. Meanwhile, objective observations (e.g., asymmetries in posture of legs skin irritation in contacts points, user's tendency to self-rotate) were collected to integrate and confirm the insights offered by the subjects' opinions.

According to the reports, the participants especially focused on issues related to comfort, leading to e.g., structural refinements of the braces (as described later in section Braces). They also paid special attention to safety: for example, this made the developers improve the gait patterns via software to approach a more stable trajectory (as explained in section Control System). These evaluation sessions resulted in the spontaneous emergence of comfort and safety as additional requirements, which were set along with those listed in the previous section. Hence, they were added to the preliminary list of five requirements addressed previously and were included in the development process to be taken into consideration for further revisions of the device.

Table 2 presents the full list of requirements set for the development of the TWIN exoskeleton.

## MECHATRONIC DESIGN OF THE TWIN LOWER LIMB EXOSKELETON

The whole development process was guided by the exploratory and formative processes described in the previous section. It

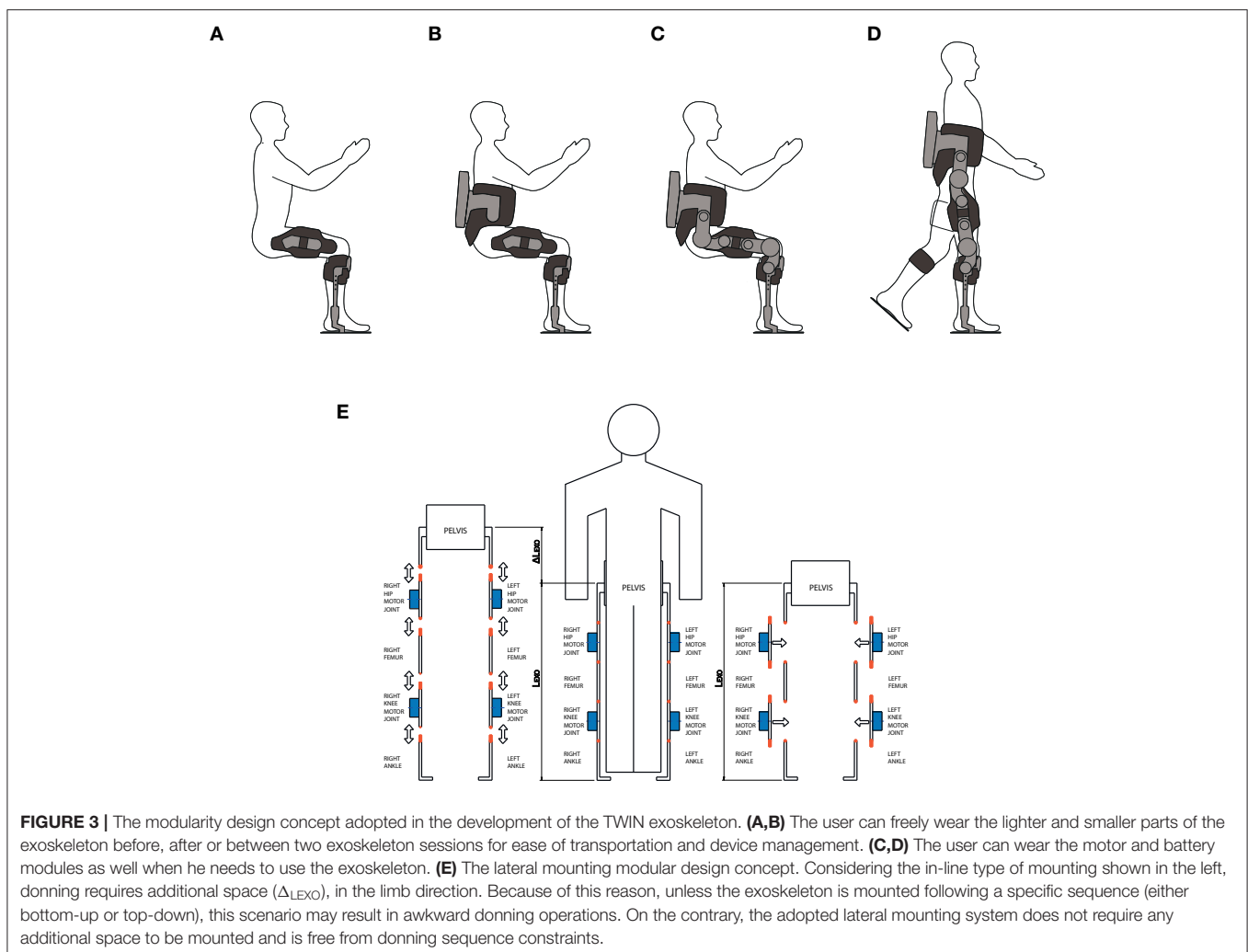
indeed featured a continuous exchange of information between developers and end users (i.e., patients and clinicians) to incrementally and iteratively validate the design choices and the exoskeleton's components (e.g., structure, braces, control) once they were implemented.

The user-centered design approach adopted in this work was not focused on the betterment of exoskeleton performance in the conventional sense: our goal was to develop novel device concepts which could enable new use-case scenarios for the improvement of usability-related aspects of the device.

## Concept Layout Design and Iterative Co-creation Process

Based on the user-centered requirements outlined in Table 2, a concept study was carried out to define possible layouts of the exoskeleton to guide the mechatronic design. Requirements #1, 2 have a few implications: (1) the device must be donned on and off by the subject quickly and autonomously (2) it should be meant for a joint use in combination with the wheelchair,

and (3) it should be compatible with personal transportation vehicles (Figure 2B). Notably, the only existing commercial exoskeleton that deals with these issues is the Parker Hannafin's Indego. It indeed presents a modular structure made of five modules (waist, R/L thigh, and R/L shank-foot) which is meant to be autonomously assembled or disassembled by the user and to facilitate transportation and donning operations. The modularity concept has therefore been integrated within this device which effectively represents a step ahead toward usability in the context of personal use: this exoskeleton is therefore considered as the reference gold standard for this work. Inspired by the design concept of the Indego exoskeleton, we developed TWIN by adopting the idea of a modular structure which could be autonomously assembled and by extremizing modularity with the goal of further impacting on user's autonomy. Indeed, the modules which compose the TWIN exoskeleton have been increased to a number of 9. These are: waist, R/L hip motor, R/L thigh link, R/L knee motor, R/L shank link, and foot. We decided to minimize the number of overall actuators (hip and knee motors only) to comply with requirements #1 and #4. One of the advantages of high modularity is that the exoskeleton can



be quickly disassembled by the user into small sub-units, so as to facilitate its management and transportation. Indeed, we decided to design a concept layout which allowed to divide the modules into two main groups. The first group includes the heavy, cumbersome and costly parts (i.e., motor modules and batteries), whereas lighter, inexpensive and “tailored” components can be classified into the second group (links and braces). This choice aims to bring direct benefits to both the production cost and usability perspectives and further differentiates our work from the Indego exoskeleton. Thanks to TWIN’s design, the patient can wear the modules that less hinder the degree of movement and autonomy, i.e., the links and braces, before, after, or between exoskeleton sessions, **Figures 3A–D**. This brings a number of usability-related benefits:

- 1) it minimizes the number of needed donning operations between sessions (only motors and batteries need to be assembled to start a session);
- 2) it greatly simplifies transportation of the device by allowing the user to carry only the motor and battery modules in a hand luggage;
- 3) it facilitates compatibility with the wheelchair and personal vehicles.

Furthermore, given the high number of modules, we strategically decided to make the motor units to be mountable laterally to further facilitate donning and assembling operations. From the usability perspective, we argue that this method is to be preferred with respect to “in-line” mounting such as that employed in the Indego exoskeleton. Indeed, the latter forces the user to perform a specific donning sequence and may result awkward as it requires additional axial space to be mounted, as shown schematically in **Figure 3E**. Instead, our approach facilitates donning and it allows the user to choose the mounting sequence that can best adapt to the specific context, **Figures 3A–D**. This is another step toward usability, which further differentiates TWIN with respect to the Indego exoskeleton.

From the production cost perspective, the extremization of modularity directly implies saving because the “tailored” parts, i.e., braces and links, which need to be produced in various sizes, are physically separated from the high cost components, i.e., batteries and motors. This facilitates economy of scale in the production of the costly modules and is therefore agreeable with Requirement #4. On the other hand, requirements #3 and #5 were not directly related to the physical layout of the exoskeleton, and were instead implemented through appropriate control, and electrical dimensioning, respectively.

Finally, the two requirements emerged in the formative phase, i.e., #6 and #7 on comfort and safety, have been considered in all aspects of the design, ranging from e.g., the development of the braces to the implementation of the gait patterns as explained in the following sections.

## System Overview and Architecture

Based on the requirements defined in **Table 2**, the anthropometry of the European population, direct comparison with other existing exoskeletons, and engineering constraints, TWIN’s specifications were broken down and set accordingly with

**TABLE 3 |** User-driven specifications of the TWIN exoskeleton.

Type	Value
Target walking speed	1.5 km/h
Max patient’s weight	110 kg
Target weight	20 kg
Battery autonomy (continuous usage)	3 h
Min-max sizes	5 <sup>th</sup> to 95 <sup>th</sup> percentile

the parameters in **Table 3**. The target walking speed was not prioritized accordingly with the results shown in **Figure 2**. Its target weight has been set to be realistically achieved using off the shelf mechatronic components. In fact, as the full weight of lower limb exoskeletons for SCI might result rather high for enabling the user to perform the operations required in autonomous use, we decided that the structure of TWIN should have been “broken down” into a number of modules, each featuring much smaller mass than that of the full device. Furthermore, the weight of the exoskeleton is supported by the structure of the device itself through the soles. Therefore, the user won’t bear the weight of the exoskeleton during use. We hence focused on providing an answer to weight issues highlighted by requirement #1 by extremizing the modularity of the device, so as to allow the user to handle small and light modules that could easily be managed individually.

The four actuation modules can be easily donned on and off by means of lateral quick release connectors placed on both ends of each actuation module, which implement the key concepts explained in the previous section to facilitate the implementation of requirements #1 and #2. The novel quick release system has been custom designed and is a crucial component as it opens up to new use-case scenarios in the field of personal use of lower limb exoskeletons. Still, the design of this subsystem is a major technical challenge that implies critical electromechanical design which must ensure the transmission of both the structural mechanical load and function of electrical connector. Indeed, this component is subject to high values of stress when the exoskeleton is in use, which need to be borne by the mechanical structure, and at the same time it needs to provide continuity in delivering voltage supply and safely stream data throughout the whole structure. Regarding the control of gait parameters, they can be set using a mobile device-based GUI, whereas each step is triggered by means of an Inertial Measurement Unit (IMU)—based system. The actuation guarantees a maximum walking speed of 1.5 km/h on patients weighing up to 110 kg. Structural parts (pelvis, femur, tibia) and braces of different sizes are provided to adapt the device to the anatomy of the patient. The battery pack is located at the back of the device and guarantees up to 3 h of continuous operation. The full device weighs 23 kg and is shown in **Figure 4**.

Finally, a custom motherboard located in the battery pack area behind the back of the user is employed as central control unit (CCU) to coordinate the actuation units and provide measurements and diagnostics. Particularly, a Xilinx XC7020



**FIGURE 4 | (A)** TWIN's modular structure and lateral mounting of the modules, **(B)** The TWIN lower limb exoskeleton in walking mode worn by a subject. The person wearing the exoskeleton gave permission for the use of her image.

Zync-7000 series system on chip (SOC) executes the high-level control.

Regarding the autonomy of the battery, this specification has been set to be sufficiently high, allowing to perform 1–2 walking session with some degree of reserve. Finally, the exoskeleton can be worn and support patients' weight so as to cover the vast majority of the European population, in the range 5<sup>th</sup>–95<sup>th</sup> percentile.

## Quick Release System

The challenge was to develop a mechanism system with lateral release which could bear the complex, multi axial, force-torque load imposed on the structure, at the same time guaranteeing patient safety, high structural stiffness to comply with requirement #3, power supply and data streaming continuity. Despite the fact that “in-line” coupling layout (e.g., Indego style) might seem preferable because it copes well with both axial load and bending moments, this choice has again been discarded to prioritize device usability and ease of donning (requirement #2) through lateral mounting. The lateral quick release system was specifically designed to require little manual effort for the patient during use, at the same time ensuring high mechanical and electrical safety, following the IEC 60601 medical electrical devices safety standard (IEC, 2020).

## Mechanics

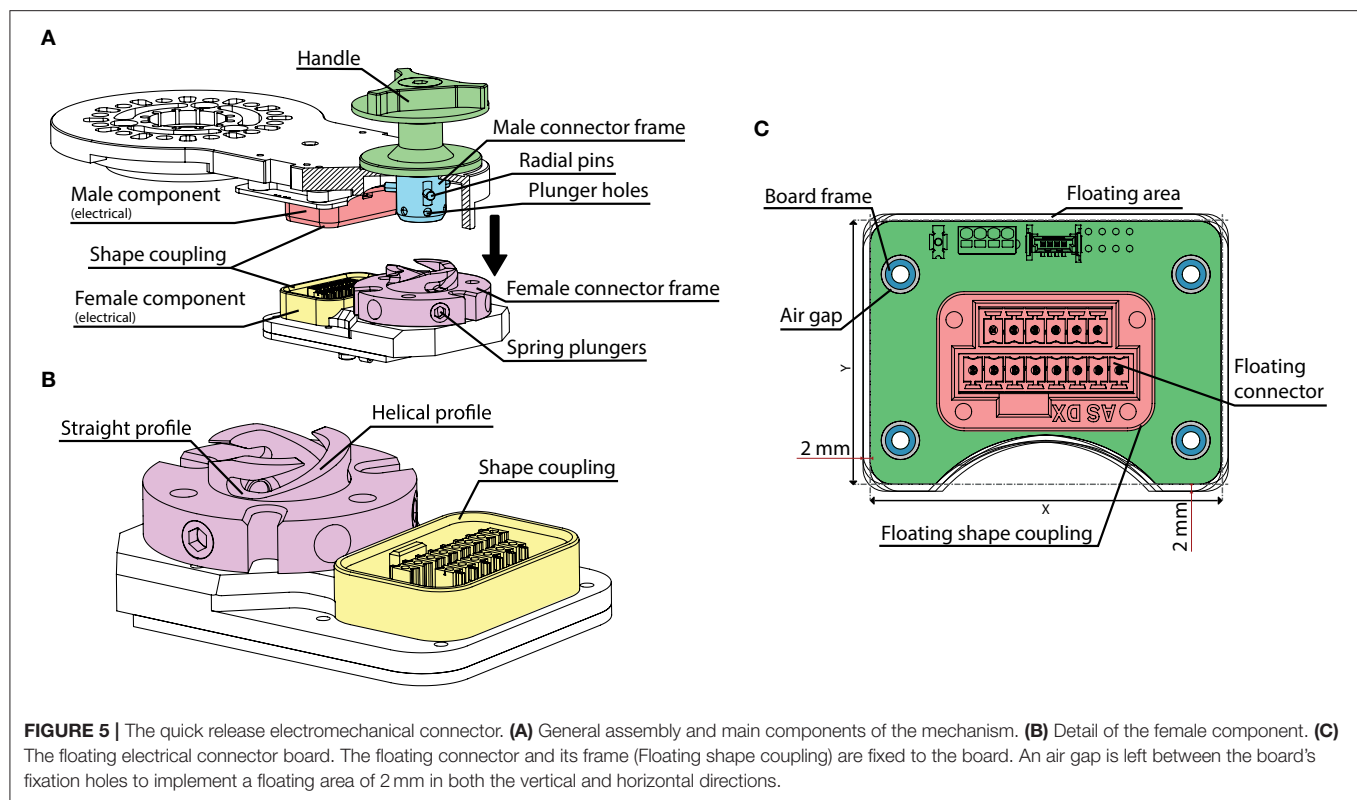
The mechanism is shown in **Figures 5A,B**: the male component is composed of a large pin that features three further small radial pins equally spaced by a 120° angle, whereas the female

counterpart is made by a hollow cylindrical shaped part that was machined to present three helical-shaped grooves. When the male part enters its counterpart, the three radial pins get engaged into the three corresponding grooves machined on the female component by means of manual application of torque on the handle in the clockwise direction. Given the helical shape of the grooves in the female part, when the user applies torque in the clockwise direction, the male part of this system, which is located to each extremity of any of the motor modules, slides along its axis until the mechanical end-stop is reached, when the pin reaches the end of the groove machined on the female part, **Figure 5B**. The groove profile, in its final part, transitions from helical to straight, to ensure the stability of the male part when engaged within the female, **Figure 5B**. Furthermore, three spring plungers have been radially arranged on the female component.

These get engaged with three corresponding holes machined on the main pin of the male component when the handle reaches its end stop, with the dual function of providing acoustic feedback to the user on the successful locking of the system and to additionally ensure mechanical locking safety, **Figure 5**. Indeed, when the plungers are engaged, they lock the male part in its end stop position to avoid accidental disengagement. Hence, to unlock this part, it is necessary to pass a certain torque threshold value which can be regulated by appropriate preload of the plungers' springs which was set to 7 Nm. Please note that, although the torques applied to the structure during exoskeleton use are significantly higher than the required level to unlock the quick disconnect system, the shape coupling profiles of this component, **Figure 5**, decouple the structural loading from the torque loading of the handle. As a result, the male and female components are stressed in traction/compression mode. The main male pin and its counterpart are both machined using 41CrAlMo7 hardened steel, while additional gas nitriding treatment has been performed on the surfaces. This allows to increase Vickers hardness to a value of HV1150, which guarantees very high wear-resistance performances and reduced friction. FEM simulation was also performed on the main components of this critical system to validate their design. The load scenario used in this simulation replicated that measured by a motorized dummy exoskeleton which was equipped with force/torque sensors (please refer to section Structure and Actuation Unit for more details on this device). To obtain this data, a healthy subject simulating leg impairment wore the exoskeleton while position controlled to perform the walking patterns described in our previous work (Vassallo et al., 2020). The worst-case load scenario is summarized in **Table 4**, where the Y axis represents longitudinal axis of the lower limb, the Z axis is the medio-lateral axis and the X axis completes the triad.

Results from this simulation confirm that the critical components, i.e., the main male pin and its counterpart, are able to withstand the load, reaching a peak stress of 441 MPa, which allows validation of the design, taking into account a safety factor of about 2. The male quick disconnect halves are placed on both ends of the actuation modules, whereas their receptacles are placed at the ends of the structural parts described in section Structure and Actuation Unit.





## Electrical Connections

Given that requirement #2 expressed the need of performing quick donning and setup, we decided to develop an embedded quick release that could incorporate electrical connections (voltage supply and CAN communication) as well, so as to allow to achieve both mechanical and electrical connection in one simple step. This solution additionally favors usability by eliminating any external cabling which could possibly result in entanglements with external objects during use. From the technological perspective, though, this constitutes a further challenge. Indeed, ensuring stable electrical continuity over a connector that is subject to considerable mechanical stress is particularly challenging, especially in this case where compactness is paramount and where the applied load is a combination of multi-axial forces and torques. To solve this issue, we designed a system which mechanically decouples the electrical connection from the structural parts of the connector. Indeed, the female electrical connector was mounted on a “floating board,” which is able to freely move on its plane up to 2 mm on both horizontal and vertical directions. This range of movement is so small that it does not pose robustness problems if all the cable routing and soldering of the terminations are made appropriately. This was achieved by means of a specific loose fit between the floating board and the structural frame, **Figure 5C**. This prevents unwanted stress to be generated by deformation of the mechanical structure when under stress. The centring between male and female electrical connectors is guaranteed by the custom-made connector frames which allowed shape coupling as shown in **Figure 5**. The electromechanical

**TABLE 4 |** Load configuration used for the FEM simulation.

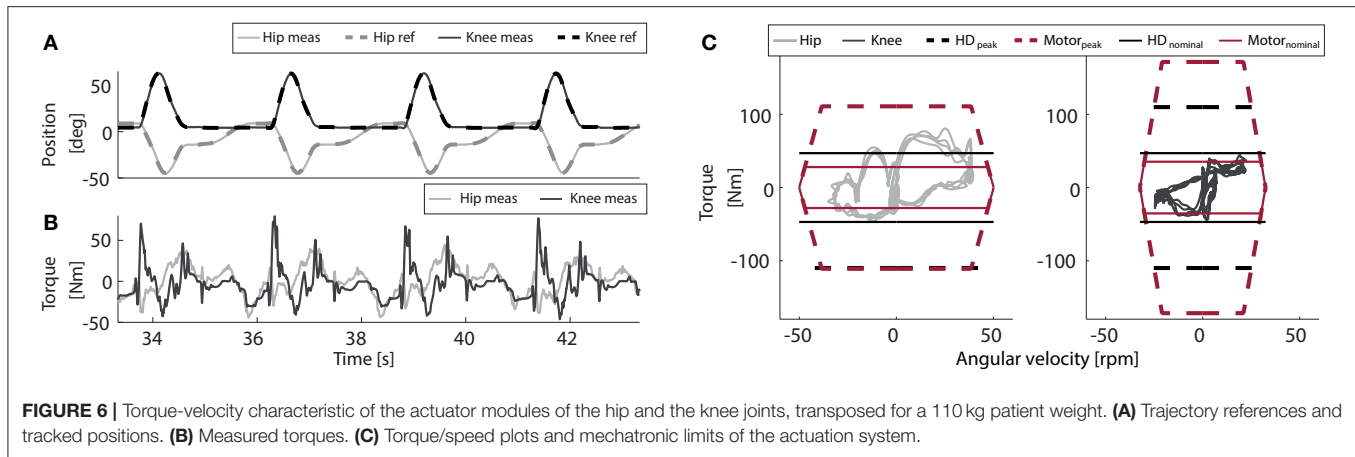
Load	X	Y	Z	Total
Force (N)	250	−300	290	486
Torque (Nm)	56	19	−45	74

design choices adopted in the development of the quick release system, have permitted to obtain the highest safety of this critical component, which additionally allowed TWIN to obtain compliance to IEC 60601 standards.

## Actuator Sizing

The dimensioning of the actuators and battery unit of the TWIN exoskeleton was based on the specifications set in **Table 3**. Given that the walking pattern of exoskeletons for this type of application is significantly different with respect to healthy subjects' physiological gait velocity/torque profiles, we decided not to use human biomechanical gait data as reference values for the design as they would result unrealistic and require significantly higher mechanical power than needed. Indeed, motion patterns replicated by exoskeletons are rather different compared to those of healthy subjects. To obtain more realistic data, we therefore developed and used a custom-made “dummy” motorized lower limb exoskeleton that was fully sensorized for the purpose of recording the load applied to the exoskeleton actuators and structure during position-controlled walking, standing and sitting and use them for appropriate actuators





dimensioning. A classical robotic trajectory was set as reference for the position-controlled system, **Figure 6A** (T1 as explained in Vassallo et al., 2020), and a healthy male subject, 60 kg, wore the exoskeleton performing a few steps simulating full leg impairment.

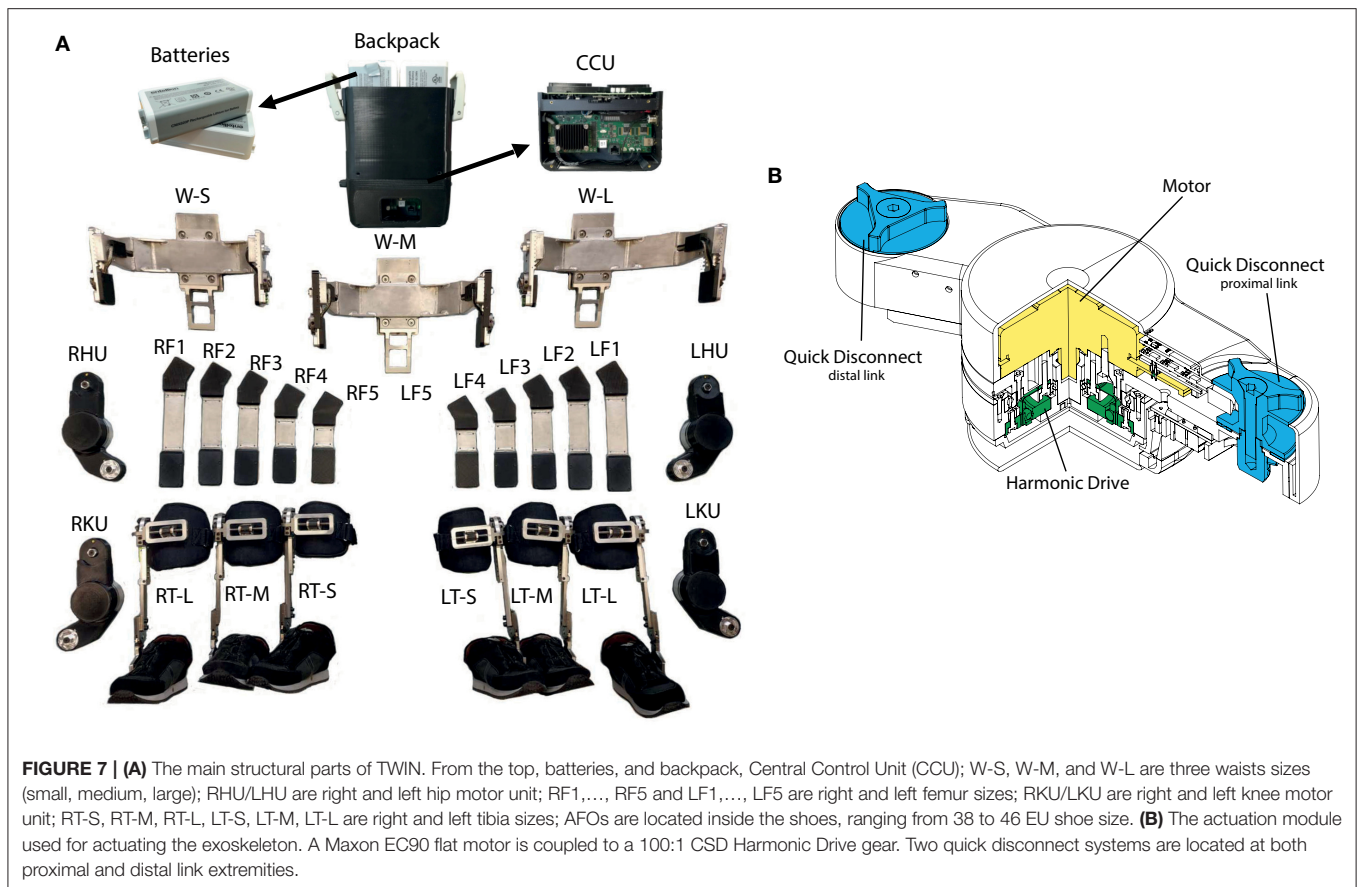
The recorded joint-space velocity-torque profiles of the knee and the hip, **Figures 6B,C**, were then scaled up to respect the patient's weight and walking speed specs set in **Table 3**, so as to properly size the motor-gearbox modules accordingly to worst-case conditions. This data was later processed by a dynamic model of the actuator module to determine an appropriate combination of motor and gearbox, which could respect the required velocity, torque and power values. A torque-velocity graph that reports the results of these simulations is shown in **Figure 6C**. All the results in **Figure 6** show that an appropriate combination to be used for the actuation of the hip and knee is composed of the brushless motor Maxon EC90 and the Harmonic Drive CSD-25-100-2A-GR-BB 100:1 gearbox. The motors employed for the knee and hip had different nominal voltages, 24 and 36 V, respectively, to meet the different torque/speed requirements of these two joints. Each motor is controlled by a custom-made board which features a PWM controlled three phase Mosfet bridge inverter, which compensates the variable input voltage with the motor control algorithm.

## Battery Units and Electronic Architecture

Regarding the battery unit, referring to requirement #5 and the specified target value set in **Table 3**, we assumed an exoskeleton's battery life of 3 h. Assuming the device operating in typical conditions, i.e., walking at the set target speed as defined in **Table 3** performed by an average european weight wearer (70.8 kg, Walpole et al., 2012), we computed the average power consumption required by the TWIN Exoskeleton to compute the task, which was about 59 W. Hence, it results that battery pack charge should be at least 177 Wh. This value, combined to a nominal voltage that is compatible with the chosen motors and a peak power output that can deal with the worst case operative conditions (subject weighing 110 kg walking at 1.5 km/h), defined the main target values for the

battery unit. We therefore designed a battery unit made by a combination of two Accutronics CMX820P Li-ion battery packs, which can deliver a total energy of 189.4 Wh and a peak power output of 482 W, with a nominal voltage of 28.8 V and maximum current peak of 15 A, which are compatible with our requirements. The batteries are mounted in a docking system that allows to change batteries when needed to simplify cabling and ease of replacement. Each pack is monitored by an internal BMS which to the motherboard via SMBus. The BMS includes safety, diagnostics, and communication functionalities. The two battery packs are paralleled by an oring ideal diode circuitry, and the current delivered to each leg is measured via shunt current monitors." Furthermore, these battery units are IEC62133 certified and can therefore assure safety of the TWIN exoskeleton accordingly with the IEC60601-1 norms.

The electronics architecture of the TWIN exoskeleton is presented in the **Supplementary Figure 1**. The main component of this system is the custom main motherboard (named SMEX in the diagram) which is based on a Xilinx Zynq-7000 SOC running a Linux OS. The SOC interfaces to a variety of sensors; including two independent IMUs, doubled for redundancy and cross checking, a battery voltage sensor and two separate leg current sensors, used for monitoring, logging, and diagnostic purposes. The custom SMEX motherboard also implements several communication peripherals, including Ethernet, Wi-Fi, and Bluetooth for diagnostics and interface to host devices (PC or tablet), two separate CAN Bus lines (one for each leg) for internal communication to the motor boards, and one SMBus line for the communication to the battery packs. The SMEX motherboard exchanges CAN bus packets with the motor control boards. Particularly, the SMEX sends to the motor control boards the reference set-points, according to the selected control strategy, while the motor control boards sends messages back regarding joint absolute position, status, and motor current readings. Each active joint features a custom motor control board, including a PWM controlled three phase Mosfet bridge inverter, to drive BLDC or PMSM motors from 18 to 60 VDC, up to 35 A motor current. The motor current is monitored via low-side shunt current monitors.



Regarding the available sensing, each joint contains a fast-shaft quadrature encoder (6,400 pulses per revolution), used for motion control, three phase hall-sensors used for commutation, and a custom slow shaft absolute potentiometer, that is used for calibration purposes and redundancy. The reference joint trajectories are treated as setpoints that are tracked by using a PI controller.

## Structure and Actuation Unit

The structure of the TWIN exoskeleton is largely made by welded Al7075 T6 aluminum alloy profiles. This choice was made to keep the overall structural weight low as well as to minimize costs as outlined by requirement #4. Four main structural parts can be identified. These are: (1) waist; (2) femur; (3) tibia; (4) foot, **Figure 7A**. The waist was designed so as to replicate a “C-shape” profile which accommodates the proportions outlined in Dreyfuss (1993). Three sizes of waist have been designed to cover the set anthropometry requirements (Dreyfuss, 1993). This part is also responsible for housing the battery pack and CCU, that are located at the back of the device in separate modules that can be disconnected separately thanks to a custom-made dock that is rigidly fixed to the waist module. This allows ease of battery replacement. The femur modules are located between the hip and the knee motors and are composed of a straight link that employs a rectangular shaped Al7075 T6 aluminum alloy profile which ends on both sides with receptacles of the

quick disconnect system. A total of six sizes of this link have been manufactured to accommodate the anatomical variation among the population with sufficient precision. Indeed, given that the gap between one size and the next is 2 cm, a maximum misalignment of 1 cm can manifest between the motor and the physiological joint<sup>1</sup>.

The tibia comes in one size that is able to fit the different patient lengths thanks to a regulation system that was designed for the purpose. The upper end mounts a quick disconnect receptacle that is employed to connect this segment to the knee motor module. The lower end of this segment connects to the foot.

The foot comprises a passive elastic ankle joint, which is then connected on its lower end to a custom carbon fiber-based footsole. Passive elasticity is implemented using a simple mechanism made of linear compression springs placed antagonistically which can be preloaded by means of two socket screws. These screws can also be employed to set the ankle joint's equilibrium point, as well as its stroke, to accommodate its configuration to each patient's need, **Figure 7A**. The ankle mechanism design was inspired by that implemented in the ReWalk exoskeleton.

<sup>1</sup>This of course holds true for measurements of the user limb lengths that are performed correctly by the clinician/physiotherapist.

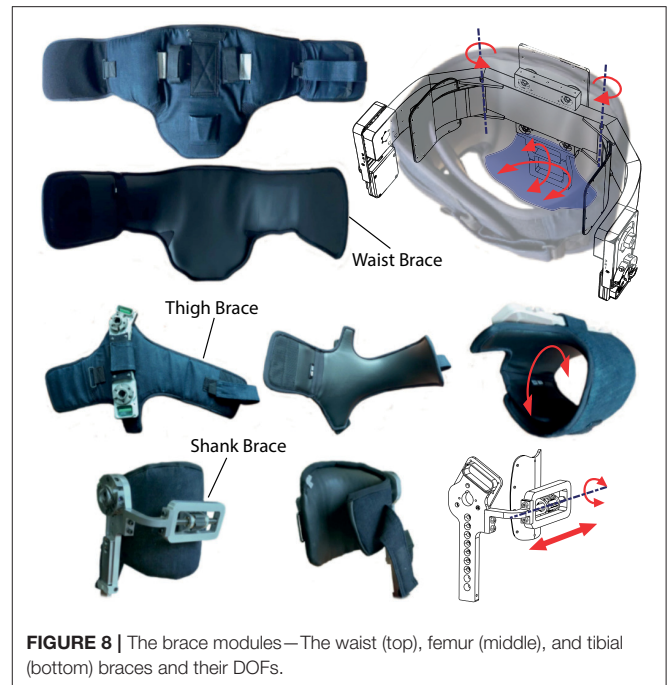
The structure has been dimensioned using the force/torque data recorded in the dummy exoskeleton in the experiments explained in section Actuator Sizing, employing a safety factor of 2.5. Finally, these calculations have been validated by means of FEM simulations.

Regarding the actuation unit, the Maxon EC90—Harmonic Drive CSD-25-100-2A-GR-BB 100:1 gearbox assembly is implemented as shown in **Figure 7B**. The proximal link is connected to the motor's frame whereas the distal link is connected to the Harmonic drive's output shaft.

## Braces

The interface between the patient and the machine stands as a critical aspect of exoskeleton development. Hence, they should converge on a variety of aspects such as: ergonomics, comfort, safety, anthropometry, and aesthetics while maintaining biomechanical and functional requirements. Although comfort did not emerge directly from the initial user need analysis phase, we implicitly took this aspect as priority during the formative phase as highlighted in section Formative Phase: Iterative Improvements of the Device where we discuss about the role of their contribution within the formative assessment of usability. Indeed, the delicate skin of SCI patients can be easily damaged by the generation of unwanted forces or pressures on the contact points. This holds true also if the user wears the braces over their own clothes as the avoidance of these unwanted effects depends on a combination of good structural design (mostly to avoid pressure concentrations in the orthogonal direction) as well as on a good choice of materials to avoid chafing effects of the brace or cloth against the user's skin. Hence, the braces must guarantee a safe and comfortable interfacing with the wearer (Requirements #6 and #7, **Table 2**) so as to in turn accommodate safe and stable walk as outlined by requirement #3. TWIN is currently equipped with a pair of thigh and shank braces for each leg and a waist brace as the uppermost connection to the patient, for a total of five human-machine interfaces **Figure 8**.

All braces employ Velcro®-based straps to achieve correct tightening during donning procedure. The inner region in contact with the patient is made of spandex material, which ensures biocompatibility and reduces shear forces on patient skin, main causes of skin lesions. The outer region is made using denim for durability. The waist brace is composed of a central portion which is directly connected to the structure by means of bolts and two lateral bands wrapped around the patient and can be tightened on the front. This brace additionally hosts a pair of stiff wings that are hinged on the waist structure and can rotate on the transverse plane: this additional DOF helps to accommodate lateral weight-shifting on the support leg during gait, while providing maximum patient-exoskeleton connection of tilting movements in the sagittal plane, achieving higher controllability of the machine's step trigger (please see section Control System). Finally, this brace houses a coccyx support connected to the waist structure, which avoids excessive lumbar hyper-lordotic postures. A semirigid shell, which can tilt in the transversal and sagittal plane, is placed on top of the coccyx support inside the brace to allow rotations of the sacrococcygeal region to avoid generation of shear stress on the patient's skin



**FIGURE 8** | The brace modules—The waist (top), femur (middle), and tibial (bottom) braces and their DOFs.

(**Figure 8**—top right). The frontal portion of the brace acts as a thoracic stabilizer preventing the patient from collapsing, which is critical for SCI patients with higher level of injury. Each thigh can partially rotate (see **Figure 8**—middle right) around the femur, which ease donning/doffing procedures. The shank brace is composed of a hinged semirigid plate which hosts the patient tibia and can tilt in the sagittal plane. The medio-lateral position of the brace can be adjusted to account for different postures or deformities in the knee joint by means of a leadscrew mechanism (see **Figure 8**—bottom right). This mechanism is inspired by that employed in the ReWalk exoskeleton shank brace design.

## CONTROL SYSTEM

As the patients targeted in this work are complete SCI, we opted for a position control-based scheme to provide full support to the patients during use. The identification of predefined gait trajectories to be employed on lower limb exoskeletons is typically obtained by fitting mathematical curves to temporal sequences of desired joint angles that are often inspired by biological gait patterns. In contrast to this, in Vassallo et al. (2020) we proposed predefined gait trajectories for the TWIN lower-limb exoskeleton, generated in Cartesian space, by using a basis function interpolation method which was designed so as to maximize stable walk as outlined by requirement #3. Such approach allows to guarantee the length and clearance of each step, despite the variation of tibia and femur lengths. Thanks to this, the trajectories are fully parametrizable to better fit user needs. In any of the gait patterns, steps are triggered by reaching a set of two torso inclination thresholds. Torso inclination



angles were measured by the IMU sensor located in backpack of the device.

## Computing the Reference Trajectory

The kinematic model of the TWIN exoskeleton is shown in **Figure 9A**. It has been developed based on Denavit-Hartenberg convention, considering the bilateral actuations of the knee and hip as  $q_1, q_3$  and  $q_2, q_4$ , respectively. Conversely, the tibia and femur links length, and hip-COM distance, are defined as  $l_T, l_F$ , and  $l_H$ . These lengths are fixed and do not change during the whole session with a patient. We define  $\theta_T$  as the tilt angle of the torso with respect to the frontal plane,  $\beta$  the flexion angle of the support ankle, and  $\theta_F$  the orientation of the swing ankle. Given the absence of sensors on the ankle joints,  $\beta$  cannot be measured. Therefore, we estimate its value, that is comprised between two values  $\beta_{\min}$  and  $\beta_{\max}$ , which are set according to the patient's need during the setup phase by using the regulation screws as explained in Section Structure and Actuation Unit.

## The Design of the Gait Pattern

The gait pattern is generated by an interpolation approach, consisting in multiplying basis functions, normalized in amplitude and over time, and depend on the desired step length  $L$  and height  $H$ . The reference trajectories are represented in the Cartesian space by the following Equations: (1)  $x_F(t) = x_F^0 + L f_x(t)$ , (2)  $z_F(t) = z_F^0 + H f_z(t)$ , (3)  $x_T(t) = x_T^0 + L g_x(t)$ , where  $(x_F, z_F)$  represent the swing foot coordinates, and  $x_T$  the torso ones.  $x_F^0, z_F^0, x_T^0$  represent the foot coordinates at the beginning of the step. The basis functions  $f_x, f_z$  define the walking shape while  $g_x$  is a 6<sup>th</sup> order polynomial. These functions are normalized and assume a value which can range from 0 to 1. A more detailed description of the definition of the basis function is given in Vassallo et al. (2020). Given the reference trajectory in the Cartesian space  $x_F, z_F, x_T$ , we compute the joint angles based on the following assumptions: (i)  $\theta_T = \beta + q_1 + q_2$  with  $\{\beta \in \mathbb{R}, \beta_{\min} \leq \beta \leq \beta_{\max}\}$ , (ii)  $\theta_T(t) = 0, \forall t \in [0, t_s]$  where  $t_s$  is the step duration.

$$q_1 = \sin^{-1} \left( \frac{x_T - (l_T \sin(\beta) + l_H \sin(\theta_T))}{l_F} \right) - \beta \quad (1)$$

$$q_2 = \theta_T - q_1 - \beta \quad (2)$$

$$q_3 = \cos^{-1} \left( \frac{a_x^2 + a_z^2 - l_F^2 - l_T^2}{2l_F l_T} \right) \quad (3)$$

$$q_4 = \tan^{-1} \left( \frac{z_F - z_T}{x_F - x_T} \right) - \tan^{-1} \left( \frac{l_T \sin(q_3)}{l_F + l_T \cos(q_3)} \right) \quad (4)$$

A representation of the gait pattern is shown in **Figures 9B,D**. Particularly, **Figure 9B** shows the basis functions, that are employed to compute the joint angle trajectories shown in **Figure 9C**. **Figure 9D** shows the corresponding cartesian representation of the foot trajectory on the sagittal plane.

An overview of the described control system is shown in **Figure 9E**: the basis function  $f_x, f_z$ , the desired step length  $L$ , the clearance  $H$ , and the step duration  $t_s$  are inputted to the high-level control, which in turn extrapolates time-continuous reference trajectories in the Cartesian space. Then, the inverse

kinematics equations of the system allow to compute the related joint angles  $q_1(t), q_2(t), q_3(t), q_4(t)$  based on the specific exoskeleton dimensions  $l_H, l_F, l_T$ . Finally, the reference joint positions are sent to the four motors via the CAN-bus. At the motor-board level, the local low-level control transforms these inputs into a PWM's duty-cycle value, which is returned by the PI controller, to drive the motor.

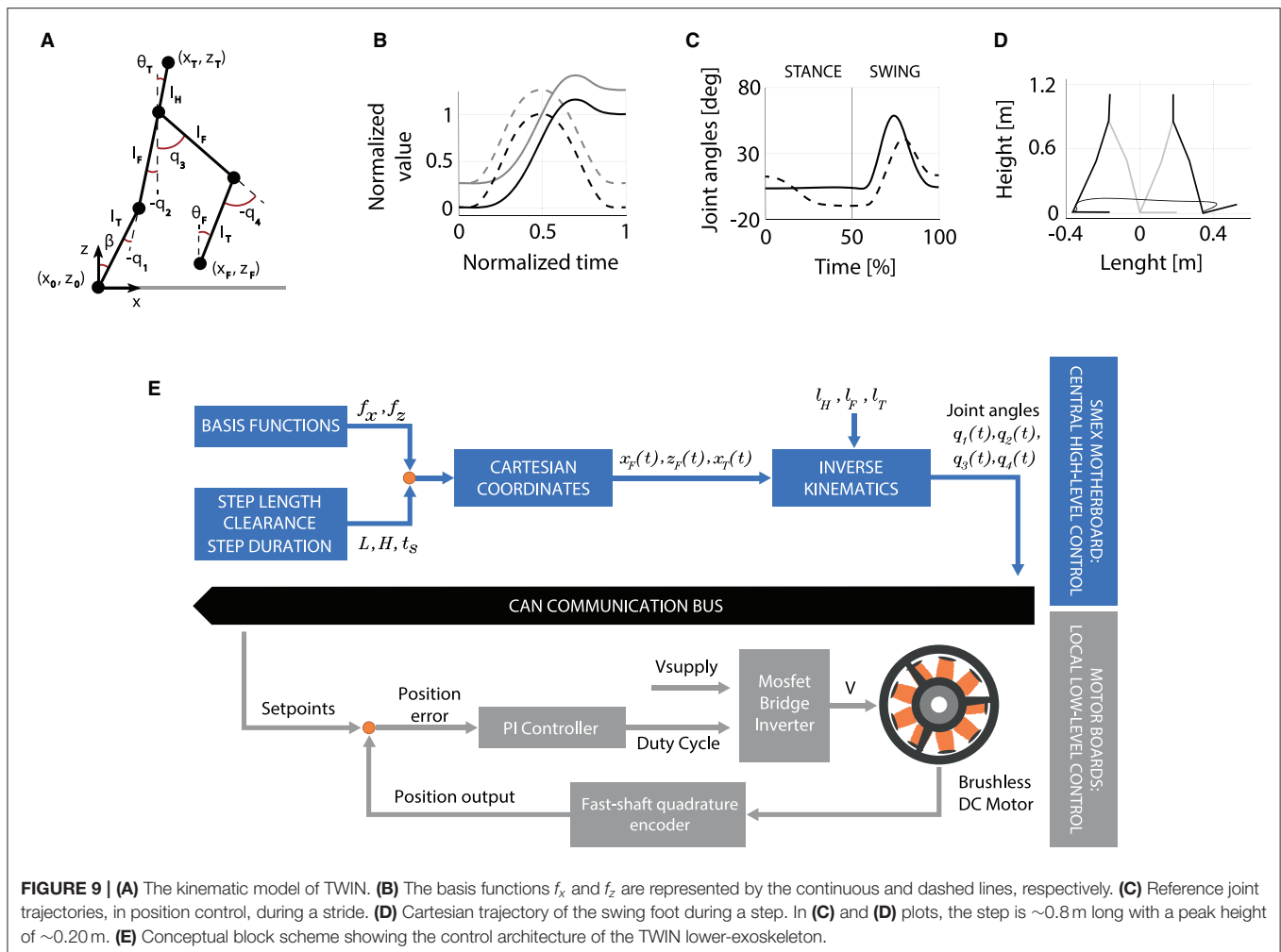
The development of the gait pattern was made to comply the following aspects: (1) stability and safety, which was priority according to requirement #3 and requirement #7, (2) similarity with those employed in existing exoskeletons, (3) experience gained in pilot trials. The resulting trajectory is characterized by a marked clearance and an emphasized heel-strike to comply with requirement #3. In fact, in humans, the heel-strike to toe-off movement has an important role, widely studied in literature: the foot arches compliance reduces metabolic energy consumption during locomotion, help balance and, consequently, improve stability (Stearne et al., 2016). Most importantly, this approach is also beneficial to the safety of the patient because it is meant to avoid the potential hazard caused by accidental stumbling (requirements #3 and #7).

## Trigger

The trigger scheme's function is to initiate steps based on the intention of the user by elaborating signals coming from the IMU sensor located in the CCU compartment. The pitch  $P$  and roll  $R$  angles are defined as the tilt of the waist unit with respect to the frontal and sagittal planes, respectively. When these angles both pass the threshold values  $P_t$  and  $R_{t\_Left}$ , or  $R_{t\_Right}$ , the step trigger is activated. These parameters can be set according to patient needs. This functionality can be observed in the plots shown in **Figure 10B**.

## MECHATRONICS SYSTEM EVALUATION

The validation of the device's mechatronics as well as a preliminary evaluation of the ergonomics and the feasibility of the designed gait trajectories have been carried out by testing the device on healthy subjects and on one SCI subject, as discussed in section Formative Phase: Iterative Improvements of the Device as part of a formative assessment of usability which focused, in this case, on the efficacy and the efficiency of the advanced prototype of TWIN which is the result of the first 36 months of development and formative phase. The subjects were asked to perform straight walk from a starting to a final point located 10 m away at their preferred speed. **Figure 10A** reports a sequence of images of the patient, while the plots of IMU data, position, torque, and of an extract of two steps are reported in **Figure 10B**. This task was freely repeated by the subject in each session—after 30 min the trials were stopped in order to monitor the conditions of the participant (especially on potentially sore areas—coccyx and tibia). The joints' torque, speed, as well as the IMU data were recorded during trials with the patient and were used to assess and validate the mechatronic design. **Figure 10B** shows the trend of lateral and frontal inclination of the exoskeleton, as well as the angular positions and torques of the joints, while the step trigger times are denoted by the vertical dotted lines.



## DISCUSSION

Thorough effort was dedicated during the whole development phase to satisfy the user-centered requirements set in the initial field research reported in **Table 2** (system portability, donning and setting autonomy, standing/walking stability, cost effectiveness, long battery life) and in the formative process (comfort, safety). These requirements involved significant implications to the mechatronics of the device according to a strict adoption of quality management system for medical devices (i.e., ISO 13485:2016), and in function of its usability, as defined by IEC 62366-1:2015. Consequently, the safety of the device (Requirement #7) was tested according to the IEC 60601 safety standards, while other usability-related aspects, like comfort, were assessed by means of a periodical analysis of feedback from both expert clinicians and users. Furthermore, a preliminary clinical evaluation was conducted on one SCI subject for a first field test of the whole system, while TWIN's distinctive features with respect to both commercial and research exoskeletons have been considered in the evaluation. These investigations enriched the formative assessment itself by exploiting user research to iteratively improve the different prototype versions of the TWIN

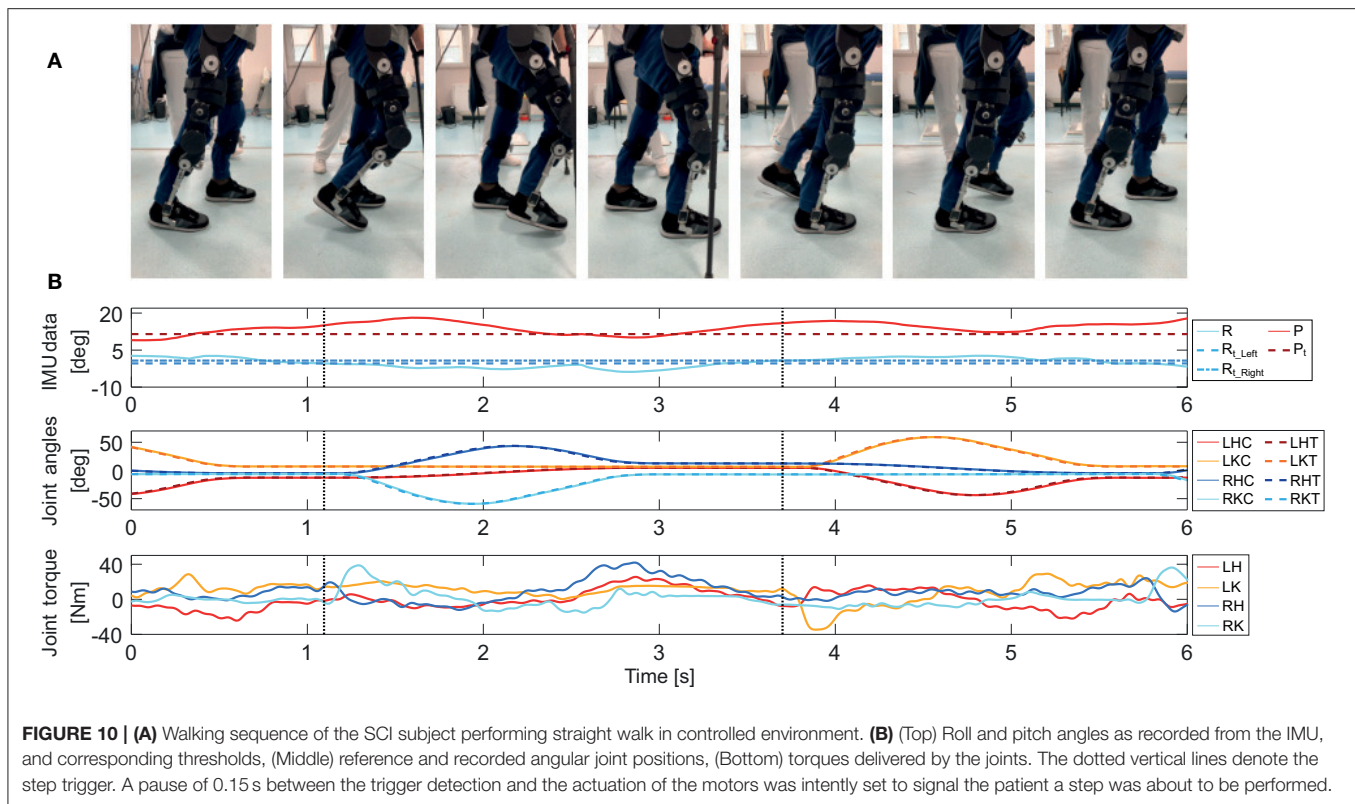
system as required by the standards of IEC for the usability engineering of medical devices.

Regarding comfort, i.e., Requirement #6, the SCI user verbally expressed high appreciation of our bracing system compared to the exoskeleton he daily uses at home, i.e., ReWalk. The user also did not report any skin injuries in the points of contact with the exoskeleton and no signs of lesion in the critically stressed areas (tibial tuberosity and sacrococcygeal). Similar positive feedback was also given by clinicians, which confirmed its suitability to operate on the delicate skin of SCI subjects. Of course, this cannot be considered as definitive validation but is in fact taken as an initial positive result to feed further iterations of the formative assessment.

Another significant outcome of the clinical test on the SCI subject is that TWIN's trajectory patterns facilitate the stability of the user due to its emphasized heel strike, as explained in detail in our previous work (Vassallo et al., 2020) and this is agreeable with respect to usability too.

Finally, from the mechatronic perspective, plots from the clinical trial on the SCI patient (**Figure 10**) demonstrate that the system can track the trajectory imposed by the CCU for straight walking at 0.35 m/s. At the same time, the delivered





**FIGURE 10 | (A)** Walking sequence of the SCI subject performing straight walk in controlled environment. **(B)** (Top) Roll and pitch angles as recorded from the IMU, and corresponding thresholds, (Middle) reference and recorded angular joint positions, (Bottom) torques delivered by the joints. The dotted vertical lines denote the step trigger. A pause of 0.15 s between the trigger detection and the actuation of the motors was intentionally set to signal the patient a step was about to be performed.

torques are below the nominal torque of the Harmonic drive and well below the peak torque value of 110 Nm. Furthermore, the values of delivered current are within the continuous operation limits of the motors and do not generate heat during functioning, meaning that the actuators operate in their nominal range. This safe operating condition, which is well-below the mechatronic operational limits of the exoskeleton, occurs because the device was operating under the following conditions: (1) the user was an expert exoskeleton user and knew how to use the machine with confidence, (2) the walking speed was about one third of the maximum allowable speed, (3) the task was performed by a user weighing 63% of the maximum allowable weight. Although further trials will be needed to validate this design, e.g., on patients with higher weight, and at higher walking speed, the obtained results are a clear indication that the mechatronic design is reasonably sized.

Furthermore, comparing TWIN with the state of the art, and focusing specifically on the requirements initially outlined in **Table 2**, we can state that Indego is the exoskeleton which best managed to address Requirements #1 and #2 (Lightweight and autonomous portability, Quick and autonomous donning, respectively), among existing commercial and research devices. In order to improve these characteristics, TWIN introduced a novel design primarily addressed to maximize autonomous use by developing a structure characterized by a higher number of modules with respect to the Indego exoskeleton, coupled with an unconventional lateral mounting solution. These features can greatly facilitate donning and allow the user to mount the modules according to the sequence that

can best adapt to the context. In addition, although we slightly exceeded the target weight (TWIN weighs 23 kg), high modularity allows users to keep the lightest (9.8 kg, i.e., 43% of the total weight) and most comfortable modules donned on when the exoskeleton is not in use, accordingly with the considerations made in sections Concept Layout Design and Iterative Co-Creation Process. We hence argue that this solution considerably simplifies autonomy of use and transportation, with the goal of facilitating independent domestic usage that is paramount to guarantee high frequency of use and therefore maximize the benefit provided by the exoskeleton training.

Regarding other requirements, most commercial exoskeletons, such as the Ekso, ReWalk, Indego, to name a few, present battery life that is lower than the target imposed by Requirement #5. Hence, TWIN also offers advantages in terms of battery life, allowing the user to make longer exoskeleton sessions, hence facilitating intensive training.

Regarding Requirement #3, all the cited exoskeletons, to the best of our knowledge, can guarantee stability when standing, whereas a dedicated comparative study would be needed to draft conclusions on walking stability. Nevertheless, we argue that, compared to the “traditional” patterns adopted by e.g., ReWalk or TWICE, the trajectory designed for TWIN may bring additional benefits related to stability because of its emphasized heel-strike which also facilitates stumble-free walking patterns (Vassallo et al., 2020).

Furthermore, considering all existing exoskeletons, there is still room for improvement on requirement #4, i.e., cost

effectiveness. Indeed, although exoskeleton companies are striving to keep low costs, the current market price of these devices make them hardly affordable to the average user. Regarding TWIN, the strategic choice to adopt standard and low-cost components in the device design will allow to set a highly competitive target price in TWIN, which will be close to that of the most inexpensive commercial lower limb exoskeletons.

To provide a general overview of the differences of TWIN's design concept and related priorities we can state that other designs might endow a stable standing/walking, cost effectiveness, long battery life, high comfort, high safety, (i.e., req. #3–7). However, most of these priorities are not jointly considered in a “holistic” way and, in most cases, are not meant to directly tackle autonomous portability and, related to this, quick and autonomous donning and setup (req. #1, 2). An exception can be made for the Indego exoskeleton which adopted a similar modular design strategy to that of TWIN, as explained in section Concept Layout Design and Iterative Co-Creation Process.

Finally, we argue that the employed user-centered approach very much fits the development of healthcare robots such as exoskeletons. Indeed, we experienced great effectiveness to plan and continuously adapt design goals and activities toward the satisfaction of user needs. In addition to this, the employed approach has demonstrated to provide a vast number of insights that drove technological as well as design choices.

## CONCLUSIONS

This work presented the design of TWIN, a novel lower limb exoskeleton for personal use of SCI subjects, and the user-centered design approach adopted for its development. This device is the result of a joint effort coming from a tight cooperation between engineers, industrial designers, physical therapists, physiatrists, and SCI patients, which jointly cooperated in an iterative development process, which started with the definition of a set of five user-centered design principles, that were subsequently integrated by two other requirements that emerged during the formative processes. An initial concept layout analysis was presented to show how this device was conceived to maximize usability. The consequent advantages and novelty of the proposed solution, which is mainly based on high modularity and lateral mounting, were highlighted, especially considering the state of the art. A series of iterative tests were implemented as part of the formative evaluation of TWIN, following the requirements established worldwide by IEC 62366-1:2015 for the usability engineering of medical devices. Moreover, preliminary results showed that the device mechatronics is capable of delivering the torque/speed profiles required for a typical exoskeleton session. Overall, the device was assessed positively by the SCI subject and expert clinicians, from both the comfort/ergonomics perspective and feasibility of the walking pattern. From this initial assessment and discussions with users and experts in the field, we claim that the successful design of personal aids must rely on detailed analyses of the needs

and the lifestyle of users. Indeed, user-centered design techniques require the implementation of careful analyses of users' need before the design of any prototype. Similarly, the formative assessment needs to be executed since the very beginning and throughout the whole development process. We believe this can only be achieved by means of a rigorous application of user-centered design and co-development approaches, as presented in this work.

Future work on TWIN will include the summative assessment of the device and its clinical evaluation on a larger subject population. In this future study, specific focus will be devoted to the quantitative evaluation of usability.

## DATA AVAILABILITY STATEMENT

The original contributions presented in the study are included in the article/**Supplementary Material**, further inquiries can be directed to the corresponding author/s.

## ETHICS STATEMENT

The studies involving human participants were reviewed and approved by Comitato Etico Interaziendale Bologna-Imola of the Pharmaceutical Department U.O.C. Farmacia Ospedale Maggiore, Bologna, Italy. The patients/participants provided their written informed consent to participate in this study. Written informed consent was obtained from the individual(s) for the publication of any potentially identifiable images or data included in this article.

## AUTHOR CONTRIBUTIONS

ML and JS conceived the study. ML wrote the first draft of this manuscript. SD'A, CV, CP, MC, SD, MD, AS, SC, GC, SS, LC, NB, CM, JS, EGu, GB, MS, ST, SM, FM, RS, EGr, and LD wrote sections of this manuscript. All authors contributed to the revision of this manuscript, and they read and approved its submitted version.

## FUNDING

This work was funded by the Istituto Nazionale per la Assicurazione contro gli Infortuni sul Lavoro (INAIL) under grant agreements POR-1 and POR-AI 1/1.

## ACKNOWLEDGMENTS

We thank Valentina Pericu and Riccardo Vaccaro for their support in the experimental data analysis and preparation of the graphical material.

## SUPPLEMENTARY MATERIAL

The Supplementary Material for this article can be found online at: <https://www.frontiersin.org/articles/10.3389/fnbot.2021.709731/full#supplementary-material>

## REFERENCES

- Berkowitz, M., O'Leary, P. K., Kruse, D. L., and Harvey, C. (1998). *Spinal Cord Injury: An Analysis of Medical and Social Costs*. New York, NY: Demos Medical Publishing.
- Bitkina, O. V., Kim, H. K., and Park, J. (2020). Usability and user experience of medical devices: an overview of the current state, analysis methodologies, and future challenges. *Int. J. Ind. Ergon.* 76, 102932. doi: 10.1016/j.ergon.2020.102932
- Brooke, J. (1996). "SUS-A quick and dirty usability scale," in *Usability Evaluation in Industry*, Vol. 189, eds B. A. Weerdmeester, I. L. McClelland, P. W. Jordan, and B. Thomas (London: CRC Press), 4–7.
- Chandran, S., Al-Sa'di, A., and Ahmad, E. (2020). "Exploring user centered design in healthcare: a literature review," *Paper Presented at the 2020 4th International Symposium on Multidisciplinary Studies and Innovative Technologies (ISMSIT)* (Istanbul). doi: 10.1109/ISMSIT50672.2020.9255313
- Dreyfuss, H. (1993). *The Measure of Man and Woman: Human Factors in Design*. New York: Whitney Library of Design.
- Esquenazi, A., Talaty, M., Packel, A., and Saulino, M. (2012). The ReWalk powered exoskeleton to restore ambulatory function to individuals with thoracic-level motor-complete spinal cord injury. *Am. J. Phys. Med. Rehabil.* 91, 911–921. doi: 10.1097/PHM.0b013e318269d9a3
- Farris, R. J., Quintero, H. A., Murray, S. A., Ha, K. H., Hartigan, C., and Goldfarb, M. (2014). A preliminary assessment of legged mobility provided by a lower limb exoskeleton for persons with paraplegia. *IEEE Trans. Neural Syst. Rehabil. Eng.* 22, 482–490. doi: 10.1109/TNSRE.2013.2268320
- Foulds, H. J. A., Bredin, S. S. D., Charlesworth, S. A., Ivey, A. C., and Warburton, D. E. R. (2014). Exercise volume and intensity: a dose–response relationship with health benefits. *Eur. J. Appl. Physiol.* 114, 1563–1571. doi: 10.1007/s00421-014-2887-9
- Fritz, H., Patzer, D., and Galen, S. S. (2019). Robotic exoskeletons for reengaging in everyday activities: promises, pitfalls, and opportunities. *Disabil. Rehabil.* 41, 560–563. doi: 10.1080/09638288.2017.1398786
- Gorgey, A. S. (2018). Robotic exoskeletons: the current pros and cons. *World J. Orthop.* 9, 112–119. doi: 10.5312/wjo.v9.i9.112
- Hart, S. G., and Staveland, L. E. (1988). Development of NASA-TLX (Task Load Index): results of empirical and theoretical research. *Adv. Psychol.* 52, 139–183. doi: 10.1016/S0166-4115(08)62386-9
- IEC. (2020). 60601-1:2020 *Medical Electrical Equipment*. IEC.
- Kendler, J., and Strohlic, A. Y. (2015). *Usability Testing of Medical Devices*. Boca Raton, FL: CRC Press.
- Kozlowski, A., Bryce, T., and Dijkers, M. (2015). Time and effort required by persons with spinal cord injury to learn to use a powered exoskeleton for assisted walking. *Top. Spinal Cord Inj. Rehabil.* 21, 110–121. doi: 10.1310/sci2102-110
- Lajeunesse, V., Vincent, C., Routhier, F., Careau, E., and Michaud, F. (2016). Exoskeletons' design and usefulness evidence according to a systematic review of lower limb exoskeletons used for functional mobility by people with spinal cord injury. *Disabil. Rehabil. Assist. Technol.* 11, 535–547. doi: 10.3109/17483107.2015.1080766
- Martin, J. L., Murphy, E., Crowe, J. A., and Norris, B. J. (2006). Capturing user requirements in medical device development: the role of ergonomics. *Physiol. Meas.* 27, R49. doi: 10.1088/0967-3334/27/8/R01
- Masia, L., and Vitiello, N. (2020). The long and winding road to symbiotic wearable robotics [young professionals]. *IEEE Robot. Automat. Magaz.* 27, 9–9. doi: 10.1109/MRA.2020.2967007
- Meijneke, C., van Oort, G., Sluiter, V., van Asseldonk, E., Tagliamonte N. L., Tamburella, F., et al. (2021). Symbion exoskeleton: design, control, and evaluation of a modular exoskeleton for incomplete and complete spinal cord injured individuals. *IEEE Trans. Neural Syst. Rehabil. Eng.* 29, 330–339. doi: 10.1109/TNSRE.2021.3049960
- Milia, P., De Salvo, F., Caserio, M., Cope, T., Weber, P., Santella, C., et al. (2016). Neurorehabilitation in paraplegic patients with an active powered exoskeleton (Ekso). *Digit. Med.* 2, 163–168. doi: 10.4103/digm.digm\_51\_16
- Pagliacci, M. C., Celani, M. G., Zampolini, M., Spizzichino, L., Franceschini, M., Baratta, S., et al. (2003). An Italian survey of traumatic spinal cord injury. The Gruppo Italiano Studio Epidemiologico Mielolesioni study. *Arch. Phys. Med. Rehabil.* 84, 1266–1275. doi: 10.1016/S0003-9993(03)00234-X
- Privitera, M. B., Evans, M., and Southee, D. (2017). Human factors in the design of medical devices—approaches to meeting international standards in the European Union and USA. *Appl. Ergon.* 59, 251–263. doi: 10.1016/j.apergo.2016.08.034
- Scherer, D., and Gouveia Filho, F. F. (2019). "Documentation template for the usability engineering process for medical devices," *Paper Presented at the World Congress on Medical Physics and Biomedical Engineering 2018* (Prague). doi: 10.1007/978-981-10-9038-7\_13
- Shah, S. G. S., and Robinson, I. (2008). Medical device technologies: who is the user? *Int. J. Healthcare Technol. Manage.* 9, 181–197. doi: 10.1504/IJHTM.2008.017372
- Simonsen, J., and Hertzum, M. (2010). "Iterative participatory design," in *Design Research* (Evanston, IL: Routledge), 34–50.
- Stearne, S. M., McDonald, K. A., Alderson, J. A., North, I., Oxnard, C. E., and Rubenson, J. (2016). The foot's arch and the energetics of human locomotion. *Sci. Rep.* 6, 19403. doi: 10.1038/srep19403
- Vassallo, C., De Giuseppe, S., Piezzo, C., Maludrottu, S., Cerruti, G., D'Angelo, M. L., et al. (2020). "Gait patterns generation based on basis functions interpolation for the TWIN lower-limb exoskeleton\*," *Paper Presented at the 2020 IEEE International Conference on Robotics and Automation (ICRA)* (Paris). doi: 10.1109/ICRA40945.2020.9197250
- Walpole, S. C., Prieto-Merino, D., Edwards, P., Cleland, J., Stevens, G., and Roberts, I. (2012). The weight of nations: an estimation of adult human biomass. *BMC Public Health* 12, 439. doi: 10.1186/1471-2458-12-439
- Wang, S., Wang, L., Meijneke, C., Asseldonk, E. V., Hoellinger, T., Cheron, G., et al. (2015). Design and control of the MINDWALKER exoskeleton. *IEEE Trans. Neural Syst. Rehabil. Eng.* 23, 277–286. doi: 10.1109/TNSRE.2014.2365697
- WHO. (2013). *International Perspectives on Spinal Cord Injury*. Available online at: [https://apps.who.int/iris/bitstream/handle/10665/94190/9789241564663\\_eng.pdf;jsessionid=\\$E0B957D71C282E0B658CF8C650A94C82?sequence=\\$1](https://apps.who.int/iris/bitstream/handle/10665/94190/9789241564663_eng.pdf;jsessionid=$E0B957D71C282E0B658CF8C650A94C82?sequence=$1)

**Conflict of Interest:** The authors declare that the research was conducted in the absence of any commercial or financial relationships that could be construed as a potential conflict of interest.

**Publisher's Note:** All claims expressed in this article are solely those of the authors and do not necessarily represent those of their affiliated organizations, or those of the publisher, the editors and the reviewers. Any product that may be evaluated in this article, or claim that may be made by its manufacturer, is not guaranteed or endorsed by the publisher.

Copyright © 2021 Laffranchi, D'Angella, Vassallo, Piezzo, Canepa, De Giuseppe, Di Salvo, Succi, Cappa, Cerruti, Scarpetta, Cavallaro, Boccardo, D'Angelo, Marchese, Saglia, Guanzioroli, Barresi, Semprini, Traverso, Maludrottu, Molteni, Sacchetti, Gruppioni and De Micheli. This is an open-access article distributed under the terms of the Creative Commons Attribution License (CC BY). The use, distribution or reproduction in other forums is permitted, provided the original author(s) and the copyright owner(s) are credited and that the original publication in this journal is cited, in accordance with accepted academic practice. No use, distribution or reproduction is permitted which does not comply with these terms.



# Wearable Robots: An Original Mechatronic Design of a Hand Exoskeleton for Assistive and Rehabilitative Purposes

Nicola Secciani<sup>1\*</sup>, Chiara Brogi<sup>1</sup>, Marco Pagliai<sup>1</sup>, Francesco Buonamici<sup>1</sup>, Filippo Gerli<sup>2</sup>, Federica Vannetti<sup>2</sup>, Massimo Bianchini<sup>3</sup>, Yary Volpe<sup>1</sup> and Alessandro Ridolfi<sup>1</sup>

<sup>1</sup> Department of Industrial Engineering, University of Florence, Firenze, Italy, <sup>2</sup> IRCCS Don Gnocchi, Don Carlo Gnocchi Foundation, Firenze, Italy, <sup>3</sup> Institute for Complex Systems, National Research Council, Sesto Fiorentino, Italy

## OPEN ACCESS

### Edited by:

Luciano Luporini Menegaldo,  
Federal University of Rio de Janeiro,  
Brazil

### Reviewed by:

Maria Elizete Kunkel,  
Federal University of São Paulo, Brazil  
Chad Gregory Rose,  
Auburn University, United States

### \*Correspondence:

Nicola Secciani  
nicola.secciani@unifi.it

**Received:** 30 July 2021

**Accepted:** 15 September 2021

**Published:** 21 October 2021

### Citation:

Secciani N, Brogi C, Pagliai M, Buonamici F, Gerli F, Vannetti F, Bianchini M, Volpe Y and Ridolfi A (2021) Wearable Robots: An Original Mechatronic Design of a Hand Exoskeleton for Assistive and Rehabilitative Purposes. *Front. Neurobot.* 15:750385. doi: 10.3389/fnbot.2021.750385

Robotic devices are being employed in more and more sectors to enhance, streamline, and augment the outcomes of a wide variety of human activities. Wearable robots arise indeed as of-vital-importance tools for telerehabilitation or home assistance targeting people affected by motor disabilities. In particular, the field of “Robotics for Medicine and Healthcare” is attracting growing interest. The development of such devices is a primarily addressed topic since the increasing number of people in need of rehabilitation or assistive therapies (due to population aging) growingly weighs on the healthcare systems of the nation. Besides, the necessity to move to clinics represents an additional logistic burden for patients and their families. Among the various body parts, the hand is specially investigated since it most ensures the independence of an individual, and thus, the restoration of its dexterity is considered a high priority. In this study, the authors present the development of a fully wearable, portable, and tailor-made hand exoskeleton designed for both home assistance and telerehabilitation. Its purpose is either to assist patients during activities of daily living by running a real-time intention detection algorithm or to be used for remotely supervised or unsupervised rehabilitation sessions by performing exercises preset by therapists. Throughout the mechatronic design process, special attention has been paid to the complete wearability and comfort of the system to produce a user-friendly device capable of assisting people in their daily life or enabling recorded home rehabilitation sessions allowing the therapist to monitor the state evolution of the patient. Such a hand exoskeleton system has been designed, manufactured, and preliminarily tested on a subject affected by spinal muscular atrophy, and some results are reported at the end of the article.

**Keywords:** wearable robot, hand exoskeleton, telerehabilitation, home assistance, mechatronics design, robotics

## 1. INTRODUCTION

The demographic, economic, social, technological, environmental, and political factors (DESTEP factors) of the last decades of the twentieth century and the first years of the twenty-first century have paved the way to the advent of Robotics for Medicine and Healthcare (Butter et al., 2008). These factors have driven a breakneck growth of robotic systems for medical purposes—equipment,



treatment, and rehabilitation. The most significant innovation and development areas are prevention and diagnostics, professional care support, surgery, assistance, and rehabilitation for disabled or chronically ill patients. WHO estimates that over 1 billion people live with disabilities<sup>1</sup>. Such a number is bound to rise because of population aging and the significant increase in chronic disorders (non-communicable diseases), for which, according to WHO<sup>2</sup>, almost 15 million people die every year, and many others lose their mobility functions. Upper-limb functions loss is one of the most impairing disabilities caused by diseases or traumas, and their recovery is seen as a rehabilitation priority (Anderson, 2004; Huang et al., 2017). For this reason, upper-limb devices, hand ones particularly, have exceptional attention in the field of Robotics for Medicine and Healthcare (Duruoz, 2016), which is arising as a powerful tool to overcome some primary limits of the standard Assistive Technology (AT).

Over the years, many different devices have been developed to recover hand functions and restore the life quality of impaired people. Some of these are already commercially available, e.g., *HandyRehab* from Zunosaki<sup>3</sup>, *exomotion*® from HKK Bionics<sup>4</sup>, *Carbonhand* from Bioservo Technologies<sup>5</sup>, or *Neomano* from neofect<sup>6</sup>. Despite their significant variability, such devices have in common some requirements (Sarac et al., 2019), such as: (i) being correctly coupled with the assisted hand; (ii) ensuring user safety and comfort; (iii) being effective in force transmission; and (iv) being as affordable and available as possible. A wide range of Hand Exoskeleton Systems (HESs), achieving at least one of these requirements, are suggested in the literature and can be distinguished according to different aspects, typically the aim, the assisted movements, mechanical design, actuation, and control systems (Troncossi et al., 2016; Meng et al., 2017; Sarac et al., 2019; Desplenter et al., 2020).

Concerning the aim, such devices can have mainly rehabilitative (Dovat et al., 2008; Tong et al., 2010; Ho et al., 2011; Lamercy et al., 2013; Cempini et al., 2014; Polygerinos et al., 2015; Diez et al., 2018; Putzu et al., 2018; Wang et al., 2018; Bouteraa et al., 2019) and assistive (In et al., 2015; Randazzo et al., 2017; Yun et al., 2017; Cappello et al., 2018; Hadi et al., 2018; Yu et al., 2019; Dittli et al., 2020; Yurkewich et al., 2020) purposes. Exoskeletons or end-effector rehabilitation robots are used for treatments—typically in clinical settings—to recover from the loss of motor functions (Maciejasz et al., 2014; Zhang et al., 2018). They are designed for repetitive training during therapies and, thus, to perform specific movements and exert high forces. Most of these have no dimension limitations since their portability is not mandatory, even if it is still preferable, e.g., the already commercially available *Gloreha* from Idrogenet<sup>7</sup> (Milia

et al., 2019) or *InMotion*® ARM from Bionick<sup>8</sup>. Their clinical outcomes are considered highly dependent on the mechanical design, the interaction with the patient, the adopted training mode, its duration and intensity, and the patient state (Huang et al., 2017; Zhang et al., 2018; Rodgers et al., 2019). Assistive devices are designed instead to help the users in the Activities of Daily Living (ADLs) (Sarac et al., 2019), e.g., holding a bottle of water or opening a door, by responding to their intentions. Therefore, they shall be comfortable to wear, lightweight, less bulky as possible while still exerting enough force to assist the wearer effectively. Moreover, they shall not force the hand in wrong poses and preserve the sense of touch. At the best of their capabilities, assistive HESs should allow movements as a healthy hand could make alone.

Recently, such a distinction is no longer clear-cut. Indeed, more wearable and portable devices make possible rehabilitation therapy in different environments from the clinical one (e.g., at home), reducing the burden on therapists or in-patient facilities (Huang et al., 2017). Besides, devices designed for assistance or at-home rehabilitation (Lamercy et al., 2013; Polygerinos et al., 2015; Randazzo et al., 2017; Cappello et al., 2018; Putzu et al., 2018; Wang et al., 2018; Bouteraa et al., 2019; Dittli et al., 2020; Yurkewich et al., 2020) can always be available for the patient, who may find it stimulating and motivating to perform these therapies in a home setting by playing a computer game or during typical ADLs (Butter et al., 2008; Maciejasz et al., 2014). Despite the significant results achieved, robot-assisted and home-based therapy effectiveness remains an open research topic (Maciejasz et al., 2014; Huang et al., 2017; Duret et al., 2019).

More designing aspects can also distinguish HESs. Regarding the assisted movements, the number of driven fingers—usually defining the number of independent motors, unless passive couplings between fingers are used—the Degrees Of Freedom (DOFs), and the interactions between hand and exoskeleton may differ. In particular, HESs can have a single interaction point on each finger, in the case of single-phalanx mechanisms (Dovat et al., 2008), or more than one, in multi-phalanx configurations (Tong et al., 2010; Ho et al., 2011; Lamercy et al., 2013; Cempini et al., 2014; Yun et al., 2017; Diez et al., 2018; Wang et al., 2018; Bouteraa et al., 2019; Dittli et al., 2020).

Also, different mechanical designs are commonly classified according to the strategies for placing the device on the hand and fingers, e.g., on the palm (Bouzit et al., 2002; Putzu et al., 2018), the back, as most of the presented solutions, or even involving the finger sides (Lamercy et al., 2013; Cempini et al., 2014; Yu et al., 2019). In addition, they can be rigid or soft exoskeletons. The first ones (Bouzit et al., 2002; Tong et al., 2010; Ho et al., 2011; Lamercy et al., 2013; Cempini et al., 2014; Yun et al., 2017; Diez et al., 2018; Wang et al., 2018; Bouteraa et al., 2019) are made of metal or plastic, transmit motion through rigid kinematic chains, and usually exert higher force than soft ones (Chiaradia et al., 2018; Chu and Patterson, 2018). Indeed, on the other side, these are made of flexible materials (In et al., 2015; Polygerinos et al., 2015; Randazzo et al., 2017; Cappello et al., 2018; Hadi et al., 2018; Putzu et al., 2018; Yu et al., 2019; Dittli et al., 2020; Yurkewich

<sup>1</sup><https://www.who.int/health-topics/disability> (accessed August 31, 2021).

<sup>2</sup><https://www.who.int/news-room/fact-sheets/detail/noncommunicable-diseases> (accessed August 31, 2021).

<sup>3</sup><https://handyrehab.com> (accessed August 31, 2021).

<sup>4</sup><https://www.hkk-bionics.de/en/exomotion-en> (accessed August 31, 2021).

<sup>5</sup><https://www.bioservo.com/healthcare/carbonhand> (accessed August 31, 2021).

<sup>6</sup><https://www.neofect.com/us/neomano> (accessed August 31, 2021).

<sup>7</sup><https://www.gloreha.com/?lang=it> (Accessed August 31, 2021).

<sup>8</sup><https://www.bioniklabs.com/products/inmotion-arm> (accessed August 31, 2021).



**TABLE 1** | The table shows the comparison between some of the most interesting assistive and rehabilitative hand exoskeletons at the current state of the art.

Devices	Actuated fingers	Wearability	Exerted force [N]	Mass [g]	Intention detection method
Ho et al. (2011)	All	/	/	500	sEMG
In et al. (2015)	Index, middle	Yes (*)	9–12	194	Wrist motion
Polygerinos et al. (2015)	All	Yes (*)	8	285	Force, position
Randazzo et al. (2017)	All	Yes (*)	5	50	EEG activity
Yun et al. (2017)	Thumb, Index, Middle	Yes (*)	/	319	sEMG
Diez et al. (2018)	All	No	12,5	/	Force, position
Hadi et al. (2018)	All	/	8	300	/
Rose and O'alley (2018)	All	Yes (*)	40	220	sEMG
Wang et al. (2018)	All	/	/	420	sEMG, voice control
Bouteraa et al. (2019)	All	Yes	/	388	sEMG
Yu et al. (2019)	All	No	22	300	/
Dittli et al. (2020)	All except for the thumb	Yes (*)	/	113	sEMG
Yurkewich et al. (2020)	All	Yes	/	377	sEMG
Carbonhand	Thumb, middle, ring	Yes (*)	5–8	85	Force
exomotion®	All	Yes (*)	/	/	Impulses of an active muscle
HandyRehab	All	Yes	/	380	sEMG
Neomano	Thumb, index, middle	Yes (*)	20	105	/

(\*) some of the parts of the HES—e.g., the power supply or actuation system—are dislocated from the hand.

et al., 2020) and are smaller and lighter than rigid ones. Recently, first hybrid solutions have been studied (Rose and O'alley, 2018) aiming to exploit the strengths of both.

Hand Exoskeleton Systems also depend on the actuation system, which can be electrical (Tong et al., 2010; Ho et al., 2011; Lambercy et al., 2013; Cempini et al., 2014; Randazzo et al., 2017; Yun et al., 2017; Diez et al., 2018; Wang et al., 2018; Bouteraa et al., 2019; Dittli et al., 2020; Yurkewich et al., 2020), pneumatic (Bouzit et al., 2002; Cappello et al., 2018; Putzu et al., 2018), hydraulic (Polygerinos et al., 2015), or realized through different working principles, e.g., using shape memory alloy actuators (Hadi et al., 2018).

Finally, exoskeletons differ in the employed method and sensors for finger pose tracking during operation, e.g., optical, flex, magnetic sensors, or finger exerted forces measuring. Such devices might also be passive or active, and they might be distinguished in the way of detecting the user intentions near correctly as possible, e.g., using surface ElectroMyoGraphic (sEMG) signals (Ho et al., 2011; Meng et al., 2017; Yun et al., 2017; Rose and O'alley, 2018; Wang et al., 2018; Bouteraa et al., 2019; Dittli et al., 2020; Yurkewich et al., 2020).

Although many alternatives exist in the literature, not all of them are fully wearable and portable solutions. It is reasonable to state that the more compact, light weight, and standalone the device, the better the wearability. Furthermore, preserving the user freedom of movement and comfort is crucial for these tools to be handy. Indeed, these are critical features that profoundly affect such device characterization (Desplenter et al., 2020), allowing them to broaden their application fields. A solution that concentrates its components as much as possible on the assisted limb is preferable concerning wearability and portability to those that displace some units (e.g., actuation or power supply) to other body parts, limiting freedom of motion (Desplenter

et al., 2020) [e.g., in a waist belt (Polygerinos et al., 2015), in the arm (In et al., 2015), in the back (Rose and O'alley, 2018; Dittli et al., 2020), and in the chest (Randazzo et al., 2017)]. For instance, forces exerted by soft structures might be increased by exploiting pneumatic or hydraulic actuators. However, these also augment the overall device weight, requiring different placement typically for both the actuators and control units (Polygerinos et al., 2015), thus limiting the user mobility. Significantly, a fully wearable and portable device can help the patient in ADLs and make available rehabilitation training in most places of daily life and thus also at home (Chu and Patterson, 2018; Wang et al., 2018). Depending on the patient state, this might prevent the constant therapist presence, who would nevertheless have to assess the rehabilitation progress periodically and guide the following training. It might reduce both the device and treatment cost and facilitate repetitive training (Huang et al., 2017).

**Table 1** summarizes some characteristics (of interest for the focus of the discussion proposed in this study) of the leading current state-of-the-art assistive and portable rehabilitation devices and some also commercially available: the actuated fingers, wearability, exerted forces, weight on the hand, and intention detection method.

The research activities of the Mechatronics and Dynamic Modeling Laboratory (MDM Lab) at the Department of Industrial Engineering (DIEF) at the University of Florence (UNIFI) have been focusing on wearable devices since 2013. The research team has developed several versions of a HES (Secciani et al., 2018), whose primary purpose is to assist users in ADLs. More strict requirements for the assistance aim led to this choice. However, such a device can also be used for rehabilitative purposes. Indeed, some preliminary tests on the patient with the HES have been carried out in a clinical setting, like a rehabilitation session, proving the device effectiveness

in assisting the user in ADLs (Secciani et al., 2019). Despite promising results, the developed prototypes all presented gaps that did not allow them to be fully wearable solutions.

Conversely, the version (Secciani et al., 2021), presented in detail here, embodies the evolution of the previous designs to overcome such wearability limits. It is essential to point out that no performance improvements have been implemented from the last version, but instead, they remain similar, mainly because of exploiting the same actuator and kinematic structure. For these reasons, the main contribution of the work reported in this study relies on the innovative mechatronic design that results in a fully wearable and portable robotic device for assisting impaired hands. In contrast to most other state-of-the-art devices, it is particularly noteworthy that the solution presented here eliminates components dislocation, maximizing the exoskeleton wearability. *Action research arm test (ARAT)* has been performed to prove the HES capabilities and evaluate its redesign pros and cons.

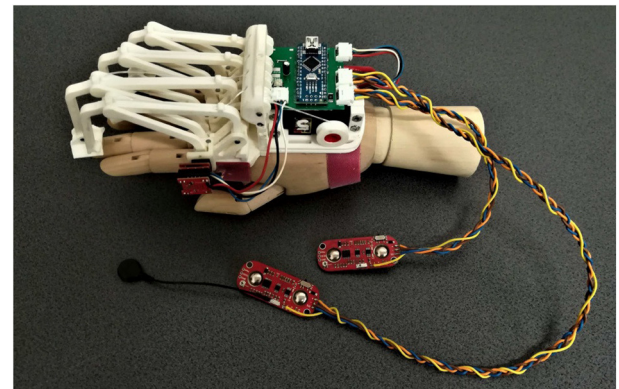
This study is organized as described below. In section 2, the main strengths and flaws of the previous prototypes will be highlighted, laying the foundations for the further development presented in this study. Section 3 will present the changes made to solve the mentioned problems. In section 4, *ARAT* and its results will be presented. The strengths and flaws of the achieved solution will be discussed in detail in Section 5, based on the conducted tests. Finally, section 6 will conclude the this study.

## 2. THE PREVIOUS PROTOTYPES: STRENGTHS AND FLAWS

This research activity has always aimed to develop an easily wearable, small, lightweight, safe, and low-cost robotic device for users with impaired hands. The HES prototype presented in detail in this study results from the evolution of three previous versions (Secciani et al., 2018). The overall architecture key points have had no changes: It has always been based on single-phalanx, single-DOF, rigid, and cable-driven finger mechanisms, acting on all the finger, except for the thumb. Each mechanism end-effectors are on the matching fingers distal phalanx. In addition, these mechanisms have been designed: (i) to be 3D-printed in Acrylonitrile Butadiene Styrene (ABS)—chosen due to its mechanical characteristics and its lightness—; (ii) to withstand forces up to 15 N on the contact point of each matching finger, which has been proved to be a reasonable value for typical manipulation tasks of ADLs (Riddle et al., 2020).

The last of the previous prototypes (the third one), shown in **Figure 1**, has been developed focusing on patient needs, aiming to have a portable, wearable, and easily customizable device for assistive and rehabilitative purposes.

The single-DOF and single-phalanx finger-handling mechanism—made lighter and less bulky without influencing the already validated kinematic model (Conti et al., 2016)—allows reproducing the complex hand kinematics using a more compact device than most of the other state-of-the-art rigid mechanisms (Lambercy et al., 2013; Yun et al., 2017; Diez et al., 2018; Bouteraa et al., 2019). For this reason, no other cumbersome components



**FIGURE 1** | The figure shows the last version of the exoskeleton prototype before the changes proposed below in this paper (Secciani et al., 2021). Specifically, the following components can be seen: (i) four planar finger mechanisms on the left; (ii) a magnetic encoder, placed upon the mechanism joint above the index finger MCP one; (iii) two sEMG sensors, the two red boards on the bottom, and cables for data transmission; (iv) a micro-controller on a green printed circuit board, in the middle top of the figure; (v) a servomotor, the black component below the micro-controller.

have been added. Only a second passive DOF per finger has been added to allow ab/adduction movements, enabling the auto-alignment between fingers and their corresponding mechanisms. An optimization procedure (Bianchi et al., 2018) has been employed so that its final geometry results to be effectively tailor-made on the patient anatomy. Customization and ab/adduction movements improve ergonomics and user comfort, avoiding constraining feelings and helping the fingers more efficiently arrange during object grasping. Such considerations allow complying with some of the crucial requirements cited in section 1 (Sarac et al., 2019).

The exploitation of a single servomotor (HS-5495BH High-Torque Servo from Hitec), unlike the solutions in **Table 1**, is another vital topic to be considered in depth. On one side, this choice positively impacts the mechanical and electronic hardware architecture since the system weight is unavoidably lower by reducing its components. Also, the control code is more straightforward, not managing the synchronized motion of more actuators. As an inevitable drawback, the independent motion of the fingers is not allowed. However, being the finger-handling mechanisms cable-driven, the grasp shape results to be deformable to different object shapes. Indeed, the patient can perform irregular grasps since the fingers can adapt—while remaining within their own *Range Of Motion*—to the objects thanks to the cable flexibility. Nevertheless, independently controlled fingers make a significant difference only with tasks involving the tip and tripod grasps, not frequently used in essential ADLs (Montagnani et al., 2016).

By powering the servomotor with 7.4 V, it can output a maximum torque of 0.735 Nm and a maximum angular speed of 6.67 rad/s; such performances have been preliminary considered and then verified suitable to exert the forces the exoskeleton has been designed for (15 N as mentioned above), which are

comparable, if not better, to the ones of the listed solutions in **Table 1**.

All the electronic components have been chosen to have a lighter, cheaper, and more intuitive device. An Arduino Nano controller board, a Bluetooth module, and a driver have been integrated on a custom Printed Circuit Board (PCB) (Secciani et al., 2019) and then placed on the user hand back. A magnetic encoder collects the angular position and velocity of the mechanism joint—to which it is applied—placed right above the index finger MCP joint, not preventing any hand function. The mechanism kinematics is solved as a function of this mechanism joint angular coordinate, which depends on the index finger's MCP joint flexion/extension angle. Such measurements are consistent also with the other fingers since they are all moved simultaneously by the HES. Two MyoWare<sup>TM</sup> Muscle Sensors from Advancer Technologies (United States), low-powered devices, have been chosen to collect epidermal EMG signals, namely sEMG signals. They can detect, interpret, and measure bioelectric signals from muscle activity. Such sensors incorporate the housing for two monopolar snap electrodes into a small breakout board ( $20.8 \times 52.3 \text{ mm}^2$ ). Despite this, the MyoWare behaves as a single bipolar sensor capable of generating two distinct differential output types. Specifically, they represent a good trade-off between the high cost of many of these sensors and problems connected with the dedicated software for managing them.

The strategy proposed (Secciani et al., 2019) for controlling this device enables intuitive management of its motion. Indeed, it is based on the user intention classification starting from myoelectric readings. The user muscular activity is measured 50 times per second, and it is translated into a command for the actuator to follow the captured intention. Such commands can be “hand opening,” “hand closing,” and “resting.” It is worth noting that the forearm muscle closeness and sEMG signal nature and noise level require high computational power machines to classify user movements accurately. Classifying just three elementary intentions has resulted in a reasonable trade-off between complexity and usability. The first two intentions imply an effective system motion, while the third represents a security state for which the device remains in its current position. The motor velocity is set to perform a complete opening gesture in about 1 s; the same applies to complete closure.

A custom Graphical User Interface (GUI) has been developed to (i) collect sEMG signals training datasets by recording them, (ii) manually draw two polygons around the points that identify the opening and closing gesture, (iii) upload the classifier parameters to the micro-controller board, and (iv) save the polygons vertices coordinates (Secciani et al., 2020). By doing so, opening or closing intentions are classified according to the polygon the corresponding points belong to. Those points that belong to both the polygons or none of them are classified as a rest intention.

Another GUI has been developed for an intermediate training phase for both the classifier and user. A 3D hand model is displayed, and it moves according to the user intention classification. The interface allows controlling the complete hand opening and closing, and the intermediate positions, helping the

user to get used to the HES and classifier. From the user point of view, straightforward device managing is one of the main goals of this version.

At this point of the study, the HES is customizable on the patient hand, compliant with it, and intuitive, thanks to the user intention detection method. Nevertheless, some flaws have remained, especially non-full device wearability and portability. During a preliminary testing phase, some criticisms in cable management and dressing the electromyographic sensors have arisen and impose severe limitations on the device use. Such tests have been carried out in the laboratory and only on healthy subjects to assess the new integrated electronics. The subjects were required to wear the MyoWare<sup>TM</sup> sensors on the forearm and trigger the servomotor motion with muscle contractions. It was observed that wrist movements could occasionally produce excessive tensions in cables connecting the sEMG sensors to the microcontroller (see **Figure 1**). Besides, these cables elasticity caused small shifts between the sensor and user skin. These displacements compromised the signal acquisition and were then translated into the so-called “motion artifacts,” which resulted in erroneous intention classifications. Therefore, cables represented a hindrance and another annoyance for the patient, preventing the HES from complete portability.

Also, the connection between the hand and exoskeleton represented a crucial issue to be solved. Such an interface was produced by sewing the device to a sports glove and then fixing it to the limb with additional Velcro bands, as in Tong et al. (2010), Ho et al. (2011), Lamercy et al. (2013), Rose and O'alley (2018), and Wang et al. (2018). However, on one side, elasticity of both these systems ensured high-grade coupling safety because of their intrinsic compliance with any possible displacement. On the other side, the same feature could cause an inconsistency between the exoskeleton actual trajectories and the fingers ones it has been designed for. Indeed, the exoskeleton motion may produce a change in its relative position to the back of the hand, not ensuring the same movements reliable repeatability.

Finally, the lack of an on-board power supply system, as also in In et al. (2015), Polygerinos et al. (2015), Randazzo et al. (2017), Diez et al. (2018), Rose and O'alley (2018), Yu et al. (2019), and Dittli et al. (2020) or in *exomotion*<sup>®</sup>, *Carbonhand* and *Neomano* devices among the commercially available ones, as visible in **Table 1**, prevented the device from being fully wearable and portable. Being an exoskeleton intended for assistive use, as already mentioned, this point was one of the most limiting since it forced the user to be connected to a power supply away from the hand.

### 3. THE NEW ARCHITECTURE

This section will present the changes made to overcome the above-mentioned issues and develop a fully wearable device. Specifically, the renewed sEMG technology, the improved ergonomics of the interface between the hand and exoskeleton, and the revamped mechatronic architecture are presented.

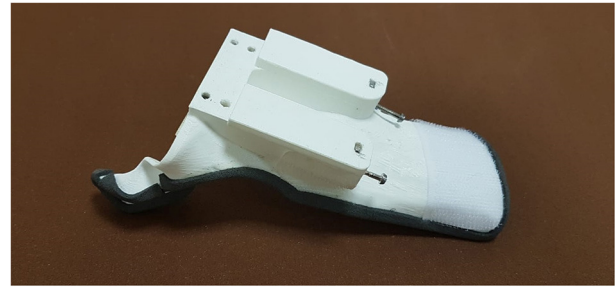




**FIGURE 2 |** The figure shows the sEMG bracelet, developed to reduced the disturbances coming from the sensor wires, with its central unit and the other two smaller ones containing the sEMG sensors.

### 3.1. Surface Electromyography Technology

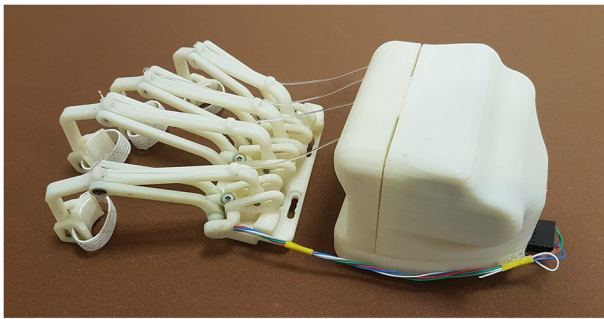
Among the several commercially available sensors, which are usually exploited to interpret the myoelectric activity (Rechy-Ramirez and Hu, 2015), sEMG sensors have also been employed in this new device version due to their capability of detecting electromyographic signal directly through the skin, as a completely non-invasive technique. Some preliminary tests have been carried out (Secciani et al., 2019), proving that the device effectively assists patients with muscular (rather than neuronal) deficits in ADLs. Indeed, as long as the user can emit controlled myoelectric signals—even if weak—the system can sample them, classify them, and then replace the musculoskeletal system. For these reasons, such a HES can be used in all cases, acute or chronic, in which the disability does not compromise the user ability to associate a motion intention with a specific muscle activation voluntarily. For this kind of application, the sEMG sensors chosen are usually placed on the antagonist muscle bands responsible for the fingers and wrist flexion/extension, which are on the *extensor digitorum* and *flexor digitorum* muscles. A first tentative bracelet for sEMG signals collection has been designed to overcome cable issues presented in section 2 and mitigate the disturbances introduced. It has been thought to be worn on the forearm. The result is shown in **Figure 2**. As visible, the sEMG bracelet consists of three cases that are 3D-printed in ABS. The central unit, the biggest one, has been thought to house the microcontroller, the Bluetooth module, and a single-cell 500 mAh Li-ion battery, while the other two hold only the sEMG sensors. Each wire between the central unit and the two sensor housings has a different function following its color: The red one is the 3.3 V line, the black one represents the ground line, sEMG signals flow in the yellow wire, while the white one represents the reference potential. Thus, the long cables, shown in **Figure 1**, connecting the sensors directly to the exoskeleton actuation system, have been removed. The servomotor command signals are now processed on-board and then sent to it thanks to the micro-controller on the exoskeleton over a Bluetooth bridge. The resulting total weight of the bracelet is around 80 g.



**FIGURE 3 |** The figure shows the 3D-printed anatomical splint with the slide and the holes for mounting the two HES modules.

### 3.2. Ergonomics

The connection between the hand and exoskeleton has been improved to make the device more comfortable for the wearer, avoiding the issues mentioned above about motion accuracy. It has been achieved by exploiting an anatomical wrist splint, which provides a sufficient rigid interface base with the forearm. A splint is meant as a device that increases, improves, or controls an impaired function of an injured segment, e.g., such a tool is usually used to support a broken bone and keep it in a fixed position or during rehabilitation treatments. It is commonly made of a thermoplastic material mouldable at relatively low temperatures (about 75°), customized and modeled by a therapist directly on the patient anatomy. Its main features are being lightweight, resistant, easy to wear and remove, washable, and continuously adaptable to the evolving patient needs. However, such a thermoformed splint does not have a support base to anchor the exoskeleton. So, a ROMER arm equipped with a 3D laser scanner—a completely portable coordinate measuring machine—has been used to acquire the splint surfaces and produce a considerable number of point clouds to create a 3D CAD model. After collecting sufficient data, the point clouds have been cleaned and smoothed using Polyworks and Geomagic Design X software. After that, the points have been triangulated, aligned, and finally merged in one only surface. The splint 3D CAD model is rebuilt starting from this optimized surface, and, by doing so, its lower surface shape accurately reproduces the forearm anatomy. Then, such a model has been modified as shown in **Figure 3**: The fingers module housing, in which there are four threaded holes for the screws employed for their attachment, and a magnetic slide for fixing the motor box has been designed. Finally, the splint has been 3D-printed in PolyLactic Acid (PLA), resulting in a thickness of 2 mm and a weight of only 42 g. A stable interface between the hand and HES is then provided by connecting it with the exoskeleton. The connection, removable whenever needed, is achieved by exploiting four screws for the finger mechanisms module, the slide, and two other screws to fix the motor box to the new splint. Among the possible functionalities of a splint, this tool employed as a part of the new prototype and presented in this study (see **Figure 3**) can be identified as an integrative splint—since it allows to compensate compromised limb functions—and



**FIGURE 4 |** The figure shows the two blocks of the HES modular structure: on the left, the fingers' mechanisms module, and on the right, the motor and control one.

one for protected mobilization—since it aims to improve specific muscle activity. Indeed, on one side, it enables to stiffen the wrist articulation so that the interaction forces between the hand and exoskeleton are spread throughout the forearm, concentrating the HES action on the fingers and giving better stability to the system. On the other side, it also provides rigid support for the thumb to keep its first phalanx in a semi-opposition state to the palm, thus facilitating object grasping by mitigating tendon retraction. Finally, even in this case, the HES can be fixed on the hand using Velcro bands, providing the interface with a bit of compliance for improved wearer comfort.

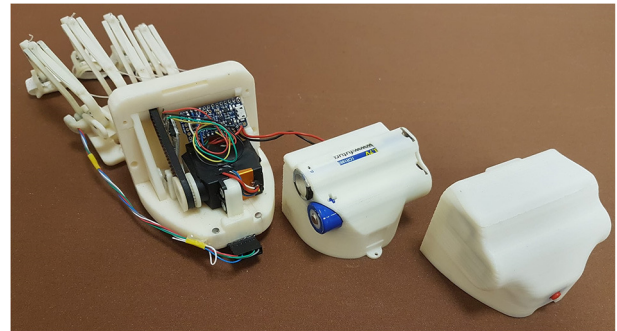
### 3.3. Overall Architecture and Power Supply System

The last and most significant changes have been made to the overall mechatronic structure, revamping the power supply and transmission system to achieve the complete portability of the device.

The first crucial difference of this new HES version is the whole system modular structure, which is now essentially divided into two blocks, shown in **Figure 4**: The one including the motor and control box is placed on the hand back, while the one that houses all the finger mechanisms is located right above the fingers.

Such a structure has been designed to minimize downtime for maintenance, whether it is programmed or not. While the back module may be subjected to sporadic changes, e.g., a smaller one may be required for a pediatric exoskeleton (Bianchi et al., 2019), the front one will be more subject to replacements due to a mobility recovery or, on the contrary, a pathology evolution. Indeed, the finger trajectories may change, and thus, their mechanisms geometry might need to be revised. So, the fingers module is connected with the 3D-printed splint thanks to four screws, easily removable. In addition, as visible in **Figure 4**, four slots are realized in this module to help regulate its position and match each mechanism with its corresponding finger correctly. The two modules total mass on the hand is 415 g.

Another variation to the previous version is about the power supply system (see **Figure 5**). It is now incorporated into the electronics case, and thus, it is no longer part of external



**FIGURE 5 |** The figure shows an exploded view of the new motor box and the three layers that compose it: on the left, the inner layer, including the transmission system, actuator, and control electronics; on the centre, the middle one containing the batteries, and, on the right, the outer one, including the switch button.

equipment but directly integrated on the hand back. This module has been modified to contain the following components: the actuator, transmission system, control electronics, batteries, and a switch button. All these elements are disposed on three different layers, as shown in **Figure 5**: The actuator, transmission system, and control electronics are into the inner one; the batteries on the middle; and the switch button on the outer one. The layer on the middle is the last externally accessible to let the user change the batteries. Such a new power supply system consists of two rechargeable 3.7 V lithium-ion batteries with 2,600 mAh capacity serially connected.

Third, also the actuation system has been subject to change. Motors have been reduced from four (on the first HES prototype) to one, resulting in an unavoidable redesign of the finger mechanisms motion transmission and, thus, the overall actuation module. Indeed, a specific cable-driven transmission has been developed: Four pulleys with different diameters, depending on the fingers dimensions, have been designed and embedded to a single secondary shaft to obtain the same angular speed for all the fingers. Instead of cable that wraps and unwinds around the pulley integral with the motor shaft, a toothed belt drive is now used so that the motor sets in motion the shaft to which the four pulleys are integral. This adjustment allows obtaining the same angular velocity for all the fingers as for the previous versions, even though their trajectories involve different cable lengths.

Finally, it is worth highlighting that, as in the previous versions, additional force sensing or actuators, e.g., Series Elastic Actuators (SEA) (Yun et al., 2017) or Force Sensitive Resistor (FSR), have not been exploited to avoid additional components that increase overall complexity, dimensions, and weight, thus limiting the portability and wearability. For this reason, the proposed HES operates only in position and speed control modes, while force control mode has not been currently implemented.



### 3.4. Hand Exoskeleton System Development and Use

So far, the changes to overcome the primary limits of the previous version and achieve a fully wearable and portable device have been presented. This subsection summarizes instead the main steps required to actually develop such a customized hand exoskeleton. Firstly, the metacarpal bones and phalanges lengths are required to solve the hand kinematics and find the trajectory of the desired fingers. Such trajectories becomes then the inputs for the optimization procedure that will calculate the link dimensions of each finger mechanism. Finger-handling mechanisms are hence customized on the patient anatomy and follow the corresponding desired trajectory as accurately as possible. Once the 3D parametric model of the whole HES has been updated in the CAD software, all the components can be 3D-printed and then assembled. While finger mechanisms change from patient to patient, the actuation and control box usually remains the same, and this is why the system is designed to be split into two principal parts as described in subsection 3.3. In parallel, an anatomical splint is developed starting from a 3D scan of the user limb and then 3D-printed. The splint becomes the main interface with the hand, and the whole system is rigidly fixed to it. Elastic rings are used to fix the device to the fingers, while the splint is fixed to the hand and forearm with velcro bands. Finally, to control the HES motion, the user has to wear the sEMG bracelet and perform a preliminary phase of system training. Such step consists of a repetition of elementary muscle contractions (i.e., opening, closing, and resisting) to match with a specific exoskeleton action (i.e., pulling cables, releasing cables, and idling). Once the classifier is properly trained, the HES is ready to be used.

The kinds of patient for whom the exoskeleton is suited for are all those who can arbitrarily contract the muscles, as it is the only way to control the motion. Besides, the device, in its current status, is capable of assisting only people with hand opening impairments.

## 4. TEST AND RESULTS

Experimental tests have been carried out to assess the new redesigned HES capabilities. The tested exoskeleton is tailor-made for a patient's hand, who has followed this research from the beginning. The subject is affected by Spinal Muscular Atrophy (SMA) type II since birth. Such a disease damaged muscular extensors of both his hands, causing their opening impairment due to tendon retroactions, and therefore, now hands are closed like fists. The tests have been performed to evaluate the HES actual effectiveness for the pilot study patient and whether improvements have been made after redesigning it, as presented in section 3. Specifically, they are used to understand whether the new HES exploitation can improve the patient assistance in ADLs, enabling him to grasp objects more effectively than when the device is not worn, if he has some advantages or disadvantages in using it, its new strengths, and remaining flaws. ARAT (De Weerd and Harrison, 1985; Yozbatiran et al., 2008) has been conducted for such experimental sessions since it evaluates

**TABLE 2 |** The table shows the ARAT items.

Grasp	G1	Block, wood, 10 cm cube (most difficult)
	G2	Block, wood, 2,5 cm cube (easiest)
	G3	Block, wood, 5 cm cube
	G4	Block, wood, 7,5 cm cube
	G5	Ball (Cricket), 7,5 cm diameter
	G6	Stone 10 x 2,5 x 1 cm
Grip	GR1	Pour water from glass to glass (most difficult)
	GR2	Tube 2,25 cm (easiest)
	GR3	Tube 1 x 16 cm
	GR4	Washer (3,5 cm diameter) over bolt
Pinch	P1	Ball bearing, 6 mm, 3rd finger and thumb (most difficult)
	P2	Marble, 1,5 cm, index finger and thumb (easiest)
	P3	Ball bearing 2nd finger and thumb
	P4	Ball bearing 1st finger and thumb
	P5	Marble 3rd finger and thumb
	P6	Marble 2nd finger and thumb
Gross movements	GM1	Place hand behind head
	GM2	Place hand on top of head
	GM3	Hand to mouth

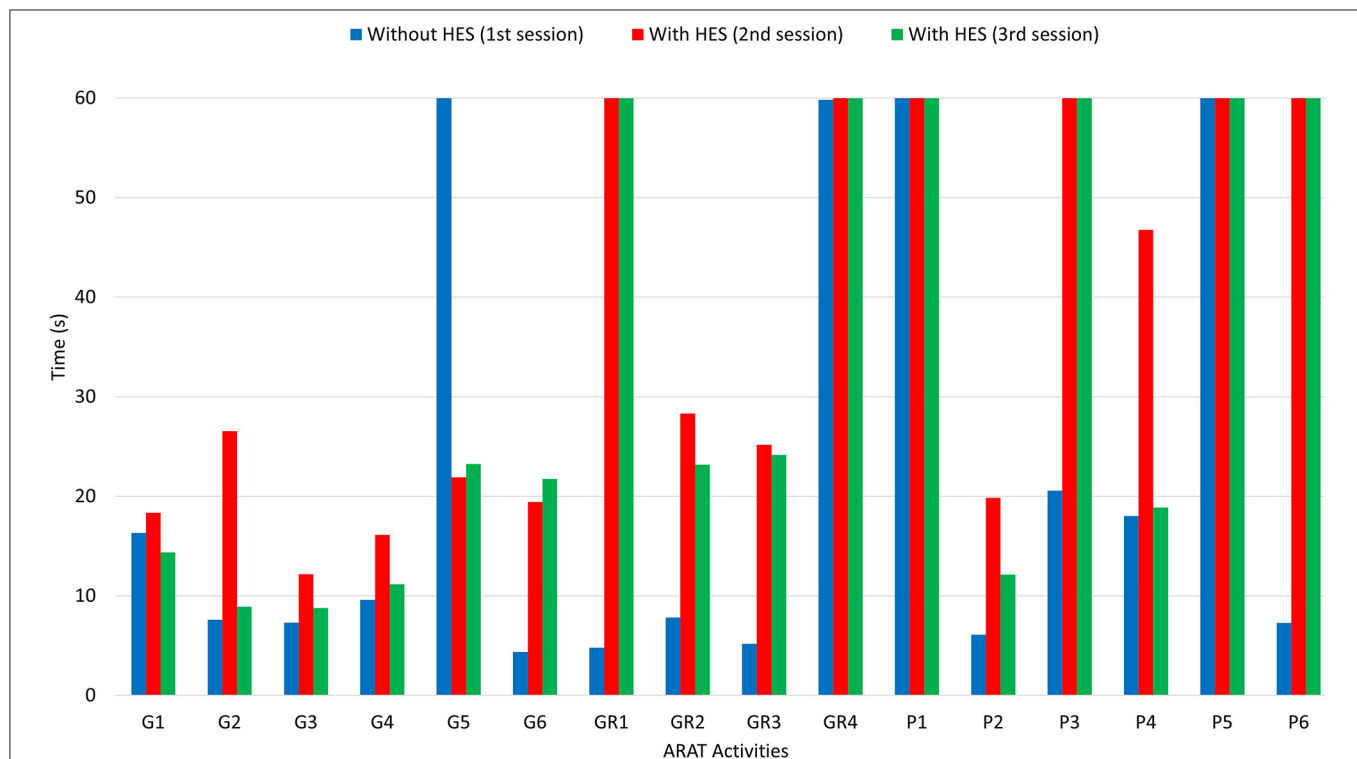
*The first column includes the four subgroups. In the second one, there are direct identifiers to each task: letters indicate the corresponding subgroup, while numbers show the order in which the tasks are proposed to the subject. The third column describes the activity explicitly to perform.*

grasp, grip, pinch, and gross arm movements, usual in daily life activities (Duruöz, 2014). It is a functional evaluation test that assesses the upper limb functions. The test takes approximately 5–15 min to administer and requires standardized equipment: various sized blocks of wood, cricket ball, stone, glasses, tubes, washer and bolt, ball bearing, and marble. Standard protocol requires the patient to be seated in a chair facing a table, with the head in a neutral position and feet on the floor. The test is organized into four subgroups corresponding to the four different motions evaluated, with 19 items presented. Each item must be grasped and lifted on a 37-cm-high shelf above the table facing the subject.

The patient performance is rated on a 4-point scale, ranging from 0 (no movement possible) to 3 (movement correctly performed). The maximum obtainable score for ARAT is 57. Each item in the four subgroups has a well-standardized presentation order: First, the patient is asked to manipulate the most challenging object of the considered subgroup. If the task is correctly performed, enabling a total score, he is credited with having scored 3 on all the remaining subtest items without performing them. However, if the patient fails the first task and scores less than 3, the most manageable object is tested. If unlikely the patient scores 0, the remaining subtest is credited with 0, and the evaluation proceeds to the following subgroup. If otherwise, the patient scores more than 0, all items in the subtest should be assessed. The standard protocol indicates that each task might run up to 60 s if the patient does not complete it before. Specifically, the items in each subgroup are shown in **Table 2**.

**TABLE 3 |** The table shows the scores obtained during the three sessions of ARAT.

Sessions	G1	G2	G3	G4	G5	G6	GR1	GR2	GR3	GR4	P1	P2	P3	P4	P5	P6	GM1	GM2	GM3	Total score
Without HES	2	2	2	2	1	2	2	2	2	2	0	2	2	2	0	2	3	3	3	36
With HES	2	2	2	2	2	2	0	2	2	0	0	2	0	2	0	0	3	3	3	29
With HES	2	2	2	2	2	2	0	2	2	0	0	2	0	2	0	0	3	3	3	29

**FIGURE 6 |** The figure shows a histogram concerning the results of the ARAT carried out. While activities are reported in the horizontal axis, the time (in seconds) needed for each one corresponds to the height of the column, readable in the vertical axis.

For this case study, experimental tests have been carried out in a clinical environment, and the patient was seated in his wheelchair facing the table. The tests have been repeated three times. In the first session, the patient carried out the test without wearing the HES, while he had to wear it during the second and third ones. The second session has been conducted considering a motor speed of 4,000 counts/s, enabling a complete closing in 1.2 s. The same applies to the complete opening. The third session has been instead performed at a 50%-increased motor speed (6,000 counts/s, allowing a complete closing/opening in 0.8 s) after finding that it did not cause discomfort to the patient.

After carrying out the first session and taking the time to perform each ARAT task, a physiotherapist helped the patient donning the sEMG bracelet and HES on the right upper limb. The two sEMG sensors have to be placed as described in subsection 3.1. The donning phase and sensor placement required about 5 min since particular attention must be paid to avoid painful movements and find the correct spot for sensors. In such a case, it has been necessary to consider the wrist muscular activity

due to the difficulty of providing strong finger extension signals without heavy fatigue. The first GUI presented in section 2 has been exploited to collect sEMG signals training datasets, draw the corresponding opening and closing gestures polygons, and upload the classifier to distinguish each intention. Instead, the second one is employed to have an intermediate training phase for the patient wearing the HES. Then, the interfaces have been closed, and the other two sessions started. **Table 3** shows the scores the physiotherapist gave to each task. It is possible to understand that the patient has no arm-motion impairments, having scored 3 points for gross movements (GM1, GM2, and GM3) wearing the HES or not. Instead, in all the other tasks, more or fewer difficulties have been found. Thus, significantly, the results concerning only the first three subgroups (G, GR, and P) are also shown in terms of time thanks to a histogram (see **Figure 6**), and they are reported for all three sessions. The histogram indicates the time (in the vertical axis) recorded to complete each task (specified instead in the horizontal axis) during different session settings. Specifically, the blue column



**FIGURE 7 |** The figure shows some pictures taken during the test: (i) on the top-left, the cricket ball grasping (G5) performed without the HES, (ii) on the top-right, the same task performed with the HES, (iii) on the bottom-left, the wooden block grasping (G1) is shown, while (iv) on the bottom-right, the alloy tube gripping (GR2) is visible.

height shows the time taken to complete the task without the HES, the red column height the time taken wearing the HES with a motor speed of 4,000 counts/s, while the green one refers to the session in which the motor speed is increased up to 6,000 counts/s. Sixty seconds has been awarded to the tasks the patient failed to complete.

The histogram shows that the times taken for grasping activities during the first and third sessions are comparable. Instead, longer times have been recorded during the second one. Besides, the HES exploitation allowed better-grasping objects. For instance, **Figure 7** shows the 7.5-cm-diameter cricket ball grasping (G5) without the HES (on the top-left) and wearing it (on the top-right). It is possible to observe that without the HES, the patient has adjusted his grasping according to the movements he can perform. On the contrary, the HES enabled the patient to fully open the hand and grasp the ball correctly and effectively. The same happened for the 10-cm-cube wooden block grasping (G1), visible in **Figure 7** bottom-left.

More difficulties have been found among grip movements wearing the HES on glasses (GR1) and washer (GR4) manipulation. Significantly, the washer is highly challenging to grip for the patient also without the HES due to its shallow thickness. Conversely, alloy tubes grips (GR2 and GR3) have been performed without the HES and wearing it, as visible in **Figure 7** bottom-right. The time taken on the second and third sessions is more than the one on the first, but also now, the HES enabled the patient to have a more correct and effective hand grip.

Finally, from **Figure 6**, it is possible to observe that the patient has found more impairments on pinch movements both with and without the HES. Indeed, he could not perform two out

**TABLE 4 |** The table compares the overall lengths and heights of the first, and the one proposed here prototypes finger mechanisms.

Fingers	First HES		New HES	
	Length [mm]	Height [mm]	Length [mm]	Height [mm]
Index	98,42	35	85,61	35,13
Middle	107,6	48	95,44	39,17
Ring	100	36	87,31	35,84
Small	74	27	71,91	29,51

of six pinch tasks during the first session, but he failed four out of six tasks during the second and third. The augmented velocity on the third session enabled times comparable with those recorded without the HES, even if they are still greater. The worsening performances are due to the overall dimensions of the finger-handling mechanisms, which, although they have been reduced compared to the first prototype ones, as visible in **Table 4**, still prevent movements in confined spaces, e.g., when the patient hand approaches the table to pinch small-size items on it. Specifically, he did not fail the task in which index and thumb fingers had to interact. Instead, when the patient had to pinch items with the middle or ring finger and thumb, such impairment did not allow him to complete the tasks.

## 5. DISCUSSION

In this section, the new exoskeleton prototype strengths and weaknesses will now be discussed. The main focus of this

study was the renewal of the system architecture to achieve a fully wearable, portable, comfortable, and tailor-made robotic device for home assistance in ADLs and telerehabilitation. The experimental tests presented in section 4 proved that such an aim had been correctly pursued. Indeed, the redesigned HES is now fully wearable and portable, and so it was for the patient throughout the tests—which lasted about 3 h, including the starting training phase and some resting breaks. The patient could perform all the sessions without much discomfort, even if he still fails some tasks. Such failures are primarily due to the HES overall dimensions that prevent tasks in confined spaces. Besides, the patient needs a more extended training period with the HES to get used to it and how the device detects his intentions. Specifically, the redesigned device enables the user to open the hand starting from a fist and then perform the grasps correctly. It also allows the patient to hold the item due to its force effectiveness until he wants to release it, and a hand opening intention detected from the sEMG sensors causes the cables to wind up.

Below, direct references to the three subsections above will be made to discuss the improvements presented on each.

**sEMG technology (subsection 3.1)**—The exploitation of sEMG sensors enables the HES control system to collect and interpret signals from muscular activity in a completely non-invasive way. Various solutions from **Table 1** exploit sEMG signals to detect the user intention (Ho et al., 2011; Yun et al., 2017; Rose and O’alley, 2018; Wang et al., 2018; Bouteraa et al., 2019; Dittli et al., 2020; Yurkewich et al., 2020), but only in Rose and O’alley (2018) and Yurkewich et al. (2020) and *HandyRehab* a bracelet, are exploited to collect such signals. The sEMG bracelet proposed in this study represents one more step toward an entirely intuitive device, free from cumbersome cables and external equipment. The advantages of such a solution are not limited to the disturbance reduction, which is achieved by physically decoupling the acquisition system from the wrist and exploiting a Bluetooth bridge for data transmission. Indeed, it has also been proved to help lighten the microcontroller workload on the exoskeleton, which is no longer slowed down by the sEMG signals sampling, preprocessing, and classification. It is worth highlighting that the Bluetooth bridge avoids cables presence and enables the system to stream sEMG data to any external platform for development and monitoring purposes, even remotely. The experimental tests conducted (and presented in the previous section) have proved that the bracelet improved the HES, being comfortably portable and effortlessly wearable, mitigating the patient feeling of constraint on the forearm due to cables.

**Ergonomics (subsection 3.2)**—An ergonomic mechanical design of a wearable assistive and rehabilitative device should guarantee kinematic compatibility with the user fingers and a comfortable mechanical-physical interface (Chiri et al., 2012). The new prototype ergonomics have been increased thanks to a tailor-made PLA splint that provides a high-stability kinematic coupling with the user limb. This feature allows the mechanisms to follow the desired finger trajectory correctly with decent repeatability. This aspect is extremely crucial to prevent the exoskeleton from forcing the hand into wrong and painful poses. Specifically, the splint avoids the poor stability that was

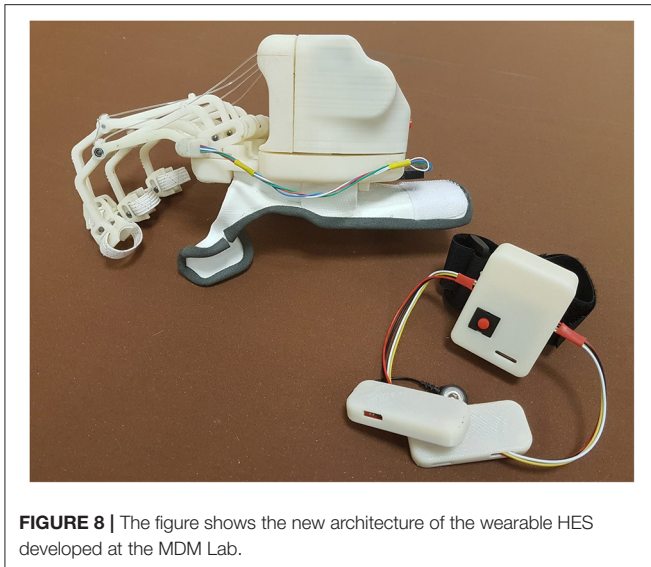
due to the glove elasticity and ensures a better distribution of efforts on the hand and forearm. Before starting tests, 1-mm-thick Neoprene adhesive strips have been added to the splint inner surface and edges to reduce direct contact with the skin and the consequent skin redness and irritation. Only a commercially available solution, the *exomotion*<sup>®</sup>, exploits the Reverse Engineering to achieve a glove and an arm splint designed for the patient, to the best of the authors’ knowledge. Its plaster casts are used in this case to mold a glove, which has to be scanned and then rebuilt. Instead, for many solutions, a simple platform to hold all the components is designed (Lambercy et al., 2013; Diez et al., 2018; Wang et al., 2018; Dittli et al., 2020). Only occasionally, it is curved according to the natural hand profile but still not tailor-made on the specific patient hand (Tong et al., 2010; Ho et al., 2011).

Although improved over previous versions, the ergonomics of the device still have plenty of room for improvement. Firstly, the splint might be improved by exploiting a reticular structure with variable stiffness, making it more breathable and fitting to the hand. Second, the development of a donning/doffing system to let the patient autonomously wear the exoskeleton would be crucial. To the best of the authors’ knowledge, there are no devices that include such a system in the literature. In its current state, this solution is only a first step toward a system fully compliant with the hand, which can provide ergonomic support to fix the exoskeleton. Also, the splint makes the HES donning/doffing phase easier, reducing the time the therapist spent on this procedure while guaranteeing noteworthy kinematic stability.

**Overall architecture and power supply system (subsection 3.3)**—The most significant innovation of this new architecture compared to the current state-of-the-art wearable robots—at least to the best of the authors’ knowledge—is undoubtedly owed to this aspect. The exoskeleton is now standalone and entirely wearable. The modular structure is differently proposed in some other devices (In et al., 2015; Polygerinos et al., 2015; Randazzo et al., 2017; Hadi et al., 2018; Rose and O’alley, 2018; Yu et al., 2019; Dittli et al., 2020), also in the commercially available ones, to enable some components dislocation and lightening the device on the hand back, against complete wearability and portability. The proposed solution makes faster and more streamlined the HES design process, its embodiment, its assembly, and its regulation on the hand, while not foreclosing the complete wearability and portability features instead. Besides, such a structure reduces the maintenance times since only the modules eventually needed can be replaced.

Toothed belt exploitation between the motor and secondary shaft makes the motion transmission more accurate and stable, preventing unexpected cable unwinding, which could cause errors during hand opening or closing. The total encapsulation of the power supply system and the electronics (including the one for processing sEMG signals) prevents the device from exposing delicate components—which otherwise should have to be placed along the upper-limb—resulting in a smaller and electrically safer design, thus not constraining the patient movements. Indeed, these changes allow achieving the following overall dimensions of the module on the hand back: 80 mm in width, 72.5 mm in length, and 70.6 mm in height. In addition, the new mechanisms





bulkiness is smaller than that of the previous prototype, as visible in **Table 4**, by streamlining the structure. It is worth noting that all the length sizes have been reduced, having removed some components. Instead, the heights have remained relatively similar to the previous one. However, such a solution results also in a worse masses distribution. Indeed, about 460 g is now concentrated on the hand back. It may sometimes produce a slight unintentional outwards hand twisting, owed to the gravity center position, which is too high to the hand. Thus, such a distribution makes the exoskeleton hard to be worn by the patient for a long time to have continuous assistance in ADLs. Instead, it could be more easily used for shorter rehabilitation exercises.

Finally, the three layers of the actuation box case improve the device usability and safety, enabling the wearer to change the exhausted batteries straightforwardly.

**Table 1** reports some of the most significant state-of-the-art devices. It is worth noting that only a few of them are fully wearable, i.e., without any components dislocated from the hand, as Bouteraa et al. (2019) and Yurkewich et al. (2020) and *HandyRehab*. Unlike (Bouteraa et al., 2019), the new HES design eliminates cables and exploits a wireless bridge for sEMG signals transmission, as in Yurkewich et al. (2020) and *HandyRehab*. Compared to the commercially available *HandyRehab* the proposed HES is specifically tailored to the patient hand, and its finger-handling mechanisms result more streamlined. Finally, it is worth comparing the new prototype with *My-HERO* presented in Yurkewich et al. (2020). They have been designed for similar purposes but with different methods. Indeed, the proposed HES is based on rigid structures, while *My-HERO* is based on a soft one. The choice of using soft elements certainly reduces the weight and encumbrance of the system: *My-HERO* results, in fact, lighter and slimmer than the proposed exoskeleton. On the other side though, exploiting mechanical components increases the overall weight but generally ensure also

greater kinematic accuracy and force effectiveness. Besides, the proposed design ensures that the palm and the lower surface of the fingers are mostly component-free; feature that, unlike the glove exploited in *My-HERO*, preserves the sense of touch. Finally, while *My-HERO* needs to establish and maintain a connection with a PC, the proposed system classifies the user intention internally, hence boosting the system portability and the user freedom of movement.

Overall, the novelty of this study lies in proposing a design that, differently from other state-of-the-art solutions, collects most of the primary crucial characteristics of assistive and rehabilitative devices (i.e., wearability, portability, safety, comfort, compliance, customization, force, and cost effectiveness). Nonetheless, the authors are well aware of the wide room for improvements left, in particular, regarding component miniaturization, thumb actuation, and independent finger movement.

## 6. CONCLUSIONS AND FUTURE PERSPECTIVES

The overall new HES mechatronic design, proposed in this article and shown in **Figure 8**, presents innovative and noteworthy aspects compared to the current state-of-the-art wearable robots for hand disabilities. The proposed solution has several strengths, of which some are inherited from the previous prototypes. The rigid mechanisms geometry and new splint-based interface are tailored to the patient hand and forearm to be as compliant as possible with its anatomy and natural movements, and thus comfortable for the patient. A single actuator exploitation considerably lightens the whole system, while using a toothed belt provides better stability to the motion transmission and acts as mechanical friction in emergency cases. Also, spaces inside the module on the hand back have been exploited to the best, which, along with not using any more cables for data transmission, prevent an annoying feeling of constraint on the forearm and increase safety. The sEMG-based intention recognition technique represents a highly intuitive way of managing the system motion. Besides, the new data transmission protocol allows for straightforward monitoring of the system status using any Bluetooth-compatible devices and thus also remotely rehabilitation treatments by performing tasks preset by the therapist. So, the new HES results to be customizable, compliant and comfortable for the patient. Its components placement does not add impairments to the user motions, also ensuring safety. The device is force effective, intuitive, and fully wearable and portable. Finally, the HES is affordable since it costs about 550€, compact since it does not exceed a standard hand size, and lightweight since it weighs less than 550 g. Therefore, the primary requirements listed in section 1 have been met. The proposed enhancements allow to achieve a solution that results in helpful for the pilot study patient mainly in grasp movements, still having some difficulties in grip ones, depending on the item shape and sizes, especially in pinch movements. Also, it can be helpful in rehabilitation sessions. Concerning this point, it is worth noting that the possibility that the patient individually



wears, uses, and removes the device depends on its conditions. If the patient cannot don the device alone, as in this study, the therapist presence is mandatory at home and in clinics.

Complete wearability and portability, safety, comfort, compliance, force effectiveness, customization, intuitiveness, and affordability are features encapsulated in this device, based on rigid mechanisms—unlike other soft solutions—and this represents the true novelty of the study.

Nevertheless, some flaws have still been and will be under investigation in the short-term future. Firstly, the cable-driven actuation needs to be replaced since, even if it can adapt well to the hand's complex kinematics, it allows active actuation only when opening. Such a solution is enough for the pilot study patient, but in enlarging the subjects that can use it, active actuation also during closing may be required. In addition, it sometimes presents a problematic reversal of motion—also happened during the experimental tests—mainly when too much cable has been unwound, thus requiring specific maintenance work to restart the HES. Second, the lack of a thumb-handling mechanism still limits usability since its opposition is crucial to achieving good dexterity in object handling. Intending to produce a complete device, the development of a thumb mechanism is now under investigation. Third, bearing in mind the mentioned considerations, the fingers' independent motion might be challenging to implement but crucial to allow different hand gestures, such as precision manipulation or pinching, and further improve ergonomics. Finally, the space on the hand back has been optimized, but the weight distribution worsens, especially for assistance purposes. Besides, the finger mechanism dimensions still prevent the HES use in confined spaces, e.g., turning a handle or pinching small items, as also happened during the ARAT.

Both component miniaturization and masses redistribution will undoubtedly improve the device usability, ergonomics, and comfort for all these reasons. Also, unlocking the wrist articulation might be considered by changing the HES support base and hand connection system. All these enhancements

represent the core of the present and future research activities of the group.

## DATA AVAILABILITY STATEMENT

The raw data supporting the conclusions of this article will be made available by the authors, without undue reservation.

## ETHICS STATEMENT

Ethical review and approval was not required for the study on human participants in accordance with the local legislation and institutional requirements. The patients/participants provided their written informed consent to participate in this study.

## AUTHOR CONTRIBUTIONS

NS: conceptualization, writing, supervision, and experimentation. CB and FG: writing, supervision, and experimentation. MP, FV, YV, and AR: conceptualization and supervision. FB: conceptualization. MB: conceptualization and experimentation. All authors contributed to the article and approved the submitted version.

## FUNDING

This work has been supported by Don Carlo Gnocchi Foundation (Italy) and three research projects: the “HOLD” project funded by the University of Florence, the “HERMES” project funded by Fondazione CR Firenze, and the “BMIFOCUS” project funded by the Tuscany Region (POR FESR 2014–2020).

## SUPPLEMENTARY MATERIAL

The Supplementary Material for this article can be found online at: <https://www.frontiersin.org/articles/10.3389/fnbot.2021.750385/full#supplementary-material>

## REFERENCES

- Anderson, K. D. (2004). Targeting recovery: priorities of the spinal cord-injured population. *J. Neurotrauma*. 21, 1371–1383. doi: 10.1089/neu.2004.21.1371
- Bianchi, M., Fanelli, F., Meli, E., Ridolfi, A., Vannetti, F., Bianchini, M., et al. (2018). Optimization-based scaling procedure for the design of fully portable hand exoskeletons. *Meccanica* 53, 3157–3175. doi: 10.1007/s11012-018-0858-7
- Bianchi, M., Secciani, N., Ridolfi, A., Vannetti, F., and Pasquini, G. (2019). Kinematics-based strategy for the design of a pediatric hand exoskeleton prototype. *Mech. Mach. Sci.* 68, 501–508. doi: 10.1007/978-3-030-03320-0\_55
- Bouteraa, Y., Abdallah, I. B., and Elmogy, A. M. (2019). Training of hand rehabilitation using low cost exoskeleton and vision-based game interface. *J. Intell. Rob. Syst.* 96, 31–47. doi: 10.1007/s10846-018-0966-6
- Bouzit, M., Burdea, G., Popescu, G., and Boian, R. (2002). The rutgers master ii-new design force-feedback glove. *IEEE/ASME Trans. Mechatron.* 7, 256–263. doi: 10.1109/TMECH.2002.1011262
- Butter, M., Rensma, A., Boxsel van, J., Kalisingh, S., Schoone, M., Leis, M., et al. (2008). Robotics for healthcare: Final report. *European Commission EC*. <http://www.ehealthnews.eu/images/stories/robotics-final-report.pdf>
- Cappello, L., Meyer, J. T., Galloway, K. C., Peisner, J. D., Granberry, R., Wagner, D. A., et al. (2018). Assisting hand function after spinal cord injury with a fabric-based soft robotic glove. *J. Neuroeng. Rehabil.* 15, 1–10. doi: 10.1186/s12984-018-0391-x
- Cempini, M., Cortese, M., and Vitiello, N. (2014). A powered finger-thumb wearable hand exoskeleton with self-aligning joint axes. *IEEE/ASME Trans. Mechatron.* 20, 705–716. doi: 10.1109/TMECH.2014.2315528
- Chiaradia, D., Xiloyannis, M., Solazzi, M., Masia, L., and Frisoli, A. (2018). “Comparison of a soft exosuit and a rigid exoskeleton in an assistive task,” in *International Symposium on Wearable Robotics*. Pisa: Springer, 415–419.
- Chiri, A., Cempini, M., De Rossi, S. M. M., Lenzi, T., Giovacchini, F., Vitiello, N., et al. (2012). On the design of ergonomic wearable robotic devices for motion assistance and rehabilitation. *Annu. Int. Conf. IEEE Eng. Med. Biol. Soc.* 2012:6124–6127. doi: 10.1109/EMBC.2012.6347391
- Chu, C.-Y., and Patterson, R. M. (2018). Soft robotic devices for hand rehabilitation and assistance: a narrative review. *J. Neuroeng Rehabil.* 15, 9. doi: 10.1186/s12984-018-0350-6

- Conti, R., Meli, E., and Ridolfi, A. (2016). A novel kinematic architecture for portable hand exoskeletons. *Mechatronics* 35, 192–207. doi: 10.1016/j.mechatronics.2016.03.002
- De Weerd, W., and Harrison, M. (1985). Measuring recovery of arm-hand function in stroke patients: a comparison of the brunstrom-fugl-meyer test and the action research arm test. *Physiotherapy Can.* 37, 65–70. doi: 10.3138/ptc.37.2.065
- Desplenter, T., Zhou, Y., Edmonds, B. P., Lidka, M., Goldman, A., and Trejos, A. L. (2020). Rehabilitative and assistive wearable mechatronic upper-limb devices: a review. *J. Rehabil. Assist. Technol. Eng.* 7:2055668320917870. doi: 10.1177/2055668320917870
- Diez, J. A., Blanco, A., Catalán, J. M., Badesa, F. J., Lledó, L. D., and García-Aracil, N. (2018). Hand exoskeleton for rehabilitation therapies with integrated optical force sensor. *Adv. Mech. Eng.* 10, 1687814017753881. doi: 10.1177/1687814017753881
- Dittli, J., Hofmann, U., Bützer, T., Lamercy, O., and Gassert, R. (2020). Remote actuation systems for fully wearable assistive devices: requirements, selection, and optimization for out-of-the-lab application of a hand exoskeleton. *Front. Rob. AI* 7:187. doi: 10.3389/frobt.2020.596185
- Dovot, L., Lamercy, O., Gassert, R., Maeder, T., Milner, T., Leong, T. C., et al. (2008). Handcare: a cable-actuated rehabilitation system to train hand function after stroke. *IEEE Trans. Neural Syst. Rehabil. Eng.* 16, 582–591. doi: 10.1109/TNSRE.2008.2010347
- Duret, C., Grosmaire, A.-G., and Krebs, H. I. (2019). Robot-assisted therapy in upper extremity hemiparesis: overview of an evidence-based approach. *Front. Neurol.* 10:412. doi: 10.3389/fneur.2019.00412
- Duruöz, M. T. (2014). “Assessment of hand functions,” in *Hand Function* New York, NY: Springer, 41–51.
- Duruoz, M. T. (2016). *Hand Function*. New York, NY: Springer.
- Hadi, A., Alipour, K., Kazeminasab, S., and Elahinia, M. (2018). Asr glove: a wearable glove for hand assistance and rehabilitation using shape memory alloys. *J. Intell. Mater. Syst. Struct.* 29, 1575–1585. doi: 10.1177/1045389X17742729
- Ho, N., Tong, K., Hu, X., Fung, K., Wei, X., Rong, W., et al. (2011). “An emg-driven exoskeleton hand robotic training device on chronic stroke subjects: task training system for stroke rehabilitation,” in *2011 IEEE International Conference on Rehabilitation Robotics* (Zurich: IEEE), 1–5.
- Huang, X., Naghdy, F., Naghdy, G., Du, H., and Todd, C. (2017). Robot-assisted post-stroke motion rehabilitation in upper extremities: a survey. *Int. J. Disabil. Hum. Dev.* 16, 233–247. doi: 10.1515/ijdh-2016-0035
- In, H., Kang, B. B., Sin, M., and Cho, K.-J. (2015). Exo-glove: a wearable robot for the hand with a soft tendon routing system. *IEEE Rob. Autom. Mag.* 22, 97–105. doi: 10.1109/MRA.2014.2362863
- Lamercy, O., Schröder, D., Zwicker, S., and Gassert, R. (2013). “Design of a thumb exoskeleton for hand rehabilitation,” in *Proceedings of the 7th International Convention on Rehabilitation Engineering and Assistive Technology* (Singapore: Singapore Therapeutic, Assistive and Rehabilitative Technologies (START) Centre), 41.
- Maciejasz, P., Eschweiler, J., Gerlach-Hahn, K., Jansen-Troy, A., and Leonhardt, S. (2014). A survey on robotic devices for upper limb rehabilitation. *J. Neuroeng. Rehabil.* 11, 1–29. doi: 10.1186/1743-0003-11-3
- Meng, Q., Meng, Q., Yu, H., and Wei, X. (2017). “A survey on semg control strategies of wearable hand exoskeleton for rehabilitation,” in *2017 2nd Asia-Pacific Conference on Intelligent Robot Systems (ACIRS)* (Wuhan: IEEE), 165–169.
- Milia, P., Peccini, M. C., De Salvo, F., Sfoldaroli, A., Grelli, C., Lucchesi, G., et al. (2019). Rehabilitation with robotic glove (gloreha) in poststroke patients. *Digit. Med.* 5, 62. doi: 10.4103/digm.digm\_3\_19
- Montagnani, F., Controzzì, M., and Cipriani, C. (2016). Independent long fingers are not essential for a grasping hand. *Sci. Rep.* 6:35545. doi: 10.1038/srep35545
- Polygerinos, P., Wang, Z., Galloway, K. C., Wood, R. J., and Walsh, C. J. (2015). Soft robotic glove for combined assistance and at-home rehabilitation. *Rob. Auton. Syst.* 73, 135–143. doi: 10.1016/j.robot.2014.08.014
- Putzu, F., Abrar, T., and Althoefer, K. (2018). “Development of a soft inflatable structure with variable stiffness for hand rehabilitation,” in *Computer/Robot Assisted Surgery (CRAS)*, Vol. 8 (London), 2.
- Randazzo, L., Iturrate, I., Perdakis, S., and Millán, J., d. R. (2017). mano: a wearable hand exoskeleton for activities of daily living and neurorehabilitation. *IEEE Rob. Autom. Lett.* 3, 500–507. doi: 10.1109/LRA.2017.2771329
- Rechy-Ramirez, E. J., and Hu, H. (2015). Bio-signal based control in assistive robots: a survey. *Digit. Commun. Netw.* 1, 85–101. doi: 10.1016/j.dcan.2015.02.004
- Riddle, M., MacDermid, J., Robinson, S., Szekeres, M., Ferreira, L., and Lalone, E. (2020). Evaluation of individual finger forces during activities of daily living in healthy individuals and those with hand arthritis. *J. Hand Ther.* 33, 188–197. doi: 10.1016/j.jht.2020.04.002
- Rodgers, H., Bosomworth, H., Krebs, H. I., van Wijck, F., Howel, D., Wilson, N., et al. (2019). Robot assisted training for the upper limb after stroke (ratuls): a multicentre randomised controlled trial. *Lancet* 394, 51–62. doi: 10.1016/S0140-6736(19)31055-4
- Rose, C. G., and O'Malley, M. K. (2018). Hybrid rigid-soft hand exoskeleton to assist functional dexterity. *IEEE Rob. Autom. Lett.* 4, 73–80. doi: 10.1109/LRA.2018.2878931
- Sarac, M., Solazzi, M., and Frisoli, A. (2019). Design requirements of generic hand exoskeletons and survey of hand exoskeletons for rehabilitation, assistive, or haptic use. *IEEE Trans. Haptics* 12, 400–413. doi: 10.1109/TOH.2019.2924881
- Secciani, N., Bianchi, M., Meschini, A., Ridolfi, A., Volpe, Y., Governi, L., et al. (2018). Assistive hand exoskeletons: the prototypes evolution at the university of florence. *Mech. Mach. Sci.* 68, 307–315. doi: 10.1007/978-3-030-03320-0\_33
- Secciani, N., Bianchi, M., Ridolfi, A., and Allotta, B. (2019). Assessment of a hand exoskeleton control strategy based on user's intentions classification starting from surface emg signals. *Biosyst. Biorobot.* 22, 440–444. doi: 10.1007/978-3-030-01887-0\_85
- Secciani, N., Pagliai, M., Buonamici, F., Vannetti, F., Volpe, Y., and Ridolfi, A. (2021). A novel architecture for a fully wearable assistive hand exoskeleton system. *Mech. Mach. Sci.* 91, 120–127. doi: 10.1007/978-3-030-55807-9\_14
- Secciani, N., Topini, A., Ridolfi, A., Meli, E., and Allotta, B. (2020). A novel point-in-polygon-based semg classifier for hand exoskeleton systems. *IEEE Trans. Neural Syst. Rehabil. Eng.* 28, 3158–3166. doi: 10.1109/TNSRE.2020.3044113
- Tong, K., Ho, S., Pang, P., Hu, X., Tam, W., Fung, K., et al. (2010). “An intention driven hand functions task training robotic system,” in *2010 Annual International Conference of the IEEE Engineering in Medicine and Biology* (Buenos Aires: IEEE), 3406–3409.
- Troncosi, M., Mozaffari-Foumashi, M., and Parenti-Castelli, V. (2016). An original classification of rehabilitation hand exoskeletons. *J. Robot. Mech. Eng. Res* 1, 17–29. doi: 10.24218/jrmer.2016.18
- Wang, D., Meng, Q., Meng, Q., Li, X., and Yu, H. (2018). Design and development of a portable exoskeleton for hand rehabilitation. *IEEE Trans. Neural Syst. Rehabil. Eng.* 26, 2376–2386. doi: 10.1109/TNSRE.2018.2878778
- Yozbatiran, N., Der-Yeghian, L., and Cramer, S. C. (2008). A standardized approach to performing the action research arm test. *Neurorehabil. Neural Repair.* 22, 78–90. doi: 10.1177/1545968307305353
- Yu, S., Perez, H., Barkas, J., Mohamed, M., Eldaly, M., Huang, T.-H., et al. (2019). A soft high force hand exoskeleton for rehabilitation and assistance of spinal cord injury and stroke individuals. *Front. Biomed. Devices* 41037:V001T09A011. doi: 10.1115/DMD2019-3268
- Yun, Y., Dancus, S., Esmatloo, P., Serrato, A., Merring, C. A., Agarwal, P., et al. (2017). “Maestro: an emg-driven assistive hand exoskeleton for spinal cord injury patients,” in *2017 IEEE International Conference on Robotics and Automation (ICRA)* (Singapore: IEEE), 2904–2910. doi: 10.1109/ICRA.2017.7989337
- Yurkewich, A., Kozak, I. J., Ivanovic, A., Rossos, D., Wang, R. H., Hebert, D., et al. (2020). Myoelectric untethered robotic glove enhances hand function and performance on daily living tasks after stroke. *J. Rehabil. Assist. Technol. Eng.* 7:2055668320964050. doi: 10.1177/2055668320964050
- Zhang, K., Chen, X., Liu, F., Tang, H., Wang, J., and Wen, W. (2018). System framework of robotics in upper limb rehabilitation on poststroke

motor recovery. *Behav. Neurol.* 2018:6737056. doi: 10.1155/2018/6737056

**Conflict of Interest:** The authors declare that the research was conducted in the absence of any commercial or financial relationships that could be construed as a potential conflict of interest.

**Publisher's Note:** All claims expressed in this article are solely those of the author and do not necessarily represent those of their affiliated organizations, or those of the publisher, the editors and the reviewers. Any product that may be evaluated in

this article, or claim that may be made by its manufacturer, is not guaranteed or endorsed by the publisher.

*Copyright © 2021 Secciani, Brogi, Pagliai, Buonamici, Gerli, Vannetti, Bianchini, Volpe and Ridolfi. This is an open-access article distributed under the terms of the Creative Commons Attribution License (CC BY). The use, distribution or reproduction in other forums is permitted, provided the original author(s) and the copyright owner(s) are credited and that the original publication in this journal is cited, in accordance with accepted academic practice. No use, distribution or reproduction is permitted which does not comply with these terms.*



# Usability Assessment of Body Controlled Electric Hand Prostheses: A Pilot Study

Sasha B. Godfrey<sup>1,2</sup>, Cristina Piazza<sup>3</sup>, Federica Felici<sup>1</sup>, Giorgio Grioli<sup>1</sup>, Antonio Bicchi<sup>1,4</sup> and Manuel G. Catalano<sup>1,2\*</sup>

<sup>1</sup> Soft Robotics for Human Cooperation and Rehabilitation, Center for Robotics and Intelligent Systems, Istituto Italiano di Tecnologia, Genoa, Italy, <sup>2</sup> Assistive and Restorative Technology Laboratory, Rehabilitation Medicine Research Center, Mayo Clinic, Rochester, MN, United States, <sup>3</sup> Department of Informatics and Munich Institute of Robotics and Machine Intelligence, Technical University of Munich, Munich, Germany, <sup>4</sup> Centro "E. Piaggio" and Dipartimento di Ingegneria Informatica, University of Pisa, Pisa, Italy

## OPEN ACCESS

### Edited by:

Josep M. Font-Llagunes,  
Universitat Politècnica de Catalunya,  
Spain

### Reviewed by:

Amit N. Pujari,  
University of Hertfordshire,  
United Kingdom  
Alejandro Zacarías,  
Instituto Politécnico Nacional (IPN),  
Mexico  
Strahinja Dosen,  
Aalborg University, Denmark

### \*Correspondence:

Manuel G. Catalano  
manuel.catalano@iit.it

**Received:** 20 March 2021

**Accepted:** 06 October 2021

**Published:** 05 November 2021

### Citation:

Godfrey SB, Piazza C, Felici F, Grioli G, Bicchi A and Catalano MG (2021) Usability Assessment of Body Controlled Electric Hand Prostheses: A Pilot Study.  
*Front. Neurobot.* 15:683253.  
doi: 10.3389/fnbot.2021.683253

Poly-articulated hands, actuated by multiple motors and controlled by surface myoelectric technologies, represent the most advanced aids among commercial prostheses. However, simple hook-like body-powered solutions are still preferred for their robustness and control reliability, especially for challenging environments (such as those encountered in manual work or developing countries). This study presents the mechatronic implementation and the usability assessment of the SoftHand Pro-Hybrid, a family of poly-articulated, electrically-actuated, and body-controlled artificial hands, which combines the main advantages of both body-powered and myoelectric systems in a single device. An assessment of the proposed system is performed with individuals with and without limb loss, using as a benchmark the SoftHand Pro, which shares the same soft mechanical architecture, but is controlled using surface electromyographic sensors. Results indicate comparable task performance between the two control methods and suggest the potential of the SoftHand Pro-Hybrid configurations as a viable alternative to myoelectric control, especially in work and demanding environments.

**Keywords:** prosthetic hand, myoelectric control, body-powered prostheses, prosthetic control, soft robotics

## 1. INTRODUCTION

Upper limb loss is disproportionately found in developing countries with trauma and war as the most common causes (World Health Organization, 2004). While disease is also a frequent cause, upper limb loss globally tends to affect a younger, working-age population (van der Sluis et al., 2009). It is therefore important that prosthetic solutions take this population into account by being economically accessible and robust to strenuous use or hostile environments. However, a 1985 study found that 75% of persons with amputation (upper, lower, and multiple) change occupation group when they return to the work-force post-amputation, moving from machining, processing, fabrication, and construction to service, clerical, and sales (Millstein et al., 1986). Additionally, only 21% returned to their pre-amputation job and more than half noted negative repercussions on career potential following amputation (Millstein et al., 1986). A recent literature review (Darter et al., 2018) found that data on returning to work post-amputation varies greatly (48–89% of individuals) but that returning to one's previous position continues to be rare and less frequent for manual rather than office work.



Active prosthetic solutions are either body-powered or electric. Most of the former are controlled using a shoulder harness that encompasses one or both shoulders (figure-of-nine or figure-of-eight, respectively) depending on the amputation(s), see **Figure 1**. Most of the latter are myoelectrical controlled, that is using muscle signals in the residual limb. Myoelectric devices are typically anthropomorphic in appearance if not in structure: most devices have a hand-shaped glove or shell covering a tri-digit structure. The newest devices, however, have five fingers and multiple motors to enable various postures. While the former is relatively simple to control, they provide only a single, rigid, C-shaped grasp. The latter, in contrast, offer more grasp modalities but place a higher cognitive burden on the user (Kuiken et al., 2016). Along with control complexity, weight tends to increase with myoelectric prosthetic complexity, due in part to the use of multiple motors (Belter et al., 2013), and robustness tends to decrease. In contrast, body-powered prostheses are most typically split-hook models and thus are not anthropomorphic. Some specific domains show better performance by one type of prosthesis over the other (Carey et al., 2017), e.g., myoelectric hands tend to be more accepted for low-intensity work, while their drawbacks, in general, render them less desirable for use in manual tasks in home and work environments and in resource-poor areas, which represent tough testing grounds for a prosthetic system. Conversely, body-powered hooks are the most used aids in such contexts. As such, many prosthesis users have more than one prosthetic device, choosing between them based on activity or setting, for example preferring one for work environments and another for social situations (Millstein et al., 1986; Dakpa and Heger, 1997).

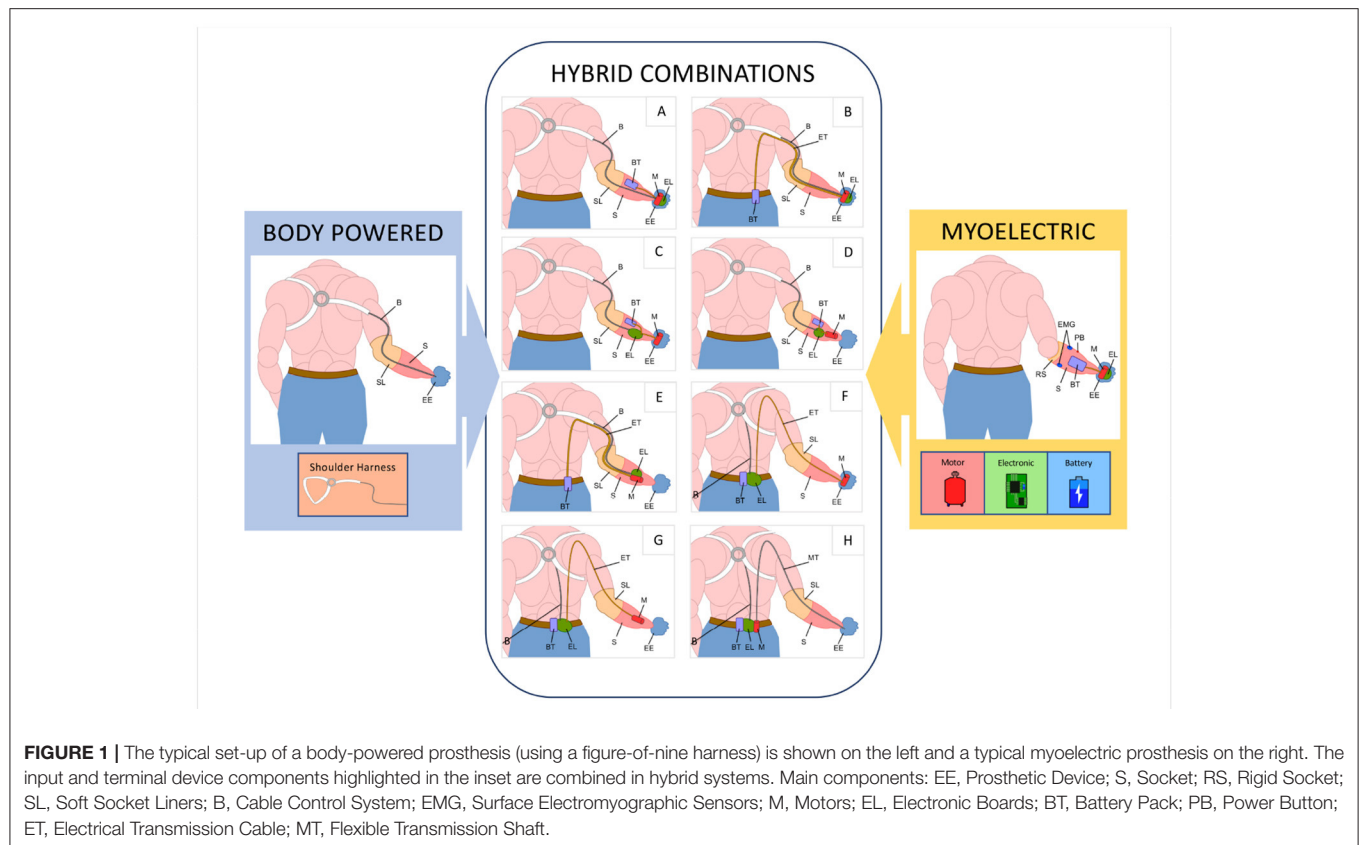
Each type has its advantages and disadvantages, and although commercial and research innovations tend toward highly-sophisticated myoelectric devices, many individuals continue to use body-powered systems (Biddiss and Chau, 2007b; Østlie et al., 2012), which have seen only minor improvements in the last century (Hashim et al., 2018). Sophisticated myoelectric technologies may be difficult to control or lack reliability and may not provide adequate support across all activities of daily living. The latter aspect is also highlighted by the outcomes of international competitions such as the Cybathlon - Powered Arm Prosthetic Race (Riener, 2016). In both editions (Cybathlon 2016 and Cybathlon 2020) approaches aiming at simple body-powered designs proved notable benefits and outperformed all myoelectric prostheses in the competition. This is not to say that one prosthesis type is superior to another. There is insufficient evidence to draw such a conclusion and ultimately the user must decide based on need, access, and other personal factors (Carey et al., 2015). Indeed, Østlie et al. (2012) surveyed 181 prosthesis users and found roughly 30% used a body-powered device as their primary prosthesis and roughly 34% used a myoelectric device. Of those users listing a secondary device, roughly 36% used a body-powered device and 27% a myoelectric one.

Looking more closely at these advantages and disadvantages, body-powered prostheses tend to be more robust and lighter than their myoelectric counterparts, with different materials available (aluminium, steel, etc.) to balance robustness and weight to suit the needs of the user. Furthermore, the shoulder harness

provides a straight-forward and easy-to-use control method with limited sensory feedback (Brown et al., 2017), at the cost of applying pressure to the axilla, which can cause discomfort or even damage to the brachial plexus over time (Fryer, 1992). Users of myoelectric devices tend to rely on visual feedback to guide movements; however, the sound of the motor is also used to inform prosthetic control (Antfolk et al., 2013). In terms of comfort, myoelectric systems require a rigid interface between the socket and the residual limb to ensure adequate contact with surface electromyographic sensors (sEMG), while body-powered systems can employ more comfortable soft socket liners, and the contact area with the residual limb can be significantly increased. Moreover, performance of sEMG drops severely when impurities, such as dirt or sweat, interpose between the sEMG and the underlying skin; this problem can be mitigated at least in part with the use of solutions such as linear transducers, switches, and other biomechanical control methods (Childress, 1992; Muzumdar, 2004). Body-powered prosthesis function does not suffer from these aspects.

This work explores the concept of a “hybrid” configuration that aims to feature robust and intuitive control in a prosthesis that is both resilient to harsh environments, highly functional, and anthropomorphic, thanks to the combination of the main advantages of both body-powered and myoelectric systems in a single device. As presented in **Figure 1**, a myoelectric hand prosthesis requires three main additional components compared to a body-powered prosthesis: a motor to actuate the device, an electronic board to control it, and a battery to power it, all generally located within the hand and socket. The approach proposed has the advantage of enabling multiple solutions through the placement of the electro-mechanical components in three possible locations: on the hand, in the socket, or on the body of the user. Considering different solutions among these, the designer can thus create a class of devices suitable for different applications.

Although current commercial prostheses are rigid, novel trends in robotic research are moving the state of the art of artificial hands in a different direction, which includes soft materials and structures and simpler actuation mechanisms (Piazza et al., 2019). Soft robotics may present a particular advantage in challenging environments by naturally being more robust to collisions and similar mis-use (Negrello et al., 2020). In Godfrey et al. (2018), we proposed the SoftHand Pro, a myoelectric prosthetic device whose movement is based on neuroscientific principles of hand joint coordination, or synergies, in line with the proposal above. Despite good results in terms of grasping capabilities, ease of use, and user acceptance (Godfrey et al., 2018), the SoftHand Pro maintains those drawbacks directly related to the use of sEMG sensors (e.g., sensitivity to dirt and dust, socket interface, costs). Moreover, functionality of myoelectric solutions is dependent on many constraints, not only connected with the technology itself but also related to clinical aspects (i.e., insufficient muscle activation in the residual limb). For these reasons, in Piazza et al. (2017), we presented the concept of the SoftHand Pro-Hybrid (SHPH), to combine the easy-to-use control of a body-powered prosthesis with the power available from an electric terminal




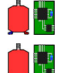

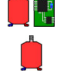


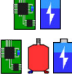

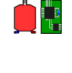


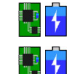



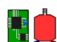



device. As introduced in the detailed analysis of Piazza et al. (2017), considering all possible combinations of components and locations, 8 potential solutions were isolated (refer to **Table 1**, for details), and one of them was briefly evaluated with only one amputee subject (an expert user of a body-powered hook). The work presented in Piazza et al. (2017) sketches the main ideas behind the platform and shows the main technical advantages of such an approach: simple control of the prosthetic hand while retaining high grip power and providing a high level of robustness, adaptivity, and resilience. However, it does not provide any clinical assessment of the platform or any information about the mechatronic designs that can be used to build all the possible solutions.

The work presented herein has as its main goal to assess the usability of a hybrid system with multiple subjects (not expert body-powered users), through the adoption of standard clinical tests, and make a comparison with a system, based on the same architecture and used as a benchmark, but activated by conventional myoelectric control (the SoftHand Pro). Given the lack of literature on specific tests to assess prostheses in work and challenging environments, we selected the ACMC test and the System Usability Scale (SUS) as our main outcome measures. The former because it takes in consideration several aspects of manipulation (e.g., the releasing or the holding phase) in the context of, but independent from, everyday tasks, and the latter because it is a standard questionnaire used to evaluate technological devices. The results of this investigation

suggest that hybrid solutions can be a valid alternative to myoelectric control, e.g., in situations that require high grip power, grasp versatility and resilience or depending on user preferences. Specifically, hybrid solutions may be more suitable for working activities and challenging environments, where the use of sEMG sensors, that can be sensitive to sweat or socket alignment, increase the overall complexity. The study extends the work in Piazza et al. (2017) exploring the usability of two of the solutions presented in that work. Furthermore, it provides a first insight into the possibility of using the SoftHand architecture to make a direct comparison between myoelectric and body-power control modes. Indeed, few studies address this topic (Edelstein and Berger, 1993; Carey et al., 2009), which is of great relevance to understanding which control modes are best suited to a user or use-case. In the opinion of the authors, these types of comparisons could help advance the research field and warrant deeper investigation in future work. To achieve these goals, we proceed as follows. Sections 2.1, 2.2, and 2.3 present the mechanical implementation of the hybrid and myoelectric solutions, while section 2.4 discusses pros and cons of each layout, with respect to a set of specifications and indications that comes from a detailed analysis of surveys and studies available in the state of art. Then, sections 2.5 and 2.6 present the assessments selected for this analysis and the protocol performed with individuals with and without limb loss. Results are presented in section 3 and discussed in section 4.

**TABLE 1** | Summary of hybrid component locations for 8 feasible solutions (Piazza et al., 2017) and, for reference, myoelectric solution (BM) component location (Godfrey et al., 2018).

SOL	HAND 	SOCKET 	EXT BOX 
A			
B			
C			
D			
E			
F			
G			
H			
BM			-

## 2. MATERIALS AND METHODS

### 2.1. SoftHand Architecture

The mechanical structure of the terminal devices considered in this work is based on the architecture of the Pisa/IIT SoftHand (Catalano et al., 2014), from which both the myoelectrically controlled and the hybrid body controlled prosthetic hands are derived. The architecture presents an anthropomorphic shape with 19 DoFs. Each finger consists of a group of rolling joints connected by elastic ligaments. The elastic bands, fixed on either side of the joint, make the system soft and safe and allow the hand to automatically return to its correct configuration, i.e., after severe dislocations. The transmission system uses one tendon that runs through the entire hand in two levels of pulleys, giving adaptivity to the overall system without a differential gear mechanism. The soft robotic mechanical design gives the hand an overall robustness with the capability of adapting its closure to the shape of objects. Phalanges and structural parts of the palm are crafted using high-performance thermoplastic materials (nylon reinforced with 35% of glass fibres), and are produced using injection molding techniques, enabling a sizable reduction of weight and costs. Such technological solutions allow the possibility of working in harsh and dangerous environments (for more details please refer to Piazza et al., 2017; Godfrey et al., 2018; Mura et al., 2018; Negrello et al., 2020). As an example of these capabilities, photo-sequence in **Figure 10** shows one of the subjects enrolled in this study performing a grasping task in an underwater setting.

### 2.2. Body Controlled SoftHand: Concept and Development

The hybrid solutions adopt the structural architecture described in section 2.1 and integrate a Hosmer body-powered wrist to interface with the socket, enabling pronosupination movements through manual wrist rotation. The idea of a

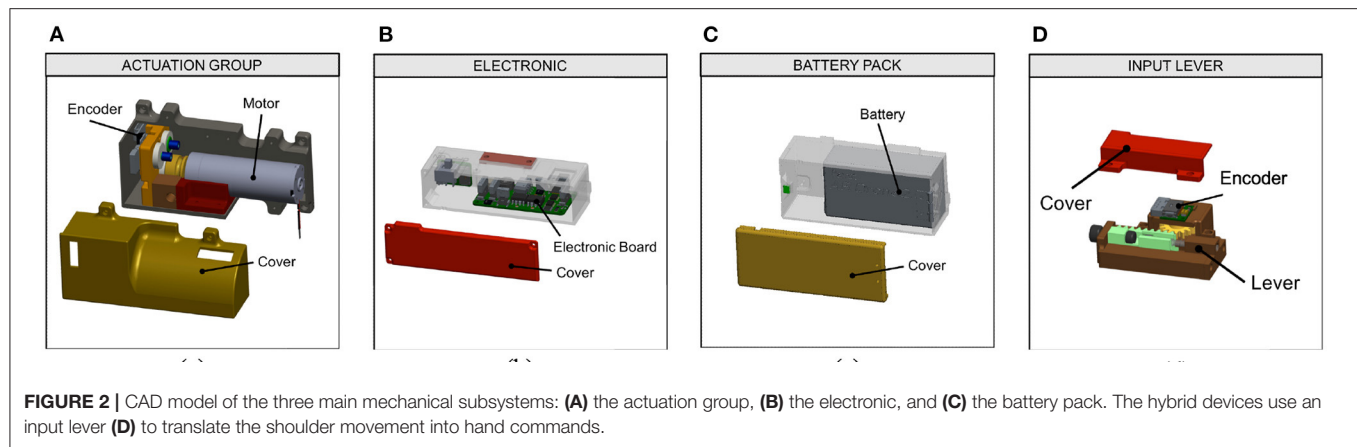
hybrid configuration can be realized in different ways. In our approach, the hybrid system uses an electromechanical lever to translate inputs from a shoulder harness to motor control. The electromechanical lever consists of a linear mechanism and spur gear. The position is read by a single encoder that transmits signals to the motor through the electronic board to command hand opening/closing.

The amount of shoulder excursion required to correctly operate the SHPH (i.e., to yield full opening/closure and switch between control modalities) is modifiable to balance comfort, ease-of-use, sensitivity, and resolution. The benefits of this mechanism are visible already in Piazza et al. (2017). These values were adjusted for each study subject at the start of each trial and, if needed, fine-tuned during the training period. Additionally, the user can use the lever to switch between two modes, voluntary-opening (VO) and voluntary-closing (VC), (Sensinger et al., 2015) by compressing the end-stroke spring on the remote or mounted lever through additional shoulder rotation. The ability to switch between modes allows users to employ whichever they were most comfortable with, both in general and, if desired, on a task-by-task basis; for example, using VO for carrying robust and/or heavy objects and VC for handling more fragile objects or for precision grasping. The other components can be grouped into three modules, each one embedding a mechanical subsystem as shown in **Figure 2**:

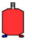


1. Actuation Group, which includes the motor and a position sensor. In our implementation, a DCX 22S + GPX 83:1 Maxon motor is used, combined with an Austrian Microsystem Magnetic Encoder.
2. Electronic Board, equipped with a Cypress PSOC microcontroller and a daisy chain RS485 Bus and several i/o connections. The board can communicate with magnetic sensors through the SSR protocol. The custom electronic board is derived from Della Santina et al. (2017);
3. Battery Pack, used to power the hand (in our implementation, an off-the-shelf battery from Parrot AirDrone 2.0 with a capacity of 1,500 mAh).

The technical specifications of the components included in the three modules are reported in **Table 2**; these can be used to evaluate all eight proposed solutions. All eight solutions are practicable and can be adapted to different situations, activities or to meet user needs.

This concept becomes clearer if we apply a multi-variate Pareto analysis (Hwang and Yoon, 2012) to the different configurations following specific criteria. Using this method, it is possible to highlight how each configuration measures against the different criteria, which ideally should be selected and customized with the user. To give a more clear example of this concept, we choose four criteria considering the critical factors motivating device abandonment and leading consumer design priorities, as stated in the literature. From Cordella et al. (2016) it is evident how comfort, function and appearance of the prosthesis are the aspects with the highest priority for users and common to all device types. In particular (Biddiss et al., 2007) highlights how, for body-powered systems, harness comfort and weight reduction are among the main problems



**TABLE 2 |** Technical specifications of the three mechanical subsystems.

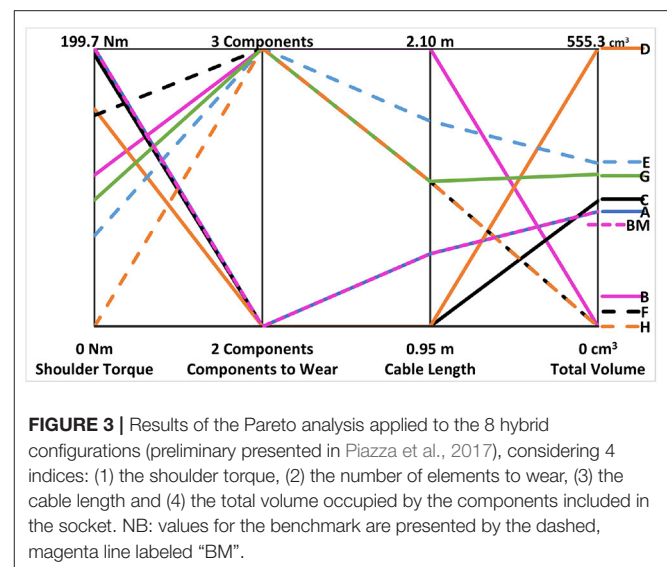
	Motor Group 	Electronic 	Battery Pack 
Weights	130 g	15 g	202 g
Dimensions	$d = 22 \text{ mm}$ , $l = 80 \text{ mm}$	$60 \times 30 \times 12 \text{ mm}$	$94 \times 66 \times 37 \text{ mm}$

experienced by the users. Moreover, it is also important to take into account characteristics specific to the user, such as the level of limb loss (Biddiss and Chau, 2007a), a factor which is strictly connected to the design of the socket and to the placement of the device electro-mechanical components. Starting from these considerations, the following criteria were selected for this study:

1. Shoulder torque, directly related to system weight and placement (Cordella et al., 2016). It is calculated considering the linear distance from the shoulder to the component using standard anthropometric measurements (average data between male and female) from McConville et al. (1980); Dempster (1955) and the weights of each component. We are not considering the weight of the terminal device and socket because, for our analysis, it will be the same in all the configurations. This criterion relates both to function as well as comfort. If the shoulder torque is excessively high, the hand will be more difficult to operate, as it will require more strength. Additionally, shoulder torque contributes to repetitive use strain and injury, typically to the brachial plexus, as mentioned above (Fryer, 1992);
2. Number of elements to wear, an important consideration in terms of comfort (Cordella et al., 2016) as well as appearance. Wearing multiple components can render the system more bulky and less aesthetically pleasing as well as potentially making the system more challenging to don and doff. The elements considered in this analysis are hand, socket and an external box. Note: as the hand and socket are necessary for all solutions, this criterion refers primarily to the external box;
3. Cable length, to connect each subsystem (both electric and driving cables) and calculated considering the distance the cables traverse across the arm and/or back following standard

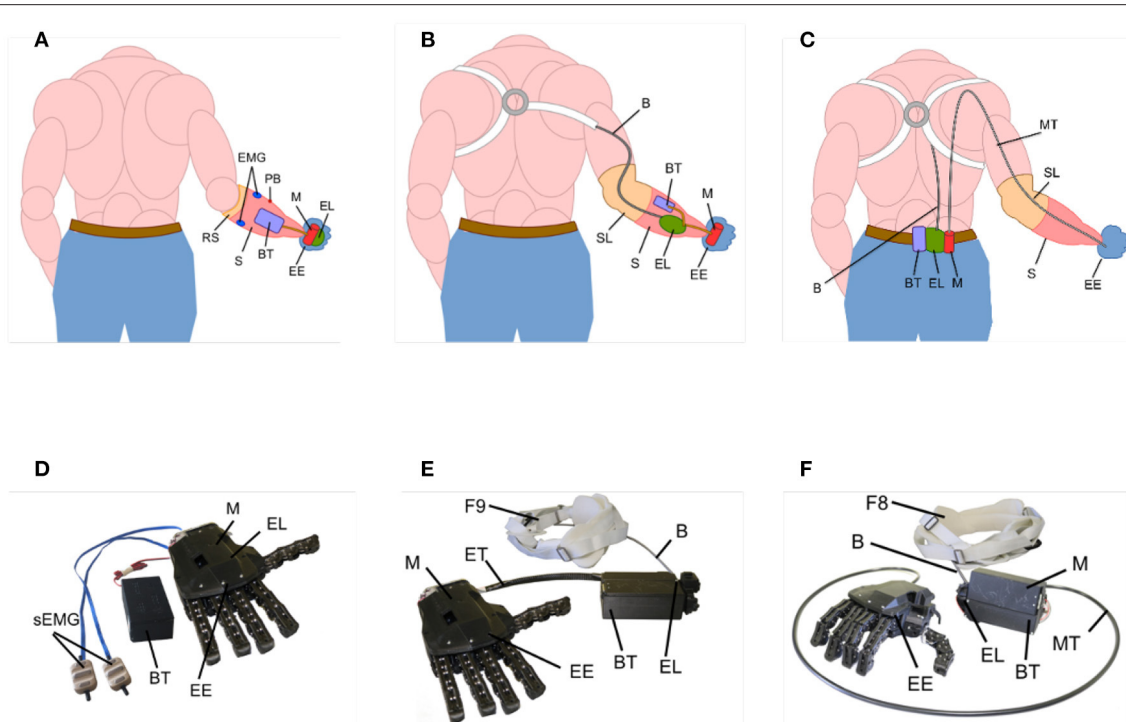
**TABLE 3 |** Data of shoulder torque, components to wear, cable length, and total volume criteria for each hybrid configuration and benchmark.

SOL	Shoulder torque (Nm)	Comp. to wear	Cable length (m)	Total vol. (cm <sup>3</sup> )
A	199.650	2	1.250	229.548
B	108.750	3	2.100	0
C	195.150	2	0.950	251.148
D	156.150	2	0.950	555.254
E	65.250	3	1.800	325.706
F	151.500	3	1.550	0
G	90.900	3	1.550	304.106
H	0	3	1.550	0
BM	199.650	2	1.250	229.548



anthropometric measurements from McConville et al. (1980); Dempster (1955). As discussed above, comfort in term of cables is highlighted as an important aspect for body-powered users (Biddiss et al., 2007). In addition to comfort, cabling can





**FIGURE 4 |** Schematic placement (A–C; Benchmark, Compact, and Hardy Configurations, respectively) of the components of the configurations tested in this study on the hand, socket, and waist of the user and pictures (D–F) of the physical devices used. EE, Prosthetic Device; S, Socket; RS, Rigid Socket; SL, Soft Socket Liners; B, Cable Control System; EMG, Surface Electromyographic Sensors; M, Motors; EL, Electronic Boards; BT, Battery Pack; PB, Power Button; BT, Battery Pack; ET, Electrical Transmission Cable; MT, Flexible Transmission Shaft; F8, Figure-of-eight Harness; F9, Figure-of-nine Harness.

affect function in terms of mechanical feasibility, as some of the user's shoulder effort is lost along the flexible transmission shaft. Additionally, cabling may affect both appearance and aesthetics depending on cable routing and the user's ability to hide cables under clothing, if desired;

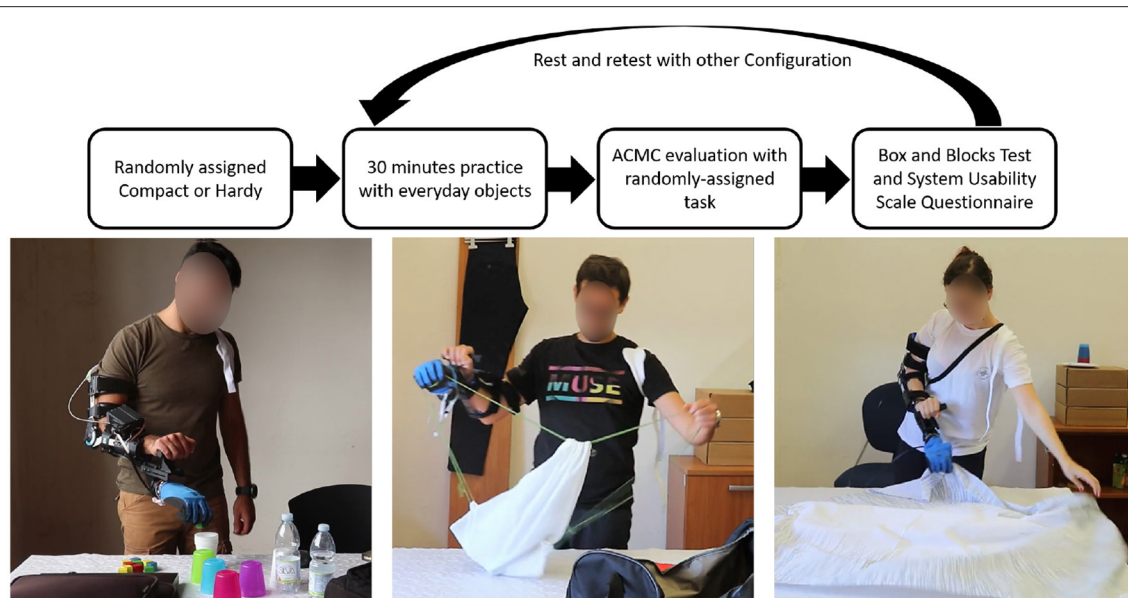
4. Total volume occupied by the components included in the socket, calculated considering the volume of each electromechanical subsystem for each case. This aspect should not be underestimated as it relates to limb length (important for function and aesthetics) and device feasibility, depending on residual limb length and especially in the case of users with distal amputation (Biddiss and Chau, 2007a).

The metrics for each criterion for the hybrid configurations are shown in **Table 3**, while the results of the analysis are presented in **Figure 3**. For each criterion, a smaller number is preferable. The goal of the Pareto analysis is to find the ideal solution considering multiple criteria, thus configurations were considered that minimized the most criteria. It should be noted that the most criteria minimized by any configuration were two; no configuration minimized three or four criteria. From the analysis, Configurations C and D minimized both "Components to Wear" and "Cable Length", while Configuration H minimizes "Shoulder Torque" and "Total Volume". Solutions where all components are integrated into the hand and socket (Configuration A, C, and D) provide the advantage of being

less cumbersome and supplying the components with at least limited protection against environmental factors such as dust or liquid. These solutions, however, depend on the length of the residual limb. For longer limb lengths, more components can be placed on the body (such as Configurations F–H), providing additional protection against environmental factors, possibly even rendering the system waterproof at the level of the hand or arm. Finally, for scenarios requiring increased grasp strength, solutions such as those in Configurations G or H could be used with more powerful motors. Considering the results of the analysis and the features of the configurations themselves, we chose to develop two different solutions. Configurations C and D minimize the same two criteria, as mentioned above. Configuration D creates 25% less shoulder torque while Configuration C requires less than half the total volume. As mentioned earlier, total volume is an essential aspect of device feasibility, usability, and acceptance and thus Configuration C was chosen over D. Configuration C was developed alongside Configuration H, as they provide very different theoretical advantages to the user.

### 2.3. Myoelectrically Controlled SoftHand

The myoelectrically controlled SoftHand Pro, used as a benchmark, adopts the structural architecture described in section 2.1, and is actuated by a DCX 22S + GPX 83:1 Maxon



**FIGURE 5 | Top:** Flow-chart of the experimental protocol. **Bottom:** Intact-limb subjects practicing with everyday objects (left) and testing the two Hybrid Configurations during tasks of daily living as part of a standardized clinical test: SHPH-C, ACMC "packing" task (middle) and SHPH-H, ACMC "setting the table" task (right).

motor (as in the hybrid configurations) mounted on the dorsal side of the hand. This hand shares the same electronic board of the hybrid hands, but can read and elaborate EMG signals provided by a pair of sensors (13E200=60, OttobockGmbH, Germany). Different standard controllers are available in the board; the one adopted in this study is based on an integral control of myoelectric signals which command the reference velocity of the motor (for more details see Godfrey et al., 2018). Finally, the hand is equipped with a standard Ottobock Quick Disconnect Wrist, enabling wrist prono-supination movements through manual wrist rotation, comparable to the Hosmer device used for the hybrid configurations.

## 2.4. Experimental Setup

Among the eight possible hybrid solutions (please refer to Table 1), the solutions which best fit the selected criteria for our analysis (extracted from the literature) were solutions C and H. These two solutions were dubbed the Compact and Hardy Configurations, solutions C and H, respectively. The SoftHand Pro (Godfrey et al., 2018), was used as a benchmark. An overview of the three solutions used in the experimental section is presented in Figure 4, highlighting the main components:

- **Benchmark Configuration**, myoelectrically controlled using 2 surface EMG sensors included directly in the socket. Motor and electronics are embedded directly in the palm of the hand.
- **Compact Configuration**, this hybrid configuration uses a figure-of-nine harness as input control. The motor is embedded in the hand, while the electronics, lever, and battery are integrated in the socket/forearm of the user.
- **Hardy Configuration** displaces all three electromechanical components to the waist. In this hybrid configuration, the

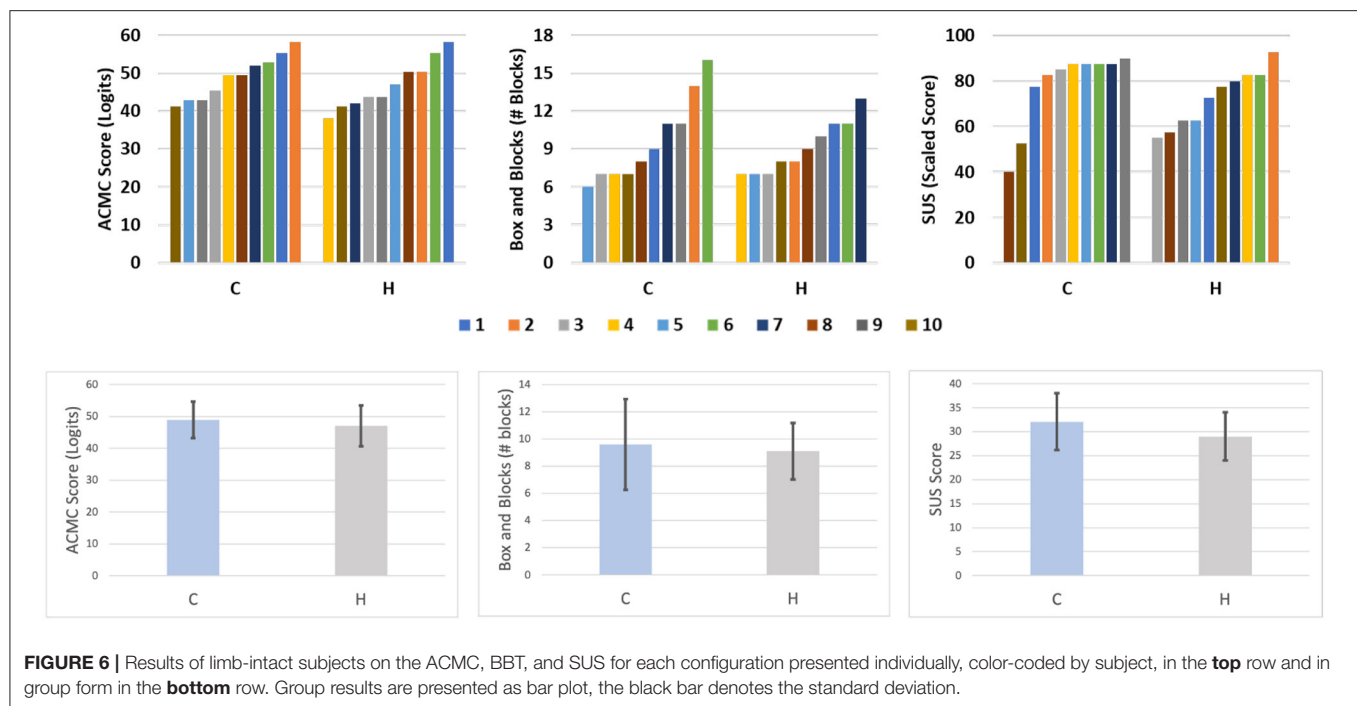
**TABLE 4 |** Demographics of subjects with limb loss.

Subj.	Age (yrs)	Sex	Time since amputation	Main prosthesis (Alt)	BP exper. level	MP exper. level
LL1	37	F	37 years	Cosmetic	Low	High
LL2	23	F	22 years	None (MP)	None	Med
LL3	41	M	7 years	BP (MP)	Low	High

MP, myoelectric prosthesis; BP, body-powered prosthesis.

actuation lever is connected to a figure-of-eight harness. A steel Bowden cable goes from the motor group to the hand-winding system, to operate hand opening and closing.

Broadly speaking, the Compact Configuration has the main components embedded in the hand and socket, which makes the system more integrated but increases the weight of the distal part and reduces resistance to liquids. In the Hardy solution, the electromechanical components are placed on the body of the user, which makes the whole system bulkier and less aesthetically pleasing but can be very effective for work environments because the total weight of the system is distributed along the body of the user and the terminal device is capable of interacting with dangerous environmental factors such as dust or liquids (see Figure 10). The Benchmark Configuration, similar to the Compact one, has the electromechanical components distributed in the hand and socket. This configuration is myoelectrically controlled so no cables are passing along the body of the user. However, the sEMG sensors are sensitive to environmental factors (i.e., liquid, dust, etc.) or impurities (i.e.,

**TABLE 5 |** Limb-intact subject results.

	<b>Solution C</b>	<b>Solution H</b>
	<b>Mean <math>\pm</math> standard deviation</b>	<b>Mean <math>\pm</math> standard deviation</b>
ACMC	49 $\pm$ 5.73	47 $\pm$ 6.45
BBT	9.6 $\pm$ 3.34	9.1 $\pm$ 2.08
SUS	77.8 $\pm$ 6.89	72.5 $\pm$ 5.01

dirt or sweat), which decreases the suitability of this system in working environments.

## 2.5. Assessment Tools

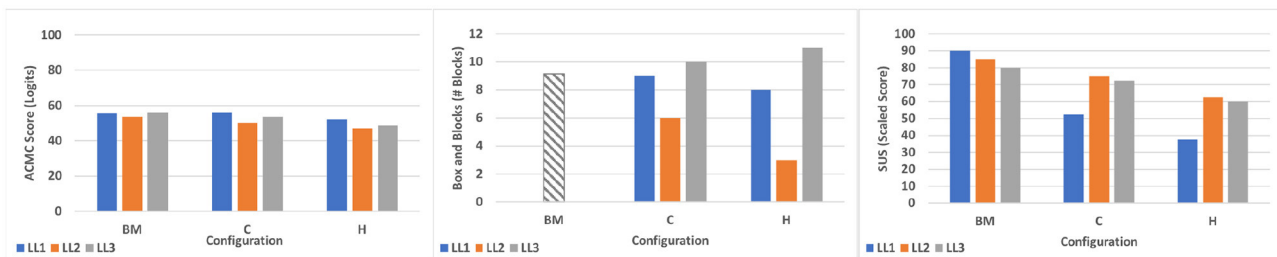
The hybrid configurations were validated with standard clinical and technology assessments (ACMC, BBT, SUS) to evaluate the strengths and weaknesses of the proposed solutions. The Assessment of Capacity for Myoelectric Control (ACMC) is a standard observational clinical test able to assess the ability to control a prosthetic hand in a daily living task (Hermansson et al., 2005). The rater may choose one among six validated tasks for the testee to perform, which reproduce hobbies or activities of daily living. The tasks were designed to feature similar types of movements in different contexts and to be interchangeable. Each item is an observable prosthetic hand movement on its own or in relation to other body parts and is scored from zero (incapable) to three (extremely capable). An algorithm (accessible online) is used to convert the raw score to ACMC logits, ranging from 0 to 100 with 100 representing ideal performance and prosthetic control. Among the different outcome measures available in the literature, the ACMC is unique, to the authors' knowledge, in breaking down tasks or actions into sub-movements of grasping, holding,

**TABLE 6 |** Limb loss subject results.

	<b>LL1</b>			<b>LL2</b>			<b>LL3</b>		
	<b>BM</b>	<b>C</b>	<b>H</b>	<b>BM</b>	<b>C</b>	<b>H</b>	<b>BM</b>	<b>C</b>	<b>H</b>
ACMC	55.4	56.3	51.9	53.7	50.3	47	56.3	53.7	48.7
BBT	-	9	8	-	6	3	-	10	11
SUS	90	52.5	37.5	85	75	62.5	80	72.5	60

The results of the three subjects with limb loss are presented as raw data.

releasing, and repetitive movements (see **Table 8**). Many tests were considered when designing the protocol, including the AM-ULA (Resnik et al., 2013) and the SHAP (Light et al., 2002). The former is rated by an experienced rater, usually an occupational or physical therapist, on the ability to perform a set of 18 ADLs and the quality of that performance, including smoothness of movements, speed, appropriateness and precision of grasp, etc. The latter is scored by time to completion of various tasks including grasping different light and heavy forms and completing ADLs; the rating is given by an algorithm that compares these times to a benchmark of able-bodied individuals. To enable comparison to a benchmark set of data, the SHAP protocol must be adhered to strictly, sometimes impeding a testee's typical way of approaching a particular task. While all three tests have strengths and weaknesses, ultimately, the ACMC was chosen as our primary outcome measure because, at this stage of device development, it allowed a better understanding of the detailed movement stages required to complete a task rather than task completion itself and focused specifically on control capacity. The Box and Blocks Test (BBT) is a standard clinical



**FIGURE 7 |** Results from subjects with limb loss testing the two hybrid configurations in comparison with the benchmark. Box and Blocks data of the benchmark are extracted from Godfrey et al. (2018).

**TABLE 7 |** Limb loss subjects average results.

	Median BM	Median C	Median H	Mean BM	Mean C	Mean H
ACMC	55.4	53.7	48.7	55.1	53.4	49.2
BBT	11.0	9	8	9.6	8.3	7.3
SUS	85	72.5	60	85	66.6	53.3

*°Data extracted from Godfrey et al. (2018).*

test to evaluate unilateral gross manual dexterity (Desrosiers et al., 1994). In the BBT, subjects are asked to move as many blocks as possible in 1 min from one compartment of a box to the other, with a vertical divider between them. The number of blocks carried over the partition is used to score the test. BBT was designed to measure hand performance in patients with neuromuscular disorders; it is often also used in prosthetic evaluations and is valid in this context (Resnik and Borgia, 2012). The System Usability Scale (SUS) is a simple, effective, and widely exploited tool for measuring the usability of a device (Brooke, 1996); it does not serve a diagnostic function nor is it limited to clinical applications. It is a 10-item questionnaire with five response options, ranging from “strongly agree” to “strongly disagree”. The subject’s scores for each question are converted to a new number between 0 and 4 based on whether the question was framed in a positive light (e.g., “I think that I would like to use this system frequently.”) or a negative one (e.g., “I found the system unnecessarily complex.”). The ten ratings are then added together and multiplied by 2.5 to convert the original cumulative score of 0–40 to 0–100.

## 2.6. Experimental Protocol

The research was performed under the oversight of the local ethics committee (Comitato Etico di Area Vasta Nord Ovest, CEAVNO), protocol number 1072. Informed Consent was obtained from all subjects. An open, crossover, experimental study was performed. The study was composed of two phases, one for each population, performed first with limb-intact subjects and subsequently with subjects with limb loss. The protocol was identical for both subject populations. Experiments with limb-intact subjects were performed first, to provide a preliminary evaluation of the usability of the two SHPH configurations, which had never undergone testing before. Then, tests with subjects

with limb loss followed, aimed at verifying limb-intact results and highlighting the advantages and disadvantages of the tested devices in comparison with a standard myoelectric configuration (SHP). Limb-intact subjects wore a forearm adapter that placed the SHPH under their natural hand. Furthermore, these subjects wore an arm brace (Innovator X Post-Op Elbow, Ossur) that restricted pronation/supination to more closely mimic the limitation or absence of this DOF in subjects with limb loss (see Figure 5). The latter subjects wore the SHP and SHPH on their typical socket or a socket made specifically for this study by a certified prosthetist.

Inclusion criteria for limb-intact subjects were 18 – 80 years of age, with normal motor and cognitive function, right-handedness, and able to understand the experimental procedures and give informed consent. For subjects with limb loss, inclusion criteria were 18–80 years of age, transradial difference, ability to understand the experimental procedures and give informed consent. Ten subjects matching the inclusion criteria, 7 males and 3 females, ranging from 25 to 32 years old, were included in the limb-intact group. The limb loss group comprised 3 subjects, 2 females and 1 male all with left transradial difference. Demographic information for the subjects with limb loss can be found in Table 4.

The set of assessments was built within the International Classification of Functioning, Disability and Health (ICF) framework. For each configuration, the experimental session consisted of brief training followed by functional testing and self-administered questionnaires on usability and pleasantness of the device tested. Configurations were presented in a pseudo-random order. In training, subjects partook in 30 min of grasping and manipulation practice, with objects of daily-living of different shapes, weights, and softness. To the authors’ knowledge, standard tests of hand function that replicate work tasks and/or a work environment have not been developed. The performance evaluation was thus composed of the Assessment of Capacity for Myoelectric Control (ACMC) test and the Box and Blocks Test (BBT). For the ACMC, four tasks among six were chosen: setting the table, packing a suitcase, preparing a dessert, and organizing the mail. The order of the four tasks of the ACMC were also pseudo-randomized. The randomization of the ACMC tasks and prosthetic configurations was adjusted to ensure a balance between the order of configurations, order of tasks, and the number of times a particular configuration was





**FIGURE 8 |** Average results of the three tested configurations for each ACMC item. The full list of items is reported in **Table 8**.

matched with a particular task. Among the authors, we have four trained and certified raters, two of whom co-scored the test. The devices were also rated using the System Usability Scale (SUS). During all procedures, comments by subjects on tests and devices were gathered. Rest periods were included as needed both within and between sessions. Overall, the entire measurement session lasted about 2 h.

### 3. RESULTS

#### 3.1. Limb-Intact Subjects

Following training, in which subjects practised both control modes (voluntary-open and voluntary-close, VO and VC, respectively) and how to switch between them, subjects were free to choose with which control mode to start the ACMC test. Out of 20 trials (2 ACMC tests across 10 subjects) only in 1 instance, or 5%, did the subject opt to start in VO. They were allowed to switch as many times as desired during the test; the number of times subjects switched volitionally was not recorded. We requested that subjects announce when they accidentally switched between voluntary-open and voluntary-close control modes. The Hardy Configuration had a higher average accidental switch rate than

the Compact Configuration ( $1.9 \pm 2.1$  and  $0.8 \pm 0.9$  switches per ACMC test, respectively).

Plots showing the results of the three tests across limb-intact subjects are presented in **Figure 6**. Group results for these subjects are presented in **Table 5**. Immediately evident from both sets of charts is the extent to which the results of the two configurations overlap. The Compact Configuration, however, appears to perform slightly better on all three tests. The distribution of the results passes the Shapiro-Wilk Test for normality and thus means were compared using a student's *t*-test and no significant differences were found between Compact and Hardy configurations. Additionally, the difference between the SHPH-C and SHPH-H in the ACMC does not exceed the value of "minimum detectable change" of 2.5 logits.

#### 3.2. Subjects With Limb Loss

Individual results from testing with subjects with limb loss can be found in **Table 6** and **Figure 7**, while group results are presented in **Table 7**. As described in section 2, our primary objective outcome measure was the ACMC. All results fall into the same category of clinical interpretation and are classified as "Generally Capable," which comprises scores between 46.7 and 57.1 logits. Furthermore, the minimum detectable change (MDC)

**TABLE 8 |** Description of the 22 items evaluated by ACMC.

A	GRIPPING
1	With Support
2	Power Grip Without Support
3	Precision Grip Without Support
4	Appropriate Force
5	In Different Positions
6	Timing
7	Coordinating Both Hands
8	Without Visual Feedback
9	Appropriate Force Without Visual Feedback
B	RE-ADJUSTING GRIP
1	Repetitive Grip and Release
2	Repetitive Grip and Release Without Visual Feedback
C	HOLDING
1	With Support
2	Without Support
3	In Motion
4	Without Visual Feedback
5	In Motion, Without Visual Feedback
D	RELEASING
1	With Support
2	Without Support
3	In Different Positions
4	Timing
5	Coordinating Both Hands
6	Without Visual Feedback

for assessments performed by the same rater is 2.5 logits. In a pair-wise, within-subject comparison of the scores, most fall outside of this range, except for LL1 SHPH-C and SHP. Between subjects, pair-wise comparisons are less than the MDC for the SHP (LL1 and LL3, and LL1 and LL2) and the SHPH-H (LL2 and LL3). Taking this into consideration, subjects LL2 and LL3 exhibited the most control capacity with the SHP followed by the SHPH-C and finally the SHPH-H. LL1 performed equivalently with the SHPH-C and the SHP and less well with the SHPH-H. **Figure 8** shows the breakdown of the scores of the ACMC for the three subjects with limb loss. Please note: the test is not designed to be evaluated based on individual items; however, these are presented to provide a more complete picture of the comparison between control modes. The items in each category increase in difficulty (along the x-axis); this increase is reflected in the overall decrease in scores along this axis. Across the 66 items (22 items per test and three subjects), SHPH-H control capacity was rated lower than that with the SHPH-C 32% of the time, equal 59% of the time, and superior 9% of the time. Capacity of control of the SHPH-C was more similar to that of the SHP, with control rated inferior, equal, and superior 20, 70, and 10% of the time, respectively. Images of two subjects with limb loss

performing various activities from the ACMC tasks with each SHPH Configuration can be found in **Figure 9**.

The SUS was used as a primary subjective outcome measure, while the BBT was a secondary outcome measure in evaluating the SHPH configurations and SHP. On the SUS, the benchmark achieved the highest scores for all three subjects, followed by the SHPH-C and then the SHPH-H. Results were more mixed for the BBT. Comparing the two SHPH configurations: LL1 and LL3 moved nearly the same number of blocks across configurations (9 and 8 blocks for LL1 and 10 and 11 blocks for LL2 for SHPH-C and SHPH-H, respectively). Both of these subjects were near the mean for the SHP (9.6) found in a previous study with 9 subjects with limb loss (Godfrey et al., 2018). Subject LL2 was markedly below this value, performing better with the SHPH-C than the SHPH-H (6 and 3 blocks, respectively).

Anecdotally, we asked subjects to report which configuration among the two SHPH they preferred overall and additionally asked which configuration's control they preferred. Note: the Compact Configuration used the figure-of-nine harness (single shoulder), while the Hardy Configuration used the figure-of-eight harness (double shoulder). Two subjects (1 and 3) preferred the Hardy Configuration in terms of control and two subjects (1 and 2) preferred the Compact Configuration overall. All subjects chose to start in VO mode for both configurations. Finally, subjects had 1, 4, and 2 involuntary switches with the Compact Configuration compared with 1, 2, and 0 with the Hardy Configuration.

## 4. DISCUSSION

The SHPH-C and SHPH-H were preliminarily validated with intact-limb subjects before testing with subjects with limb loss. Among these subjects, the Compact Configuration slightly outperformed the Hardy Configuration on all three outcome measures (ACMC, BBT, SUS), but not significantly so. Additionally, it is worth noting the clustering of SUS scores, in particular for the Compact Configuration. These scores approach the upper limit of the SUS, and the clustering could suggest either a ceiling effect of the measure or simply agreement among those who rated the configurations more positively. The Compact configuration has more weight distal to the torso but is less cumbersome in terms of donning and wearing (using a figure-of-nine harness and socket, with nothing else worn on the body). One of the limitations of the study was that the Hardy Configuration was noticeably slower than the other configurations due to friction in the Bowden cable limiting transmission of motion from the motor to the hand. It is difficult to infer the impact of this issue: one might expect a significantly slower hand to show drastically decreased performance in the BBT, while this was not the case. Slower movement, especially among subjects with limited training could have resulted in more precise movements as they allowed the subject more time to adjust the grasp and hand position during closure. This phenomenon could be reflected in the BBT results for the Hardy Configuration compared to the Compact: the slower hand could mask some of the variability seen between subjects



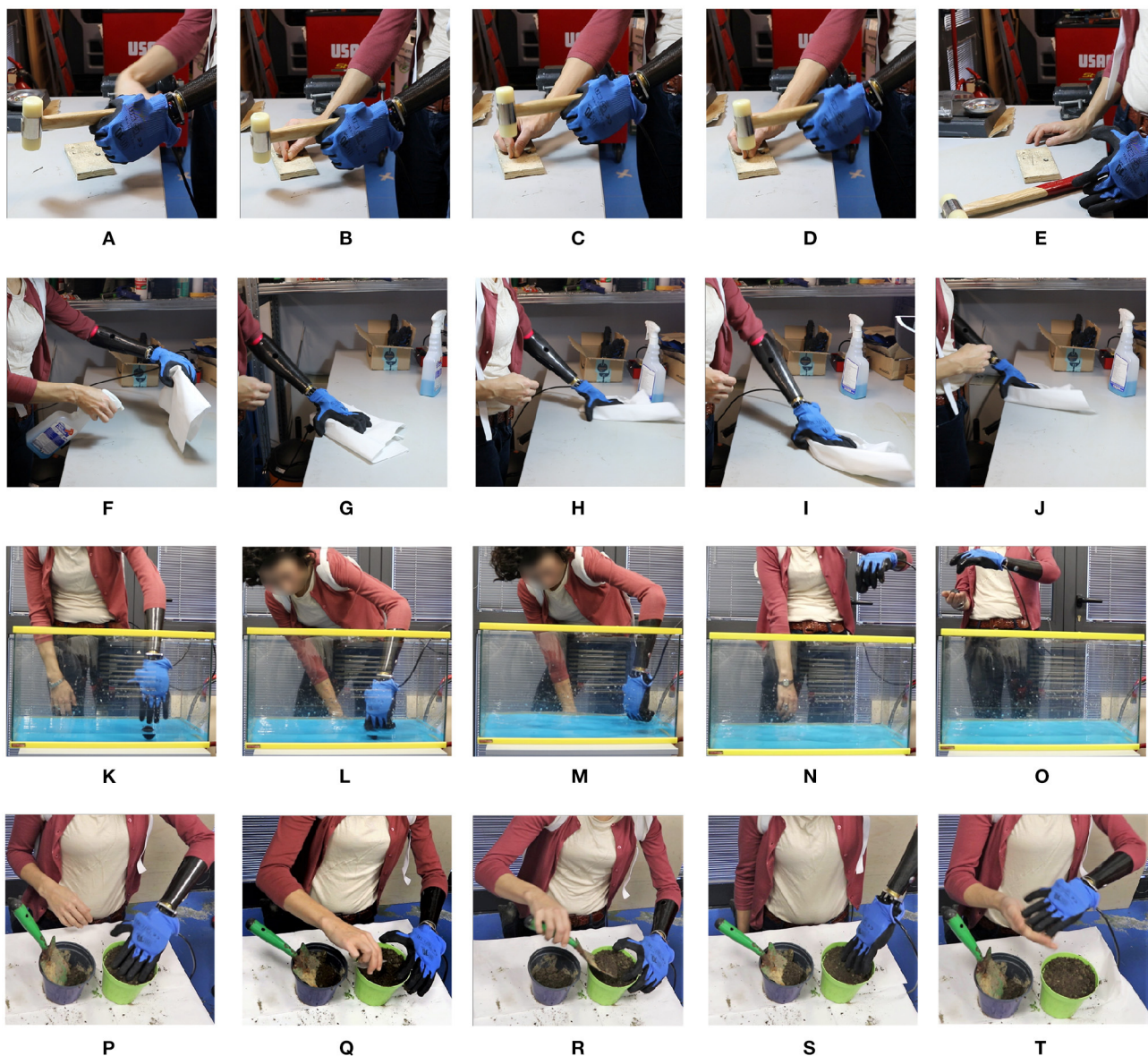
**FIGURE 9 |** (A–J) are still images of the various activities performed in the ACMC “packing” task, while (K–T) are taken from the ACMC “setting the table” task. The subject is using the Compact Configuration in the packing task and the Hardy Configuration in the setting the table task.

with the Compact Configuration. This decreased speed could nevertheless have been a contributing factor in the less-favorable subjective ratings.

In the comparison between myoelectrical- and body-controlled electric devices, the main objective outcome measure of this study, the ACMC, showed subjects with limb loss were able to perform at the “Generally Capable” level with all three devices tested. These subjects had more experience with myoelectric control compared to body-powered and all had some exposure to the SHP in the past. Despite this advantage, they were able to reach the same clinical level with the SHPH after limited training, and in one instance (LL1, SHPH-C) reach a score equivalent

to that with the SHP. The limb-intact group shows a much wider range of results on the ACMC, with control of the SHPH-C being rated “Somewhat Capable” 4 times (5 times for the SHPH-H), 5 times “Generally Capable” (4 times for the SHPH-H), and 1 time “Extremely Capable” for each configuration. The notable difference in the range of scores between the limb-intact and limb-loss groups is reasonable given the different levels of exposure to prosthetic technology. It is to be expected that longer-term users could leverage their experience, both with other prostheses and control methods as well as with the SHP, to perform reasonably well on the ACMC while the limb-intact group would acquire mastery of the prosthesis and its control at





**FIGURE 10 |** Still images from various work tasks performed by a subject with limb-loss using the Hardy Configuration. From top to bottom the tasks are: hammering a nail (A–E), wiping down a work surface (F–J), retrieving an item in water (K–O), and planting seeds (P–T).

different rates. As mentioned earlier, the ACMC individual item scores should be examined with care as the test is designed to be taken as a whole. These data can still provide interesting insight: for example, it is reasonable to infer that subjects' performance, in particular in challenging tasks such as grasping or holding without visual feedback and/or in motion, relates not only to the subject's capacity in performing a particular task but also to their confidence in that capacity. It is worth noting that all three subjects reached the maximum across all "Holding" items with the SHP but only one subject did with the SHPH-H and none with the SHPH-C. This could be due to the limited exposure to body-powered prosthesis control and a resultant lack of confidence in using it. Furthermore, the individual items

show that the slightly lower performance with the SHPH-H in comparison with the SHPH-C is not due to a major decrease in performance in any one specific category but rather to a slight underperformance across the range of items. Additionally, to our knowledge, there are no standardized tests that replicate a work environment. As the SHPH class of devices was designed in large part for work environments and manual tasks, one of the subjects with limb-loss performed several relevant tasks following study completion. Still images from these tasks are presented in **Figure 10** and consist of hammering a nail, submerging the hand in water to retrieve an item, wiping down a work surface, and planting seeds. These tasks were chosen because they require high forces and/or recreate environments and tasks that are



typically challenging for prostheses, including exposure to dirt and immersion in water. Videos of the subject completing the various tasks are available as a multimedia attachment to the present work. While not the result of a standard test, these successful attempts support the idea that the SHPH could be a high-functioning prosthetic device in these environments. In the future, this aspect will be explored more in-depth.

In future studies, one could study the trade-off in comfort between distal weight, that over the long-term would likely induce fatigue, and simplicity of donning and wearing by providing subjects with limb loss longer exposure to the Compact and Hardy Configurations. To minimize the likelihood of a training effect, beyond randomizing the order, similar comparisons in the future could lengthen the training session prior to testing the first configuration or use a proxy to increase training time. For example, future SHPH tests could include an initial training session with the myoelectrical controlled SHP to familiarize the subject with the terminal device and/or a standard body-powered prosthesis to better internalize the control scheme. Since both configurations performed similarly well on the objective outcome measures, future work will also focus on improving the mechanical implementation of the Hardy Configuration. In particular, as mentioned above, optimizing the speed of the terminal device, streamlining donning, and adjusting the configuration to be less bulky would likely improve device performance and acceptance.

## 5. CONCLUSIONS

In this work, we presented and assessed two different prototypes of the SoftHand Pro-Hybrid that integrate the use of soft robotic technologies with non-EMG based controls. In a preliminary validation with subjects without limb loss, both Configurations performed well, with the Compact Configuration slightly outperforming the Hardy in both objective and subjective tests. We then tested both of these Configurations with three subjects with limb loss and compared these results to the myoelectrically controlled SHP, used as a benchmark. This group had similar results with the Compact slightly outperforming the Hardy configuration on the APMC and the benchmark outperforming both in two out of three subjects. Across configurations, however, all three subjects were rated as “Generally Capable” on the APMC with all three configurations. Despite the limited number of subjects, this pilot study suggests the reliability of the SHPH configurations and the possibility to use hybrid solutions as a valid alternative to myoelectric control, especially in challenging environments. Improvements in the speed of the Hardy Configuration may improve both subjective and objective evaluations. Additionally, it is possible that further exposure to

and more intensive training with the SHPH configurations could help improve performance. Encouraging results also open new avenues for the design of a different class of prosthetic device (i.e., partial hands) based on a similar hybrid method.

## DATA AVAILABILITY STATEMENT

The original contributions presented in the study are included in the article/**Supplementary Material**, further inquiries can be directed to the corresponding author/s.

## ETHICS STATEMENT

The studies involving human participants were reviewed and approved by Comitato Etico di Area Vasta Nord Ovest, CEAVNO. The patients/participants provided their written informed consent to participate in this study.

## AUTHOR CONTRIBUTIONS

SBG and FF performed the experiments. SBG, CP, GG, and MC performed the data analysis and designed the experimental setup. All authors contributed to writing the manuscript and designed the study.

## FUNDING

This project has received funding from the European Union’s Horizon 2020 ERC programme under the Grant Agreement No. 810346 (Natural Bionics) and by the European Research Council under the Proof of Concept Grant SoftHand Pro-H (No. 727536). The content of this publication is the sole responsibility of the authors. The European Commission or its services cannot be held responsible for any use that may be made of the information it contains.

## ACKNOWLEDGMENTS

The authors thank qbrobotics for their support in all aspects of this study. We also thank Giacomo Dinuzzi, Manuel Barbarossa, Simona Casini, Mattia Poggiani, and Vinicio Tincani for the help in the building of prototypes and tests.

## SUPPLEMENTARY MATERIAL

The Supplementary Material for this article can be found online at: <https://www.frontiersin.org/articles/10.3389/fnbot.2021.683253/full#supplementary-material>

## REFERENCES

- Antfolk, C., D’Alonzo, M., Rosén, B., Lundborg, G., Sebelius, F., and Cipriani, C. (2013). Sensory feedback in upper limb prosthetics. *Expert Rev. Med. Devices* 10, 45–54. doi: 10.1586/erd.12.68
- Belter, J. T., Segil, J. L., Dollar, A. M., and Weir, R. F. (2013). Mechanical design and performance specifications of anthropomorphic prosthetic hands: a review. *J. Rehabil. Res. Dev.* 50:599. doi: 10.1682/JRRD.2011.10.0188
- Biddiss, E., Beaton, D., and Chau, T. (2007). Consumer design priorities for upper limb prosthetics. *Disabil. Rehabil. Assist. Technol.* 2, 346–357. doi: 10.1080/17483100701714733
- Biddiss, E., and Chau, T. (2007a). The roles of predisposing characteristics, established need, and enabling resources on upper extremity prosthesis use and abandonment. *Disabil. Rehabil. Assist. Technol.* 2, 71–84. doi: 10.1080/17483100601138959

- Biddiss, E. A., and Chau, T. T. (2007b). Upper limb prosthesis use and abandonment: a survey of the last 25 years. *Prosthet. Orthot. Int.* 31, 236–257. doi: 10.1080/0309364060094581
- Brooke, J. (1996). SUS-a quick and dirty usability scale. *Usabil. Eval. Industry* 189, 4–7.
- Brown, J. D., Kunz, T. S., Gardner, D., Shelley, M. K., Davis, A. J., and Gillespie, R. B. (2017). An empirical evaluation of force feedback in body-powered prostheses. *IEEE Trans. Neural Syst. Rehabil. Eng.* 25, 215–226. doi: 10.1109/TNSRE.2016.2554061
- Carey, S. L., Dubey, R. V., Bauer, G. S., and Highsmith, M. J. (2009). Kinematic comparison of myoelectric and body powered prostheses while performing common activities. *Prosthet. Orthot. Int.* 33, 179–186. doi: 10.1080/03093640802613229
- Carey, S. L., Lura, D. J., and Highsmith, M. J. (2015). Differences in myoelectric and body-powered upper-limb prostheses: systematic literature review. *J. Rehabil. Res. Dev.* 52, 247–262. doi: 10.1682/JRRD.2014.08.0192
- Carey, S. L., Lura, D. J., and Highsmith, M. J. (2017). Differences in myoelectric and body-powered upper-limb prostheses: systematic literature review. *J. Prosthet. Orthot.* 29, 4–16. doi: 10.1097/JPO.0000000000000159
- Catalano, M. G., Grioli, G., Farnioli, E., Serio, A., Piazza, C., and Bicchi, A. (2014). Adaptive synergies for the design and control of the Pisa/IIT SoftHand. *Int. J. Robot. Res.* 33, 768–782. doi: 10.1177/0278364913518998
- Childress, D. S. (1992). “Upper-limb prosthetics: control of limb prostheses,” in *Atlas of Limb Prosthetics: Surgical, Prosthetic, and Rehabilitation Principles*, eds H. K. Bowker and J.W. Michael (Rosemont, IL: American Academy of Orthopedic Surgeons).
- Cordella, F., Ciancio, A. L., Sacchetti, R., Davalli, A., Cutti, A. G., Guglielmelli, E., et al. (2016). Literature review on needs of upper limb prosthesis users. *Front. Neurosci.* 10:209. doi: 10.3389/fnins.2016.00209
- Dakpa, R., and Heger, H. (1997). Prosthetic management and training of adult upper limb amputees. *Curr. Orthopaed.* 11, 193–202. doi: 10.1016/S0268-0890(97)90034-7
- Darter, B. J., Hawley, C. E., Armstrong, A. J., Avellone, L., and Wehman, P. (2018). Factors influencing functional outcomes and return-to-work after amputation: a review of the literature. *J. Occupat. Rehabil.* 28, 656–665. doi: 10.1007/s10926-018-9757-y
- Della Santina, C., Piazza, C., Gasparri, G. M., Bonilla, M., Catalano, M. G., Grioli, G., et al. (2017). The quest for natural machine motion: an open platform to fast-prototyping articulated soft robots. *IEEE Robot. Automat. Mag.* 24, 48–56. doi: 10.1109/MRA.2016.2636366
- Dempster, W. T. (1955). *Space Requirements of the Seated Operator, Geometrical, Kinematic, and Mechanical Aspects of the Body with Special Reference to the Limbs*. Technical report, Michigan State University, East Lansing, MI. doi: 10.21236/AD0087892
- Desrosiers, J., Bravo, G., Hébert, R., Dutil, É., and Mercier, L. (1994). Validation of the box and block test as a measure of dexterity of elderly people: reliability, validity, and norms studies. *Arch. Phys. Med. Rehabil.* 75, 751–755. doi: 10.1016/0003-9993(94)90130-9
- Edelstein, J., and Berger, N. (1993). Performance comparison among children fitted with myoelectric and body-powered hands. *Arch. Phys. Med. Rehabil.* 74, 376–380.
- Fryer, C. (1992). “Upper-limb prosthetics: harnessing and controls for body-powered devices,” in *Atlas of Limb Prosthetics: Surgical, Prosthetic, and Rehabilitation Principles*, eds H. K. Bowker and J. W. Michael (Rosemont, IL: Mosby Inc.).
- Godfrey, S., Zhao, K., Theuer, A., Catalano, M., Bianchi, M., Breighner, R., et al. (2018). The softand pro: functional evaluation of a novel, flexible, and robust myoelectric prosthesis. *PLoS ONE* 13:e0205653. doi: 10.1371/journal.pone.0205653
- Hashim, N. A., Abd Razak, N. A., Abu Osman, N. A., and Gholizadeh, H. (2018). Improvement on upper limb body-powered prostheses (1921–2016): a systematic review. *Proc. Instit. Mech. Eng. H J. Eng. Med.* 232, 3–11. doi: 10.1177/0954411917744585
- Hermansson, L. M., Fisher, A. G., Bernspång, B., and Eliasson, A.-C. (2005). Assessment of capacity for myoelectric control: a new rasch-built measure of prosthetic hand control. *J. Rehabil. Med.* 37, 166–171. doi: 10.1080/16501970410024280
- Hwang, C.-L., and Yoon, K. (2012). *Multiple Attribute Decision Making: Methods and Applications a State-of-the-Art Survey*, Vol. 186. Berlin: Springer Science & Business Media.
- Kuiken, T. A., Miller, L. A., Turner, K., and Hargrove, L. J. (2016). A comparison of pattern recognition control and direct control of a multiple degree-of-freedom transradial prosthesis. *IEEE J. Transl. Eng. Health Med.* 4, 1–8. doi: 10.1109/JTEHM.2016.2616123
- Light, C. M., Chappell, P. H., and Kyberd, P. J. (2002). Establishing a standardized clinical assessment tool of pathologic and prosthetic hand function: normative data, reliability, and validity. *Arch. Phys. Med. Rehabil.* 83, 776–783. doi: 10.1053/apmr.2002.32737
- McConville, J. T., Clauser, C. E., Churchill, T. D., Cuzzi, J., and Kaleps, I. (1980). *Anthropometric Relationships of Body and Body Segment Moments of Inertia*. Technical report, Anthropology Research Project Inc., Yellow Springs, OH. doi: 10.21236/ADA097238
- Millstein, S., Heger, H., and Hunter, G. (1986). Prosthetic use in adult upper limb amputees: a comparison of the body powered and electrically powered prostheses. *Prosthet. Orthot. Int.* 10, 27–34. doi: 10.3109/03093648609103076
- Mura, D., Barbarossa, M., Dinuzzi, G., Grioli, G., Caiti, A., and Catalano, M. G. (2018). A soft modular end effector for underwater manipulation: a gentle, adaptable grasp for the ocean depths. *IEEE Robot. Automat. Mag.* 25, 45–56. doi: 10.1109/MRA.2018.2871350
- Muzumdar, A. (2004). *Powered Upper Limb Prostheses: Control, Implementation and Clinical Application*. Berlin: Springer Science & Business Media. doi: 10.1007/978-3-642-18812-1
- Negrello, F., Friedl, W., Grioli, G., Garabini, M., Brock, O., Bicchi, A., et al. (2020). Benchmarking hand and grasp resilience to dynamic loads. *IEEE Robot. Automat. Lett.* 5, 1780–1787. doi: 10.1109/LRA.2020.2969180
- Østlie, K., Lesjö, I. M., Franklin, R. J., Garfelt, B., Skjeldal, O. H., and Magnus, P. (2012). Prosthesis use in adult acquired major upper-limb amputees: patterns of wear, prosthetic skills and the actual use of prostheses in activities of daily life. *Disabil. Rehabil. Assist. Technol.* 7, 479–493. doi: 10.3109/17483107.2011.653296
- Piazza, C., Catalano, M. G., Godfrey, S. B., Rossi, M., Grioli, G., Bianchi, M., et al. (2017). The SoftHand Pro-H: a hybrid body-controlled, electrically powered hand prosthesis for daily living and working. *IEEE Robot. Automat. Mag.* 24, 87–101. doi: 10.1109/MRA.2017.2751662
- Piazza, C., Grioli, G., Catalano, M., and Bicchi, A. (2019). A century of robotic hands. *Annu. Rev. Control Robot. Auton. Syst.* 2, 1–32. doi: 10.1146/annurev-control-060117-105003
- Resnik, L., Adams, L., Borgia, M., Delikat, J., Disla, R., Ebner, C., et al. (2013). Development and evaluation of the activities measure for upper limb amputees. *Arch. Phys. Med. Rehabil.* 94, 488–494. doi: 10.1016/j.apmr.2012.10.004
- Resnik, L., and Borgia, M. (2012). Reliability and validity of outcome measures for upper limb amputation. *J. Prosthet. Orthot.* 24, 192–201. doi: 10.1097/JPO.0b013e31826ff91c
- Riener, R. (2016). The Cybathlon promotes the development of assistive technology for people with physical disabilities. *J. Neuroeng. Rehabil.* 13:49. doi: 10.1186/s12984-016-0157-2
- Sensinger, J. W., Lipsey, J., Thomas, A., and Turner, K. (2015). Design and evaluation of voluntary opening and voluntary closing prosthetic terminal device. *J. Rehabil. Res. Dev.* 52, 63–76. doi: 10.1682/JRRD.2014.03.0087
- van der Sluis, C. K., Hartman, P. P., Schoppen, T., and Dijkstra, P. U. (2009). Job adjustments, job satisfaction and health experience in upper and lower limb amputees. *Prosthet. Orthot. Int.* 33, 41–51. doi: 10.1080/03093640802555917
- World Health Organization (2004). *The Rehabilitation of People With Amputations*. US Dept. of Defense; MossRehab amputee Rehabilitation Program (2004)

**Conflict of Interest:** AB, MC, and GG are cofounders and shareholders of qrobotics s.r.l., a company producing robotic hands and components of the SoftHand Pro used in the experiments reported in this paper.

The remaining authors declare that the research was conducted in the absence of any commercial or financial relationships that could be construed as a potential conflict of interest.

**Publisher's Note:** All claims expressed in this article are solely those of the authors and do not necessarily represent those of their affiliated organizations, or those of the publisher, the editors and the reviewers. Any product that may be evaluated in this article, or claim that may be made by its manufacturer, is not guaranteed or endorsed by the publisher.

*Copyright © 2021 Godfrey, Piazza, Felici, Grioli, Bicchi and Catalano. This is an open-access article distributed under the terms of the Creative Commons Attribution License (CC BY). The use, distribution or reproduction in other forums is permitted, provided the original author(s) and the copyright owner(s) are credited and that the original publication in this journal is cited, in accordance with accepted academic practice. No use, distribution or reproduction is permitted which does not comply with these terms.*



# Assessment of a Robotic Walker in Older Adults With Parkinson's Disease in Daily Living Activities

Sergio D. Sierra M.<sup>1</sup>, Daniel E. Garcia A.<sup>1</sup>, Sophia Otálora<sup>1</sup>, María Camila Arias-Castro<sup>2</sup>, Alejandro Gómez-Rodas<sup>2,3</sup>, Marcela Múnera<sup>1</sup> and Carlos A. Cifuentes<sup>1\*</sup>

<sup>1</sup> Department of Biomedical Engineering, Colombian School of Engineering Julio Garavito, Bogotá, Colombia, <sup>2</sup> Programa de Fisioterapia, Fundación Universitaria del Área Andina, Pereira, Colombia, <sup>3</sup> Programa Ciencias del Deporte y la Recreación, Universidad Tecnológica de Pereira, Pereira, Colombia

## OPEN ACCESS

### Edited by:

Francisco Romero Sánchez,  
University of Extremadura, Spain

### Reviewed by:

Farong Gao,  
Hangzhou Dianzi University, China  
Matteo Lafranchi,  
Italian Institute of Technology (IIT), Italy

### \*Correspondence:

Carlos A. Cifuentes  
carlos.cifuentes@escuelaing.edu.co

**Received:** 16 July 2021

**Accepted:** 09 November 2021

**Published:** 14 December 2021

### Citation:

Sierra M. SD, Garcia A. DE, Otálora S, Arias-Castro MC, Gómez-Rodas A, Múnera M and Cifuentes CA (2021) Assessment of a Robotic Walker in Older Adults With Parkinson's Disease in Daily Living Activities. *Front. Neurobot.* 15:742281. doi: 10.3389/fnbot.2021.742281

The constant growth of the population with mobility impairments, such as older adults and people suffering from neurological pathologies like Parkinson's disease (PD), has encouraged the development of multiple devices for gait assistance. Robotic walkers have emerged, improving physical stability and balance and providing cognitive aid in rehabilitation scenarios. Different studies evaluated human gait behavior with passive and active walkers to understand such rehabilitation processes. However, there is no evidence in the literature of studies with robotic walkers in daily living scenarios with older adults with Parkinson's disease. This study presents the assessment of the AGoRA Smart Walker using Ramps Tests and Timed Up and Go Test (TUGT). Ten older adults participated in the study, four had PD, and the remaining six had underlying conditions and fractures. Each of them underwent a physical assessment (i.e., Senior Fitness, hip, and knee strength tests) and then interacted with the AGoRA SW. Kinematic and physical interaction data were collected through the AGoRA walker's sensory interface. It was found that for lower limb strength tests, older adults with PD had increases of at least 15% in all parameters assessed. For the Sit to Stand Test, the Parkinson's group evidenced an increase of 23%, while for the Chair Sit and Reach Test (CSRT), this same group was only 0.04 m away from reaching the target. For the Ramp Up Test (RUT), the subjects had to make a greater effort, and significant differences ( $p$ -value = 0.04) were evidenced in the force they applied to the device. For the Ramp Down Test (RDT), the Parkinson's group exhibited a decrease in torque, and there were statistically significant differences ( $p$ -value = 0.01) due to the increase in the complexity of the task. In the Timed Up and Go Test (TUGT), the subjects presented significant differences in torque ( $p$ -value of 0.05) but not in force ( $p$ -value of 0.22) due to the effect of the admittance controller implemented in the study. Finally, the results suggested that the walker, represents a valuable tool for assisting people with gait motor deficits in tasks that demanded more physical effort adapting its behavior to the specific needs of each user.

**Keywords:** smart walker, Parkinson's disease, daily living activities, senior fitness, timed up and go, older adults



## 1. INTRODUCTION

Human gait is a locomotion process in which the human body moves forward, alternating support in both lower limbs (Vaughan, 2003). Different musculoskeletal and neurological pathologies considerably affect balance and stability during this process (Mrozowski et al., 2007; Sammer et al., 2012; Pirker and Katzenschlager, 2017). In particular, stroke and spinal cord injuries are strongly related to locomotion disorders and significantly affect people's motor skills (Ghenot et al., 2012; Cifuentes and Frizera, 2016). Parkinson's disease (PD) is another brain disorder that disrupts these capabilities (World Health Organization, 2006). The gradual decline of cognitive faculties (Nieuwboer et al., 2001; Buchman et al., 2011; Belghali et al., 2017) and the neuromuscular system in the older adults (Ghenot et al., 2012; Poewe et al., 2017) are also associated with these pathologies. Besides, it is worth highlighting that PD is the second most common neuro-degenerative disorder affecting between 2 and 3% of the population aged 65 or older (Poewe et al., 2017).

The WHO estimates that the proportion of the population with mobility difficulties has been slowly and substantially rising, reaching 15% of the global population nowadays (World Health Organization, 2015). The United Nations also states that the world's population of older people will double in the next 3 decades, increasing from 9.3% in 2020 to 16% in 2050 (United Nations, 2020). Thus, mobility problems are common in older people and individuals with functional and cognitive disorders (Brown and Flood, 2013; Pedersen et al., 2014; Mikolajczyk et al., 2018). Several assistive devices have been developed to improve impaired locomotion abilities (Cifuentes and Múnera, 2022).

Concretely, mobility assistive devices help people overcome and compensate for physical disabilities by sustaining or improving their functioning and independence in clinical and daily situations (Van der Loos et al., 2016). One such device is traditional walkers with basic and low-cost mechanical systems, as well as, partial body weight support and stabilization. Nevertheless, such walkers compromise the balance and energy costs of the user, not to mention that fall prevention and overall safety are not very efficient (Neto et al., 2015; Sierra et al., 2022a). Another limitation of conventional devices is that they do not fully and correctly address cognitive and sensory assistance, which is of great importance for people with physical limitations (Mitzner et al., 2014; Jenkins and Draper, 2015; Geravand et al., 2016). Therefore, Smart Walkers (SWs) emerged, integrating robotic technologies to mitigate these drawbacks.

Smart Walkers are a potential tool for gait training and assistance due to their simple mechanical structures and multiple interaction interfaces (Scheidegger et al., 2019; Aristizabal-Aristizabal et al., 2022; Cifuentes and Múnera, 2022). The main functionalities of these devices include autonomous navigation systems (Papageorgiou et al., 2016), safety and obstacle avoidance modules (Sierra et al., 2018), biomechanical monitoring (Caetano et al., 2016; Alves et al., 2017; Sierra et al., 2021), user intention detection mechanisms (Lacey and Rodriguez-Losada, 2008), path-following modules (Sierra et al., 2022b), and people detection systems (Sierra et al., 2019). Also, these strategies provide a natural and safe interaction with the user in dynamic

and complex environments (Neto et al., 2015). Therefore, they are often referred to as Human-Robot Interaction Interfaces (HRI) and Human-Robot-Environment Interaction Interfaces (HREI) (Sierra et al., 2019).

Several case studies report the effects of robotic walkers. As presented in Chugo et al. (2009), Jun et al. (2011), Yoon et al. (2012), and Werner et al. (2020), the efficacy and user satisfaction with sit-to-stand assistance systems provided by the walker is evaluated. These studies analyze how the device impacts the stability and balance of the subjects when the task is combined with a brief walk. Although relevant results are presented in terms of improved performance during the tests, there is no evidence of studies where the difficulty of the tests is increased with the aim of both physically and cognitively stimulating the user (i.e., more extended gait tasks and turns before the subject sits down). On the other hand, other studies have also been presented where the effect of the walker on the gait pattern of the subjects in scenarios that emulate daily activities (Wang et al., 2014; Lindemann et al., 2016, 2017; Costamagna et al., 2019; Mundt et al., 2019).

Studies involving subjects suffering from neurological diseases have been also reported (Martins et al., 2015; Bayon et al., 2016; Moreira et al., 2019). Regarding subjects with Parkinson's disease, some studies focused on interaction strategies to improve the experience during the task (Mou et al., 2012; Zhang et al., 2018). These kinds of studies evaluated the level of assistance provided by the device and how it influenced the speed, cadence, and stability of the users (Cubo et al., 2003; Kegelmeier et al., 2013; Wu et al., 2020). However, exploration of the kinematic effects of robotic walkers in this population remains scarce. In particular, there is insufficient evidence of the validation of these devices in more dynamic environments that emulate daily tasks. Furthermore, at the time of the writing of this manuscript, no studies compare the performance of people with PD with other focal groups with different physical and neurological conditions.

In this sense, the main contribution of this study is the comparison of the kinematic performance of a group of older adults with PD vs. a group of older adults with metabolic diseases, joint diseases, and fractures. This assessment was conducted when the older adults were interacting with the AGoRA SW in tests such as Up Ramps, Down Ramps, and Timed Up and Go. Besides, it presents and analyzes how the robotic device helps to compensate for the limitation of the subjects in the tasks that demanded more physical effort. Additionally, this study analyzes how the physical conditions of the subjects and the interaction strategy of the walker influence the results obtained. For this purpose, the Senior Fitness Test (SFT), lower limb strength tests, and a human-robot interaction strategy were necessary for this study.

## 2. MATERIALS AND METHODS

This section describes the robotic platform used during the study and the interaction strategy proposed to provide an appropriate level of assistance to the user. Moreover, this part details the tests performed and the experimental setup, and the data collected in each of them.

## 2.1. Robotic Platform Description

The Pioneer LX research platform (Omron Adept Technologies, Pleasanton, CA, USA) referred to as the AGoRA SW was used for this study. As presented in Sierra et al. (2019), this device was adapted to emulate the structural frame of a conventional assistive walker by attaching two forearm support handlebars to the main deck of the platform (refer to **Figure 1**).

This platform equips an onboard computer running a Linux operating system distribution compatible with the Robotic Operating System (ROS) framework. Moreover, features different sensors, actuators, and processing units such as (1) two motorized wheels and two caster wheels that provide propulsion and stability to the walker; (2) two encoders and an inertial measurement unit (IMU) to estimate the position and orientation of the device; (3) a 2D light detection and ranging (LiDAR) sensor (S300 Expert, SICK, Waldkirch, Germany) to sense the environment and detect obstacles; (4) two ultrasonic plates to detect objects at low height; (5) two triaxial load cells (MTA400, FUTEK, Irvine, CA, USA) to estimate the user's navigation commands; (6) an HD camera (LifeCam Studio, Microsoft, Redmond, WA, USA) for human detection; and (7) a 2D laser rangefinder (Hokuyo URG-04LX-UG01, Osaka, Japan) to estimate the user's gait parameters (Sierra et al., 2019).

## 2.2. System Operation

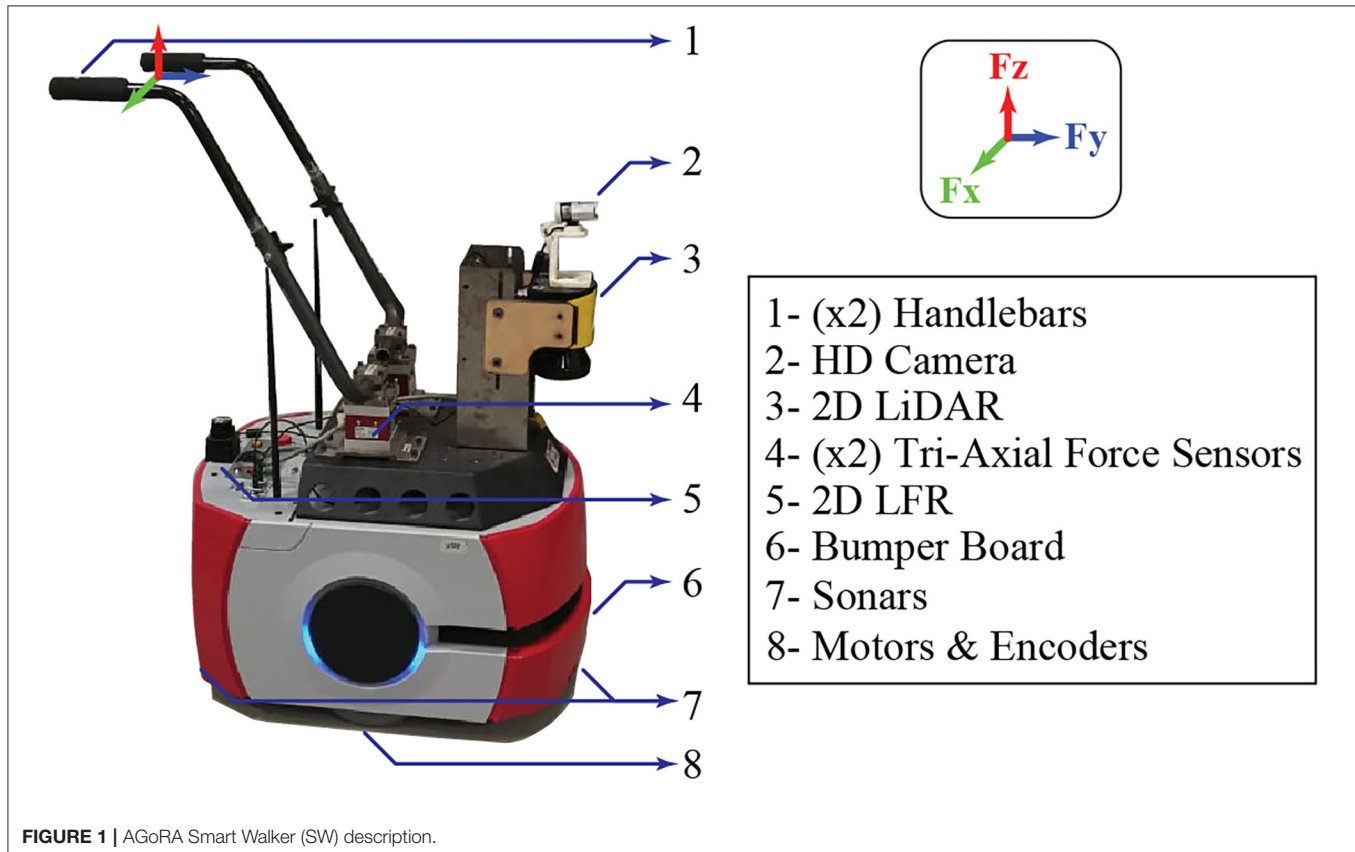
In this study, the architecture described in **Figure 2** was implemented. The overall system is composed of two main

modules: (1) a signal processing module, which is in charge of filtering the signals from the force sensors and generating the corresponding resulting forces and torques, and (2) an admittance controller, which converts the user's movement intention to speed commands to provide an appropriate level of assistance when they interact with the SW.

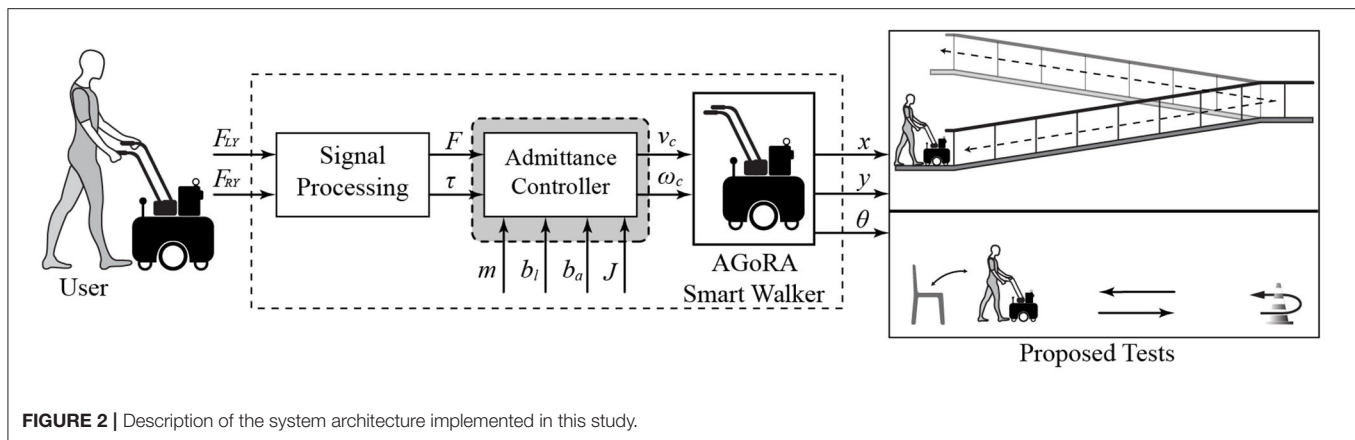
### 2.2.1. Signal Processing Module

As presented in (Sierra et al., 2019) between the SW force sensors and the user's handlebar points, there is a vertical misalignment (refer to **Figure 1**). Supported by previous studies (Sierra et al., 2019, 2021), this implies that the resulting forces along the  $y$ -axis and  $z$ -axis read by the sensors will combine the forces along the  $y$ -axis and  $z$ -axis at the support points. However, it is possible to estimate that the forces along the  $y$ -axis provide essential information related to the user's motion intention. Similarly, the forces along the  $z$ -axis are a directly proportional estimation of the user's support on the device. At the same time, the forces along the  $x$ -axis are discarded, since they do not provide relevant information (Sierra et al., 2019). These signals are contaminated with some noise sources, related to the natural oscillatory pattern of gait (Brodie et al., 2015) and vibrations associated with irregularities in the floor (Sierra et al., 2019), which implies that these signals require additional filtering and conditioning treatment to remove such artifacts.

Hence, the same filtering strategy presented in Sierra et al. (2019) is implemented in this study, which mainly consists of



**FIGURE 1** | AGoRA Smart Walker (SW) description.



four steps: (1) averaging the force signals along the  $z$ -axis, which contain information related to the oscillatory movements of the user's trunks, then (2) a band-pass filter is applied to remove all high-frequency components (1-2 Hz cutoff frequencies), then (3) the resulting signal cadence is estimated, thanks to the weighted fourier linear combiner filter (Frizera et al., 2010), and finally (4) the oscillatory components of the forces along the  $y$ -axis of each sensor are removed by introducing the cadence into a fourier linear combiner filter (Frizera Neto et al., 2010).

After performing this process, it is possible to estimate the force ( $F$ ) and the resulting torque ( $t$ ) and, thus, have an indicator that provides relevant information of the physical interaction between the SW and the user. Equations (1) and (2) describe how the signals are finally obtained:

$$\vec{F} = \vec{F}'_{LY} + \vec{F}'_{RY}, \quad (1)$$

$$\vec{\tau} = (\vec{F}'_{LY} - \vec{F}'_{RY}) * \frac{d}{2}. \quad (2)$$

$\vec{F}'_{LY}$  and  $\vec{F}'_{RY}$  are the filtered force signals from both handlebars, and  $d$  is the separation between the load cells of the device, which for this case is 0.3 m. It is essential to highlight that the force provides information about the user's intention when starting to walk, while the torque supplies information about the user's intention when turning.

### 2.2.2. Interaction Strategy

Admittance controllers, widely used in SWs, are dynamic models that allow the robotic device to respond efficiently to the user's motion intentions (Jiménez et al., 2019). This sort of strategy allows to virtually modify the mechanical impedance of the walker, allowing to emulate different levels of assistance (Jiménez et al., 2019; Sierra et al., 2021, 2022b). With these controllers, it is possible to generate speed commands according to the user's exerted force and torque. Depending on the controller's constants, the SW can resemble lightweight device or a heavy device (Sierra et al., 2021). Thus, the purpose of these strategies is to provide users with feelings of easiness and naturalness during physical interaction with the robotic walker.

This study implements two admittance controllers to generate linear and angular velocities from the force and torque signals applied by the user on the handlebars. The controllers model the SW as a first-order *mass-damper* system and the outputs are linear ( $v$ ) and angular ( $\omega$ ) velocities, as described in Equations (3) and (4):

$$L(s) = \frac{v(s)}{F(s)} = \frac{\frac{1}{m}}{s + \frac{b_l}{m}}, \quad (3)$$

$$A(s) = \frac{\omega(s)}{\tau(s)} = \frac{\frac{1}{J}}{s + \frac{b_a}{J}}, \quad (4)$$

where  $m$  is the walker's virtual mass,  $J$  is the virtual moment of inertia of the walker, and  $b_l$  and  $b_a$  are damping constants. These equations describe the transfer function of each controller.  $L(s)$  stands for Linear System, and  $A(s)$  stands for Angular System. It was necessary to adjust the values of the controller parameters to achieve an appropriate SW behavior. For this purpose, the virtual mass ( $m$ ), inertia ( $J$ ), and damping constants ( $b_l$  and  $b_a$ ) were adjusted after several experimental tests with healthy subjects (Sierra et al., 2021). In particular, the following values were used:  $m = 0.5$  kg,  $b_l = 4$  N.s/m,  $J = 2.1$  kg.m<sup>2</sup>/rad, and  $b_a = 2$  N.m.s/rad.

Regarding mass and inertia, low values were required since the AGoRA walker is a heavy robotic platform (70.2 kg). The inertia value was designed to be at least two times the virtual mass to ensure balance and stability during walking.

### 2.3. Experimental Protocol

This section describes the implemented experimental protocol to assess the interaction between the users and the AGoRA SW during the proposed tests. Additionally, it presents the physical assessment tests that were performed on each of them.

#### 2.3.1. Session Environment

This study took place at the Innovation and Technological Development Center (ITDC) of the Technological University of Pereira. The tests were performed jointly with physiotherapists and professors from the Areandina University Foundation.

### 2.3.2. Participant Recruitment

- Inclusion criteria: Adults over 65 years of age who present some type of physical or cognitive condition that will significantly affect their gait cycle.
- Exclusion criteria: Subjects who did not present pathologies associated with alterations of normal gait parameters were excluded from the study.

A group of subjects that were actively attending a rehabilitation program was formally recruited to participate in the clinical study. The ethics committee previously approved the study, and all participants read and signed the written informed consent. The group was conformed by ten subjects (5 men, 5 women,  $69.5 \pm 8.44$  y.o,  $1.61 \pm 0.08$  m,  $66.35 \pm 14.93$  kg), 4 of them had PD and, the remaining 6 had metabolic and joint diseases, and some had previous fractures. **Table 1** describes the demographic data of the participants.

### 2.3.3. Session Procedure

Before starting the tests, participants had to fill out an informed consent form to ensure that they had voluntarily expressed their intention to participate in the research. Participants only had to attend one session (i.e., a total of 10 sessions were conducted.), which was divided into two stages: (1) physical validation tests and (2) tests with the robotic walker. The participant had 1 h of rest between each of these to prevent them from becoming fatigued or experiencing any kind of muscular load.

The first stage aimed at determining the physical condition of the subjects. Several tests evaluated their levels of resistance, strength, and flexibility. Specifically, a digital dynamometer (microFET2, Hoggan Scientific, USA) was used to measure the force exerted by both the hip and the knee. Measurements with this type of device have been shown to be valid and reliable

(Kawaguchi and Babcock, 2010). In the case of the hip, for the assessment of flexor and extensor strength, participants were placed supine with the hip flexed at approximately  $90^\circ$ . Abductor and adductor strength were measured while participants were lying on their side with  $0^\circ$  of hip flexion/extension. Additionally, for knee extensor and flexor strength, participants were required to be seated with approximately  $90^\circ$  hip and  $90^\circ$  knee flexion (Mintken et al., 2007; Stevens-Lapsley et al., 2010). Participants performed a series of maximal voluntary isometric contractions (MVIC) preceded by two submaximal warm-up contractions. All participants received visual targets and solid verbal encouragement during each MVIC to assist in obtaining maximal effort. All MVICs were performed by allowing the patient to increase the force to maximal capacity gradually; the maximal effort was maintained for 3–5 s. Patients were allowed 30-s rest periods between repetitions.

Furthermore, the physical capabilities and functional skills of the participants were assessed using the SFT (Rikli and Jones, 2013; Hesseberg et al., 2015). The following tests were performed:

- Sit to Stand Test (SST): This test consisted of counting the number of times the participant stood up from a chair with his arms crossed on his chest for 30 s. The purpose of this test was to evaluate the strength and resistance of the subjects' legs.
- Arm Curl Test (ACT): This test consisted of counting how many times the participant managed to bend the forearm with a weight (5 pounds for women, 8 pounds for men) for 30 s. This test aimed to measure the strength and resistance of the subjects in their upper limbs.
- Chair Sit and Reach Test (CSRT): This test consisted of measuring the distance the participant was missing to reach the toe (minus score) or beyond the toe (plus score). While sitting on the edge of a chair, one leg should be bent and the foot flat on the floor, while the other leg was extended straight in front of the hip with the heel on the floor and the foot ankle  $90^\circ$ . The person leaned forward at the hip while sliding the hands along the extended leg (the position was held for 3 s). The purpose of this test was to evaluate the flexibility of the lower limbs of the subjects.
- Back Scratch Test (BST): This test consisted of measuring the distance between (or overlap of) the middle fingers behind the back when attempting to touch the middle fingers of both hands together behind the back. Such a test was intended to measure the overall range of movement of the subjects' shoulders.
- Six Minutes Walking Test (6MWT): This test is used as an endurance test and is often used as a general indicator of overall physical performance and mobility in older adults (Heerink et al., 2009). In this sense, the participants were instructed to walk over a flat hallway without running or jogging, and they were allowed to stop and rest during the test. Considering the test duration, a walking circuit was used, where the subject had to make a U-turn every 30 m. For this test, it was necessary to instrument the user with the G-WALK sensor (BTS G-Sensor, BTS Bioengineering, USA) to extract average speed and cadence parameters (BTS Bioengineering, 2019).

**TABLE 1** | Summary of demographic data of the volunteers who participated in the clinical study.

Subject	Group	Gender	Age	Weight [kg]	Height [m]	IMC	Pathology
1	PK	Male	70	83	1.73	28	Parkinson
2		Male	71	59	1.66	22	Parkinson
3		Male	70	82	1.70	28	Parkinson
4		Female	70	57	1.63	22	Parkinson
5	MJF	Female	68	74	1.55	31	Arterial Hypertension Osteoarthritis
6		Female	67	57	1.58	23	Hypothyroidism Osteoporosis
7		Female	71	61	1.53	26	High Blood Pressure Osteoporosis
8		Male	72	70	1.64	26	Epicondylitis Osteoporosis
9		Female	67	50	1.47	23	Triple Ankle Fracture
10		Male	69	70	1.62	27	Tibial Plate Fracture

Parkinson group (PK) is the group suffering from PD and, MJF is the group of older adults with metabolic, joint diseases, and fractures.



In both cases (i.e., lower limb strength tests and SFT), each participant had to perform three repetitions, except in the 6MWT, because of the time and distance covered by the user, only one repetition is sufficient (Rikli and Jones, 2013). These measurements were averaged and reported.

The second stage of the study compared the kinematic performance of both groups when they interacted with the AGoRA SW in everyday scenarios. The following tests were proposed:

- **Ramps:** The subjects were asked to walk up (RUT) and down (RDT) a ramp with the AGoRA Walker. Each user had to walk three times on the ramp-up and then three times on the ramp down (refer to **Figure 3**).
- **Timed Up and Go test (TUGT):** This is a clinical assessment test widely used to assess balance and walking ability in elderly populations (Heerink et al., 2009). A modified version of this test was used to be suitable during walker-assisted gait. Specifically, the subjects were asked to rise from a chair, walk at their usual pace a distance of 3 m, make a U-turn around a cone, walk back to the chair, and sit down (Heerink et al., 2009). Due to the use of the walker, users had to make a final turn before reaching the chair (refer to **Figure 3**).

Finally, data were acquired through the sensory interface of the AGoRA Walker. Specifically, the interaction force and torque, walker speeds, and trial duration were recorded. Moreover, to estimate additional parameters of the subject, the G-WALK sensor was used (BTS Bioengineering, 2019). This device supplied the most relevant parameters related to each trial, such as the subject's speed, cadence, gait cycle duration, and the number of cycles.

**Figure 4** summarizes the procedure and tests that were performed to evaluate this study.

### 2.3.4. Statistical Analysis

Descriptive statistics were used to report the results of the study. The significance level of all tests was set at 0.05. To determine the distribution of the information collected, the Shapiro-Wilk normality test was performed. To evaluate statistically significant differences, two types of tests were performed. In the case of parametric data, the non-paired *t*-test was performed. Regarding non-parametric data, Mann-Whitney tests were performed.

## 2.4. Ethics Statement

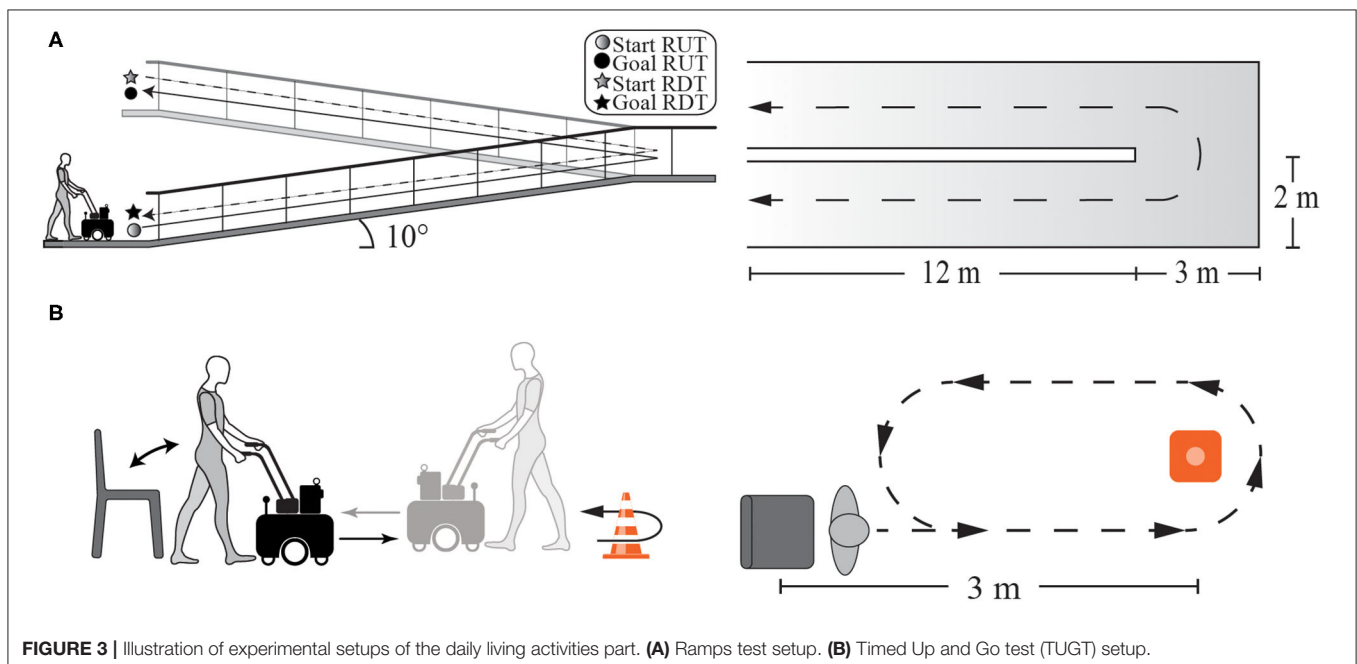
The University Research Ethics Committee approved this experimental protocol. Participants were informed of the scope and purpose of the experiment, and as explained above, their written informed consent was obtained before the study. Additionally, participants were free to leave the study whenever they chose to do so.

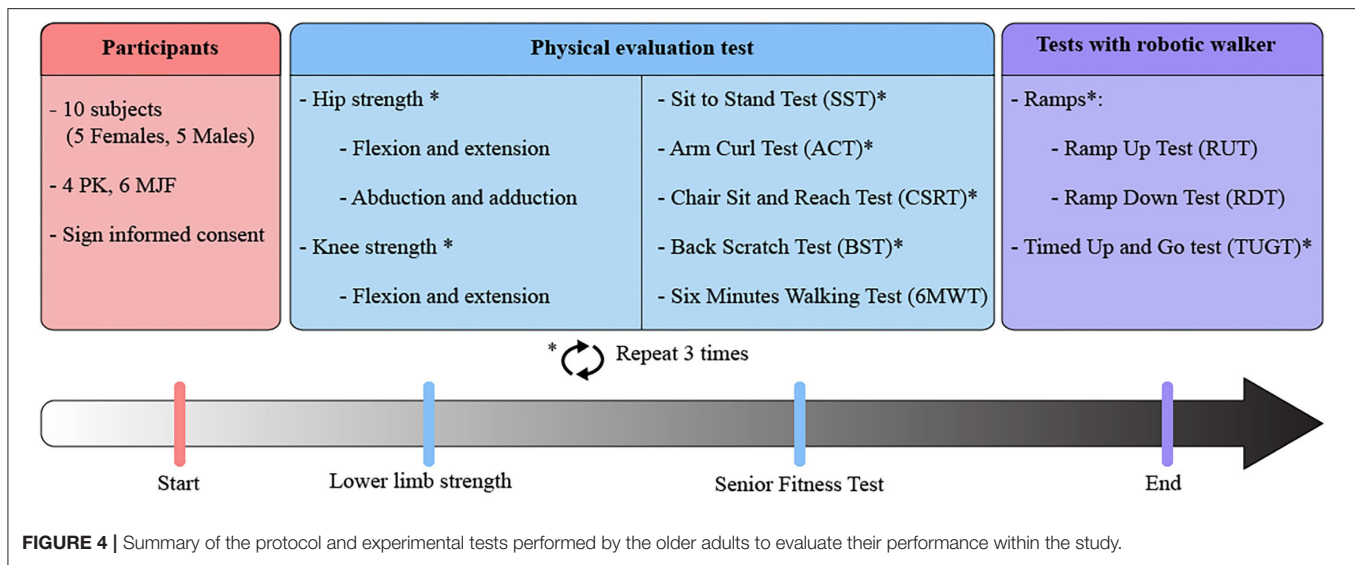
## 3. RESULTS

Five hundred forty-six trials divided into 10 sessions were performed. Kinematic and interaction parameters were measured, such as users' gait spatio-temporal parameters, the interaction force and torque, trial average duration, and walking distance. This section describes the results obtained during the study.

### 3.1. Physical Condition Assessment Results

The data provided by the digital dynamometer were used to estimate the condition of the participants' lower limbs. **Table 2** summarizes the strength values for the hip and knee of each group (i.e., PK and MJF). The dominant side of both groups was the right side, allowing a direct comparison between them.





**FIGURE 4 |** Summary of the protocol and experimental tests performed by the older adults to evaluate their performance within the study.

**TABLE 2 |** Force data obtained from the lower limb strength of the participants.

Join	Parameter	Side	PK	MJF	<i>p-value</i>
Hip	Flexion [N]	Right	198.10 ± 20.64*	147.13 ± 27.73*	<b>0.02</b>
		Left	166.94 ± 67.34*	142.27 ± 29.19*	<b>0.04</b>
	Extension [N]	Right	139.60 ± 19.05*	128.40 ± 37.76	<b>0.01</b>
		Left	127.98 ± 24.35*	126.62 ± 53.41	<b>0.05</b>
	Abduction [N]	Right	127.89 ± 27.21*	108.03 ± 18.22*	<b>&lt;0.01</b>
		Left	126.33 ± 17.77*	98.69 ± 23.85*	<b>0.04</b>
Knee	Adduction [N]	Right	118.20 ± 2.71*	95.81 ± 45.28	<b>&lt;0.01</b>
		Left	117.46 ± 29.41*	92.94 ± 40.11*	<b>&lt;0.01</b>
	Flexion [N]	Right	147.71 ± 25.63*	118.81 ± 29.96*	<b>0.03</b>
		Left	147.03 ± 25.63*	95.62 ± 31.12*	<b>0.05</b>
	Extension [N]	Right	185.83 ± 13.38*	166.53 ± 93.40*	<b>0.04</b>
		Left	185.44 ± 41.06*	155.83 ± 74.65*	<b>&lt;0.01</b>

Asterisks indicate the data have a normal distribution. *P-values* in bold indicate significant differences between groups.

Regarding hip flexion and extension, **Table 2** shows how the group of older adults with Parkinson presented better results. The MJF group presented a reduction of 25.7% (right limb) and 17.34% (left limb) compared to the PK group during flexion tests. Besides, significant differences were found between both groups (*p-value* of 0.02). In extension, the strength values in both the right and left were more remarkable for the PK group. Although this parameter presented significant differences, there is not a great discrepancy in the strength measurements for the left hemisphere since the Parkinson group presented a mean of 127.98 N and the group of older adults presented a mean of 126.62 N.

Concerning the movements of abduction and adduction, both parameters presented statistically significant differences. On the right side, the PK group showed an increase compared to the MJF group of 18.38% in abduction, while in adduction, such

**TABLE 3 |** Senior Fitness Test (SFT) results.

Test	PK	MJF	<i>p-value</i>
SST [repetitions]	11 ± 1.63*	10 ± 2.61*	<b>0.02</b>
ACT [repetitions]	13 ± 2.16*	14 ± 4.38*	0.74
CSRT [m]	-0.12 ± 0.09*	0.04 ± 0.02*	<b>0.03</b>
BST [m]	-0.20 ± 0.04*	0.09 ± 0.06*	0.06
6MWT [m]	395.4 ± 190.28*	383.2 ± 157.36*	0.53

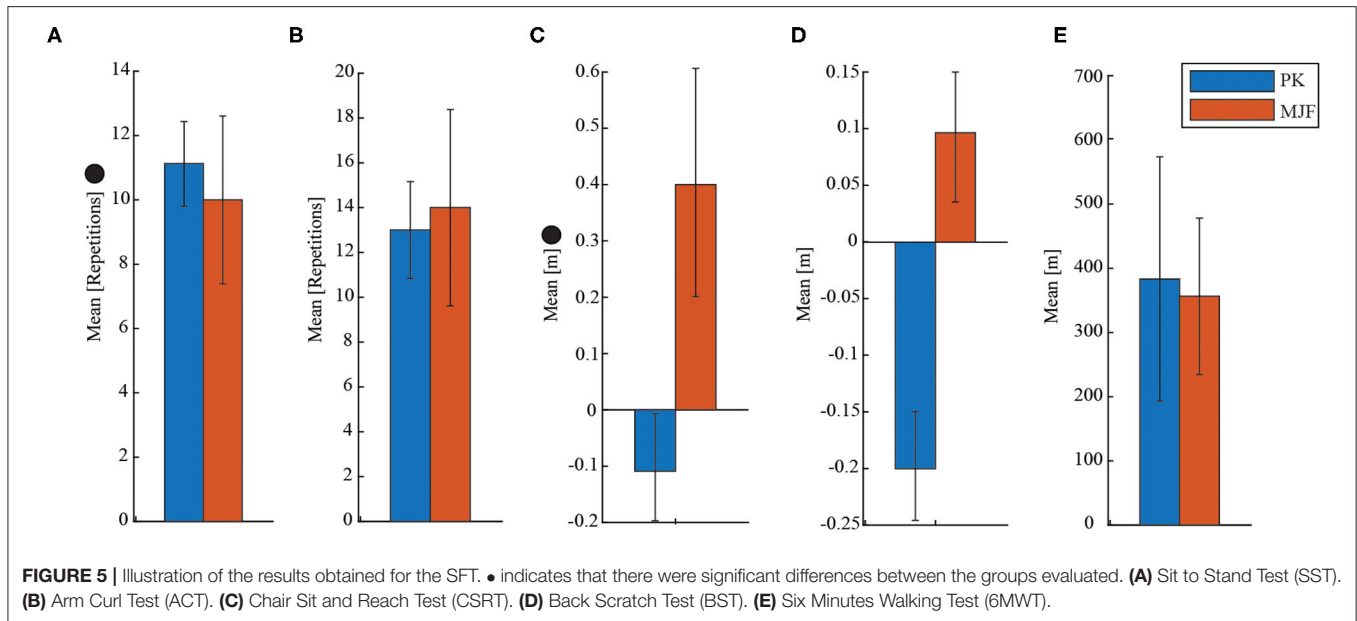
*P-values* in bold indicate significant differences between groups. Asterisks indicate a normal distribution of the data.

an increase was 23.37%. The difference between the groups was considerably more significant for the left side since, for both parameters, the increase exceeded 25%.

**Table 2** presents the results obtained in the flexion and extension measurements of the participants. The MJF group presented a mean value of 118.81 N vs. a 137.71 N by the PK group in flexion for the right hemisphere, representing an increase of 15.90%. This behavior did not change for the left side, as the PK group exhibited a 43.31% increase. Regarding joint extension, the MJF group presented in each case lower results. Also, significant differences were found in the two parameters.

On the other hand, **Table 3** presents the results obtained from the SFTs. It can be observed that for the ACT and BST, which evaluated the upper body condition of the subjects, there were no significant differences (*p-values* of 0.74 and 0.06, respectively). This behavior was maintained for the 6MWT (*p-value* of 0.53), which was used as a general indicator of the older adults' overall physical performance and mobility. The remaining tests, which evaluated the lower body condition of the subjects, presented statistically significant differences.

For SST, although there were statistically significant differences, the PK group was only one repetition above the MJF group. Likewise, the group with metabolic and joint diseases showed greater flexibility in the lower limb (CSRT, refer

**TABLE 4** | Results obtained for the Ramp Up Test (RUT).

RUT	PK	MJF	p-value
SW speed [m/s]	0.71 ± 0.07	0.61 ± 0.07	<b>&lt;0.01</b>
User speed [m/s]	0.70 ± 0.07*	0.61 ± 0.07*	<b>&lt;0.01</b>
Cadence [steps/min]	86.46 ± 3.28*	83.10 ± 5.28*	<b>0.02</b>
Cycle Duration [s]	1.39 ± 0.05*	1.45 ± 0.09*	<b>0.04</b>
No. Cycles	35.36 ± 4.36*	39.10 ± 4.77*	<b>0.01</b>
Trial Duration [s]	49.01 ± 5.34	56.70 ± 7.24*	<b>&lt;0.01</b>
Max frc_y [N]	7.35 ± 0.88*	9.70 ± 1.05	<b>0.04</b>
Mean frc_y [N]	2.40 ± 0.28*	2.76 ± 0.28*	<b>0.04</b>
Max. trq_z [N.m]	4.44 ± 0.93*	4.86 ± 0.99	0.09
Mean trq_z [N.m]	0.01 ± 0.48*	0.03 ± 0.29*	0.27

The p-values in bold indicate significant differences between the two groups, whereas the asterisks indicate that the data have a normal distribution.

**TABLE 5** | Results obtained in the Ramp Down Test (RDT).

RDT	PK	MJF	p-value
SW speed [m/s]	0.62 ± 0.07	0.56 ± 0.10	<b>0.03</b>
User speed [m/s]	0.62 ± 0.07*	0.56 ± 0.10	<b>0.05</b>
Cadence [steps/min]	104.67 ± 6.64*	96.78 ± 11.09*	<b>&lt;0.01</b>
Cycle Duration [s]	1.15 ± 0.07*	1.35 ± 0.13*	<b>&lt;0.01</b>
No. Cycles	45.24 ± 8.77*	48.77 ± 9.84	<b>&lt;0.01</b>
Trial Duration [s]	51.62 ± 6.89*	60.13 ± 19.05	<b>0.04</b>
Max frc_y [N]	6.66 ± 0.65*	9.09 ± 0.83*	<b>0.02</b>
Mean frc_y [N]	2.19 ± 0.21*	4.73 ± 0.40*	<b>&lt;0.01</b>
Max. trq_z [N.m]	7.20 ± 0.94*	9.05 ± 0.92*	<b>0.03</b>
Mean trq_z [N.m]	1.55 ± 0.14	1.91 ± 0.28	<b>&lt;0.01</b>

Asterisks indicate that the data followed a normal distribution. Bolded p-values indicate that there were statistically significant differences between groups.

to Table 3) as they were 0.04 m ahead of the toe, while the PK group was 0.12 m short of the target. Also, there were significant differences between the two groups. In addition to the above, to illustrate the behavior of these results, Figure 5 shows their distribution in a bar chart with the SD.

### 3.2. Kinematic and Physical Interaction Results

Several indicators were estimated using the data collected by the force sensors of the walker and the G-WALK sensor. To characterize the users' gait, parameters such as gait speed, cadence, average gait cycle duration, and the number of gait cycles were calculated. To evaluate the physical interaction between the participant and the walker, the mean force in the y-axis and z-axis were estimated, as well as, the maximum values.

Table 4 shows the kinematic and physical interaction data in the RUT, except the parameters related to the torque in the z-axis, the remaining ones presented statistically significant differences. In terms of user and device speed, the PK group exhibited better results. Nevertheless, for cadence, cycle time, number of cycles, test duration, and the force impressed to the walker on the axis, the MJF group presented higher values supporting the previous results. However, for the y-axis force, very similar results were obtained.

Further, as shown in Table 5, the kinematic and physical interaction parameters presented significant differences in their totality. For the speed of the walker and the user, the PK group showed better results. For the parameters related to the subject's cycles, cadence, and trial duration, the MJF group presented values below the remaining older adults. However, for user-generated force and torque, the MJF group exhibited considerably higher results.

Regarding the TUGT, **Table 6** summarizes the obtained results. Due to the nature of the test, since the user's speed is measured even before the user starts to move forward with the

**TABLE 6** | Results obtained for the Timed Up and Go Test (TUGT).

TUGT	PK	MJF	p-value
SW speed [m/s]	0.36 ± 0.09	0.32 ± 0.06	<b>&lt;0.01</b>
User speed [m/s]	0.32 ± 0.08	0.29 ± 0.06	<b>&lt;0.01</b>
Cadence [steps/min]	105.72 ± 13.87*	110.61 ± 29.58*	<b>0.04</b>
Cycle Duration [s]	1.17 ± 0.15*	1.13 ± 0.29	<b>0.05</b>
No. Cycles	38.82 ± 5.16*	36.59 ± 10.21*	<b>0.02</b>
Trial Duration [s]	32.33 ± 3.82*	42.50 ± 7.34*	<b>&lt;0.01</b>
Max frc_y [N]	6.65 ± 0.67	6.68 ± 1.16*	0.74
Mean frc_y [N]	1.24 ± 0.27*	1.57 ± 0.31*	0.22
Max. trq_z [N.m]	5.51 ± 0.80*	6.07 ± 1.25	<b>0.03</b>
Mean trq_z [N.m]	0.27 ± 0.54	0.13 ± 0.85	<b>0.05</b>

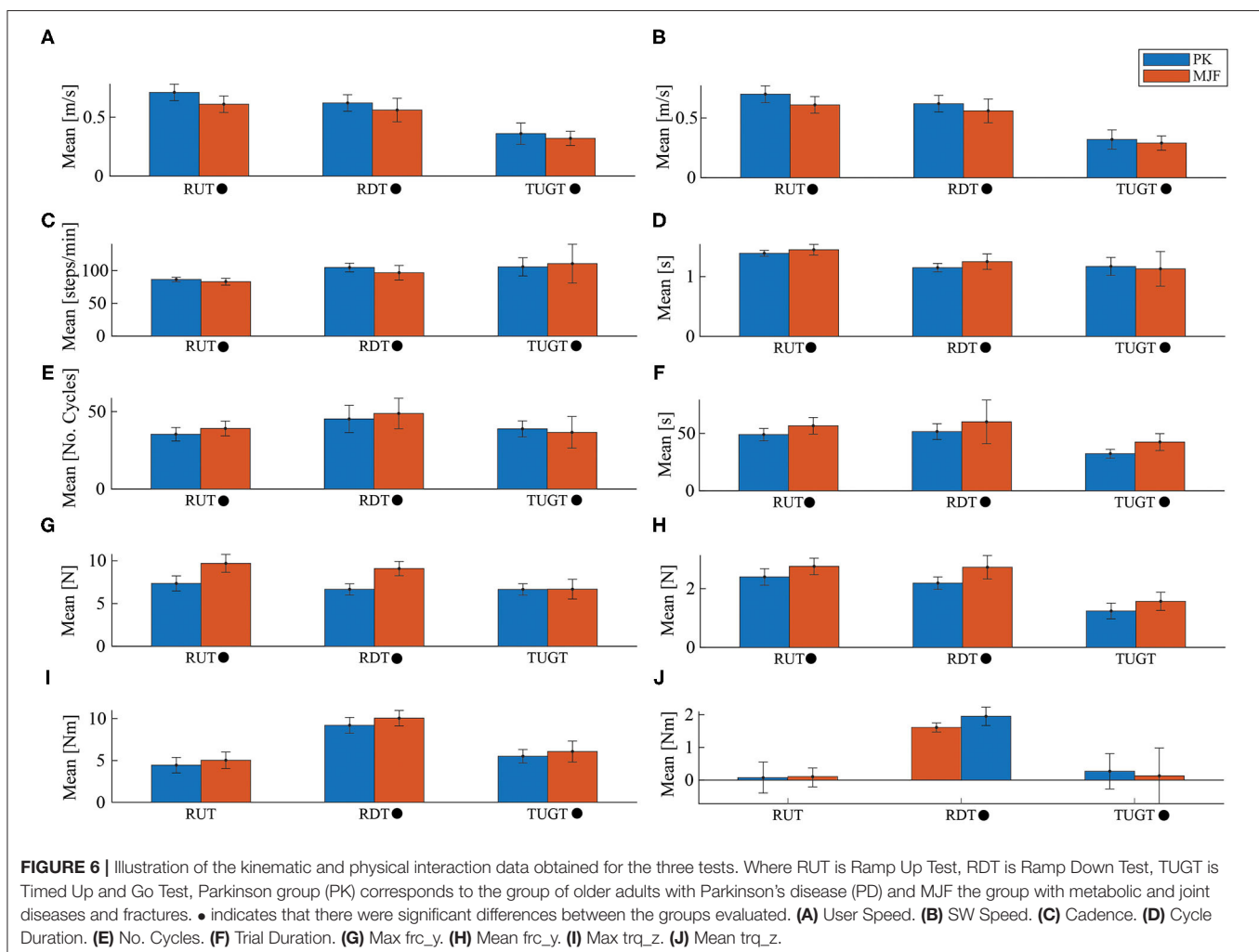
The bold parameters indicate significant differences between the two groups, whereas the asterisks indicate that the data have a normal distribution.

walker (i.e., in the standing and sitting stage), the parameters related to these speeds presented slight differences. In contrast to the previous tests, the cadence of the MJF group is higher than that of the PK group. Thus, the cycle length and the number of cycles of the group with PD are also higher. However, the PK group managed to finish the test in less time (32.33 s) than the other group (42.50 s). On the other hand, for the *y*-axis strength, both groups presented very similar results, adding that there were no significant differences. For the *z*-axis torque, which provides information on the user's support on the device, the PK group presented lower values.

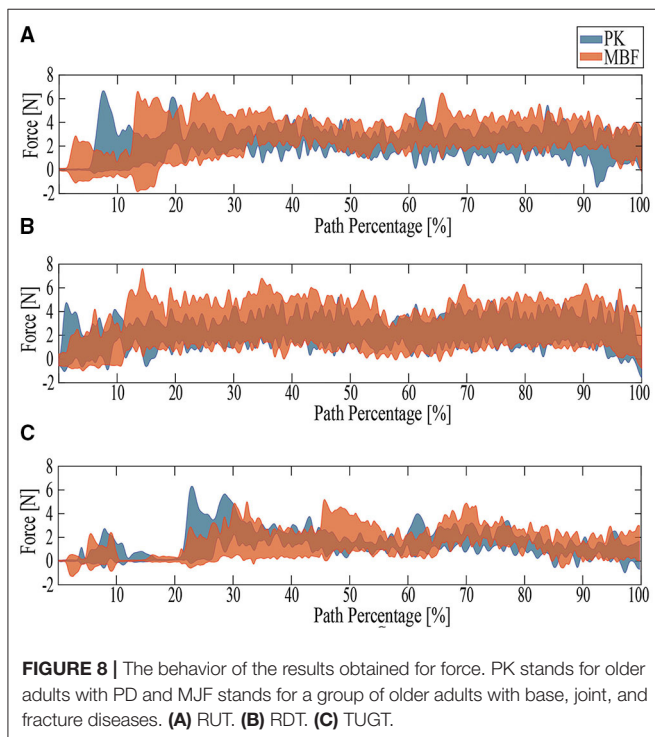
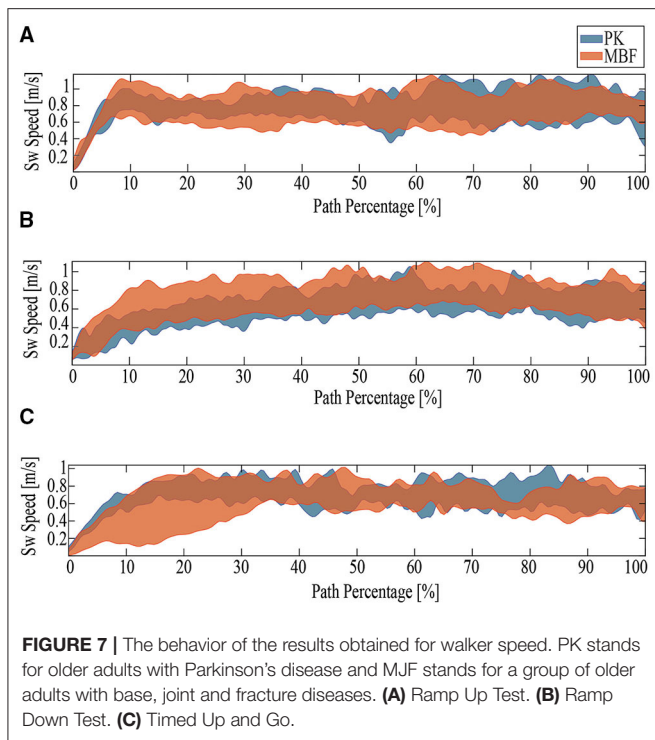
**Figure 6** summarizes the parameters evaluated for the three proposed tests. **Figures 7–9** show the walker speed, force, and torque behavior. For these illustrations, the data from all participants were averaged and the SD was used.

## 4. DISCUSSION

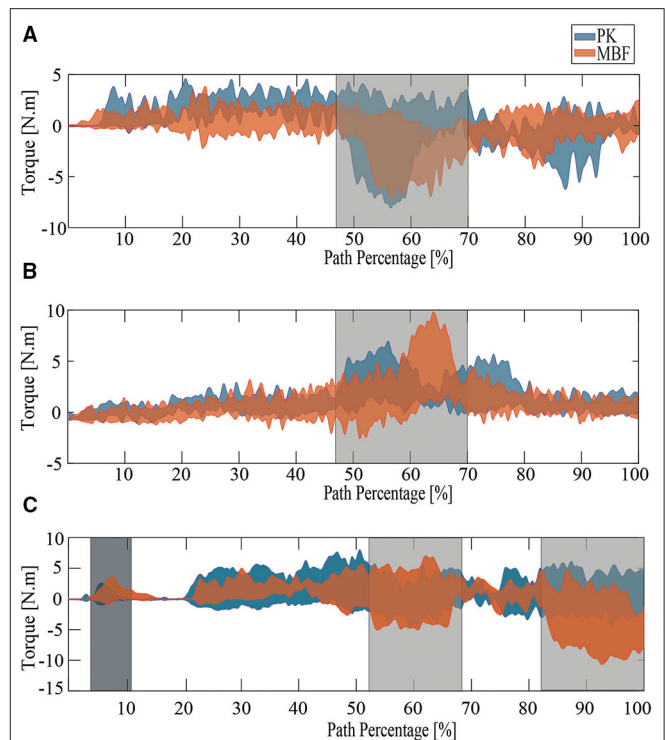
In this study, there were no cases of misunderstanding of the behavior and operation of the AGoRA SW, and no cases of collisions were reported. Besides, it is essential to highlight that







the sample size of this study is considered small. However, studies of similar samples have been reported with this type of devices, as well as, with older adults with Parkinson's and other diseases (Mou et al., 2012; Zhang et al., 2018; Mundt et al., 2019). According to the results presented in the previous section, it was



observed that the physical condition of the subjects significantly influences the participants' performance using the device.

#### 4.1. Physical Condition Assessment

The results shown in **Table 2** indicate that the adults with PD were in better condition. For the hip strength, there was a considerable reduction in the MJF group compared to the PPK. Although PK group was expected to have lower hip strength (Inkster et al., 2003; Skinner et al., 2019), our results are supported by the fact that there are joint disorders (such as osteoarthritis and osteoporosis), which in advanced stages, affect and weaken the hip extensor and flexor muscles (Jerez-Mayorga et al., 2019). In Rydevik et al. (2010) and Judd et al. (2014), similar results were obtained, where a group of older adults with osteoarthritis exhibited a 10–25% deficit in hip muscle strength.

In terms of knee flexion and extension, the average deficit in this joint is less than that in the hip for the PK group. Moreover, the PK group flexion-extension outcomes were considerably higher than the MJF group. Such an increase was of more than 40% and statistically significant differences were found for the left limb flexion, mainly due to an older adult who had a fracture of the tibial plate in the MJF group. As presented in Gaston et al. (2005), when these types of fractures have not been given

sufficient time for recovery, significant impairment of muscle movement and function can occur.

For the SFTs, the results presented in **Table 3** were relevant to determining the participants' overall functional capacity, agility, dynamic balance, aerobic endurance, and upper and lower extremity muscular strength. The PK group exhibited better results in the Sit to Stand Test SST and significant differences were found (refer to **Figure 5**). These results are related to those previously obtained in the strength tests since the older adults in the MJF group showed a considerable reduction. Similarly, in Zijlstra et al. (2012) it is shown how Parkinson patients exhibit acceptable performance in this type of test.

Upper limb strength and endurance is another fitness parameter that was measured with the ACT. As shown in **Figure 5**, despite the slight increase in the number of repetitions in the test by MJF, there were no significant differences. Some older adults in this group who had osteoporosis and epicondylitis may have influenced the obtained results. Epicondylitis is an injury characterized by pain in the external aspect of the elbow, in the region of the epicondyle (Walz et al., 2010). Whereas, osteoporosis is a bone disease characterized by a decrease in the density of bone tissue and resulting in an exaggerated fragility of the bones (on Osteoporosis et al., 2001). In this sense, very similar results to those shown in Adamo et al. (2015) were obtained, indicating that participants with these pathologies show a significant deficit, compromising their physical abilities.

There was not much discrepancy in the mean values obtained for the CSRT results. However, significant differences were found in this parameter (refer to **Figure 5**). As in the previous test, this one presents values below normal. Additionally, these results are supported by the fact that older adults with Parkinson's present a direct relationship between the degree of stiffness their body experiences, generated by the disorder and the passing of years (Inkster et al., 2003).

In the opposite case, the MJF group presented better results for the BST, despite not showing significant differences (refer to **Figure 5**). Regarding the 6MWT the results were as expected. Even though, the PK group covered a slightly greater distance, there were no significant differences (refer to **Figure 5**). This last could be related to the fact that adults with PD cannot maintain a constant pace when making very long trips. As presented in Falvo and Earhart (2009), the Parkinson's group obtains similar results because of the subjects' impaired balance and predisposition to falls. For this reason and as presented in Mou et al. (2012), Zhang et al. (2018), and Wu et al. (2020), devices such as SWs can help reduce the risk factors for falls and help to maintain constant kinematic parameters such as speed and cadence of the participant in very long distances.

## 4.2. Kinematic and Physical Interaction

As for the Ramp Up Test (RUT), the PK group presented better results concerning user speed (refer to **Figure 6**), walker speed (refer to **Figures 6, 7**), and cadence (refer to **Figure 6**). In contrast, the MJF group obtained higher values in the cycle time, the number of cycles, and test duration (refer to **Figure 6**), meaning an inferior performance. This type of test

involve muscles such as the glutes, hamstrings, and quadriceps (Lindemann et al., 2017), thus the flexion-extension results of the PK group support their better performance in the RUT. These results can also be seen in the force exerted by the users (refer to **Figure 8**), due to the considerable effort that the older adults in the MJF group had to make. This significant increase is also supported by the low performance in the hip and knee strength tests by this group. Given the weakened lower limbs in the MJF group, the participants felt the need to rely on the device to compensate for this deficit. However, there were no significant differences in the torque values as shown in **Figures 6, 9**, which is consistent with the nature of the test (i.e., the majority of the test with straight sections).

These results might classify the AGoRA SW as a potential tool for gait retraining and rehabilitation. Considering the participant's effort and the natural deterioration of their lower limbs, the implemented admittance controller could be adjusted to emulate a lighter or heavier platform according to the requirements of the subject.

Regarding the Ramp Down Test (RDT), the PK group also obtained better results. When comparing the behavior of the kinematic and physical interaction parameters during both ramp tests, similar results were observed in terms of user and walker speed (refer to **Figures 6, 7**). Slight changes were obtained in cadence, gait cycle time, and the number of cycles. These results are supported by the fact that uphill walking resulted in slower speeds because of the natural effort of the test. In addition, the peak force and torque (refer to **Figures 8, 9**, respectively) exerted by the users were considerably higher in the downhill ramp tests. Because the device exhibited higher moments of inertia during the downhill tests, subjects required greater efforts to perform the mid-ramp turn. These results are supported by the ACT (refer to **Table 3**), since adults with PD presented a 7.1% reduction in this test, indicating the natural deterioration of the lower limbs. For this reason, and unlike the previous test, there are significant differences in the torque generated in the z-axis. Similar results were obtained in Lindemann et al. (2017). In this study, they highlight how a SW reduces under-performance in subjects' gait and shows how the kinematic parameters (cadence, speed, cycles) are substantially reduced in the downhill tests.

Finally, during the TUGT, users were asked to lean on the device to stand out of the chair. To prevent the admittance controller from generating velocities, the device motors were remotely deactivated. This leaning event was observed as an initial spike in the force and torque signal. As seen in **Figures 6, 8**, the force signals did not exhibit many discrepancies, and there was no evidence of significant differences. Regarding the torque, it is essential to highlight that the MJF group showed higher values (refer to **Figures 6, 9**). These findings suggest that users saw in the intelligent walker a possibility to compensate for this deficit in the musculature (Judd et al., 2014). Moreover, compared to the previous tests, which required more physical effort from the subjects, the TUGT showed lower force (refer to **Figure 6**) and torque (**Figure 6**) values. This indicates the efficiency and usefulness of the admittance controller in emulating a lighter platform.

## 5. CONCLUSIONS AND FUTURE WORK

This study presented the assessment of the AGoRA SW in daily life scenarios with two groups of older adults. One group had PD and the other group had underlying diseases, joint diseases, and fractures. Physical validation tests were performed and relevant results were found in the relationship between this condition and the performance in tests with the walker. One of the main findings of this study is related to the relationship between users' pathologies and their physical condition. As previously discussed, PD is a brain disorder that causes progressive cognitive and motor deterioration producing tremors, rigidity and difficulty in walking, balance, and coordination. However, it was found that pathologies such as osteoarthritis in advanced stages can further affect the physical condition of the subjects and their performance in activities of daily living.

Interesting results related to the kinematic and interaction parameters during the RUT were found. Although the RUT demands that the user has to apply a more significant effort even to the point of opposing the movement intention, it could induce muscle training during rehabilitation processes. In addition, this test could be complemented by adjusting the level of assistance of the AGoRA SW to meet the specific needs of each user. More resistive assistance levels induce slower gait patterns compared to studies reported in the literature. This could be interpreted as a safety strategy, as slower gait patterns could help users avoid collisions and stumbling while walking. In addition, the strength data collected during the RUT provided information on potential muscle training applications. Furthermore, as evidenced in the TUGT, the AGoRA SW can guarantee a natural and adequate interaction in scenarios where no significant effort is required from the users. This can be evidenced in the force values, as there were slight discrepancies but no significant differences. This indicates that despite the participant's physical condition and pathology, the AGoRA walker can assist efficiently.

One of the main limitations of this study is that it lacks EMG information that provides insights related to the participant's physical interaction and evolution with this technique in the different tests. As mentioned before, another limitation of this research is the sample size. However, this study is the first approach to comparing the performance of two groups of older adults with different physical and cognitive characteristics.

Finally, future study will be focused on evaluating at AGoRA SW with a bigger group of participants. The MJF group will include older adults with other pathologies that significantly affect their gait patterns. Besides, standardized scales will be included to determine the stage of the disease and how this

may influence the results. Future studies will also include biomechanical analyses.

## DATA AVAILABILITY STATEMENT

The datasets presented in this study can be found in online repositories. The names of the repository/repositories and accession number(s) can be found at: <https://figshare.com/s/51dce22f5a718d759927>.

## ETHICS STATEMENT

The studies involving human participants were reviewed and approved by Ethical Committee of the Colombian School of Engineering Julio Garavito. The patients/participants provided their written informed consent to participate in this study.

## AUTHOR CONTRIBUTIONS

SS, DG, SO, MA-C, AG-R, MM, and CC contributed to the conception and design of the study. SS, MM, and CC conceptualized the study and designed the methodology. AG-R recruited the participants. SS, DG, and MA-C conducted the experimental trials. DG, MA-C, and SO performed data curation and processing. DG wrote the original manuscript. SS, AG-R, MM, and CC provided feedback on the manuscript. AG-R, MM, and CC supervised the study. MM and CC managed the funding resources. All authors have read and accepted the published version of the manuscript.

## FUNDING

This study was supported by the Ministry of Science, Technology, and Innovation of Colombia (Grant 801-2017) and (Grant 845-2020) and the Colombian School of Engineering Julio Garavito Funds.

## ACKNOWLEDGMENTS

The authors wish to acknowledge the voluntary participation of all subjects during the study. In addition, the authors would like to thank the Innovation and Technological Development Center for facilitating the use of their facilities and the physiotherapy professors and students of the Areandina University Foundation of Pereira who were on hand at every stage of the study. Finally, to the Ethics Committee of the Colombian School of Engineering Julio Garavito for allowing and approving the realization of this research.

## REFERENCES

- Adamo, D. E., Talley, S. A., and Goldberg, A. (2015). Age and task differences in functional fitness in older women: comparisons with senior fitness test normative and criterion-referenced data. *J. Aging Phys. Act.* 23, 47–54. doi: 10.1123/JAPA.2012-0317
- Alves, J., Seabra, E., Caetano, I., and Santos, C. P. (2017). "Overview of the asbgo++ smart walker," in *2017 IEEE 5th Portuguese Meeting on Bioengineering (ENBENG)* (Coimbra: IEEE), 1–4.

- Aristizabal-Aristizabal, J., Ferro-Rugeles, R., Lancheros-Vega, M., Sierra M. S. D., Múnera, M., and Cifuentes, C. A. (2022). *Fundamentals for the Design of Smart Walkers, 1st Edn, Vol. 1* Cham: Springer International Publishing.
- Bayon, C., Ramírez, O., Del Castillo, M. D., Serrano, J. I., Raya, R., Belda-Lois, J. M., et al. (2016). "Cpwalker: robotic platform for gait rehabilitation in patients with cerebral palsy," in *2016 IEEE International Conference on Robotics and Automation (ICRA)* (Stockholm: IEEE), 3736–3741.
- Belghali, M., Chastan, N., Cignetti, F., Davenne, D., and Decker, L. M. (2017). Loss of gait control assessed by cognitive-motor dual-tasks: pros and cons in



- detecting people at risk of developing alzheimer's and parkinson's diseases. *Geroscience* 39, 305–329. doi: 10.1007/s11357-017-9977-7
- Brodie, M. A. D., Beijer, T. R., Canning, C. G., and Lord, S. R. (2015). Head and pelvis stride-to-stride oscillations in gait: validation and interpretation of measurements from wearable accelerometers. *Physiol. Meas.* 36, 857–872. doi: 10.1088/0967-3334/36/5/857
- Brown, C. J., and Flood, K. L. (2013). Mobility limitation in the older patient: a clinical review. *JAMA* 310, 1168–1177. doi: 10.1001/jama.2013.276566
- BTS Bioengineering (2019). G-WALK.
- Buchman, A. S., Boyle, P. A., Leurgans, S. E., Barnes, L. L., and Bennett, D. A. (2011). Cognitive function is associated with the development of mobility impairments in community-dwelling elders. *Am. J. Geriatr. Psychiatry* 19, 571–580. doi: 10.1097/JGP.0b013e3181ef7a2e
- Caetano, I., Alves, J., Gonçalves, J., Martins, M., and Santos, C. P. (2016). “Development of a biofeedback approach using body tracking with active depth sensor in asbgo smart walker,” in *2016 International Conference on Autonomous Robot Systems and Competitions (ICARSC)* (Bragança: IEEE), 241–246.
- Chugo, D., Asawa, T., Kitamura, T., Songmin, J., and Takase, K. (2009). “A motion control of a robotic walker for continuous assistance during standing, walking and seating operation,” in *2009 IEEE/RSJ International Conference on Intelligent Robots and Systems* (Bangkok: IEEE), 4487–4492.
- Cifuentes, C. A., and Frizera, A. (2016). *Human-Robot Interaction Strategies for Walker-Assisted Locomotion*, volume 115 of *Springer Tracts in Advanced Robotics*. Cham: Springer International Publishing.
- Cifuentes, C. A. and Múnera, M. (2022). *Interfacing Humans and Robots for Gait Assistance and Rehabilitation 1st Edn*, Vol. 1. Cham: Springer International Publishing.
- Costamagna, E., Thies, S. B., Kenney, L. P., Howard, D., Lindemann, U., Klenk, J., et al. (2019). Objective measures of rollator user stability and device loading during different walking scenarios. *PLoS ONE* 14:e0210960. doi: 10.1371/journal.pone.0210960
- Cubo, E., Moore, C. G., Leurgans, S., and Goetz, C. G. (2003). Wheeled and standard walkers in parkinson's disease patients with gait freezing. *Parkinsonism Relat. Disord.* 10, 9–14. doi: 10.1016/S1353-8020(03)00060-9
- Falvo, M. J., and Earhart, G. M. (2009). Six-minute walk distance in persons with parkinson disease: a hierarchical regression model. *Arch. Phys. Med. Rehabil.* 90, 1004–1008. doi: 10.1016/j.apmr.2008.12.018
- Frizera Neto, A., Gallego, J. A., Rocon, E., Pons, J. L., and Ceres, R. (2010). Extraction of user's navigation commands from upper body force interaction in walker assisted gait. *BioMed. Eng. Online*. Vitória 9, 1–16. doi: 10.1186/1475-925X-9-37
- Frizera, A., Gallego, J., Rocon de Lima, E., Abellanas, A., Pons, J., and Ceres, R. (2010). “Online cadence estimation through force interaction in walker assisted gait,” in *ISSNIP Biosignals and Biorobotics Conference 2010* (Vitoria), 1–5.
- Gaston, P., Will, E., and Keating, J. (2005). Recovery of knee function following fracture of the tibial plateau. *J. Bone Joint Surg.* 87, 1233–1236. doi: 10.1302/0301-620X.87B9.16276
- Geravand, M., Werner, C., Hauer, K., and Peer, A. (2016). An integrated decision making approach for adaptive shared control of mobility assistance robots. *Int. J. Soc. Robot.* 8, 631–648. doi: 10.1007/s12369-016-0353-z
- Gheno, R., Cepparo, J. M., Rosca, C. E., and Cotten, A. (2012). Musculoskeletal disorders in the elderly. *J. Clin. Imaging Sci.* 2:39. doi: 10.4103/2156-7514.99151
- Heerink, M., Kröse, B., Wielinga, B., and Evers, V. (2009). “Measuring the influence of social abilities on acceptance of an interface robot and a screen agent by elderly users,” in *People and Computers XXIII Celebrating People and Technology - Proceedings of HCI 2009*, Cambridge, 430–439.
- Hesseberg, K., Bentzen, H., and Bergland, A. (2015). Reliability of the senior fitness test in community-dwelling older people with cognitive impairment. *Physiother. Res. Int.* 20, 37–44. doi: 10.1002/pri.1594
- Inkster, L. M., Eng, J. J., MacIntyre, D. L., and Stoessl, A. J. (2003). Leg muscle strength is reduced in Parkinson's disease and relates to the ability to rise from a chair. *Mov. Disord.* 18, 157–162. doi: 10.1002/mds.10299
- Jenkins, S., and Draper, H. (2015). Care, monitoring, and companionship: views on care robots from older people and their carers. *Int. J. Soc. Robot.* 7, 673–683. doi: 10.1007/s12369-015-0322-y
- Jerez-Mayorga, D., Ríos, L. J. C., Reyes, A., Delgado-Floody, P., Payer, R. M., and Requena, I. M. G. (2019). Muscle quality index and isometric strength in older adults with hip osteoarthritis. *PeerJ* 7:e7471. doi: 10.7717/peerj.7471
- Jiménez, M. F., Monllor, M., Frizera, A., Bastos, T., Roberti, F., and Carelli, R. (2019). Admittance controller with spatial modulation for assisted locomotion using a smart walker. *J. Intell. Robot. Syst.* 94, 621–637. doi: 10.1007/s10846-018-0854-0
- Judd, D. L., Thomas, A. C., Dayton, M. R., and Stevens-Lapsley, J. E. (2014). Strength and functional deficits in individuals with hip osteoarthritis compared to healthy, older adults. *Disabil. Rehabil.* 36, 307–312. doi: 10.3109/09638288.2013.790491
- Jun, H.-G., Chang, Y.-Y., Dan, B.-J., Jo, B.-R., Min, B.-H., Yang, H., et al. (2011). “Walking and sit-to-stand support system for elderly and disabled,” in *2011 IEEE International Conference on Rehabilitation Robotics* (Zurich: IEEE), 1–5.
- Kawaguchi, J. K., and Babcock, G. (2010). Validity and reliability of handheld dynamometric strength assessment of hip extensor and abductor muscles. *Athlet. Train. Sports Health Care* 2, 11–17. doi: 10.3928/19425864-20101221-04
- Kegelmeyer, D. A., Parthasarathy, S., Kostyk, S. K., White, S. E., and Kloos, A. D. (2013). Assistive devices alter gait patterns in Parkinson disease: advantages of the four-wheeled walker. *Gait Posture* 38, 20–24. doi: 10.1016/j.gaitpost.2012.10.027
- Lacey, G. J., and Rodriguez-Losada, D. (2008). The evolution of guido. *IEEE Robot. Autom. Mag.* 15, 75–83. doi: 10.1109/MRA.2008.929924
- Lindemann, U., Schwenk, M., Klenk, J., Kessler, M., Weyrich, M., Kurz, F., et al. (2016). Problems of older persons using a wheeled walker. *Aging Clin. Exp. Res.* 28, 215–220. doi: 10.1007/s40520-015-0410-8
- Lindemann, U., Schwenk, M., Schmitt, S., Weyrich, M., Schlicht, W., and Becker, C. (2017). Effect of uphill and downhill walking on walking performance in geriatric patients using a wheeled walker. *Z. Gerontol. Geriatr.* 50, 483–487. doi: 10.1007/s00391-016-1156-4
- Martins, M., Santos, C., Frizera, A., and Ceres, R. (2015). A review of the functionalities of smart walkers. *Med. Eng. Phys.* 37, 917–928. doi: 10.1016/j.medengphy.2015.07.006
- Mikolajczyk, T., Ciobanu, I., Badea, D. I., Iliescu, A., Pizzamiglio, S., Schauer, T., et al. (2018). Advanced technology for gait rehabilitation: an overview. *Adv. Mech. Eng.* 10:1687814018783627. doi: 10.1177/1687814018783627
- Mintken, P. E., Carpenter, K. J., Eckhoff, D., Kohrt, W. M., and Stevens, J. E. (2007). Early neuromuscular electrical stimulation to optimize quadriceps muscle function following total knee arthroplasty: a case report. *J. Orthop. Sports Phys. Ther.* 37, 364–371. doi: 10.2519/jospt.2007.2541
- Mitzner, T. L., Chen, T. L., Kemp, C. C., and Rogers, W. A. (2014). Identifying the potential for robotics to assist older adults in different living environments. *Int. J. Soc. Robot.* 6, 213–227. doi: 10.1007/s12369-013-0218-7
- Moreira, R., Alves, J., Matias, A., and Santos, C. (2019). Smart and assistive walker-asbgo: rehabilitation robotics: a smart-walker to assist ataxic patients. *Adv. Exp. Med. Biol.* 1170, 37–68. doi: 10.1007/978-3-030-24230-5\_2
- Mou, W.-H., Chang, M.-F., Liao, C.-K., Hsu, Y.-H., Tseng, S.-H., and Fu, L.-C. (2012). “Context-aware assisted interactive robotic walker for parkinson's disease patients,” in *2012 IEEE/RSJ International Conference on Intelligent Robots and Systems* (Vilamoura-Algarve: IEEE), 329–334.
- Mrozowski, J., Awrejcewicz, J., and Bamberki, P. (2007). Analysis of stability of the human gait. *J. Theor. Appl. Mech.* 45, 91–98. Available online at: <http://www.ptmts.org.pl/jtam/index.php/jtam/article/view/v45n1p91>
- Mundt, M., Batista, J. P., Markert, B., Bollheimer, C., and Laurentius, T. (2019). Walking with rollator: a systematic review of gait parameters in older persons. *Eur. Rev. Aging Phys. Act.* 16, 1–9. doi: 10.1186/s11556-019-0222-5
- Neto, A. F., Elias, A., Cifuentes, C., Rodriguez, C., Bastos, T., and Carelli, R. (2015). “Smart walkers: Advanced robotic human walking-aid systems,” in *Intelligent Assistive Robots* (Cham: Springer), 103–131.
- Nieuwboer, A., Dom, R., De Weerd, W., Desloovere, K., Fieus, S., and Broens-Kaucsik, E. (2001). Abnormalities of the spatiotemporal characteristics of gait at the onset of freezing in parkinson's disease. *Mov. Disord.* 16, 1066–1075. doi: 10.1002/mds.1206
- NIH Consensus Development Panel on Osteoporosis Prevention, Diagnosis, and Therapy (2001). Osteoporosis prevention, diagnosis, and therapy. *JAMA* 285, 785–795. doi: 10.1001/jama.285.6.785
- Papageorgiou, X. S., Chalvatzaki, G., Lianos, K.-N., Werner, C., Hauer, K., Tzafestas, C. S., et al. (2016). “Experimental validation of human pathological gait analysis for an assisted living intelligent robotic walker,” in *2016 6th IEEE International Conference on Biomedical Robotics and Biomechanics (BioRob)* (Singapore: IEEE), 1086–1091.



- Pedersen, M. M., Holt, N. E., Grande, L., Kurlinski, L. A., Beauchamp, M. K., Kiely, D. K., et al. (2014). Mild cognitive impairment status and mobility performance: an analysis from the boston rise study. *J. Gerontol. Ser. A Biomed. Sci. Med. Sci.* 69, 1511–1518. doi: 10.1093/gerona/glu063
- Pirker, W., and Katzenschlager, R. (2017). Gait disorders in adults and the elderly. *Wiener Klinisch. Wochensh.* 129, 81–95. doi: 10.1007/s00508-016-1096-4
- Poewe, W., Seppi, K., Tanner, C. M., Halliday, G. M., Brundin, P., Volkman, J., et al. (2017). Parkinson disease. *Nat. Rev. Dis. Primers* 3, 1–21. doi: 10.1038/nrdp.2017.13
- Rikli, R. E., and Jones, C. J. (2013). *Senior Fitness Test Manual*. Human kinetics.
- Rydevik, K., Fernandes, L., Nordsletten, L., and Risberg, M. A. (2010). Functioning and disability in patients with hip osteoarthritis with mild to moderate pain. *J. Orthop. Sports Phys. Ther.* 40, 616–624. doi: 10.2519/jospt.2010.03346
- Sammer, G., Uhlmann, T., Unbehau, W., Millonig, A., Mandl, B., Dangschat, J., et al. (2012). Identification of mobility-impaired persons and analysis of their travel behavior and needs. *Transport. Res. Rec.* 2320, 46–54. doi: 10.3141/2320-06
- Scheidegger, W. M., de Mello, R. C., Sierra M., S. D., Jimenez, M. F., Munera, M. C., Cifuentes, C. A., et al. (2019). “A novel multimodal cognitive interaction for walker-assisted rehabilitation therapies,” in *2019 IEEE 16th International Conference on Rehabilitation Robotics (ICORR)* (Toronto: IEEE), 905–910.
- Sierra, M. S. D., Arciniegas-Mayag, L., Bautista, M., Pinto-Bernal, M. J., Cespedes, N., Múnera, M., et al. (2022a). *Introduction to Robotics for Gait Assistance and Rehabilitation, 1st Edn*, Vol. 1. Cham: Springer International Publishing.
- Sierra, M. S. D., Garzón, M., Munera, M., Cifuentes, C. A., et al. (2019). Human-robot-environment interaction interface for smart walker assisted gait: Agora walker. *Sensors* 19:2897. doi: 10.3390/s19132897
- Sierra, M. S. D., Jiménez, M. F., Frizera-Neto, A., Múnera, M., and Cifuentes, C. A. (2022b). *Control Strategies for Human-Robot-Environment Interaction in Assisted Gait With Smart Walkers*. Cham: Springer International Publishing.
- Sierra, M. S. D., Múnera, M., Provot, T., Bourgain, M., Cifuentes, C. A., et al. (2021). Evaluation of physical interaction during walker-assisted gait with the agora walker: strategies based on virtual mechanical stiffness. *Sensors* 21:3242. doi: 10.3390/s21093242
- Sierra, S. D., Molina, J. F., Gómez, D. A., Múnera, M. C., and Cifuentes, C. A. (2018). “Development of an interface for human-robot interaction on a robotic platform for gait assistance: Agora smart walker,” in *2018 IEEE Andescon* (Santiago de Cali: IEEE), 1–7.
- Skinner, J. W., Christou, E. A., and Hass, C. J. (2019). Lower extremity muscle strength and force variability in persons with parkinson disease. *J. Neurol. Phys. Ther.* 43, 56–62. doi: 10.1097/NPT.0000000000000244
- Stevens-Lapsley, J. E., Balter, J. E., Kohrt, W. M., and Eckhoff, D. G. (2010). Quadriceps and hamstrings muscle dysfunction after total knee arthroplasty. *Clin. Orthop. Relat. Res.* 468, 2460–2468. doi: 10.1007/s11999-009-1219-6
- United Nations (2020). *World Population Ageing 2020 Highlights: Living Arrangements of Older Persons*. United Nations.
- Van der Loos, H. M., Reinkensmeyer, D. J., and Guglielmelli, E. (2016). “Chapter 64: Rehabilitation and health care robotics,” in *Springer Handbook of Robotics* (Cham: Springer International Publishing), 1685–1728.
- Vaughan, C. L. (2003). Theories of bipedal walking: an odyssey. *J. Biomech.* 36, 513–523. doi: 10.1016/S0021-9290(02)00419-0
- Walz, D. M., Newman, J. S., Konin, G. P., and Ross, G. (2010). Epicondylitis: pathogenesis, imaging, and treatment. *Radiographics* 30, 167–184. doi: 10.1148/rg.301095078
- Wang, T., Dune, C., Merlet, J.-P., Gorce, P., Sacco, G., Robert, P., et al. (2014). “A new application of smart walker for quantitative analysis of human walking,” in *European Conference on Computer Vision* (Cham: Springer), 464–480.
- Werner, C., Geravand, M., Korondi, P. Z., Peer, A., Bauer, J. M., and Hauer, K. (2020). Evaluating the sit-to-stand transfer assistance from a smart walker in older adults with motor impairments. *Geriatr. Gerontol. Int.* 20, 312–316. doi: 10.1111/ggi.13874
- World Health Organization (2006). *Neurological Disorders: Public Health Challenges*. World Health Organization.
- World Health Organization (2015). *World Report on Ageing and Health*. World Health Organization.
- Wu, H.-K., Chen, H.-R., Chen, W.-Y., Lu, C.-F., Tsai, M.-W., and Yu, C.-H. (2020). A novel instrumented walker for individualized visual cue setting for gait training in patients with parkinson's disease. *Assist. Technol.* 32, 203–213. doi: 10.1080/10400435.2018.1525442
- Yoon, S. H., Jun, H. G., Dan, B. J., Jo, B. R., and Min, B. H. (2012). “Hidden marker position estimation during sit-to-stand with walker,” in *2012 Annual International Conference of the IEEE Engineering in Medicine and Biology Society* (San Diego: IEEE), 1940–1943.
- Zhang, M., Artan, N. S., Gu, H., Dong, Z., Burina Ganatra, L., Shermon, S., et al. (2018). Gait study of Parkinson's disease subjects using haptic cues with a motorized walker. *Sensors* 18:3549. doi: 10.3390/s18103549
- Zijlstra, A., Mancini, M., Lindemann, U., Chiari, L., and Zijlstra, W. (2012). Sit-stand and stand-sit transitions in older adults and patients with Parkinson's disease: event detection based on motion sensors versus force plates. *J. Neuroeng. Rehabil.* 9, 1–10. doi: 10.1186/1743-0003-9-75

**Conflict of Interest:** The authors declare that the research was conducted in the absence of any commercial or financial relationships that could be construed as a potential conflict of interest.

**Publisher's Note:** All claims expressed in this article are solely those of the authors and do not necessarily represent those of their affiliated organizations, or those of the publisher, the editors and the reviewers. Any product that may be evaluated in this article, or claim that may be made by its manufacturer, is not guaranteed or endorsed by the publisher.

Copyright © 2021 Sierra M., Garcia A., Otálora, Arias-Castro, Gómez-Rodas, Múnera and Cifuentes. This is an open-access article distributed under the terms of the Creative Commons Attribution License (CC BY). The use, distribution or reproduction in other forums is permitted, provided the original author(s) and the copyright owner(s) are credited and that the original publication in this journal is cited, in accordance with accepted academic practice. No use, distribution or reproduction is permitted which does not comply with these terms.



# Adaptation Strategies for Personalized Gait Neuroprosthetics

Anne D. Koelewijn<sup>1\*</sup>, Musa Audu<sup>2,3</sup>, Antonio J. del-Ama<sup>4</sup>, Annalisa Colucci<sup>5</sup>, Josep M. Font-Llagunes<sup>6,7</sup>, Antonio Gogeochea<sup>8</sup>, Sandra K. Hnat<sup>2,3</sup>, Nathan Makowski<sup>2,9</sup>, Juan C. Moreno<sup>10</sup>, Mark Nandor<sup>2,11</sup>, Roger Quinn<sup>2,11</sup>, Marc Reichenbach<sup>12,13</sup>, Ryan-David Reyes<sup>2,3</sup>, Massimo Sartori<sup>8</sup>, Surjo Soekadar<sup>5</sup>, Ronald J. Triolo<sup>2,3</sup>, Mareike Vermehren<sup>5</sup>, Christian Wenger<sup>14</sup>, Utku S. Yavuz<sup>15</sup>, Dietmar Fey<sup>13</sup> and Philipp Beckerle<sup>16</sup>

<sup>1</sup> Biomechanical Data Analysis and Creation (BIOMAC) Group, Machine Learning and Data Analytics Lab, Faculty of Engineering, Friedrich-Alexander-Universität Erlangen-Nürnberg, Erlangen, Germany, <sup>2</sup> Department of Veterans Affairs, Louis Stokes Cleveland and Veterans Affairs Medical Center, Advanced Platform Technology Center, Cleveland, OH, United States, <sup>3</sup> Department of Biomedical Engineering, Case Western Reserve University, Cleveland, OH, United States, <sup>4</sup> Applied Mathematics, Materials Science and Technology and Electronic Technology Department, Rey Juan Carlos University, Mostoles, Spain, <sup>5</sup> Clinical Neurotechnology Lab, Neuroscience Research Center (NWFZ), Department of Psychiatry and Neurosciences, Charité - Universitätsmedizin Berlin, Berlin, Germany, <sup>6</sup> Biomechanical Engineering Lab, Department of Mechanical Engineering and Research Centre for Biomedical Engineering, Universitat Politècnica de Catalunya, Barcelona, Spain, <sup>7</sup> Institut de Recerca Sant Joan de Déu, Esplugues de Llobregat, Spain, <sup>8</sup> Department of Biomechanical Engineering, Faculty of Engineering Technology, University of Twente, Enschede, Netherlands, <sup>9</sup> Department of Physical Medicine and Rehabilitation, MetroHealth Medical Center, Cleveland, OH, United States, <sup>10</sup> Neural Rehabilitation Group, Department of Translational Neuroscience, Cajal Institute, CSIC, Madrid, Spain, <sup>11</sup> Department of Mechanical Engineering, Case Western Reserve University, Cleveland, OH, United States, <sup>12</sup> Chair of Computer Engineering, Brandenburg University of Technology Cottbus-Senftenberg, Cottbus, Germany, <sup>13</sup> Chair for Computer Architecture, Department of Computer Science, Faculty of Engineering, Friedrich-Alexander-Universität Erlangen-Nürnberg, Erlangen, Germany, <sup>14</sup> IHP-Leibniz Institut Fuer Innovative Mikroelektronik, Frankfurt (Oder), Germany, <sup>15</sup> Biomedical Signals and Systems Group, University of Twente, Enschede, Netherlands, <sup>16</sup> Chair of Autonomous Systems and Mechatronics, Department of Electrical Engineering, Artificial Intelligence in Biomedical Engineering, Faculty of Engineering, Friedrich-Alexander-Universität Erlangen-Nürnberg, Erlangen, Germany

## OPEN ACCESS

### Edited by:

Zlatko Matjacic,  
University Rehabilitation Institute  
(Slovenia), Slovenia

### Reviewed by:

Carlos A. Cifuentes,  
Escuela Colombiana de Ingeniería  
Julio Garavito, Colombia  
Dong Hyun Kim,  
Korea Advanced Institute of Science  
and Technology, South Korea

### \*Correspondence:

Anne D. Koelewijn  
anne.koelewijn@fau.de

**Received:** 30 July 2021

**Accepted:** 18 November 2021

**Published:** 16 December 2021

### Citation:

Koelewijn AD, Audu M, del-Ama AJ, Colucci A, Font-Llagunes JM, Gogeochea A, Hnat SK, Makowski N, Moreno JC, Nandor M, Quinn R, Reichenbach M, Reyes R-D, Sartori M, Soekadar S, Triolo RJ, Vermehren M, Wenger C, Yavuz US, Fey D and Beckerle P (2021) Adaptation Strategies for Personalized Gait Neuroprosthetics. *Front. Neurobot.* 15:750519. doi: 10.3389/fnbot.2021.750519

Personalization of gait neuroprosthetics is paramount to ensure their efficacy for users, who experience severe limitations in mobility without an assistive device. Our goal is to develop assistive devices that collaborate with and are tailored to their users, while allowing them to use as much of their existing capabilities as possible. Currently, personalization of devices is challenging, and technological advances are required to achieve this goal. Therefore, this paper presents an overview of challenges and research directions regarding an interface with the peripheral nervous system, an interface with the central nervous system, and the requirements of interface computing architectures. The interface should be modular and adaptable, such that it can provide assistance where it is needed. Novel data processing technology should be developed to allow for real-time processing while accounting for signal variations in the human. Personalized biomechanical models and simulation techniques should be developed to predict assisted walking motions and interactions between the user and the device. Furthermore, the advantages of interfacing with both the brain and the spinal cord or the periphery should be further explored. Technological advances of interface computing architecture should focus on learning on the chip to achieve further personalization. Furthermore,

energy consumption should be low to allow for longer use of the neuroprosthesis. In-memory processing combined with resistive random access memory is a promising technology for both. This paper discusses the aforementioned aspects to highlight new directions for future research in gait neuroprosthetics.

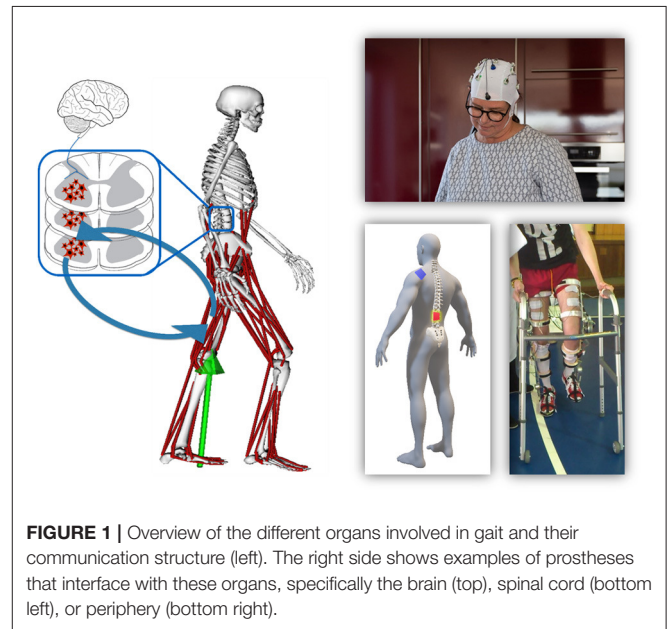
**Keywords:** neuroprosthesis, resistive random access memory, neural interface, personalized devices, perspective, embedded artificial intelligence

## 1. INTRODUCTION

Gait neuroprostheses aim to restore function in persons with paralysis caused by various injuries, diseases, or dysfunctions in the central or peripheral nervous system, e.g., a stroke, cerebral palsy (CP) or a spinal cord injury (SCI). Interfaces with the brain, spinal cord or the periphery are appropriate (**Figure 1**), whereas the type and location of the interface is highly dependent on the user's abilities and remaining possibilities for voluntary control. Development of gait neuroprostheses should focus on user-friendliness, and aim to maximize speed and safety, while minimizing fall risk. Furthermore, systems should be portable and easy-to-use to achieve their adoption in real-life environments.

Despite some individual success using interfaces with the brain (e.g., Ajiboye et al. 2017), spinal cord (e.g., Wagner et al. 2018), and periphery (e.g., Nandor et al. 2021), widespread application of neuroprostheses is still limited. One of the main challenges are differences between and within individuals. Between individuals, there is significant heterogeneity in the target population, which requires personalization of stimulation, stimulus timing and intensity, and the possible extent of additional motorized assistance. With “personalization,” we mean that every patient is provided with an individualized neuroprosthesis. This personalization can be done on the hardware and software level. It can be achieved offline through modeling and simulation, or online through adaptation of the stimulation scheme to the patient's current abilities. Personalizing the intervention is currently a time intensive process of trial and error by a human expert. Automation of this process with expert systems that can learn the optimal combinations of muscular and motor activation for a given individual would increase accessibility of gait neuroprostheses (Seel et al., 2016). Over time, due to fatiguing or improved function after rehabilitation, individuals might benefit from different stimulation patterns, which requires stimulation to be adaptive (Del-Ama et al., 2014).

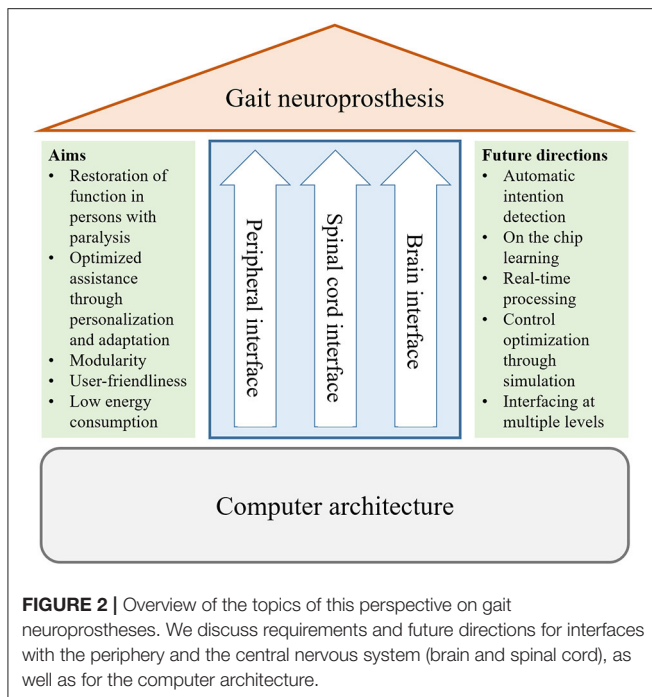
The development of adaptive interfaces and personalized devices requires an interdisciplinary approach involving clinicians, neuroscientists, engineers, and computer scientists. The effectiveness of gait neuroprostheses can be quantitatively assessed by measuring the gait speed, where desired gait speeds suitable for community use are between 0.8 and 1.2 m/s (Robinett and Vondran, 1988; Lapointe et al., 2001), or by measuring the metabolic energy expenditure while using the device (Asselin et al., 2015; Evans et al., 2015; Miller et al., 2016). Other acceptable metrics could be gait outcomes such as kinematics or symmetry (Hayes et al., 2020). Furthermore, limits for comfortable and tolerable stimulation should be defined



**FIGURE 1** | Overview of the different organs involved in gait and their communication structure (left). The right side shows examples of prostheses that interface with these organs, specifically the brain (top), spinal cord (bottom left), or periphery (bottom right).

for each user. **Figure 2** provides an overview of the different aims and future directions that are described in this paper. Movement analyses and simulations are required to understand pathological gait patterns and to tailor assistance, while the design should also be modular and user friendly. Artificial intelligence (AI) would allow control algorithms to be adapted to each individual user, and potentially over the course of rehabilitation. Furthermore, AI has the potential to process data, e.g., electroencephalography and electromyography, accurately in real-time, which is challenging due to the noisiness of these measurements. Adoption of AI in gait neuroprostheses requires development of new software and hardware for efficient on-chip learning, which should also focus on low energy consumption to allow for daily use of the device.

In this perspective paper, the organizers, speakers, and authors of the mini symposium “Adaptation Strategies for Personalized Gait Neuroprosthetics” which was held during the 10<sup>th</sup> International IEEE/EMBS Conference on Neural Engineering (NER) in May 2021, summarize and extend their contributions and discussions to point out directions for future research. The workshop comprised talks and discussion from experts working on assistive and rehabilitative neuroprostheses and exoskeletons. This perspective covers three topics: interfacing with the periphery, interfacing with the central nervous system, and requirements of interface computing architectures. We



discuss and provide a perspective on current research and future directions.

## 2. INTERFACING WITH THE PERIPHERY

Interfacing with the peripheral nervous system is a promising method to address specific functional deficits (Wilson et al., 2019). Through user-specific stimulation via surface, percutaneous, or implanted electrodes, muscles can perform a majority of the work for particular tasks. By implementing hybrid actuation approaches combining neural stimulation of affected muscles with robotic assistance, lower extremity function can be restored for patients with gait impairments, who can still drive the main features of the walking cycle by their healthy or preserved muscles. By bringing together neuroprosthetic and wearable robotic approaches, those hybrid concepts combine physiologic benefits by activating the other paralyzed and paretic lower limb muscles through neural stimulation, reducing the demand on external robotic assistance, and augmenting volitional and programmed movements to enhance safety, stability, and endurance.

Neuromechanical simulations of such neuromuscular, biomechanical, and mechanical interactions can be used to optimize the performance of users, hardware design (e.g., reduce size, weight or energy consumption), and controller design (e.g., seamless motor/muscle actuation and appropriate sensory feedback) (Alonso et al., 2012; Crago et al., 2014; García-Vallejo et al., 2016; Uchida et al., 2016; Sreenivasa et al., 2017; Michaud et al., 2019; Sauder et al., 2019). Dynamic simulations of the system composed of the human and the neuroprosthesis can predict the combined human-neuroprosthesis response, allow

for device and control customization to maximize walking ability, and improve our understanding of the interaction between human and device for new movement conditions. We advocate to extend computational neuromusculoskeletal models to encompass paralysis-related muscular constraints (Alonso et al., 2012; García-Vallejo et al., 2016) and auxiliary assistive devices (e.g., crutches/walker, orthoses, exoskeletons, etc.) (Febrer-Nafria et al., 2020, 2021) to achieve subject-specific model-based optimization of the device and its control. Then, such simulations might reveal insights into biomechanical effects such as altered recruitment, reduced force production due to atrophy, fatigue effects, or abnormal synergies (Shin et al., 2018). However, creating a personalized neuromusculoskeletal model of a patient is still challenging, since the exact underlying neurological problems of a patient are difficult to extract, and simulations cannot include the variability in muscle responses over time. Experimental validation of simulated clinical outcomes is therefore required (De Groote and Falisse, 2021; Fregly, 2021). Furthermore, even though simulations can provide insight into the required stimulation pattern, the stimulation needs to be adjusted in practice due to the variability in muscle response.

To adapt to the individual user, modular and adjustable hardware and control solutions can be implemented on a joint-need basis, and adapted to different anthropometrics, available muscles and their capabilities, as well as the neurological conditions (Del-Ama et al., 2014; Makowski et al., 2021; Nandor et al., 2021). Control in particular requires an adaptive approach that continuously updates muscle stimulation and electric motor actuation, and potentially prioritizes muscle activity through commanding motors in a trajectory-free ballistic paradigm while monitoring and managing muscle fatigue. To achieve seamless integration of auxiliary assistive devices, control strategies might rely on sensors onboard the human and the machine to measure user-device interaction (Lancini et al., 2016; Ugurlu et al., 2020) and should favor low impedances so the user's muscles can backdrive the device (Foglyano et al., 2016; Beckerle et al., 2017). Wearable kinematic sensing based on inertial measurement units is expected to provide equivalent performance to marker-based approaches. To this end, recent works propose to integrate inertial measurement units into musculoskeletal modeling workflows (Dorschky et al., 2019, 2020; Al Borno et al., 2021; Guidolin et al., 2021). Beyond this, sensory data from the limbs and muscles could be used to improve control and increase muscle performance by improved fatigue management compared to current methods based on muscle activity estimation (Alibeji et al., 2017; Mohamad et al., 2017).

## 3. INTERFACING WITH THE CENTRAL NERVOUS SYSTEM

Neural interfacing technologies connected to the CNS, the spinal cord (Wagner et al., 2018) and the brain (Ajiboye et al., 2017) have shown promising results, achieving restoration of control of extremities. While myographic control can provide more reliable and versatile assistance, there is increasing evidence that



only stimulation at the CNS level can trigger motor recovery (Soekadar et al., 2015; Cervera et al., 2018). Moreover, when there is no voluntary control of the periphery, an interface to the central nervous system might be the only remaining approach to restore movement or communication (Birbaumer et al., 2014). Most neural interfaces focus on either the brain or the spinal cord, but recently, pioneering studies also investigate combinations, either of the brain and the spinal cord, or the brain and the periphery (Dixon et al., 2016; Shulga et al., 2021).

For the spinal cord, a key goal is to interface with specific motor circuitries responsible for locomotion. Commonly, invasive interfaces are used (Hochberg et al., 2006, 2012; Wagner et al., 2018), which require complex setups to infer neural information of movement intention. Noninvasive approaches, which combine high-density electromyography, blind source separation and neuromechanical modeling, could offer an inexpensive alternative. Although high-density electromyography records spatiotemporal myoelectric activity at the periphery level, it underlies interfering information from spinal neural cells (i.e., alpha motor neurons). Blind source separation (Holobar et al., 2009; Negro et al., 2016) enables separating the interfering activity from neural sources, thereby retrieving the activity of actual motor neuron pools. In turn, the decoded neural firing events can be employed to drive comprehensive neuromusculoskeletal models (Sartori et al., 2016, 2017). Such an interface allows for the activity of actual motor neuron pools to be decoded by separating the interference activity from the neural source. This technique is currently used for characterizing motor neurons during voluntary contractions (Farina and Holobar, 2016) and reflex movements (Yavuz et al., 2015) in healthy and impaired (Holobar et al., 2012) individuals. Moreover, other applications include studying the neuromechanical response to external devices (Farina et al., 2014; Gogea-scoechea et al., 2020). This technique can therefore extend current open-loop rehabilitation techniques into closed-loop neuro-modulative approaches. However, its use is mostly limited to isometric contractions or slow dynamic contractions, mainly due to computational challenges related to the assumption that motor units are stationary and real-time implementation of the method. Both model-free AI (e.g., machine and deep learning techniques) (Chen et al., 2020; Clarke et al., 2020) and model-based techniques (e.g., data-driven mechanistic modeling) (Sartori and Sawicki, 2021) are explored to enable real-time implementation, which would allow mechanical and neural adaptations to exoskeleton training and neurostimulation to be predicted.

Besides providing intuitive and seamless assistive control, an important goal at the level of the brain is to promote neuroplastic changes and foster functional connectivity between central motoneurons and inactive and/or silent peripheral motoneurons (Donati et al., 2016). By decoding movement intention and gait characteristics in real time, invasive and non-invasive brain-computer interfaces can directly infer the user's intention to move, optimizing rehabilitation outcomes (Soekadar et al., 2015; Mrachacz-Kersting et al., 2016). Non-invasive brain-computer interfaces can assess large-scale brain oscillatory activity directly, through electroencephalography or magnetoencephalography, or

indirectly, by measuring the brain's energy expenditure (Liew et al., 2016; Soekadar et al., 2021). Invasive brain-computer interfaces typically exploit the user's ability to train the electrical activity in their brain, which is recorded by electrocorticography or multielectrode arrays (Hochberg et al., 2012; Ajiboye et al., 2017). The future of individualized brain-computer interfaces interventions relies on advanced algorithms for automated detection of brain states and self-adapting neurofeedback, as well as on hybrid neural interfaces, integrating different biosignals, e.g., electroencephalography, electromyography, or electrooculography, to allow for a more robust and safe control in real-life applications (Witkowski et al., 2014; Soekadar et al., 2016). To enable a broad adoption of brain-computer interfaces in real-life environments for clinics and home use, portable and easy-to-use systems need to be designed, requiring comfortable electroencephalography-headsets that minimize preparation time and allow self-applicability. Furthermore, new machine learning approaches are needed to optimize calibration time without inflating the number of sensors.

Instead of focusing on interfacing solely with either the brain, central nervous system, or periphery, the next generation of gait neuroprostheses for movement rehabilitation may aim to develop an interface on multiple levels. The advantage is that the paired activation of pre- and post-synaptic motoneurons at the level of the spinal cord is crucial for facilitating the re-wiring of functional connections after spinal cord injury (Dixon et al., 2016; Shulga et al., 2021). Motor cortex activity can also be used to control spinal cord stimulation (Capogrosso et al., 2016) instead of external control using a mobile app (Wagner et al., 2018). Adapting the parameters of peripheral stimulation to the ongoing neural activity has also proven to play a key role in fostering neuroplastic reorganization (Mrachacz-Kersting et al., 2016; Bonizzato et al., 2018). Therefore, we envision the implementation of brain-computer interfaces that allow for personalized adaptive modulation of brain activity and alpha motor circuitries.

## 4. INTERFACE WITH THE EMBEDDED COMPUTER ARCHITECTURE

The main requirements for interface computing architectures of gait neuroprosthetics are that the system is personalizable and adaptable, it should consume as little energy as possible, such that the system can be used optimally for at least a full day, and data processing should happen in real-time. Embedded AI for neuroprosthetics is a promising approach to achieve these requirements, as it has the potential to be real-time, while the computing technology and electronics are attached to the body or even implanted inside the body. The importance of a corresponding computer architecture in neuroprosthesis has been emphasized (Vassanelli and Mahmud, 2016; Ielmini and Wong, 2018), specifically to develop a suitable neuronal architecture to interface with the brain. However, no implementations exist so far, and therefore the further development and prototyping of concepts is of utmost importance (Mikhaylov et al., 2020). To achieve personalization

and adaptability, a main challenge is to perform online learning on the embedded AI. In contrast, today's embedded AI only allow inference, while networks are trained offline. This training is computationally intensive and consumes much energy. To achieve low energy consumption and real-time processing for training as well as inference on the chip, the embedded AI should be implemented as low-energy circuits.

An important step to achieve low energy consumption in embedded AI is to use in-memory processing, i.e., operations on data are performed analogously or digitally directly in the memory. Low-energy consumption is inherent for analog processing, since no digital conversion is required, while specialized hardware architectures without a central processing unit can greatly decrease energy consumption since long data paths are avoided. Using non-volatile storage ensures that no information is lost when power is switched off, what can be done when no data processing is required, e.g., when a person wearing a neuroprosthesis stops and does not walk. Accordingly, reloading weights after activation is not required. Many international groups currently study applications of non-volatile memory for neural networks and enhanced computing technologies, e.g., utilizing such memory as synaptic elements for artificial neural networks (Hu et al., 2018; Zhang et al., 2020).

Resistive random access memory (ReRAM) has compared to other non-volatile memory technologies, like e.g., Phase Change Memories, the advantage (Ielmini and Wong, 2018) to further decrease energy consumption, due to a unique combination of multi-level programming and a high density of integration (Milo et al., 2019). Furthermore, ReRAMs are potentially compatible with the most commonly used chip technology, complementary metal-oxide-semiconductor process manufacturing. Multi-level programming means that multiple bits can be stored on one ReRAM device. Therefore, weights and matrix multiplications of a neural network can be stored inside one ReRAM cell, and a neural network can be implemented by saving all network weights directly on the chip (Perez et al., 2020). As a result, external memory access is avoided, which can lower the energy consumption drastically (Knödtel et al., 2020). The high-density integration on the chip allows for the ReRAM cells to be closely attached to digital computation units, which decreases energy consumption by avoiding long data paths on the chip. The use of ReRAM technology yielded a 95% reduction in energy consumption for the classification of bio-signals for atrial fibrillation compared to a traditional approach (Pechmann et al., 2021). Therefore, ReRAM technology is a promising candidate for realization of personalized gait neuroprostheses relying on artificial neural networks in digital (e.g., as ReRAM storage for weights) and analog in-memory processing (e.g., as an in-memory processing element itself).

However, several challenges exist for ReRAM technology to be implemented on a neuroprosthesis. Currently, storage of up to three bits on each ReRAM cell is possible (Milo et al., 2021). However, energy consumption for reading out information increases when more bits are stored on a cell. This

trade-off between energy consumption for read out and energy saving from in-memory processing should be further investigated to minimize overall energy consumption. Furthermore, storage elements using ReRAM technology have a larger device-to-device variability than traditional storage elements, which use volatile technology. In particular, this device-to-device variability is a problem for multi-bit storing (Fritscher et al., 2021b), which is desired for embedded AI. Also the variability of switching parameters and energy overheads of analog-to-digital and digital-to-analog conversion is still a challenge for the reliable use of ReRAMs as well as their comparatively low endurance, i.e., the number of allowable switching cycles of the ReRAM cells. This is particularly challenging for neuroprostheses, which have higher time series data analysis requirements than e.g., a ReRAM based analyser for detecting atrial fibrillation. To achieve this, new research should address special training methods that account for tolerable fluctuations by using learning techniques such as noisy training or dropout layers (Fritscher et al., 2021a).

## 5. SUMMARY AND CONCLUSION

Neuroprostheses can potentially restore function through external activation of the central or peripheral nervous system. We have presented our perspective on current challenges of and future directions in the development of neuroprostheses in stimulation of the peripheral and central nervous systems, and outlined technical approaches to appropriate computer architectures, as also summarized in **Figure 2**. A paramount challenge is to restore mobility by effectively combining neuroprosthetic and wearable robotic approaches and to align neuroprostheses to the individual user's needs and capabilities.

To this end, predictive simulations of the human-machine system in dynamic tasks appear to be a promising approach to customize design and control. Still, predictive simulations can only provide rough representations of a paralysis and its highly individual constraints, which cannot yet be covered by recent neuromuscular modeling approaches, which, in turn, hampers user-specific control and stimulation. We suggest that future work should focus on improving neuromechanical simulations of user-device interaction based on experimental data, e.g., obtaining muscle parameters on the bench and in real applications, and aim at prioritizing muscle activity over robotic assistance. Combining a deeper understanding of neuromechanical dynamics, particularly muscle-group excitation through the central nervous system, with multimodal sensor networks distributed across the human and the device could foster model-based monitoring and management of muscle fatigue.

For the central nervous system, real-time data processing, ease of use of systems, and combining interfacing at multiple levels are important future directions. Real-time data processing is required to extract useful information from noisy measurements of brain or spinal cord activity in a useful

way. AI is a promising approach to enable this real-time data processing, while also allowing for personalization, and limiting the number of sensors required, improving ease of use. Portable and easy-to-use systems should be designed to allow for the adoption of neuroprostheses in real-life. Furthermore, the combination of stimulation at the brain and the spinal cord or the periphery should be further explored, since these combinations were shown to have benefits over stimulation at only one of these levels, and thereby improve rehabilitation outcomes.

Regarding technological advances of the interface to the computing architecture, a main current challenge is to achieve low-energy electronics, real-time data processing, and learning on the chip. Embedded AI has the potential to process data in real-time, and allows for learning and inference on the chip. To achieve low-energy consumption, the embedded AI should use in-memory processing combined with ReRAM technology. To allow the use of ReRAM technology in gait neuroprostheses, we need further research in combining ReRAM technology as multi-bit storage cells with complementary metal-oxide-semiconductor process manufacturing, the commonly-used chip technology. Furthermore, the functionality of the ReRAM cells should be expanded to improve reliability and mitigate the effect its device-to-device variability.

In conclusion, a close cooperation between computer architects, electrical engineers, material scientist, medical experts, and biomechanical experts is required to design appropriate neuroprostheses that are tailored to the user's need, adaptable, easy-to-use, and consume little energy.

## DATA AVAILABILITY STATEMENT

The original contributions presented in the study are included in the article/supplementary material, further inquiries can be directed to the corresponding author.

## REFERENCES

- Ajiboye, A. B., Willett, F. R., Young, D. R., Memberg, W. D., Murphy, B. A., Miller, J. P., et al. (2017). Restoration of reaching and grasping movements through brain-controlled muscle stimulation in a person with tetraplegia: a proof-of-concept demonstration. *Lancet* 389, 1821–1830. doi: 10.1016/S0140-6736(17)30601-3
- Al Borno, M., O'Day, J., Ibarra, V., Dunne, J., Seth, A., Habib, A., et al. (2021). Opensense: An open-source toolbox for inertial-measurement-unit-based measurement of lower extremity kinematics over long durations. *bioRxiv*. doi: 10.1101/2021.07.01.450788
- Alibeji, N., Kirsch, N., and Sharma, N. (2017). An adaptive low-dimensional control to compensate for actuator redundancy and fes-induced muscle fatigue in a hybrid neuroprosthesis. *Control Eng. Pract.* 59, 204–219. doi: 10.1016/j.conengprac.2016.07.015
- Alonso, J., Romero, F., Pàmies-Vilà, R., Llugrís, U., and Font-Llagunes, J. M. (2012). A simple approach to estimate muscle forces and orthosis actuation in powered assisted walking of spinal cord-injured subjects. *Multibody Syst. Dyn.* 28, 109–124. doi: 10.1007/s11044-011-9284-5
- Asselin, P., Knezevic, S., Kornfeld, S., Ciriogliaro, C., Agranova-Breyer, I., and Bauman, W. A. (2015). Heart rate and oxygen demand of powered

## AUTHOR CONTRIBUTIONS

AK coordinated the writing process, the development of the paper structure, and integration of individual contributions. PB and DF supported this for the whole paper. MA, AJd-A, JMF-L, SH, NM, JCM, MN, RQ, R-DR, RJT, and PB mainly contributed to section 2. AC, AG, MS, SS, MV, USY, and AK mainly contributed to section 3. MR, CW, and DF mainly contributed to section 4. All authors contributed to the article and approved the submitted version.

## FUNDING

AK is funded by a faculty endowment by adidas AG. MA, SKH, NM, MN, RJQ, R-DR, RJT are supported by NSF CPS grant 1739800, VA Merit Reviews A2275-R and 3056, and the NIH (5T32EB004314-15, R01 NS040547-13). MS and AG are funded by the European Research Council (ERC) under the European Union's Horizon 2020 research and innovation programme (Grant agreement No. 803035). AJd-A, JMF-L, and JCM are supported by coordinated grants RTI2018-097290-B-C31/C32/C33 (TAILOR project) funded by MCIN/AEI/10.13039/501100011033 and by "ERDF A way of making Europe". MR is funded by the Lo3-ML project by the Federal Ministry for Education, Science and Technology (BMBF) (Funding No. 16ES1142K). AC, SS, and MV were supported by the European Research Council (ERC) under the project NGBMI (759370), the Einstein Stiftung Berlin, the ERA-NET NEURON project HYBRIDMIND (BMBF, 01GP2121A and -B) and the BMBF project NEO (13GW0483C).

## ACKNOWLEDGMENTS

The authors thank the organizers of IEEE/EMBS NER conference in 2021 for the opportunity to hold the mini symposium Adaptation Strategies for Personalized Gait Neuroprosthetics as part of the conference.

- exoskeleton-assisted walking in persons with paraplegia. *J. Rehabil. Res. Dev.* 52, 147. doi: 10.1682/JRRD.2014.02.0060
- Beckerle, P., Salvietti, G., Unal, R., Prattichizzo, D., Rossi, S., Castellini, C., et al. (2017). A human-robot interaction perspective on assistive and rehabilitation robotics. *Front. Neurobot.* 11:24. doi: 10.3389/fnbot.2017.00024
- Birbaumer, N., Gallegos-Ayala, G., Wildgruber, M., Silvoni, S., and Soekadar, S. R. (2014). Direct brain control and communication in paralysis. *Brain Topogr.* 27, 4–11. doi: 10.1007/s10548-013-0282-1
- Bonizzato, M., Pidpruzhnykova, G., DiGiovanna, J., Shkorbatova, P., Pavlova, N., Micera, S., et al. (2018). Brain-controlled modulation of spinal circuits improves recovery from spinal cord injury. *Nat. Commun.* 9, 1–14. doi: 10.1038/s41467-018-05282-6
- Capogrosso, M., Milekovic, T., Borton, D., Wagner, F., Moraud, E. M., Mignardot, J.-B., et al. (2016). A brain-spine interface alleviating gait deficits after spinal cord injury in primates. *Nature* 539, 284–288. doi: 10.1038/nature20118
- Cervera, M. A., Soekadar, S. R., Ushiba, J., Millán, J., d., R., Liu, M., et al. (2018). Brain-computer interfaces for post-stroke motor rehabilitation: a meta-analysis. *Ann. Clin. Transl. Neurol.* 5, 651–663. doi: 10.1002/acn3.544
- Chen, C., Yu, Y., Sheng, X., and Zhu, X. (2020). Analysis of motor unit activities during multiple motor tasks by real-time emg decomposition: perspective



- for myoelectric control. *Annu. Int. Conf. IEEE Eng. Med. Biol. Soc.* 2020, 4791–4794. doi: 10.1109/EMBC44109.2020.9176362
- Clarke, A. K., Atashzar, S. F., Del Vecchio, A., Barsakcioglu, D., Muceli, S., Bentley, P., et al. (2020). Deep learning for robust decomposition of high-density surface emg signals. *IEEE Trans. Biomed. Eng.* 68, 526–534. doi: 10.1109/TBME.2020.3006508
- Crago, P. E., Makowski, N. S., and Cole, N. M. (2014). Contributions to muscle force and emg by combined neural excitation and electrical stimulation. *J. Neural Eng.* 11, 056022. doi: 10.1088/1741-2560/11/5/056022
- De Groote, F., and Falisse, A. (2021). Perspective on musculoskeletal modelling and predictive simulations of human movement to assess the neuromechanics of gait. *Proc. R. Soc. B* 288, 20202432. doi: 10.1098/rspb.2020.2432
- Del-Ama, A. J., Gil-Agudo, Á., Pons, J. L., and Moreno, J. C. (2014). Hybrid gait training with an overground robot for people with incomplete spinal cord injury: a pilot study. *Front. Hum. Neurosci.* 8:298. doi: 10.3389/fnhum.2014.00298
- Dixon, L., Ibrahim, M. M., Santora, D., and Nikou, M. (2016). Paired associative transspinal and transcortical stimulation produces plasticity in human cortical and spinal neuronal circuits. *J. Neurophysiol.* 116, 904–916. doi: 10.1152/jn.00259.2016
- Donati, A. R., Shokur, S., Morya, E., Campos, D. S., Moiola, R. C., Gitti, C. M., et al. (2016). Long-term training with a brain-machine interface-based gait protocol induces partial neurological recovery in paraplegic patients. *Sci. Rep.* 6, 1–16. doi: 10.1038/srep30383
- Dorschky, E., Nitschke, M., Martindale, C. F., van den Bogert, A. J., Koelewijn, A. D., and Eskofier, B. M. (2020). Cnn-based estimation of sagittal plane walking and running biomechanics from measured and simulated inertial sensor data. *Front. Bioeng. Biotechnol.* 8:604. doi: 10.3389/fbioe.2020.00604
- Dorschky, E., Nitschke, M., Seifer, A.-K., van den Bogert, A. J., and Eskofier, B. M. (2019). Estimation of gait kinematics and kinetics from inertial sensor data using optimal control of musculoskeletal models. *J. Biomech.* 95:109278. doi: 10.1016/j.jbiomech.2019.07.022
- Evans, N., Hartigan, C., Kandilakis, C., Pharo, E., and Clesson, I. (2015). Acute cardiorespiratory and metabolic responses during exoskeleton-assisted walking overground among persons with chronic spinal cord injury. *Top. Spinal. Cord. Inj. Rehabil.* 21, 122–132. doi: 10.1310/sci2102-122
- Farina, D., and Holobar, A. (2016). Characterization of human motor units from surface emg decomposition. *Proc. IEEE* 104, 353–373. doi: 10.1109/JPROC.2015.2498665
- Farina, D., Jiang, N., Rehbaum, H., Holobar, A., Graimann, B., Dietl, H., et al. (2014). The extraction of neural information from the surface emg for the control of upper-limb prostheses: emerging avenues and challenges. *IEEE Trans. Neural Syst. Rehabil. Eng.* 22, 797–809. doi: 10.1109/TNSRE.2014.2305111
- Febrer-Nafria, M., Pallarès-López, R., Fregly, B. J., and Font-Llagunes, J. M. (2020). Comparison of different optimal control formulations for generating dynamically consistent crutch walking simulations using a torque-driven model. *Mech. Mach. Theory* 154:104031. doi: 10.1016/j.mechmachtheory.2020.104031
- Febrer-Nafria, M., Pallarès-López, R., Fregly, B. J., and Font-Llagunes, J. M. (2021). Prediction of three-dimensional crutch walking patterns using a torque-driven model. *Multibody Syst. Dyn.* 51, 1–19. doi: 10.1007/s11044-020-09751-z
- Foglyano, K. M., Schnellenberger, J. R., Kobetic, R., Lombardo, L., Pinaut, G., Selkirk, S., et al. (2016). Accelerometer-based step initiation control for gait-assist neuroprostheses. *J. Rehabil. Res. Dev.* 53, 919–932. doi: 10.1682/JRRD.2015.09.0188
- Fregly, B. J. (2021). A conceptual blueprint for making neuromusculoskeletal models clinically useful. *Appl. Sci.* 11:2037. doi: 10.3390/app11052037
- Fritscher, M., Knödtel, J., Mallah, M., Pechmann, S., Perez-Bosch Quesada, E., Rizzi, T., et al. (2021a). “Mitigating the effects of RRAM process variation on the accuracy of artificial neural networks,” in *Proc. 21st International Conference on Embedded Computer Systems: Architectures, Modeling and Simulation (SAMOS 2021)* (Pythagorion).
- Fritscher, M., Knödtel, J., Reiser, D., Mallah, M., Pechmann, S., Fey, D., et al. (2021b). “Simulating large neural networks embedding mlc rram as weight storage considering device variations,” in *2021 IEEE 12th Latin America Symposium on Circuits and System (LASCAS)*, (Arequipa: IEEE), 1–4.
- García-Vallejo, D., Font-Llagunes, J. M., and Schiehlen, W. (2016). Dynamical analysis and design of active orthoses for spinal cord injured subjects by aesthetic and energetic optimization. *Nonlinear. Dyn.* 84, 559–581. doi: 10.1007/s11071-015-2507-1
- Gogeaascoechea, A., Kuck, A., Van Asseldonk, E., Negro, F., Buitenweg, J. R., Yavuz, U. S., et al. (2020). Interfacing with alpha motor neurons in spinal cord injury patients receiving trans-spinal electrical stimulation. *Front. Neurol.* 11:493. doi: 10.3389/fneur.2020.00493
- Guidolin, M., Petrea, R. A. B., Roberto, O., Reggiani, M., Menegatti, E., and Tagliapietra, L. (2021). “On the accuracy of imus for human motion tracking: a comparative evaluation,” in *2021 IEEE International Conference on Mechatronics (ICM)* (Kashiwa: IEEE), 1–6.
- Hayes, S. C., White, M., White, H. S. F., and Vanicek, N. (2020). A biomechanical comparison of powered robotic exoskeleton gait with normal and slow walking: an investigation with able-bodied individuals. *Clin. Biomech.* 80:105133. doi: 10.1016/j.clinbiomech.2020.105133
- Hochberg, L. R., Bacher, D., Jarosiewicz, B., Masse, N. Y., Simeral, J. D., Vogel, J., et al. (2012). Reach and grasp by people with tetraplegia using a neurally controlled robotic arm. *Nature* 485, 372–375. doi: 10.1038/nature11076
- Hochberg, L. R., Serruya, M. D., Friehs, G. M., Mukand, J. A., Saleh, M., Caplan, A. H., et al. (2006). Neuronal ensemble control of prosthetic devices by a human with tetraplegia. *Nature* 442, 164–171. doi: 10.1038/nature04970
- Holobar, A., Farina, D., Gazzoni, M., Merletti, R., and Zazula, D. (2009). Estimating motor unit discharge patterns from high-density surface electromyogram. *Clin. Neurophysiol.* 120, 551–562. doi: 10.1016/j.clinph.2008.10.160
- Holobar, A., Glaser, V., Gallego, J., Dideriksen, J. L., and Farina, D. (2012). Non-invasive characterization of motor unit behaviour in pathological tremor. *J. Neural Eng.* 9, 056011. doi: 10.1088/1741-2560/9/5/056011
- Hu, M., Graves, C. E., Li, C., Li, Y., Ge, N., Montgomery, E., et al. (2018). Memristor-based analog computation and neural network classification with a dot product engine. *Adv. Mater.* 30, 1705914. doi: 10.1002/adma.201705914
- Ielmini, D., and Wong, H.-S. P. (2018). In-memory computing with resistive switching devices. *Nat. Electron.* 1, 333–343. doi: 10.1038/s41928-018-0092-2
- Knödtel, J., Fritscher, M., Reiser, D., Fey, D., Breiling, M., and Reichenbach, M. (2020). “A model-to-circuit compiler for evaluation of dnn accelerators based on systolic arrays and multibit emerging memories,” in *2020 9th International Conference on Modern Circuits and Systems Technologies (MOCAS)* (Bremen: IEEE), 1–6.
- Lancini, M., Serpelloni, M., Pasinetti, S., and Guanziroli, E. (2016). Healthcare sensor system exploiting instrumented crutches for force measurement during assisted gait of exoskeleton users. *IEEE Sens. J.* 16, 8228–8237. doi: 10.1109/JSEN.2016.2579738
- Lapointe, R., Lajoie, Y., Serresse, O., and Barbeau, H. (2001). Functional community ambulation requirements in incomplete spinal cord injured subjects. *Spinal Cord.* 39, 327–335. doi: 10.1038/sj.sc.3101167
- Liew, S.-L., Rana, M., Cornelsen, S., Fortunato de Barros Filho, M., Birbaumer, N., Sitaram, R., et al. (2016). Improving motor corticothalamic communication after stroke using real-time fmri connectivity-based neurofeedback. *Neurorehabil. Neural Repair.* 30, 671–675. doi: 10.1177/1545968315619699
- Makowski, N. S., Campean, A., Lambrecht, J. M., Buckett, J. R., Coburn, J. D., Hart, R. L., et al. (2021). Design and testing of stimulation and myoelectric recording modules in an implanted distributed neuroprosthetic system. *IEEE Trans. Biomed. Circ. Syst.* 15, 281–293. doi: 10.1109/TBCAS.2021.3066838
- Michaud, F., Mouzo, F., Lugris, U., and Cuadrado, J. (2019). Energy expenditure estimation during crutch-orthosis-assisted gait of a spinal-cord-injured subject. *Front. Neurobot.* 13:55. doi: 10.3389/fnbot.2019.00055
- Mikhaylov, A., Pimashkin, A., Pigareva, Y., Gerasimova, S., Gryaznov, E., Shchanikov, S., et al. (2020). Neurohybrid memristive cmos-integrated systems for biosensors and neuroprosthetics. *Front. Neurosci.* 14:358. doi: 10.3389/fnins.2020.00358
- Miller, L. E., Zimmermann, A. K., and Herbert, W. G. (2016). Clinical effectiveness and safety of powered exoskeleton-assisted walking in patients with spinal cord injury: systematic review with meta-analysis. *Med. Devices (Auckl)* 9:455. doi: 10.2147/MDER.S103102
- Milo, V., Glukhov, A., Pérez, E., Zambelli, C., Lepri, N., Mahadevaiah, M. K., et al. (2021). Accurate program/verify schemes of resistive switching memory



- (rram) for in-memory neural network circuits. *IEEE Trans. Electron. Devices*. 68, 3832–3837. doi: 10.1109/TED.2021.3089995
- Milo, V., Zambelli, C., Olivo, P., Pérez, E., K., Mahadevaiah, M., et al. (2019). Multilevel hfo2-based rram devices for low-power neuromorphic networks. *APL Mater.* 7, 081120. doi: 10.1063/1.5108650
- Mohamad, N. Z., Hamzaid, N. A., Davis, G. M., Abdul Wahab, A. K., and Hasnan, N. (2017). Mechanomyography and torque during fes-evoked muscle contractions to fatigue in individuals with spinal cord injury. *Sensors* 17:1627. doi: 10.3390/s17071627
- Mrachacz-Kersting, N., Jiang, N., Stevenson, A. J. T., Niazi, I. K., Kostic, V., Pavlovic, A., et al. (2016). Efficient neuroplasticity induction in chronic stroke patients by an associative brain-computer interface. *J. Neurophysiol.* 115, 1410–1421. doi: 10.1152/jn.00918.2015
- Nandor, M., Kobetic, R., Audu, M., Triolo, R., and Quinn, R. (2021). A muscle-first, electromechanical hybrid gait restoration system in people with spinal cord injury. *Front. Rob. AI* 8:645588. doi: 10.3389/frobt.2021.645588
- Negro, F., Muceli, S., Castronovo, A. M., Holobar, A., and Farina, D. (2016). Multi-channel intramuscular and surface emg decomposition by convolutive blind source separation. *J. Neural Eng.* 13, 026027. doi: 10.1088/1741-2560/13/2/026027
- Pechmann, S., Mai, T., Potschka, J., Reiser, D., Reichel, P., Breiling, M., et al. (2021). A low-power RRAM memory block for embedded, multi-level weight and bias storage in artificial neural networks. *Micromachines* 12:1277. doi: 10.3390/mi12111277
- Perez, E., González Ossorio, Ó., Duenas, S., Castan, H., Garcia, H., and Wenger, C. (2020). Programming pulse width assessment for reliable and low-energy endurance performance in al: Hfo2-based rram arrays. *Electronics* 9, 864. doi: 10.3390/electronics9050864
- Robinet, C. S., and Vondran, M. A. (1988). Functional ambulation velocity and distance requirements in rural and urban communities: a clinical report. *Phys. Ther.* 68, 1371–1373. doi: 10.1093/ptj/68.9.1371
- Sartori, M., Lloyd, D. G., and Farina, D. (2016). Neural data-driven musculoskeletal modeling for personalized neurorehabilitation technologies. *IEEE Trans. Biomed. Eng.* 63, 879–893. doi: 10.1109/TBME.2016.2538296
- Sartori, M., and Sawicki, G. S. (2021). Closing the loop between wearable technology and human biology: A new paradigm for steering neuromuscular form and function. *Progr. Biomed. Eng.* 3, 023001. doi: 10.1088/2516-1091/abe3e0
- Sartori, M., Yavuz, U., S., and Farina, D. (2017). In vivo neuromechanics: decoding causal motor neuron behavior with resulting musculoskeletal function. *Sci. Rep.* 7, 1–14. doi: 10.1038/s41598-017-13766-6
- Sauder, N. R., Meyer, A. J., Allen, J. L., Ting, L. H., Kesar, T. M., and Fregly, B. J. (2019). Computational design of fastfes treatment to improve propulsive force symmetry during post-stroke gait: a feasibility study. *Front. Neurobot.* 13:80. doi: 10.3389/fnbot.2019.00080
- Seel, T., Werner, C., Raisch, J., and Schauer, T. (2016). Iterative learning control of a drop foot neuroprosthesis—generating physiological foot motion in paretic gait by automatic feedback control. *Control Eng. Pract.* 48:87–97. doi: 10.1016/j.conengprac.2015.11.007
- Shin, H., Suresh, N. L., Rymer, W. Z., and Hu, X. (2018). Relative contribution of different altered motor unit control to muscle weakness in stroke: a simulation study. *J. Neural Eng.* 15, 016014. doi: 10.1088/1741-2552/aa925d
- Shulga, A., Lioumis, P., Kirveskari, E., Savolainen, S., and Mäkelä, J. P. (2021). A novel paired associative stimulation protocol with a high-frequency peripheral component: A review on results in spinal cord injury rehabilitation. *Eur. J. Neurosci.* 53, 3242–3257. doi: 10.1111/ejn.15191
- Soekadar, S., Witkowski, M., Gómez, C., Opisso, E., Medina, J., Cortese, M., et al. (2016). Hybrid eeg/eog-based brain/neural hand exoskeleton restores fully independent daily living activities after quadriplegia. *Sci. Robot* 1, 32–96. doi: 10.1126/scirobotics.aag3296
- Soekadar, S. R., Birbaumer, N., Slutzky, M. W., and Cohen, L. G. (2015). Brain-machine interfaces in neurorehabilitation of stroke. *Neurobiol. Dis.* 83, 172–179. doi: 10.1016/j.nbd.2014.11.025
- Soekadar, S. R., Kohl, S. H., Mihara, M., and von Lüthmann, A. (2021). Optical brain imaging and its application to neurofeedback. *Neuroimage Clin.* 30:102577. doi: 10.1016/j.nicl.2021.102577
- Sreenivasa, M., Millard, M., Felis, M., Mombaur, K., and Wolf, S. I. (2017). Optimal control based stiffness identification of an ankle-foot orthosis using a predictive walking model. *Front. Comput. Neurosci.* 11:23. doi: 10.3389/fncom.2017.00023
- Uchida, T. K., Seth, A., Pouya, S., Dembia, C. L., Hicks, J. L., and Delp, S. L. (2016). Simulating ideal assistive devices to reduce the metabolic cost of running. *PLoS ONE* 11:e0163417. doi: 10.1371/journal.pone.0163417
- Ugurlu, B., Oshima, H., Sariyildiz, E., Narikiyo, T., and Babic, J. (2020). Active compliance control reduces upper body effort in exoskeleton-supported walking. *IEEE Trans. Hum. Mach. Syst.* 50, 144–153. doi: 10.1109/THMS.2019.2961969
- Vassanelli, S., and Mahmud, M. (2016). Trends and challenges in neuroengineering: toward “intelligent” neuroprostheses through brain-“brain inspired systems” communication. *Front. Neurosci.* 10:438. doi: 10.3389/fnins.2016.00438
- Wagner, F. B., Mignardot, J.-B., Le Goff-Mignardot, C. G., Demesmaeker, R., Komi, S., Capogrosso, M., et al. (2018). Targeted neurotechnology restores walking in humans with spinal cord injury. *Nature* 563, 65–71. doi: 10.1038/s41586-018-0649-2
- Wilson, R. D., Bryden, A. M., Kilgore, K. L., Makowski, N., Bourbeau, D., Kowalski, K. E., et al. (2019). Neuromodulation for functional electrical stimulation. *Phys. Med. Rehabil. Clin.* 30, 301–318. doi: 10.1016/j.pmr.2018.12.011
- Witkowski, M., Cortese, M., Cempini, M., Mellinger, J., Vitiello, N., and Soekadar, S. R. (2014). Enhancing brain-machine interface (bmi) control of a hand exoskeleton using electrooculography (eog). *J. Neuroeng. Rehabil.* 11, 1–6. doi: 10.1186/1743-0003-11-165
- Yavuz, U., S., Negro, F., Sebik, O., Holobar, A., Frömmel, C., et al. (2015). Estimating reflex responses in large populations of motor units by decomposition of the high-density surface electromyogram. *J. Physiol.* 593, 4305–4318. doi: 10.1113/JP270635
- Zhang, W., Gao, B., Tang, J., Yao, P., Yu, S., Chang, M.-F., et al. (2020). Neuro-inspired computing chips. *Nat. Electron.* 3, 371–382. doi: 10.1038/s41928-020-0435-7

**Conflict of Interest:** The authors declare that the research was conducted in the absence of any commercial or financial relationships that could be construed as a potential conflict of interest.

**Publisher's Note:** All claims expressed in this article are solely those of the authors and do not necessarily represent those of their affiliated organizations, or those of the publisher, the editors and the reviewers. Any product that may be evaluated in this article, or claim that may be made by its manufacturer, is not guaranteed or endorsed by the publisher.

Copyright © 2021 Koelewijn, Audu, del-Ama, Colucci, Font-Llagunes, Gogea-coechea, Hnat, Makowski, Moreno, Nandor, Quinn, Reichenbach, Reyes, Sartori, Soekadar, Triolo, Vermehren, Wenger, Yavuz, Fey and Beckerle. This is an open-access article distributed under the terms of the Creative Commons Attribution License (CC BY). The use, distribution or reproduction in other forums is permitted, provided the original author(s) and the copyright owner(s) are credited and that the original publication in this journal is cited, in accordance with accepted academic practice. No use, distribution or reproduction is permitted which does not comply with these terms.



# A Novel Clinical-Driven Design for Robotic Hand Rehabilitation: Combining Sensory Training, Effortless Setup, and Large Range of Motion in a Palmar Device

Raphael Rätz<sup>1</sup>, François Conti<sup>2</sup>, René M. Müri<sup>3</sup> and Laura Marchal-Crespo<sup>1,4\*</sup>

<sup>1</sup> Motor Learning and Neurorehabilitation Laboratory, ARTORG Center for Biomedical Engineering Research, University of Bern, Bern, Switzerland, <sup>2</sup> Force Dimension, Nyon, Switzerland, <sup>3</sup> Department of Neurology, University Neurorehabilitation, University Hospital Bern (Inselspital), University of Bern, Bern, Switzerland, <sup>4</sup> Department of Cognitive Robotics, Delft University of Technology, Delft, Netherlands

## OPEN ACCESS

### Edited by:

Luciano Luperini Menegaldo,  
Federal University of Rio de Janeiro,  
Brazil

### Reviewed by:

Ye Ma,  
Ningbo University, China  
J. Michael Hermann,  
University of Edinburgh,  
United Kingdom

### \*Correspondence:

Laura Marchal-Crespo  
l.marchalcrespo@tudelft.nl

**Received:** 27 July 2021

**Accepted:** 12 November 2021

**Published:** 20 December 2021

### Citation:

Rätz R, Conti F, Müri RM and Marchal-Crespo L (2021) A Novel Clinical-Driven Design for Robotic Hand Rehabilitation: Combining Sensory Training, Effortless Setup, and Large Range of Motion in a Palmar Device.  
*Front. Neurobot.* 15:748196.  
doi: 10.3389/fnbot.2021.748196

Neurorehabilitation research suggests that not only high training intensity, but also somatosensory information plays a fundamental role in the recovery of stroke patients. Yet, there is currently a lack of easy-to-use robotic solutions for sensorimotor hand rehabilitation. We addressed this shortcoming by developing a novel clinical-driven robotic hand rehabilitation device, which is capable of fine haptic rendering, and that supports physiological full flexion/extension of the fingers while offering an effortless setup. Our palmar design, based on a parallelogram coupled to a principal revolute joint, introduces the following novelties: (1) While allowing for an effortless installation of the user's hand, it offers large range of motion of the fingers (full extension to 180° flexion). (2) The kinematic design ensures that all fingers are supported through the full range of motion and that the little finger does not lose contact with the finger support in extension. (3) We took into consideration that a handle is usually comfortably grasped such that its longitudinal axis runs obliquely from the metacarpophalangeal joint of the index finger to the base of the hypothenar eminence. (4) The fingertip path was optimized to guarantee physiologically correct finger movements for a large variety of hand sizes. Moreover, the device possesses a high mechanical transparency, which was achieved using a backdrivable cable transmission. The transparency was further improved with the implementation of friction and gravity compensation. In a test with six healthy participants, the root mean square of the human-robot interaction force was found to remain as low as 1.37 N in a dynamic task. With its clinical-driven design and easy-to-use setup, our robotic device for hand sensorimotor rehabilitation has the potential for high clinical acceptance, applicability and effectiveness.

**Keywords:** robotic hand rehabilitation, clinical acceptability, neurorehabilitation, sensorimotor, haptics, clinical-driven, grasp, transparency

# 1. INTRODUCTION

With about 17 million people worldwide that experience a stroke each year, stroke remains a major cause of disability (Feigin et al., 2014). Up to 75% of stroke survivors suffer from long-term arm and hand impairments (Lai et al., 2002), which leads to a severe impact on patients' capability of performing activities of daily living and compromises their autonomy (Mercier et al., 2001; Hunter and Crome, 2002). To maximize recovery, clinical evidence suggests that patients should embark in active (Lotze, 2003), long (Kwakkel et al., 2004; Nielsen et al., 2015), high-intensity (Tollár et al., 2021), and repetitive functional task-specific practice (French et al., 2016). Sensory training is also highly recommended (Turville et al., 2019), as several studies have associated somatosensory impairment at baseline with poorer motor function and recovery after stroke (Meyer et al., 2014; Rowe et al., 2017). However, in practice, high-intensity therapy is labor-intensive, and training duration can be limited by the endurance and availability of the therapists, possibly reducing therapy outcomes. Furthermore, most of the current therapies target primarily improving motor functions, neglecting the sensory aspects of neurorehabilitation (Bolognini et al., 2016; Gassert and Dietz, 2018; Handelzalts et al., 2021).

The ideal neurorehabilitation training could be provided by robotic devices as robots can deliver high-intensity training in a motivating and engaging virtual environment (Brütsch et al., 2010; Lo et al., 2010; Gassert and Dietz, 2018; Bernardoni et al., 2019). However, despite the increasing number of robotic devices developed in the recent years for hand rehabilitation, the majority of these solutions has never been tested in clinical settings. One of the main obstacles listed for their poor clinical acceptance is high complexity—e.g., long setup times and overabundant functionalities (Balasubramanian et al., 2010). Furthermore, recent meta-analyses concluded that traditional robotic training yields similar or even inferior outcomes to conventional therapy, especially in activities of daily living (Bertani et al., 2017; Veerbeek et al., 2017). This is not surprising, since current rehabilitation robots only provide general assistance to perform rather artificial movements that are far from being functional. Current robot-aided interventions rely on abstract visual feedback while somatic (i.e., tactile and proprioceptive) feedback is underutilized. However, the perception of forces from the interaction with virtual environments conveys essential information for fine motor control and learning, e.g., during object grasping and manipulation (Huang et al., 2007; Danion et al., 2012; Özen et al., 2021). Thus, robots that enhance somatic information through haptic rendering—i.e., the provision of simulated interactive forces with virtual objects—might promote functional gains by leveraging practice in an enriched multisensory environment (Gassert and Dietz, 2018).

To evaluate the current state of the art on robotic hand rehabilitation, we performed an in-depth literature research and compared the found hand rehabilitation devices based on degrees of freedom (DoF), range of motion (RoM), available force, setup, and haptic rendering capabilities (see comparison table of hand rehabilitation devices in the **Supplementary Material**). Actuated

hand rehabilitation devices can be distinguished in wearable exoskeletons, soft robotic gloves, grounded end-effectors, and grounded exoskeletons. The distinction between grounded exoskeletons and end-effector devices can be ambiguous in the case of hand rehabilitation devices, yet it is generally accepted that exoskeletons exert a high degree of control over individual joints and limb segments (Gassert and Dietz, 2018).

Wearable exoskeletons are usually mounted dorsally and often provide a large range of finger motion through sophisticated mechanisms that ensure coincident centres of rotation with the anatomical finger joints (Sarac et al., 2019). While some exoskeletons are principally designed to allow patients to perform rehabilitation exercises (e.g., Ho et al., 2011; Pu et al., 2020), others focus on assisting in activities of daily living (e.g., Hasegawa et al., 2008; Gasser et al., 2017; Hong et al., 2019). Because wearable exoskeletons tend to be cumbersome to install (Aggogeri et al., 2019), there has been an increasing effort to develop self-aligning (e.g., Zhang et al., 2014; Cempini et al., 2015; Leonardis et al., 2015; Sarac et al., 2016) as well as highly portable and mechanically simple exoskeletons [e.g., Tenoexo (Bützer et al., 2020), Mano (Randazzo et al., 2018)] to improve usability and ease of setup.

Similar to mechanically simple exoskeletons, soft-robotic gloves appear to be a promising alternative to complex exoskeletons for grasping assistance. They are often actuated by cables [e.g., CADEX (Kim and Park, 2018), Grasp Glove (Popov et al., 2017), CHAD (Huang et al., 2020), (Xu et al., 2020; Alnajjar et al., 2021)] or soft pneumatic actuators (e.g., Yap et al., 2016), which results in lightweight designs. Furthermore, they generally exhibit an excellent range of motion. The donning of soft robotic gloves has been facilitated by an open palm in the Glorea (Borboni et al., 2016) or a zipper on the palmar side of the glove in the BiomHED (Lee et al., 2014). Nevertheless, they require an advanced level of dexterity and finger mobility from the patients to be setup easily (Sarac et al., 2019).

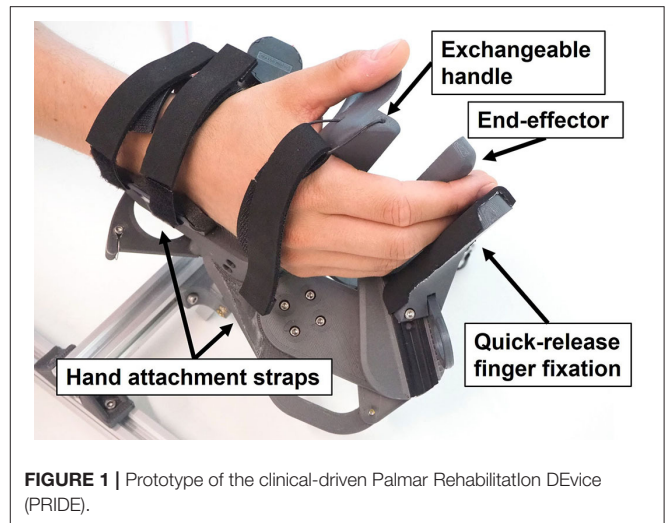
While exoskeletons as well as soft robotic gloves create opportunities to integrate rehabilitation in activities of daily living, the vast majority of them is difficult to setup for patients suffering from compromised finger mobility due to spasticity or hypertonía (Tsai et al., 2019), which greatly limits the potential for interventions with these devices. Although a few wearable exoskeletons or soft robotic gloves are capable of haptic rendering [e.g., (Li et al., 2011; Sandoval-Gonzalez et al., 2016; Decker and Kim, 2017), CyberForce (CyberGlove Systems, USA), see **Supplementary Material** for further details], most of them do not yield this functionality. Due to their design, exoskeletons often allow to provide tactile sensory information by directly interacting with physical objects during exercises (e.g., Wang et al., 2018). Yet, the richness of sensory stimulation is limited to the properties of the physically available objects during therapy. Soft robotic gloves, on the other hand, generally have the disadvantage that the fingertips are covered, which might attenuate sensations from real-world object handling. Dedicated haptic devices, however, are able to provide rich sensory information with adjustable intensity, and importantly, can adapt continuously to the patients' specific needs and performance.

Several end-effector devices have been specifically developed to provide haptic feedback. The HIRO-III (Hioki et al., 2011) is a haptic interface that resembles a robotic hand with fingers that interact individually with the subject's fingertips. The underactuated orthosis of Sooraj et al., employs a three-bar linkage mechanism to individually actuate the fingertips and offers a large range of motion (Sooraj et al., 2013). Frisoli et al. proposed a high-fidelity haptic interface for thumb and index finger of the hand (Frisoli et al., 2007) with potential application in sensorimotor rehabilitation. The ReHapticKnob is a two DoF device (i.e., grasping and pronosupination) specifically designed to have excellent haptic rendering capabilities (Metzger et al., 2011). However, similar to the cable-driven HandCARE robot (Dovat et al., 2008) or the commercially available Amadeo<sup>®</sup> (TyroMotion, Austria), the fingertips are attached to a linear axis and do not move along a physiological (i.e., spiral-shaped) finger path. The reachMAN2 is a haptic device for reach and grasp training with a palmar handle—i.e., the handle is largely in contact with the palmar side of the hand. The Alpha-Prototype II (Masia et al., 2007) is a palmar robotic handle with an axially symmetrical design capable of high-quality haptic rendering. It is—similar to other palmar end-effector devices [e.g., (Just et al., 2019), InMotion<sup>®</sup> Arm/Hand (Bionik Labs, Canada)]—relatively simple to setup. However, current palmar devices generally suffer from a limited range of motion.

When it comes to grounded hand exoskeletons, Ueki et al. developed a device for hand and wrist rehabilitation that controls 18 DoF (Ueki et al., 2012) employing dedicated linkage mechanisms for each finger. The HEXORR, developed by Schabowsky et al. (2010), is a grounded robotic exoskeleton which implements simultaneous movements of index to little finger with a large range of motion. The FINGER exoskeleton (Taheri et al., 2014) is highly backdrivable and can be used for proprioceptive training of two fingers. The hand module Manovo<sup>®</sup> Power (Hocoma, Switzerland) offers one DoF (i.e., coupled finger and thumb motion), uses straps for an easy setup, but provides only limited finger flexion. Finally, The Gentle/G hand module (Loureiro and Harwin, 2007) provides basic haptic rendering and allows to interact with virtual environments. It is equipped with a hinge mechanism that allows to open the hand fixations for a quick setup.

Based on the reviewed studies, there is a clear need for a new actuated hand rehabilitation device that is easy to setup while allowing for a large range of finger motion, and that provides physical assistance as well as somatic sensations to practice meaningful functional tasks in an engaging virtual environment. To address the unsatisfied needs in robotic sensorimotor rehabilitation, we aimed at developing a novel clinical-driven robotic hand rehabilitation device that is capable of high quality haptic rendering and that supports physiological full flexion/extension of the fingers while offering an effortless setup.

To maximize acceptance and usability of our novel device, we conducted a survey with 33 participants (therapists, nurses, and physicians working in neurerehabilitation) to gather clinical requirements (Rätz et al., 2021). The results from this survey

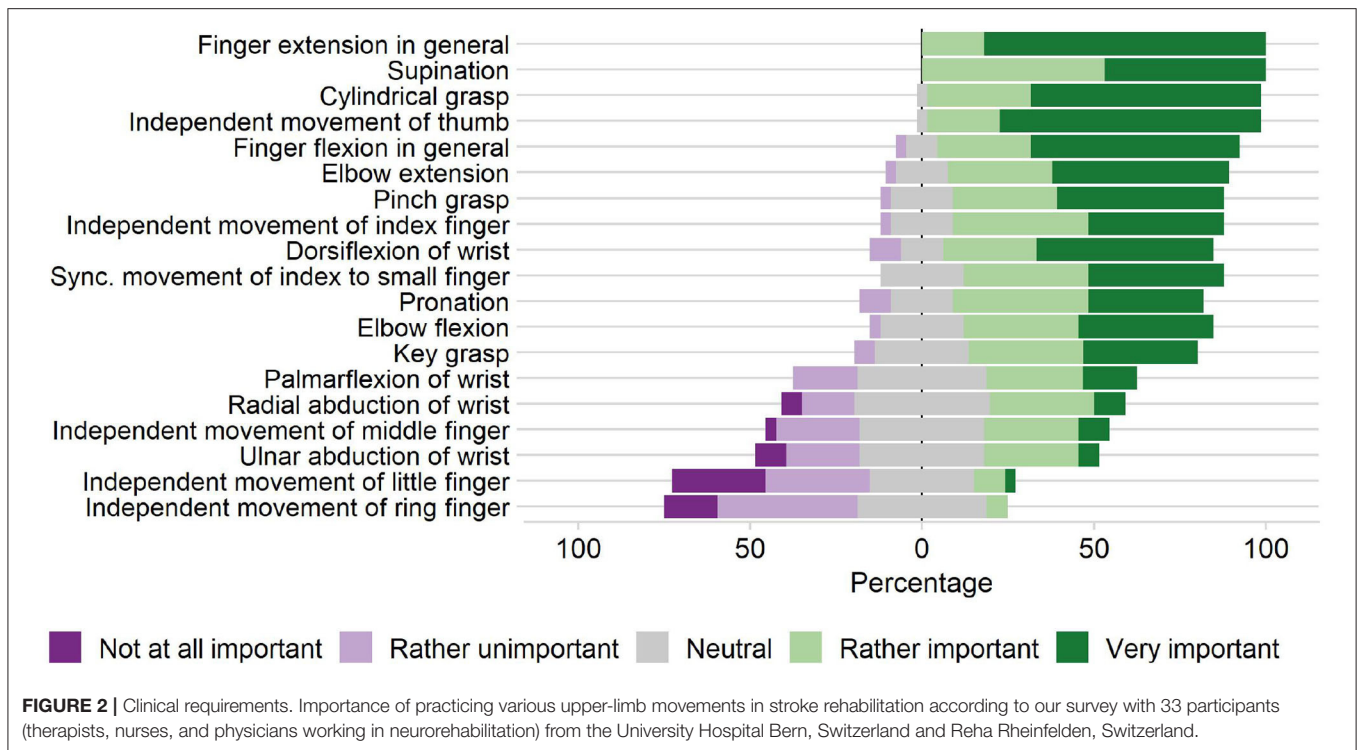


confirmed that a simple and short setup is essential for the clinical acceptability and applicability of robotic devices in rehabilitation. Furthermore, finger extensions were reported as crucial movements to be trained. To fulfill these clinical requirements, we combined novel optimization methods that incorporate not only mechanical considerations (i.e., simple setup, fine haptic capabilities, accommodating diverse hand sizes), but importantly, also anatomical considerations (i.e., large physiological range of motion, different lengths of individual fingers, ergonomic grasp). Here, we present the resulting optimal design, the Palmar Rehabilitation Device (PRIDE) (Figure 1), which introduces the following novelties:

1. A large range of motion (from 180° flexion to full extension) of the fingers, while allowing for an effortless installation of the patient's hand. This is achieved by designing the handle to have a compact cylindrical shape during the setup phase.
2. Our kinematic design ensures that all fingers are supported through the full range of motion and that the little finger does not lose contact with the handle during extension.
3. In our design, we took into consideration that the human hand usually grasps a cylindrical object in a way that it is not orthogonal to the longitudinal axis of the hand. Instead, it runs obliquely from the metacarpophalangeal joint of the index finger to the base of the hypothenar eminence.
4. The end-effector path was optimized to guarantee physiologically correct finger movements for a large variety of hand sizes.

In the upcoming sections, we present the requirements as well as the mechanical design and control of our prototype. First, the requirements are established based on clinical needs, anatomical constraints, and mechanical considerations. A kinematic design that satisfies all the requirements is then proposed and optimized based on anthropometric data. The mechanical realization and the control thereof are then described, including friction and gravity compensation to enhance transparency. Finally, we present results from a preliminary test with healthy participants to characterize the device's haptic capabilities.





## 2. METHODS

### 2.1. Requirements

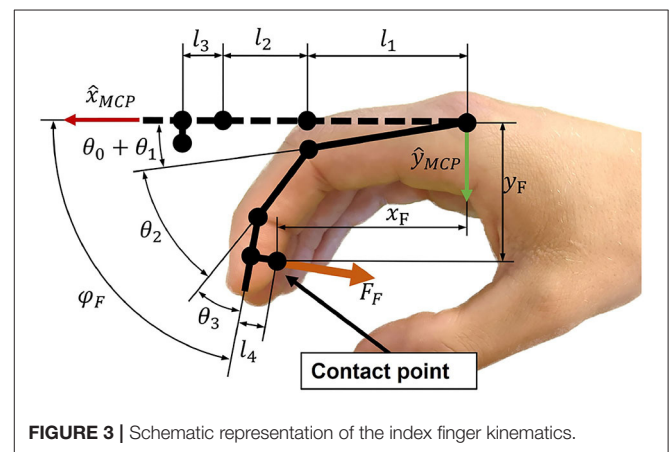
#### 2.1.1. Clinical Requirements

Prior to the novel device development, we conducted a survey with 33 clinical professionals (therapists, nurses, and physicians working in neurorehabilitation) from the University Hospital Bern, Switzerland and Reha Rheinfelden, Switzerland, to gather the clinical requirements for a robotic device targeting sensory-motor rehabilitation of the upper-limbs (Rätz et al., 2021). We found that grasping, eating, and personal hygiene are amongst the most important activities of daily living to be exercised. Finger and wrist extensions were reported as relevant movements to be trained. In subsequent on-site discussions with therapists during the device development, we further particularized full finger extensions as a crucial clinical requirement. Moreover, the results of our survey indicated a higher relevance of training the index finger compared to middle, ring and small finger (**Figure 2**). Importantly, the majority of the clinicians would like to spend less than 10 min (median of 5 min) to set up the robotic device. A complete list of the survey results can be found in Rätz et al. (2021).

#### 2.1.2. Anatomical Requirements

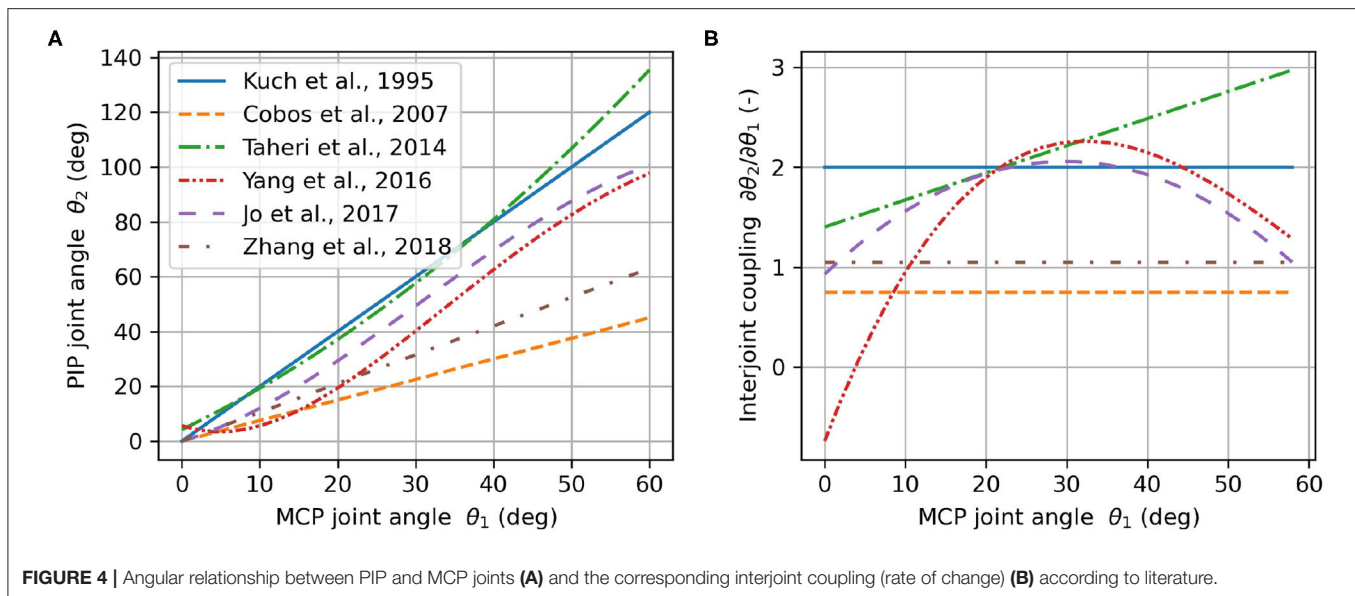
##### *Finger Model and Interjoint Couplings*

To support physiological finger movements, we first need to understand the path that is described by a finger in a grasping motion. To this end, a kinematic model of the fingers is required. We utilized the three DoF kinematic model depicted in **Figure 3**. The metacarpophalangeal (MCP;  $\theta_1$ ), proximal interphalangeal (PIP;  $\theta_2$ ) and distal interphalangeal (DIP;  $\theta_3$ )



joints were considered as one DoF hinge joints. The angle  $\theta_0$  denotes the initial angle of the MCP joint. The abduction and adduction of the fingers were assumed to be zero. Further, all joints axes were assumed to be parallel to  $\hat{z}_{MCP}$ , which constrains the finger movements to be within the  $xy$ -plane (**Figure 3**). The finger tip angle w.r.t. to the metacarpal bone is denoted as  $\varphi_F$ . The fingertip position coordinates  $x_F$  and  $y_F$  as well as  $\varphi_F$  are computed by Equation (1), whereby  $c_{01}$  is the short form of  $\cos(\theta_0 + \theta_1)$ , etc.

$$\begin{aligned} x_F &= l_1 c_{01} + l_2 c_{012} + l_3 c_{0123} - l_4 s_{0123} \\ y_F &= l_1 s_{01} + l_2 s_{012} + l_3 s_{0123} + l_4 c_{0123} \\ \varphi_F &= \sum_{i=0}^3 \theta_i \end{aligned} \quad (1)$$



**FIGURE 4 |** Angular relationship between PIP and MCP joints **(A)** and the corresponding interjoint coupling (rate of change) **(B)** according to literature.

We assumed that consecutive finger joint positions can be described as a function of the preceding finger joints. These interjoint couplings  $n_{12}$  and  $n_{23}$  were defined as follows:

$$\begin{aligned}\theta_2 &= n_{12}\theta_1 \\ \theta_3 &= n_{23}\theta_2 = n_{12}n_{23}\theta_1\end{aligned}\quad (2)$$

It is generally accepted that there is an approximately constant anatomical coupling between the DIP and PIP joints that lies in the range of  $n_{23} \in [0.65, 0.75]$  for the index finger (Hahn et al., 1995; Cobos et al., 2007; Mentzel et al., 2011) while the movements of the MCP and PIP joints are independent to each other. It is, for example, possible to fully flex the PIP joint while extending the MCP joint and vice-versa. The typical relation of the MCP and PIP joint angles  $n_{12}$  during grasping for healthy individuals has been subject to investigation and has been described as linear (Kuch and Huang, 1995; Cobos et al., 2007; Zhang et al., 2018), quadratic (Taheri et al., 2014), cubic (Jo et al., 2017), or even quartic (Yang et al., 2016) (**Figures 4A,B**). Based on this large and inconsistent variety of identified MCP-PIP interjoint couplings, we argue that a constant coupling between MCP and PIP joint angles can be assumed, which results in a physiologically correct and comfortable grasping motion. For the development of our prototype, the value of this constant coupling was chosen to be in the range of  $n_{12} \in [1.25, 1.75]$ . This allows to reduce the three DoF finger model in Equation (1) to a one DoF model.

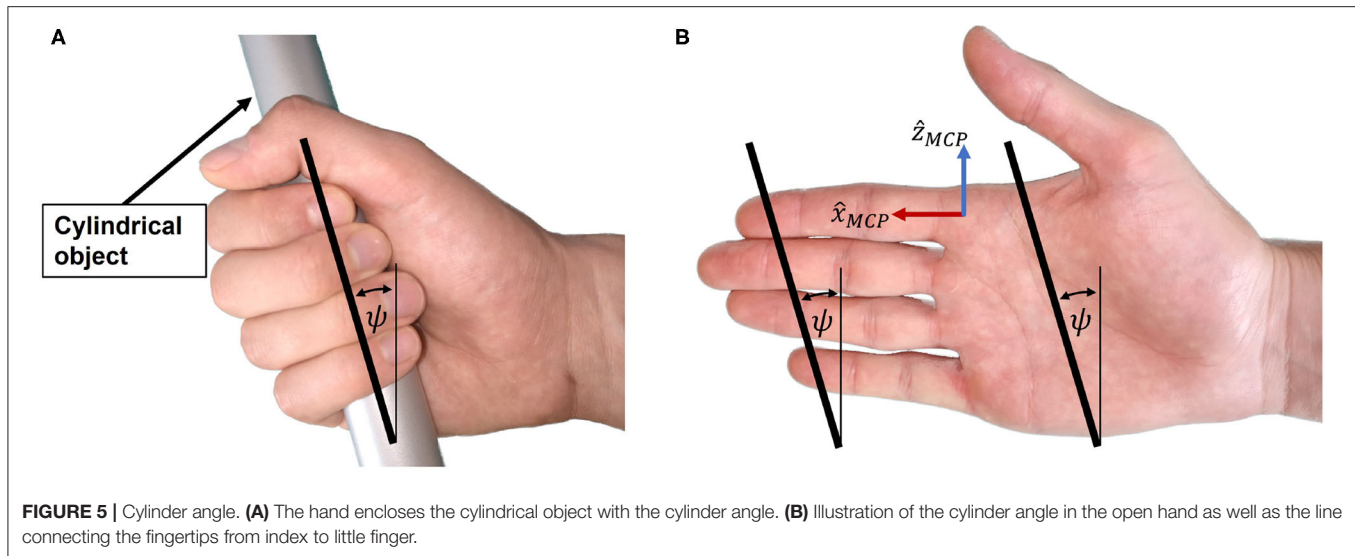
### Cylindrical Grasping

When holding a cylindrical object using full palmar prehension, the longitudinal axis of the cylindrical object usually runs obliquely from the MCP joint of the index finger to the base of the hypothenar eminence (Napier, 1956). We refer to the angle of this longitudinal axis relative to the transverse axis of the hand in **Figure 5A** as *cylinder angle*, as introduced by Buchholz

(Buchholz, 1992). A wide range of cylinder angles, from  $10^\circ$  to  $30^\circ$ , has been reported in literature (Kapandji, 1982; Buchholz, 1992).

If a straight line is traced in the coronal plane through the center of the distal segment of the index finger and the center of the distal segment of the little finger (**Figure 5B**), the angle between this line and the transverse axis of the hand happens to be similar to the cylinder angle  $\psi$ . Importantly, this is also the case if the same line is traced when the hand is closed (**Figure 5A**). The straight line connecting the centers of the distal segments of index and little finger appears to be parallel to the longitudinal axis of a cylindrical object in a cylindrical grasp with flexed (**Figure 5A**) or extended (prior to grasping, **Figure 5B**) fingers. This is due to a combination of several factors: First, the length of each finger is different, with the little finger being the shortest. Second, the MCP joint of each finger has a different proximodistal position with the MCP joint of the little finger being the most proximal (Vergara et al., 2018). Third, as described by Kapandji (Kapandji, 1982), the last three fingers—i.e., middle finger, ring finger and little finger—not only move in the sagittal plane when flexed, but in an oblique plane latero-medially, with the small finger moving in the most oblique plane. Last, the increased functional range of motion of the MCP joints of ring and little finger (Hayashi and Shimizu, 2013) bring their fingertips in a more proximal position in a cylindrical grasp.

Because of the apparent resemblance of the cylinder angle and the angle deduced from the line through the fingertips of index and little finger, we assume these angles to be equivalent and denote them both by  $\psi$  as indicated in **Figure 5B**. To enable a natural cylindrical grasp, we require our kinematic design to respect this angle, which we assumed to be  $\psi = 25^\circ$  based on estimations of the fingertip positions of index and little finger using (Garrett, 1970a,b; Vergara et al., 2018).



### 2.1.3. Design Requirements

#### Easy Setup

After stroke, patients often suffer from spasticity (Urban et al., 2010), leading to involuntary chronic joint flexion. This presents an insuperable barrier for the usage of devices that require finger extension during setup. Thus, to facilitate the admission of patients with spasticity into robotic rehabilitation, it would be advantageous to perform the patients' setup with their hands being closed. We, therefore, aimed at designing a device that possesses a compact, cylindrical-shaped geometry during setup, which allows to slide the patient's closed fist on the device.

The simultaneous clinical requirement of being able to practice full finger extension movements and the design requirement of a compact handle to facilitate the setup, impose the need of a large range of motion of the fingers. We determined a fingertip full flexion angle  $\varphi_F$  of  $180^\circ$  as a reasonable value for a closed hand and  $\varphi_F$  of  $0^\circ$  at fingers full extension. This choice represents a compromise between compactness of the handle during setup, full finger extension, and mechanical feasibility.

#### Fingertip Forces During Grasping

Including all digits, the human hand is capable of approximately 500 N grasping force (100 N for the thumb during a key grasp) (Hasser, 1995; Rickert, 2010). Wiker et al. report that a value of 15% of the maximum voluntary finger contraction, corresponding to 75 N in the fingertips, is an upper bound for the comfortable long-term use of a haptic interface (Wiker et al., 1989). A lower bound can be deducted from the peak force that is required to extend moderately spastic/hypertonic fingers. In literature, values ranging from approximately 15 N (Kamper et al., 2006) to 25 N, (15 N for the thumb) (Nycz et al., 2018) are reported. Thus, a minimum continuous fingertip force of  $F_{F,min} = 30$  N was considered as an adequate value for the development of our haptic device. The force during practice was decided to be applied on the last segment of the fingers, which corresponds to natural grasping. This would further promote

sensory stimulation at the fingertips where the highest density of cutaneous mechanoreceptors is located (Vallbo and Johansson, 1984).

#### Accounting for Different Hand Sizes

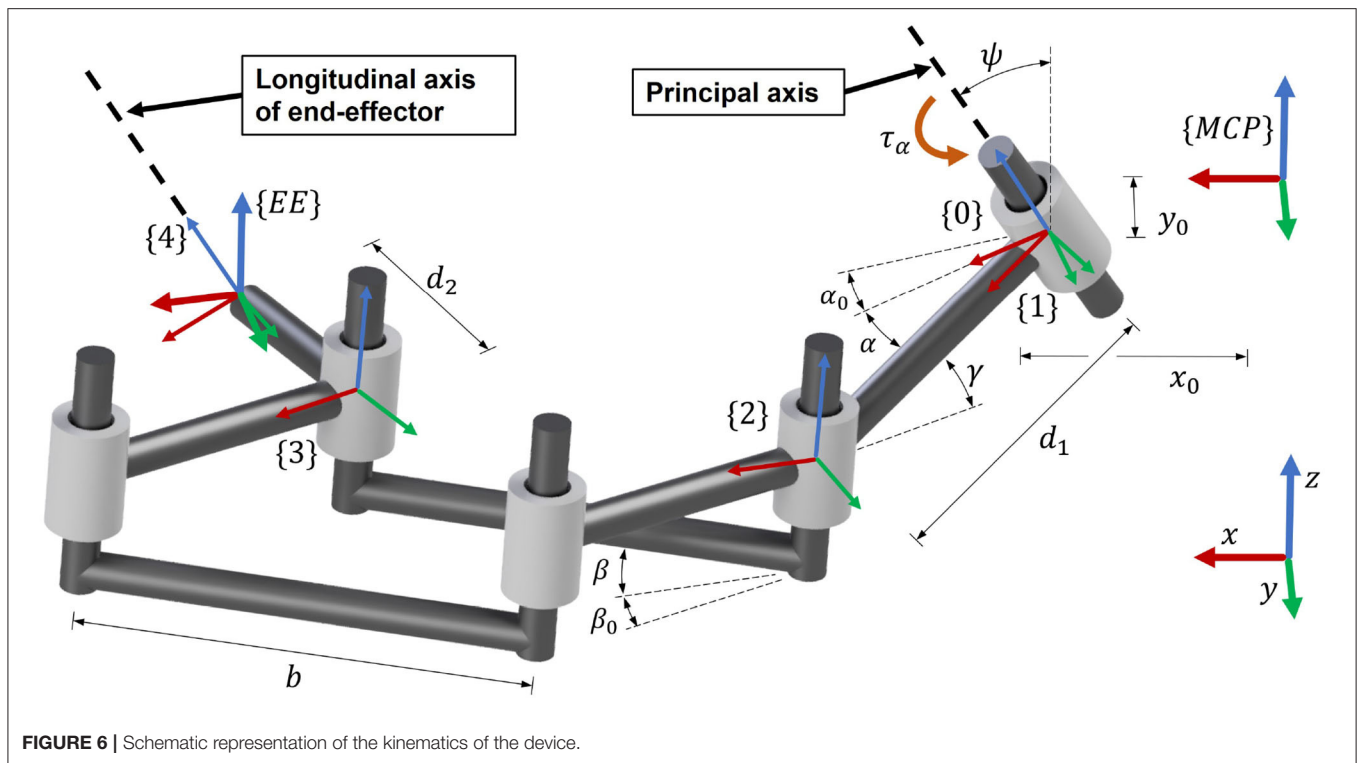
In order to increase the clinical practicability of our solution, we aimed to design a device that could be used by patients with a variety of hand proportions, i.e., from the 5th percentile of women's hand size to the 95th percentile of men's hand size. Exhaustive measurements of hand proportions are reported in the NASA Man-System Integration Standards (NASA, 1995), in the studies of Garrett (1970a,b) and by Vergara et al. (2018). Buchholz et al. represent the length of each finger segment as a percentage of the total hand length (Buchholz et al., 1992). Their estimations agree with the findings of Van Der Hulst et al. (2012). For our development, we utilized the values reported by Garrett and Buchholz et al., and we assumed that all the proportions of finger segments scale linearly with the hand size.

#### Enhanced Transparency

Haptic interactions can be finely rendered without the need of adding expensive/bulky force sensors by employing open-loop impedance control (Hatzfeld and Kern, 2014). Yet, this requires that our mechanical design is inherently transparent, i.e., possesses low static friction, low backlash, and high backdrivability. A highly backdrivable design also has the advantage of being inherently safe in case of a power cut-off. Cable-driven transmissions could be good candidates to achieve high transparency and are already successfully employed in many haptic devices (e.g., Mali and Munih, 2006; Pezent et al., 2017; Buongiorno et al., 2018).

## 2.2. Mechanical Design

In our solution, we employ a palmar design—i.e., the main area of contact between the device and the hand is between the handle and the palm (Figure 1). While the metacarpal



bones of the hand are fixed on the handle using straps, the fingertips are attached to an end-effector, which moves the fingertips along a specific path. In this paper, we refer to the *end-effector* as the part of our device which interacts with the user's fingertips. While a large part of the distal finger segments might touch the end-effector, the contact point between a fingertip and the end-effector is defined to be in the center of the palmar side of the distal finger segment (Figure 3). After finding an adequate kinematic architecture for our device based on clinical, anatomical and design requirements, the synthesis of the mechanical design parameters was performed utilizing an optimization approach (see section *Optimization of Design Parameters*). The key idea of this optimization was to find the position of hands of different sizes on the device such that their respective fingertip paths overlap when performing a cylindrical grasp.

Motivated by the results of our survey, which highlights the relevance of training natural index finger movements (Rätz et al., 2021), the kinematic design was realized focusing on the index fingertip path. When performing a cylindrical grasp, the fingertips approximately describe a spiral around the MCP joints, which consists of a rotary movement around a principal revolute axis with a successively decreasing momentary radius. To accomplish that the robot end-effector follows this spiral-like movement, a parallelogram coupled to a principal revolute joint was chosen (Figure 6). Within this design, the parallelogram moves as a function of the rotation  $\alpha$  of the principal revolute joint, and hence, requires only one actuator. Furthermore, this solution uses solely revolute bearings, which typically possess lower friction values and require less maintenance than

linear bearings because their races are less exposed and can be more easily protected from dust than the rails of linear bearings.

To achieve a natural cylindrical grasp, the cylinder angle  $\psi$  (Figure 5) was introduced into the system design. We found that a remarkably natural grasping motion can be obtained when the orientation of the handle's longitudinal axis (corresponding to the orientation of a straight line connecting the centers of the fingertips of index and little finger as shown in Figure 5) is invariant to the world frame during the entire range of motion. In particular, this allows the small finger to stay in contact with the end-effector and avoids that it slides off the end-effector during the entire range of motion. Thus, we tilted the entire mechanism forwards, including the principal (actuated) revolute joint, with an angle  $\psi$  (Figure 6) w.r.t. the transverse axis of the hand. The fingertip support (end-effector) was then designed to be parallel to this tilted principal axis of rotation in order to keep its orientation during the entire range of motion. Note that the tilted parallelogram would result in a vertical movement of the end-effector. To reduce this undesired vertical movement to the minimum, the parallelogram was inclined backwards in the opposite direction by an angle  $\gamma$  (Figure 6). This angle  $\gamma$  will be subject to the optimization of the design parameters after the derivation of the kinematics.

The kinematics of the robot end-effector were derived using homogeneous transformation matrices  ${}^A_B T$ , representing frame  $\{B\}$  in frame  $\{A\}$ . The frame  $\{MCP\}$  is attached to the MCP joint of the index finger, while frame  $\{EE\}$  is attached to the end-effector. The short forms  $D_x, D_y, D_z$  and  $R_x, R_y, R_z$  denote a local translation or rotation respectively (Craig, 2005). The



kinematic chain is schematically represented in **Figure 6** and mathematically described by Equations (3) to (9).

$$\begin{aligned} {}^{MCP}_0T &= D_x(x_0)D_y(y_0)R_y(\psi)R_z(\alpha_0) \\ {}^0_1T &= R_z(\alpha) \\ {}^1_2T &= D_x(d_1)R_y(-\gamma)R_z(-\beta_0) \\ {}^2_3T &= R_z(-\beta)D_x(b)R_z(\beta) \\ {}^3_4T &= R_z(\beta_0)D_y(-d_2)R_y(\gamma)R_z(-\alpha_0) \end{aligned} \quad (3)$$

$${}^{MCP}_4T = {}^{MCP}_0T {}^0_1T {}^1_2T {}^2_3T {}^3_4T = \begin{bmatrix} \hat{x}_4 & \hat{y}_4 & \hat{z}_4 & p_4 \\ 0 & 0 & 0 & 1 \end{bmatrix} \quad (4)$$

$$\hat{x}_{EE} = \frac{\hat{y}_4 \times \hat{z}_{MCP}}{\|\hat{y}_4 \times \hat{z}_{MCP}\|} \quad (5)$$

$$\hat{y}_{EE} = \hat{z}_{MCP} \times \hat{x}_{EE} \quad (6)$$

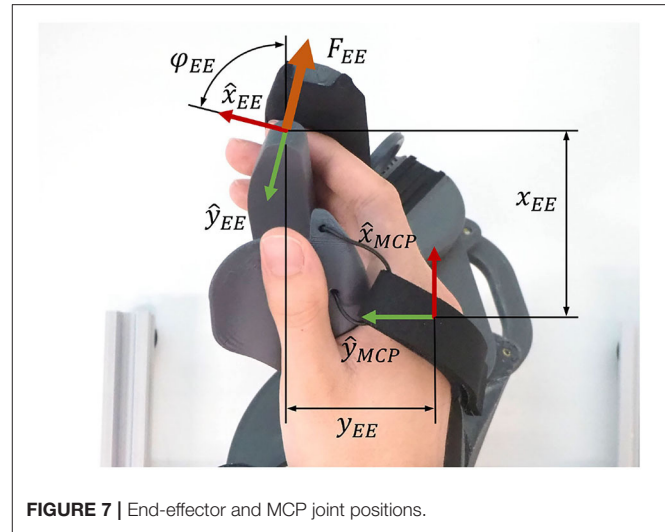
$$\hat{z}_{EE} = \hat{z}_{MCP} \quad (7)$$

$$p_{EE} = p_4 \quad (8)$$

$${}^{MCP}_{EE}T = \begin{bmatrix} \hat{x}_{EE} & \hat{y}_{EE} & \hat{z}_{MCP} & p_{EE} \\ 0 & 0 & 0 & 1 \end{bmatrix} \quad (9)$$

The matrix  ${}^{MCP}_0T$  describes the transformation from the MCP joint frame  $\{MCP\}$  to the frame  $\{0\}$ . The local  $z$ -axis vector  $\hat{z}_0$  is coincident with the axis of the principal revolute joint. Actuating this joint by introducing a rotation of  $\alpha$  leads to frame  $\{1\}$ . The following transformation  ${}^1_2T$  places the frame  $\{2\}$  on the first revolute joint of the parallelogram. The next transformation,  ${}^2_3T$ , describes the translation from the input to the output of the parallelogram. The  ${}^3_4T$  is a transformation that places frame  $\{4\}$  into the end-effector position, whereby  $\hat{z}_4$  is always parallel to the principal revolute axis  $\hat{z}_0$ . The final transformation  ${}^{MCP}_{EE}T$ , which expresses the transformation from the MCP joint to the end-effector, is obtained by constructing  $\hat{x}_{EE}$  and  $\hat{y}_{EE}$  and utilizing the position vector  $p_{EE}$  obtained from Equation (8). The vectors  $\hat{x}_{EE}$  and  $\hat{y}_{EE}$  (Equations 5 and 6) are computed such that  $\hat{x}_{EE}$  represents the end-effector orientation and are based on the anatomical constraint that the fingertip always moves in the  $xy$ -plane of the MCP joint frame  $\{MCP\}$ . The angle  $\alpha_0 + \alpha$  denotes the angle of the principal axis of rotation, while the angle  $\beta_0 + \beta$  is the angular opening of the parallelogram. The angle  $\alpha$  describes the rotation introduced by the actuator ( $\alpha \geq 0^\circ$ ). The initial angles  $\alpha_0$  and  $\beta_0$  are constant design parameters that need to be optimized. The parallelogram opening angle  $\beta$  was chosen to be proportional to the angle  $\alpha$  (with fixed ratio  $n_{\alpha\beta}$ , Equation 10) to avoid a too complex mechanical design.

$$\beta = n_{\alpha\beta}\alpha \quad (10)$$



**FIGURE 7** | End-effector and MCP joint positions.

The end-effector position coordinates  $x_{EE}$ ,  $y_{EE}$  and  $z_{EE}$  are obtained from  $p_{EE}$  (**Figure 7**). The end-effector angle  $\varphi_{EE}$ , corresponds to the angle between  $\hat{x}_{EE}$  and  $\hat{x}_{MCP}$  and is computed by Equation (11). For the upcoming synthesis of the mechanical design parameters, this angle was bounded to  $\varphi_{EE} \in [-90^\circ, 270^\circ]$ .

$$\varphi_{EE} = \text{sign}((\hat{x}_{EE} \times \hat{x}_{MCP}) \cdot \hat{z}_{MCP}) \arccos(\hat{x}_{EE} \cdot \hat{x}_{MCP}) \quad (11)$$

## 2.3. Optimization of the Design Parameters

Once the kinematic architecture was decided, we searched for the most suitable set of design parameters by performing an optimization. This optimization step aims to find the optimal position of hands of different sizes on the handle such that their respective fingertip paths overlap. By achieving this, it suffices for the device to track only one common fingertip path, independently of finger sizes. This allowed us to engineer our device without any adjustable moving parts which would have resulted in complicated adjustment mechanisms. Instead, different hand sizes are accommodated by the use of size-specific handles, which can be exchanged within seconds. Four different index finger sizes (*small*, *small-medium*, *medium-large*, *large*) were considered in the optimization, the smallest being the 5th percentile of women and the largest being the 95th percentile of men, according to anthropometric databases. The two intermediate finger sizes were linearly interpolated.

The optimization step required the definition of an adequate cost function whose minimization would result in optimal design parameters. The cost function was defined with two goals in mind:

1. Find interjoint couplings  $n_{12}$  and  $n_{23}$  as well as MCP joint positions  $(x_0, y_0)$  and initial MCP angles  $\theta_0$  for various hand sizes, such that the overlap of the resulting fingertip paths of different hand sizes is maximized.

- Find mechanical design parameters (linkage lengths and orientations) such that the robot end-effector closely tracks these overlapping fingertip paths.

In the synthesis of mechanical linkage systems via optimization, the target path is usually known. A common technique is to define the so-called precision points that discretize the target path. These are points along the target path—often at a regular interval—through which the end-effector of the linkage mechanism is supposed to move. In the optimization step, the mechanical design parameters are optimized such that the position difference between the end-effector and these precision points is minimal (Goulet et al., 2016). However, in our case, the target path was not known prior to the optimization. Instead, we needed to simultaneously find the end-effector path as well as a fingertip path for each hand size.

Nevertheless, we had to discretize the still unknown paths. The number of discrete points along the end-effector path was selected to be  $n = 10$ . A specific point on this path is referred to by the index  $j$ . The number of hand sizes that were included in the optimization is  $m = 4$  and a specific finger size is referred to by  $i$ . In the upcoming equations, superscripts are used to denote the discretization step  $j$  and hand size  $i$ .

To make sure that the fingertip and end-effector paths are optimized along the entire range of motion of the fingers, the optimization variables  $\Delta\theta^{(i)}$  were introduced. Because the optimal start and end points of the finger paths may slightly differ for each hand size, a hand-size-specific, constant discretization step size was required, defined by  $\Delta\theta^{(i)} > 0$ . Without this variable, the optimization algorithm might only consider arbitrary, unequally spaced sections of the paths. To allow for a slightly different starting point of the fingertip path of each hand size, the variable  $\theta_0 \in [-5^\circ, 5^\circ]$  was introduced in Equation (1).

The problem formulation is stated in Equation (12) with the optimization variable vector  $\mathbf{x} = [u, v, \alpha]^T$ . The design parameters are constrained to be within the lower bound  $\mathbf{x}_L$  and the upper bound  $\mathbf{x}_U$ .

$$\min_{\mathbf{x}} \sum_{k=1}^6 f_k(\mathbf{x}) \quad (12)$$

$$\text{s.t. } \mathbf{x}_L \leq \mathbf{x} \leq \mathbf{x}_U$$

Each entry in  $\mathbf{x}$  corresponds to a set of design parameters. The mechanical design parameters are included in  $v = [d_1, d_2, b, \alpha_0, \beta_0, \gamma, n_{\alpha\beta}]$ , where each element is a scalar. The rotation around the principal axis  $\alpha$  is  $1 \times mn$ , with  $m$  denoting the number of considered hand sizes ( $m = 4$ ) and  $n$  the number of discretized points along the end-effector path ( $n = 10$ ). The design parameters related to the finger kinematics are included in  $u = [x_0, y_0, \theta_0, n_{12}, n_{23}, \Delta\theta]$ , i.e., the MCP positions ( $x_0, y_0$ ), initial MCP joint angles  $\theta_0$ , interjoint couplings  $n_{12}$  and  $n_{23}$  and  $\Delta\theta$  (Figure 4). The upper and lower bounds  $\mathbf{x}_L$  and  $\mathbf{x}_U$  were either defined by anatomical constraints (e.g.,  $n_{12} \in [1.25, 1.75]$  and  $n_{23} \in [0.65, 0.75]$ ) or they were defined such that a reasonable search space for the global optimization was

achieved that excludes mechanically infeasible solutions (e.g., very long linkage lengths).

The angle  $\theta_1^{(i,j)}$  which is needed to compute the fingertip coordinates  $x_F^{(i,j)}$  and  $y_F^{(i,j)}$  as well as  $\varphi_F^{(i,j)}$  using Equation (1) is computed in Equation (13). All elements in  $u$  are  $1 \times m$ , except  $\theta_0$ , which is  $1 \times (m - 1)$  (the initial MCP joint angle  $\theta_0$  of the smallest finger is 0 to avoid redundant optimization variables).

$$\theta_1^{(i,j)} = j \Delta\theta^{(i)} + \theta_0^{(i)} \quad (13)$$

The cost function in Equation (12) consists of a weighted sum of six individual cost functions, each contributing to a specific meaningful goal. Each individual cost function is weighted by specific weights  $w_\varphi, w_z, w_{\varphi, \text{end}}, w_{\text{end}}, w_{\text{start}}$ , and  $w_\eta$ .

- $f_1(x)$ : This is the fundamental cost function that drives the end-effector path ( $x_{EE}, y_{EE}, \varphi_{EE}$ ) to overlay with the fingertip paths ( $x_F, y_F, \varphi_F$ ) for each point in the path ( $j \in \{1, n\}$ ) and each hand size ( $i \in \{1, m\}$ ).

$$f_1(x) = \frac{1}{mn} \sum_{i=1}^m \sum_{j=1}^n (x_{EE}^{(i,j)} - x_F^{(i,j)})^2 + (y_{EE}^{(i,j)} - y_F^{(i,j)})^2 + w_\varphi (\varphi_{EE}^{(i,j)} - \varphi_F^{(i,j)})^2 \quad (14)$$

- $f_2(x)$ : This individual cost function ensures that there is minimal variation in the  $z$ -direction ( $z_{EE}$ ) along the end-effector entire movement.

$$f_2(x) = w_z \frac{1}{m(n-1)} \sum_{i=1}^m \sum_{j=1}^{n-1} (z_{EE}^{(i,j+1)} - z_{EE}^{(i,j)})^2 \quad (15)$$

- $f_3(x)$ : This ensures that the angles at the last point ( $j = n$ ) of the fingertip path ( $\varphi_F$ ) and the end-effector path ( $\varphi_{EE}$ ) are close to  $\varphi_{\text{end}} = 180^\circ$ .

$$f_3(x) = w_{\varphi, \text{end}} \frac{1}{m} \sum_{i=1}^m (\varphi_{EE}^{(i,n)} - \varphi_{\text{end}})^2 + (\varphi_F^{(i,n)} - \varphi_{\text{end}})^2 \quad (16)$$

- $f_4(x)$ : This individual cost function enforces that the last position ( $j = n$ ) of the finger paths ( $x_F, y_F$ ) from different hand sizes ( $i \in \{1, m\}$ ) coincide when the fingers are fully flexed.

$$f_4(x) = w_{\text{end}} \frac{1}{1-m} \sum_{i=1}^{m-1} (x_F^{(i+1,n)} - x_F^{(i,n)})^2 + (y_F^{(i+1,n)} - y_F^{(i,n)})^2 \quad (17)$$

- $f_5(x)$ : This individual cost function reinforces that the robot end-effector and each corresponding fingertip position coincide at the initial point of the paths ( $j = 1$ ). Without this term, the differences between the start of the fingertip paths and the start of the end-effector path tend to be rather large in the  $x$ -direction. This is especially undesired because in full extension (quasi-aligned in  $x$ -direction, depending on  $\theta_0$ ), the fingers are in a singular configuration (or quasi-singular, depending on  $\theta_0$ ) with respect to the  $x$ -direction.

$$f_5(x) = w_{\text{start}} \frac{1}{m} \sum_{i=1}^m (x_{EE}^{(i,1)} - x_F^{(i,1)})^2 + (y_{EE}^{(i,1)} - y_F^{(i,1)})^2 \quad (18)$$

- $f_6(x)$ : This term minimizes the difference between the largest and smallest mechanical advantage along the range of motion. The mechanical advantage  $\eta$  of the mechanism describes the relation between the input torque at the principal revolute axis  $\tau_\alpha$  and the end-effector force orthogonal to the fingertip  $F_{EE}$  (see **Figure 7**). It is computed by using the Jacobian in the end-effector frame  ${}^{EE}J$  (Equation 19) and varies as a function of the rotation  $\alpha$  of the principal axis. Note that the end-effector force  $F_{EE}$  is always pointing in  $y$ -direction of the  $\{EE\}$  frame (see **Figure 6**). Therefore, the  $y$ -component of  ${}^{EE}J$  is extracted in Equation (20) to compute the mechanical advantage.

$${}^{EE}J = {}^{MCP}_{EE}R^T \frac{\partial \mathbf{p}_{EE}}{\partial \alpha} \quad (19)$$

$$\eta(\alpha) = \frac{\partial y_{EE}}{\partial \alpha} = \frac{F_{EE}}{\tau_\alpha} = -\frac{1}{[0 \ 1 \ 0]{}^{EE}J} \quad (20)$$

The addition of this individual cost function is important as variations in the mechanical advantage of a mechanism modify its dynamic behavior and, consequently, its haptic rendering capabilities. Therefore, we want to minimize variations of the mechanical advantage to promote consistent haptic rendering along the entire range of motion of the device.

$$f_6(x) = w_\eta (\max(\eta) - \min(\eta))^2 \quad (21)$$

Due to the non-convex nature of the cost function, a global optimization algorithm was required. The differential evolution algorithm was selected, which was first proposed by Storn and Price (2002) and that has already been successfully applied for the synthesis of mechanical linkage systems (Acharyya and Mandal, 2009; Peñuñuri et al., 2011). The implementation of the “best1bin” strategy in the Python package SciPy (Virtanen et al., 2020) was employed with a relative convergence tolerance of 0.005.

## 2.4. Further Transparency Enhancements: Friction and Gravity Compensation

We aimed at developing a device that is transparent by design. Nevertheless, undesired friction, Coriolis, centrifugal, and gravitational forces could still lower the transparency of a haptic device (Hatzfeld and Kern, 2014), which could possibly also limit self-initiated hand movements, especially in patients who suffer from severe hand paresis. To prevent these disturbing torques from hampering our hand device transparency, we modeled, identified, and compensated the friction and gravitational disturbance forces. Because the gravitational forces and friction cannot be distinguished as seen from the motor, they were modeled and identified simultaneously. The Coriolis and centrifugal forces were neglected in the proposed model, as our solution has low inertias and the target operational speed is relatively low—we estimated a required maximum speed of  $\dot{\alpha} = 500^\circ/\text{s}$  based on grasping speeds of stroke patients from Lang et al. (2005) and taking into account the varying mechanical advantage of our device.

We **modeled** the viscous and Coulomb friction and gravitational forces,  $\tilde{\tau}_{dist}$ , following Equation (22), with the parameters to be identified  $a_0, a_1, a_2$ , and  $a_3$ .

$$\tilde{\tau}_{dist} = a_0 \sin(\alpha + a_1) + a_2 \dot{\alpha} + a_3 \text{sign}(\dot{\alpha}) \quad (22)$$

To **identify** the model parameters, we employed an empirically tuned PI velocity controller to track trapezoidal velocity profiles with target velocities  $\dot{\alpha} = 5, 10, 15, \dots, 150^\circ/\text{s}$ . The start and the end of the constant velocity plateaus were always located at the same positions by adjusting the acceleration phase (i.e.,  $\alpha = 20^\circ$ , and  $\alpha = 160^\circ$ , respectively). The required torques to sustain the constant velocities—i.e., the output of the PI controller—as well as the velocity and position were recorded at 1 kHz. The proposed model in Equation (22) was fitted to the recorded values by means of a least squares optimization using the trust region reflective algorithm in Python (Virtanen et al., 2020).

We **implemented** the disturbance torque compensation using Equation (23), with the sinusoidal term accounting for the gravitational torque, the second term accounting for viscous friction, and the last one for Coulomb friction.

$$\tau_{comp} = a_0 \sin(\alpha + a_1) + a_2 \dot{\alpha}_{filt} + b_0 a_3 \tanh(b_1 \dot{\alpha}_{filt}) \quad (23)$$

Note that the sign function in Equation (22) was replaced by a hyperbolic tangent function in Equation (23) to obtain a smooth transition around zero speed. A new parameter  $b_1$  was included in the hyperbolic tangent such that the output of the function reaches 0.95 at a speed of  $\pm 5^\circ/\text{s}$ . We also added a second parameter ( $b_0 = 0.6$ ) to slightly reduce the compensation of the Coulomb friction and ensure that the device remains passive (Schabowsky et al., 2010). The velocity  $\dot{\alpha}_{filt}$  was computed by backwards differentiation of  $\alpha$  which was obtained from the encoder and subsequent filtering with a first-order Butterworth low pass filter (cut-off frequency  $f_c = 16 \text{ Hz}$ ).

## 2.5. Evaluation of the Haptic Capabilities of PRIDE

A common measure of **transparency** is the human-robot interaction force in free space (i.e., in the absence of any rendered interaction with virtual objects), which should be minimal (Bernstein et al., 2005; Van Dijk et al., 2013; Just et al., 2018). To benchmark the transparency of the device, six right-handed participants (1 female, 5 male, aged 22 to 36 years, with hand sizes: 1 small, 2 small-medium, 3 medium-large and 1 large) without any known hand impairments were asked to perform finger flexion and extension movements with their right hand installed on the device. Ethical review and approval was not required for the study on human participants in accordance with the local legislation and institutional requirements. The participants provided their written informed consent to participate in this study.

The participants, who were naive to the device/task, were asked to open and close their hands repeatedly in a natural and comfortable manner without reaching the mechanical end-stops of the device. Our goal was to evaluate the transparency of

the prototype by measuring the interaction forces during these movements with and without gravity and friction compensation. We equipped the device with a handle corresponding to the participants' individual hand sizes. To obtain comparable measurements, a certain movement frequency was imposed. This was achieved by presenting rhythmic auditive cues to the participants. A metronome was used to present cues with 20, 40, and 60 beats per minute (BPM). The participants were instructed that one movement (flexion or extension) should last one beat. To help the participants with the timing—especially in the 20 BPM condition—we introduced two intermediate beats with a different pitch.

For each movement frequency (i.e., 20, 40, and 60 BPM) and condition (i.e., with and without gravity and friction compensation), participants performed 12 flexion and extension movements, which we refer to as one sequence. The interaction force between the fingers and the fingertip support was measured with a force sensor (TAL 221, SparkFun Electronics, USA) and recorded at  $\approx 80$  Hz (OpenScale with custom firmware, SparkFun Electronics, USA). The root mean square (RMS) of the interaction forces was computed for each sequence of 12 movements. To evaluate the effectiveness of the friction and gravity compensation, the differences in the RMS of the interaction force were evaluated by a two-way repeated measures ANOVA with gravity and friction compensation (on/off) and BMP (20/40/60 BPM) as within-subject factors.

To demonstrate the device's **capability to render** interaction forces with virtual tangible objects, a virtual wall was also implemented and evaluated in a second benchmark experiment with one healthy participant. Virtual walls are usually represented by either a force derived from a linear virtual spring and damper or by a torque derived from a rotational virtual spring and damper in the end-effector space. In the context of grasping, a virtual wall based on a linear spring and damping, orthogonal to the fingertips would be the obvious choice. However, the orientation of the end-effector force of our device  $F_{EE}$  (and opposing fingertip force  $F_F$ ) depends on  $\alpha$ . Consequently, to represent a meaningful virtual wall, based on a linear virtual spring and damper, it was needed to linearize the movement of the end-effector along  $\hat{y}_{EE}$ . The penetration depth of the fingers into the virtual wall should be relatively small, and therefore, the penetration depth  $\Delta y_{EE}$  can be computed employing the following linearization Equation (24):

$$\Delta y_{EE} \approx \frac{\partial y_{EE}}{\partial \alpha} \Delta \alpha = \frac{1}{\eta} \Delta \alpha \quad (24)$$

where  $\Delta \alpha$  is the penetration depth in the joint space of the primary axis and  $\eta$  is the mechanical advantage. The momentary linear speed of the end-effector  $\dot{y}_{EE}$  is computed using Equation (25):

$$\dot{y}_{EE} = \frac{1}{\eta} \dot{\alpha}_{filt} \quad (25)$$

The interaction force between the fingers and the virtual wall  $F_{wall}$  is then computed with Equation (26) with  $K$  and  $B$  being the desired virtual spring and damping values.

$$F_{wall} = \begin{cases} K \Delta y_{EE} + B \dot{y}_{EE} & \text{if } \Delta y_{EE} > 0 \\ 0 & \text{else} \end{cases} \quad (26)$$

This force is then transferred to a motor torque  $\tau_{mot}$  using Equation (27). The friction and gravity compensation torque  $\tau_{comp}$  was added in Equation (27) for an accurate rendering of the virtual wall. The term  $n_{mot,\alpha}$  represents a transmission ratio which translates the motor torque to the torque at the principal axis of rotation, i.e.,  $\tau_\alpha = \tau_{mot} n_{mot,\alpha}$ .

$$\tau_{mot} = \frac{1}{n_{mot,\alpha}} \frac{1}{\eta} F_{wall} + \tau_{comp} \quad (27)$$

To evaluate the haptic capabilities of the device, a virtual wall was rendered at different positions and the stability regions were evaluated by one additional participant (male, age 29, medium-large hand size). For a given virtual damping  $B$ , the virtual spring constant  $K$  was manually varied in steps of  $\pm 2$  N/mm until the maximum value of  $K$ , which did not introduce any perceivable oscillations, was found. The stability of the wall was judged according to the criteria proposed by Colgate and Brown (Colgate and Brown, 1994). Contrary to the interaction force evaluation of the device transparency, the test person in this second evaluation was familiarized with the device and the notion of virtual wall stability prior to the evaluation.

## 3. RESULTS

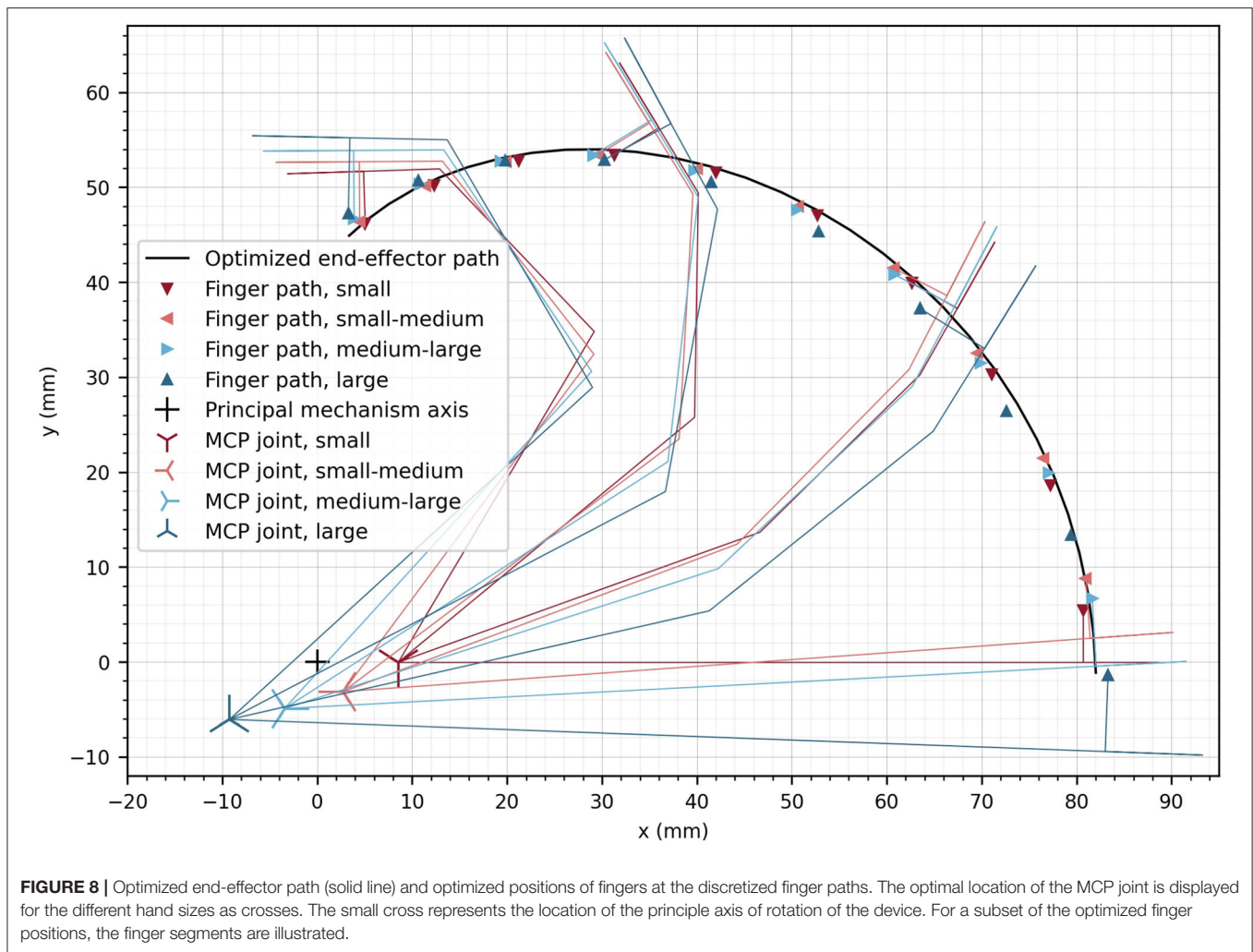
### 3.1. Optimized Design Parameters

The resulting optimal end-effector path as well as the path of the contact point of the corresponding index finger of each hand size (i.e., four different sizes from small to large) were obtained upon convergence of the differential evolution algorithm after 2425 iterations (**Figure 8**). Furthermore, the corresponding MCP joint positions, which were found for each hand size, are indicated in **Figure 8** with crosses. The deviation of the end-effector path compared to the fingertip paths measured as the mean Euclidean distance between the end-effector points and the corresponding fingertip contact points (for all hand sizes and all discretization steps) remained small (1.14 mm).

The angular deviation of the fingertip angle  $\varphi_F$  with respect to the device end-effector angle  $\varphi_{EE}$  is represented in **Figure 9A** as a function of  $\alpha$ . The mean deviation across finger sizes and full range of motion is only  $3.78^\circ$ . The largest deviations are observed as the finger reach full extension (i.e.,  $\approx 9^\circ$  for the two smallest hand sizes for  $\alpha = 0^\circ$ ). Nevertheless, the observed deviations are within an acceptable range as it would anyway not be possible to drastically constrain the fingertip angle on the device in a comfortable manner. Due to this certain angular compliance from the fingertip fixation, the obtained angular deviations are not noticeable when using the device.

In the optimization, the difference between the fingertip  $z$ -position and the end-effector  $z$ -position was not included.





Instead, the mean  $z$ -position of the end-effector can simply be considered during the mechanical design as a constant offset. However, the variation of the  $z$ -position of the end-effector (in direction of  $\hat{z}_{EE}$ ) was desired to be zero because the fingertips move in the  $xy$ -plane of  $\{MCP\}$ , and has consequently, been minimized in the optimization. The end-effector vertical variation after optimization remains small along the complete end-effector path with a mean deviation of 0.380 mm (Figure 9B). The peak-to-peak vertical variation is less than 1.5 mm, which is not perceptible when using the device.

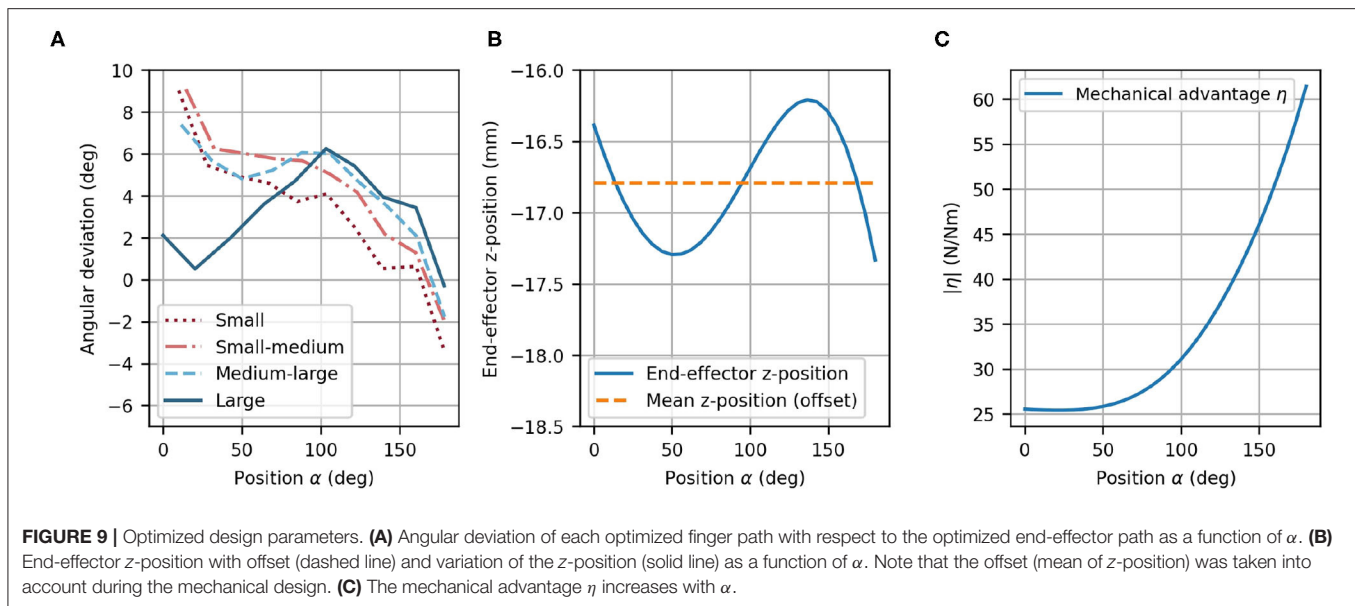
The mechanical advantage (Figure 9C) depends on  $\alpha$  and ranges from  $\eta = 25.4 \text{ N/Nm}$  to  $\eta = 61.4 \text{ N/Nm}$ . This results in a change of mechanical advantage along the full range of motion by a factor of 2.42. While  $\eta$  remains low for small values of  $\alpha$ , it increases above  $\alpha \approx 50^\circ$ .

### 3.2. Hardware and Mechanical Realization

The main structure of the resulting robotic hand module design includes a parallelogram with one main arm and a set of bearings, which can be mechanically solicited in any direction. A second

light-weight arm with small bearings, which only transmits forces along its longitudinal axis, completes the parallelogram structure (Figure 10A). The parallelogram in the prototype was displaced w.r.t. to its original location within the  $xy$ -plane of frame  $\{2\}$ . This shift of the parallelogram does not modify the kinematic chain because the corresponding offsets were added between frame  $\{3\}$  and the end-effector frame. However, the shift allows to adapt the mechanical design in order to avoid collisions between the mechanical structure and the user's forearm during finger flexion. Because these offsets would have been redundant in the optimization, they were added during the design of the actual prototype.

The PRIDE prototype was manufactured using a combination of 3D printed parts. Carbon-reinforced polylactic acid (PLA) was employed for structural parts and standard PLA for parts that are touched during use (Figure 10). Square aluminium profiles were employed for structural support. For each of the four hand sizes, a specific handle was designed such that it locates a hand of the corresponding size according to the size-specific MCP joint offsets  $x_0$  and  $y_0$ , which were obtained from the optimization. To design ergonomic handles and to consider the different depths



and breaths of fingers for different hand sizes, anthropometric data from Vergara et al. (2018) was consulted. In each handle, we integrated a cushioned strap which allows to attach the metacarpal bones of the hand. To constrain wrist movements, a wrist rest with two cushioned straps was designed. Finally, to allow the fingers to execute extension movements (Figure 11), a fingertip fixation with a quick-release mechanism was added on the dorsal side of the fingers. All of these fixations were designed to promote a fast and effortless setup as demonstrated in Figure 12.

The actuation of the principal axis is performed by a capstan transmission to reduce the needed motor torque (Figure 10B). A capstan transmission satisfies all listed mechanical requirements in terms of transparency, i.e., it is backlash-free, highly backdrivable, and has low friction. A drive pulley with 7 mm diameter, actuated by a brushed DC motor (RE30, Maxon Motor AG, Switzerland) that includes an encoder with 1,000 ticks per revolution (4,000 in quadrature) drives a large output drum (see Figure 10). The requirement on the minimum force on the fingertips ( $F_{F,min} = 30$  N) and the minimal mechanical advantage resulted in a output drum of diameter 156 mm. The motor is driven by a custom controller board based on the ones employed in the Sigma.7 haptic device (Force Dimension, Switzerland) and controlled with an update rate of 1 kHz from a PC with a Linux operating system.

The parallelogram is designed to move with a constant mechanical coupling  $n_{\alpha\beta}$  w.r.t to the position of the principal axis  $\alpha$ . To retain the low-backlash and high backdrivability of the cable actuation, this coupling was also designed using a cable transmission. The shifting of the parallelogram (Figure 10A) causes the principal axis and the revolute axes of the parallelogram to be skew. A cable transmission is, therefore, also a good solution to easily couple these skew axes of rotation. Small idler pulleys were used to guide the cables from a stationary pulley in frame  $\{0\}$  (whose axis

is aligned with  $\hat{z}_0$ ) to a pulley driving the parallelogram. They were arranged so that they need minimal space (see Figures 10C,D).

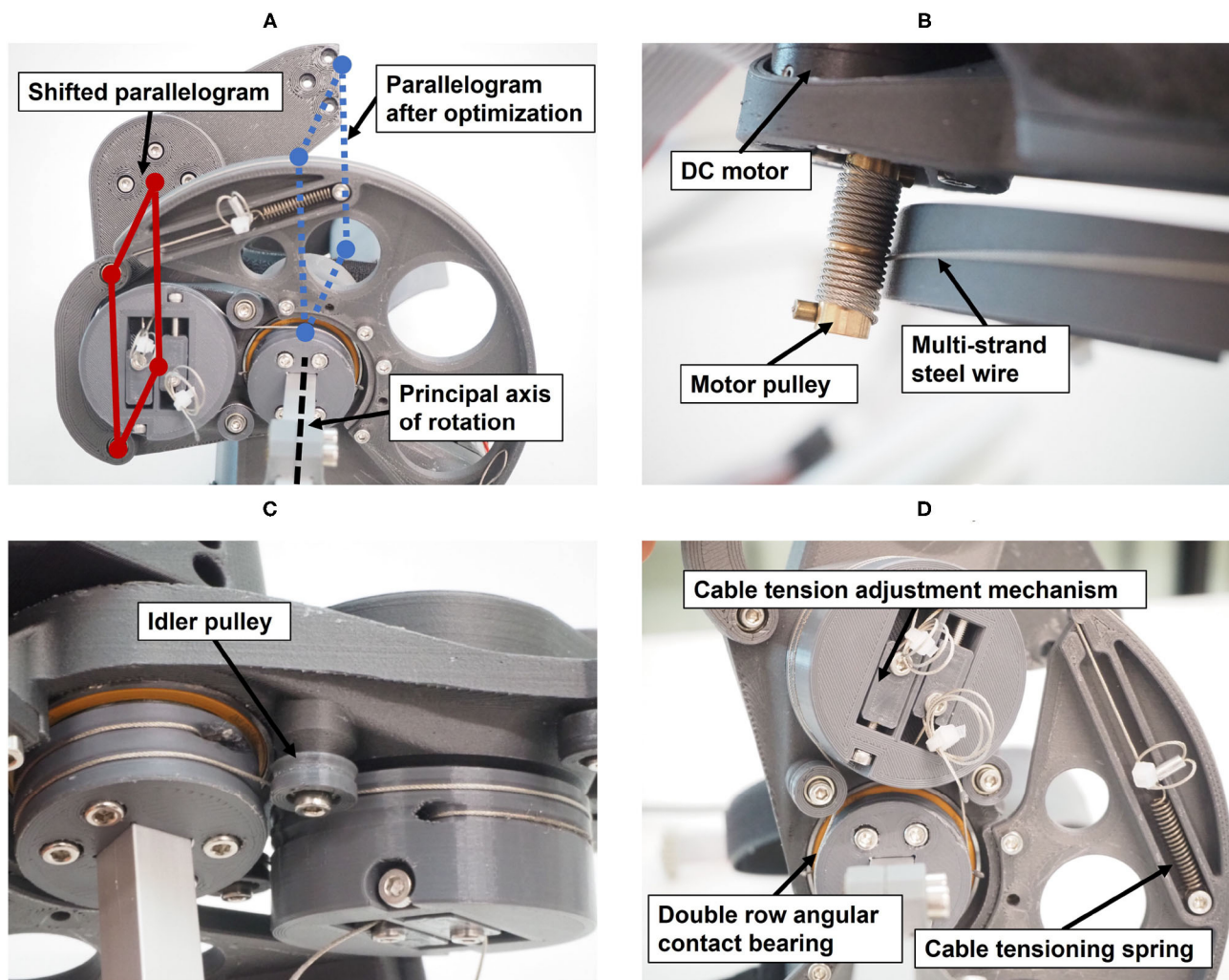
### 3.3. Transparency and Virtual Wall Tests

The transparency test revealed a RMS human-robot interaction force of 2.96 N before the compensation of disturbance forces. The addition of gravity and friction compensation reduced this value to 1.37 N for all movement frequencies—i.e., BPM—combined (Table 1). The results of the repeated measures ANOVA revealed a statistically significant main effect of the compensation ( $p < 0.001$ ) and a non-significant effect of BPM ( $p = 0.055$ ) as well as interaction effect ( $p = 0.094$ ). Hence, the effectiveness of the gravity and friction compensation to enhance transparency was confirmed. Figure 13 shows the interaction forces for each participant as a function of the end-effector position  $\alpha$ .

The stability regions—i.e., the areas beneath the plotted points—resulting from the interaction with virtual walls at different positions ( $\alpha = 60^\circ$ ,  $90^\circ$  and  $120^\circ$ ) are depicted in Figure 14. Note that as the wall position increases—i.e., for larger  $\alpha$ —the stable region becomes larger.

## 4. DISCUSSION

In this article, we present PRIDE (Palmar Rehabilitation DEvice), a novel device for sensorimotor hand rehabilitation based on clinical and anatomical requirements gathered from interviews and questionnaires with clinical personnel. Clinicians reported that special attention should be paid to high usability and effortless setup and that the device should support the practice of finger flexion/extension (Rätz et al., 2021). This is in agreement with the findings of Lang et al., who report that poor grasping performance post-stroke is related to a lack of adequate finger extension ability (Lang et al., 2009). Further requirements were

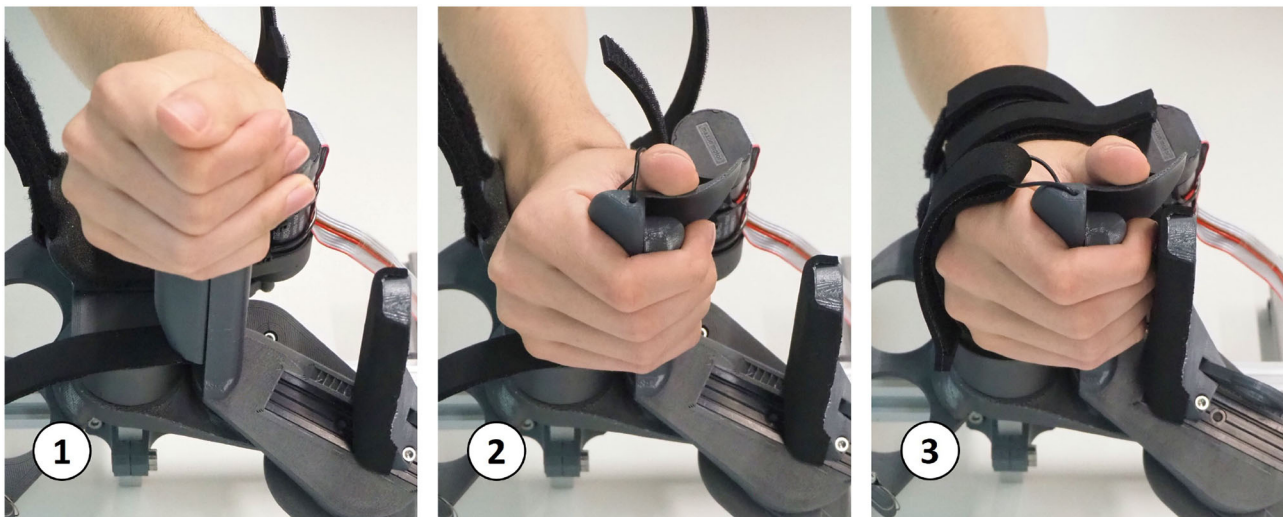


**FIGURE 10 |** Technical details of the prototype: **(A)** View from below showing the shifted parallelogram. **(B)** Actuation of the principal axis of rotation through a capstan transmission. **(C)** Actuation of the parallelogram, including idler pulley for cable guidance. **(D)** Cable tensioning mechanisms.



**FIGURE 11 |** Hand movement sequence from full finger extension to 180° flexion for a hand of size *medium-large*.





**FIGURE 12 |** Setup sequence: a hand with flexed fingers can easily be slid onto the handle. Then, within a few seconds, the wrist and hand straps can be tightened and the fingertip fixation can be adjusted.

**TABLE 1 |** RMS of human-robot interaction forces (N) during continuous finger flexion and extension movements at different frequencies.

Compensation	BPM			
	20	40	60	Combined
Off	3.02 (0.52)	2.90 (0.64)	2.96 (0.71)	2.96 (0.62)
On	1.55 (0.49)	1.36 (0.48)	1.20 (0.47)	1.37 (0.50)

*The values inside the brackets denote the standard deviation.*

established based on anatomical considerations—e.g., different lengths of the individual fingers within a hand—as well as ergonomic aspects in cylindrical grasping. The need for a device with high-quality haptic rendering capabilities to provide sensorimotor neurorehabilitation added further mechanical requirements, e.g., high backdrivability, low backlash, and high transparency.

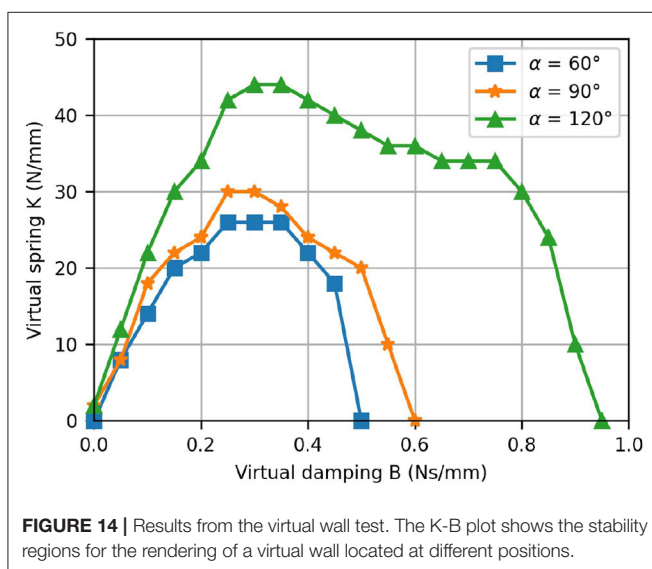
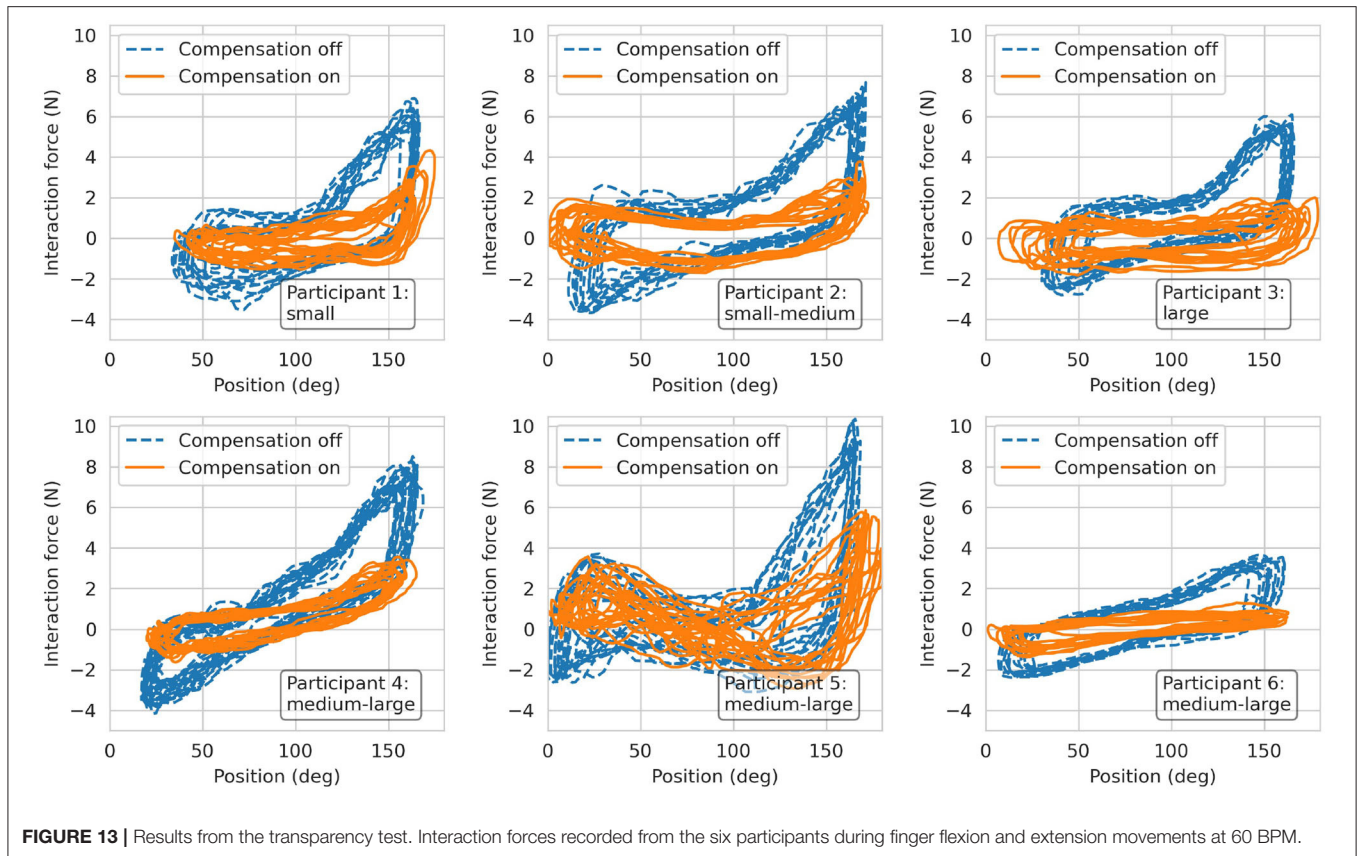
A novel kinematic design based on a novel architecture with only one actuator was developed to meet the gathered clinical, anatomical, and design requirements. To accommodate patients with different hand sizes, our device accurately tracks and supports the fingertip paths of hands of various sizes. To achieve this, we performed an optimization based on anthropometric data from hands of different sizes and anatomical considerations (e.g., constant interjoint coupling) to determine the device mechanical design parameters. In a feasibility test with seven healthy young participants with different hand sizes, the specific functionalities of the device were demonstrated, namely, physiological finger movements with large range of motion, quick setup, high transparency, and fine haptic rendering. In the following subsections, we discuss the novelties of our hand rehabilitation haptic device, the study limitations, and future work.

#### 4.1. Our Palmar Device Allows for an Effortless Installation of the Patient's Hand While Offering Large Physiological Finger Flexion/Extension Motions

The rapidly growing number of published works on hand rehabilitation shows that a great number of hand rehabilitation devices have been developed for research and commercial purposes [see our comparison table in the **Supplementary Material** and (Bos et al., 2016; Gassert and Dietz, 2018)]. Our literature research on hand rehabilitation devices resulted in a total of 54 devices, both commercial [e.g., Amadeo<sup>®</sup> (TyroMotion, Austria), Manovo<sup>®</sup> Power (Hocoma, Switzerland)] or research prototypes (e.g., Taheri et al., 2014; Zhu et al., 2014; Cheng et al., 2018). Nevertheless, only a few of these devices were developed with strong focus on high usability and easy setup (e.g., Masia et al., 2007; Yap et al., 2016; Randazzo et al., 2018; Bützer et al., 2020). While hand exoskeletons are inherently difficult to setup in patients suffering from spasticity due to their complexity (Aggogeri et al., 2019), grounded end-effector devices generally compromise the range of finger motion (e.g., Masia et al., 2007; Zhu et al., 2014; Just et al., 2019) and/or are not able to guarantee physiological movements of the fingers (e.g., Dovat et al., 2008; Hioki et al., 2011; Metzger et al., 2011).

To maximize the clinical applicability and acceptance of our novel device, we collaborated closely with clinical personnel. We began our development by conducting a survey with 33 healthcare professionals while we continuously integrated feedback from therapists in several prototype iterations. The repeatedly mentioned need for an effortless and rapid patient setup from our clinical partners, led us to the development of a palmar device with a compact handle geometry. This allows to install even a clenched hand on the device by sliding it onto the handle, similar to Just et al. (2019). The reported need for intensive training of





finger extension movements motivated us to develop a design that supports finger movements from full flexion up to full extension. Thus, in a minimally actuated device, we could fulfill two important clinical requirements: a quick effortless setup and training of physiological full finger flexion/extension movements.

## 4.2. The Kinematic Solution Ensures That All Fingers Are Supported Through the Full Range of Motion and That the Little Finger Does Not Lose Contact in Finger Extension

To accommodate for the different lengths of the individual fingers of a given hand, the contact points of the fingers with the robot end-effector were defined to lie on a line which was rotated by an angle  $\psi = 25^\circ$  relative to the transverse axis of the hand. This was especially important to not lose contact between the little finger and the robot end-effector during finger extension due to its generally shorter length w.r.t. the other fingers. Keeping the orientation of the longitudinal axis of the end-effector invariant during the entire range of finger motion, resulted in a remarkably natural grasping motion. Our resulting novel kinematic design is—to the best of our knowledge—the first palmar device for sensorimotor hand rehabilitation which supports physiological movements for index, middle, ring and little finger over a range of motion as large as  $\varphi_F \in [0^\circ, 180^\circ]$ .

## 4.3. Our Design Allows for a Natural Cylindrical Grasp

We took into consideration that cylindrical objects are usually grasped such that the longitudinal axis of the object runs obliquely from the MCP joint of the index finger to the base of the hypothenar eminence by rotating the cylindrical handle forwards by  $\psi = 25^\circ$  w.r.t. to  $\hat{z}_{MCP}$ . In combination with the

aforementioned invariant orientation of the longitudinal axis of the end-effector, we ensured that the fingertip of the little finger is more proximal than the fingertip of the index finger through the entire range of motion (see **Figure 11**) which results in a natural, functional cylindrical grasp. To better understand this, it should be noted that the MCP joint of the little finger is generally located in a more proximal and more palmar position than the MCP of the index finger. Further, Hayashi et al., report a higher functional range of motion of the MCP joints of ring and little finger compared to index and middle finger during power grasps (Hayashi and Shimizu, 2013). These findings may explain why the fingertip of the little finger is not only more proximal in full extension—as one might expect due to the shorter length—but along the full motion of a cylindrical grasp up to full flexion.

Yet, even though we achieved a natural cylindrical grasp by tilting the handle and the end-effector, it comes with a drawback: Apart from full finger extension or flexion, the effective finger force applied at the end-effector also has a vertical component along  $\hat{z}_{EE}$ , which is not considered in  $F_F$ —i.e., the finger force  $F_F$  is applied with a certain, position-dependent angle (maximum value of  $25^\circ$  at  $\alpha = 90^\circ$ ) relative to the end-effector. This could potentially result in slipping or sensations of tangential forces on the fingertips.

#### 4.4. The Device Guarantees Physiologically Correct Finger Movements for a Large Variety of Hand Sizes

Due to the achieved large range of motion, our device needed some kind of adjustment for different hand sizes. This is contrary to other palmar devices with a smaller range of motion like the handle of Just et al. (2019) or Alpha-Prototype II (Masia et al., 2007), which do not require any adjustments for different finger sizes (see comparison table in **Supplementary Material**). Nonetheless, based on the clinicians' feedback, we aimed to avoid any adjustments of the moving parts of the device because they would have resulted in a drastical increase of complexity and long setup times (e.g., Schabowsky et al., 2010; Cheng et al., 2018; Marconi et al., 2019). Instead, we engineered several handles—that can be exchanged within a few seconds—to position hands of different sizes such that their respective fingertip paths overlap. These engineered handles allow to position the MCP joints of different hand sizes in optimal locations to grant the device end-effector to track only one common fingertip path, independently of the hand size. To achieve this goal, constant interjoint couplings were considered, which, even if it is a simplification of the biomechanical functioning of the hand, results in physiological movements of the fingers. Intermediate meetings with therapists confirmed that exchangeable handles are appreciated and valued as a considerable advantage compared to adjustment of the device itself. Furthermore, the exchangeability facilitates the cleaning and disinfection of the device, which leads again to shorter setup times.

The synthesis of the mechanical design was performed utilizing a differential evolution optimization algorithm (Storn and Price, 2002) due to the non-convex nature of the problem.

Four representative hand sizes, from small to large according to anthropometric databases (Garrett, 1970a,b; Buchholz et al., 1992; Vergara et al., 2018), were included. The goal was to simultaneously find mechanical design parameters as well as the common fingertip path for various hand sizes. A cost function, consisting of a set of individually weighted functions, was developed to find suitable design parameters. Having too many weights in a cost function can potentially lead to cumbersome and inefficient trial and error tuning of the weights (Yang, 2014). However, each of the utilized individual functions has an intuitive meaning, which allowed us to define the weights with relative ease. This cost function could also have been partially replaced by non-linear constraints. Yet, it would have been challenging to define and justify the bounds of these constraints.

Using this optimization approach, we found design parameters with a mean Cartesian position and angular difference between the optimized points of the finger paths and the end-effector path of 1.14 mm, respectively  $3.77^\circ$ . The higher angular deviations compared to the Cartesian position deviations are desired and can be explained by the attribution of the weights in the cost function, as an angular deviation of  $3^\circ$  was equally penalized as a 1 mm Cartesian deviation in our defined cost function.

With our chosen kinematic design, a certain vertical movement of the end-effector can not be eliminated completely, but we were able to reduce it enough (peak-to-peak less than 1.5 mm) to not be perceptible nor uncomfortable. It has to be noted though, that an even more appropriate movement of the end-effector could possibly be found by actively including the kinematics of all four fingers in the design optimization. However, this would have needed a reliable database for all MCP, PIP, and DIP joint positions and orientations of different hand sizes, as the joint axes of the middle, ring, and little fingers are not parallel to the transverse axis of the hand (Kapandji, 1982).

#### 4.5. PRIDE Allows for High-Quality Haptic Rendering

The large intrinsic mechanical advantage of our design, in combination with the selected capstan cable transmission, allows to achieve high grasping forces without the need for additional gearing to increase the motor torque. As a result, the mechanical transmission is highly backdrivable and transparent. Even though no force sensors were utilized for the control of our novel device, the RMS of the user-robot interaction forces reached a maximum of only 2.96 N during a highly dynamic task. We further significantly reduced these undesirable interaction forces to a maximum of 1.37 N, by modeling, identifying, and compensating the friction and gravitational disturbance forces. These residual forces are on a similar level as other haptic devices for hand rehabilitation, e.g., Metzger et al. declare interaction forces of 1.5 N for the ReHapticKnob (Metzger et al., 2012), Schabowsky et al. report approximately 2 N (with an assumed finger length of 100 mm) for the HEXORR (Schabowsky et al., 2010), and Endo et al. report an impressive 0.1 N per finger for the HIRO III haptic interface (Endo et al., 2011). Unfortunately,

the interaction force has not been systematically reported in any of the other reviewed devices.

The friction compensation could be further ameliorated by improving the speed resolution of our device or by implementing a more sophisticated speed estimation algorithm, e.g., by using first-order adaptive windowing (Janabi-Sharifi et al., 2000) or a Kalman filter (Taheri et al., 2014). The gravity compensation torque estimation could also be improved by using a more accurate model instead of the suggested sinusoidal approximation, e.g., by taking into account all moving parts of the kinematic chain. Finally, bearings with less static friction could be used, or a force sensor could be permanently integrated into the handle to perform closed-loop impedance control, at the expense of a more costly solution.

The measured K-B plot demonstrated the excellent haptic rendering capabilities of our device as the achieved stability regions are comparable to other devices which were specifically built for high-fidelity haptic hand rehabilitation. For the ReHapticKnob, maximum values of  $K = 50 \text{ N/mm}$ , respectively  $B = 0.25 \text{ Ns/mm}$  were reported (Metzger et al., 2012). The ETH Mike achieves values of  $K = 8 \text{ N/mm}$  and  $B = 0.04 \text{ Ns/mm}$  (assuming a lever-arm of 100 mm). In **Figure 14**, it is apparent that the stability region depends on the position of the virtual wall and increases with the position. This can be explained by the varying mechanical advantage, which has two effects. First, it modifies the device inertias and, especially, the reflected inertia of the motor. Second, it also inherently improves the speed resolution as the fingers are more flexed. That said, the fundamental drawbacks of K-B plots should also be noted. The stability of a virtual wall depends on the user interaction—i.e., the admittance of the user's hand. Besides, even though Colgate and Brown provide a definition for the stability of a virtual wall, the wall might be perceived slightly different across different users (Colgate and Brown, 1994).

## 4.6. Study Limitations

Our design procedure suffers from some limitations. First, we did not investigate how more complex interjoint relations (e.g., polynomial) would have affected the mechanical design of the device. By altering the spiral-like movement of the fingertips, this could potentially have resulted in a different end-effector path with lower variation of the mechanical advantage. Furthermore, for our standardized handle sizes, we assumed hand breadths and finger thicknesses to scale proportionally to hand lengths. This might result in inadequate handles, and therefore, suboptimal hand positioning for certain hands. Finally, the choice of 3D printing as manufacturing process, although enabling us to iterate numerous times after feedback from therapists, might have limited the rigidity of the device due to the characteristics of the employed 3D printing materials. Albeit no deflection is visible during normal usage, the (potentially) low stiffness of our 3D printed parts could result in an inaccurate representation of the virtual wall rigidity  $K$  because any deflection of the end-effector caused by deformations of the parts cannot be sensed by the motor encoder.

The device benchmarking also suffers from a couple of limitations. First, for the performed robot-user interaction force

measurements, we assumed that all interactions forces occur orthogonal to the longitudinal direction of the fingertip in the  $xy$ -plane of the end-effector frame. However, especially if the participant's hand was flexed, it is likely that also tangential forces in the direction of  $\hat{x}_{EE}$  were transmitted to the end-effector. This could have influenced the force measurements and might explain the observed between-subjects variance, especially in hand-flexed poses. Secondly, the sample size in the interaction force evaluation was rather small. However, given the highly significant main effect observed in the two-way repeated measures ANOVA, it is unlikely that larger sample sizes and/or any other statistical test (e.g., non-parametric) would have shown a non-significant effect of the friction compensation.

Finally, it is currently possible—for a healthy participant—to actively pull the fingertips out of the fingertip fixation. Although it did not occur by accident during the experiments, participants pointed out that this could be a design limitation. The fingertips are constraint by the palmar end-effector contact surface and the dorsal quick-release finger fixation. This allows for an optimal transmission of the forces that occur during a grasp, but does only slightly restrict movements along the longitudinal fingertip axis. Currently, the cushioning of the dorsal fixation does not account for different diameters of the individual fingers, which results in non-uniform pressure on the fingertips and consequently a suboptimal fingertip fixation.

## 4.7. Future Work

While our prototype is functional, it could be further improved with future work. The compact handle geometry introduced a challenging aspect to the design of the handle: Without a thumb rest, the thumb could easily collide with the fingertips of the fingers attached to the end-effector. This is particularly problematic if the thumb is flexed while the end-effector is in extension. During the movement of the end-effector back to flexion, the thumb could get pinched, which must be strictly prevented. The integration of a thumb rest, which prevents this issue, makes the design of the different handles notably challenging. In future developments, this thumb rest should be addressed and improved. Ideally, the device should be extended by an active or passive mechanism which allows the thumb to move into opposition and/or flexion to practice precision grasp. At the same time, the dorsal fixation of the fingertips could be further ameliorated to rule out any involuntary release of the fingertips, i.e., by extending it to the proximal direction and by improving the cushioning. Future work also includes the development of a solution for training the left hand. A mirrored version will be built to allow for training left and right hands or to perform bi-manual tasks.

Finally, the novel device was designed with high usability and low setup times in mind. Although preliminary tests with healthy participants confirmed that the setup is quick and only takes a few seconds, its usability needs to be evaluated with brain-injured patients with different spasticity levels. In future experiments with brain-injured patients, we will further evaluate the clinical practicability of the design.

## 5. CONCLUSION

In this paper, we presented a novel robotic device for sensorimotor hand rehabilitation. The design is strongly motivated by a set of clinical, anatomical, and mechanical requirements that we established prior to the development. After carrying out the design synthesis via an optimization approach, a functional prototype was built and its haptic capabilities demonstrated in a preliminary test with seven participants. With the clinical-driven design, our robotic hand rehabilitation device has the potential to enable sensorimotor hand rehabilitation for patients with various levels of hand impairment. Moreover, we hope that our design approach will raise the awareness of clinical acceptance and applicability in future research and development of hand rehabilitation devices.

## DATA AVAILABILITY STATEMENT

The datasets presented in this study can be found in online repositories. The names of the repository/repositories and accession number(s) can be found below: <https://zenodo.org/record/5542327>.

## ETHICS STATEMENT

Ethical review and approval was not required for the study on human participants in accordance with the local legislation and institutional requirements. The patients/participants provided their written informed consent to participate in this study.

## AUTHOR CONTRIBUTIONS

RR and LM-C developed the kinematics as well as the mechanical components of the device. RR and RM established the requirements and conducted meetings with therapists from the Department of Neurology, University Hospital Bern

(Inselspital), Switzerland to discuss intermediate prototypes. FC contributed to the development of the motor control electronics and firmware. RR and LM-C edited and revised the manuscript. All authors contributed to the article and approved the submitted version.

## FUNDING

The present research was supported by the Innosuisse grant 32213.1 IP-CT Novel Clinical-Driven Robot-Assisted Sensorimotor Therapy in collaboration with Force Dimension (Switzerland). The funder was not involved in the study design, collection, analysis, interpretation of data, the writing of this article, or the decision to submit it for publication. This work was also supported by the Swiss National Science Foundation through the Grant PP00P2163800.

## ACKNOWLEDGMENTS

The authors are grateful for the numerous fruitful discussions with the therapists of the Department of Neurology, University Hospital Bern (Inselspital), Switzerland. In this regard, special thanks go to Isabelle Lehmann, Irène Thaler, and Magdalena Eichenberger for the organization of the meetings. The authors would also like to thank Gabriel Gruener for his advice regarding the kinematic structure of the device and mathematical representation thereof. Furthermore, the support and advice of Force Dimension (Switzerland)—particularly Patrick Helmer—during the development of the prototype was highly appreciated.

## SUPPLEMENTARY MATERIAL

The Supplementary Material for this article can be found online at: <https://www.frontiersin.org/articles/10.3389/fnbot.2021.748196/full#supplementary-material>

## REFERENCES

- Acharyya, S. K., and Mandal, M. (2009). Performance of EAs for four-bar linkage synthesis. *Mech. Mach. Theory* 44, 1784–1794. doi: 10.1016/j.mechmachtheory.2009.03.003
- Aggogeri, F., Mikolajczyk, T., and O’Kane, J. (2019). Robotics for rehabilitation of hand movement in stroke survivors. *Adv. Mech. Eng.* 11:168781401984192. doi: 10.1177/1687814019841921
- Alnajjar, F., Umari, H., Ahmed, W. K., Gochoo, M., Vogan, A. A., Aljumaily, A., et al. (2021). CHAD: compact hand-assistive device for enhancement of function in hand impairments [Formula presented]. *Robot. Auton. Syst.* 142:103784. doi: 10.1016/j.robot.2021.103784
- Balasubramanian, S., Klein, J., and Burdet, E. (2010). Robot-assisted rehabilitation of hand function. *Curr. Opin. Neurol.* 23, 661–670. doi: 10.1097/WCO.0b013e32833e99a4
- Bernardoni, F., Ozen, O., Buetler, K., and Marchal-Crespo, L. (2019). “Virtual reality environments and haptic strategies to enhance implicit learning and motivation in robot-assisted training,” in *2019 IEEE 16th International Conference on Rehabilitation Robotics (ICORR)* (Toronto, ON: IEEE), 760–765. doi: 10.1109/ICORR.2019.8779420
- Bernstein, N., Lawrence, D., and Pao, L. (2005). “Friction modeling and compensation for haptic interfaces,” in *First Joint Eurohaptics Conference and Symposium on Haptic Interfaces for Virtual Environment and Teleoperator Systems* (Pisa: IEEE), 290–295. doi: 10.1109/WHC.2005.59
- Bertani, R., Melegari, C., De Cola, M. C., Bramanti, A., Bramanti, P., and Calabró, R. S. (2017). Effects of robot-assisted upper limb rehabilitation in stroke patients: a systematic review with meta-analysis. *Neurol. Sci.* 38, 1561–1569. doi: 10.1007/s10072-017-2995-5
- Bionik Labs (2021). *InMotion ARM/HAND*. Available online at: <https://www.bioniklabs.com/products/inmotion-arm-hand> (accessed July 22, 2021).
- Bolognini, N., Russo, C., and Edwards, D. J. (2016). The sensory side of post-stroke motor rehabilitation. *Restorat. Neurol. Neurosci.* 34, 571–586. doi: 10.3233/RNN-150606
- Borboni, A., Mor, M., and Faglia, R. (2016). Gloreha-hand robotic rehabilitation: design, mechanical model, and experiments. *J. Dyn. Syst. Measure. Control Trans. ASME* 138, 111003-1–111003-12. doi: 10.1115/1.4033831
- Bos, R. A., Haarman, C. J., Stortelder, T., Nizamis, K., Herder, J. L., Stienen, A. H., et al. (2016). A structured overview of trends and technologies used in dynamic hand orthoses. *J. Neuroeng. Rehabil.* 13:62. doi: 10.1186/s12984-016-0168-z



- Brütsch, K., Schuler, T., Koenig, A., Zimmerli, L., Koeneke, S. M., Lünenburger, L., et al. (2010). Influence of virtual reality soccer game on walking performance in robotic assisted gait training for children. *J. Neuroeng. Rehabil.* 7. doi: 10.1186/1743-0003-7-15
- Buchholz, B. (1992). A kinematic model of the human hand to evaluate its prehensile capabilities. *J. Biomech.* 25, 149–162. doi: 10.1016/0021-9290(92)90272-3
- Buchholz, B., Taylor, P., Armstrong, T. J., and Goldstein, S. A. (1992). Anthropometric data for describing the kinematics of the human hand. *Ergonomics* 35, 261–273. doi: 10.1080/00140139208967812
- Buongiorno, D., Sotgiu, E., Leonardi, D., Marcheschi, S., Solazzi, M., and Frisoli, A. (2018). WRES: a novel 3 DoF WRist ExoSkeleton with tendon-driven differential transmission for neuro-rehabilitation and teleoperation. *IEEE Robot. Automat. Lett.* 3, 2152–2159. doi: 10.1109/LRA.2018.2810943
- Bützer, T., Lambercy, O., Arata, J., and Gassert, R. (2020). Fully wearable actuated soft exoskeleton for grasping assistance in everyday activities. *Soft Robot.* 8, 128–143. doi: 10.1089/soro.2019.0135
- Cempini, M., Cortese, M., and Vitiello, N. (2015). A powered finger–thumb wearable hand exoskeleton with self-aligning joint axes. *IEEE/ASME Trans. Mechatron.* 20, 705–716. doi: 10.1109/TMECH.2014.2315528
- Cheng, L., Chen, M., and Li, Z. (2018). Design and control of a wearable hand rehabilitation robot. *IEEE Access* 6, 74039–74050. doi: 10.1109/ACCESS.2018.2884451
- Cobos, S., Ferre, M., Sánchez-Urán, M., and Ortego, J. (2007). Constraints for realistic hand manipulation. *Proc. Presence* 2007, 369–370.
- Colgate, J., and Brown, J. (1994). “Factors affecting the Z-Width of a haptic display,” in *Proceedings of the 1994 IEEE International Conference on Robotics and Automation* (San Diego, CA), 3205–3210. doi: 10.1109/ROBOT.1994.351077
- Craig, J. J. (2005). *Introduction to Robotics: Mechanics and Control*. Pearson.
- CyberGlove Systems (2021). *CyberForce*. Available online at: <http://www.cyberglovesystems.com/cyberforce> (accessed July 22, 2021).
- Danion, F., Diamond, J. S., and Flanagan, J. R. (2012). The role of haptic feedback when manipulating nonrigid objects. *J. Neurophysiol.* 107, 433–441. doi: 10.1152/jn.00738.2011
- Decker, M., and Kim, Y. (2017). “A hand exoskeleton device for robot assisted sensory-motor training after stroke,” in *2017 IEEE World Haptics Conference, WHC 2017* (Munich), 436–441. doi: 10.1109/WHC.2017.7989941
- Dovat, L., Lambercy, O., Gassert, R., Maeder, T., Milner, T., Chee, T. L., et al. (2008). HandCARE: a cable-actuated rehabilitation system to train hand function after stroke. *IEEE Trans. Neural Syst. Rehabil. Eng.* 16, 582–591. doi: 10.1109/TNSRE.2008.2010347
- Endo, T., Kawasaki, H., Mouri, T., Ishigure, Y., Shimomura, H., Matsumura, M., et al. (2011). Five-fingered haptic interface robot: HIRO III. *IEEE Trans. Hapt.* 4, 14–27. doi: 10.1109/TOH.2010.62
- Feigin, V. L., Forouzanfar, M. H., Krishnamurthi, R., Mensah, G. A., Connor, M., Bennett, D. A., et al. (2014). Global and regional burden of stroke during 1990–2010: findings from the Global Burden of Disease Study 2010. *Lancet* 383, 245–255. doi: 10.1016/S0140-6736(13)61953-4
- French, B., Thomas, L. H., Coupe, J., McMahon, N. E., Connell, L., Harrison, J., et al. (2016). Repetitive task training for improving functional ability after stroke. *Cochrane Database Syst. Rev.* 11:CD006073. doi: 10.1002/14651858.CD006073.pub3
- Frisoli, A., Simoncini, F., Bergamasco, M., and Salsedo, F. (2007). Kinematic design of a two contact points haptic interface for the thumb and index fingers of the hand. *J. Mech. Des.* 129, 520–529. doi: 10.1115/1.2712219
- Garrett, J. W. (1970a). *Anthropometry of the Air Force Female Hand*. US Department of the Air Force. doi: 10.21236/AD0710202
- Garrett, J. W. (1970b). *Anthropometry of the Hands of Male Air Force Flight Personnel*. US Department of the Air Force. doi: 10.21236/AD0709883
- Gasser, B. W., Bennett, D. A., Durrrough, C. M., and Goldfarb, M. (2017). “Design and preliminary assessment of Vanderbilt hand exoskeleton,” in *IEEE International Conference on Rehabilitation Robotics* (London), 1537–1542. doi: 10.1109/ICORR.2017.8009466
- Gassert, R., and Dietz, V. (2018). Rehabilitation robots for the treatment of sensorimotor deficits: a neurophysiological perspective. *J. Neuroeng. Rehabil.* 15:46. doi: 10.1186/s12984-018-0383-x
- Goulet, V., Li, W., Cheong, H., Iorio, F., and Quimper, C.-G. (2016). “Four-bar linkage synthesis using non-convex optimization,” in *Lecture Notes in Computer Science*, ed M. Rueher (Cham: Springer) 618–635. doi: 10.1007/978-3-319-44953-1\_39
- Hahn, P., Krimmer, H., Hradetzky, A., and Lanz, U. (1995). Quantitative analysis of the linkage between the interphalangeal joints of the index finger. *J. Hand Surg.* 20B, 696–699. doi: 10.1016/S0266-7681(05)80139-1
- Handelzalts, S., Ballardini, G., Avraham, C., Pagano, M., Casadio, M., and Nisky, I. (2021). Integrating tactile feedback technologies into home-based telerehabilitation: opportunities and challenges in light of COVID-19 pandemic. *Front. Neurobot.* 15:617636. doi: 10.3389/fnbot.2021.617636
- Hasegawa, Y., Mikami, Y., Watanabe, K., and Sankai, Y. (2008). “Five-fingered assistive hand with mechanical compliance of human finger,” in *2008 IEEE International Conference on Robotics and Automation* (Pasadena, CA: IEEE), 718–724. doi: 10.1109/ROBOT.2008.4543290
- Hasser, C. J. (1995). Force-reflecting anthropomorphic handmaster requirements. *Am. Soc. Mech. Eng. Dyn. Syst. Control Divis.* 57, 663–674.
- Hatzfeld, C., and Kern, T. A. (2014). *Engineering Haptic Devices - A Beginner's Guide*. London: Springer-Verlag. doi: 10.1007/978-1-4471-6518-7
- Hayashi, H., and Shimizu, H. (2013). Essential motion of metacarpophalangeal joints during activities of daily living. *J. Hand Therapy* 26, 69–74. doi: 10.1016/j.jht.2012.10.004
- Hioki, M., Kawasaki, H., Sakaeda, H., Nishimoto, Y., and Mouri, T. (2011). Finger rehabilitation support system using a multifingered haptic interface controlled by a surface electromyogram. *J. Robot.* 2011, 1–10. doi: 10.1155/2011/167516
- Ho, N. S. K., Tong, K. Y., Hu, X. L., Fung, K. L., Wei, X. J., Rong, W., et al. (2011). “An EMG-driven exoskeleton hand robotic training device on chronic stroke subjects: task training system for stroke rehabilitation,” in *2011 IEEE International Conference on Rehabilitation Robotics* (Zürich: IEEE), 1–5. doi: 10.1109/ICORR.2011.5975340
- Hocoma (2021). *ManovoPower*. Available online at: <https://www.hocoma.com/solutions/armeo-power/modules/> (accessed July 22, 2021).
- Hong, M. B., Kim, S. J., Ihn, Y. S., Jeong, G.-C., and Kim, K. (2019). KULEX-hand: an underactuated wearable hand for grasping power assistance. *IEEE Trans. Robot.* 35, 420–432. doi: 10.1109/TRO.2018.2880121
- Huang, F. C., Gillespie, R. B., and Kuo, A. D. (2007). Visual and haptic feedback contribute to tuning and online control during object manipulation. *J. Motor Behav.* 39, 179–193. doi: 10.3200/JMBR.39.3.179-193
- Huang, H., Zhu, A., Song, J., Tu, Y., Shi, X., and Guo, Z. (2020). “Characterization and evaluation of a cable-actuated flexible hand exoskeleton,” in *2020 17th International Conference on Ubiquitous Robots, UR 2020* (Kyoto), 56–61. doi: 10.1109/UR49135.2020.9144871
- Hunter, S., and Crome, P. (2002). Hand function and stroke. *Rev. Clin. Gerontol.* 12, 68–81. doi: 10.1017/S0959259802012194
- Janabi-Sharifi, F., Hayward, V., and Chen, C.-S. (2000). Discrete-time adaptive windowing for velocity estimation. *IEEE Trans. Control Syst. Technol.* 8, 1003–1009. doi: 10.1109/87.880606
- Jo, I., Lee, J., Park, Y., and Bae, J. (2017). “Design of a wearable hand exoskeleton for exercising flexion/extension of the fingers,” in *2017 International Conference on Rehabilitation Robotics (ICORR)* (London: IEEE), 1615–1620. doi: 10.1109/ICORR.2017.8009479
- Just, F., Gunz, D., Duarte, J., Simonetti, D., Riener, R., and Rauter, G. (2019). “Improving usability of rehabilitation robots: hand module evaluation of the ARMin exoskeleton,” in *Biosystems & Biorobotics*, eds M. Carrozza, S. Micera, and J. Pons (Cham: Springer International Publishing), 80–84. doi: 10.1007/978-3-030-01887-0\_16
- Just, F., Özen, Ö., Bösch, P., Bobrovsky, H., Klamroth-Marganska, V., Riener, R., et al. (2018). Exoskeleton transparency: feed-forward compensation vs. disturbance observer. *Automatisierungstechnik* 66, 1014–1026. doi: 10.1515/auto-2018-0069
- Kamper, D. G., Fischer, H. C., Cruz, E. G., and Rymer, W. Z. (2006). Weakness is the primary contributor to finger impairment in chronic stroke. *Arch. Phys. Med. Rehabil.* 87, 1262–1269. doi: 10.1016/j.apmr.2006.05.013
- Kapandji, I. A. (1982). *Physiology of the Joints, Volume 1, Upper Limb*. 5th edition. Edn. H.
- Kim, D. H., and Park, H.-S. (2018). “Cable actuated dexterous (CADEX) glove for effective rehabilitation of the hand for patients with neurological diseases,”

- in 2018 *IEEE/RSJ International Conference on Intelligent Robots and Systems (IROS)* (Madrid: IEEE), 2305–2310. doi: 10.1109/IROS.2018.8594336
- Kuch, J., and Huang, T. (1995). "Vision based hand modeling and tracking for virtual teleconferencing and telecollaboration," in *Proceedings of IEEE International Conference on Computer Vision* (Cambridge, MA), 666–671. doi: 10.1109/ICCV.1995.466875
- Kwakkel, G., van Peppen, R., Wagenaar, R. C., Wood Dauphinee, S., Richards, C., Ashburn, A., et al. (2004). Effects of augmented exercise therapy time after stroke. *Stroke* 35, 2529–2539. doi: 10.1161/01.STR.0000143153.76460.7d
- Lai, S.-M., Studenski, S., Duncan, P. W., and Perera, S. (2002). Persisting consequences of stroke measured by the stroke impact scale. *Stroke* 33, 1840–1844. doi: 10.1161/01.STR.0000019289.15440.F2
- Lang, C. E., DeJong, S. L., and Beebe, J. A. (2009). Recovery of thumb and finger extension and its relation to grasp performance after stroke. *J. Neurophysiol.* 102, 451–459. doi: 10.1152/jn.91310.2008
- Lang, C. E., Wagner, J. M., Bastian, A. J., Hu, Q., Edwards, D. F., Sahrmann, S. A., et al. (2005). Deficits in grasp versus reach during acute hemiparesis. *Exp. Brain Res.* 166, 126–136. doi: 10.1007/s00221-005-2350-6
- Lee, S. W., Landers, K. A., and Park, H. S. (2014). Development of a biomimetic hand exotendon device (BiomHED) for restoration of functional hand movement post-stroke. *IEEE Trans. Neural Syst. Rehabil. Eng.* 22, 886–898. doi: 10.1109/TNSRE.2014.2298362
- Leonardis, D., Barsotti, M., Loconsole, C., Solazzi, M., Troncosi, M., Mazzotti, C., et al. (2015). An EMG-controlled robotic hand exoskeleton for bilateral rehabilitation. *IEEE Trans. Hapt.* 8, 140–151. doi: 10.1109/TOH.2015.2417570
- Li, J., Zheng, R., Zhang, Y., and Yao, J. (2011). iHandRehab: an interactive hand exoskeleton for active and passive rehabilitation. *IEEE Int. Conf. Rehabil. Robot.* 2011:5975387. doi: 10.1109/ICORR.2011.5975387
- Lo, A. C., Guarino, P. D., Richards, L. G., Haselkorn, J. K., Wittenberg, G. F., Federman, D. G., et al. (2010). Robot-assisted therapy for long-term upper-limb impairment after stroke. *N. Engl. J. Med.* 362, 1772–1783. doi: 10.1056/NEJMoa0911341
- Lotze, M. (2003). Motor learning elicited by voluntary drive. *Brain* 126, 866–872. doi: 10.1093/brain/awg079
- Loureiro, R. C., and Harwin, W. S. (2007). "Reach & grasp therapy: design and control of a 9-DOF robotic neuro-rehabilitation system," in 2007 *IEEE 10th International Conference on Rehabilitation Robotics* (Noordwijk: IEEE), 757–763. doi: 10.1109/ICORR.2007.4428510
- Mali, U., and Munih, M. (2006). HIFE-haptic interface for finger exercise. *IEEE/ASME Trans. Mechatron.* 11, 93–102. doi: 10.1109/TMECH.2005.863363
- Marconi, D., Baldoni, A., McKinney, Z., Cempini, M., Crea, S., and Vitiello, N. (2019). A novel hand exoskeleton with series elastic actuation for modulated torque transfer. *Mechatronics* 61, 69–82. doi: 10.1016/j.mechatronics.2019.06.001
- Masia, L., Krebs, H. I., Cappa, P., and Hogan, N. (2007). Design and characterization of hand module for whole-arm rehabilitation following stroke. *IEEE/ASME Trans. Mechatron.* 12, 399–407. doi: 10.1109/TMECH.2007.901928
- Mentzel, M., Benlic, A., Wachter, N. J., Gulkin, D., Bauknecht, S., and Gülke, J. (2011). The dynamics of motion sequences of the finger joints during fist closure. *Handchirurgie Mikrochirurgie Plastische Chirurgie* 43, 147–154. doi: 10.1055/s-0031-1271804
- Mercier, L., Audet, T., Hebert, R., Rochette, A., and Dubois, M.-F. (2001). Impact of motor, cognitive, and perceptual disorders on ability to perform activities of daily living after stroke. *Stroke* 32, 2602–2608. doi: 10.1161/hs1101.098154
- Metzger, J.-C., Lambercy, O., Chapuis, D., and Gassert, R. (2011). "Design and characterization of the ReHapticKnob, a robot for assessment and therapy of hand function," in 2011 *IEEE/RSJ International Conference on Intelligent Robots and Systems* (San Francisco, CA), 3074–3080. doi: 10.1109/IROS.2011.6094882
- Metzger, J.-C., Lambercy, O., and Gassert, R. (2012). "High-fidelity rendering of virtual objects with the ReHapticKnob - novel avenues in robot-assisted rehabilitation of hand function," in 2012 *IEEE Haptics Symposium (HAPTICS)* (Vancouver, BC: IEEE), 51–56. doi: 10.1109/HAPTIC.2012.6183769
- Meyer, S., Karttunen, A. H., Thijs, V., Feys, H., and Verheyden, G. (2014). How do somatosensory deficits in the arm and hand relate to upper limb impairment, activity, and participation problems after stroke? A systematic review. *Phys. Therapy* 94, 1220–1231. doi: 10.2522/ptj.20130271
- Napier, J. R. (1956). The prehensile movements of the human hand. *J. Bone Joint Surg.* 38, 902–913. doi: 10.1302/0301-620X.38B4.902
- NASA (1995). *Man-Systems Integration Standards - Anthropometry and Biomechanics*. Available online at: <https://msis.jsc.nasa.gov/sections/section03.htm> (accessed July 21, 2021).
- Nielsen, J. B., Willerslev-Olsen, M., Christiansen, L., Lundbye-Jensen, J., and Lorentzen, J. (2015). Science-based neurerehabilitation: recommendations for neurerehabilitation from basic science. *J. Motor Behav.* 47, 7–17. doi: 10.1080/00222895.2014.931273
- Nycz, C. J., Meier, T. B., Carvalho, P., Meier, G., and Fischer, G. S. (2018). Design criteria for hand exoskeletons: measurement of forces needed to assist finger extension in traumatic brain injury patients. *IEEE Robot. Automat. Lett.* 3, 3285–3292. doi: 10.1109/LRA.2018.2852769
- Özen, Ö., Buetler, K. A., and Marchal-Crespo, L. (2021). Promoting motor variability during robotic assistance enhances motor learning of dynamic tasks. *Front. Neurosci.* 14:600059. doi: 10.3389/fnins.2020.600059
- Peñuñuri, F., Peón-Escalante, R., Villanueva, C., and Pech-Oy, D. (2011). Synthesis of mechanisms for single and hybrid tasks using differential evolution. *Mech. Mach. Theory* 46, 1335–1349. doi: 10.1016/j.mechmachtheory.2011.05.013
- Pezent, E., Rose, C. G., Deshpande, A. D., and O'Malley, M. K. (2017). "Design and characterization of the OpenWrist: A robotic wrist exoskeleton for coordinated hand-wrist rehabilitation," in 2017 *International Conference on Rehabilitation Robotics (ICORR)* (Pezent: IEEE), 720–725. doi: 10.1109/ICORR.2017.8009333
- Popov, D., Gaponov, I., and Ryu, J. H. (2017). Portable exoskeleton glove with soft structure for hand assistance in activities of daily living. *IEEE/ASME Trans. Mechatron.* 22, 865–875. doi: 10.1109/TMECH.2016.2641932
- Pu, S. W., Pei, Y. C., and Chang, J. Y. (2020). Decoupling finger joint motion in an exoskeletal hand: a design for robot-assisted rehabilitation. *IEEE Trans. Indus. Electron.* 67, 686–697. doi: 10.1109/TIE.2019.2912793
- Randazzo, L., Iturrate, I., Perdakis, S., and Millán, J. D. (2018). Mano: a wearable hand exoskeleton for activities of daily living and neurerehabilitation. *IEEE Robot. Automat. Lett.* 3, 500–507. doi: 10.1109/LRA.2017.2771329
- Rätz, R., Müri, R. M., and Marchal-Crespo, L. (2021). "Assessment of clinical requirements for a novel robotic device for upper-limb sensorimotor rehabilitation after stroke," in *Proceedings of the 5th International Conference on Neurerehabilitation (ICNR2020)*, eds D. Torricelli, M. Akay, and J. L. Pons (Vigo: Springer International Publishing).
- Rickert, M. (2010). *Funktionelle normwerte und einflussfaktoren an unterarm und hand gesunder männlicher erwachsener* (Ph.D. thesis). Ludwig-Maximilians-Universität München, Munich, Germany.
- Rowe, J. B., Chan, V., Ingemanson, M. L., Cramer, S. C., Wolbrecht, E. T., and Reinkensmeyer, D. J. (2017). Robotic assistance for training finger movement using a hebbian model: a randomized controlled trial. *Neurerehabil. Neural Repair* 31, 769–780. doi: 10.1177/1545968317721975
- Sandoval-Gonzalez, O., Jacinto-Villegas, J., Herrera-Aguilar, I., Portillo-Rodriguez, O., Tripicchio, P., Hernandez-Ramos, M., et al. (2016). Design and development of a hand exoskeleton robot for active and passive rehabilitation. *Int. J. Adv. Robot. Syst.* 13. doi: 10.5772/62404
- Sarac, M., Solazzi, M., and Frisoli, A. (2019). Design requirements of generic hand exoskeletons and survey of hand exoskeletons for rehabilitation, assistive, or haptic use. *IEEE Trans. Hapt.* 12, 400–413. doi: 10.1109/TOH.2019.2924881
- Sarac, M., Solazzi, M., Sotgiu, E., Bergamasco, M., and Frisoli, A. (2016). Design and kinematic optimization of a novel underactuated robotic hand exoskeleton. *Meccanica* 52, 749–761. doi: 10.1007/s11012-016-0530-z
- Schabowsky, C. N., Godfrey, S. B., Holley, R. J., and Lum, P. S. (2010). Development and pilot testing of HEXORR: hand EXOskeleton rehabilitation robot. *J. Neuroeng. Rehabil.* 7:36. doi: 10.1186/1743-0003-7-36
- Sooraj, R., Akshay, N., Jeevan, T. G., and Bhavani, R. R. (2013). Design and analysis of a parallel haptic orthosis for upper limb rehabilitation. *Int. J. Eng. Technol.* 5, 444–451.
- Storn, R., and Price, K. (2002). Differential evolution - a simple and efficient adaptive scheme for global optimization over continuous spaces. *Entomol. Exp. Appl.* 103, 239–248. doi: 10.1023/A:1008202821328
- Taheri, H., Rowe, J. B., Gardner, D., Chan, V., Gray, K., Bower, C., et al. (2014). Design and preliminary evaluation of the FINGER rehabilitation robot: controlling challenge and quantifying finger individuation during musical computer game play. *J. Neuroeng. Rehabil.* 11:10. doi: 10.1186/1743-0003-11-10

- Tollár, J., Nagy, F., Csutorás, B., Prontvai, N., Nagy, Z., Török, K., et al. (2021). High frequency and intensity rehabilitation in 641 subacute ischemic stroke patients. *Arch. Phys. Med. Rehabil.* 102, 9–18. doi: 10.1016/j.apmr.2020.07.012
- Tsai, Y.-L., Huang, J.-J., Pu, S.-W., Chen, H.-P., Hsu, S.-C., Chang, J.-Y., et al. (2019). Usability assessment of a cable-driven exoskeletal robot for hand rehabilitation. *Front. Neurobot.* 13:3. doi: 10.3389/fnbot.2019.00003
- Turville, M. L., Cahill, L. S., Matyas, T. A., Blennerhassett, J. M., and Carey, L. M. (2019). The effectiveness of somatosensory retraining for improving sensory function in the arm following stroke: a systematic review. *Clin. Rehabil.* 33, 834–846. doi: 10.1177/0269215519829795
- TyroMotion (2021). *Amadeo*. Available online at: <https://tyromotion.com/en/products/amadeo/> (accessed July 22, 2021).
- Ueki, S., Kawasaki, H., Ito, S., Nishimoto, Y., Abe, M., Aoki, T., et al. (2012). Development of a hand-assist robot with multi-degrees-of-freedom for rehabilitation therapy. *IEEE/ASME Trans. Mechatron.* 17, 136–146. doi: 10.1109/TMECH.2010.2090353
- Urban, P. P., Wolf, T., Uebele, M., Marx, J. J., Vogt, T., Stoeter, P., et al. (2010). Occurrence and clinical predictors of spasticity after ischemic stroke. *Stroke* 41, 2016–2020. doi: 10.1161/STROKEAHA.110.581991
- Vallbo, A. B., and Johansson, R. S. (1984). Neurobiology related to touch sensation. *Hum. Neurobiol.* 3, 3–14.
- Van Der Hulst, F. P., Schätzle, S., Preusche, C., and Schiele, A. (2012). “A functional anatomy based kinematic human hand model with simple size adaptation,” in *Proceedings - IEEE International Conference on Robotics and Automation* (St Paul, MN), 5123–5129. doi: 10.1109/ICRA.2012.6225350
- Van Dijk, W., Van Der Kooij, H., Koopman, B., Van Asseldonk, E. H., and Van Der Kooij, H. (2013). “Improving the transparency of a rehabilitation robot by exploiting the cyclic behaviour of walking,” in *IEEE International Conference on Rehabilitation Robotics*. doi: 10.1109/ICORR.2013.6650393
- Veerbeek, J. M., Langbroek-Amersfoort, A. C., van Wegen, E. E. H., Meskers, C. G. M., and Kwakkel, G. (2017). Effects of robot-assisted therapy for the upper limb after stroke. *Neurorehabil. Neural Repair* 31, 107–121. doi: 10.1177/1545968316666957
- Vergara, M., Agost, M. J., and Gracia-Ibáñez, V. (2018). Dorsal and palmar aspect dimensions of hand anthropometry for designing hand tools and protections. *Hum. Fact. Ergon. Manuf. Serv. Indus.* 28, 17–28. doi: 10.1002/hfm.20714
- Virtanen, P., Gommers, R., Oliphant, T. E., Haberland, M., Reddy, T., Cournapeau, D., et al. (2020). SciPy 1.0: fundamental algorithms for scientific computing in Python. *Nat. Methods* 17, 261–272. doi: 10.1038/s41592-020-0772-5
- Wang, D., Meng, Q., Meng, Q., Li, X., and Yu, H. (2018). Design and development of a portable exoskeleton for hand rehabilitation. *IEEE Trans. Neural Syst. Rehabil. Eng.* 26, 2376–2386. doi: 10.1109/TNSRE.2018.2878778
- Wiker, S. F., Elaine, H., and Zik, J. (1989). “Teleoperator comfort and psychometric stability: criteria for limiting master-controller forces of operation and feedback during telemanipulation,” in *NASA Conference on Space Telerobotics*, 99–107.
- Xu, D., Wu, Q., and Zhu, Y. (2020). Development of a soft cable-driven hand exoskeleton for assisted rehabilitation training. *Indus. Robot* 48, 189–198. doi: 10.1108/IR-06-2020-0127
- Yang, J., Xie, H., and Shi, J. (2016). A novel motion-coupling design for a jointless tendon-driven finger exoskeleton for rehabilitation. *Mech. Mach. Theory* 99, 83–102. doi: 10.1016/j.mechmachtheory.2015.12.010
- Yang, X.-S. (2014). “Multi-objective optimization,” in *Nature-Inspired Optimization Algorithms* (Oxford: Elsevier), 197–211. doi: 10.1016/B978-0-12-416743-8.00014-2
- Yap, H. K., Lim, J. H., Goh, J. C. H., and Yeow, C.-H. (2016). Design of a soft robotic glove for hand rehabilitation of stroke patients with clenched fist deformity using inflatable plastic actuators. *J. Med. Dev.* 10, 5–10. doi: 10.1115/1.4033035
- Zhang, F., Hua, L., Fu, Y., Chen, H., and Wang, S. (2014). Design and development of a hand exoskeleton for rehabilitation of hand injuries. *Mech. Mach. Theory* 73, 103–116. doi: 10.1016/j.mechmachtheory.2013.10.015
- Zhang, Y., Deng, H., and Zhong, G. (2018). Humanoid design of mechanical fingers using a motion coupling and shape-adaptive linkage mechanism. *J. Bionic Eng.* 15, 94–105. doi: 10.1007/s42235-017-0007-3
- Zhu, T. L., Klein, J., Dual, S. A., Leong, T. C., and Burdet, E. (2014). “ReachMAN2: a compact rehabilitation robot to train reaching and manipulation,” in *IEEE International Conference on Intelligent Robots and Systems (IROS)* (Chicago, IL), 2107–2113. doi: 10.1109/IROS.2014.6942845

**Conflict of Interest:** FC is currently employed by Force Dimension (Switzerland), which provided the motors and drivers for the mechanical realization of the prototype as part of their engagement as industrial partner in the Innosuisse project 32213.1 IP-CT “Novel Clinical-Driven Robot-Assisted Sensorimotor Therapy.” The involvement of FC was limited to the development of the prototype and verification of the technical correctness of the manuscript. Our work does neither evaluate, nor promote any commercial devices of Force Dimension.

The remaining authors declare that the research was conducted in the absence of any commercial or financial relationships that could be construed as a potential conflict of interest.

**Publisher’s Note:** All claims expressed in this article are solely those of the authors and do not necessarily represent those of their affiliated organizations, or those of the publisher, the editors and the reviewers. Any product that may be evaluated in this article, or claim that may be made by its manufacturer, is not guaranteed or endorsed by the publisher.

Copyright © 2021 Rätz, Conti, Müri and Marchal-Cresco. This is an open-access article distributed under the terms of the Creative Commons Attribution License (CC BY). The use, distribution or reproduction in other forums is permitted, provided the original author(s) and the copyright owner(s) are credited and that the original publication in this journal is cited, in accordance with accepted academic practice. No use, distribution or reproduction is permitted which does not comply with these terms.



# Development and Electromyographic Validation of a Compliant Human-Robot Interaction Controller for Cooperative and Personalized Neurorehabilitation

Stefano Dalla Gasperina<sup>1,2\*</sup>, Valeria Longatelli<sup>1,2</sup>, Francesco Braghin<sup>2,3</sup>,  
Alessandra Pedrocchi<sup>1,2†</sup> and Marta Gandolla<sup>1,2</sup>

<sup>1</sup> NeuroEngineering and Medical Robotics Laboratory (NearLab), Department of Electronics, Information and Bioengineering, Politecnico di Milano, Milan, Italy, <sup>2</sup> WE-COBOT Lab, Polo Territoriale di Lecco, Politecnico di Milano, Lecco, Italy,

<sup>3</sup> Department of Mechanical Engineering, Politecnico di Milano, Milan, Italy

## OPEN ACCESS

### Edited by:

Massimo Sartori,  
University of Twente, Netherlands

### Reviewed by:

Sang Wook Lee,  
The Catholic University of America,  
United States

Suncheol Kwon,  
National Rehabilitation Center,  
South Korea  
Arvid Keemink,  
University of Twente, Netherlands

### \*Correspondence:

Stefano Dalla Gasperina  
stefano.dallagasperina@polimi.it

### †ORCID:

Stefano Dalla Gasperina  
orcid.org/0000-0002-3466-8397  
Alessandra Pedrocchi  
orcid.org/0000-0001-9957-2786

**Received:** 30 June 2021

**Accepted:** 12 November 2021

**Published:** 18 January 2022

### Citation:

Dalla Gasperina S, Longatelli V,  
Braghin F, Pedrocchi A and  
Gandolla M (2022) Development and  
Electromyographic Validation of a  
Compliant Human-Robot Interaction  
Controller for Cooperative and  
Personalized Neurorehabilitation.  
*Front. Neurobot.* 15:734130.  
doi: 10.3389/fnbot.2021.734130

**Background:** Appropriate training modalities for post-stroke upper-limb rehabilitation are key features for effective recovery after the acute event. This study presents a cooperative control framework that promotes compliant motion and implements a variety of high-level rehabilitation modalities with a unified low-level explicit impedance control law. The core idea is that we can change the haptic behavior perceived by a human when interacting with the rehabilitation robot by tuning three impedance control parameters.

**Methods:** The presented control law is based on an impedance controller with direct torque measurement, provided with positive-feedback compensation terms for disturbances rejection and gravity compensation. We developed an elbow flexion-extension experimental setup as a platform to validate the performance of the proposed controller to promote the desired high-level behavior. The controller was first characterized through experimental trials regarding joint transparency, torque, and impedance tracking accuracy. Then, to validate if the controller could effectively render different physical human-robot interaction according to the selected rehabilitation modalities, we conducted tests on 14 healthy volunteers and measured their muscular voluntary effort through surface electromyography (sEMG). The experiments consisted of one degree-of-freedom elbow flexion/extension movements, executed under six high-level modalities, characterized by different levels of (i) corrective assistance, (ii) weight counterbalance assistance, and (iii) resistance.

**Results:** The unified controller demonstrated suitability to promote good transparency and render both compliant and stiff behavior at the joint. We demonstrated through electromyographic monitoring that a proper combination of stiffness, damping, and weight assistance could induce different user participation levels, render different physical human-robot interaction, and potentially promote different rehabilitation training modalities.

**Conclusion:** We proved that the proposed control framework could render a wide variety of physical human-robot interaction, helping the user to accomplish the task while



exploiting physiological muscular activation patterns. The reported results confirmed that the control scheme could induce different levels of the subject's participation, potentially applicable to the clinical practice to adapt the rehabilitation treatment to the subject's progress. Further investigation is needed to validate the presented approach to neurological patients.

**Keywords:** neurorehabilitation, human robotics, compliant control, impedance control, electromyography, physical human-robot interaction

## 1. INTRODUCTION

Worldwide, stroke is a leading cause of death and permanent disability (Johnson et al., 2016). Although the global mortality of stroke has decreased in the past decades, the incidence and the effects of the disease are expected to increase (Gorelick, 2019). Consequently, the burden of stroke is still likely to produce long-term impairment, limitations during activities of daily living, and compromise the social participation of most stroke survivors. In most cases, rehabilitation treatment is required for an effective recovery, besides partial spontaneous recovery. Indeed, physical therapy fosters the motor relearning process during post-stroke rehabilitation. Nevertheless, only 5–20% of people with initial upper limb impairment after stroke completely recover lost functionalities (French et al., 2016). In the past years, the literature proposed upper limb robot-assisted rehabilitation as a method to stimulate motor relearning through repetitive, high-intensity, and task-oriented functional training (Winstein et al., 2016; Duret et al., 2019). Since the 90s, several upper-limb robotic devices have been designed, but only a few of them effectively reached the market, probably due to controversial results obtained in clinical trials (Ambrosini et al., 2019).

Recent systematic reviews show that robotic rehabilitation could produce better, or at least equivalent, outcomes than conventional therapy in both the International Classification of Functioning, Disability and Health (ICF) Body and Activity domains (Veerbeek et al., 2017; Mehrholz et al., 2018, 2020). Moreover, given that traditional passive mobilization limits neuroplasticity, a more customizable and adaptable control approach, facilitating subject's engagement and motivation, could lead to better effectiveness of the treatment (Marchal-Crespo and Reinkensmeyer, 2009). Thus, the effectiveness of the robotic rehabilitation therapy strongly depends on the capability of the system to guide natural coordinated motion, promote physiological muscular contraction, and induce the patient to cooperate as much as possible. This is why a key component of effective robot-mediated therapy is a good cooperative and adaptable control solution, which can be tailored to the single user being able to follow his/her progress.

With this study, we first analyze the robot-mediated rehabilitation modalities proposed in the literature. We investigate the availability of low-level control strategies that can be exploited to promote the desired haptics and physical human-robot interaction. Finally, we present the description of a low-level unified controller for upper-limb rehabilitation that is capable of assisting patients in a compliant manner and that

promotes most of the robot-mediated training modalities used in clinics.

The fundamental concept of the proposed approach relies on the availability of a unified compliant controller, which could change the level of assistance and resistance according to the patient's performances and contribution, toward the paradigms of personalization and continuity of care. The core idea is that by tuning three control parameters, we can change the perceived haptics of the test-bed when interacting with the human arm. We validated this concept by monitoring surface EMG while asking (healthy) subjects to modulate their volitional contribution to correctly fulfill the required task.

### 1.1. Structure of the Study

This study is structured as follows. Section 2 defines the rehabilitation training modalities used in upper-limb robot-assisted therapy and their low-level control implementation challenges. The core idea of this study is presented in section 3, which explains how high-level modalities have been integrated with a low-level unified compliant controller. Section 4 presents the experimental design implemented to test the controller, and the results are exposed in section 5. Finally, sections 6 and 7 draw the discussion and conclusion of the Chapter.

## 2. RELATED STUDY AND NOVEL CONTRIBUTION

### 2.1. Robot-Mediated Rehabilitation

Robot-mediated rehabilitation has been largely investigated since the 1990s. The literature agrees that the goal of robots should be to induce motor plasticity in subjects undergoing rehabilitation treatment and, therefore, to improve their motor recovery (Huang and Krakauer, 2009). Therefore, robot-mediated control algorithms were designed and developed, taking inspiration from motor learning and neurophysiological aspects (Krakauer, 2006; Reinkensmeyer et al., 2016; Iandolo et al., 2019). Consequently, different high-level training modalities were proposed to promote motor recovery at different stages of the disease. Such modalities are in turn embodied by low-level controllers that are capable of shaping the physical human-robot interaction (pHRI) according to the residual capabilities of the user, i.e., the aim of researchers is to design controllers that minimize the interaction forces between the robot and the human while motivating the subject and guaranteeing the completion of the rehabilitation task. In other words, the robot should cooperate with the patient

along with the rehabilitation treatment as a therapist would do, changing the levels of assistance, resistance, and motion correction based on the progression of the motor recovery. Over the past decade, several reviews on exoskeletal control for robot-assisted rehabilitation have been proposed in the literature. However, the researchers proposed several taxonomies and categorizations at various levels of abstraction (Marchal-Crespo and Reinkensmeyer, 2009; Basteris et al., 2014; Meng et al., 2015; Gull et al., 2020). In this study, we will use the term “training modalities” for “high-level” desired rehabilitation behaviors and the term “control strategies” for their “low-level” control scheme implementation. Generally, the training modalities for upper-limb rehabilitation are characterized by three main features: (i) corrective assistance, which implies that, given a pre-defined task, the system also corrects the movement when the subject moves away from the desired trajectory; (ii) weight counterbalance assistance, which refers to the ability of the robot to support and compensate the weight and the dynamics of the impaired limb; and (iii) resistance, which relates to training strategies that make the movement more difficult to perform, thus engaging the subject and stimulating the motor control learning process (Basteris et al., 2014; Proietti et al., 2016). When describing the cooperation between robot and human, in this study, we propose a terminology that describes the expected subject's behavior during interaction. For example, “Passive mode” will refer to subject-passive/robot-active training.

On top of these general definitions, it can be observed that one of the most critical areas in rehabilitation robotics is implementing the desired high-level modalities within the robot's hardware.

## 2.2. The Role of Compliant Control in Neurorehabilitation

Our concept relies on the concept of compliant and cooperative motion, i.e., the robot should behave transparently with respect to human activity, and eventually enhance user-driven movements. Compliant motion, by definition refers to the capability of the robotic system to generate movement and, simultaneously, undergo movement if external forces are applied. Typically, the perceived compliance can be implemented either through mechanical compliance, for example by using soft joints instead of rigid joints, or through compliant controllers (Calanca et al., 2016; Keemink et al., 2018). Moreover, these approaches intrinsically improve back-drivability and safety during human-robot interaction (Vallery et al., 2008).

From a low-level point of view, achieving compliant motion is a fundamental, yet challenging, task in rehabilitation robotics. In fact, if achieving the rigid behavior of the robot can be considered a trivial task, obtaining its opposite can be challenging since the low-level controller should reject the disturbances introduced by the robot hardware. At the same time, one of the key characteristics of the motor recovery process is not to limit, in any way, any intention of movement coming from the user and, possibly, of guiding the subject's voluntary movements toward the correct task execution. Compliant motion in rehabilitation

robotics can, thus, be addressed as a compromise between good trajectory tracking and minimization of interaction forces.

Usually, rehabilitation robots and exoskeletons are provided with high-ratio transmission gearboxes that are kinematically inefficient, and that can introduce static and viscous friction. In this scenario, the perceived compliance cannot be guaranteed by the back-drivability of the motor itself. Still, it can be implemented by adding an elastic element in series with the actuation unit, i.e., series elastic actuators (SEA) (Crea et al., 2016; Calanca et al., 2017; Chen et al., 2019; Wu et al., 2019) or with compliant controllers that add virtual springs and dampers to shape the virtual mechanical impedance at the joint.

In the literature, several low-level controllers have been proposed to achieve compliant motion, and in turn, to implement the previously described training modalities. Among all, impedance control is one of the most common approaches, and it has been demonstrated to be a very efficient solution for neurorehabilitation (Mehdi and Boubaker, 2012). The impedance control belongs to those control schemes that permit a compliant pHRI. It implements dynamic control that relates force/torque and position: a torque/force output is generated from a position input. In particular, impedance control is characterized by a nested loop architecture. An inner torque-feedback loop implements the transparent behavior and promotes mechanical compliance (i.e., it “softens” the control). An outer position-feedback loop corrects for trajectory tracking errors by applying forces or torques aimed at the completion of the task (i.e., it “stiffens” the control). Furthermore, two different variants of the impedance control can be identified. When the actuation unit is inherently back-drivable, the torque control can be implemented through an open-loop current control loop (i.e., implicit impedance). In the other cases, a load-cell or an elastic element is exploited in series as a feedback signal for the closed-loop torque control loop (i.e., explicit impedance) (Calanca et al., 2016; Schumacher et al., 2019).

## 2.3. Available Control Strategies for Upper-Limb Exoskeletons

Regarding the rehabilitation domain, both impedance controllers in joint-space (Pehlivan et al., 2015; Just et al., 2017; Kim et al., 2017) and the Cartesian-space have been developed (Krebs et al., 2003; Frisoli et al., 2009; Ruiz et al., 2009; Mao and Agrawal, 2012). In joint-space impedance, the virtual mechanical elements are implemented in the joint-space with torsional spring and damper. The compliant behavior is given independently at each joint of the robot. Instead, with the Cartesian-space controller, virtual linear springs and dampers are connected to the robot end-effector in three-dimensional directions. Each direction is responsible for one of the three dimensions of the impedance ellipsoid computed at the robot end-effector. For example, in Kim et al. (2017), the baseline low-level control strategy of the Harmony robot, which is a bimanual upper-body exoskeleton for post-stroke rehabilitation, is based on a SEA-based joint-space impedance control that promotes the coordinated motion of the shoulder, through the assistance of the scapulohumeral rhythm (Kim and Deshpande,

2015). Specifically, for each joint, the deformation of the elastic element is used to estimate the generated torque at the joint axis. Then, an outer position-feedback is added to correct for task deviation. The dynamic model of the exoskeleton is formulated with a recursive Euler-Newton algorithm, and a feedforward term is added to compensate for gravity, friction, and dynamic torques. Similarly, the ARMin exoskeleton (Nef et al., 2007; Guidali et al., 2011; Just et al., 2017) is another example of an upper-limb exoskeleton for post-stroke rehabilitation based on a Proportional-Derivative (PD) position-feedback control that supports both the arm weight and provides assistance to the movement by virtually constraining the motion through stiffness/damping guidance. On top of this controller, the authors included online adaptive compensation algorithms to compensate for friction, elastic elements, and gravity terms (Just et al., 2018, 2020). On the other side, Frisoli et al. (2009) developed a Cartesian-space impedance-controlled exoskeleton to discriminate the end-effector reference trajectory from its orthogonal trajectory. In detail, two concurrent low-level impedance controllers act along the tangential and orthogonal directions of the trajectory, providing different virtual stiffness levels along with such directions and promoting a virtual tunnel that follows the Cartesian-space desired trajectory. Further evolution of impedance-based controllers involves the adaptation of the assistance according to the performances of the subject (Pehlivan et al., 2015; Perez-Ibarra et al., 2015; Pérez-Ibarra et al., 2019). Proietti et al. (2015) developed an exoskeleton controller based on adaptive techniques that can actively modulate the stiffness of the robotic device in function of the subject's activity. Instead, Pneu-WREX researchers developed a model-based adaptive control that learns from the patient's ability and provides support in completing movement while guaranteeing mechanical compliance (Wolbrecht et al., 2008). They implemented a Cartesian-space impedance control law, to which they added a feedforward term characterized by a non-linear sliding mode control scheme. The assistance-as-needed adaptation was achieved by adding a learning factor, which iteratively corrects the feedforward contribution, and a force decay, which reduces the support when the subject is able to perform the movement correctly.

This study identifies a compliant control framework that implements multiple high-level human-robot interaction modalities with a unique low-level explicit impedance control law. A similar compliant controller has already been implemented in other robots for neurorehabilitation (de Oliveira et al., 2019). Researchers already proposed that a mixture of assistance, correction, and resistance with impedance control laws could be used to gradually increase the amount of expected voluntary muscle activity. However, the generalization and validation of these approaches through the assessment of human volitional activity is still lacking.

To this aim, we employ an impedance-based controller to render different human-robot interaction modalities, and we demonstrate that the proposed controller can induce different levels of subject participation. We validate this approach by measuring the muscular voluntary effort of healthy volunteers through surface electromyographic (sEMG) monitoring. The

experiments consist of elbow flexion/extension tasks executed under six different assistance and resistance levels by 14 healthy participants, who are instructed to self-tune their volitional contribution according to the effort needed to fulfill the tracking task.

### 3. UNIFIED COMPLIANT CONTROL FRAMEWORK

In this section, we introduce a compliant control framework based on an explicit impedance control law, capable of fulfilling different requirements and features, such as favoring good transparency of the joint, compensating for the weight of the robot and the supported limb, assisting the motion along the desired trajectory, recovering from task deviations, or even challenging the user by applying resistance or increased gravity to the motion.

The controller relies on the concepts of compliant control and, in particular, impedance control. The overall scheme of the proposed controller is presented in **Figure 1**. The idea is to employ a control architecture based on multiple nested control loops.

The outer impedance loop implements the virtual mechanical impedance  $I(s)$ , which is in charge of correcting for deviations from the desired angular position and providing the anti-gravity compensation of the robot-human system. Namely, the outer loop provides the force-field assistance toward the completion of the task. We expect this assistance to be adaptable according to the desired training mode.

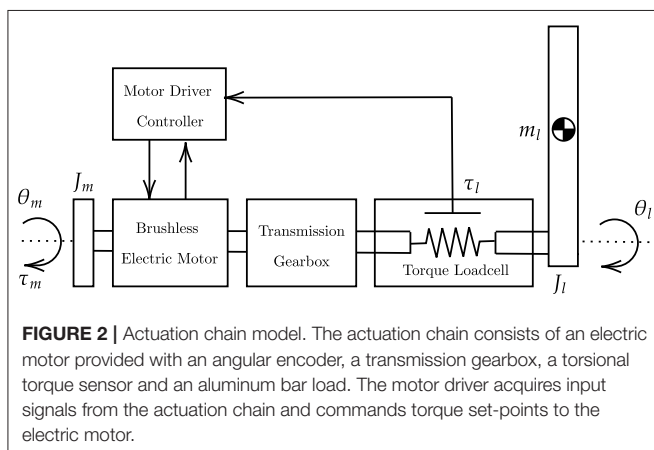
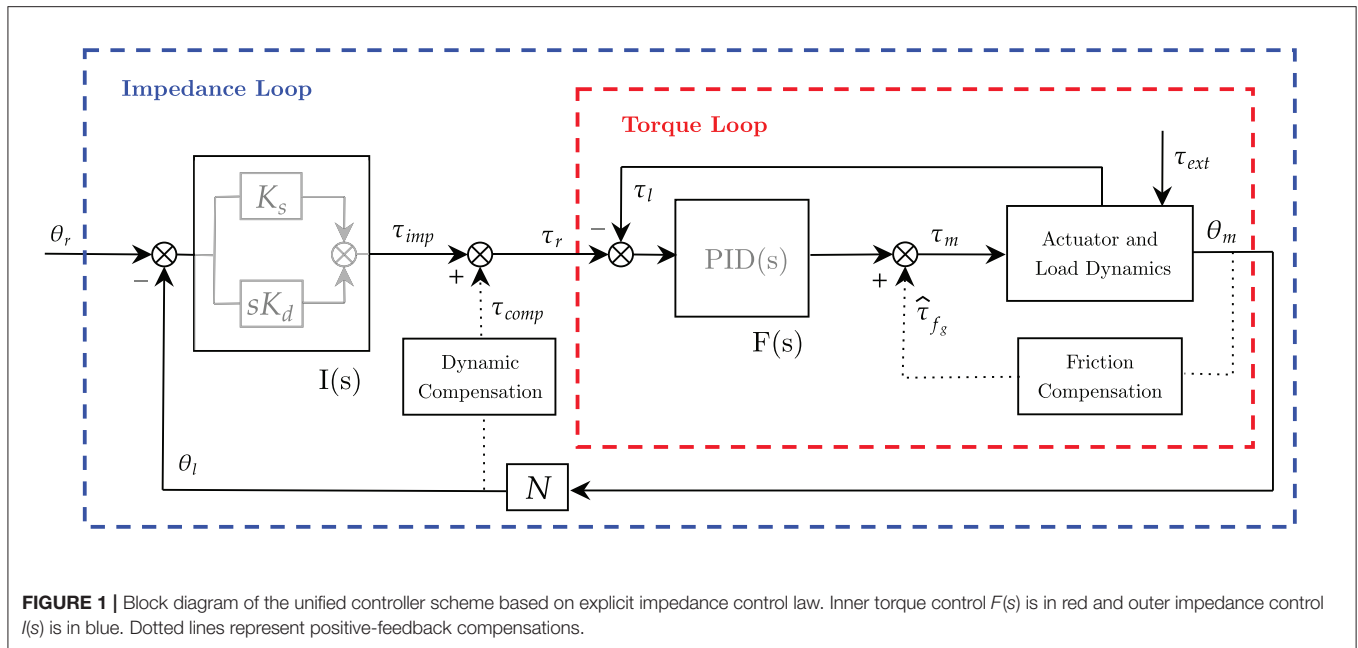
The inner torque loop  $F(s)$  is in charge of controlling the torque output at the load axis. It is aimed at promoting compliant behavior (i.e., mainly rejecting friction) and guaranteeing high-fidelity torque control. The inner torque control loop is employed to obtain an “explicit” feedback signal of the torque generated by the motor that rejects friction disturbances.

While the inner torque loop is supposed to be fast enough to neglect its dynamics, and its control parameters are kept fixed to exhibit stability, the outer loops (e.g., impedance loop and gravity compensation term) are characterized by adjustable parameters, to be adapted according to the desired pHRI.

In this study, we consider an exemplary single-degree-of-freedom joint, shown in **Figure 2**, as a platform to validate the controller and its functionalities as it interacts with the human arm. The actuation chain is composed of an electric motor coupled with a high-ratio transmission gearbox. The unit is also provided with an incremental encoder that measures the joint angle, and a reaction torsional load-cell provides torque feedback at the output load axis. The dynamics of the one degree-of-freedom actuation system is as follows:

$$\tau_l = (\tau_m - J_m \ddot{\theta}_m - \eta_m \dot{\theta}_m - \tau_{fg})N + \tau_{ext} \quad (1)$$

where  $\theta_m$  is the motor displacement,  $\tau_m$  and  $\tau_l$ , respectively, represent the motor torque and the load torque measured at the load-cell, and  $\tau_{ext}$  is the externally applied torque. The generated motor torque  $\tau_m$  is converted in the acceleration of the rotor ( $\ddot{\theta}_m$ ) with inertia  $J_m$  in the dissipation of the motor damping  $\eta_m$  and



friction  $\tau_{f_g}$  of the transmission gearbox. The resulting torque is then amplified by the gear ratio  $N$  and transferred to the output axis ( $\theta_l$  of **Figure 2**).

### 3.1. Torque Control (Inner Loop)

The inner torque loop of an impedance controller can be implemented both as an open-loop (i.e., implicit impedance) or a closed-loop (i.e., explicit impedance) torque controller. In literature, Hogan first presented an implicit impedance controller that exploits an open-loop torque controller based on motor current control (Hogan, 1985, 1989). However, it requires inherent back-drivability, that can only be achieved with the low-ratio transmission or direct-drive actuators (Calanca et al., 2016). Several other approaches are available to compensate for undesired gearbox inefficiency. Model-based force estimation (Wolbrecht et al., 2008) or disturbance observer-based control

schemes (Just et al., 2018) are common solutions. More often, torque sensors can be used to explicitly measure the actual generated torque and/or the subject's applied effort to be used as feedback in a closed-loop formulation (Focchi et al., 2016; Masud et al., 2018). In our study, since we consider high-ratio transmissions and the open-loop formulation would require a good friction model to achieve high-fidelity torque control, we opted for torque-controlled joints that are provided with torsional load-cells at each joint. In fact, torque-controlled robots are capable of producing very low impedance, which is essential to encourage users' voluntary contribution. In this form, the inner torque control  $F(s)$  is in charge of making sure that the measured torque output ( $\tau_l$ ) follows the outer loop control variable ( $\tau_r$ ). From the reference torque level to be actuated ( $\tau_r$ ), the inner torque loop estimates the target torque of the actuator ( $\tau_m$ ) through a Proportional-Integrative-Derivative (PID) controller, with feedback from the torsional load-cell ( $\tau_l$ ), that in the Laplace form is (2):

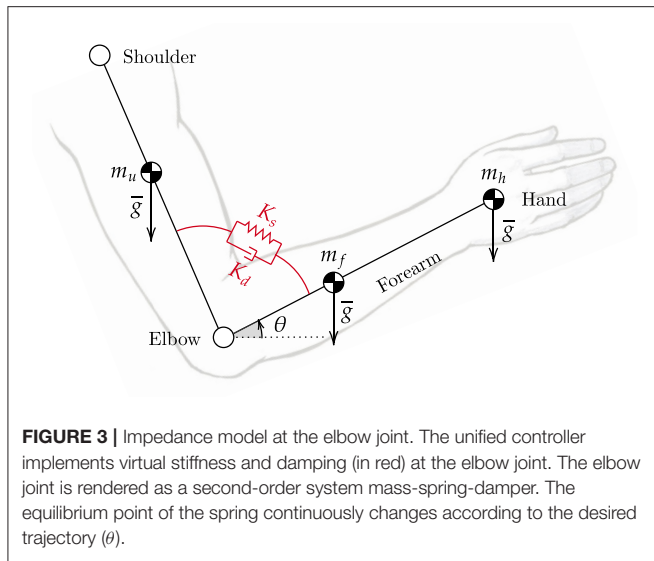
$$F(s) = K_p + K_i/s + K_d s \quad (2)$$

To compensate for static and viscous friction introduced by high-ratio gearboxes, an additional feedforward friction compensation ( $\hat{\tau}_{f_g}$ ), modeled as in Wit et al. (1998), has been added at the inner loop level, as shown in **Figure 1**. The compensation can be divided into Coulomb friction and velocity-dependent friction:

$$\hat{\tau}_{f_g} = \tau_c \tanh(\dot{\theta}/\dot{\theta}_c) + f_v \dot{\theta} \quad (3)$$

where  $\tau_c$  is the Coulomb friction torque,  $\dot{\theta}$  is the measured joint velocity,  $\dot{\theta}_c$  is the Coulomb joint velocity threshold, and  $f_v$  is the viscous friction coefficient. The hyperbolic tangent function ensures the Coulomb term to be continuous and smooth across





$\dot{\theta} = 0$  in order to avoid undesired oscillations. The  $\hat{\tau}_{f_g}$  term is summed up to the torque PID control signal and fed as input to the actuator current control. The actual torque actuated at the load axis is then measured by the load-cell ( $\tau_l$ ) and fed back to the PID controller to track the reference torque ( $\tau_r$ ).

According to Calanca et al. (2016), the inner torque loop dynamics should not influence the outer loop. Thus, the inner loop is usually implemented at a higher control frequency. In our study, as previously stated, the torque loop is supposed to be fast enough to neglect its dynamics with respect to the outer impedance loop. Consequently, the torque control loop should be considered an ideal torque source and only serves as a baseline for the impedance control loop.

As suggested by Focchi et al. (2016), the parameters tuning of the explicit inner torque loop strongly influences the stability of the system. We decided to empirically tailor the inner controller to exhibit stable behavior throughout the full range of achievable impedance at the outer loop. For this reason and to avoid unstable conditions, the inner loop is operated with fixed parameters, which are considered constant regardless of the desired high-level mode.

### 3.2. Impedance Control (Outer Loop)

The impedance control can be regarded as an outer position loop that takes a reference in terms of angular position (i.e.,  $\theta_r$ ) and, by means of a virtual mechanical impedance, produces a reference torque (i.e.,  $\tau_r$ ) that in turn is fed to the inner torque loop. The total reference torque can be seen as composed of two contributions, as in Equation (4). The feedback impedance-based term, namely  $\tau_{imp}$ , corrects for tracking errors and dampens undesired oscillations. The feedforward term  $\tau_{comp}$  compensates for the dynamic model of the robot and the weight of the wearer's limb.

$$\tau_r = \tau_{imp} + \tau_{comp} \quad (4)$$

Instead, the measured torque at the load axis consists of the actual torque generated by the robotic system and can be broken down into four main components, as shown in Equation (5):

$$\tau_l = \tau_{comp} + \tau_{imp} + \tau_{ext} + \tau_{res} \quad (5)$$

where  $\tau_{comp}$  and  $\tau_{imp}$  represent the actuation torques commanded to the motor,  $\tau_{ext}$  indicates the external torque that the user exerts to the joint, and  $\tau_{res}$  represents the residual disturbance torque that the inner torque controller can not reject.

#### 3.2.1. Feedback Impedance-Based Term

To derive the feedback impedance-based term (i.e.,  $\tau_{imp}$ ), considering a first order impedance, the transfer function  $I(s)$  between the reference target ( $\theta_s$ ) and the impedance-based torque term ( $\tau_{imp}$ ) is characterized by two parameters: virtual spring ( $K_s$ ) and virtual damper ( $D_d$ ), and it can be implemented in the well-known form Equation (6):

$$I(s) = K_s + sD_d \quad (6)$$

that in the time domain becomes Equation (7):

$$\tau_{imp} = K_s(\theta_d - \theta) + D_d(\dot{\theta}_d - \dot{\theta}) \quad (7)$$

where  $\tau_{imp}$  is the desired impedance control torque that is used as a set-point by the inner torque loop, while  $\theta_d$  and  $\theta$  are, respectively, the desired and measured joint angle positions.

The virtual stiffness, by means of the virtual spring constant  $K_s$ , pulls the joint link toward its desired configuration (i.e., the spring corrects for deviations from its equilibrium point, which is continuously adapted to follow the desired angular trajectory). At the same time, the virtual damper ( $D_d$ ) dissipates the spring energy and damps oscillations. Overall, the role of these parameters is to render, as shown in **Figure 3** for the elbow joint, a second-order system by virtualizing a spring-damper component within the impedance control law. When dealing with robotic rehabilitation, the desired angular velocity might not be available, especially when the task trajectory is updated in real-time to follow the subject's intention of movement. In such cases, we can neglect the reference velocity term ( $\dot{\theta}_d$ ) in the previous (Equation 7). In this way, the damping term is related to the absolute velocity instead of the error velocity. The virtual damper is fixed to the ground frame, resulting in always-resistive damping of the system.

#### 3.2.2. Feedforward Weight and Dynamics Compensation Term

A feedforward torque reference term that accounts for the dynamics of the robot and for weight of the arm is added at the impedance control level.

For the sake of simplicity, in this section, we consider the general single-degree-of-freedom joint shown in **Figure 3**, which can be reduced to a rigid pendulum system. The torque acting at the load axis can be described

with the dynamic equation of the system, which includes both the robot and the human, as follows Equation (8):

$$\tau = J_l \ddot{\theta} + f_l \dot{\theta} + G(\theta) \quad (8)$$

where  $J_l$  is the inertia moment,  $f_l$  is the viscous friction at the load axis, and  $G$  represents gravitational torques for both the link and the forearm. Compensating for the inertial component of the dynamic model requires the estimation of inertia moments and the computation of the acceleration by twice-differentiating the encoder position. These operations can raise many difficulties and undesired uncertainties that are in turn fed to the controller as positive-feedback terms. Inertia compensation can, thus, make the system non-passive and can jeopardize the coupled stability of the human-exoskeleton system (Kim et al., 2014). Additionally, in robotic rehabilitation, the desired arm movements are usually slow, leading to neglectable effects due to the dynamic terms of Equation (8). For these reasons, in our study, we only compensate for gravitational and viscous frictional torques.

We, therefore, introduce the simplified compensation term:

$$\tau_{comp} = \hat{f}_l \dot{\theta} + \hat{G}_{link}(\theta) + \hat{G}_{wc}(\theta) \quad (9)$$

where  $\hat{f}_l$  is the estimated viscous friction coefficient,  $\hat{G}_{link}$  represents the weight compensation term for the robot components, and  $\hat{G}_{wc}$  represents the weight compensation of the human component. The weight compensation term for the robot can be modeled as in Equation (10):

$$\hat{G}_{link}(\theta) = mgl \cos \theta \quad (10)$$

where  $m$  is the robot link mass,  $l$  is its center-of-mass distance, and  $g$  is the gravitational acceleration.

As for the gravitational compensation term of the human ( $\hat{G}_{wc}$ ), we need to make explicit reference to the single-degree-of-freedom joint used as a demonstrative example (Figure 3). Of course, this can be generalized to any joint of interest. We have included vertical forces applied at the centers of mass of the forearm and hand. The position of the center of mass and the weight of the limbs can be derived from the anthropometric tables presented in Winter (2009). The level of weight assistance can be regulated by means of a weighting factor (ranging from 0 to 100%) that accounts for misalignment and uncertainties in the anthropometric data as in Equation (11):

$$\hat{G}_{wc}(\theta) = W_f(m_f l_f + m_h l_h)g \cos \theta \quad (11)$$

where  $W_f$  is the weighting factor,  $m_f$  and  $m_h$  are the masses of forearm and hand, while  $l_f$  and  $l_h$  are their centers of mass. With this dynamic compensation, only inertial, centrifugal, and residual frictional torques are to be overcome if the user wants to perform a voluntary movement (i.e., they are not included in the compensation term).

The feedforward compensation torque formulation can be obviously generalized if an  $n$ -degree-of-freedom robot is concerned. In such cases, the dynamics compensation terms can also include Coriolis and centrifugal torques. Such feedforward

compensation can be computed from centralized inverse dynamics algorithms, such as closed-form solutions or more computationally efficient recursive Euler-Newton approaches (Moubarak et al., 2010; Ragonesi et al., 2013; Kim et al., 2017; Just et al., 2020).

### 3.3. Human-Robot Interaction Modalities

In this study, we took inspiration from literature control modalities for robot-mediated therapy, and we selected six high-level human-robot interaction modalities, ranging from passive mobilization to challenging modalities. In this section, we first describe the motor learning rationale and the desired high-level behavior for each mode. Then, we propose a match between the high-level behavior and a set of control parameters that can render the desired behavior. The claim regards the adjustment of stiffness, damping, and weight-compensation assistance to render different pHRI levels. We underline that the parameters are adapted only at the higher level as the torque control loop serves as an internal loop to promote compliant behavior and improve the torque tracking accuracy.

#### Passive Mode (P)

The *P* mode should be exploited during the preliminary stages of the rehabilitation process. The robot helps the patient to track a predefined trajectory to improve the limb range of motion and reduce muscular atrophy or tendon retractions (Masiero et al., 2007). When the system is operated in *P* mode, the robot performs the movement without accounting for the user's intentional activity. Stiffness  $K_s$  and damping  $D_d$  control gains are greater than in other modes, rendering a stiffer behavior of the joint, and the torque feedforward term ( $\tau_{comp}$ ) is used to compensate for the user's arm weight. However, in this mode, the trajectory tracking is not as accurate as in position control, as the impedance control intrinsically introduces a tolerance dead-band. Nevertheless, this is not a critical aspect for rehabilitation robots since the crucial feature is to limit the interaction forces with the human limb.

#### Corrective Mode (C)

*Corrective* modalities are used when patients have some voluntary muscular contractions, but the generated strength is not sufficient to perform complete and functional movements. The robot provides assistance when the participant is not capable of fulfilling the task, and generates a force-field to push the arm toward the desired path (Basteris et al., 2014). In this mode, subjects generate the minimum effort needed to accomplish the desired task. The user is actively involved in the movement, and the robot partially assists the motion. The *C* mode is implemented with impedance-based assistance. Lower values for both virtual stiffness and damping are used with respect to the *P*, rendering a more compliant and softer behavior of the robot, i.e., the user is allowed to deviate from the trajectory.

#### Weight Counterbalance Mode (W)

The *W* mode can be applied to perceive a microgravity environment. This effect is obtained through the counterbalancing assistance term that is computed according to

the configuration of the user's arm. In this mode, the subject is wholly involved in the task, and if the voluntary activity is not sufficient to fulfill the exercise, the robot does not apply for any corrective assistance. Indeed, the controller is not programmed to follow a predefined exercise task. At low-level, the virtual stiffness is removed, and a low damping value is used to avoid undesired oscillations and dampen the motion.

### Transparent Mode (T)

In *T* mode, the user performs the task, and the robot follows the movement without assisting (nor resisting) the movement. In other words, this mode enables the robot to be dynamically transparent to users' voluntary movements, by compensating the exoskeleton weight at each configuration along with the task. Regarding its implementation, the low impedance behavior is achieved by means of a null-torque controller provided only with the compensation for the robot weight. Neither assistance nor resistance is provided.

### Resistive Mode (R)

The *R* mode has been introduced to further engage the patient along with his/her progression, i.e., when most of the motor functionalities have been (hopefully) relearned, but the subject still has to gain some muscular tone. In fact, robots with torque-controlled joints can also realize an aquatic therapy-like environment by providing weight support and allowing user-driven free motions with or without viscous resistance (Kong et al., 2010; Song et al., 2014). To implement such behavior, this mode adds a viscous-like resistance to the movement while compensating for the robot dynamics. No impedance-based assistance is present, and the controller resists the movement by applying a viscous frictional torque, which is inversely proportional to the movement velocity.

### Hypergravity Mode (H)

The *H* mode amplifies the effect of gravity during the movement. This mode can be used to challenge the subject during the exercise and to focus the training on postural anti-gravity muscles. In particular, instead of counterbalancing the limb weight, the controller adds additional virtual weight, applied at the centers of mass of the limb, that gives the feeling of doing the task with weight, or, in other words, of doing the exercise in a hyper-gravity environment.

Overall, qualitative guidelines suggest that high-impedance implementation should be used to stiffen the control law, imposing the subject's movement along the task trajectory. Contrarily, low-impedance gains should be exploited to render more compliant and softer behavior of the robot, i.e., the controller promotes voluntary movements, and the user is allowed to deviate from the trajectory. Finally, we usually increased the damping not only to reduce overshoots and oscillations but also to introduce a baseline kinematic error, which should engage the user when following the desired trajectory. However, a trade-off in the impedance parameters is needed to induce a physiological muscular activation aimed at completing the task in an assisted-as-needed fashion. Regarding the weight counterbalance, the mathematical model does not

**TABLE 1 |** The proposed parameters used with the unified compliant controller to render the selected high-level human-robot interaction modalities.

Human-robot interaction modalities		Weight ( $W_f$ ) (%)	Stiffness ( $K_s$ ) (Nm/rad)	Damping ( $D_d$ ) (Nms/rad)
Passive	P	75	50.0	10.0
Corrective	C	0	5.0	1.0
Weight counterbalance	W	75	0.0	0.1
Transparent	T	0	0.0	0.1
Resistive	R	0	0.0	3.5
Hypergravity	H	-100	0.0	0.5

$K_s$  and  $D_d$  relate to the impedance-based term. The  $W_f$  parameter corresponds to the weighting factor for the feedforward compensation of Equation (11) and it was manually tuned to 75% to avoid overcompensating for the user's arm weight.

always entail a real experience of weight relief for the end-user. As a consequence, we adapted the level of anti-gravity support by means of the weighting factor  $W_f$ , which was tuned to 75%. Indeed, in the implementation of anti-gravity exoskeletons, a 100% compensation could hinder the user during anti-gravity movements, and it is suggested to compensate for a fraction of the full dynamics (Näf et al., 2018).

To define the quantitative values of stiffness, damping and weight assistance for each mode, we separately ran some preliminary tests on two healthy subjects, which were not recruited for the rehabilitation modalities assessment to avoid bias. The parameters of the controller were empirically determined according to the perceived behavior.

Table 1 shows the parameters that we used for the human-robot interaction modalities validation, as described in section 3.3.

## 4. METHODS

To assess the validity of the proposed control framework and its ability to promote different human-robot interaction modalities, we considered a typical actuation joint for a general upper-limb exoskeleton, and we used it as a platform to test and verify the performances of the proposed controller. As previously explained, the controller is first characterized regardless of the volitional human activity, then the perceived pHRI is assessed on elbow flexion/extension movements throughout the proposed modalities. In detail, the validation of the control framework is presented in two different steps: i) assessment of the performances of the control loops 4.2, and ii) electromyographic validation of the unified compliant control operating in the proposed rehabilitation modalities 4.3.

### 4.1. Experimental Set-Up

The actuation is provided by a brushless DC motor (EC-45 flat, Maxon Motor AG, Switzerland), coupled with a planetary gearhead with a transmission ratio of 156:1 (GP-42-C, Maxon Motor AG, Switzerland). The electric motor provides a nominal torque of about 120 mNm. Thus, given the ratio and the efficiency of the transmission, the gear motor is able to provide

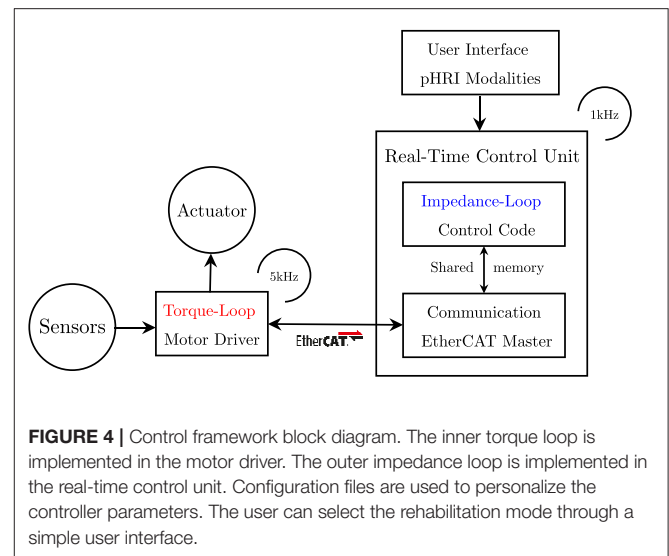
at the load side a maximum constant torque of about 15 Nm and a peak torque of about 18.5 Nm. An incremental encoder reads the rotor position with a resolution of 2,048 counts per revolution, leading to a resolution of  $0.001^\circ$  at the load side. Finally, a reaction torsional load-cell (TRT-200, Transducer Techniques, CA, USA) is connected to the gearbox output shaft to sense the torque acting on the joint of the robot. With the aim of testing the control in the interaction with the human motion, we designed a one-degree-of-freedom robotic system to provide assistance to the elbow during flexion-extension tasks, similar to the one presented by Lobo-Prat et al. (2016). In particular, the rotational axis of the system is aligned with the user's elbow joint. An aluminum bar is attached to the load-cell and is fixed to the user's forearm by means of an ergonomic arm cuff. The arm cuff is equipped with padded fabric which minimizes interaction forces between the rigid shell and the arm. Adhesive strips are used to fix it to the arm cuff. The user's elbow rests over a soft foam surface, and the arm cuff position can be adjusted according to the forearm length to improve the comfort and alignment of the rotation axis. The unified controller described in section 3 is implemented in a real-time control system, based on Linux patched with PREEMPT RT, and runs at a cycle time of 1 ms. The control hardware architecture shown in **Figure 4** relies on the EtherCAT field-bus, which guarantees good performances on distributed networks, and assures a reliable, deterministic, stable, and low-latency communication between the control unit and the connected hardware. In particular, the motor driver (Mini Torque Driver, Esmacat, US) is connected to the control system *via* the EtherCAT communication, and a real-time C++ master application, based on the Simple Open-Source EtherCAT Master (SOEM) library, is implemented to handle the communication with the motor and sensors. The real-time control unit also implements the outer impedance/position loop at 1 kHz, the feedforward compensations, and the trajectory generation. The low-level torque control is instead implemented in the motor driver at 5 kHz.

The experimental set-up and its connection are described in **Figure 5B**, while its final realization is shown in **Figure 5A**. The main features of the presented experimental set-up are reported in **Table 2**.

## 4.2. Actuation and Control Characterization

The characterization of the controller was conducted on a single healthy subject as its performances are to be assessed regardless of the subject's performance and involvement.

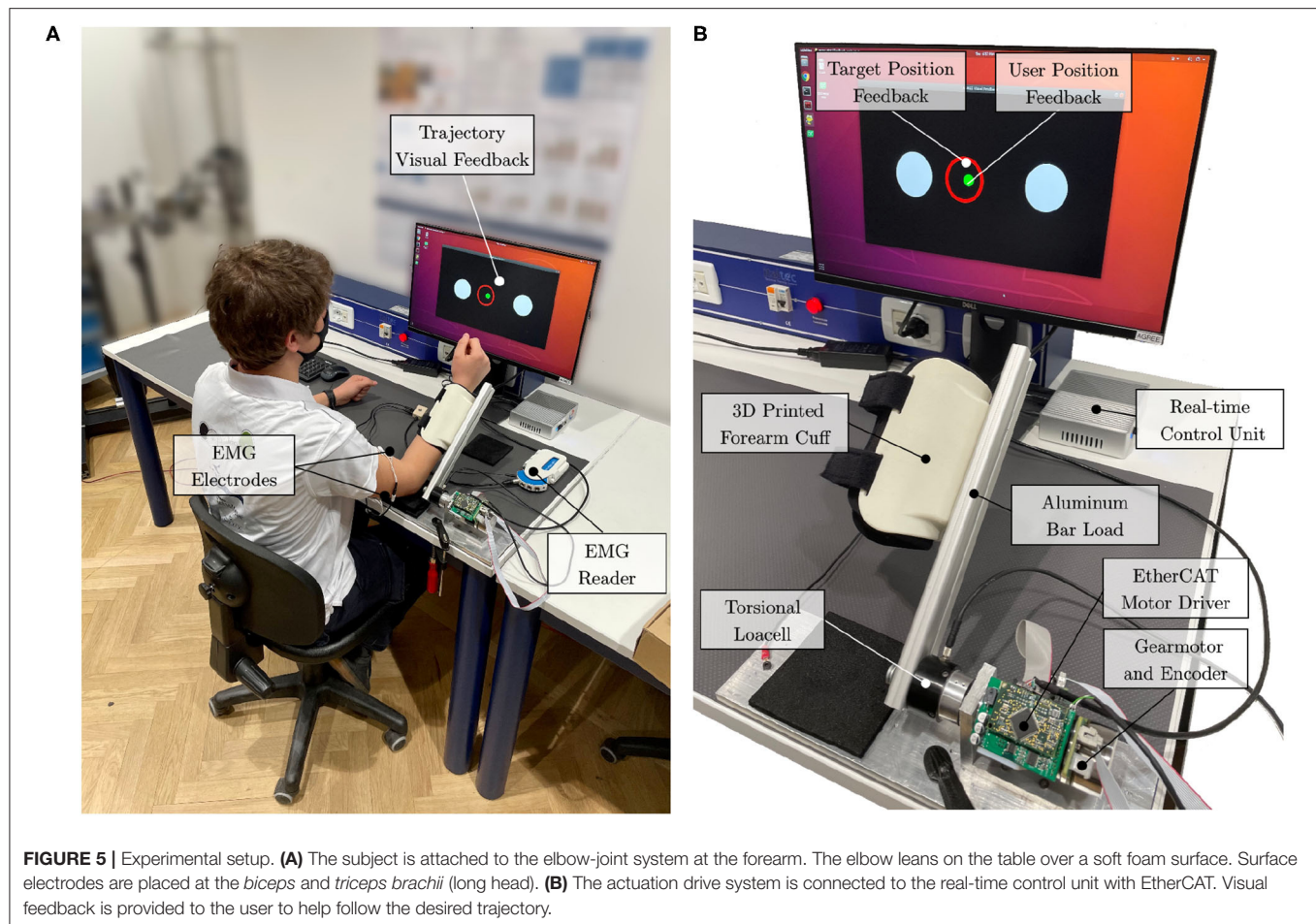
First, we assessed the capability of the system to promote physical human-robot transparency, defined in literature as to how good the robot is at rejecting torque disturbances and at limiting resistance during subjects' voluntary motion (Zanotto et al., 2013). To validate the need of employing the inner torque closed-loop and consequently to assess the ability of the unified compliant controller to improve transparency, open-loop (current-based) null-torque control was compared to closed-loop (loadcell-based) null-torque control. To this aim, we asked a healthy subject to perform movements spanning the whole available range of motion (i.e.,  $0^\circ$  to  $+90^\circ$ ) with



the elbow one-degree-of-freedom test-bed at various velocities ranging from  $-1.0$  to  $1.0$  rad/s in two conditions: i) back-driving movements operating the joint with no active control. In this condition, the inner loop is disabled and the mechanical backdrivability of the joint is sensed; ii) back-driving movements operating the joint in closed-loop null-torque control: The inner torque control follows a null torque reference. We measured the torque output from the torque sensor, while the position and velocity of the joint axis were obtained from the embedded incremental encoder. We computed the maximum residual resistive torques, which should be lower for better transparency.

Second, to assess the accuracy of the torque control, we analyzed the frequency response of the inner closed-loop. We set the drive system at its mechanical end-stop, and we commanded sinusoidal torque profiles to the actuator torque control at different frequencies, ranging from 0.5 to 4 Hz. We evaluated the differences between the commanded torque and the measured torque curves using Root Mean Squared Error (RMSE) and Peak Error (PE) values, which are measures of the accuracy of the torque-control loop and both should be as small as possible. Finally, we computed the Pearson correlation coefficients to evaluate torque fidelity at each frequency, which should be greater than 90% for high similarity levels (Mukaka, 2012). At last, we investigated the performance of the impedance control, and we estimated the accuracy of the rendered torsional impedance values that the system was able to generate. The robot was commanded in impedance at the vertical equilibrium point ( $\theta = 0^\circ$ ), and external torques were exerted to the joint-link system. The experiment was repeated at different stiffness/damping values. The displacement from the equilibrium point (in radians) at stiffness values of 5, 10, 20, and 40 Nm/rad has been evaluated and related to the measured torque output. One should verify that the experimental stiffness matches the commanded one.





**TABLE 2 |** The main features and specifications of the developed experimental set-up.

Specifications	Value
Nominal torque	15 Nm
Max. Peak torque	18.5 Nm
Max. Velocity	4.4 rad/s
Gearbox ratio (N)	156:1
Range-of-motion	0° +110°
Torque control frequency	5 kHz
Impedance control frequency	1 kHz

Performances of the torque control and impedance control loops are discussed in section 5.1.

### 4.3. Human-Robot Interaction Modalities Validation

The testing protocol was performed on healthy subjects, and it was approved by the ethical committee of Politecnico di Milano.

The protocol involved the execution of elbow flexion/extension tasks with the elbow-joint developed set-up (Section 4.1). The system was connected to the dominant arm of the user, and the user performed elbow flexion and extension

movements following the six implemented rehabilitation strategies. Their sequence was randomized to avoid learning or fatigue effects, that could have biased the results. For each mode, the user performed 15 elbow flexion/extension repetitions. The user was instructed to perform the movements following visual feedback (**Figure 5A**). The visual interface showed the movement to be tracked and the actual position of the joint. The desired movement speed was kept the same across all modalities.

The goal of the task was to correctly track a moving trajectory, and the performance was the resultant of the sum of the contribution of the torque provided by the human and the motor. In this view, healthy subjects can modulate their contribution to the movement. Thus, we have been able to monitor different human contribution levels while keeping the task performance constant.

As proposed in Hogan (1984), the movement of the human arm, when coupled with a robot, can be described by a minimum jerk trajectory. In this study, we defined the nominal trajectory by means of a symmetric fifth order  $\beta$ -function (Krebs et al., 1999) as in Equation 12. The nominal trajectory starts with the forearm lying on the table (i.e., 0°), then the flexion/extension movement

is performed in about 8 s as in **Figure 6A**.

$$\theta_r(t) = P_0 + P_1(t - P_2)^{P_3}(P_4 - t)^{P_5}, P_2 \leq t \leq P_4 \quad (12)$$

$$P_1 = \frac{A_0}{\frac{P_4 - P_2}{2}(P_3 + P_5)} \quad (13)$$

where the  $P_n$  parameters are used to configure the desired trajectory.  $P_0$  represents the initial position offset,  $P_2$  and  $P_4$  are the start and the stop time,  $P_3$  and  $P_5$  are the interpolators' orders for the raising and falling phases, and  $P_1$  is related to movement amplitude  $A_0$  by means of Equation (13). **Figure 6B** shows the desired  $\beta$ -function trajectory for the elbow flexion/extension movement.

#### 4.3.1. Outcome Measures

We recorded the kinematic and dynamic data from the robot sensors. Commanded and measured angular position, velocity and torques were sampled at a frequency of 1 kHz. Torque data were low-pass filtered with a Butterworth filter of the third order and a cut-off frequency of 20 Hz. To investigate how subjects adapted their motion control to various assistance (or resistance) levels, and to posit if the experiments were comparable, we assessed the kinematics variability. In particular, to evaluate if the subjects performed comparable trajectories across all modalities and, as a consequence, if we could posit that all the subjects performed the same movements, we computed the RMSE between the commanded and the measured angular position across all repetitions, subjects, and modalities.

To validate the implemented control strategies and to investigate how they affect the user's behavior, we also registered the muscular activity. In particular, we recorded the *biceps* and *triceps* (long head) muscles, as shown in **Figure 5B**. The sEMG signal was recorded at a frequency of 1 kHz with a wireless EMG reader (Sessantaquattro, OTbioelettronica, Italy). EMG signals were pre-processed following a standard approach that includes high-pass filtering with a third-order Butterworth filter at 10 Hz, rectification, and low-pass filtering with a third-order Butterworth filter at 4 Hz (Gandolla et al., 2018). We normalized signals for each participant with respect to 80% of the maximum contraction during the whole experimental session, preventing normalization by spurious EMG spikes (Ricamato and Hidler, 2005). We computed the integrated EMG (iEMG) as a marker of voluntary muscle drive as the area under the curve of the normalized EMG signal (Androwis et al., 2018).

#### 4.3.2. Statistical Analysis

Outcome measures were collected for each subject and for each control mode. All output indices were computed separately for the flexion and extension movements. Results are expressed as medians and inter quartile ranges (IQR) [25th - 75th percentiles]. Given the reduced sample size, the Friedman test was performed to detect possible significant changes in the RMSE and iEMG indices across different control strategies. *Post-hoc* comparisons with Bonferroni correction were used to identify statistically significant differences between the six modalities. All statistical analyses have been performed in MATLAB (version R2020b) and IBM SPSS Statistics (version 27).

## 5. RESULTS

### 5.1. Actuation and Control Characterization Results

As for the capability of the compliant controller to promote physical human-robot transparency, results demonstrated that the closed-loop torque controller reduced the residual frictional torques, from 2.0 to 0.3 Nm. As shown in **Figures 7A,B**, when the robot is operated in closed-loop null-torque control, better transparency is achieved within a range of  $-1.0$ – $1.0$  rad/s, which are typical maximum velocities for a rehabilitation exercise (Neilson, 1972). The maximum residual resistive torques during back-driving movements were perceived as negligible by the user that was performing the experiment. This result confirms that employing a loadcell-based torque control loop permits to achieve higher transparency of the joint and better torque tracking.

To measure the torque control accuracy, we performed sinusoidal torque profiles, as shown in **Figure 8**. The differences between the commanded torque and the measured torque curves were computed to assess the accuracy of the inner closed-loop torque control. Results showed torque output RMSE of 0.12, 0.30, 0.33, and 0.49 Nm, respectively, for 0.5, 1.0, 2.0, and 4.0 Hz. The maximum (PE) of about 0.90 Nm was obtained at 4.0 Hz in correspondence to sudden changes (i.e., at the inversion of velocity). Pearson correlation coefficients resulted equal to 99.62 ( $f = 0.5$  Hz), 98.06 ( $f = 1$  Hz), 97.55 ( $f = 2$  Hz), and 94.71% ( $f = 4$  Hz), demonstrating a high-fidelity torque control.

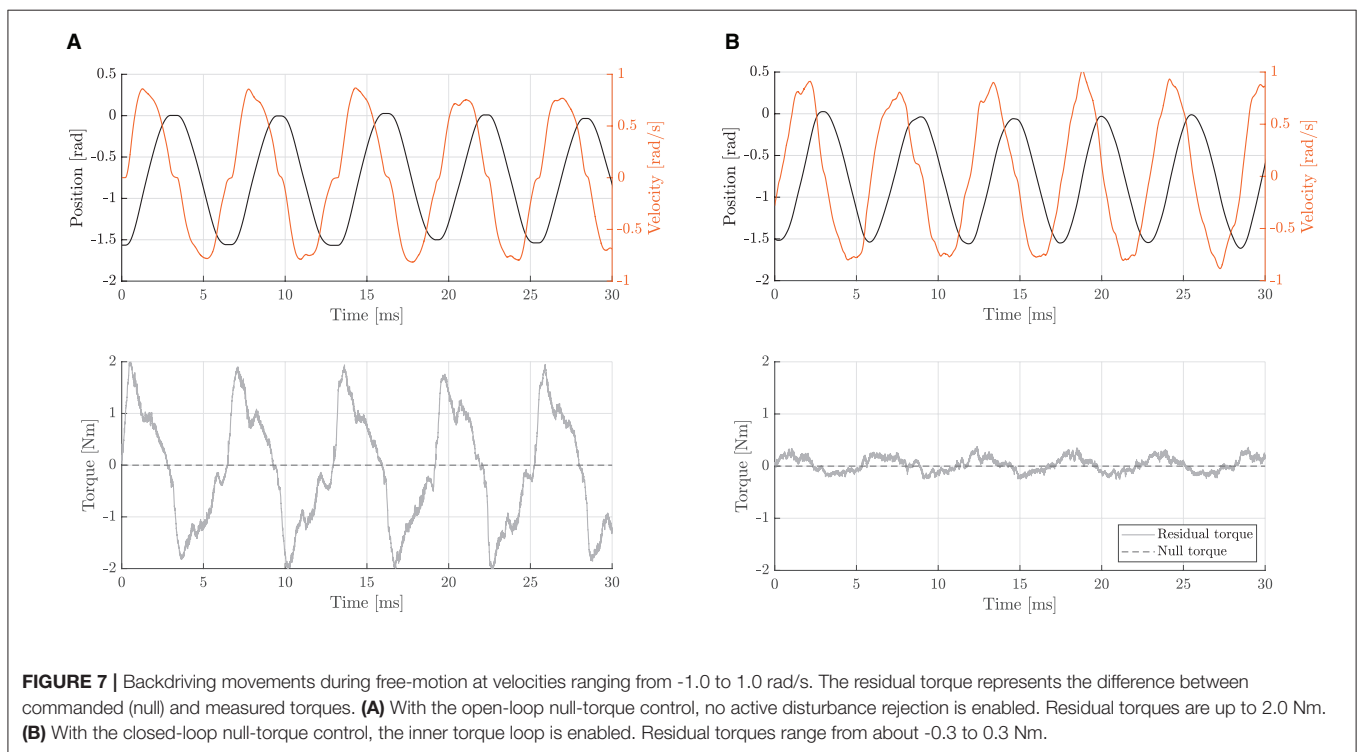
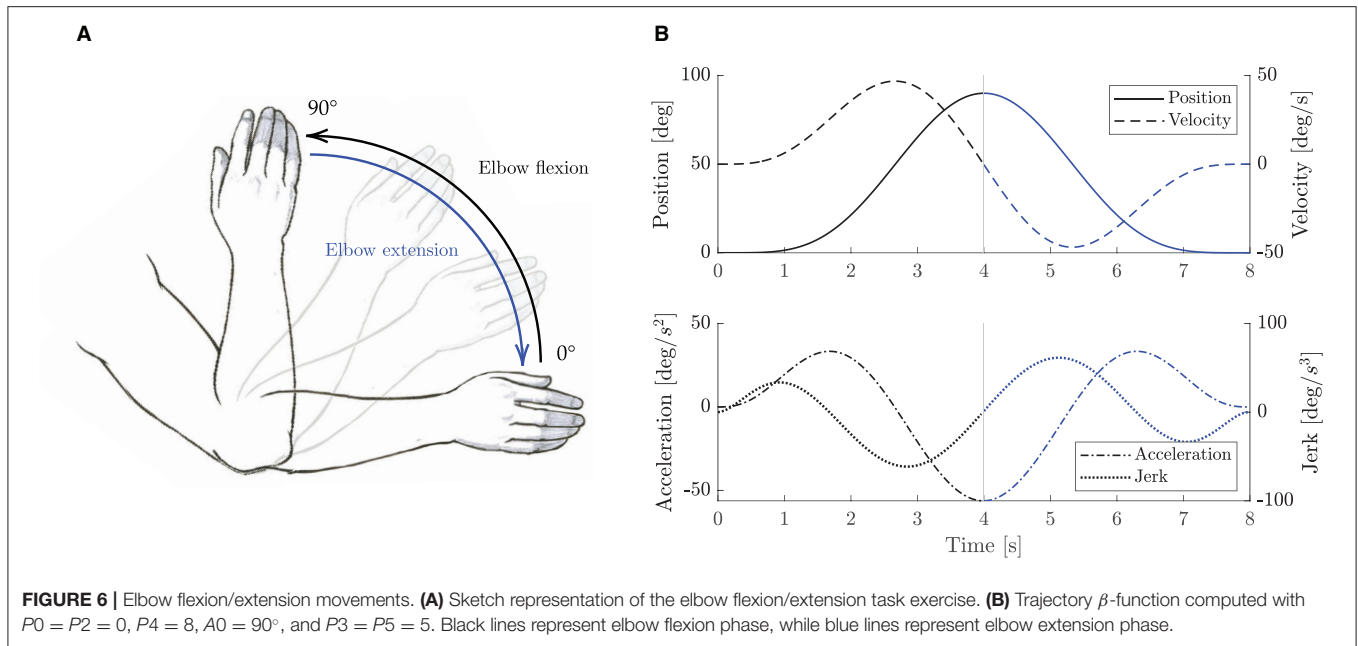
As for the performances of the impedance controller, **Figure 9** shows the relationship between the generated torque output (in Nm) and the displacement from the equilibrium point (in rad) at stiffness values of 5, 10, 20, and 40 Nm/rad. Notably, the fitted values from the experimental data demonstrate a good stiffness accuracy, resulting in an average relative error of  $3.3 \pm 0.3\%$  with respect to desired values.

### 5.2. Human-Robot Interaction Modalities Validation Results

We assessed the capability of the controller to implement the proposed high-level modalities by measuring the perceived pHRI through the monitoring of the voluntary muscular effort of healthy participants. We recruited 14 healthy volunteers, with a median age of 25 years, [24–27] IQR.

#### 5.2.1. Kinematics Variability Assessment

The results of the trajectory tracking RMSE of the elbow joint reported that the overall average tracking error was  $3.38 \pm 1.29$  degrees, and the maximum detected RMSE was 5.73 degrees (about 0.1 radians). The Friedman test rejected the null hypothesis that data came from the same distribution ( $p < 0.0001$ ). The *post-hoc* analysis revealed that only RMSE data of the *P* mode significantly differed from all the other groups ( $p < 0.01$ ). As expected, since we are using an impedance control logic, which does not guarantee an accurate position tracking, and since no effort was required from the user, in *P* mode, we can notice higher errors, but the trajectory variability is minimal. Finally, in *W* mode, by which the controller does not correct for



trajectory deviation, the tracking RMSE was slightly higher than in the other modalities.

### 5.2.2. Electromyographic Monitoring

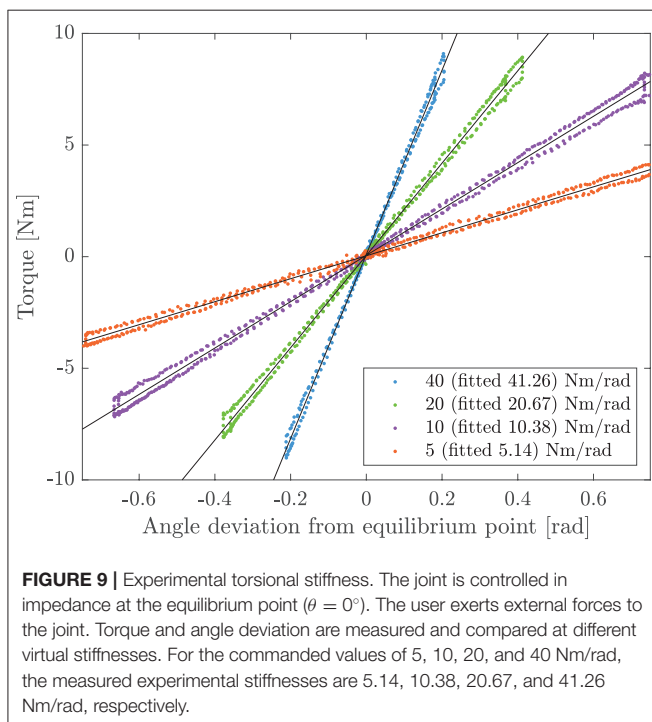
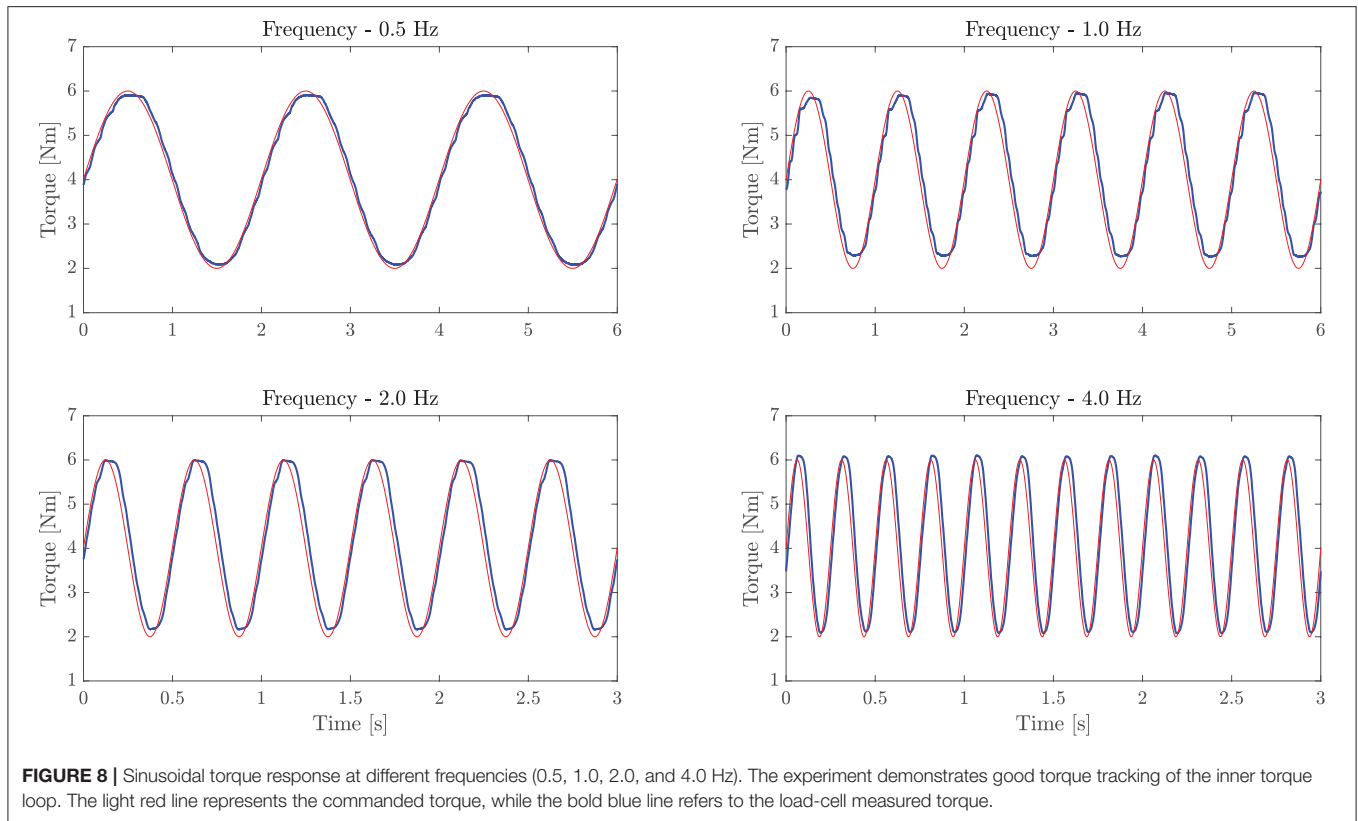
In **Figure 10**, we present the average envelope profiles of muscular contraction (*biceps* and *triceps brachii*), and the torque output for each of the presented high-level modalities.

Furthermore, the iEMG results are reported in **Figure 11** for each high-level mode. The Friedman test revealed significant differences among training modalities for the iEMG index for

the four conditions analyzed (i.e., *biceps* and *triceps* contraction during elbow flexion and extension phases) ( $p < 0.0001$ ). Therefore, we performed further analysis to separately compare each rehabilitation mode with the others. The results of the *post-hoc* analysis are shown in **Tables 3, 4**.

### Passive Mode (P)

In *P* mode, the robot entirely performs the movement, and the subjects were asked to simulate the “passive” behavior by relaxing their muscles along the movement, and by not counteracting to



residual trajectory errors. As expected, the normalized activation of biceps and triceps was minimal, which confirmed the user's "passive" behavior (Figure 10). Considering the biceps activation during the flexion phase, we found a significant difference (i.e.,

$p < 0.05$ ) for all modalities except *W* mode. Instead, triceps contraction during the extension phase resulted in significant difference with *W*, *R*, and *H* modes (Table 3).

#### Corrective Mode (C)

When in *C* mode, the activation of the biceps was not statistically different with respect to the *T* mode ( $p = 1$ ), while it was different from the others. The triceps activation plot shows no significant muscular activity during movement in favor of gravity. In fact, the triceps iEMG was not significantly different from the *P* mode where all the muscles are relaxed ( $p = 0.055$ ). The *C* mode also demonstrates similarity to the *T* mode, by which the user substantially uses the contribution gravity in the extension phase, and therefore, the triceps activation is almost null.

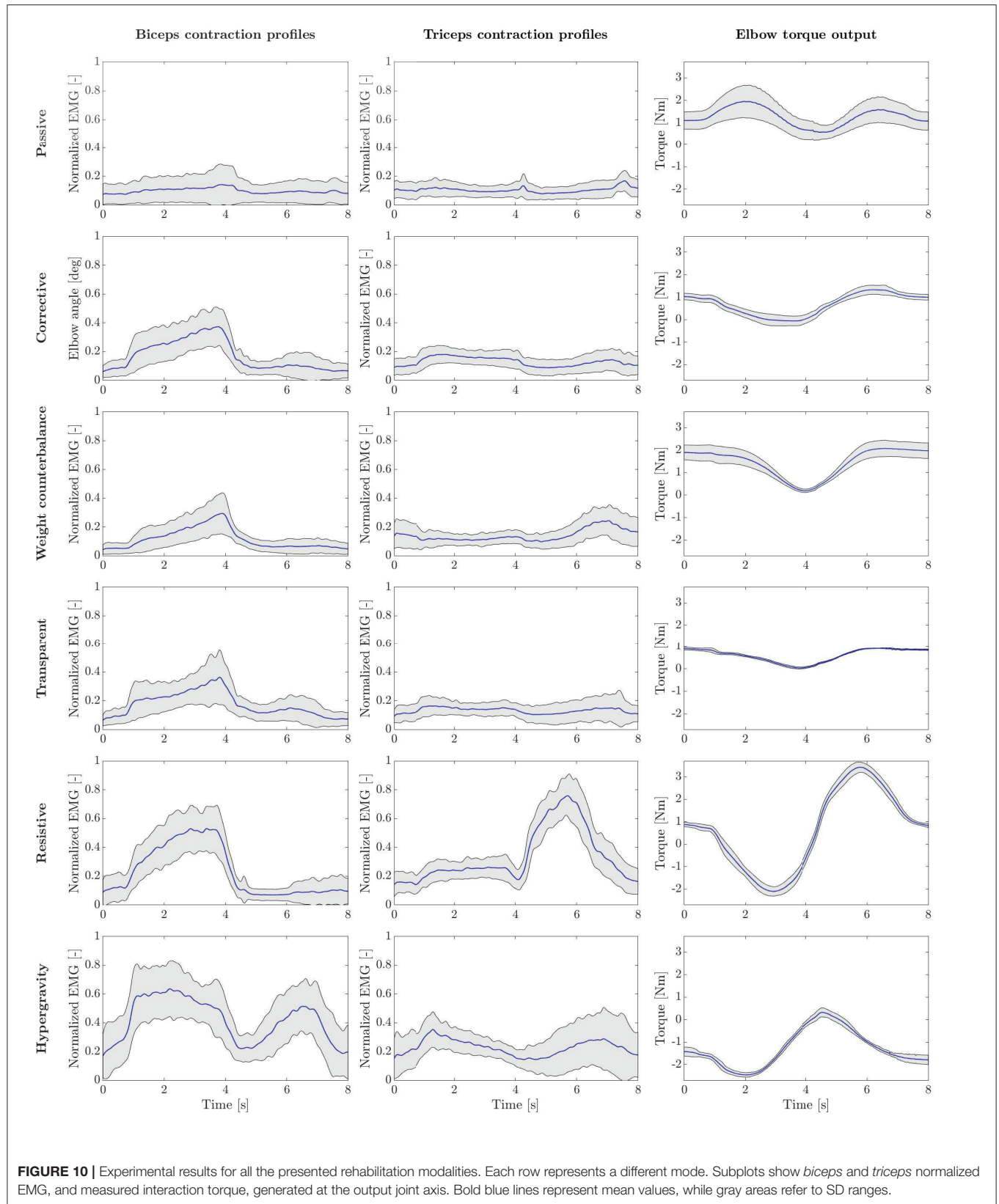
#### Weight Counterbalance Mode (W)

The trials performed in *W* mode showed that the biceps contracted during the lifting phase, and the triceps during the descending phase. Triceps contraction during the extension phase was slightly higher than in *C* mode, as the user could not exploit the effect of gravity to complete the movement and had to contract the antagonist muscles to counteract the robot weight counterbalance.

#### Transparent Mode (T)

Averagely, the users contracted the biceps during the elbow flexion phase and continued to contract during the elbow extension phase to slow down the downward movement. Since the movement was performed against gravity, the triceps





**FIGURE 10 |** Experimental results for all the presented rehabilitation modalities. Each row represents a different mode. Subplots show *biceps* and *triceps* normalized EMG, and measured interaction torque, generated at the output joint axis. Bold blue lines represent mean values, while gray areas refer to SD ranges.

muscle was not significantly activated. We can also observe that both biceps and triceps activation profiles of the *T* mode are substantially similar to *C* mode (Figure 10). This result is confirmed by the iEMG ( $p > 0.05$ ).

#### Resistive Mode (*R*)

In *R* mode, we can observe high biceps contraction during the elbow flexion phase and triceps contraction during the elbow extension. The activation of the biceps during the elbow flexion was significantly higher than all modalities ( $p < 0.05$ ), except the *H* mode. During the elbow extension phase, we observed triceps contraction significantly greater than all the other training modes.

#### Hypergravity Mode (*H*)

The *H* mode involved especially the biceps muscles. Indeed, in Figure 10, we can observe a great muscular contraction of the biceps during both elbow flexion and extension. The biceps iEMG index during the elbow flexion phase was significantly different from all modalities ( $p \leq 0.05$ ), except from the *R* one ( $p = 1$ ), where the users were contracting the biceps to overcome the resistance offered by the robot. During the elbow extension, instead, we observed biceps muscular activation significantly higher than all the other training modalities ( $p \leq 0.001$ ).

#### 5.2.3. Torque Output Results

Regarding the torque output results presented in Figure 10, the right plots show the torque output generated by the elbow-joint system to the users' arm interface. In *P* mode, the measured torque consisted of the torque generated by the motor to complete the task. Such torque is equal to the inverse-dynamic torque needed to passively move the human-robot system along the desired trajectory, besides residual torques that are not rejected by the torque controller. In *C* mode, the measured torque mainly corresponds to the impedance-based torque employed to correct path deviations. Since the participants were well-performing in the task, the torque variability is limited, and it corresponds to the anti-gravity torque of the elbow test-bed, similar to *T* mode. In *W* mode, the system compensates for arm weight, which varies according to the wearer's characteristics. This explains the greater variability and the greater amplitude of torque profiles. In *T* mode, instead, the robot only compensates its weight, with no trajectory correction. Accordingly, the measured torque profiles show a smaller variance, and the trend goes with the cosine of the joint position, as described in Equation (10). The *R* mode shows that torque trends are inversely proportional to the task velocity, demonstrating a viscous frictional behavior. Finally, a visual inspection shows that in *H* mode, the torque output was opposite to the *P* mode. In fact, the assistance in *P* mode was pushing the arm in the opposite direction with respect to the *H* mode, in which the torque output is aligned with the gravity direction.

## 6. DISCUSSION

The literature proposed several high-level training modalities for effective post-stroke rehabilitation treatment. However, their implementation strongly depends on the developed robotic systems. For example, the Harmony exoskeleton exploits an explicit SEA-based impedance controller (Kim et al., 2017), which is similar to our approach, while other exoskeletons, such as ARMin, use instead implicit impedance controllers to promote rehabilitation exercises (Nef et al., 2007; Khan et al., 2015). However, the generalization of these approaches to a large variety of human-robot interaction modalities, their integration in a unified low-level compliant controller, and the validation of the perceived pHRI through the assessment of the voluntary human effort have not been investigated yet.

We developed a compliant controller based on impedance control and implemented it on a test-bed for the elbow flexion/extension. This study aims at validating the proposed unified control framework through two sets of experiments. We first characterized the controller performances. Then, we evaluated the muscular engagement of healthy subjects by operating the robot in six high-level training modalities.

### 6.1. Actuation and Control Characterization

As a first step, we identified a suitable actuation configuration that could be exploited to create a compliant joint for upper-limb rehabilitation robots. We used actuators along with load-cell feedback to provide high-fidelity torque control. In this way, low-impedance behavior can be achieved, and the robot can behave compliantly with respect to the subject, encouraging residual voluntary movements. On top of this configuration, we proposed a generalized explicit impedance-based control law, which includes positive-feedback terms for friction compensation and arm weight counterbalance. We tested the unified controller performances with an elbow flexion-extension test-bed. The experimental results showed that the developed set-up, combined with the proposed low-level controller, exhibited very low impedance at the joint level, imposing negligible resistive torques (less than 0.3 Nm) on the user's free-motion movements. Notably, since the impedance-based corrective term of the unified controller is superimposed to the *T* control mode, achieving a baseline dynamic transparent behavior was a fundamental step to implement compliant rehabilitation strategies. We can conclude that the inner-loop is expected not to influence the high-level behavior, and it can be considered an ideal torque source.

Due to the developed controller's inner explicit torque feedback control, most of the disturbance torques introduced by the high-ratio gearbox could be rejected, without the need for accurate model-based compensation. With these results, we demonstrated that the proposed approach was effective in implementing different virtual stiffness and damping values, that were performed by the robot with good accuracy.

### 6.2. Human-Robot Interaction Modalities Validation

With the developed system, we proposed a set of parameters that could implement various levels of pHRI. Specifically, we

**TABLE 3 |** *P*-values results of the *post-hoc* analysis comparing integrated EMG (iEMG) index among training modalities during elbow flexion movement.

Muscular contraction during elbow flexion phase						
Biceps	P	C	W	T	R	H
P	—					
C	<b>&lt;0.001</b> ↑	—				
W	0.101	<b>&lt;0.001</b> ↓	—			
T	<b>&lt;0.001</b> ↑	1	<b>0.002</b> ↑	—		
R	<b>&lt;0.001</b> ↑	<b>&lt;0.001</b> ↑	<b>&lt;0.001</b> ↑	<b>0.001</b> ↑	—	
H	<b>&lt;0.001</b> ↑	<b>&lt;0.001</b> ↑	<b>&lt;0.001</b> ↑	<b>&lt;0.001</b> ↑	1	—
Triceps	P	C	W	T	R	H
P	—					
C	0.055	—				
W	0.620	0.831	—			
T	0.101	0.081	1.000	—		
R	<b>0.003</b> ↑	<b>0.014</b> ↑	<b>0.002</b> ↑	<b>0.002</b> ↑	—	
H	<b>0.005</b> ↑	<b>0.011</b> ↑	<b>&lt;0.001</b> ↑	<b>0.001</b> ↑	1.000	—

Bold values indicate significant differences between muscular contraction obtained with row and column modalities. Up and down arrows are used to specify if the mode represented in the selected row has significantly higher (↑) or lower (↓) muscular contraction than the mode represented in the respective column of the table.

**TABLE 4 |** *P*-values results of the *post-hoc* analysis comparing iEMG index among training modalities during elbow extension movement.

Muscular contraction during elbow extension phase						
Biceps	P	C	W	T	R	H
P	—					
C	1.000	—				
W	1.000	1.000	—			
T	<b>0.004</b> ↑	1.000	<b>0.013</b> ↑	—		
R	<b>0.043</b> ↑	1.000	0.125	1.000	—	
H	<b>&lt;0.001</b> ↑	<b>&lt;0.001</b> ↑	<b>&lt;0.001</b> ↑	<b>&lt;0.001</b> ↑	<b>&lt;0.001</b> ↑	—
Triceps	P	C	W	T	R	H
P	—					
C	0.272	—				
W	0.101	1.000	—			
T	0.226	1.000	1.000	—		
R	<b>&lt;0.001</b> ↑	<b>0.002</b> ↑	<b>&lt;0.001</b> ↑	<b>0.006</b> ↑	—	
H	<b>0.013</b> ↑	<b>0.011</b> ↑	0.229	<b>0.004</b> ↑	<b>0.009</b> ↑	—

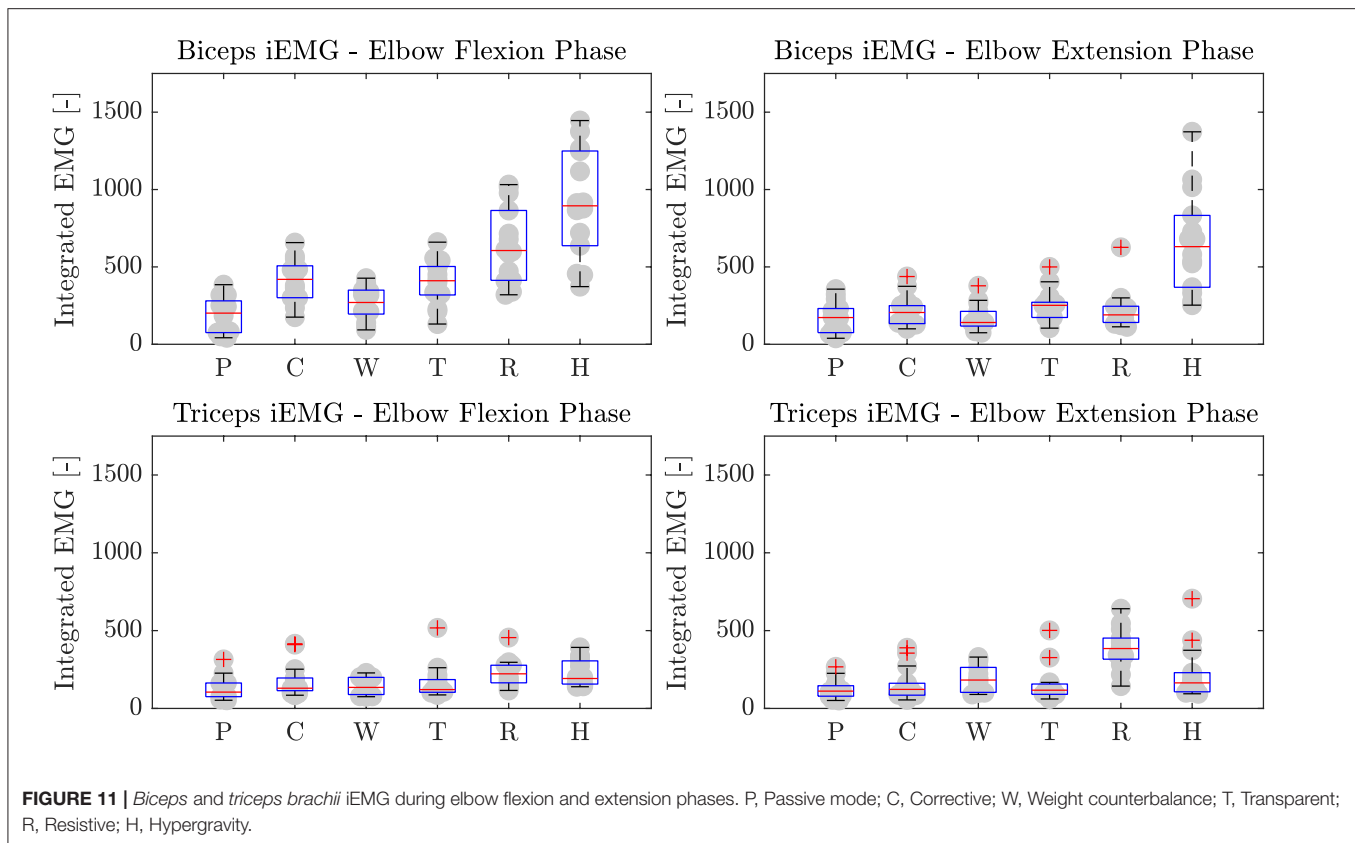
Bold values indicate significant differences between muscular contraction obtained with row and column modalities. Up and down arrows are used to specify if the mode represented in the selected row has significantly higher (↑) or lower (↓) muscular contraction than the mode represented in the respective column of the table.

combined assistance, correction, and resistance to promote a collaborative controller that implements different high-level training modalities. All the previously presented discrete robot-mediated training strategies can be viewed as different points of a continuum of corrective assistance, counterbalance assistance, and resistance. We underline that this study aims not to define a single set of parameters but to test the hypothesis that the parameter space—if properly explored—can be exploited to move across different rehabilitation scenarios. In particular, we included and tested six rehabilitation modalities, as described in section 3.3.

In this study, we evaluated the capability of the proposed framework to realize a wide range of pHRI by measuring the

voluntary muscular activity of healthy subjects in a controlled and replicable experimental protocol. We compared the biceps and triceps muscular activity of 14 healthy subjects under the identified rehabilitation modalities. At the same time, the angular position followed by users and the torque output generated by the elbow-joint system were measured.

The kinematics experimental results demonstrated that the subjects could keep full control of the robotic link while performing elbow flexion/extension tasks. Consequently, the results confirm two crucial hypotheses. First, participants' kinematics performances did not show significant difference across the presented training modalities. Second, all the subjects were able to follow the desired trajectory within the maximum



tolerance of about 0.1 radians (about 5.73 degrees). For these reasons, we posit that, under all tested conditions, all subjects could fulfill the required motor tasks in terms of trajectory tracking, range of movement and timing, no matter the level of assistance/resistance provided. Thus, we could compare the electromyographic data across modalities. We observed trajectory tracking to be less accurate than in a position controlled system (especially for the *P* mode). In fact, the impedance control scheme, due to the pure spring-damper correction, introduces bias offset errors to the trajectory tracking control problem that are not negligible. Contrarily, a position control scheme would reject such errors, but it would not provide compliant behavior with the human arm. Furthermore, in applications by which the robot is coupled with a fragile human arm, achieving precise positioning is not a critical aspect, but it is more important to avoid high interaction torques that can be uncomfortable or potentially hazardous to the wearer.

As desired, we observed that the different human-robot interaction modalities implemented with the unified controller induced different muscular activation patterns, both in *biceps* and *triceps brachii*, according to the selected training mode. The interaction modalities ranged from a full robot action with almost null muscular contribution (*P* mode), to training paradigms where the robot resists and challenges the users, requiring them an extra muscular effort to accomplish the task (*R* and *H* modes).

The *T* mode was considered the baseline reference since it describes the behavior by which neither assistance nor resistance

is provided to the user during the task. In fact, the muscular effort registered in *T* mode corresponds to the natural free task execution. During elbow-flexion, we observed a medium biceps contraction, while the triceps were characterized by a slight co-contraction. During the extension phase, instead, a modulated contraction of the biceps is used to control the downward motion provided by gravity, while the triceps were again not significantly activated, given that the movement was performed in favor of gravity.

We also observed that both *C* and *W* modes promoted similar biceps contractions that are significantly higher with respect to *P* mode. However, when the weight counterbalance was active (i.e., *W* mode), the triceps experienced greater contraction with respect to the other training modalities. Therefore, these results indicate that such modalities induced the physiological contraction of biceps muscles, and that the controller was inducing slightly greater motor antagonistic activation when weight counterbalance assistance was present. Comparing results obtained in *T* mode with the *C* mode, we could interestingly observe that the activation profiles in the two modalities were comparable, despite the *C* mode allowing a reduced effort and avoid any fail in task execution, providing assistance whether the user is not capable of completing the task or is too slow.

We can also observe that, given that the participants were performing controlled movements (i.e., healthy subjects followed a trajectory pre-defined in position and velocity) with comparable performances, the controller was able to induce muscular



patterns in the *C* and *W* modes that are not significantly different from the baseline *T* mode. We can also verify that the torque output in these modalities almost followed the robot weight counterbalance torque (i.e., *T* mode) and that the residual dynamic torque to complete the tasks was generated by users' voluntary contraction. Therefore, we can derive that the proposed control system could correctly implement the assist-as-needed paradigm, helping the user to accomplish the task while inducing the physiological muscular activation pattern.

Instead, in *R* and *H* modes, the statistical analysis confirmed that, for both biceps and triceps, significant greater muscular contraction levels were reached with respect to other modalities. In particular, the *H* mode can be regarded as equivalent to gym-like exercises. In fact, the robot trained the biceps along with the whole movement, during both elbow flexion and extension movements, as if the user was performing the task with payload weights. On the contrary, in *R* mode, the robot trained both muscles during the task: the biceps contracted during the flexion phase, and the triceps during the extension phase.

These results demonstrated that the proposed unified controller could provide low-impedance and high-impedance correction, low-resistance and high-resistance behavior, rendering different levels of pHRI and inducing different levels of muscular contraction and subject's involvement.

### 6.3. Potential Impacts for Neurorehabilitation

From the rehabilitation point of view, the goal is to achieve efficient motor control that should be as similar as possible to the free task scenario, i.e., the *T* mode. Purely corrective strategies (such as *C* mode), around the desired trajectory, modulate the assistance without impacting the muscle recruitment strategy but guaranteeing the completion of the task. Instead, we noticed that in the *W* mode, which involved anti-gravity compensation, the triceps contracted during the extension phase. This implies agonist-antagonist coordination that is entirely different from the natural one, and therefore, it could potentially induce unnatural muscular synergies. From these experimental trials, we observed that anti-gravity compensation of the human arm could induce non-physiological muscular activation, potentially leading to maladaptive plasticity. In this view, a purely corrective approaches might be more effective. However, further investigation is needed to confirm this hypothesis, involving upper arm and forearm tests on the target population.

Finally, the proposed *R* and *H* methods were able to motivate and induce challenging exercises to the subject, training both agonist and antagonist muscles. For this reason, the presented approach could also be applied to the recovery from sports and orthopedic injuries. We claim that the controller could be initially employed to assist the motion during the early stages of the physiotherapy and then—by switching modalities—to improve the muscle mass recovery.

Overall, the controller and the developed hardware confirmed suitability for implementing the training modalities needed for effective physical therapy treatment. With these advancements, we can conclude that the proposed compliant controller might assist the subject along the upper-limb rehabilitation

treatment process, from stages when the patient is completely hemiplegic toward the functional recovery of the limb. Future studies will involve the application of this approach to post-stroke patients to assess its efficacy toward motor recovery. Although we developed a compliant joint for the elbow training, future studies can involve the translation of the proposed solution to multi-degrees-of-freedom applications. Indeed, the joint-space control scheme can be replicated for each joint of the robotic chain, and more sophisticated centralized algorithms for arm weight compensation can be implemented.

## 7. CONCLUSION

In this study, we presented and validated a human-robot cooperative controller for upper-limb robot-mediated neurorehabilitation. The design of the control framework took inspiration from motor learning and neurophysiological aspects, which suggest that good collaboration between the impaired subject and the therapeutic device is preferred to induce effective motor recovery in neurological survivors. In this sense, we found strong evidence that the proposed controller guaranteed dynamic transparency—to promote users' voluntary movements—and produced variable assistance and resistance levels—to tune the rehabilitation treatment according to the subject's performance and involvement.

We demonstrated through electromyographic monitoring that a proper combination of stiffness, damping and weight assistance could properly induce various levels of muscular activation and the subject's participation, namely promoting different human-robot interaction modalities. We believe that since a collaborative controller should provide the minimal amount of assistance to complete the tasks, the presented high-level modalities can be considered as different points of a continuum, and we posit that they can be potentially selectable according to the stage of motor recovery, involving the subject in the completion of the rehabilitation treatment. Our results suggest that the presented collaborative framework is suitable for these purposes. Future studies will extend this approach to multiple degrees of freedom robots and investigate the optimal adaptation control law that makes the controller learn and adapt to the subject's performances in a therapist-like manner. Finally, the efficacy of such a controller on neurological motor recovery will be assessed on post-stroke patients in future studies.

## DATA AVAILABILITY STATEMENT

The raw data supporting the conclusions of this article will be made available by the authors, without undue reservation.

## ETHICS STATEMENT

All the experiments that involved human subjects were approved by the Ethical Committee of Politecnico di Milano (Opinion n. 13/2021). All participants provided written informed consent to

participate in the study. Written informed consent was obtained from the individual(s) for the publication of any potentially identifiable images or data included in this article.

## AUTHOR CONTRIBUTIONS

SD, MG, AP, and FB conceived the presented idea. SD developed the theory and implemented control architecture. SD, MG, and VL conceived testing protocols and performed data analysis. SD and VL performed measurements and drafted the manuscript. All authors discussed the results and contributed to the final manuscript and made a significant contribution

to the review of the manuscript, read, and approved the final manuscript.

## FUNDING

We gratefully acknowledge the funding provided by the AGREE project (Regione Lombardia, Pre-commercial procurement, Ref. ARCA\_2018\_132).

## ACKNOWLEDGMENTS

We thank the volunteers who participated in the study.

## REFERENCES

- Ambrosini, E., Dalla Gasperina, S., Gandolla, M., and Pedrocchi, A. (2019). "Upper-limb exoskeletons for stroke rehabilitation," in *Mediterranean Conference on Medical and Biological Engineering and Computing* (Coimbra: Springer), 1722–1728.
- Andrews, G. J., Pilkar, R., Ramanujam, A., and Nolan, K. J. (2018). Electromyography assessment during gait in a robotic exoskeleton for acute stroke. *Front. Neurol.* 9:630. doi: 10.3389/fneur.2018.00630
- Basteris, A., Nijenhuis, S. M., Stienen, A. H., Buurke, J. H., Prange, G. B., and Amirabdollahian, F. (2014). Training modalities in robot-mediated upper limb rehabilitation in stroke: a framework for classification based on a systematic review. *J. Neuroeng. Rehabil.* 11:111. doi: 10.1186/1743-0003-11-111
- Calanca, A., Muradore, R., and Fiorini, P. (2016). A review of algorithms for compliant control of stiff and fixed-compliance robots. *IEEE/ASME Tran. Mechatron.* 21, 613–624. doi: 10.1109/TMECH.2015.2465849
- Calanca, A., Muradore, R., and Fiorini, P. (2017). Impedance control of series elastic actuators: Passivity and acceleration-based control. *Mechatronics* 47, 37–48. doi: 10.1016/j.mechatronics.2017.08.010
- Chen, T., Casas, R., and Lum, P. S. (2019). An elbow exoskeleton for upper limb rehabilitation with series elastic actuator and cable-driven differential. *IEEE Trans. Rob.* 35, 1464–1474. doi: 10.1109/TRO.2019.2930915
- Crea, S., Cempini, M., Moise, M., Baldoni, A., Trigili, E., Marconi, D., et al. (2016). "A novel shoulder-elbow exoskeleton with series elastic actuators," in *2016 6th IEEE International Conference on Biomedical Robotics and Biomechatronics (BioRob)* (Singapore: IEEE), 1248–1253.
- de Oliveira, A. C., Warburton, K., Sulzer, J. S., and Deshpande, A. D. (2019). "Effort estimation in robot-aided training with a neural network," in *2019 International Conference on Robotics and Automation (ICRA)* (Montreal, QC: IEEE), 563–569.
- Duret, C., Grosmaire, A. G., and Krebs, H. I. (2019). Robot-assisted therapy in upper extremity hemiparesis: overview of an evidence-based approach. *Front. Neurol.* 10:412. doi: 10.3389/fneur.2019.00412
- Focchi, M., Medrano-Cerda, G. A., Boaventura, T., Frigerio, M., Semini, C., Buchli, J., et al. (2016). Robot impedance control and passivity analysis with inner torque and velocity feedback loops. *Control Theory Technol.* 14, 97–112. doi: 10.1007/s11768-016-5015-z
- French, B., Thomas, L. H., Coupe, J., McMahon, N. E., Connell, L., Harrison, J., et al. (2016). Repetitive task training for improving functional ability after stroke. *Cochrane Database Syst. Rev.* 11:CD006073. doi: 10.1002/14651858.CD006073.pub3
- Frisoli, A., Salsedo, F., Bergamasco, M., Rossi, B., and Carboncini, M. C. (2009). A force-feedback exoskeleton for upper-limb rehabilitation in virtual reality. *Appl. Bionics Biomech.* 6, 115–126. doi: 10.1155/2009/378254
- Gandolla, M., Guanzirio, E., D'Angelo, A., Cannaviello, G., Molteni, F., and Pedrocchi, A. (2018). Automatic setting procedure for exoskeleton-assisted overground gait: proof of concept on stroke population. *Front. Neurobot.* 12:10. doi: 10.3389/fnbot.2018.00010
- Gorelick, P. B. (2019). The global burden of stroke: persistent and disabling. *Lancet Neurol.* 18, 417–418. doi: 10.1016/S1474-4422(19)30030-4
- Guidali, M., Duschau-Wicke, A., Broggi, S., Klamroth-Marganska, V., Nef, T., and Riener, R. (2011). A robotic system to train activities of daily living in a virtual environment. *Med. Biol. Eng. Comput.* 49, 1213–1223. doi: 10.1007/s11517-011-0809-0
- Gull, M. A., Bai, S., and Bak, T. (2020). A review on design of upper limb exoskeletons. *Robotics* 9, 16. doi: 10.3390/robotics9010016
- Hogan, N. (1984). An organizing principle for a class of voluntary movements. *J. Neurosci.* 4, 2745–2754. doi: 10.1523/JNEUROSCI.04-11-0274.5.1984
- Hogan, N. (1985). Impedance control: an approach to manipulation: part I-theory. *J. Dyn. Syst. Meas. Control Trans. ASME* 107, 1–7. doi: 10.1115/1.3140702
- Hogan, N. (1989). "Controlling impedance at the man/machine interface," in *1989 IEEE International Conference on Robotics and Automation* (Scottsdale, AZ: IEEE Computer Society), 1626–1627.
- Huang, V. S., and Krakauer, J. W. (2009). Robotic neurorehabilitation: a computational motor learning perspective. *J. Neuroeng. Rehabil.* 6, 1–13. doi: 10.1186/1743-0003-6-5
- Iandolo, R., Marini, F., Semprini, M., Laffranchi, M., Mugnosso, M., Cherif, A., et al. (2019). Perspectives and challenges in robotic neurorehabilitation. *Appl. Sci.* 9, 3183. doi: 10.3390/app9153183
- Johnson, W., Onuma, O., Owolabi, M., and Sachdev, S. (2016). Stroke: a global response is needed. *Bull. World Health Organ.* 94, 634. doi: 10.2471/BLT.16.181636
- Just, F., Özen, Ö., Bösch, P., Bobrovsky, H., Klamroth-Marganska, V., Riener, R., et al. (2018). Exoskeleton transparency: Feed-forward compensation vs. disturbance observer. *Automatisierungstechnik* 66, 1014–1026. doi: 10.1515/auto-2018-0069
- Just, F., Özen, Ö., Tortora, S., Klamroth-Marganska, V., Riener, R., and Rauter, G. (2020). Human arm weight compensation in rehabilitation robotics: efficacy of three distinct methods. *J. Neuroeng. Rehabil.* 17, 1–17. doi: 10.1186/s12984-020-0644-3
- Just, F., Özen, Ö., Tortora, S., Riener, R., and Rauter, G. (2017). "Feedforward model based arm weight compensation with the rehabilitation robot armin," in *2017 International Conference on Rehabilitation Robotics (ICORR)* (London: IEEE), 72–77.
- Keemink, A. Q., van der Kooij, H., and Stienen, A. H. (2018). Admittance control for physical human-robot interaction. *Int. J. Rob. Res.* 37, 1421–1444. doi: 10.1177/0278364918768950
- Khan, A. M., Yun, D.-w., Ali, M. A., Han, J., Shin, K., and Han, C. (2015). "Adaptive impedance control for upper limb assist exoskeleton," in *2015 IEEE International Conference on Robotics and Automation (ICRA)* (Seattle, WA: IEEE), 4359–4366.
- Kim, B., and Deshpande, A. D. (2015). "Controls for the shoulder mechanism of an upper-body exoskeleton for promoting scapulohumeral rhythm," in *2015 IEEE International Conference on Rehabilitation Robotics (ICORR)* (Singapore: IEEE), 538–542.
- Kim, B., Rodot, A., and Deshpande, A. D. (2014). "Impedance control based on a position sensor in a rehabilitation robot," in *ASME 2014 Dynamic Systems and Control Conference. American Society of Mechanical Engineers Digital Collection* (San Antonio, TX).

- Kim, G., Lim, S. Y., Kim, H. J., Lee, B. J., Seo, S. C., Cho, K. H., et al. (2017). Is robot-assisted therapy effective in upper extremity recovery in early stage stroke? - a systematic literature review. *J. Phys. Ther. Sci.* 29, 1108–1112. doi: 10.1589/jpts.29.1108
- Kong, K., Moon, H., Jeon, D., and Tomizuka, M. (2010). Control of an exoskeleton for realization of aquatic therapy effects. *IEEE/ASME Trans. Mechatron.* 15, 191–200. doi: 10.1109/TMECH.2010.2041243
- Krakauer, J. W. (2006). Motor learning: its relevance to stroke recovery and neurorehabilitation. *Curr. Opin. Neurol.* 19, 84–90. doi: 10.1097/01.wco.0000200544.29915.cc
- Krebs, H. I., Aisen, M. L., Volpe, B. T., and Hogan, N. (1999). Quantization of continuous arm movements in humans with brain injury. *Proc. Natl. Acad. Sci. U.S.A.* 96, 4645–4649. doi: 10.1073/pnas.96.8.4645
- Krebs, H. I., Palazzolo, J. J., Dipietro, L., Ferraro, M., Krol, J., Ranekleiv, K., et al. (2003). Rehabilitation robotics: performance-based progressive robot-assisted therapy. *Auton. Robots.* 15, 7–20. doi: 10.1023/A:1024494031121
- Lobo-Prat, J., Kooren, P. N., Janssen, M. M., Keemink, A. Q., Veltink, P. H., Stienen, A. H., et al. (2016). Implementation of emg-and force-based control interfaces in active elbow supports for men with duchenne muscular dystrophy: a feasibility study. *IEEE Trans. Neural Syst. Rehabil. Eng.* 24, 1179–1190. doi: 10.1109/TNSRE.2016.2530762
- Mao, Y., and Agrawal, S. K. (2012). Design of a cable-driven arm exoskeleton (carex) for neural rehabilitation. *IEEE Trans. Rob.* 28, 922–931. doi: 10.1109/TRO.2012.2189496
- Marchal-Crespo, L., and Reinkensmeyer, D. J. (2009). Review of control strategies for robotic movement training after neurologic injury. *J. Neuroeng. Rehabil.* 6, 1–15. doi: 10.1186/1743-0003-6-20
- Masiero, S., Celia, A., Rosati, G., and Armani, M. (2007). Robotic-assisted rehabilitation of the upper limb after acute stroke. *Arch. Phys. Med. Rehabil.* 88, 142–149. doi: 10.1016/j.apmr.2006.10.032
- Masud, N., Smith, C., and Isaksson, M. (2018). Disturbance observer based dynamic load torque compensator for assistive exoskeletons. *Mechatronics* 54, 78–93. doi: 10.1016/j.mechatronics.2018.07.003
- Mehdi, H., and Boubaker, O. (2012). Stiffness and impedance control using lyapunov theory for robot-aided rehabilitation. *Int. J. Soc. Rob.* 4, 107–119. doi: 10.1007/s12369-011-0128-5
- Mehrholz, J., Pohl, M., Platz, T., Kugler, J., and Elsner, B. (2018). Electromechanical and robot-assisted arm training for improving activities of daily living, arm function, and arm muscle strength after stroke. *Cochrane Database Syst. Rev.* 2015:CD006876. doi: 10.1002/14651858.CD006876.pub5
- Mehrholz, J., Pollock, A., Pohl, M., Kugler, J., and Elsner, B. (2020). Systematic review with network meta-analysis of randomized controlled trials of robotic-assisted arm training for improving activities of daily living and upper limb function after stroke. *J. Neuroeng. Rehabil.* 17, 1–14. doi: 10.1186/s12984-020-00715-0
- Meng, W., Liu, Q., Zhou, Z., Ai, Q., Sheng, B., and Xie, S. S. (2015). Recent development of mechanisms and control strategies for robot-assisted lower limb rehabilitation. *Mechatronics* 31, 132–145. doi: 10.1016/j.mechatronics.2015.04.005
- Moubarak, S., Pham, M. T., Moreau, R., and Redarce, T. (2010). Gravity compensation of an upper extremity exoskeleton. *Ann. Int. Conf. IEEE Eng. Med. Biol.* 2010, 4489–4493.
- Mukaka, M. M. (2012). A guide to appropriate use of correlation coefficient in medical research. *Malawi Med. J.* 24, 69–71. Available online at: <https://www.ajol.info/index.php/mmj/article/view/81576>
- Näf, M. B., Koopman, A. S., Baltrusch, S., Rodriguez-Guerrero, C., Vanderborght, B., and Lefeber, D. (2018). Passive back support exoskeleton improves range of motion using flexible beams. *Front. Robot. AI* 5:72. doi: 10.3389/frobt.2018.00072
- Nef, T., Mihelj, M., and Riener, R. (2007). Armin: a robot for patient-cooperative arm therapy. *Med. Biol. Eng. Comput.* 45, 887–900. doi: 10.1007/s11517-007-0226-6
- Neilson, P. D. (1972). Speed of response or bandwidth of voluntary system controlling elbow position in intact man. *Med. Biol. Eng.* 10, 450–459. doi: 10.1007/BF02474193
- Pehlivan, A. U., Losey, D. P., and O'Malley, M. K. (2015). Minimal assist-as-needed controller for upper limb robotic rehabilitation. *IEEE Trans. Rob.* 32, 113–124. doi: 10.1109/TRO.2015.2503726
- Perez-Ibarra, J. C., Siqueira, A. A., and Krebs, H. I. (2015). Assist-As-needed ankle rehabilitation based on adaptive impedance control. *IEEE Int. Conf. Rehabil. Rob.* 2015, 723–728. doi: 10.1109/ICORR.2015.7281287
- Pérez-Ibarra, J. C., Siqueira, A. A., Silva-Couto, M. A., De Russo, T. L., and Krebs, H. I. (2019). Adaptive impedance control applied to robot-aided neuro-rehabilitation of the ankle. *IEEE Rob. Autom. Lett.* 4, 185–192. doi: 10.1109/LRA.2018.2885165
- Proietti, T., Crocher, V., Roby-Brami, A., and Jarrasse, N. (2016). Upper-limb robotic exoskeletons for neurorehabilitation: a review on control strategies. *IEEE Rev. Biomed. Eng.* 9, 4–14. doi: 10.1109/RBME.2016.2552201
- Proietti, T., Jarrassé, N., Roby-Brami, A., and Morel, G. (2015). “Adaptive control of a robotic exoskeleton for neurorehabilitation,” in *2015 7th International IEEE/EMBS Conference on Neural Engineering (NER)* (Montpellier: IEEE), 803–806.
- Ragonesi, D., Agrawal, S. K., Sample, W., and Rahman, T. (2013). Quantifying anti-gravity torques for the design of a powered exoskeleton. *IEEE Trans. Neural Syst. Rehabil. Eng.* 21, 283–288. doi: 10.1109/TNSRE.2012.2222047
- Reinkensmeyer, D. J., Burdet, E., Casadio, M., Krakauer, J. W., Kwakkel, G., Lang, C. E., et al. (2016). Computational neurorehabilitation: modeling plasticity and learning to predict recovery. *J. Neuroeng. Rehabil.* 13, 1–25. doi: 10.1186/s12984-016-0148-3
- Ricamato, A. L., and Hidler, J. M. (2005). Quantification of the dynamic properties of emg patterns during gait. *J. Electromyogr. Kinesiol.* 15, 384–392. doi: 10.1016/j.jelekin.2004.10.003
- Ruiz, A. F., Rocon, E., and Forner-Cordero, A. (2009). Exoskeleton-based robotic platform applied in biomechanical modelling of the human upper limb. *Appl. Bionics Biomech.* 6, 205–216. doi: 10.1155/2009/647178
- Schumacher, M., Wojtusch, J., Beckerle, P., and von Stryk, O. (2019). An introductory review of active compliant control. *Rob. Auton. Syst.* 119, 185–200. doi: 10.1016/j.robot.2019.06.009
- Song, Z., Guo, S., Pang, M., Zhang, S., Xiao, N., Gao, B., et al. (2014). Implementation of resistance training using an upper-limb exoskeleton rehabilitation device for elbow joint. *J. Med. Biol. Eng.* 34, 188–196. doi: 10.5405/jmb.e.1337
- Vallery, H., Veneman, J., Van Asseldonk, E., Ekkelenkamp, R., Buss, M., and Van Der Kooij, H. (2008). Compliant actuation of rehabilitation robots. *IEEE Rob. Autom. Mag.* 15, 60–69. doi: 10.1109/MRA.2008.927689
- Veerbeek, J. M., Langbroek-Amersfoort, A. C., Van Wegen, E. E., Meskers, C. G., and Kwakkel, G. (2017). Effects of robot-assisted therapy for the upper limb after stroke: a systematic review and meta-analysis. *Neurorehabil. Neural Repair.* 31, 107–121. doi: 10.1177/154596831666957
- Winstein, C. J., Stein, J., Arena, R., Bates, B., Cherney, L. R., Cramer, S. C., et al. (2016). Guidelines for adult stroke rehabilitation and recovery: a guideline for healthcare professionals from the american heart association/american stroke association. *Stroke* 47, e98–e169. doi: 10.1161/STR.0000000000000098
- Winter, D. A. (2009). *Biomechanics and Motor Control of Human Movement*. John Wiley & Sons.
- Wit, C. C. D., Olsson, H., Åström, K. J., Gäfvert, M., and Lischinsky, P. (1998). Friction models and friction compensation. *Eur. J. Control* 4, 176–195. doi: 10.1016/S0947-3580(98)70113-X
- Wolbrecht, E. T., Chan, V., Reinkensmeyer, D. J., and Bobrow, J. E. (2008). Optimizing compliant, model-based robotic assistance to promote neurorehabilitation. *IEEE Trans. Neural Syst. Rehabil. Eng.* 16, 286–297. doi: 10.1109/TNSRE.2008.918389
- Wu, K.-Y., Su, Y.-Y., Yu, Y.-L., Lin, C.-H., and Lan, C.-C. (2019). A 5-degrees-of-freedom lightweight elbow-wrist exoskeleton for forearm fine-motion rehabilitation. *IEEE/ASME Trans. Mechatron.* 24, 2684–2695. doi: 10.1109/TMECH.2019.2945491
- Zanotto, D., Lenzi, T., Stegall, P., and Agrawal, S. K. (2013). Improving transparency of powered exoskeletons using force/torque sensors on

the supporting cuffs. *IEEE Int. Conf. Rehabil. Rob.* 2013:6650404. doi: 10.1109/ICORR.2013.6650404

**Conflict of Interest:** SD, FB, AP, and MG hold shares in AGADE srl, Milan, Italy.

The remaining author declares that the research was conducted in the absence of any commercial or financial relationships that could be construed as a potential conflict of interest.

**Publisher's Note:** All claims expressed in this article are solely those of the authors and do not necessarily represent those of their affiliated organizations, or those of

the publisher, the editors and the reviewers. Any product that may be evaluated in this article, or claim that may be made by its manufacturer, is not guaranteed or endorsed by the publisher.

Copyright © 2022 Dalla Gasperina, Longatelli, Braghin, Pedrocchi and Gandolla. This is an open-access article distributed under the terms of the Creative Commons Attribution License (CC BY). The use, distribution or reproduction in other forums is permitted, provided the original author(s) and the copyright owner(s) are credited and that the original publication in this journal is cited, in accordance with accepted academic practice. No use, distribution or reproduction is permitted which does not comply with these terms.





# Evaluation of Optimal Control Approaches for Predicting Active Knee-Ankle-Foot-Orthosis Motion for Individuals With Spinal Cord Injury

Miriam Febrer-Nafria<sup>1,2\*</sup>, Benjamin J. Fregly<sup>3</sup> and Josep M. Font-Llagunes<sup>1,2</sup>

<sup>1</sup> Biomechanical Engineering Lab, Department of Mechanical Engineering and Research Centre for Biomedical Engineering, Universitat Politècnica de Catalunya, Barcelona, Spain, <sup>2</sup> Health Technologies and Innovation, Institut de Recerca Sant Joan de Déu, Esplugues de Llobregat, Spain, <sup>3</sup> Department of Mechanical Engineering, Rice University, Houston, TX, United States

## OPEN ACCESS

### Edited by:

Hong Qiao,  
University of Chinese Academy of  
Sciences, China

### Reviewed by:

Monireh Ahmadi Bani,  
University of Social Welfare and  
Rehabilitation Sciences, Iran  
Zhijun Zhang,  
South China University of  
Technology, China

### \*Correspondence:

Miriam Febrer-Nafria  
miriam.febrer@upc.edu

**Received:** 27 July 2021

**Accepted:** 08 December 2021

**Published:** 24 January 2022

### Citation:

Febrer-Nafria M, Fregly BJ and  
Font-Llagunes JM (2022) Evaluation of  
Optimal Control Approaches for  
Predicting Active  
Knee-Ankle-Foot-Orthosis Motion for  
Individuals With Spinal Cord Injury.  
*Front. Neurobot.* 15:748148.  
doi: 10.3389/fnbot.2021.748148

Gait restoration of individuals with spinal cord injury can be partially achieved using active orthoses or exoskeletons. To improve the walking ability of each patient as much as possible, it is important to personalize the parameters that define the device actuation. This study investigates whether using an optimal control-based predictive simulation approach to personalize pre-defined knee trajectory parameters for an active knee-ankle-foot orthosis (KAFO) used by spinal cord injured (SCI) subjects could potentially be an alternative to the current trial-and-error approach. We aimed to find the knee angle trajectory that produced an improved orthosis-assisted gait pattern compared to the one with passive support (locked knee). We collected experimental data from a healthy subject assisted by crutches and KAFOs (with locked knee and with knee flexion assistance) and from an SCI subject assisted by crutches and KAFOs (with locked knee). First, we compared different cost functions and chose the one that produced results closest to experimental locked knee walking for the healthy subject (angular coordinates mean RMSE was 5.74°). For this subject, we predicted crutch-orthosis-assisted walking imposing a pre-defined knee angle trajectory for different maximum knee flexion parameter values, and results were evaluated against experimental data using that same pre-defined knee flexion trajectories in the real device. Finally, using the selected cost function, gait cycles for different knee flexion assistance were predicted for an SCI subject. We evaluated changes in four clinically relevant parameters: foot clearance, stride length, cadence, and hip flexion ROM. Simulations for different values of maximum knee flexion showed variations of these parameters that were consistent with experimental data for the healthy subject (e.g., foot clearance increased/decreased similarly in experimental and predicted motions) and were reasonable for the SCI subject (e.g., maximum parameter values were found for moderate knee flexion). Although more research is needed before this method can be applied to choose optimal active orthosis controller parameters for specific subjects, these findings suggest that optimal control prediction of crutch-orthosis-assisted walking using biomechanical models might be used in place of the trial-and-error method to select the best maximum knee flexion angle during gait for a specific SCI subject.

**Keywords:** biomechanics, direct collocation, optimal control, spinal cord injury, knee-ankle-foot orthosis, exoskeleton, human motion prediction

## INTRODUCTION

Walking impairment after spinal cord injury leads to a decreased quality of life, other serious health conditions (e.g., heart disease, high blood pressure), and substantial health care costs. Gait restoration can be partially achieved using active orthoses or exoskeletons, together with some type of external support for balance (e.g., crutches or a walker). In recent years, researchers have developed an active knee-ankle-foot orthosis (KAFO) for individuals with spinal cord injury that retain some hip mobility (Font-Llagunes et al., 2020). This assistive device locks the knee during the stance phase and imposes a pre-specified knee angle trajectory during the swing phase. Allowing knee flexion during swing, as opposed to a passive KAFO that locks the knee throughout the gait cycle, improves the gait pattern by increasing gait speed, stride length, and cadence while decreasing step width and lateral displacement of the center of mass (Font-Llagunes et al., 2020). In general, these modifications in gait patterns result in increased balance, reduced compensatory strategies, and decreased energy consumption (Michaud et al., 2019). To improve the walking ability of each patient as much as possible, it is important to personalize conveniently the parameters that define the device actuation, which may be different for each subject (Zhang et al., 2017; Cardona et al., 2020; Fricke et al., 2020) and may lead to undesired walking patterns if they are not correctly specified.

Exoskeleton controller parameters are usually manually adjusted based on subjective information, e.g., asking users which condition they prefer (MacLean and Ferris, 2019) or based on physiotherapists' visual assessment of basic gait parameters like foot clearance (Koopman et al., 2013). Personalization of the pre-specified orthosis knee motion parameter values for each spinal cord-injured (SCI) subject is typically done by following an experimental trial-and-error approach, which possesses significant limitations: (1) it is time-consuming and cumbersome for patients, (2) it is based on physiotherapist subjective intuition, (3) it necessitates training for physiotherapists when they start using this new device, and (4) it may lead to adverse events like falls if parameter values are not correctly specified. Because of these limitations, it is currently very difficult to select experimentally an optimal set of knee motion parameter values for a specific individual such that the assisted gait pattern is improved as much as possible. Therefore, a more objective way of evaluating different combinations of parameter values, which may also reduce required patient testing time, is needed.

Computational methods to identify assistive device design parameters or to tune their control parameters automatically have been developed in previous studies. In Fricke et al.'s study (Fricke et al., 2020), an algorithm to tune the assistance of a robotic gait trainer automatically was compared to manually-tuned assistance for 10 people with neurological disorders (six strokes and four spinal cord injuries). The authors concluded that automatic tuning of exoskeleton parameters is quicker than manual tuning and presents good performance, although clinical trials are needed to determine whether these apparent advantages result in better clinical outcomes. In Zhang et al.'s study (Zhang et al., 2017), a method for real-time identification

of exoskeleton control parameters that minimize the metabolic energy cost of human walking was developed, and it was found that optimized assistance patterns varied widely across participants, demonstrating the importance of customization. Other studies used musculoskeletal models to estimate the user's kinetic parameters to control in real-time an exoskeleton (Cardona et al., 2020) or to simulate assisted human motion for identifying design parameters of assistive devices (García-Vallejo et al., 2016; Ong et al., 2016; Uchida et al., 2016). Moreover, optimal control has recently been used to identify the optimal spring characteristics of an ankle-foot orthosis that minimizes muscle effort (Sreenivasa et al., 2017), to predict subject-exoskeleton combined motion when lifting a box using a lower back exoskeleton (Millard et al., 2017), and to simulate a sit-to-stand transition using a lower limb exoskeleton (Serrancolí et al., 2019). Finding the correct optimal control problem formulation for the generation of new impaired or assisted walking motions is a current challenge (Mombaur, 2016; Falisse et al., 2019; De Groote and Falisse, 2021). In the study of Meyer et al. (2016), stroke patient walking was predicted at different speeds. In this work, in addition to minimizing joint jerk, the cost function included various tracking terms (upper body joint angles and lower body joint torques, muscle activations, or synergy activations), following the assumption that under different conditions the subject would try to find a solution close to what he did in the nominal case. In Sauder et al.'s study (Sauder et al., 2019), a personalized functional electrical stimulation treatment for fast-speed treadmill training was designed for an individual post-stroke. In that study, the cost function included minimization of joint jerk and minimization of inter-limb propulsive force asymmetry, which was the targeted gait improvement parameter. Finally, Febrer-Nafria et al. (2021) recently found that a multi-term cost function combining minimization of joint jerk, joint torque change, joint mechanical power, and angular momentum predicted four-point crutch walking well without tracking experimental data. All of these studies show that combining subject-specific models with optimal control methods is a promising approach to design patient-specific treatments, including the personalization of active orthoses for SCI subjects.

This study investigates whether the use of a computational approach to personalize pre-defined knee trajectory parameters for an active KAFO could potentially be a better choice than the current trial-and-error approach. This investigation does not compare directly the simulation approach with manual tuning but rather explores optimal control problem formulations that allow different pre-defined assistive knee angle trajectories to be simulated, thereby permitting identification of the best walking pattern for a specific individual with SCI. This goal has been pursued by using a new optimal control problem formulation for predicting crutch-orthosis-assisted walking of an SCI subject wearing the presented active orthoses, given as an initial guess the subject's gait without knee flexion-extension assistance (i.e., locked knee) and imposing a specific pre-defined knee angle trajectory. In this way, the experimental trial-and-error process of manually adjusting these knee motion parameters for each patient could potentially be avoided with improvement being

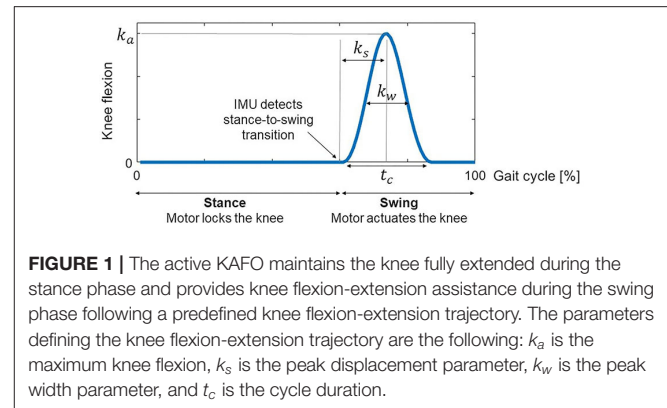
estimated quantitatively. Such improvement has been defined in terms of change in clinically meaningful/relevant measurements, such as foot clearance, stride length, cadence, and hip flexion range of motion (ROM). In this work, the maximum knee flexion angle parameter, which is usually the first one tuned in the trial-and-error approach, has been investigated. Before applying the simulation pipeline to a specific SCI subject, the simulation pipeline was developed and evaluated using experimental data collected from a healthy subject. The main reason for using healthy subject data first was to enable a complete experimental evaluation of the predictive simulation approach. While the healthy subject could place each foot correctly on one force plate while walking using active orthoses and instrumented crutches, the SCI subject could not. First, an optimal control problem formulation for predicting crutch-orthosis-assisted walking was defined comparing different cost functions and evaluating them against experimental data (locked knee case for the healthy subject). Next, using the selected cost function, motions with knee flexion assistance for two different sets of knee angle trajectory parameter values were predicted, and changes in clinical measurements with respect to predicted locked knee motion were evaluated. Finally, using the selected cost function, locked knee motion and different motions with knee flexion assistance were predicted for an SCI subject. Given the subject's gait with passive supports, different knee trajectories (with four different maximum knee flexion angle parameters) were tested computationally. In this case, improvements in gait pattern were quantified in terms of changes in clinical measurements with respect to predicted locked knee motion. These results represent a step forward in the computational personalization of pre-defined knee angle trajectories for the control of an active KAFO for SCI subjects. We consider that having a simulation tool that allows testing of different pre-defined knee motions for a specific SCI subject model, with the aim of finding a more balanced and improved assisted gait pattern (with respect to the standard locked knee motion), will overcome the limitations of manual personalization of pre-specified knee motion parameter values and will result in an improved assisted motion for each SCI subject.

## MATERIALS AND METHODS

### Orthosis Description and Current Personalization Methods

#### Orthosis Description and Function

The active KAFO used in our study is intended for patients with SCI with some remaining motor function at the hip but who cannot control their knee and ankle muscles. These patients can walk using passive KAFOs (which avoid knee flexion and ankle dorsiflexion), which are custom-tailored to the subject, and crutches. However, the resulting gait is unnatural and exhausting due to the compensatory strategies associated with straight knee walking. The active KAFO provides knee flexion-extension assistance during the swing phase and maintains the knee fully extended during the stance phase, thanks to actuation provided by a brushless direct current motor combined with a



**FIGURE 1 |** The active KAFO maintains the knee fully extended during the stance phase and provides knee flexion-extension assistance during the swing phase following a predefined knee flexion-extension trajectory. The parameters defining the knee flexion-extension trajectory are the following:  $k_a$  is the maximum knee flexion,  $k_s$  is the peak displacement parameter,  $k_w$  is the peak width parameter, and  $t_c$  is the cycle duration.

harmonic drive transmission. In contrast to a passive KAFO, allowing knee flexion during swing improves the gait pattern by increasing balance, reducing compensatory strategies, and decreasing energy consumption (Michaud et al., 2019; Font-Llagunes et al., 2020). The active orthosis has a fixed ankle joint that keeps the foot perpendicular to the shank, and the length of the shank and the thigh links can be adjusted to fit the anthropometry of the user. Regarding the orthosis controller, inertial measurement unit (IMU) data are used to identify the time instant when the knee flexion-extension cycle must be triggered at swing phase initiation (stance-to-swing transition). Then, a proportional–integral–derivative (PID) control with feedforward velocity and acceleration is used to keep the knee in full extension during the stance phase (straight leg, knee locked) and perform a pre-defined knee flexion-extension trajectory after detection of the stance-to-swing transition (Font-Llagunes et al., 2020):

$$\theta(t) = \frac{k_a}{2} \left[ 1 - \cos\left(\frac{2\pi}{t_c}t - k_s \sin\left(\frac{\pi}{t_c}t\right) - k_w \sin\left(\frac{2\pi}{t_c}t\right) \right) \right], \quad 0 \leq t \leq t_c \quad (1)$$

where  $\theta(t)$  is the pre-defined angle trajectory for each knee during the swing phase,  $k_a$  is the maximum knee flexion,  $k_s$  is the peak displacement parameter,  $k_w$  is the peak width parameter, and  $t_c$  is the flexion-extension cycle duration (Figure 1). The parameters defining the knee angle trajectory ( $k_a$ ,  $k_s$ ,  $k_w$  and  $t_c$ ) may be personalized to each subject so as to maximize their walking ability.

#### The Current Procedure for Personalizing Knee Angle Parameters

The current personalization method is based on manual tuning of the parameters that define the knee angle trajectory (Equation 1). Usually, the starting point is based on a default set of parameters that have worked for other patients. The patient walks with this set of values, and stride length and stance time for each leg are obtained from the device IMU measurements. In addition to this feedback, the physiotherapist measures relevant kinematic and spatiotemporal parameters that are usually used as outcome measures in clinical studies of lower-limb exoskeletons

(Rodríguez-Fernández et al., 2021). One of the most important parameters is foot clearance, as the ankle of the orthosis is fixed at  $90^\circ$ . If there is not enough hip and knee flexion, the toes can catch the ground during the swing phase, which may produce a fall (Koopman et al., 2013; Begg et al., 2019; Di Natali et al., 2019; Fricke et al., 2020). Stride length and cadence are also important to indicate improvements in walking patterns (Koopman et al., 2013; Rasouli and Reed, 2020; Rodríguez-Fernández et al., 2021). Finally, hip flexion ROM is a good indicator of foot clearance and stride length (Cardona et al., 2020; Fricke et al., 2020; Rasouli and Reed, 2020; Rodríguez-Fernández et al., 2021). Moreover, bilateral symmetry in hip flexion is associated with bilateral symmetry in the gait pattern. Based on all of these clinical observations and measurements, some parameter values are modified in an iterative process based on the physiotherapist's experience. The first parameters that are modified are maximum knee flexion  $k_a$ , which is the most critical one, and peak width  $k_w$ . In some cases, especially if the patient presents some spasticity, the peak displacement parameter  $k_s$ , which indicates flexion/extension duration ratio, is also modified.

## Development and Evaluation of the Prediction Framework Using Healthy Subject Data

In this work, experimental data were collected for two subjects, one healthy and one with SCI, both assisted by a pair of active KAFOs and a pair of forearm crutches. The simulation pipeline was developed and evaluated using the experimental data of the healthy subject and was later applied to predict SCI subject motion with different knee angle trajectories. A summary of the steps followed is provided below, and details regarding each step for the healthy subject are explained in this subsection, and for the SCI subject in the following subsection:

- 1) Collection of experimental data from the healthy subject
- 2) Computational model development for the healthy subject
- 3) Testing of different cost function formulations using healthy subject data with locked knee angle to identify the best formulation
- 4) Evaluation of the best cost function from step 3) using healthy subject data with different knee angle trajectories
- 5) Collection of experimental data from the SCI subject
- 6) Computational model development for the SCI subject
- 7) Evaluation of the best cost function from step 3) using SCI subject data with locked knee angle
- 8) Application of the best cost function from step 3) to predict SCI subject motion with different knee angle trajectories

### Experimental Data Collection

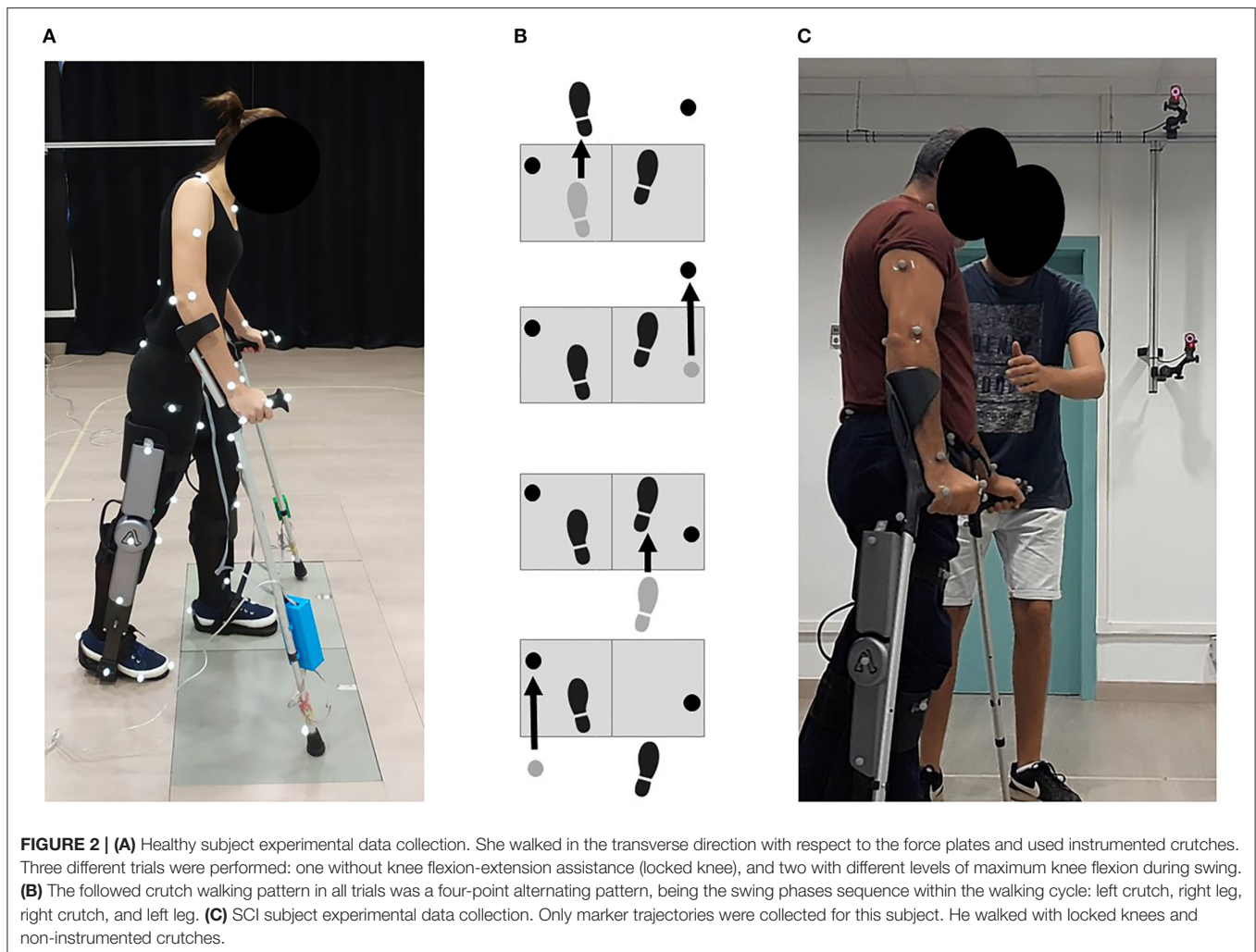
To find the most suitable problem formulation for predicting crutch-orthosis-assisted walking, we collected experimental gait data from a healthy subject walking with two active orthoses and crutches. The subject was a female (age 29 years, mass 54 kg, height 1.62 m) and the gait data were collected at the UPC Motion Analysis Laboratory in the Department of Mechanical Engineering of the Barcelona School of Industrial Engineering

(ETSEIB) (**Figure 2A**). The reason for collecting experimental data from a healthy subject first was that it was easier for the subject to step correctly with one foot on each force plate while using wired instrumented crutches, thus providing a complete set of experimental data (synchronized marker trajectory, force plate, and crutch measurements). Moreover, orthosis kinematic performance is the same for a healthy subject as for a patient with SCI, since the knee controller follows a predefined flexion-extension angle and the IMUs detect the stance-to-swing transition event the same way in both cases. Three different trials were performed: one without knee flexion-extension assistance (locked knee) and two with different levels of maximum knee flexion during swing ( $35^\circ$  and  $45^\circ$ ). The crutch walking pattern used in all trials was a four-point alternating pattern with the following crutch placement sequence within the walking cycle: left crutch, right leg, right crutch, and left leg (**Figure 2B**). Collected data included marker trajectories, ground reactions (two force plates), and crutch forces (instrumented crutches). Surface marker motion was recorded at 100 Hz by tracking 53 passive reflective markers using 16 optical infrared cameras (OptiTrack V100:R2, NaturalPoint Inc., Corvallis, OR, USA). Ground reaction forces and moments were measured at the same sampling frequency by two force plates (AccuGait, AMTI, Watertown, MA, USA) located on the floor at the center of the capture workspace. Crutch-ground reaction forces were obtained from two custom-made instrumented crutches possessing 12 strain gauges each that sampled at 89 Hz (Sardini et al., 2015). Crutch data were interpolated to 100 Hz to match the sampling rate of the marker trajectory and force plate data.

### Computational Model Development

A torque-driven model of the healthy subject with assistive devices was developed by incorporating a pair of forearm crutches and a pair of active orthoses into a currently available full-body model (Rajagopal et al., 2016) in OpenSim (Delp et al., 2007; Seth et al., 2018). The model possessed  $n_q = 31$  degrees of freedom (DOF): six DOF between the pelvis and the ground (i.e., absolute translation and rotation), three for each hip, one for each knee, three for the lumbosacral joint, three for each shoulder, two for each elbow, and two for each wrist. Each DOF was associated with a model or joint coordinate  $q_i$  ( $i = 1, \dots, n_q$ ) in the order shown above, which formed the  $n_q$ -dimensional vector of generalized coordinates  $\mathbf{q}$ . The model was scaled to the subject using the OpenSim Scale Tool, and a static trial was collected for this purpose. Each forearm crutch was incorporated into the model as a rigid body welded to the corresponding hand segment. The geometry and mass of each crutch were measured, and the crutch inertia tensor was obtained from simple rigid-body models. The active orthoses consisted of two segments (corresponding to thigh and shank-foot) with dimensions and inertial properties taken from CAD models of the real prototype. Each orthosis segment was attached to the corresponding lower limb segment using a weld joint (i.e., no relative motion was permitted between bodies). The ankle, subtalar and metatarsophalangeal joints were locked at  $0^\circ$  due to the presence of the orthosis mechanical constraints. No joints were defined between the orthosis links, i.e., the knee orthosis





joint was considered to be perfectly aligned with the subject's knee joint. Despite being a simplification, this approach can be considered realistic as the orthoses were tightly attached to the subject with Velcro straps using front support at the shank and back support at the thigh and with a ratchet strap on each foot.

One representative gait cycle was selected for each condition (locked knee, 35 and 45° of knee flexion) and used in all subsequent model development and optimal control problem formulation tasks. The gait cycle was selected to use all available foot-ground reactions, which did not correspond to a complete crutch-gait cycle. The cycle started at left crutch off (LCO), and for the initial right leg stance phase, no force plate measurements were available. The subject walked in a transverse direction with respect to the force plates, which allowed clean placement of each foot on each force plate. Unfortunately, the subject was not able to place the crutches off the force plates at the same time (**Figure 2B**). This fact necessitated the crutch-ground reaction forces being subtracted from the force plate measurements to calculate the foot-ground reactions. The OpenSim Inverse Kinematics (IK) Tool was used to calculate joint coordinates for the full-body model (henceforth referred to as “experimental

joint coordinates”). These joint coordinates and the measured foot- and crutch-ground reactions served as inputs to the OpenSim Inverse Dynamics (ID) Tool, which was used to obtain the “experimental joint torques.”

To model foot- and crutch-ground interactions, we used viscoelastic contact models whose parameter values were calibrated using an optimal control tracking problem. The foot-ground contact model consisted of 16 spring-damper units on each foot. The normal force in each element was generated using a linear spring with non-linear damping (Jackson et al., 2016), and the tangential force in each element was calculated using a simple continuous friction model (Jackson et al., 2016). The crutch-ground contact model consisted of a sphere at the tip of the crutch that could contact a plane representing the ground. The normal force was obtained using a Hertzian elastic point contact model with non-linear damping (Hunt and Crossley, 1975), and the tangential force model was the same as for the foot-ground contact model. The parameters of the foot-ground and crutch-ground contact models (i.e., spring stiffnesses, non-linear damping coefficients, dynamic friction coefficients) were calibrated by solving a direct collocation optimal control

problem (Febrer-Nafria et al., 2021). The experimental locked knee trial motion and forces (joint angles, joint torques, and ground reactions) were tracked simultaneously while adjusting contact model parameter values that were assumed to be the same for both feet and both crutches.

### Optimal Control Problem Formulations Comparison

Crutch-orthosis-assisted walking prediction problems were formulated as direct collocation optimal control problems (OCPs) using implicit skeletal dynamics (Van Den Bogert et al., 2011; Meyer et al., 2016; Falisse et al., 2019; Sauder et al., 2019) and were solved using the optimal control software GPOPS-II (Rao et al., 2014). Joint coordinates, velocities, accelerations, and torques were states in the problem, and joint jerk, joint torque change, and ground reactions were included as controls (Febrer-Nafria et al., 2021). Cycle duration, stride length, and relative duration of foot swing, crutch swing, and multiple support were considered free parameters in the optimization, and their values were bounded according to measured values (mean experimental value  $\pm$  a specific tolerance). Initial guesses for all states and controls were the experimental values for the locked knee trial, as we considered that the prediction of assisted walking should be close to this initial motion.

The skeletal equations of motion obtained from OpenSim were included implicitly as algebraic path constraints (Van Den Bogert et al., 2011). An Inverse Dynamics (ID) analysis was performed at each iteration using the OpenSim C++ API (version 3.3), and the system kinematic state was used to calculate the generalized forces and torques (which included the six residual loads acting on the pelvis). Path constraints limited the residual loads to be within a specific tolerance (1 N, 1 Nm). The velocity of some specific points (midpoint for feet and tip for crutches) during the stance phase was bounded to avoid sliding. Periodicity was imposed for joint angles, joint torques, and normal contact forces. The symmetry between right and left foot-crutch mediolateral distance was imposed at the initial and final time. Mean speed for the pelvis anterior-posterior translation was limited within a specified tolerance.

Different cost function formulations were investigated based on published studies that predicted 3D full-body walking for clinical applications (Meyer et al., 2016; Sauder et al., 2019; Febrer-Nafria et al., 2021), considering only terms related to joint-level mechanics. Cost function terms were divided into three different groups: tracking terms ( $J_{\text{track}}$ ) that were closely reproduced, optimality terms ( $J_{\text{opt}}$ ) that were minimized, and regularization terms ( $J_{\text{reg}}$ ) that were also minimized (Equation 2):

$$J = \int_{t_0}^{t_f} (J_{\text{track}}(\mathbf{x}, \mathbf{u}) + J_{\text{opt}}(\mathbf{x}, \mathbf{u}) + 0.01 J_{\text{reg}}(\mathbf{u})) dt \quad (2)$$

where  $t_0$  and  $t_f$  are the initial and final simulation times, respectively,  $\mathbf{x}$  is the vector of states, and  $\mathbf{u}$  is the vector of controls. Tracking terms included lumbar and hip flexion joint torque and upper limb joint angles; optimality terms included segment local angular momentum, joint mechanical power, and knee motor torque; regularization terms included

**TABLE 1 |** Cost function terms considered in this work.

<b>Tracking terms</b> ( $J_{\text{track}}$ )	Tracking of lumbar and hip flexion joint torque	$\sum_{i=\{1,5,9:11\}} (\tau_{\text{exp},i} - \tau_i)^2$
	Tracking of upper limb joint angles	$\sum_{i=18}^{n_q} (q_{\text{exp},i} - q_i)^2$
<b>Optimality terms</b> ( $J_{\text{opt}}$ )	Minimization of segment local angular momentum	$\sum_{i=1}^{n_b} \ L_i\ ^2$
	Minimization of joint mechanical power	$\sum_{i=7}^{n_q} (\dot{q}_i - \dot{q}_{i-6})^2$
	Minimization of knee motor torque	$\sum_{i=\{4,8\}} \tau_i^2$
<b>Regularization terms</b> ( $J_{\text{reg}}$ )	Minimization of sum of squared joint jerk	$\sum_{i=1}^{n_q} \ddot{q}_i^2$
	Minimization of sum of squared joint torque change	$\sum_{i=1}^{n_q-6} \dot{\tau}_i^2$

Tracking terms included (1) the sum of the squared error of lumbar and hip flexion joint torque, being  $\tau_{\text{exp},i}$  and  $\tau_i$  the  $i^{\text{th}}$  component of the vector of experimental joint torques  $\tau_{\text{exp}}$  and of predicted joint torques  $\tau$ , respectively; and (2) the sum of the squared error of upper limb joint angles, being  $q_{\text{exp},i}$  and  $q_i$  the  $i^{\text{th}}$  component of the vector of experimental joint coordinates  $q_{\text{exp}}$  and of predicted joint coordinates  $q$ , respectively. Optimality terms included (1) the sum of the squared norms of the segment angular momenta, being  $n_b$  the number of rigid bodies in the model and  $L_i$  the segment angular momentum at the center of mass of the  $i^{\text{th}}$  rigid body (or segment) of the model; (2) the sum of squared mechanical powers, computed for each lumbar joint coordinate, being  $\dot{q}_i$  the  $i^{\text{th}}$  component of the vector of joint velocities  $\dot{\mathbf{q}}$ ; and  $\tau_{i-6}$  the  $(i-6)^{\text{th}}$  component of the vector of joint torques  $\tau$ ; and (3) the squared value of the two knee torques, being  $\tau_i$  the  $i^{\text{th}}$  component of the vector of joint torques  $\tau$ . Regularization terms included (1) the sum of squared joint jerks, being  $\ddot{q}_i$  the  $i^{\text{th}}$  component of the vector of joint jerks  $\ddot{\mathbf{q}}$ ; and (2) the sum of squared joint torque changes, being  $\dot{\tau}_i$  the  $i^{\text{th}}$  component of the vector of joint torque change  $\dot{\tau}$ . To give more importance to the tracking and optimality criteria, a weight of 0.01 was placed on the regularization terms (minimization of joint jerk and minimization of torque change), for all the different combinations.

joint jerk and joint torque change (Table 1). Different multi-term cost functions were implemented using two or more of these terms, and locked knee crutch-orthosis-assisted walking was predicted for each one of them. All cost function terms were scaled to be of a similar magnitude. To give more importance to the tracking and optimality criteria, we placed a weight of 0.01 on the regularization terms (minimization of joint jerk and minimization of torque change) for all combinations. Convergence and accuracy of simulation results predicted with each cost function were compared. Convergence was evaluated taking into account the number of iterations and computation time required to find an optimal solution, while accuracy was evaluated by computing the root mean square error (RMSE) between predicted and experimental joint angles and ground reactions. The cost function for which the best results were obtained was chosen to be used for all other crutch-orthosis-walking predictions generated in this study.

### Evaluation of the Selected Cost Function

To assess the ability of this prediction framework to perform virtual tests of pre-defined knee motion trajectories, we used the previously chosen cost function to predict assisted motions with knee flexion. In our simulations, we assumed that the IMU sensors detected correctly the stance-to-swing transition event and that the knee motor was capable of following the desired

knee trajectory. Knee angle trajectory was defined according to Equation 1 using as maximum knee flexion  $k_a$  the exact value that was reached in the experimental trials. To quantify the performance of our simulation framework for testing virtually pre-defined knee motion trajectories, we computed RMSEs between predicted and experimental joint coordinates, joint torques, and ground reactions. Moreover, the following clinical measures that are usually used by physiotherapists in the trial-and-error process of manual tuning of knee angle trajectory parameters were computed: foot clearance, stride length, hip flexion ROM, and cadence. Foot clearance was obtained by computing the lowest vertical position of the toes' body origin in the OpenSim model during the swing phase for each foot. Stride length was computed as the mean value between feet and crutches stride length. Hip flexion ROM was computed as the right and left hip flexion ROM over the whole gait cycle. These clinical measures were evaluated by checking the improvements in assisted motions (with knee flexion) compared to locked knee motion.

## Application of the Prediction Framework Using SCI Subject Data

Once the crutch-orthosis-assisted walking prediction framework was developed and evaluated for the healthy subject, we applied it to test different pre-defined assistive knee angle trajectories for an SCI subject. This subject was able to walk with orthoses without knee flexion-extension assistance (locked knee) and non-instrumented crutches. We hypothesized that the same cost function would work for the SCI subject as for the healthy subject (Falisse et al., 2019), both for locked knee and flexed knee motions. We assumed that foot- and crutch-ground contact model parameters were the same as for the healthy subject, as the crutches and active orthoses used for both subjects were the same, and foot support of the orthoses contacted directly with the ground (i.e., the sole of the feet was the same for both subjects).

## Experimental Data Collection

The subject selected for this study was a young adult male (40 years old, mass 72 kg, and height 1.72 m) that suffered paraplegia after a spinal hemangioma. He had an incomplete transverse spinal cord syndrome below the 10th thoracic neurological segment (T10), classified at level B in the ASIA Impairment Scale (AIS). Sensory but not motor function was preserved below the level of injury. During the experimental capture, it was difficult for the patient to walk with the instrumented crutches (as they included wires and electronic modules on each crutch) and to place one foot cleanly on each force plate. For these reasons, the experimental capture was done with non-instrumented crutches, thus collecting only marker trajectories. One trial with locked knees was recorded to be used as an initial guess for the different prediction problems (Figure 2C).

## Computational Model Development

A torque-driven model of the SCI subject with crutches and active orthoses was developed following a similar approach as for the healthy subject. To take into account the SCI subject impairment, we limited hip joint torque production according to

the functional state of the subject. Following an approach similar to Sreenivasa et al. (2017), we assumed that the SCI subject used 80% of his hip motor capacity during the experimental capture with passive orthoses and crutches. Another difference with respect to the healthy subject model was that for the SCI subject, the total torque acting at the knee corresponded to the assistive motor torque since the subject's knee muscles were not functional. This torque was limited to  $\pm 34$  Nm, which is the peak torque that the electric motor can provide. To obtain the reference values for hip joint torques, we solved an optimal tracking problem that tracked joint coordinates obtained from IK while minimizing joint jerk. Ground reactions were obtained from foot-ground and crutch-ground contact models using the parameter values obtained for the healthy subject. Hip joint torques were then limited assuming that the reference values obtained from this tracking problem were 80% of the maximum values.

## Evaluation of the Selected Cost Function

To evaluate the convenience of using the same cost function for predicting locked knee crutch-orthosis-assisted walking for an SCI subject, we computed the RMSE between predicted and experimental joint angles (obtained after IK analysis).

## Knee Motion Strategy Testing

Knowing the subject's gait with locked knees, we computationally tested different knee angle trajectories, having all parameters fixed and modifying the knee maximum flexion parameter  $k_a$ . This parameter is usually the one that is varied first in the trial-and-error adaptation process. Four different motions were predicted with the following levels of knee flexion: 20, 30, 40, and 50°. Joint torques and ground reactions obtained from the locked knee tracking problem were used as the initial guess for the predictive simulations. To evaluate the performance of our simulation framework for testing virtually pre-defined knee motion trajectories for an SCI subject, we computed foot clearance, stride length, hip flexion ROM, and cadence, and we compared these clinical measures among all predicted motions. The maximum knee flexion value that produced the most improved walking motion was selected as the best candidate for this SCI subject.

## RESULTS

Different cost functions for predicting locked knee crutch-orthosis-assisted walking were explored, combining one or more tracking, optimality, and regularization terms. Overall, we found that minimizing joint jerk helped the problem converge more quickly and satisfied mesh error tolerance at the first mesh iteration. We also found that minimizing lumbar joint mechanical power, segment angular momentum (especially torso), and motor torque helped the problem converge with fewer iterations and lower joint angle errors. Moreover, we found that having joint torque as a state and joint torque change as a control worked better than having joint torque as a control. Based on these results, we chose the following cost function for predicting crutch-orthosis-assisted walking:

**TABLE 2 |** Convergence (number of iterations and computation time) and accuracy (mean RMSE for angular coordinates and ground reactions) for all predictive simulations.

Subject			Healthy			SCI				
Trial			H0	H35	H45	S0	S20	S30	S40	S50
Convergence	N iterations		322	759	582	153	125	197	990	414
	Computation time		27 min	2 h 26 min	1 h 51 min	13 min	25 min	40 min	3 h 12 min	1 h 23 min
Mean RMSE	Angular coordinates [°]	Pelvis + torso	4.88	6.95	6.24	10.67	-	-	-	-
		Upper limbs	6.46	12.65	10.76	5.74	-	-	-	-
		Lower limbs	5.13	8.57	9.57	10.61	-	-	-	-
		All	5.74	10.26	9.45	8.19	-	-	-	-
	Ground reactions [N, Nm]	Normal	55.40	90.71	53.84	-	-	-	-	-
		Tangential	14.35	15.19	13.03	-	-	-	-	-
		Moment	6.90	11.07	9.58	-	-	-	-	-

The name for each trial indicates the subject ("H" for healthy and "S" for SCI subject), followed by the maximum knee flexion angle in degrees. For the SCI subject, only errors in angular coordinates for the locked knee case (S0) were computed, according to the available experimental data.

minimization of lumbar mechanical power, all segment angular momentum, motor torque, joint jerk, and joint torque change. Using this cost function, an optimal solution for the healthy subject with locked knee was found in 27 min, and mean RMSE was 5.34° for joint angles, 55.40 N for normal forces (feet and crutches), and 14.35 N for tangential forces (feet and crutches) (Table 2). Overall, the lowest mean RMSEs for all joint angles were found for the healthy subject with locked knee motion (5.74°), followed by the SCI subject with locked knee motion (8.19°), and finally the healthy subject with 45° knee flexion (9.45°) and 35° knee flexion (10.26°) (Table 2). For the healthy subject, higher errors were found for upper limb joint angles, whereas for the SCI subject, errors were higher for the lower limbs.

Two different crutch-orthosis-assisted gait cycles were predicted for the healthy subject (with maximum knee flexion values of 35 and 45°, respectively), imposing the knee angle trajectory from the collected experimental trials. We assumed that the same cost function would work for predicting both locked knee and flexed knee-assisted walking. The computation time required to converge was higher than for the locked knee case, up to 2 h 30 min (Table 2). Mean RMSE for joint angles was 10.26° for 35° of predicted knee flexion motion and 9.45° for 45° of predicted knee flexion motion. In both cases, the lowest mean RMSE was for pelvis and torso joint angles (<7°) and the highest was for upper limbs angles (10.7–12.6°). Hip flexion was predicted better than were hip adduction and hip rotation, with predicted angle trajectories showing peaks at the same cycle times as in the experimental data (Figure 3). Regarding ground reaction forces, the mean RMSE for normal forces was higher for 35° knee flexion motion (90.71 N) compared to locked knee motion but was similar for 45° knee flexion motion (53.84 N) (Table 2). Errors in tangential forces were comparable for locked knee and both flexed knee motions (13–15 N). In all cases, predicted foot and crutch weight-bearing was consistent with the experimental ground reaction forces (Figure 4).

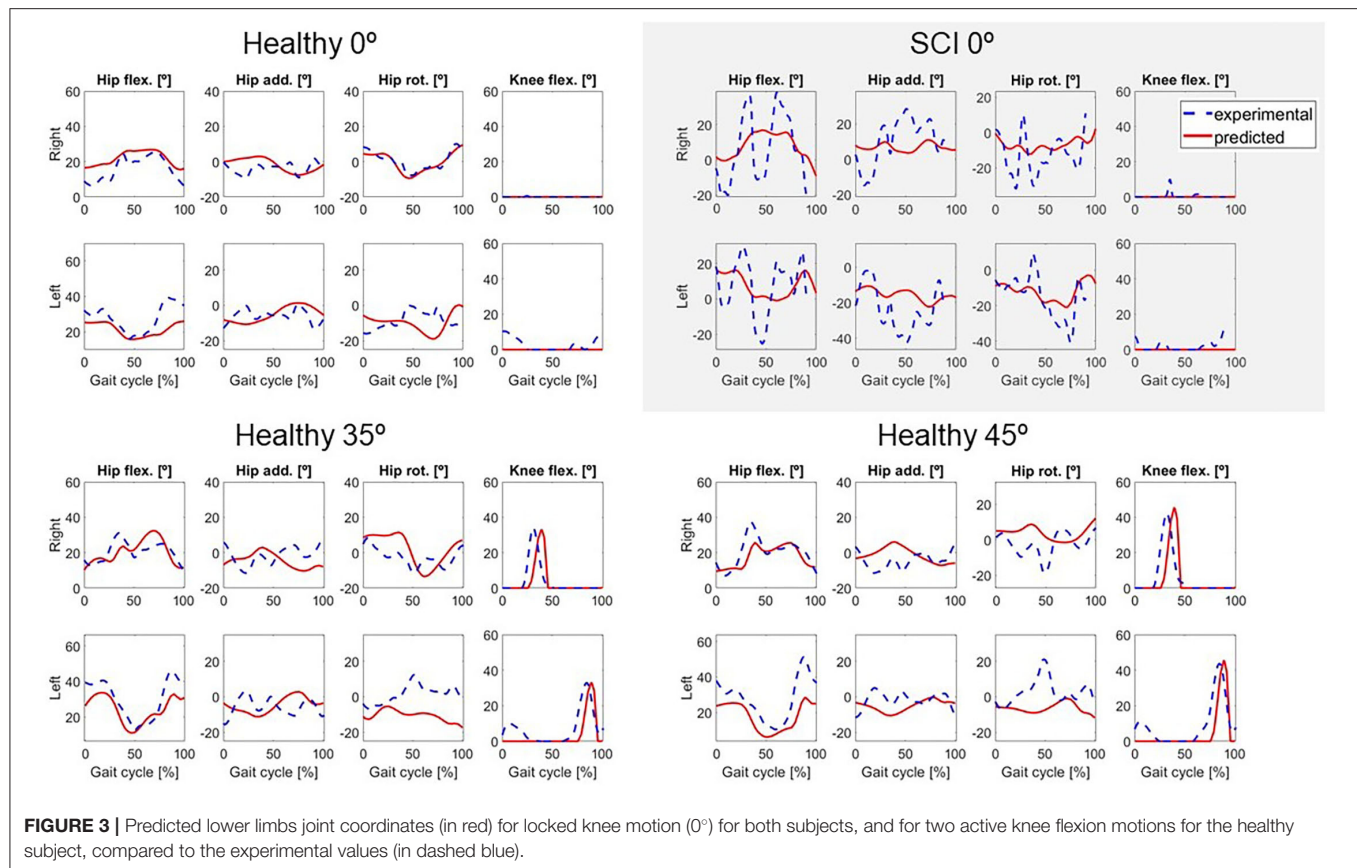
Changes in foot clearance, stride length, and cadence were in general well-predicted for the healthy subject. When comparing

flexed knee motions with respect to locked knee motions, foot clearance increased for 35° and decreased for 45° in both experimental and predicted motions (Figure 5). Stride length and cadence increased for both flexed knee motions, and stride length was higher for 45° compared to 35° in both experimental and predicted motions. Compared to locked knee motion, hip flexion ROM also increased for flexed motions in experimental and predicted motions. However, there was a difference between the trend in predicted motions compared to experimental motions: in the experimental motions, hip flexion ROM increased for 35 and 45° with respect to the locked knee case, but in the predicted motions, it increased for 35° and decreased for 45°.

In general, the locked knee predicted gait pattern for the SCI subject had a lower ROM for each joint coordinate (Figure 3) and less mediolateral movement (in the frontal plane) compared to experimental measurements. Stride length and cadence were comparable in experimental and predicted motions (0.51 m for both motions and 30.23 steps/min and 27.26 steps/min, respectively). Foot clearance was higher, and symmetry improved in the predicted motion (4.82 and 4.72 cm, for right and left foot, respectively, compared to 3.60 and 1.50 cm), whereas hip flexion ROM was lower, and symmetry decreased in the predicted motion (26 and 17°, for right and left hip, respectively, compared to 58 and 54°). Regarding ground reactions, predicted normal forces were higher for the right side (peak value of 0.75 body weight (BW) for right foot and 0.34 BW for right crutch) compared to the left side (peak value for 0.68 BW for left foot and 0.16 BW for left crutch) (Figure 4).

Four additional crutch-orthosis-assisted gait cycles were predicted for the SCI subject with maximum knee flexion angle increasing from 20 to 50° in increments of 10°. Optimal solutions were found in a mean time of 1 h 20 min, with a maximum computation time of 3 h 12 min (Table 2). In general, compared with locked knee predicted motion, all four clinical measures improved for predicted motions with knee flexion (Figure 5). Maximum values of foot clearance (right: 5.56 cm, left: 6.16 cm) were found for 30° of maximum knee flexion, maximum values for stride length (0.54 m), and hip flexion ROM (right: 40.09°,





**FIGURE 3 |** Predicted lower limbs joint coordinates (in red) for locked knee motion (0°) for both subjects, and for two active knee flexion motions for the healthy subject, compared to the experimental values (in dashed blue).

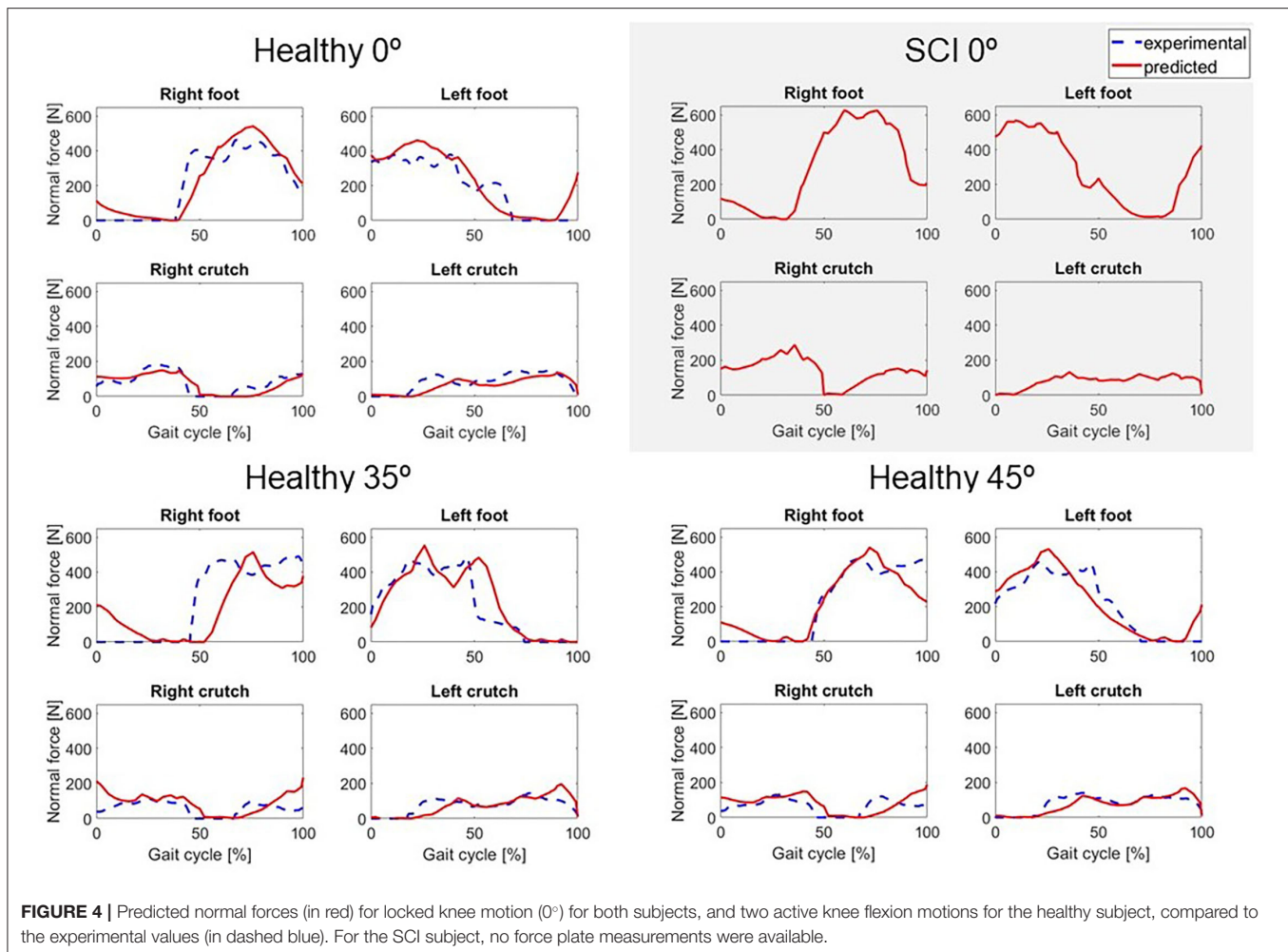
left: 26.31°) were found for 40° of maximum knee flexion, and maximum value for cadence was found for 50° knee flexion (33.37 steps/min).

## DISCUSSION

In this work, we developed an optimal control prediction approach to test different pre-defined knee angle trajectories of an active orthosis to assist the gait of SCI subjects. We compared different cost functions and chose the one that produced results closest to experimental locked knee crutch-orthosis-assisted walking for a healthy subject. Having as an initial guess the experimental motion for the locked knee case, we predicted crutch-orthosis-assisted walking imposing knee flexion using different maximum knee flexion parameters to define the knee angle trajectory along the gait cycle. For the healthy subject, two different maximum knee flexion angles were imposed for which experimental walking data were available. For the SCI subject, no experimental walking data for flexed knee motion were available, and four different maximum knee flexion angles were imposed in the simulations. We evaluated changes in four simulated clinical measures that are usually considered by physiotherapists to decide the best set of parameters for a specific patient (foot clearance, stride length, cadence, and hip flexion ROM). These changes were consistent with those observed in the experimental motions for the healthy subject and were reasonable for the SCI

subject. These findings suggest that it may be beneficial to use optimal control predictions of crutch-orthosis-assisted walking in place of the current trial-and-error method to select the best maximum knee flexion angle for a specific SCI subject.

Changes in the clinical measures were generally predicted well for the healthy subject. For the healthy subject collected motions, we found that having knee flexion-extension assistance produced better results for stride length, hip flexion ROM, and cadence, as all of these measures increased for both maximum knee flexion angles (35 and 45°) compared to the locked knee case. These changes are related to improved assisted motion and are linked, as having increased knee flexion is associated with having increased hip flexion (Escalante et al., 1999), and generally increased hip flexion is correlated with a longer stride length (Schulz et al., 2008). For the predicted motions, having knee flexion assistance also produced increased values for hip flexion ROM, stride length, and cadence. In the case of stride length and cadence, the trend observed in experimental measurements was also observed in the predicted motions (higher values for 45° compared to 35°). However, in the case of hip flexion ROM, higher values were obtained for 45° in experimental motions and 35° in predicted motions. Thus, this trend in hip flexion was not well-captured by the optimal control problem, though in both experimental and predicted motions with knee flexion assistance, hip flexion ROM was higher than in the locked knee case. Moreover, the asymmetry between right and left hip flexion ROM

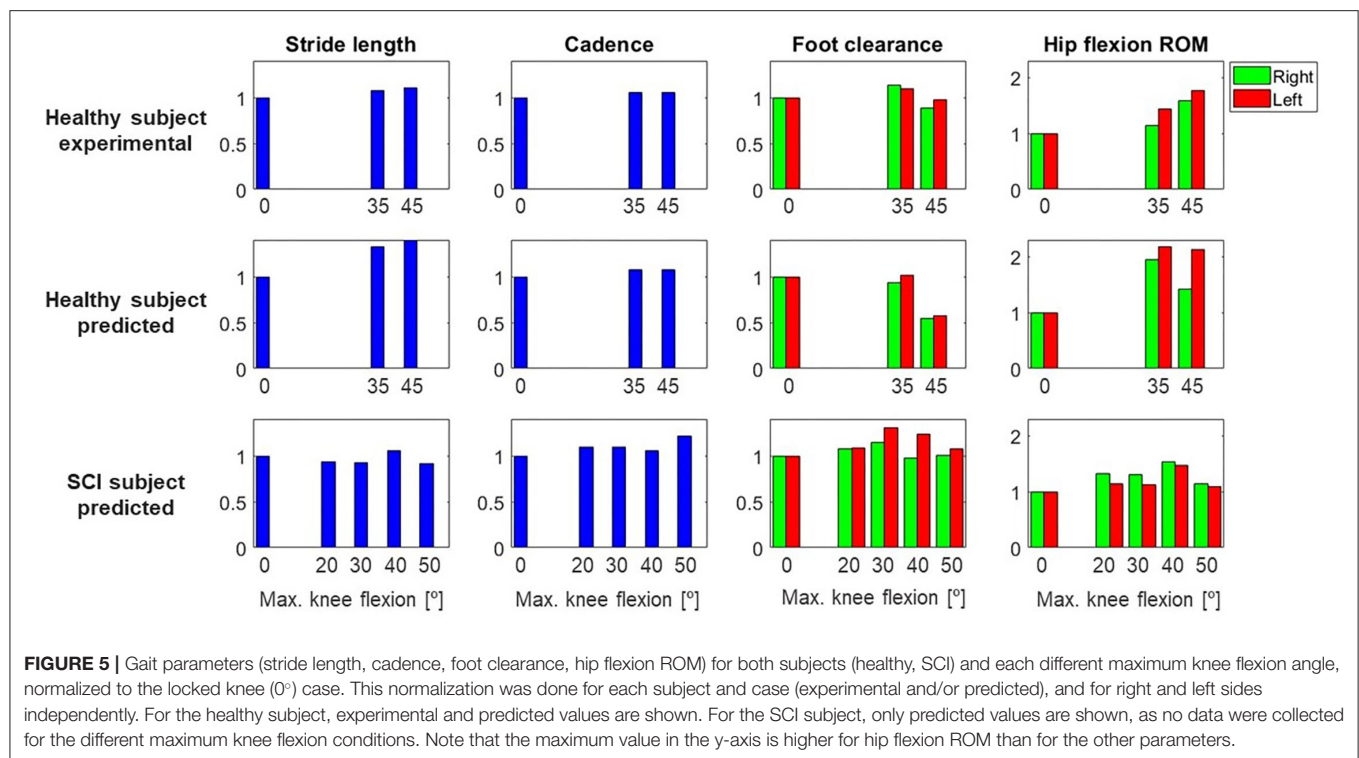


**FIGURE 4 |** Predicted normal forces (in red) for locked knee motion ( $0^\circ$ ) for both subjects, and two active knee flexion motions for the healthy subject, compared to the experimental values (in dashed blue). For the SCI subject, no force plate measurements were available.

observed in the experimental motions (left hip flexion ROM was higher than right hip flexion ROM) was also observed in the predicted motions. Foot clearance with respect to the locked knee case increased in the experimental motions for  $35^\circ$  but decreased for  $45^\circ$ . This trend was also observed in the predicted motions, where left foot clearance increased for  $35^\circ$  (and right foot clearance remained almost equal) and both feet clearance decreased for  $45^\circ$ .

Considering the four clinically relevant measures, our results suggest that for this particular SCI subject,  $30^\circ$  or  $40^\circ$  of maximum knee flexion may produce the best-assisted motion. Compared to locked knee prediction, foot clearance generally increased for knee flexion assistance. This outcome is desirable when using lower limb exoskeletons, since straight knee gait and drop foot gait reduce foot clearance (Koopman et al., 2013; Yeung et al., 2018). For both legs, the best case was for  $30^\circ$ , which produced foot clearances of 5.56 and 6.16 cm (right and left, respectively) compared to 4.82 and 4.72 cm (same order) in the locked knee case. Stride length was in general slightly lower for flexed knee motions compared to locked knee motion but slightly increased for  $40^\circ$ . Hip flexion ROM clearly increased for all flexed knee motions. The highest values were obtained for  $40^\circ$  and the lowest

for  $50^\circ$ . There was also asymmetry in hip flexion ROM, with the right hip flexion ROM being higher, as was also observed in the experimental motion. For  $40^\circ$ , the highest values of hip flexion ROM and stride length were obtained. Cadence increased slightly for all flexed knee motions, with the highest value of 33.37 steps/min occurring for  $50^\circ$  compared to 27.26 steps/min in the locked knee predicted motion. These results are reasonable if we relate them to knee kinematics during normal walking. In normal gait, the knee flexion-extension cycle starts at a terminal stance and ends at a terminal swing (Perry, 1992). During knee flexion, the ankle dorsiflexes, which increases foot clearance, and during knee extension, the ankle eccentrically plantar flexes as the cycle enters terminal swing. In our simulations, it should be noted that only the maximum knee flexion was modified for the different predictions, meaning that the flexion-extension cycle had the same allotted time to reach maximum knee flexion across all the conditions. As a result, the knee flexion-extension motion was faster for the  $50^\circ$  condition compared to the  $30^\circ$  condition and may have impacted hip flexion, leading to a shorter stride length. However, the increased speed of the knee flexion-extension cycle may have created a momentum effect and therefore led to a higher cadence.



Evaluating the assisted motion and choosing the best set of parameters for a specific subject, manually or computationally, is not always straightforward. In this work, compared to locked knee motion, we found for both subjects that clinical measures improved for assisted motions with knee flexion until a certain peak knee flexion was reached (around 35° for the healthy subject and between 30 and 40° for the SCI subject), with results worsening with higher knee flexion values. This trend was observed both experimentally (for the healthy subject) and computationally (for both subjects) and coincided with what the authors have observed in different training sessions with SCI subjects wearing the lower limb active orthosis. However, it is not clear how these clinical measures should be interpreted, e.g., if some of them improve while others do not for the same set of parameters. Usually, exoskeleton parameters are manually adjusted based on subjective evaluation, e.g., asking users which condition they prefer (MacLean and Ferris, 2019) or based on physiotherapists' visual assessment on basic gait parameters like foot clearance (Koopman et al., 2013). For our active orthosis, some objective values are added to the physiotherapist's subjective evaluation, as the device provides real-time feedback of stride length and weight-bearing time on each leg. However, the evaluation is still done subjectively by the physiotherapist, who decides how to tune the orthosis parameters manually based on both subjective assessment and objective measurements. Simulation (or automatic tuning) presents some advantages compared to trial-and-error tuning: it is quicker (Fricke et al., 2020), and many parameter sets can be virtually tested without the risk of trying a combination that will not work and could be harmful to the patient. Despite these advantages, there is no

clinical evidence to date that the automatic tuning of assisted motions results in better clinical outcomes (Fricke et al., 2020). It is difficult to develop a system that objectively takes into account all of the factors that a physiotherapist evaluates whilst assisting a patient to walk. It could be that for a specific parameter set, some important clinical measures improve while others do not, and one clinical parameter could be more critical for one patient than for others. Before this method can be applied to choose optimal knee control parameters for a specific subject, more research is needed to understand better and define objectively the targeted assisted gait pattern for the patient according to functional status.

Although trends in clinical measures were well-predicted for the healthy subject, in some cases absolute predicted values differed from experimental values. Cadence was well-predicted: 37 steps/min and 40 steps/min in locked and flexed knee motions, respectively, in both experimental and predicted results. For foot clearance, a lower value was generally found for predicted motions compared to experimental motions, with the highest difference being 2.10 cm for the left leg with a 45° maximum knee flexion angle. Stride length and hip flexion ROM were also lower in predicted motions compared to experimental motions. Stride length was 14 cm lower for predicted locked knee motion compared to experimental conditions (0.51 vs. 0.37 m) and 4–5 cm lower for predicted flexed knee motions. Hip flexion ROM was up to 12° lower in predicted vs. experimental conditions for locked knee motion and up to 18° lower for flexed knee motion. These reductions in stride length and hip flexion ROM were mainly caused by lower joint angle ROMs in predicted motions compared to experimental motions (Figure 3), which also resulted in lower foot clearance.



Differences in joint angles and ground reaction forces between predicted and experimental motions were lowest for the healthy subject with locked knee condition (that is, for the case for which the cost function was selected). This finding may indicate that different cost functions should be used for locked/flexed knee and healthy/SCI subjects, or, if healthy and pathological human gaits emerge from similar control strategies (Falisse et al., 2019), that the appropriate cost function has not yet been identified, and other terms should be added that may play an important role only for the SCI subject. Further research is needed to determine the best cost function for predicting assisted walking of SCI subjects. This effort will require the collection of a complete set of experimental data (including marker trajectories and foot-and crutch-ground reactions). Moreover, the best cost function for simulating crutch walking may be different than the best one for simulating normal walking. As far as the authors know, there is only one study that predicts crutch-assisted walking using a 3D full-body model (Febrer-Nafria et al., 2021). In the SCI subject lower limbs, only the hip is actuated by muscles, and the hip ROM was not well-predicted. This result may be caused by the fact that hip motion was controlled by net torque actuators instead of individual muscle-tendon units. Meyer et al. (2016) found that predicting walking under new conditions was more accurate if muscles rather than net torque actuators were used to generate the motion, with muscles controlled by synergies instead of individual muscle activations producing the most accurate walking predictions. Therefore, we hypothesize that including muscles in the model and controlling them by synergies could improve the prediction results. However, for that approach, it would be challenging to calibrate muscle-tendon model parameter values for patients with SCI. Moreover, when we tested whether adding more tracking terms might improve the predicted motions (Meyer et al., 2016), we did not find a clear improvement compared to cost functions without tracking terms. Given our results, we believe that adding targeted tracking terms could produce more subject-specific assisted motions following a pattern closer to the one chosen initially by the patient with a locked knee. Even though the cost function requires further investigation, these results are promising as we have been able to predict changes in crutch-orthosis-assisted walking motions that are in good (for the healthy subject) or reasonable (for the SCI subject) agreement with experimental trends. Our hypothesis is that by finding a cost function that predicts the locked knee condition better, we will be able to predict walking motions with knee flexion assistance more reliably, and changes from locked to flexed knee conditions will be maintained.

This work possesses several limitations. First of all, no training or learning process was performed by the healthy subject, and experimental data were collected before the subject was used to walking with the active orthoses. Therefore, some clinical measures could be different after such a training process. Moreover, only two different levels of maximum knee flexion were tested for the healthy subject, and the maximum value was the only knee angle trajectory parameter varied. For the clinical application, the assisted gait of a single SCI subject was simulated, and only one of the parameters that define the knee angle trajectory was explored. Although maximum

knee flexion is the most critical parameter, it would also be interesting to predict how varying the other three parameters would affect the predicted motion. In addition, we assumed that the stance-to-swing transition event was perfectly detected during the simulation. Gait event detection is done using IMUs in the real device, and some threshold parameters need to be adjusted as well. In future experiments, we will start with some training sessions, and we will collect data for different values of all parameters that define the knee angle trajectory and gait event detection. In this way, we will be able to assess if some parameters are more subject-dependent and others more general. Another limitation was that we did not directly compare manual tuning using a trial-and-error process with the computational or simulation tuning. This comparison process would be complex, as different aspects should be taken into account: (1) time and effort of the physiotherapist to find these values, (2) time and effort of the patient, (3) if different physiotherapists find different values, and (4) if both methods produce similar results in terms of the better-assisted motion. A benefit of using a computational model would be to obtain a personalized default set of parameters that could then be easily tuned in the clinic. This approach would reduce fitting time and would be safer for the patient, as there would be less risk of adverse events than when using non-personalized parameters. An adverse event like a fall would have a big impact on the patient's health and confidence in the technology. We hypothesize that in general, the set of parameters provided by the model will work well for the patient, though there will always be particular cases where the manual tuning of this initial set of parameters will be needed. These cases include patients who fatigue over the session or have changing levels of spasticity or pain. These aspects are currently not considered in the model, and therefore, it might be necessary to tune the initial set of parameters to accommodate these issues. In future work, how to include fatigue, spasticity, or pain in the model should be investigated. Another potentially complicating factor is that the cost function might vary with time. Regarding the active KAFO modeling, in this work, the knee motor modeling was simplified. We assumed that the knee flexion angle trajectory was followed correctly, and that maximum knee flexion was reached. However, we observed experimentally that maximum flexion was lower than the targeted value. In future work, we will investigate how to include actuator dynamics (Nguyen et al., 2020). Finally, we considered the same knee flexion angle trajectory for both right and left legs, but asymmetry was observed in the trials in both healthy and SCI subjects. In the future, we will investigate if the assisted knee flexion trajectory should be different for both legs to achieve a more symmetric gait pattern.

In conclusion, this study explored the feasibility of using a computational approach to personalize the pre-defined knee trajectory parameters for an active KAFO for SCI subjects. We developed an optimal control prediction approach to test different pre-defined knee angle trajectories of an active orthosis to assist the gait of SCI subjects. We checked if our optimal control approach was capable of correctly predicting assisted motions for different values of maximum knee flexion angle, evaluating results against experimental data collected from a healthy subject assisted by the active orthoses. While trends in



clinical measures were well-predicted, absolute predicted values differed from experimental values in some cases. We applied the framework to predict assisted gaits of an SCI subject with four different maximum knee flexion values. To the best of the authors' knowledge, no study in the literature has addressed how to formulate optimal control problems to predict novel crutch-orthosis-assisted walking motions using 3D full-body models. Although more research is needed before this method can be used to choose optimal knee control parameters for a specific subject, our findings suggest that optimal control prediction of crutch-orthosis-assisted walking using biomechanical models might possess benefits over the current trial-and-error method used to select the best maximum knee flexion angle for a specific SCI subject. Having a simulation tool that allows different pre-defined knee motions to be tested on a specific SCI subject model, with the aim of finding a more balanced and improved assisted gait pattern (with respect to the standard locked knee motion), could overcome limitations of the current manual personalization process and could yield an improved assisted motion for each SCI subject.

## DATA AVAILABILITY STATEMENT

The datasets presented in this article are not readily available because participants have not given written informed consent to make them publicly available. Requests to access the datasets should be directed to miriam.febrer@upc.edu.

## ETHICS STATEMENT

The studies involving human participants were reviewed and approved by Research Committee of Universitat Politècnica

de Catalunya. The patients/participants provided their written informed consent to participate in this study. Written informed consent was obtained from the individual(s) for the publication of any potentially identifiable images or data included in this article.

## AUTHOR CONTRIBUTIONS

MF-N ran the experimental data collection sessions, processed all experimental data, performed all modeling work, formulated and ran all optimal control problems, and wrote a first draft of the manuscript. JF-L and BF planned and supervised the entire project, assisted with the development of optimal control problem formulations, evaluated optimal control results, and helped with revising the manuscript. All authors contributed to the article and approved the submitted version.

## FUNDING

This work was conducted with support from the Grants DPI2015-65959-C3-2-R and RTI2018-097290-B-C33 funded by MCIN/AEI/10.13039/501100011033 and by "ERDF A way of making Europe", and the Leonardo Grant for Researchers and Cultural Creators 2018 funded by the BBVA Foundation.

## ACKNOWLEDGMENTS

We thank Mr. Ivan Camps for his time and collaboration with the experimental captures, and Dr. Joan Vidal and Mr. Mark Wright from the Neurorehabilitation Hospital Institut Guttmann for their valuable discussion and support during this work.

## REFERENCES

- Begg, R., Galea, M. P., James, L., Sparrow, W. A. T., Levinger, P., Khan, F., et al. (2019). Real-time foot clearance biofeedback to assist gait rehabilitation following stroke: a randomized controlled trial protocol. *Trials* 20, 1–7. doi: 10.1186/s13063-019-3404-6
- Cardona, M., García Cena, C. E., Serrano, F., and Saltaren, R. (2020). ALICE: conceptual development of a lower limb exoskeleton robot driven by an on-board musculoskeletal simulator. *Sensors (Switzerland)* 20:789. doi: 10.3390/s20030789
- De Groote, F., and Falisse, A. (2021). Perspective on musculoskeletal modelling and predictive simulations of human movement to assess the neuromechanics of gait. *Proc. R. Soc.* 288: 20202432. doi: 10.1098/rspb.2020.2432
- Delp, S., Anderson, F. C., Arnold, A. S., Loan, P., Habib, A., John, C. T., et al. (2007). OpenSim: open-source software to create and analyze dynamic simulations of movement. *IEEE Trans. Biomed. Eng.* 54, 1940–1950. doi: 10.1109/TBME.2007.901024
- Di Natali, C., Poliero, T., Sposito, M., Graf, E., Bauer, C., Pauli, C., et al. (2019). Design and evaluation of a soft assistive lower limb exoskeleton. *Robotica* 37, 2014–2034. doi: 10.1017/S0263574719000067
- Escalante, A., Lichtenstein, M. J., Dhanda, R., Cornell, J. E., Hazuda, H. P., and Antonio, S. (1999). Determinants of hip and knee flexion range: results from the San Antonio longitudinal study of aging. *Arthritis Care Res.* 12, 8–18. doi: 10.1002/1529-0131(199902)12:1<8::AID-ART3>3.0.CO;2-2
- Falisse, A., Serranoli, G., Dembia, C. L., Gillis, J., Jonkers, I., and De Groote, F. (2019). Rapid predictive simulations with complex musculoskeletal models suggest that diverse healthy and pathological human gaits can emerge from similar control strategies. *J. R. Soc. Interface* 16:20190402. doi: 10.1098/rsif.2019.0402
- Febrer-Nafria, M., Pallarès-López, R., Fregly, B. J., and Font-Llagunes, J. M. (2021). Prediction of three-dimensional crutch walking patterns using a torque-driven model. *Multibody Syst. Dyn.* 51, 1–19. doi: 10.1007/s11044-020-09751-z
- Font-Llagunes, J. M., Lugiés, U., Clos, D., Alonso, F. J., and Cuadrado, J. (2020). Design, control, and pilot study of a lightweight and modular robotic exoskeleton for walking assistance after spinal cord injury. *J. Mech. Robot.* 12:031008. doi: 10.1115/1.4045510
- Fricke, S. S., Bayón, C., Der Kooij, H. Van, and Edwin, E. H. (2020). Automatic versus manual tuning of robot-assisted gait training in people with neurological disorders. *J. Neuroeng. Rehabil.* 17, 1–15. doi: 10.1186/s12984-019-0630-9
- García-Vallejo, D., Font-Llagunes, J. M., and Schiehlen, W. (2016). Dynamical analysis and design of active orthoses for spinal cord injured subjects by aesthetic and energetic optimization. *Nonlinear Dyn.* 84, 559–581. doi: 10.1007/s11071-015-2507-1
- Hunt, K. H., and Crossley, F. R. E. (1975). Coefficient of restitution interpreted as damping in vibroimpact. *J. Appl. Mech. Am. Soc. Mech. Eng.* 42, 440–445. doi: 10.1115/1.3423596
- Jackson, J. N., Hass, C. J., and Fregly, B. J. (2016). Development of a subject-specific foot-ground contact model for walking. *J. Biomech. Eng.* 138:091002. doi: 10.1115/1.4034060
- Koopman, B., Van Asseldonk, E. H. F., and Van Der Kooij, H. (2013). Selective control of gait subtasks in robotic gait training: foot clearance support in stroke survivors with a powered exoskeleton. *J. Neuroeng. Rehabil.* 10, 1–21. doi: 10.1186/1743-0003-10-3

- MacLean, M. K., and Ferris, D. P. (2019). Energetics of walking with a robotic knee exoskeleton. *J. Appl. Biomech.* 35, 320–326. doi: 10.1123/jab.2018-0384
- Meyer, A. J., Eskinazi, I., Jackson, J. N., Rao, A. V., Patten, C., and Fregly, B. J. (2016). Muscle synergies facilitate computational prediction of subject-specific walking motions. *Front. Bioeng. Biotechnol.* 4:77. doi: 10.3389/fbioe.2016.00077
- Michaud, F., Mouzo, F., Ligris, U., and Cuadrado, J. (2019). Energy expenditure estimation during crutch-orthosis-assisted gait of a spinal-cord-injured subject. *Front. Neurobot.* 13:55. doi: 10.3389/fnbot.2019.00055
- Millard, M., Sreenivasa, M., and Mombaur, K. (2017). Predicting the motions and forces of wearable robotic systems using optimal control. *Front. Robot. AI* 4:41. doi: 10.3389/frobt.2017.00041
- Mombaur, K. (2016). “Optimal control for applications in medical and rehabilitation technology: challenges and solutions,” in *Advances in Mathematical Modeling, Optimization and Optimal Control, Springer Optimization*, eds J.-B. Hiriart-Urruty, A. Korytowski, H. Maurer, and M. Szymkat (New York, NY: Springer), 103–145. doi: 10.1007/978-3-319-30785-5\_5
- Nguyen, V. Q., LaPre, A. K., Price, M. A., Umberger, B. R., and Sup, F. C. (2020). Inclusion of actuator dynamics in simulations of assisted human movement. *Int. J. Numer. Method. Biomed. Eng.* 36, 1–13. doi: 10.1002/cnm.3334
- Ong, C. F., Hicks, J. L., and Delp, S. L. (2016). Simulation-based design for wearable robotic systems: an optimization framework for enhancing a standing long jump. *IEEE Trans. Biomed. Eng.* 63, 894–903. doi: 10.1109/TBME.2015.2463077
- Perry, J. (1992). *Gait Analysis: Normal and Pathological Function*. New York, NY: McGraw-Hill. doi: 10.1097/01241398-199211000-00023
- Rajagopal, A., Dembia, C. L., DeMers, M., Delp, D., Hicks, J. L., and Delp, S. (2016). Full body musculoskeletal model for muscle-driven simulation of human gait. *IEEE Trans. Biomed. Eng.* 9294, 1–1. doi: 10.1109/TBME.2016.2586891
- Rao, A. V., Benson, D. a., Darby, C., Patterson, M., Francolin, C., et al. (2014). GPOPS- II: a MATLAB software for solving multiple-phase optimal control problems using hp-adaptive gaussian quadrature collocation methods and sparse nonlinear programming. *ACM Trans. Math. Softw.* 37, 1–39. doi: 10.1145/1731022.1731032
- Rasouli, F., and Reed, K. B. (2020). Walking assistance using crutches: a state of the art review. *J. Biomech.* 98:109489. doi: 10.1016/j.jbiomech.2019.109489
- Rodríguez-Fernández, A., Lobo-Prat, J., and Font-Llagunes, J. M. (2021). Systematic review on wearable lower-limb exoskeletons for gait training in neuromuscular impairments. *J. Neuroeng. Rehabil.* 18, 1–21. doi: 10.1186/s12984-021-00815-5
- Sardini, E., Serpelloni, M., and Lancini, M. (2015). Wireless instrumented crutches for force and movement measurements for gait monitoring. *IEEE Trans. Instrum. Meas.* 64, 3369–3379. doi: 10.1109/TIM.2015.2465751
- Sauder, N. R., Meyer, A. J., Allen, J. L., Ting, L. H., Kesar, T. M., and Fregly, B. J. (2019). Computational design of FastFES treatment to improve propulsive force symmetry during post-stroke gait: a feasibility study. *Front. Neurobot.* 13:80. doi: 10.3389/fnbot.2019.00080
- Schulz, B. W., Ashton-Miller, J. A., and Alexander, N. B. (2008). The effects of age and step length on joint kinematics and kinetics of large out-and-back steps. *Clin. Biomech.* 23, 609–618. doi: 10.1016/j.clinbiomech.2008.01.006
- Serranoli, G., Falisse, A., Dembia, C. L., Vantilt, J., Tanghe, K., Lefeber, D., et al. (2019). Subject-exoskeleton contact model calibration leads to accurate interaction force predictions. *IEEE Trans. Neural Syst. Rehabil. Eng.* 27, 1597–1605. doi: 10.1109/TNSRE.2019.2924536
- Seth, A., Hicks, J. L., Uchida, T. K., Habib, A., Dembia, C. L., Dunne, J. J., et al. (2018). OpenSim: simulating musculoskeletal dynamics and neuromuscular control to study human and animal movement. *PLoS Comput. Biol.* 14:e1006223. doi: 10.1371/journal.pcbi.1006223
- Sreenivasa, M., Millard, M., Felis, M. L., Mombaur, K., and Wolf, S. I. (2017). Optimal control based stiffness identification of an ankle-foot orthosis using a predictive walking model. *Front. Comput. Neurosci.* 11:23. doi: 10.3389/fncom.2017.00023
- Uchida, T. K., Seth, A., Pouya, S., Dembia, C. L., Hicks, J. L., and Delp, S. L. (2016). Simulating ideal assistive devices to reduce the metabolic cost of running. *PLoS ONE* 11:e0163417. doi: 10.1371/journal.pone.0163417
- Van Den Bogert, A. J., Blana, D., and Heinrich, D. (2011). Implicit methods for efficient musculoskeletal simulation and optimal control. *Procedia IUTAM* 2, 297–316. doi: 10.1016/j.piutam.2011.04.027
- Yeung, L. F., Ockenfeld, C., Pang, M. K., Wai, H. W., Soo, O. Y., Li, S. W., et al. (2018). Randomized controlled trial of robot-assisted gait training with dorsiflexion assistance on chronic stroke patients wearing ankle-foot-orthosis. *J. Neuroeng. Rehabil.* 15, 1–12. doi: 10.1186/s12984-018-0394-7
- Zhang, J., Fiers, P., Witte, K. A., Jackson, R. W., Poggensee, K. L., Atkeson, C. G., et al. (2017). Human-in-the-loop optimization of exoskeleton assistance during walking. *Science (80-.)* 356, 1280–1284. doi: 10.1126/science.aal5054

**Conflict of Interest:** The authors declare that the research was conducted in the absence of any commercial or financial relationships that could be construed as a potential conflict of interest.

**Publisher's Note:** All claims expressed in this article are solely those of the authors and do not necessarily represent those of their affiliated organizations, or those of the publisher, the editors and the reviewers. Any product that may be evaluated in this article, or claim that may be made by its manufacturer, is not guaranteed or endorsed by the publisher.

Copyright © 2022 Febrer-Nafria, Fregly and Font-Llagunes. This is an open-access article distributed under the terms of the Creative Commons Attribution License (CC BY). The use, distribution or reproduction in other forums is permitted, provided the original author(s) and the copyright owner(s) are credited and that the original publication in this journal is cited, in accordance with accepted academic practice. No use, distribution or reproduction is permitted which does not comply with these terms.



# A Hybrid 3D Printed Hand Prosthesis Prototype Based on sEMG and a Fully Embedded Computer Vision System

Maria Claudia F. Castro<sup>1\*</sup>, Wellington C. Pinheiro<sup>2</sup> and Glauco Rigolin<sup>1</sup>

<sup>1</sup> Electrical Engineering Department, Centro Universitário FEI, São Bernardo do Campo, Brazil, <sup>2</sup> Mechanical Engineering Department, Centro Universitário FEI, São Bernardo do Campo, Brazil

This study presents a new approach for an sEMG hand prosthesis based on a 3D printed model with a fully embedded computer vision (CV) system in a hybrid version. A modified 5-layer Smaller Visual Geometry Group (VGG) convolutional neural network (CNN), running on a Raspberry Pi 3 microcomputer connected to a webcam, recognizes the shape of daily use objects, and defines the pattern of the prosthetic grasp/gesture among five classes: Palmar Neutral, Palmar Pronated, Tripod Pinch, Key Grasp, and Index Finger Extension. Using the Myoware board and a finite state machine, the user's intention, depicted by a myoelectric signal, starts the process, photographing the object, proceeding to the grasp/gesture classification, and commands the prosthetic motors to execute the movements. Keras software was used as an application programming interface and TensorFlow as numerical computing software. The proposed system obtained 99% accuracy, 97% sensitivity, and 99% specificity, showing that the CV system is a promising technology to assist the definition of the grasp pattern in prosthetic devices.

**Keywords:** hand prosthesis, computer vision, myoelectric signal, convolutional neural network, 3D printed

## OPEN ACCESS

### Edited by:

Francisco Romero Sánchez,  
University of Extremadura, Spain

### Reviewed by:

Vikram Shenoy Handiru,  
Center for Mobility and Rehabilitation  
Engineering Research, Kessler  
Foundation, United States  
Javier Andrés-Esperanza,  
University of Jaume I, Spain

### \*Correspondence:

Maria Claudia F. Castro  
mclaudia@fei.edu.br

**Received:** 31 July 2021

**Accepted:** 07 December 2021

**Published:** 24 January 2022

### Citation:

Castro MCF, Pinheiro WC and  
Rigolin G (2022) A Hybrid 3D Printed  
Hand Prosthesis Prototype Based on  
sEMG and a Fully Embedded  
Computer Vision System.  
*Front. Neurobot.* 15:751282.  
doi: 10.3389/fnbot.2021.751282

## 1. INTRODUCTION

The main function of the human hand and upper limb is to grasp and manipulate objects. Thus, this loss affects the ability of the amputees to carry out activities of daily living, leading to a significant impact on their independence and quality of life. Today there are some sophisticated commercial robot hands available in the market, such as iLimb Ultra and iLimb Quantum by Össur (2021b,a) and Bebionic Hand and Michelangelo Prosthetic Hand by Ottobock (2021a,b). However, the need for affordable prosthetic devices has driven the development of 3D printing systems in order to enable their use by a greater number of people. OpenBionics (2021) and InMoov (2021) are open-source initiatives for the development of affordable, lightweight, and modular myoelectric prosthetic devices that can be easily reproduced with commercially available materials.

The simple structural design of DC or servo motor wired-driven mechanisms controlled by a surface myoelectric signal (sEMG) became popular (Abarca et al., 2019; Ku et al., 2019; Sureshbabu et al., 2019; Mohammadi et al., 2020; Wahit et al., 2020; Khan et al., 2021). The sEMG control can be as simple as an on-off control scheme, proportional where movement velocity depends on the muscle contraction intensity, and even by pattern recognition, which classifies the sEMG into grip pattern classes, have also been used (Geethanjali, 2016). However, while in the former, the number of possible grasp patterns is limited, the success of the latter in clinical applications depends on the users' ability to generate distinct commands in a reproducible manner, being difficult to amputees. Users may get frustrated and stop using the prosthesis quickly (Scheme and Englehart, 2011; Jiang et al., 2012; Palermo et al., 2017; Zhai et al., 2017).

Computer vision (CV) can help the system to better understand the visual world, simulating tasks in the same way that human vision does. Algorithms that give a visual perception to the system can, for example, identify the type of object to be picked up and associate it with the appropriate grasp to be performed.

Dosen et al. (2010) and Dosen and Popovic (2010) proposed a simple scheme, using a web camera and an ultrasound distance sensor. After processing grayscale images at a resolution of  $320 \times 240$  pixels, using LabView 2009 running on a standard laptop (dual-core 2 GHz Pentium), they extracted parameters such as the lengths of the long and short axes and the orientation angle of the long axis concerning the horizontal axis of the image plane. Based on the object size and series of rules, one of four grasp types was selected, being pinch, key grasp, palmar, or spherical.

The InMoov hand was modified by Sidher and Shen (2017) enabling the opposability of the thumb and the introduction of two cameras and proximity sensors on the palm, allowing object detection and automatic grasp definition. Two Raspberry Pi 3 (RPI3) were used to control the cameras, and the control of the servos was achieved by an Arduino Mega, all controlled by a Matlab algorithm running on a PC. However, in Sidher (2017) tests were made only with geometrical objects with a tripod grasp.

DeGol et al. (2016) proposed the inclusion of a CV based on a convolutional neural network (CNN) with an architecture based on the VGG-VeryDeep-16 in a prosthesis for the automatic selection of the grasp to be performed into five classes: power grasp, pinch, tripod pinch, tool, and key grasps. The system achieved 93.2% accuracy running on an NVIDIA Tegra GPU for image processing.

In Andrade et al. (2017), the image captured by an embedded camera was processed on an external server through the Inception-v3 and Tensorflow, and the suggested grasp returned to the local processing unit, an RPI3. The user could accept or cancel the result. If accepted, the resulting grasp pattern went to the V-rep simulator system, which had 14 grasp pattern possibilities: relaxed hand, active index finger, tool, abducted thumb, index flexion, hook, key grasp, use with a computer mouse, open palm, pinch, power, precision gripper opening, precision gripper closing, and tripod pinch. The Myo armband was used to trigger a state machine to take a picture, validate a proposed grasp, ask for another grasp, or cancel an operation, using “wave in,” “wave out,” and “fist” contractions.

Another study that also used a CV system with a two-layer CNN to classify objects into their respective grasp patterns was presented by Ghazaei et al. (2017). Over 500 objects from Amsterdam and Newcastle Grasp Libraries were categorized into four grasp classes, named: pinch, tripod, palmar wrist neutral, and palmar wrist pronated. The classification accuracy in the offline tests reached 75%. In a real-time experiment with a set of the novel as well as seen but randomly-rotated objects, the system achieved an overall score of 84%, implemented in MATLAB on a Lenovo laptop with an Intel Core i7-4559U CPU (2.10 GHz).

A multimodal system was proposed by Shi et al. (2019) combining eye tracking, CV, sEMG, and an Inertial Measurement Unit (IMU) integrated into the HIT AID Hand prosthetic device. The Kinect 2.0 (Microsoft, USA), a 3D Camera, collected color,

depth, and infrared scene images from the user's perspective. The selection of the target objects was through gazing (Eye-Tracking), and the grasp pattern was defined among four based on a convolutional network model. The user controls the prosthesis in collaboration with both sEMG and IMU.

A more sophisticated system was proposed by Shi et al. (2020) showing that depth data play an important role in a grasp pattern definition. Adopting bimodal data scheme, grayscale, and depth information, they improved in 12% the classification accuracy using four types of grasp patterns, named tripod, cylindrical, lateral, and spherical. A specific dataset was built using Kinect 2.0 with objects of different sizes and shapes. After alignment and filtering, color image with reduced resolution, grayscale images, and depth images (all in  $32 \times 32$ ) were used as the inputs of the two channels of independent convolutional networks, based on the Cifar-10 model, running on a personal Laptop (Intel Core i5-3210M, 2.5 GHz, 64 bits, Win10) and connected to a prosthetic device. sEMG control was also provided, based on two finite state machines set up to divide the hand control into coding and motion states. The system accuracy was 93.9%, and the tripod grasp was the main misclassification pattern.

As can be seen, image processing systems usually use robust external computers (CPU), which make the application unfeasible for daily living activities context. The best classification rate was 93% achieved by both Shi et al. (2020) and DeGol et al. (2016). The first used a 3D camera providing depth data and two channels of independent convolutional networks based on the Cifar-10 model for four classes (cylindrical, key grasp, spherical, and tripod), while the latter used a 16-layer VGG-VeryDeep-16 convolution neural network for five classes (power grasp, pinch grasp, tool grasp, 3-jaw chuck, and key grasp).

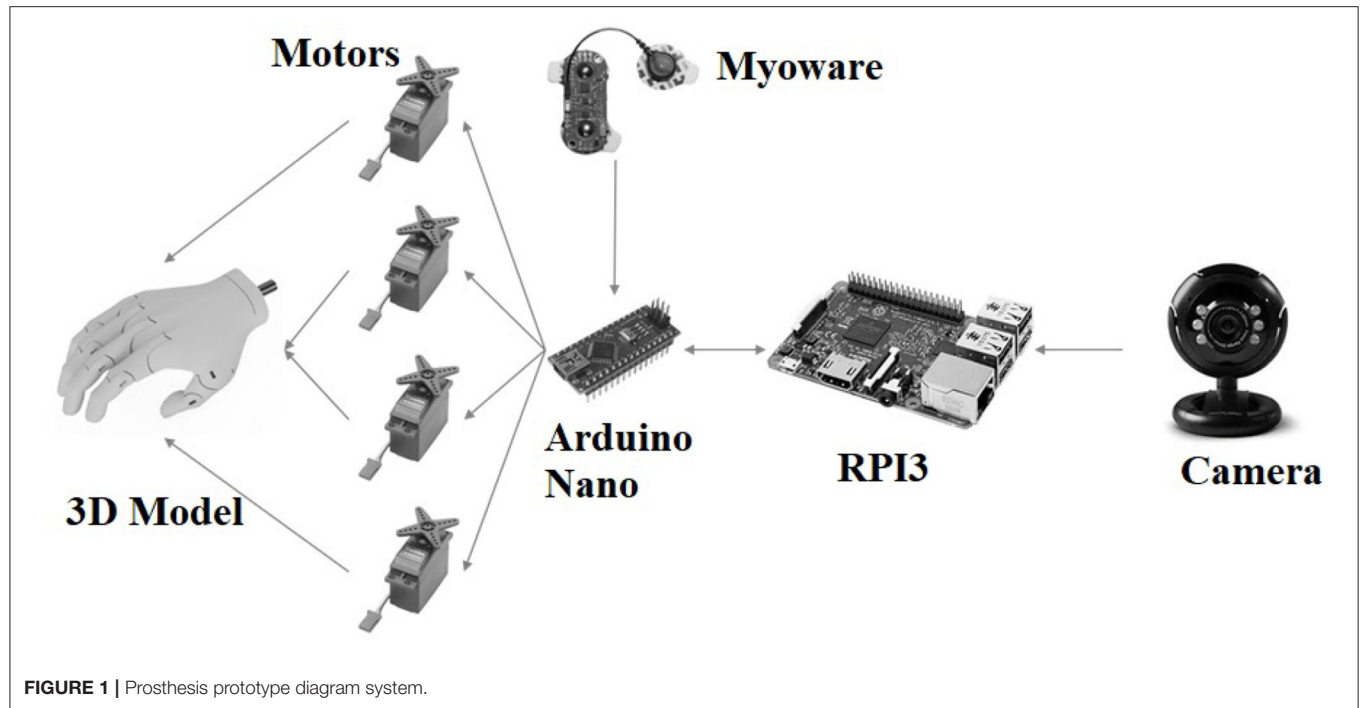
Within this context, a new intelligent hybrid prosthesis model is proposed, commanded by a simple sEMG system aided by a fully embedded CV system. A modified 5-layer SmallerVGG convolutional neural network classifies objects regarding the hand gestures used to interact with them without explicitly identifying them. The system offers five modes: palmar grasp with the wrist in a neutral position and with the wrist pronated, tripod pinch, key grasp, and the index finger extension gesture. This intelligent model facilitates and will speed up the process of learning and using the prosthesis.

## 2. MATERIALS AND METHODS

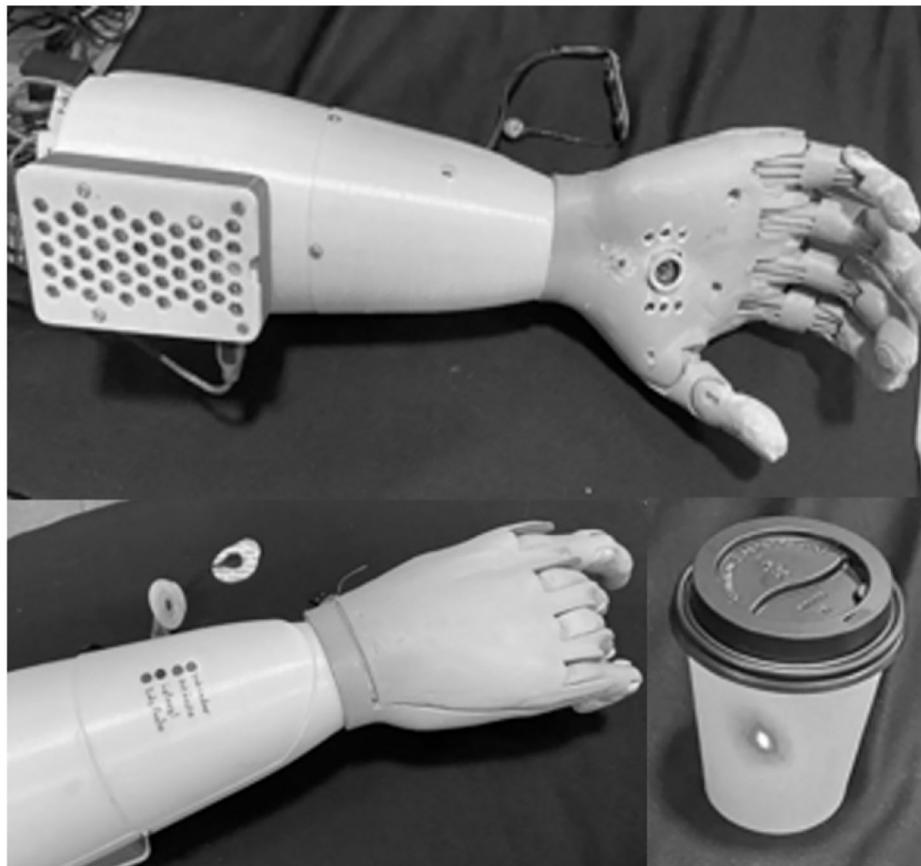
### 2.1. System Design

The prosthesis prototype system (**Figure 1**) is composed of a 3D printed model, an Arduino Nano board, a Myoware sEMG system, a CV system, and an RPI3. The 3D model was based on Buchanan's Kwawu Arm 2.0 and printed on lactic polyacid (PLA). The Arduino system commands the start of image processing, opening, and closing of the prosthesis using servo motors, based on the user's intention detected by the sEMG system and a finite state machine. The CV system is responsible for capturing the image of the object the user wants to grasp, and a CNN,





**FIGURE 1** | Prosthesis prototype diagram system.



**FIGURE 2** | 3D prosthesis prototype with the camera, laser point, and LEDs.

running on the RPI3, classifies it according to the five hand posture patterns.

The 3D prosthesis model was modified after being printed for the camera, laser point, and LEDs installation. A USB camera, APP-TECH model of 16 Megapixels, and a laser point indicator were installed in the palm area, as shown in **Figure 2**. The laser point indicates the object to be photographed and handled by the user. LEDs on the back of the prosthesis prototype inform which grasp class was proposed by the neural classifier.

## 2.2. Control System

The sEMG system is comprised of the Myoware Muscle Sensor from Advancer Technologies. It is an Arduino-powered all-in-one sEMG board with adjustable gain, providing the raw and the envelope of the filtered and rectified signal. In this application, the latter was used. The wearable design allows the disposable electrode attachment directly to the board through embedded electrode connectors. Adhesive disposable electrodes from Meditrace were used to capture sEMG signals. The Arduino Nano board, which makes the analog/digital conversion, has a sampling rate of 9,600 samples per second and 10 bits of resolution.

The control system is expressed by a finite state machine, which diagram can be seen in **Figure 3**. For each supra threshold muscle contraction, the control system receives an input pulse. A muscle contraction activates the laser point, so the user visually confirms the object to be picked up, photographs it, and starts the classification process by the CNN. The pattern chosen by the neural network is displayed on the LEDs on the back of the prosthesis. The user has two options: reject and restart the process or accept and command the movement. In the latter, another muscle contraction defines the object release, and the prosthesis returns to its initial condition.

The total estimated time for this state machine to grasp the object since rest is 1.4 s, excluding the time the user takes to accept the suggested grasp pattern. The estimated time for each sEMG pulse is 100 ms, the laser point takes 350 ms, the classification time since camera activation was less than 250 ms, and the time for motor activation and movement was approximately 600 ms.

A 5-layer VGG network (Rosebrock, 2018a,b), a modified version of the VGG-16 (Simonyan and Zisserman, 2015), was used. The input image with  $96 \times 96$  pixels  $\times$  3 channels passes through a  $3 \times 3$  convolution filter, followed by a linear rectified function (RELU) and a normalization function (BATCH). The network's first pooling layer uses a  $3 \times 3$  matrix to reduce image dimensionality to  $32 \times 32$  pixels. In the consecutive layers, the dimension of the convolution filters is changed from 32 to 64 and finally from 64 to 128. In all intermediate layers, the DROPOUT function is applied, which disconnects 25% of the layer's neurons to reduce overfitting. The final layer is fully connected through the DENSE function that uses a linear rectifier activation function and then goes through a SOFTMAX function to return the value of the probability of classification of each class. Keras software was used as an application programming interface and TensorFlow as numerical computing software.

The training and validation phases were conducted on a Mac mini 2012 computer (2.3 GHz, quad-core i7, 16 GB) and the final CNN model run on the RPI3 (1.2 GHz, Quad-Core Broadcom BCM2837, 1 GB, running with the Raspbian system) for the final testing. The algorithm converts the images to grayscale and resizes them to  $96 \times 96$  pixels. All images contain a single object, black background, and were taken with ambient lighting.

## 2.3. Experiments

Three experiments were carried out using images from the Newcastle Grasp Library (NGL) associated with the Amsterdam Library of Object Images (ALOI), while the final tests were carried out with a set of 24 objects (**Figure 4**) plus 14 keyboard images, establishing a total of 182 images not presented in the training/validation set. This set of images allowed comparisons of experiment performance.

For experiment 1, the objective was to compare the classification results of the modified 5-layer SmallerVGG network with the experiment of Ghazaei et al. (2017). The training/validation set had 7,632 images for the pinch classification pattern, 11,810 images for the tripod pinch, 8,777 images for the palmar grasp with neutral wrist position (neutral), and 11,304 images for the palmar grasp with pronated wrist (pronated). The 182 images for the test phase had 42 images for the pinch classification pattern, 42 for the tripod, 42 for neutral, and 56 for the pronated.

Due to the experiment 1 results, changes were made to the experiment 2 dataset, eliminating images of objects with similar shapes from different classes, choosing only tripod pinch (between the precision grasps), and adding the key grasp class. The CNN training set had 6,900 images for the tripod pinch, 8,345 images for the neutral pattern, 8,280 images for the pronated, and 2,188 images for the key grasp class. The tests were performed with 70 images for the tripod pinch, 42 for neutral, 56 for pronated, and 14 for the key grasp.

For experiment 3, 8,354 images were added to the experiment 2 dataset, being 3,210 computer keyboard images, 2,808 musical keyboard images, and 2,336 tablet images. Classifications from these three new image classes result in the index finger extension movement. The tests were performed with 182 images being 70 for the tripod pinch pattern, 42 for neutral, 42 for pronated, 14 for key grasp pattern, and 14 for index finger extension.

For the test phases mentioned before, a set of 24 objects, like those used by Ghazaei et al. (2017) (**Figure 4**), plus 14 images of keyboards and tablets were used, establishing a total of 182 images allowing for result comparisons. Just as Ghazaei et al. (2017), seven images for each object with random angles of view were presented to the classifier.

## 3. RESULTS

**Table 1** shows the confusion matrix and **Table 2** shows the sensitivity, specificity, and accuracy values, for experiment 1. It can be noted from **Table 1** that pinch and pronated patterns had an excellent result, with almost 100% of classification (41 from 42 and 51 from 56, respectively). On the other hand, a huge misclassification (41 from 42 trials) appeared for the tripod





**FIGURE 5** | Different tube positions allowing the use of different grasps, such as pronated palmar, tripod, pinch, and neutral palmar.

pattern that was classified as pinch, and a smaller one appeared for the neutral pattern (11 from 42 trials) that was classified as pronated. Following these results, **Table 2** reflect the impact of the right and wrong classifications for each pattern, showing a high sensitivity, but lower specificity for pinch, a very low sensitivity, but high specificity for tripod, a low sensitivity, but high specificity for neutral, and high sensitivity and specificity for pronated.

**Table 3** shows the confusion matrix and **Table 4** shows the sensitivity, specificity, and accuracy values, for experiment 2. In **Table 3**, it can be noted that all patterns had an excellent result, with almost 100% of classification, resulting in high sensitivities, specificities, and accuracies up to 96%.

**Table 5** shows the confusion matrix and **Table 6** shows the sensitivity, specificity, and accuracy values, for experiment 3. In this experiment, despite having one more class, the results of **Table 5** showed almost 100% of classification with very low misclassifications, resulting in high sensitivities, specificities, and accuracies up to 98%.

## 4. DISCUSSION

Defining the type of grasp to pick up objects is not as easy as it may seem because there is no consensus. Even with studies like Feix et al. (2016) and Abbasi et al. (2019), which propose grasp taxonomies, the number of grasp patterns is impractical in such type of system. Furthermore, it is reasonable to pick up an object in different ways, whether it is in the same position or if it is arranged in different orientations, as shown in **Figure 5**. Thus, it is often a matter of convention.

The proposed 5-layer SmallerVGG trained in experiment 1, with the same image dataset as Ghazaei et al. (2017), achieved an accuracy of 84%, with new objects, as shown in **Table 2**. The same result was reached by the original work with new and seen images but randomly-rotated objects. The

misclassifications, shown in **Table 1**, resulted in a high sensitivity but low specificity for pinch, a very low sensitivity but high specificity for tripod, and a low sensitivity but high specificity for neutral (**Table 2**). Sensitivity is a measure of how well a test can identify true positives, and specificity is a measure of how well a test can identify true negatives. The overall result for experiment 1 was sensitivity equal to 68% and specificity equal to 89%, which will frustrate the user and make the system non-functional. Since the classification feature was based on object shapes, the explanation of these misclassifications was the arrangement of objects with similar shapes in different classes. Clear examples can be seen in **Figures 6** and **7**. **Figure 6** shows objects with rectangular shape, and despite the possibility of using both neutral and pronated palmar grasps to pick them, as the system use the shape as a classification feature, it is not reasonable to have them into different classes. The same situation occurs for the balls with different sizes of **Figure 7**.

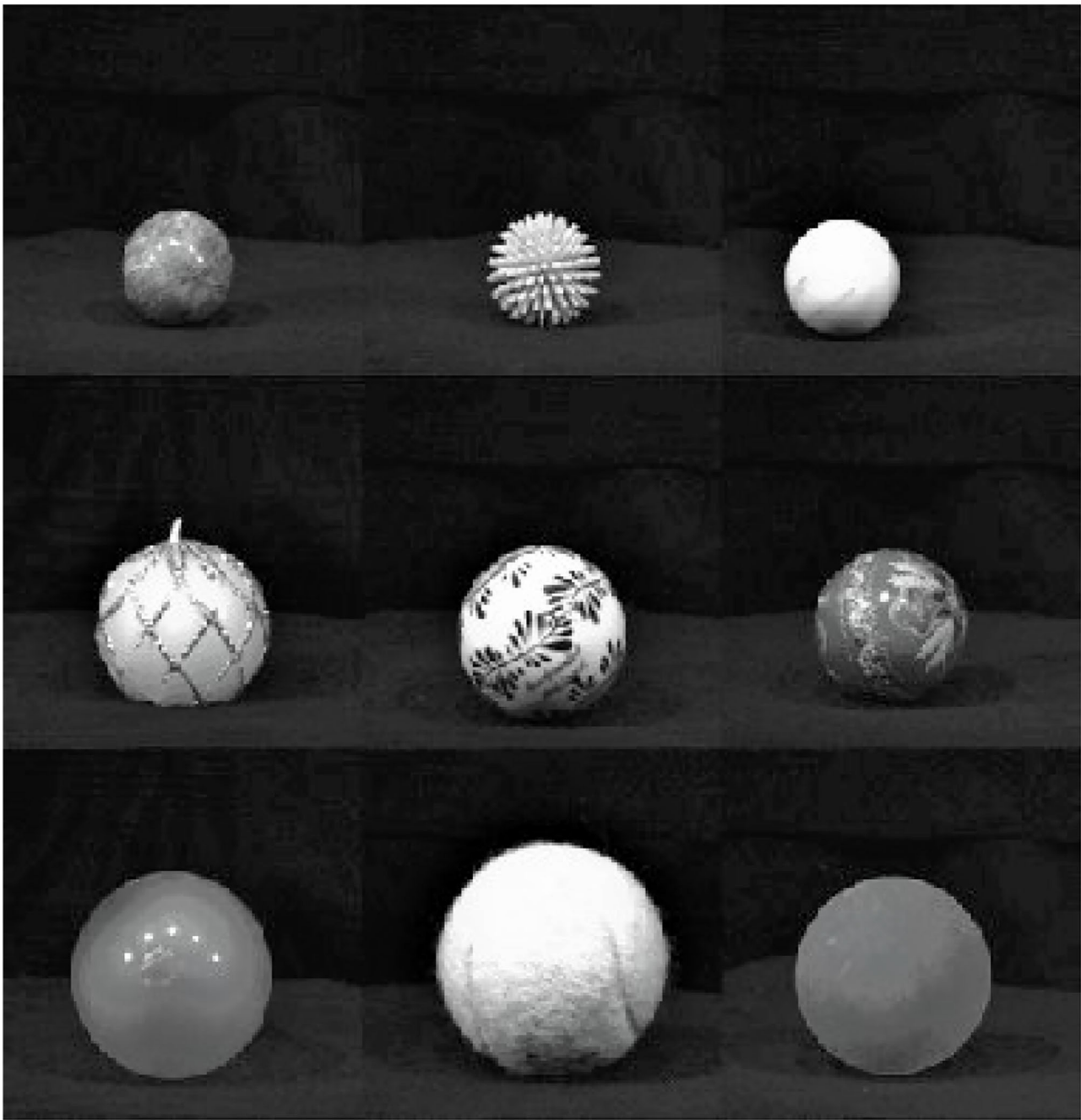
In order to resolve this incompatibility and have a better model, changes were made to the experiment 2 dataset, eliminating images of objects with similar shapes of different classes, choosing only tripod pinch between the precision grasps, since it covers both types of objects, and adding the key grasp class due to its importance, according to Feix et al. (2016) and aiming to keep the same number of classes. These modifications improved the accuracy to 98%, sensitivity to 96%, and specificity to 99% as shown in **Table 4**, for experiment 2, proving the fragility of the original image bank.

In experiment 3, the proposed 5-layer CNN trained with the modified image bank added with the extension index class obtained 99% of accuracy, 97% of sensitivity, and 99% of specificity as shown in **Table 6**. It can be said that the proposed CNN, trained for the neutral and pronated palmar grasps, tripod pinch, and key grasp, recognizes patterns, while for the computer and music keyboards, and tablet classes, the network recognize objects. Even with only five convolutional layers, the SmallerVGG





**FIGURE 6 |** Objects with similar shapes placed in different classes: first line neutral palmar, second and third lines pronated palmar.



**FIGURE 7** | Objects with similar shapes placed in different classes: pinch, tripod, and pronated palmar, respectively.

network showed high accuracy in classifying these patterns and objects in a hybrid configuration.

Comparing the sensitivity and specificity values, experiments 2 and 3 showed greater effectiveness in classification than experiment 1, due to the consistency of the image dataset, presenting a smaller number of false-negative and false-positive results, showing the importance of the adequacy of the image set for the success of the

classification. These results contribute to user satisfaction and system functionality.

Compared with other works in the literature that used a CV system to define the grasp patterns for the prosthesis, the proposed system with a 5-layer SmallerVGG CNN achieved an accuracy higher than those proposed by DeGol et al. (2016) and Shi et al. (2020) that presented accuracies of 93% with a bimodal data scheme and a VGG-VeryDeep-16, respectively.

**TABLE 1** | Confusion matrix for experiment 1.

	Pinch	Tripod	Neutral	Pronated	Total
Pinch	41	0	0	1	42
Tripod	41	1	0	0	42
Neutral	0	0	31	11	42
Pronated	3	2	0	51	56
Total	85	3	31	63	182

**TABLE 2** | Performance metrics of experiment 1 [Se, sensitivity (%); Sp, specificity (%); Acc, accuracy (%)].

	Se	Sp	Acc
Pinch	98	69	75
Tripod	2	99	76
Neutral	74	100	94
Pronated	91	90	91
Total	68	89	84

**TABLE 3** | Confusion matrix for experiment 2.

	Tripod	Neutral	Pronated	Key grasp	Total
Tripod	68	0	0	2	70
Neutral	0	41	1	0	42
Pronated	0	0	54	2	56
Key grasp	3	0	0	11	14
Total	71	41	55	15	182

**TABLE 4** | Performance metrics of experiment 2 [Se, sensitivity (%); Sp, specificity (%); Acc, accuracy (%)].

	Se	Sp	Acc
Tripod	97	97	97
Neutral	98	100	99
Pronated	96	99	98
Key grasp	79	98	96
Total	96	99	98

**TABLE 5** | Confusion matrix for experiment 3.

	Tripod	Neutral	Pronated	Key grasp	Index finger ext.	Total
Tripod	68	0	0	2	0	70
Neutral	0	42	0	0	0	42
Pronated	0	0	41	0	1	42
Key grasp	1	0	0	12	1	14
Index finger ext.	0	0	0	0	14	14
Total	69	42	41	14	16	182

Using an RPI 3 microcomputer instead of a computer for real-time analysis associated with a 3D printed model prosthesis turned the project into a low-cost portable prototype. It is a

**TABLE 6** | Performance metrics of experiment 3 [Se, sensitivity (%); Sp, specificity (%); Acc, accuracy (%)].

	Se	Sp	Acc
Tripod	97	99	98
Neutral	100	100	100
Pronated	98	100	99
Key grasp	86	99	98
Index finger extension	100	99	99
Total	97	99	99

full embedded control system, with higher accuracy than those proposed by Dosen et al. (2010), Dosen and Popovic (2010), Ghazaei et al. (2017), and Shi et al. (2020) in which the processing was done in a separate unit as a standard PC.

Moreover, the proposed hand prosthesis prototype focused on a more natural appearance, incorporating a discreet webcam in the palm, unlike the proposals by DeGol et al. (2016), Ghazaei et al. (2017), Dosen et al. (2010), and Dosen and Popovic (2010) who used an external webcam. The Arduino Nano board used to command the servos can be substituted, as the RPI3 can perform this task. This change would reduce the internal wires and cables and increase the space available inside the prosthesis prototype body.

The Myoware sensor board has a gain adjustment of the sEMG signal, and the software has a threshold adjustment, which allows for the customization required for each user due to the sEMG electrode positioning and physical conditions. Despite its simplicity, it seems to be enough to the proposed application of state machine trigger, instead of a more sophisticated one such as Myo armband as used by Andrade et al. (2017) or Delsys Trigno used by Ghazaei et al. (2017).

The total estimated time for the state machine to grasp the object since rest is approximately 1.4 s, which is reasonable for prosthetic control. However, the time taken for the user to confirm the grasp pattern was not considered. The time for each sEMG pulse was estimated at 100 ms, and it depends on the user's ability to fast contract above the selected threshold. The laser point of 350 ms aims only to confirm the selected object to be grasped. The classification time since camera activation was approximately 250 ms, and the time for motor activation and movement was approximately 600 ms.

Ghazaei et al. (2017) reported 150 ms for the average time needed for pre-processing and classification in computer-based real-time performance analysis, and 300 ms using a short flexion contraction above a threshold. Sidher (2017) reported classification times varying from 223 ms to 1.963 s for geometrical objects using RPI 3. Compared with the previous studied, the proposed system control presents promising behavior.

On the other hand, the presented prototype did not intend to be a final prosthesis proposal but a proof of concept of the feasibility of a fully embedded hybrid system based on a hybrid approach using sEMG and CV to overcome the limitations of the strict sEMG control systems. Therefore, the experiments reported in this study were related to the CV technical aspects.

Some improvements could be performed, such as adding new classes to the CV classification system or some common gestures as a user choice option via the sEMG finite state machine. Examples of the first are parallel extension, hook, and power grip, and for the latter are point (index finger extension), ok sign, and thumbs up.

Furthermore, the results were obtained in a controlled environment, with fixed prototype distance and height related to the object. These parameters could change the classification accuracies due to the classifier model's dependence on object shape patterns. Adding distance sensors like Dosen et al. (2010), Dosen and Popovic (2010), and Sidher (2017) did, seem reasonable to overcome the problem of similar shape but different size objects, as shown in **Figure 7**.

Therefore, the prosthesis's functional performance evaluation in a clinical trial is essential to guarantee its effectiveness. The Southampton Hand Assessment Procedure (SHAP) is a well-known, simple, and replicable protocol based on the assessment of the effectiveness of the prosthetic device with a focus on performing a set of tasks by the user (Light et al., 2002; Andres-Esperanza et al., in press). Dosen et al. (2010) showed that the average time to accomplish the "reach, pick up and place" task with 13 healthy subjects decreases with training, reaching approximately 10 s after 100 trials. Shi et al. (2020) reported an average time of 6.4 s in an experimental protocol with four healthy subjects performing a total of 320 trials, comparing Vision-EMG and Coding-EMG control. Ghazaei et al. (2017) reported an average time of 7s for two trans-radial amputee volunteers to accomplish the "reach, pick up, and place" task. However, this evaluation is not the focus of this study and will be the subject of future investigation.

## 5. CONCLUSION

This study presented a hybrid 3D printed hand prosthesis prototype based on an sEMG controlled finite state machine and a fully embedded CV system. A modified 5-layer Smaller Visual Geometry Group (VGG) CNN running on an RPi 3 connected to a webcam recognizes the shape of daily use objects and defines the grasp/gesture pattern for the prosthetic prototype. The sEMG signal, representing the user's intention, starts the process and commands the prosthetic motors to movement execution.

## REFERENCES

- Abarca, V. E., Flores, K. M., and Elias, D. (2019). "The octa hand: an affordable multi-grasping 3d-printed robotic prosthesis for transradial amputees," in *5th International Conference on Control, Automation and Robotics* (Beijing: IEEE), 92–97. doi: 10.1109/ICCAR.2019.8813417
- Abbasi, B., Sharifzadeh, M., Noohi, E., Parastegari, S., and Zefran, M. (2019). "Grasp taxonomy for robot assistants inferred from finger pressure and flexion," in *International Symposium on Medical Robotics (ISMR)* (Atlanta, GA: IEEE), 1154–1159. doi: 10.1109/ISMR.2019.8710191
- Andrade, D. T. G., Ishikawa, A., Munoz, A. D., and Rohmer, E. (2017). "A hybrid approach for the actuation of upper limb prostheses based on computer vision," in *Latin American Robotics Symposium (LARS)*

The proposed system obtained 99% accuracy, 97% sensitivity, and 99% specificity for grasping objects from neutral and pronated palmar grasp, tripod pinch, key grasp, and index finger extension gesture. Compared with other studies in the literature that used a CV system for prosthetics, the proposed system achieved a higher accuracy with a full embedded system. Furthermore, it is a low-cost technology with a reduced user training time, considering the simple use of sEMG.

This study showed that the use of a vision system to help define the pattern of grasping and manipulating objects is a promising alternative and that studies in this area should be performed. For the continuity of this study, it is proposed the improvement of the prosthesis for thumb movement; prosthetic functional performance evaluation in clinical measurements to guarantee its effectiveness.

## DATA AVAILABILITY STATEMENT

The raw data supporting the conclusions of this article is available at: <https://doi.org/10.5281/zenodo.5749745>.

## AUTHOR CONTRIBUTIONS

GR was the engineer and developer of all presented platforms. MC masterfully coordinated the work and was a major contributor in writing the manuscript. WP contributed to reviewing the manuscript. All authors read and approved the final manuscript.

## FUNDING

This study was financed in part by the Coordenação de Aperfeiçoamento de Pessoal de Nível Superior—Brazil (CAPES)—Finance Code 001.

## ACKNOWLEDGMENTS

The authors would like to thank the CAPES and FAPESP for their support.

and 2017 Brazilian Symposium on Robotics (SBR) (Curitiba: IEEE), 1–6. doi: 10.1109/SBR-LARS-R.2017.8215308

- Andres-Esperanza, J., Iserte-Vilar, J. L., Llop-Harillo, I., and Perez-Gonzalez, A. (in press). Affordable 3D-printed tendon prosthetic hands: expectations and benchmarking questioned. *Eng. Sci. Technol. Int. J.* doi: 10.1016/j.jestch.2021.08.010
- DeGol, J., Akhtar, A., Manja, B., and Bretl, T. (2016). "Automatic grasp selection using a camera in a hand prosthesis," in *IEEE Eng Med Biol Soc. (Orlando, FL: IEEE)*, 431–434. doi: 10.1109/EMBC.2016.7590732
- Dosen, S., Cipriani, C., Kostic, M., Controzzi, M., Carrozza, M. C., and Popovic, D. B. (2010). Cognitive vision system for control of dexterous prosthetic hands: experimental evaluation. *J. Neuroeng. Rehabil.* 7, 1–14. doi: 10.1186/1743-0003-7-42



- Dosen, S., and Popovic, D. B. (2010). Transradial prosthesis: artificial vision for control of prehension. *Artif. Organs* 35, 37–48. doi: 10.1111/j.1525-1594.2010.01040.x
- Feix, T., Romero, J., Schmiedmayer, H.-B., Dollar, A. M., and Kragic, D. (2016). The grasp taxonomy of human grasp types. *IEEE Trans. Hum. Mach. Syst.* 46, 66–77. doi: 10.1109/THMS.2015.2470657
- Geethanjali, P. (2016). Myoelectric control of prosthetic hand: stat-of-the-art review. *Med. Devices Evid. Res.* 9, 247–255. doi: 10.2147/MDER.S91102
- Ghazaei, G., Alameer, A., Degenaar, P., Morgan, G., and Nazarpour, K. (2017). Deep learning-based artificial vision for grasp classification in myoelectric hands. *J. Neural Eng.* 14, 1–18. doi: 10.1088/1741-2552/aa6802
- InMoov (2021). *Hand and Forarm*. Available online at: <http://inmoov.fr/hand-and-forarm/> (accessed May 15, 2021).
- Jiang, N., Dosen, S., Muller, K.-R., and Farina, D. (2012). Myoelectric control of artificial limbs—Is there a need to change focus? *IEEE Signal Process. Mag.* 29, 150–152. doi: 10.1109/MSP.2012.2203480
- Khan, S. S. A., Ferdous, S. J., and Chakraborty, S. (2021). Design and development of a 3D printed myoelectric-controlled prosthesis hand using sEMG sensor. *Int. J. Biomed. Biol. Eng.* 15, 10127–10134. Available online at: <https://publications.waset.org/10011734/pdf>
- Ku, I., Lee, G. K., Park, C. Y., Lee, J., and Jeong, E. (2019). Clinical outcomes of a low-cost single-channel myoelectric-interface three-dimensional hand prosthesis. *Arch. Plastic Surg.* 46, 303–310. doi: 10.5999/aps.2018.01375
- Light, C. M., Chappell, P. H., and Kyberd, P. J. (2002). Establishing a standardized clinical assessment tool of pathologic and prosthetic hand function: normative data, reliability, and validity. *Arch. Phys. Med. Rehabil.* 83, 776–783. doi: 10.1053/apmr.2002.32737
- Mohammadi, A., Lavranos, J., Zhou, H., Mutlu, R., Alici, G., Tan, Y., et al. (2020). A practical 3D-printed soft robotic prosthetic hand with multi-articulating capabilities. *PLoS ONE* 15:e0232766. doi: 10.1371/journal.pone.0232766
- Openbionics (2021). *Prosthetic hands*. Available online at: <https://openbionics.org/affordableprostheticshands/> (accessed May 15, 2021).
- Össur (2021a). *i-limb Quantum*. Available online at: <https://www.ossur.com/en-us/prosthetics/arms/i-limb-quantum?tab=specification> (accessed May 15, 2021).
- Össur (2021b). *i-limb Ultra*. Available online at: <https://www.ossur.com/en-us/prosthetics/arms/i-limb-ultra> (accessed May 15, 2021).
- Ottobock (2021a). *Bebionic*. Available online at: <https://www.ottobockus.com/prosthetics/upper-limb-prosthetics/solution-overview/bebionic-hand/> (accessed June 15, 2021).
- Ottobock (2021b). *Michelangelo Prosthetic Hand*. Available online at: <https://www.ottobockus.com/prosthetics/upper-limb-prosthetics/solution-overview/michelangelo-prosthetic-hand/> (accessed May 15, 2021).
- Palermo, F., Cognolato, M., Gijbarts, A., Muller, H., Caputo, B., and Atzori, M. (2017). “Repeatability of grasp recognition for robotic hand prosthesis control based on SEMG data,” in *International Conference on Rehabilitation Robotics (ICORR)* (London: IEEE), 1–7. doi: 10.1109/ICORR.2017.8009405
- Rosebrock, A. (2018a). *Keras and Convolutional Neural Networks (CNNs)*. Available online at: <https://www.pyimagesearch.com/2018/04/16/keras-and-convolutional-neural-networks-cnns/> (accessed June 27, 2021).
- Rosebrock, A. (2018b). *Pyimagesearch - smallerVGGNet: Multi-Label Classification With Keras*. Available online at: <https://www.pyimagesearch.com/2018/05/07/multi-label-classification-with-keras/> (accessed June 27, 2021).
- Scheme, E., and Englehart, K. (2011). Electromyogram pattern recognition for control of powered upper-limb prostheses: state of the art and challenges for clinical use. *J. Rehabil. Res. Dev.* 48, 643–659. doi: 10.1682/JRRD.2010.09.0177
- Shi, C., Qi, L., Yang, D., Zhao, J., and Liu, H. (2019). “A novel method of combining computer vision, eye-tracking, EMG, and IMU to control dexterous prosthetic hand,” in *IEEE International Conference on Robotics and Biomimetics (Dali: IEEE)*, 2614–2618. doi: 10.1109/ROBIO49542.2019.8961582
- Shi, C., Yang, D., Zhao, J., and Liu, H. (2020). Computer vision-based grasp pattern recognition with application to myoelectric control of dexterous hand prosthesis. *IEEE Trans. Neural Syst. and Rehabil. Eng.* 28, 2090–2098. doi: 10.1109/TNSRE.2020.3007625
- Sidher, A. (2017). *Prosthesis design and object recognition based grasping of a 3d printed anthropomorphic artificial hand* (Master’s thesis). University of Nevada, Reno, United States.
- Sidher, A., and Shen, Y. (2017). “Improving a 3D-printed artificial anthropomorphic hand using the human hand model,” in *IEEE International Conference on Real-time Computing and Robotics (RCAR)* (Okinawa: IEEE), 739–744. doi: 10.1109/RCAR.2017.8311952
- Simonyan, K., and Zisserman, A. (2015). “Very deep convolutional networks for large-scale image recognition,” in *International Conference on Learning Representations (ICLR)* (San Diego, CA), 1–14.
- Sureshbabu, A. V., Rass, D., and Zimmermann, M. (2019). “A lightweight transradial hand prosthesis with a variable position thumb and thermoregulation,” in *19th International Conference on Advanced Robotics (ICAR)* (Belo Horizonte: IEEE), 61–68. doi: 10.1109/ICAR46387.2019.8981665
- Wahit, M. A. A., Ahmad, S. A., Marhaban, M. H., Wada, C., and Izhar, L. I. (2020). 3D printed robot hand structure using four-bar linkage mechanism for prosthetic application. *Sensors* 20, 1–22. doi: 10.3390/s20154174
- Zhai, X., Jelfs, B., Chan, R. H. M., and Tin, C. (2017). Self-recalibrating surface EMG pattern recognition for neuroprosthesis control based on convolutional neural network. *Front. Neurosci.* 11:379. doi: 10.3389/fnins.2017.00379

**Conflict of Interest:** The authors declare that the research was conducted in the absence of any commercial or financial relationships that could be construed as a potential conflict of interest.

**Publisher’s Note:** All claims expressed in this article are solely those of the authors and do not necessarily represent those of their affiliated organizations, or those of the publisher, the editors and the reviewers. Any product that may be evaluated in this article, or claim that may be made by its manufacturer, is not guaranteed or endorsed by the publisher.

Copyright © 2022 Castro, Pinheiro and Rigolin. This is an open-access article distributed under the terms of the Creative Commons Attribution License (CC BY). The use, distribution or reproduction in other forums is permitted, provided the original author(s) and the copyright owner(s) are credited and that the original publication in this journal is cited, in accordance with accepted academic practice. No use, distribution or reproduction is permitted which does not comply with these terms.



# Wearable Power-Assist Locomotor for Gait Reconstruction in Patients With Spinal Cord Injury: A Retrospective Study

Soichiro Koyama<sup>1</sup>, Shigeo Tanabe<sup>1</sup>, Takeshi Gotoh<sup>2</sup>, Yuta Taguchi<sup>2</sup>, Masaki Katoh<sup>2</sup>, Eiichi Saitoh<sup>3</sup>, Yohei Otaka<sup>3</sup> and Satoshi Hirano<sup>3\*</sup>

<sup>1</sup> Faculty of Rehabilitation, School of Health Sciences, Fujita Health University, Toyoake, Japan, <sup>2</sup> Department of Rehabilitation, Fujita Health University Hospital, Toyoake, Japan, <sup>3</sup> Department of Rehabilitation Medicine I, School of Medicine, Fujita Health University, Toyoake, Japan

## OPEN ACCESS

### Edited by:

Massimo Sartori,  
University of Twente, Netherlands

### Reviewed by:

Nicola Lotti,  
Heidelberg University, Germany  
Michele Xiloyannis,  
ETH Zürich, Switzerland

### \*Correspondence:

Satoshi Hirano  
sshirano@fujita-hu.ac.jp

**Received:** 14 September 2021

**Accepted:** 11 January 2022

**Published:** 18 February 2022

### Citation:

Koyama S, Tanabe S, Gotoh T, Taguchi Y, Katoh M, Saitoh E, Otaka Y and Hirano S (2022) Wearable Power-Assist Locomotor for Gait Reconstruction in Patients With Spinal Cord Injury: A Retrospective Study. *Front. Neurobot.* 16:775724. doi: 10.3389/fnbot.2022.775724

Wearable robotic exoskeletons (WREs) have been developed from orthoses as assistive devices for gait reconstruction in patients with spinal cord injury. They can solve some problems encountered with orthoses, such as difficulty in independent walking and standing up and high energy consumption during walking. The Wearable Power-Assist Locomotor (WPAL), a WRE, was developed based on a knee–ankle–foot orthosis with a single medial hip joint. The WPAL has been updated seven times during the period from the beginning of its development, in 2005, to 2020. The latest version, launched as a commercialized model in 2016, is available for medical facilities. In this retrospective study, which included updated results from previous reports, all data were extracted from development research records from July 2007 to December 2020. The records were as follows: patient characteristics [the number of participants, injury level, and the American Spinal Injury Association Impairment Scale (AIS) score], the total number of WPAL trials when aggregating the cases with all the versions or only the latest version of the WPAL, and maximum walking performance (functional ambulation category [FAC], distance, and time of continuous walking). Thirty-one patients participated in the development research. The levels of spinal cord injury were cervical (C5–C8), upper thoracic (T3–T6), lower thoracic (T7–T12), and lumbar (L1) in 10, 5, 15, and 1 of the patients, respectively. The numbers of patients with AIS scores of A, B, C, and D were 20, 7, 4, and 0, respectively. The total number of WPAL trials was 1,785, of which 1,009 were used the latest version of the WPAL. Twenty of the patients achieved an FAC score of 4 after an average of 9 (median 8, range 2–22) WPAL trials. The continuous walking distance and time improved with the WPAL were compared to the orthosis. We confirmed that the WPAL improves walking independence in people with a wide range of spinal cord injuries, such as cervical spinal cord injuries. Further refinement of the WPAL will enable its long-term use at home.

**Keywords:** wearable robotic exoskeleton, gait, paraplegia, tetraplegia, clinical experience

## INTRODUCTION

Traumatic spinal cord injury (SCI) is one of the most devastating events that occur after various accidents. Long-term motor, sensory, and autonomic dysfunction caused by traumatic SCI have a tremendous effect on the daily life of patients and their families. The incidence rates of traumatic SCI per 1 million people per year were 14 cases in Austria (Majdan et al., 2016), 18 cases in Switzerland (Chamberlain et al., 2015), and 10 cases in Denmark (Bjornshave Noe et al., 2015), representing almost 180,000 cases annually worldwide in 2014 (Lee et al., 2014). Similarly, the annual incidence of SCI is approximately 54 cases per 1 million people in the United States, which is approximately 17,900 new SCI cases in 2021 (NSCIS Center, 2021). In Japan, the estimated incidence of traumatic SCI, excluding the grade E in the Frankel scale, that is, defined as no neurological deficit/complete recovery, was 49 cases per 1 million people annually in 2010 (Miyakoshi et al., 2020).

The majority of patients with motor-complete SCI often rely on a wheelchair as a mobility device in activities of daily living because a wheelchair is energy efficient and enables patients to safely perform their daily activities. However, long-term inactivity due to wheelchair use results in various medical problems [e.g., joint contraction (Kunkel et al., 1993), pressure sores (Verschuere et al., 2011), osteoporosis (Varacallo et al., 2021), and psychosocial problems as a result of a relatively low eye level (Dijkers, 1999; Levins et al., 2004)]. For patients with SCI, the opportunity to stand and walk occasionally is important from both physical and psychosocial perspectives.

In the past few decades, various wearable robotic exoskeletons (WREs) have been developed for stand and gait reconstruction in patients with motor-complete SCI. They offer the opportunity to walk in home and community environments by moving the paretic legs of patients with partial or complete SCI in a reciprocal stepping pattern (Fisahn et al., 2016; Miller et al., 2016; Palermo et al., 2017; Tan et al., 2021). Arazpour et al. (2013) reported that the gait, speed, and endurance of patients with SCI using WREs are superior to those of patients using either reciprocating gait or hip-knee-ankle-foot orthoses (Arazpour et al., 2013). The oxygen consumption and heart rate during gait training with WRE are slightly increased compared with that during sitting and standing, and the load during gait training with WRE is less than that with conventional orthoses (Asselin et al., 2015; Yatsuya et al., 2018).

We have previously reported the effects of the Wearable Power-Assist Locomotor (WPAL) on walking ability and gait pattern in patients with various levels of SCI. The first report shared the basic concept of WPAL development and a comparison of walking performance between the WPAL and the conventional Primewalk orthosis (Tanabe et al., 2013b). The report showed that the WPAL has a lower physiological cost index and involves less muscle activity in the upper limbs during walking, compared with the Primewalk orthosis (Tanabe

et al., 2013b). We also reported gait pattern, the basic training procedure, and gait performance of the WPAL in seven patients with SCI at the thoracic level of injury (T6–T12) (Tanabe et al., 2013a). In addition, we found that continuous walking time and distance were prolonged with the WPAL compared with orthotic walking in 12 patients with SCI (Hirano et al., 2015). The WPAL significantly decreased the physiological cost index, heart rate, and modified Borg score during the 6-min walking test compared with conventional knee-ankle-foot orthoses in six other patients with SCI (Yatsuya et al., 2018). Recently, we have reported that the WPAL improves walking ability more than conventional orthoses in patients with cervical SCI (Fuse et al., 2019).

The objective of this study was to summarize all data that include updated results from previous reports, about physical characteristics, and walking abilities of patients with SCI, from the development research records in clinical practice from July 2007 to December 2020. The present findings are potentially useful for gait performance comparison with other robots, a meta-analysis of the effects of WREs in patients with SCI, and evidence-based selection of WREs for patients with SCI.

## MATERIALS AND METHODS

### Study Design and Participants

In this retrospective study, we included 31 patients with SCI in our university from 2007 to 2020, regardless of being inpatients or outpatients. The causes of spinal cord injury were traumatic spinal cord injury in 24 patients, spinal cord infarction in 3 patients, encephalomyelitis in 1 patient, radiation myelitis in 1 patient, hemorrhage from the thoracic spinal cord cavernous hemangioma in 1 patient, and acute thoracic spinal epidural hematomas in 1 patient. The principal inclusion criteria for participation were as follows: (1) patients with motor paralysis [American Spinal Injury Association Impairment Scale (AIS) classification A–C] who had a neurological level of injury from C3 to L1; (2) a height of 155–180 cm; (3) a weight <80 kg; and (4) sufficient upper limb muscle strength (to the extent that the patient can transfer independently). All patients provided written informed consent prior to study participation. This study was performed in accordance with the principles of the Declaration of Helsinki and conducted after receiving approval from the ethics committee of our university (approval number: CR18-035).

The exclusion criteria were as follows: (1) progressive disease (excluding disuse syndrome); (2) difficulty in communication due to dementia or impaired consciousness; (3) high risk of fracture of the lower limbs or spine (e.g., severe osteoporosis); (4) uncontrolled hypertension (resting systolic blood pressure >180 mmHg and diastolic blood pressure >120 mmHg); (5) uncontrolled tachycardia (ventricular rate >120 beats per min); and (6) limitation of movement due to impaired cardiac or respiratory function (e.g., shortness of breath when using a wheelchair).

### Design of WPAL

A detailed basic design of the WPAL has been published previously (Tanabe et al., 2013a,b, 2017). The main structures, such as frames and motors, were placed between the lower

**Abbreviations:** AIS, American Spinal Injury Association Impairment Scale; FAC, functional ambulation category; SCI, spinal cord injury; WPAL, Wearable Power-Assist Locomotor; WRE, wearable robotic exoskeletons.

limbs. The frame was connected by a single mechanical hip joint medially under the perineum. The mechanical hip joint had a sliding structure that curves anterior-posteriorly based on the structure of Primewalk orthosis (Suzuki et al., 2005). The sliding structure enables the virtual center of rotation of the robotic hip joint to be closer to the physiological center of the hip joint. Six motors were located in the hip, knee, and ankle joints. The ranges of motion were as follows: hip, 40° (flexion 25°-extension 15°); knee, 120° (flexion 120°-extension 0°); and ankle, 50° (dorsiflexion 35°-plantar flexion 15°). Each joint used an individual custom-made brushless DC servomotor, which was compact to fit between the legs (24 V, 78 W, peak torque of 4 Nm, speed range from 0 to 1,000 deg/s). The weight of the WPAL was approximately 13 kg; however, the patient did not feel the weight because one foot was always on the ground. The use of a customized walker with motor control circuitry and batteries ensured safety and eliminated the need for the patients to carry the device themselves. Two lever switches and two button switches were installed on both handgrips of the walker to enable the patients to operate it themselves. The WPAL could also be put on and removed by the patient; a skilled patient could do this within approximately 2 min.

## Operating the WPAL

The WPAL is equipped with the following five modes: (1) standing-up mode, (2) adjustment mode for the ankle joint angle during standing, (3) walking mode, (4) sitting-down mode, and (5) manipulation mode for the knee joint while putting on or removing the WPAL. Each mode is selected by pressing the button attached to the left grip of the walker. When the WPAL user presses a button, only the indicator lamp for the currently selected mode lights up on the control panel mounted on the front bar of the walker to indicate the currently selected mode. **Figure 1** shows a state transition diagram for the WPAL operation and control.

In the standing-up mode, pressing the button attached to the right grip of the walker for 0.5 s will start the WPAL in motion from the sitting position. The user stands up by moving the body's center of gravity slightly forward and pushes the walker slightly downward and backward using residual functions in accordance with the movement of the WPAL. In the adjustment mode for the ankle joint angle during standing, the user can adjust the ankle joint angle for a stable standing posture by pulling the lever attached below the grip of the walker. Pulling the lever on the left side increases the dorsiflexion angle of the ankle joint, and pulling the lever on the right side increases the plantar flexion angle of the ankle joint. This function is necessary because each patient with SCI has a different ankle joint angle for a stable standing posture. In the walking mode, the WPAL motion is started by pressing the button attached to the right grip of the walker for 0.5 s. In this mode, the user is able to select the first step of walking (left or right). If the user selects the left side for the first step, the user has to shift the center of gravity to the right side to start walking smoothly. The WPAL moves both lower limbs alternately and constantly. WPAL users have to move their center of gravity laterally rhythmically with the WPAL motion using residual upper limb and trunk muscles and move the walker

forward at the appropriate time in the gait cycle of the WPAL. WPAL motion is stopped when the user pulls the levers on both sides simultaneously for a few seconds. In the sitting-down mode, the WPAL motion is started by pressing the right button for 0.5 s in the standing position. The sitting-down motion of the WPAL is caused first by plantar flexion of the ankle joint, followed by flexion of the knee joint. The user needs to lean forward with their trunk and maintain the posture until full flexion to the pre-programmed angle of the knee joint of the WPAL for sitting in the wheelchair. In the manipulation mode of the knee joint for putting on and removing the WPAL, the user can manipulate the knee joint of the WPAL by using the lever attached under the grip of the walker. The user flexes the knee joint of the WPAL by pulling the lever under the left grip. This action is used when the user wants to put on the WPAL from a wheelchair. In contrast, pulling the right lever extends the knee joint of the WPAL. This action enables the user to remove the WPAL while on the wheelchair after the sitting-down motion.

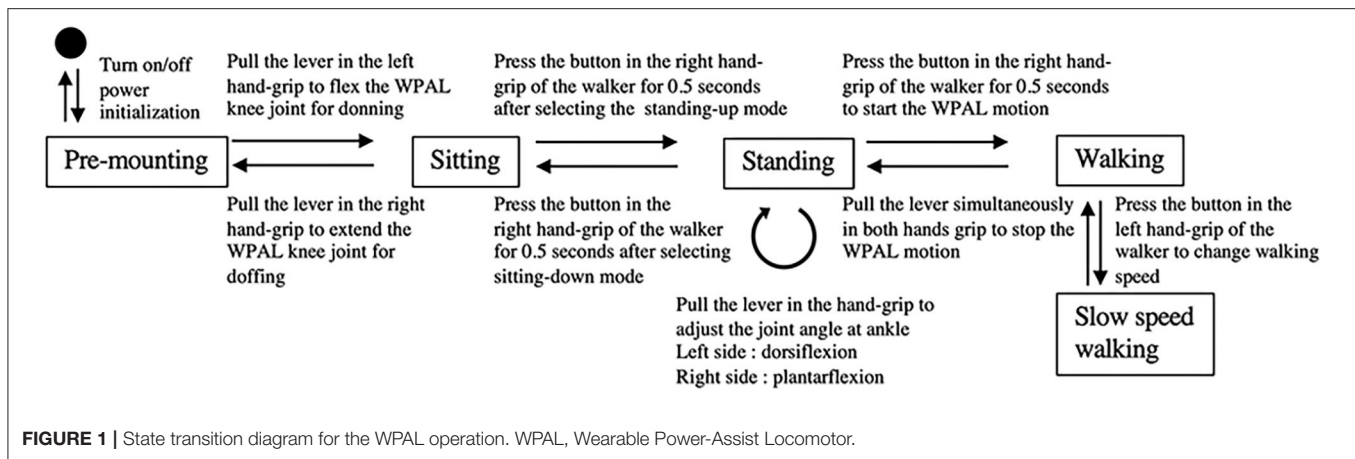
## Gait Training Procedure

The WPAL moves both lower limbs in a constant rhythm. WPAL users need to shift their lateral weight rhythmically in accordance with the WPAL motions. We have recommended five stages of gait training to achieve independent walking with the WPAL and a specialized wheeled walker (Tanabe et al., 2013a,b, 2017). In the initial four stages of gait training, the exercises are performed under the suspension system to prevent falls and reduce excessive fear of falling. The harness of the suspension system is set to slack without partially supporting the body weight. The first stage is a stepping exercise in the parallel bars. Before walking with the WPAL, the user learns to use the upper limbs and trunk muscles to perform a lateral weight shift with appropriate timing while keeping their center of gravity forward and backward, referring to a beeping sound produced in time with the walking rhythm. Subsequently, the user performs the same motions as the driving WPAL. The second stage is walking in the parallel bars. The step time is gradually shortened to approximately 1.5 s. The stride length is gradually increased to approximately 200 mm. The third stage is a walking exercise on a treadmill with a slow speed (approximately 0.1–0.3 km/h). Through continuous walking for a long period, the WPAL user can learn stable and rhythmic lateral weight shifts. The fourth stage is a walking exercise with a specialized wheeled walker. The user operates the WPAL using buttons or triggers installed on the grip of the walker. The final stage is a walking exercise without suspension using a specialized wheeled walker. Consensus decision-making is made between a certified physical therapist and a rehabilitation physician as to whether to proceed to the next stage. Patients also practice standing up and sitting down and donning/doffing of the WPAL during trials.

## Data Collection and Analysis

The development history of the WPAL was obtained from research records and interviews with members of the WPAL development team (rehabilitation physician, physical therapist, prosthetist and orthotist, and engineer). In the research records, medical doctors or physical therapists in the team recorded, on





a daily basis, the details of training, any troubles related to the training as well as the robots, and all other necessary information, such as the version of the robots. Interviews were conducted to confirm the contents of the research records if needed. The number of WPAL trials was calculated from the detailed trial data from 2007 to 2020 in the development research records. However, the WPAL trials included a few exceptional cases where the trial did not contain gait training with the WPAL; instead, the trial was used for fine-tuning the WPAL motion and three-dimensional gait analysis with the WPAL and/or the orthosis only. If the name of the patient was not recorded, we included only the total number of WPAL trials. The number of WPAL trials for each patient was calculated for those whose names were listed in the detailed trial data. The number of WPAL trials to reach a functional ambulation category (FAC) score of 4 was also counted from the development research records. The reasons for the discontinuation of the WPAL trials were also collected from the development research records. Motor function was assessed using the AIS score. The evaluation was performed by a rehabilitation physician and the physical therapist in charge, and the score was agreed upon by both parties. Gait performance using the WPAL was measured in terms of the maximum continuous walking distance and time. However, the maximum run time of the WPAL is 120 min owing to the battery capacity. The Kolmogorov-Smirnov test was used to evaluate the pattern of data distribution. Since the normality of the data was not confirmed, the FAC score and maximal continuous walking distance and time were compared between the orthosis and WPAL using the Wilcoxon signed-rank test. The FAC score was used for all patients with both orthotic and WPAL records, and the maximum continuous walking distance and time were used for patients who reached an FAC score of 4 only. Adverse events, such as falls, were recorded by a certified physiotherapist who supervised the patient while walking with the WPAL. The patients were divided into four groups according to the level of injury: cervical (C5–C8), upper thoracic (T1–T6), lower thoracic (T7–T12), and lumbar. If the SCI level of the patient was different between the left and right sides, the higher level was defined as the injury level. The practice was performed for 1 or 1.5 h per day, i.e., preparatory exercises. All statistical analyses were performed with SPSS version 25 (SPSS




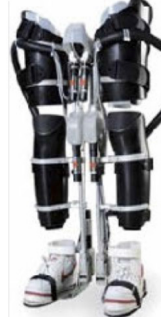




Inc., Chicago, IL, USA). Any values of  $p < 0.05$  were considered statistically significant.

## RESULTS

### Development History of WPAL

The WPAL, developed in collaboration with Aska Corporation and Tomei Brace Co. in 2005, is a walking-assist robot for people with SCI, based on the design concept of a knee–ankle–foot orthosis with a single medial hip joint (Primewalk) (Suzuki et al., 2005) (Table 1 and Figure 2). From the Primewalk, which was the basis of the WPAL, to the commercialized current model, seven major updates were implemented to improve the design and control system. The first version was a Primewalk with a total of five motors attached one to the hip joint, two to both knee joints, and two to both ankle joints. Six months later, a hip joint motor was mounted on both sides for a total of six motors in the second version. In 2007, the motors were newly developed with the support of the New Energy and Industrial Technology Development Organization in the third version. In 2008, the thigh and lower leg cuffs were made smaller and lighter. The orthotic parts were improved so that the thigh and lower leg cuffs were independent in the fourth version. When patients with SCI used the WPAL to walk, the orthotic parts were first attached to the thigh and lower leg cuffs; then, they were connected to the robotic part by themselves. This connecting procedure between the cuff and robotic part was the same as that in the current system. The shape of the footplate was also improved. In 2010, in the fifth version, the motor was improved by attaching a cover. In 2011, we developed a universal cuff and improved the positioning of the robot and the cuff fixation part in the sixth version. In 2016, the seventh and current WPAL model began commercialization for medical and social service organizations. The touchscreen tablet PC for control and settings was placed in front of the walker. Until August 2007, we used the direct current (DC) brush motors manufactured by Maxon of Switzerland. Then, we developed a new brushless servo motor that had two advantages for our robot. First, the motor allows long-term use because of better heat dissipation and lower friction. Second, it can be installed between both the lower limbs. Consequently, we introduced minor updates (mainly improvement in heat

**TABLE 1** | Development history of the Wearable Power-Assist Locomotor (WPAL).

Version	0	1	2	3
Date	4/1998	11/2005	3/2006	8/2007
Feature	Primewalk	<ul style="list-style-type: none"> <li>• Base on primewalk</li> <li>• Five commercially motors (1 hip, 2 knee, 2 ankle)</li> </ul>	<ul style="list-style-type: none"> <li>• Base on primewalk</li> <li>• Six commercially motors (2 hip, 2 knee, 2 ankle)</li> </ul>	<ul style="list-style-type: none"> <li>• Development of specialized motors</li> <li>• Improvement of orthotics parts</li> </ul>
Picture				
Version	4	5	6	7
Time	1/2008	7/2010	12/2011	10/2016
Feature	<ul style="list-style-type: none"> <li>• Miniaturization of femoral and lower leg cuff</li> <li>• Change in the don/doff method</li> <li>• Improvement of foot shape</li> </ul>	<ul style="list-style-type: none"> <li>• Development of motor cover and control box</li> <li>• Improvement of servo motor</li> <li>• New servo amplifier</li> </ul>	<ul style="list-style-type: none"> <li>• Development of universal cuff</li> <li>• cuff mounting bracket adjustment mechanism</li> <li>• Adjustable leg length</li> </ul>	<ul style="list-style-type: none"> <li>• New design</li> <li>• Improved casting module</li> <li>• Improved motor</li> <li>• New display unit</li> <li>• Adoption of tablet</li> </ul>
Picture				

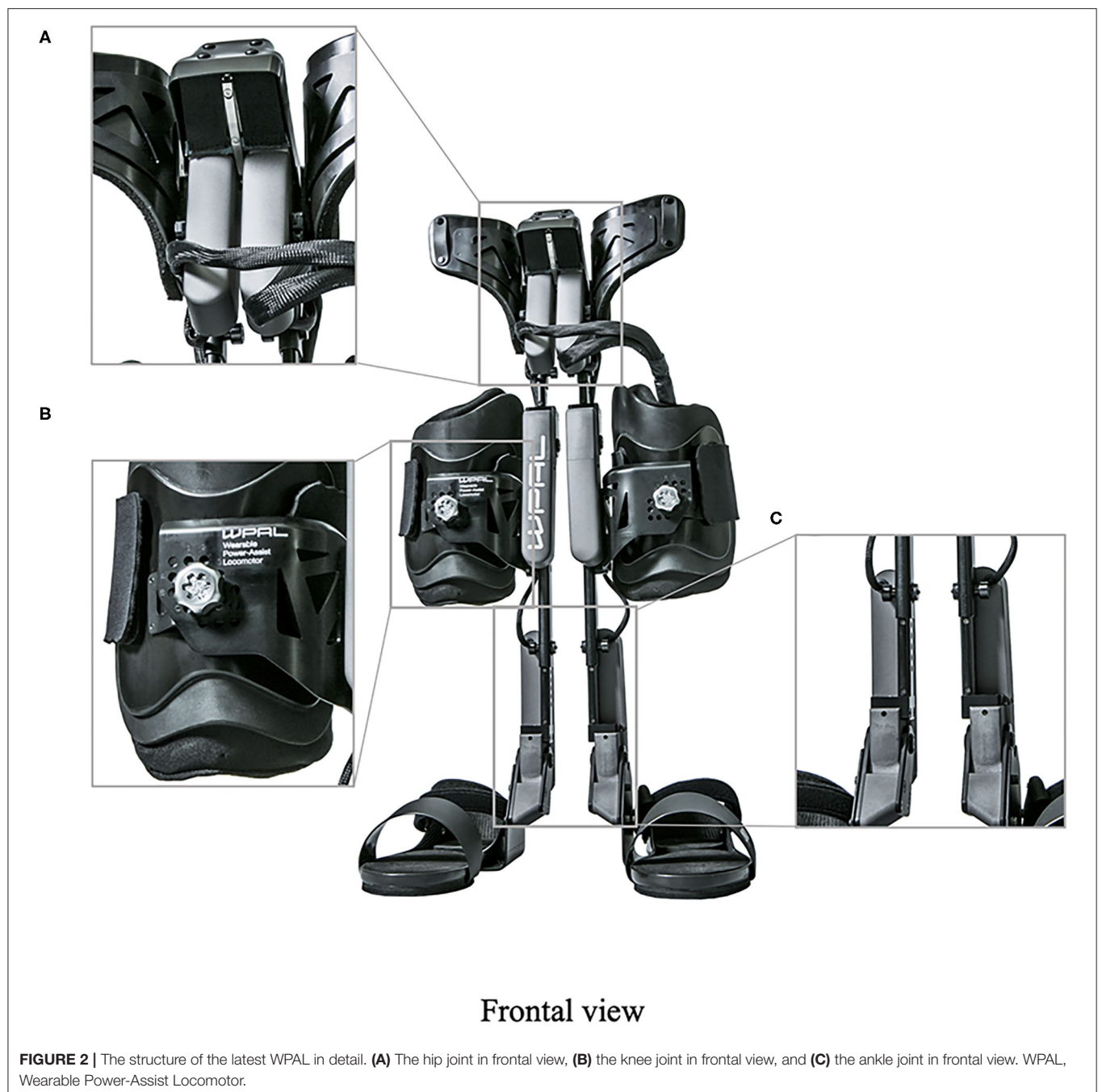
resistance) in the motor. The currently used dedicated motor can never be damaged by heat.

## Number of WPAL Trials

The SCI level was cervical (C5–C8) in 10 patients, upper thoracic (T3–T6) in 5 patients, lower thoracic (T7–T12) in 15 patients, and lumbar (L1) in one patient. The proportions of patients with AIS scores of A, B, C, and D were 20, 7, 4, and 0, respectively (**Table 2**). The total number of WPAL trials was 1,785, of which 1,009 used the latest WPAL version, and the names of the patients were not recorded in the 88 development research records. Three falls due to mechanical errors in the battery control system and the servo motor system associated with lower limb spasticity in patients with SCI were observed. No severe incidents, such as bone

fractures and skin injuries, that require unusual treatment were observed.

The mean number of WPAL trials for each patient was 55 (range 2–252) from 2007 to 2020. For the latest WPAL version, the mean number of WPAL trials for each patient was 51 (range 1–181). The person with the highest number of WPAL trials had an injury at T12 (AIS, A) and had the longest continuous walking distance and time. The most frequent reasons for discontinuation of WPAL gait training were social reasons unrelated to WPAL trials (10 patients), such as job-hunting and being busy with work, and discontinuation due to medical problems (5 patients). Twenty patients reached an FAC score of 4. The mean number of WPAL trials to reach an FAC score of 4 was 9 (median 8, range 2–22) in all patients and 13 (median 13, range 8–17) in the cervical group, 12 (median 12, range 8–16) in the upper thoracic group, 8 (median 8, range 2–22) in the lower thoracic group, and 6 in



the lumbar group. However, 2 patients were excluded from these analyses due to missing data. The mean number of days taken to achieve an FAC score of 4 under the WPAL usage condition was 143 days (median 126, 16–555). Patients who reached an FAC score of 4 continued the WPAL trials. The mean number of continued WPAL trials was 66 (median 39, range 6–247). The number of continued WPAL trials varied among the patients due to factors unrelated to the WPAL trials, such as work. The mean duration following achievement of an FAC score of 4 was 1,221 days (median 763, 65–4,058) in December 2020.

## Gait Performance

**Table 3** and **Figure 3** show the results of the gait performance in terms of the FAC scores and continuous walking distance and time when using the WPAL and the orthosis. Thirteen patients had improved FAC scores using the WPAL compared with those using the orthosis, whereas two patients had a decreased FAC score using the WPAL compared with those using the orthosis. In all patients using the WPAL, the continuous walking distance and time ranged from 5.0 to 2375.0 m (median 80 m) and from 0.5 to 120.0 min (median 10 min), respectively. Contrarily, when using

**TABLE 2 |** Patient characteristic and number of WPAL trials.

Level of injury (R/L)	Age	Sex	AIS	First year of trial	Number of WPAL trials	Frequency of WPAL trials per month	Current state	Reason for discontinuation
<b>Cervical</b>								
C5/C5	44	Male	A	2018	3	3.0	End	Pain of upper limb
C5/C6	36	Male	B	2018	23	1.0	Ongoing	–
C6/C6	72	Male	B	2012	20	0.2	Ongoing	–
C6/C6	30	Female	B	2018	79	3.0	Ongoing	–
C6/T10	33	Male	A	2015	144	2.4	Ongoing	–
C7/C7	28	Male	A	2016	72	1.5	Ongoing	–
C7/C7	51	Male	B	2017	18	3.0	Ongoing	–
C7/C7	44	Male	C	2019	5	5.0	End	Social reasons
T1/C7	60	Male	B	2017	27	0.9	Ongoing	–
T1/C8	23	Male	B	2015	10	2.0	End	Hypertension
<b>Upper thoracic</b>								
T3/T3	36	Male	A	2019	13	3.3	Ongoing	–
T4/T4	63	Male	A	2013	9	0.4	End	Social reasons
T6/T6	60	Male	A	2007	39	1.6	End	Orthostatic hypotension
T6/T6	61	Female	A	2008	99	1.4	End	Social reasons
T6/T6	43	Male	A	2008	50	1.7	End	Cellulitis
<b>Lower thoracic</b>								
T7/T7	32	Male	A	2016	118	2.0	Ongoing	–
T7/T7	84	Male	C	2018	18	6.0	Ongoing	–
T8/T8	36	Male	A	2015	50	0.4	Ongoing	–
T8/T8	53	Male	A	2011	15	5.0	End	Social reasons
T9/T9	49	Male	A	2008	43	1.4	End	Pressure sore
T10/T10	20	Female	B	2012	4	0.5	End	Social reasons
T10/T10	22	Male	A	2014	14	1.6	End	Social reasons
T10/T10	64	Male	A	2015	208	3.9	Ongoing	–
T11/T11	54	Male	A	2012	29	4.8	End	Social reasons
T11/T11	51	Male	C	2012	7	1.4	End	Social reasons
T12/T12	42	Male	A	2007	179	1.3	Ongoing	–
T12/T12	33	Male	A	2008	25	0.8	End	Social reasons
T12/T12	40	Male	A	2014	10	0.7	End	Social reasons
T12/T12	26	Male	A	2014	38	0.9	Ongoing	–
T12/T12	40	Male	A	2015	252	3.9	Ongoing	–
<b>Lumbar</b>								
L1/L1	35	Female	C	2019	48	2.5	Ongoing	–

WPAL, Wearable Power-Assist Locomotor.

the orthosis, the continuous walking distance and time ranged from 3.5 to 879.0 m (median 40 m) and from 1.9 to 61.0 min (median 6 min), respectively. For the 20 patients who achieved an FAC score of 4 using the WPAL, the continuous walking distance and time ranged from 20 to 2,375 m (median 99 m) and from 3 to 120 min (median 10 min), respectively. For using orthosis in the patients who achieved an FAC score of 4 using the WPAL, the continuous walking distance and time ranged from 9 to 879 m (median 40 m) and from 2 to 61 min (median 6 min), respectively. The FAC scores in the 26 patients in whom measurements were made for both the orthosis and WPAL, and the maximal continuous walking distance in eight patients who achieved an FAC score of 4 using both devices was significantly

higher for the WPAL than for the orthosis ( $p = 0.005$  and  $0.012$ , respectively). However, the difference in the maximal continuous walking time in the eight patients who achieved an FAC score of 4 was not statistically significant between the WPAL and the orthosis ( $p = 0.091$ ).

## DISCUSSION

In this retrospective study that includes updated results from previous reports, all data were extracted from development research records from 2007 to 2020. The present findings confirm that the WPAL improves walking ability in patients with a wide range of SCIs compared with the orthosis, such as cervical SCI.



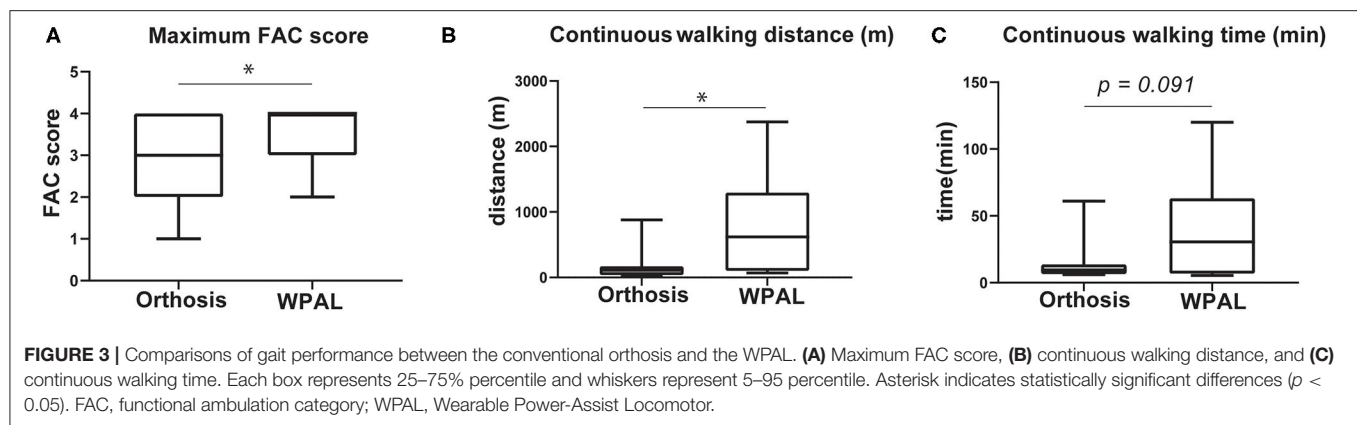
**TABLE 3 |** Gait performance.

Level of injury (R/L)	Maximum FAC score		Number of WPAL trials to reach a FAC score of 4	Consecutive walking distance (m)		Consecutive walking time (min)	
	Orthosis	WPAL		Orthosis	WPAL	Orthosis	WPAL
Cervical							
C5/C5	1	2		–	–	–	–
C5/C6	4	3		–	20.3	–	11.1
C6/C6	1	2		–	–	–	–
C6/C6	3	3		3.5	50.4	2.7	18.2
C6/T10	3	4	Missing data	10.2	69.9	6.1	5.5
C7/C7	4	4	8	36.5	69.3	14.2	6.4
C7/C7	1	2		–	–	–	–
C7/C7	–	–		–	–	–	–
T1/C7	3	4	17	9.2	49.0	1.9	5.8
T1/C8	–	–		–	–	–	–
Upper thoracic							
T3/T3	–	4	13	–	154.1	–	14.5
T4/T4	2	3		–	5.0	–	0.5
T6/T6	2	4	16	20.0	30.0	5.0	4.5
T6/T6	2	4	10	40.0	80.0	5.0	9.5
T6/T6	4	4	8	40.0	80.0	8.0	8.0
Lower thoracic							
T7/T7	4	4	8	21.9	163.8	7.5	5.5
T7/T7	1	2		–	–	–	–
T8/T8	–	4	9	–	76.2	–	5.9
T8/T8	2	4	9	20.0	20.0	3.0	3.0
T9/T9	3	4	12	57.0	99.0	6.0	12.0
T10/T10	2	2		–	–	–	–
T10/T10	4	4	2	110.0	185.0	6.0	10.0
T10/T10	4	4	5	131.0	1052.0	12.0	51.0
T11/T11	3	4	7	40.0	76.0	5.0	9.5
T11/T11	4	4	Missing data	–	–	–	–
T12/T12	4	4	22	107.0	1095.0	6.0	64.0
T12/T12	3	4	8	44.0	220.0	6.0	18.0
T12/T12	4	3		–	–	–	–
T12/T12	4	4	5	186.0	1362.3	11.0	60.5
T12/T12	4	4	5	879.0	2375.0	61.0	120.0
Lumbar							
L1/L1	–	4	6	–	123.9	–	7.3

For the first time, we summarized the development history of the WPAL in this study. During this study period, the WPAL was updated seven times. The main updates were related to the safety and appearance of the device for the purpose of improved usability. Contrarily, the medial-type hip joint system without the trunk orthosis has not changed. Additionally, the location and number of motors have not changed since 2006. We believe that the development history would be helpful for devising a new gait-assisted robot (e.g., development order and required period of development). To the best of our knowledge, there is one report about the differences in the updates of the robots. Guanzirolì et al. compared two different gait patterns using the Rewalk™ (ReWalk Robotics Ltd., Yokneam, Israel) between first- and second-generation

software control; the latter had better synchronization between the hip and knee kinematics based on healthy kinematics and kinetics profiles for improvement of the quality of the gait pattern (Guanzirolì et al., 2019). They reported an extension of the 6-min walking test and an improvement in the 10-m walking test.

The mean number of WPAL trials to reach an FAC score of 4 using a rolling walker was 9 in all patients and 13 in the cervical group, 12 in the upper thoracic group, 8 in the lower thoracic group, and 6 in the lumbar group. Some studies have reported the number of WRE trials required to walk with a walking aid and physical assistance (Esquenazi et al., 2012; Hartigan et al., 2015; Kozłowski et al., 2015; Guanzirolì et al., 2019; Tsai et al., 2021) (**Table 4**). Esquenazi et al. reported that



**TABLE 4 |** Summary results of previous studies and the present study.

References	Patients	Level of injury	Device	The degree of gait independence with the device	Number of gait training using the devices
Esquenazi et al. (2012)	12 (motor-complete)	T3–T12	ReWalk™	Independent	24 (max)
Guanziroli et al. (2019)	13 (motor-complete)	T4–L4	ReWalk™	Independent	22 (mean)
Tsai et al. (2021)	8 (motor-complete)	T1–T11	ReWalk™	Independent	30 (median)
Kozłowski et al. (2015)	7 (4 motor-complete) (3 motor-incomplete)	C4–T10	Exso	Minimal assistance (6 patients)	8 (median)
				Contact guard and close supervision (5 patients)	15 (median)
Hartigan et al. (2015)	3 (motor-complete)	C5–7	Indego	Minimal/ moderate (3 patients)	5
	5 (4 motor-complete) (1 motor-incomplete)	T1–8		Supervision (2 patients)	
	8 (7 motor-complete) (1 motor-incomplete)	T9–L1		Minimal assistance (3 patients)	
				Supervision (6 patients)	
				Minimal assistance (2 patients)	
Present study	31 (motor-complete)	C5–L1	WPAL	Independent (20 patients)	9 (mean)*

\*The mean number of WPAL trials to reach an FAC score of 4 using a rolling walker. WPAL, Wearable Power-Assist Locomotor; FAC, functional ambulation category.

all the 12 patients with a motor-complete SCI (T3–T12 injury level) were able to walk independently without physical assistance using the ReWalk™ system (ReWalk Robotics Ltd., Yokneam, Israel) for at least 50–100 m continuously, for a period of at least 5–10 min continuously, after up to 24 trials (Esquenazi et al., 2012). Guanziroli et al. reported that 13 patients with a motor-complete SCI (T4–L4 injury level) required a mean of 22 trials to achieve independent walking using ReWalk™ with crutches (Guanziroli et al., 2019). Tsai et al. reported that eight patients with motor-complete SCIs (T1–T11 injury level) required a median of 30 (range 7–90) trials to achieve independent walking using ReWalk™ with crutches within a median of 111 days (range 87–210 days) (Tsai et al., 2021). Kozłowski et al. reported that 6 of 7 patients with motor-complete

(4) or incomplete (3) SCIs (C4–T10 injury level) achieved walking using the Exso system (Exso Bionics, Richmond, CA, USA) with a front-wheeled walker or Lofstrand crutches and minimal assistance in a median of 8 trials, and 5 of them achieved walking with contact guard and close supervision assistance in a median of 15 trials (Kozłowski et al., 2015). Hartigan et al. reported three patients with motor-complete tetraplegia (C5–C7 injury level) who were able to walk after 5 WRE trials using a bilateral platform rolling walker with the minimal or moderate assistance of one therapist (Hartigan et al., 2015). In addition, six of the eight patients with motor-complete SCIs (T9–L1 injury level) were able to walk with supervised assistance using forearm crutches or a rolling walker (Hartigan et al., 2015). Regarding the level of injury, the WPAL was able to achieve

walking independence with a rolling walker within a relatively small number of trials.

The maximum continuous walking time and distance using the WPAL were 120 min and 2,375 m, respectively. The maximum run time of WPAL is 120 min owing to the battery capacity. This result suggests that the WPAL has sufficient walking performance for it to be utilized at home and in the community. van Dijksseldonk et al. (2020) investigated the number of WREs used in home and community environments in 14 patients with SCIs at an injury level of T4 to L1 (van Dijksseldonk et al., 2020). This previous study reported that the estimated median active time is 46 (range 19–84) min, during which the median estimated total distance covered is 243 (range 22–1,367) m, and the median estimated maximal distance covered without rest is 120 (range 12–1,125) m (van Dijksseldonk et al., 2020).

In the present study, 10 patients with cervical SCIs practiced the WPAL gait. All patients with cervical SCIs who reached an FAC score of 4 in the WPAL gait had longer continuous walking distances; however, two patients had shorter continuous walking time compared with those using an orthosis. The results of the longer walking distance with shorter walking time for WPAL than for orthosis suggests that WPAL walking requires a more quick and constant lateral weight shift than orthotic walking. A previous study reported that a patient is required to make a quick and constantly lateral weight shift with WPAL motion during the WPAL gait. This rhythmic lateral weight shift is produced by the lateral force using the upper limbs (Tanabe et al., 2017). Even with other WREs, independent rhythmic lateral weight shifts during walking are difficult for patients with cervical SCIs. Many previous studies reported that other WREs require assistance for walking in patients with cervical SCIs (Hartigan et al., 2015; Kozłowski et al., 2015; Benson et al., 2016; Birch et al., 2017). A previous study reported that two patients with cervical SCIs (a motor-complete C8 and a motor-incomplete C4) were able to walk over 100 m using an Ekso powered exoskeleton with supervision or minimal assistance (Kozłowski et al., 2015). Benson et al. (2016) reported that one patient with motor-incomplete C7 lesions, who could walk without using an exoskeleton, was able to walk up to 91 m in a 6-min walk test using the ReWalk™ (Benson et al., 2016). Hartigan et al. (2015) reported that patients with three motor-complete cervical SCIs (one C5 and two C6 lesions) were able to walk an average distance of 64 m in a 6-min walk test using an Indego exoskeleton (Parker Hannifin Corporation) and a bilateral platform rolling walker with minimal or moderate assistance from one therapist (Hartigan et al., 2015). Birch et al. (2017) reported that five patients with cervical SCIs with motor-incomplete injury (three C4 and two C6 lesions) were able to perform a timed up and go test in a mean of 302 s (95% CI  $\pm$  49.6 s) with one assistant for three patients and two assistants for two patients using the REX robotic exoskeleton (Rex Bionics) (Birch et al., 2017). In the present study, patients with C5–C6 lesions did not reach an FAC score of 4 using the WPAL, on equality with using other WREs. However, patients with C7 lesions, even with motor-complete SCIs, reached an FAC score of 4 even in patients with motor-complete because the WPAL has a high standing

stability, which is a structural characteristic similar to medial-type orthoses (Saitoh et al., 1996; Tanabe et al., 2013b; Koyama et al., 2016).

For using WPAL, the number of gait training to achieve independent gait was tended to less than other robots. In addition, WPAL tended to achieve independent gait in patients with cervical SCI compared with other robots. However, previous studies determined the number of gait training in advance during study periods and reported the degree of gait independence after completing total sessions of gait training. In future studies, it is necessary to compare the number of gait training to acquire independent walking with the gait-assisted robot among different robots in the same patients with SCI, rather than studies with a predetermined number of gait training.

In this study, the number and frequency of WPAL trials differed among patients. A previous study suggested that the time required to learn to safely walk with WREs is affected by the learning capacity, level of injury and completeness of SCI, and the user's strength and endurance levels (Kandilakis and Sasso-Lance, 2021). In the future, we need to clarify the rate of achievement of independent walking by configuring the previous number and frequency of WPAL trials. Moreover, the accumulation of clinical trials using WREs helps to elucidate the optimal number of training sessions and the frequency per week.

In this study, patients were able to continue the WPAL trial even after reaching an FAC score of 4 if they wished. In the future, the long-term effects of habitual walking using the WPAL on physical functions should be examined. Prolonged sitting in a wheelchair is associated with an increased risk of all-cause mortality (Rezende et al., 2016). Patients with SCIs commonly engage in less physical activity compared with healthy adults (Haisma et al., 2006; van den Berg-Emons et al., 2010). According to the physical activity guidelines, patients with SCIs should engage in at least 30 min of moderate- to vigorous-intensity aerobic exercise three times per week for cardiometabolic health benefits (Martin Ginis et al., 2018). Some studies reported that walking with WREs has numerous beneficial effects on pulmonary function (Xiang et al., 2021), bladder function (Chun et al., 2020), and sitting balance (Tsai et al., 2021). Habitual walking exercises using the WPAL three times a week for a long time may provide health benefits for patients with SCIs.

Long-term use in the community and its effects should be examined. Another robot is already being used in daily life situations (van Dijksseldonk et al., 2020). Further refinement of the WPAL will enable its long-term use in homes. The common prevent factor for long-term use is that a wheelchair is a very safe and comfortable mobility device for daily transportation in patients with SCI. Because the homes of wheelchair users are remodeled to make them accessible for wheelchair users, they can live without walking or standing. However, the robots have the advantage when patients with SCI perform cooking, washing, and cleaning (windows and shelves that cannot be reached on the wheelchair). Kandilakis et al. reported that the goal of robotic exoskeleton use is not to replace a wheelchair,

but to create a supplemental means of mobility, exercise, or activities of daily living (Kandilakis and Sasso-Lance, 2021). We also believe that the alternate usage between robots and wheelchairs is the goal in the near future. A beneficial point of the WPAL is that it is possible to move using a wheelchair with the WPAL attached to their lower limbs because the WPAL has motors installed between both the lower limbs and no trunk support orthosis.

Further important development points for all robots, such as the WPAL, are the stair climbing, the lateral movement in a standing position, the ease of transporting the robots and the walking aids, the lightweight of the robots, the ease of donning/doffing them, the easy maintenance, high sound/waterproofing property, and fall prevention or detection system. For these, it is necessary to improve elemental technologies, such as the motors and the materials used for the robots. Lastly, we should examine whether the WPAL can improve or recover motor function in patients with motor-incomplete injury by partial motor assistance rather than complete motor assistance.

## DATA AVAILABILITY STATEMENT

The original contributions presented in the study are included in the article/supplementary material, further inquiries can be directed to the corresponding author.

## REFERENCES

- Arazpour, M., Bani, M. A., Hutchins, S. W., and Jones, R. K. (2013). The physiological cost index of walking with mechanical and powered gait orthosis in patients with spinal cord injury. *Spinal Cord*. 51, 356–359. doi: 10.1038/sc.2012.162
- Asselin, P., Knezevic, S., Kornfeld, S., Ciriogliaro, C., Agranova-Breyter, I., Bauman, W. A., et al. (2015). Heart rate and oxygen demand of powered exoskeleton-assisted walking in persons with paraplegia. *J. Rehabil. Res. Dev.* 52, 147–158. doi: 10.1682/JRRD.2014.02.0060
- Benson, I., Hart, K., Tussler, D., and van Middendorp, J. J. (2016). Lower-limb exoskeletons for individuals with chronic spinal cord injury: findings from a feasibility study. *Clin. Rehabil.* 30, 73–84. doi: 10.1177/0269215515575166
- Birch, N., Graham, J., Priestley, T., Heywood, C., Sakel, M., Gall, A., et al. (2017). Results of the first interim analysis of the RAPPER II trial in patients with spinal cord injury: ambulation and functional exercise programs in the REX powered walking aid. *J. Neuroeng. Rehabil.* 14, 60. doi: 10.1186/s12984-017-0274-6
- Bjornshave Noe, B., Mikkelsen, E. M., Hansen, R. M., Thygesen, M., and Hagen, E. M. (2015). Incidence of traumatic spinal cord injury in Denmark, 1990–2012: a hospital-based study. *Spinal Cord*. 53, 436–440. doi: 10.1038/sc.2014.181
- Chamberlain, J. D., Deriaz, O., Hund-Georgiadis, M., Meier, S., Scheel-Sailer, A., Schubert, M., et al. (2015). Epidemiology and contemporary risk profile of traumatic spinal cord injury in Switzerland. *Inj. Epidemiol.* 2, 28. doi: 10.1186/s40621-015-0061-4
- Chun, A., Asselin, P. K., Knezevic, S., Kornfeld, S., Bauman, W. A., Korsten, M. A., et al. (2020). Changes in bowel function following exoskeletal-assisted walking in persons with spinal cord injury: an observational pilot study. *Spinal Cord*. 58, 459–466. doi: 10.1038/s41393-019-0392-z
- Dijkers, M. P. (1999). Correlates of life satisfaction among persons with spinal cord injury. *Arch. Phys. Med. Rehabil.* 80, 867–876. doi: 10.1016/S0003-9993(99)90076-X
- Esquenazi, A., Talaty, M., Packel, A., and Saulino, M. (2012). The ReWalk powered exoskeleton to restore ambulatory function to individuals with thoracic-level motor-complete spinal cord injury. *Am. J. Phys. Med. Rehabil.* 91, 911–921. doi: 10.1097/PHM.0b013e318269d9a3
- Fisahn, C., Aach, M., Jansen, O., Moisi, M., Mayadev, A., Pagarigan, K. T., et al. (2016). The effectiveness and safety of exoskeletons as assistive and rehabilitation devices in the treatment of neurologic gait disorders in patients with spinal cord injury: a systematic review. *Global Spine J.* 6, 822–841. doi: 10.1055/s-0036-1593805
- Fuse, I., Hirano, S., Saitoh, E., Otaka, Y., Tanabe, S., Katoh, M., et al. (2019). Gait reconstruction using the gait assist robot WPAL in patients with cervical spinal cord injury. *Jap. J. Compr. Rehabil. Sci.* 10, 88–95. doi: 10.11336/jjcrs.10.88
- Guanziroli, E., Cazzaniga, M., Colombo, L., Basilico, S., Legnani, G., and Molteni, F. (2019). Assistive powered exoskeleton for complete spinal cord injury: correlations between walking ability and exoskeleton control. *Eur. J. Phys. Rehabil. Med.* 55, 209–216. doi: 10.23736/S1973-9087.18.05308-X
- Haisma, J. A., van der Woude, L. H., Stam, H. J., Bergen, M. P., Sluis, T. A., and Bussmann, J. B. (2006). Physical capacity in wheelchair-dependent persons with a spinal cord injury: a critical review of the literature. *Spinal Cord*. 44, 642–652. doi: 10.1038/sj.sc.3101915
- Hartigan, C., Kandilakis, C., Dalley, S., Clausen, M., Wilson, E., Morrison, S., et al. (2015). Mobility outcomes following five training sessions with a powered exoskeleton. *Top. Spinal Cord Inj. Rehabil.* 21, 93–99. doi: 10.1310/sci2102-93
- Hirano, S., Saitoh, E., Tanabe, S., Katoh, M., Shimizu, Y., Yatsuya, K., et al. (2015). Comparison between gait-assisting robot (WPAL) and bilateral knee-ankle-foot orthoses with a medial single hip joint in gait reconstruction for patients with paraplegia. *Jap. J. Compr. Rehabil. Sci.* 6, 21–26. doi: 10.11336/jjcrs.6.21
- Kandilakis, C., and Sasso-Lance, E. (2021). Exoskeletons for personal use after spinal cord injury. *Arch. Phys. Med. Rehabil.* 102, 331–337. doi: 10.1016/j.apmr.2019.05.028

## ETHICS STATEMENT

The studies involving human participants were reviewed and approved by Institutional Review Board of Fujita Health University. The patients/participants provided their written informed consent to participate in this study.

## AUTHOR CONTRIBUTIONS

SK performed the data collection, analysis, writing original draft and review, editing, designing the research, and project administration. ST designed the research, writing—original draft, writing—review, and editing. TG and YT participated in data collection, analysis, and writing original draft. MK, ES, YO, and SH participated in data collection, writing original draft, writing review and editing, directed the research, project administration, and supervision. All authors contributed to the article and approved the submitted version.

## FUNDING

This work was supported by a grant-in-aid of Basic Technology Development for Practical Application of Human Support Robots [8068149], Practical Development of Industrial Technology [8080694] by New Energy and Industrial Technology Development Organization (NEDO), and the JSPS KAKENI, Grant Number 20K11223.



- Koyama, S., Tanabe, S., Saitoh, E., Hirano, S., Shimizu, Y., Katoh, M., et al. (2016). Characterization of unexpected postural changes during robot-assisted gait training in paraplegic patients. *Spinal Cord*. 54, 120–125. doi: 10.1038/sc.2015.138
- Kozlowski, A. J., Bryce, T. N., and Dijkers, M. P. (2015). Time and effort required by persons with spinal cord injury to learn to use a powered exoskeleton for assisted walking. *Top. Spinal Cord Inj. Rehabil.* 21, 110–121. doi: 10.1310/sci2102-110
- Kunkel, C. F., Scremin, A. M., Eisenberg, B., Garcia, J. F., Roberts, S., and Martinez, S. (1993). Effect of “standing” on spasticity, contracture, and osteoporosis in paralyzed males. *Arch. Phys. Med. Rehabil.* 74, 73–78.
- Lee, B. B., Cripps, R. A., Fitzharris, M., and Wing, P. C. (2014). The global map for traumatic spinal cord injury epidemiology: update 2011, global incidence rate. *Spinal Cord*. 52, 110–116. doi: 10.1038/sc.2012.158
- Levins, S. M., Redenbach, D. M., and Dyck, I. (2004). Individual and societal influences on participation in physical activity following spinal cord injury: a qualitative study. *Phys. Ther.* 84, 496–509. doi: 10.1093/ptj/84.6.496
- Majdan, M., Brazinova, A., and Mauritz, W. (2016). Epidemiology of traumatic spinal cord injuries in Austria 2002–2012. *Eur. Spine J.* 25, 62–73. doi: 10.1007/s00586-015-3985-z
- Martin Ginis, K. A., van der Scheer, J. W., Latimer-Cheung, A. E., Barrow, A., Bourne, C., Carruthers, P., et al. (2018). Evidence-based scientific exercise guidelines for adults with spinal cord injury: an update and a new guideline. *Spinal Cord*. 56, 308–321. doi: 10.1038/s41393-017-0017-3
- Miller, L. E., Zimmermann, A. K., and Herbert, W. G. (2016). Clinical effectiveness and safety of powered exoskeleton-assisted walking in patients with spinal cord injury: systematic review with meta-analysis. *Med. Devices* 9, 455–466. doi: 10.2147/MDER.S103102
- Miyakoshi, N., Suda, K., Kudo, D., Sakai, H., Nakagawa, Y., Mikami, Y., et al. (2020). A nationwide survey on the incidence and characteristics of traumatic spinal cord injury in Japan in 2018. *Spinal Cord*. 59, 626–634. doi: 10.1038/s41393-020-00533-0
- NSCIS Center (2021). *Facts and Figures at a Glance*. Birmingham, AL: University of Alabama at Birmingham.
- Palermo, A. E., Maher, J. L., Baunsgaard, C. B., and Nash, M. S. (2017). Clinician-focused overview of bionic exoskeleton use after spinal cord injury. *Top. Spinal Cord Inj. Rehabil.* 23, 234–244. doi: 10.1310/sci2303-234
- Rezende, L. F. M., Sa, T. H., Mielke, G. I., Viscondi, J. Y. K., Rey-Lopez, J. P., and Garcia, L. M. T. (2016). All-cause mortality attributable to sitting time: analysis of 54 countries worldwide. *Am. J. Prev. Med.* 51, 253–263. doi: 10.1016/j.amepre.2016.01.022
- Saitoh, E., Suzuki, T., Sonoda, S., Fujitani, J., Tomita, Y., and Chino, N. (1996). Clinical experience with a new hip-knee-ankle-foot orthotic system using a medial single hip joint for paraplegic standing and walking. *Am. J. Phys. Med. Rehabil.* 75, 198–203. doi: 10.1097/00002060-199605000-00010
- Suzuki, T., Sonoda, S., Saitoh, E., Murata, M., Uno, A., Shimizu, Y., et al. (2005). Development of a novel type of shoe to improve the efficiency of knee-ankle-foot orthoses with a medial single hip joint (Primewalk orthoses): a novel type of shoe for Primewalk orthosis. *Prosthet. Orthot. Int.* 29, 303–311. doi: 10.1080/03093640500465195
- Tan, K., Koyama, S., Sakurai, H., Teranishi, T., Kanada, Y., and Tanabe, S. (2021). Wearable robotic exoskeleton for gait reconstruction in patients with spinal cord injury: a literature review. *J. Orthop. Translat.* 28, 55–64. doi: 10.1016/j.jot.2021.01.001
- Tanabe, S., Hirano, S., and Saitoh, E. (2013a). Wearable Power-Assist Locomotor (WPAL) for supporting upright walking in persons with paraplegia. *NeuroRehabilitation*. 33, 99–106. doi: 10.3233/NRE-130932
- Tanabe, S., Koyama, S., Saitoh, E., Hirano, S., Yatsuya, K., Tsunoda, T., et al. (2017). Clinical feasibility of gait training with a robotic exoskeleton (WPAL) in an individual with both incomplete cervical and complete thoracic spinal cord injury: a case study. *NeuroRehabilitation*. 41, 85–95. doi: 10.3233/NRE-171460
- Tanabe, S., Saitoh, E., Hirano, S., Katoh, M., Takemitsu, T., Uno, A., et al. (2013b). Design of the Wearable Power-Assist Locomotor (WPAL) for paraplegic gait reconstruction. *Disabil. Rehabil. Assist. Technol.* 8, 84–91. doi: 10.3109/17483107.2012.688238
- Tsai, C. Y., Asselin, P. K., Hong, E., Knezevic, S., Kornfeld, S. D., Harel, N. Y., et al. (2021). Exoskeletal-assisted walking may improve seated balance in persons with chronic spinal cord injury: a pilot study. *Spinal Cord Ser. Cases* 7, 20. doi: 10.1038/s41394-021-00384-8
- van den Berg-Emons, R. J., Bussmann, J. B., and Stam, H. J. (2010). Accelerometry-based activity spectrum in persons with chronic physical conditions. *Arch. Phys. Med. Rehabil.* 91, 1856–1861. doi: 10.1016/j.apmr.2010.08.018
- van Dijksseldonk, R. B., van Nes, I. J. W., Geurts, A. C. H., and Keijsers, N. L. W. (2020). Exoskeleton home and community use in people with complete spinal cord injury. *Sci. Rep.* 10, 15600. doi: 10.1038/s41598-020-72397-6
- Varacallo, M., Davis, D. D., and Pizzuttillo, P. (2021). *Osteoporosis in Spinal Cord Injuries, [Updated 2021 June 3] in StatPearls*. Treasure Island, FL: StatPearls Publishing. Available online at: <https://www.ncbi.nlm.nih.gov/books/NBK526109/>
- Verschuere, J. H., Post, M. W., de Groot, S., van der Woude, L. H., van Asbeck, F. W., and Rol, M. (2011). Occurrence and predictors of pressure ulcers during primary in-patient spinal cord injury rehabilitation. *Spinal Cord*. 49, 106–112. doi: 10.1038/sc.2010.66
- Xiang, X. N., Zong, H. Y., Ou, Y., Yu, X., Cheng, H., Du, C. P., et al. (2021). Exoskeleton-assisted walking improves pulmonary function and walking parameters among individuals with spinal cord injury: a randomized controlled pilot study. *J. Neuroeng. Rehabil.* 18, 86. doi: 10.1186/s12984-021-00880-w
- Yatsuya, K., Hirano, S., Saitoh, E., Tanabe, S., Tanaka, H., Eguchi, M., et al. (2018). Comparison of energy efficiency between Wearable Power-Assist Locomotor (WPAL) and two types of knee-ankle-foot orthoses with a medial single hip joint (MSH-KAFO). *J. Spinal Cord Med.* 41, 48–54. doi: 10.1080/10790268.2016.1226701

**Conflict of Interest:** The authors declare that the research was conducted in the absence of any commercial or financial relationships that could be construed as a potential conflict of interest.

**Publisher's Note:** All claims expressed in this article are solely those of the authors and do not necessarily represent those of their affiliated organizations, or those of the publisher, the editors and the reviewers. Any product that may be evaluated in this article, or claim that may be made by its manufacturer, is not guaranteed or endorsed by the publisher.

Copyright © 2022 Koyama, Tanabe, Gotoh, Taguchi, Katoh, Saitoh, Otaka and Hirano. This is an open-access article distributed under the terms of the Creative Commons Attribution License (CC BY). The use, distribution or reproduction in other forums is permitted, provided the original author(s) and the copyright owner(s) are credited and that the original publication in this journal is cited, in accordance with accepted academic practice. No use, distribution or reproduction is permitted which does not comply with these terms.



# Performance of Impedance Control-Based Strategies in Power-Assisted Wheelchairs: A Predictive Simulation Study

Vinicius Ishimoto Cuerva, Marko Ackermann\* and Fabrizio Leonardi

Department of Mechanical Engineering, Centro Universitário FEI, São Bernardo do Campo, Brazil

## OPEN ACCESS

### Edited by:

Josep M. Font-Llagunes,  
Universitat Politècnica de Catalunya,  
Spain

### Reviewed by:

Marta Russo,  
Policlinico Tor Vergata, Italy  
Miriam Febrer-Nafria,  
Universitat Politècnica de Catalunya,  
Spain

### \*Correspondence:

Marko Ackermann  
mackermann@fei.edu.br

**Received:** 31 October 2021

**Accepted:** 31 January 2022

**Published:** 04 March 2022

### Citation:

Cuerva VI, Ackermann M and  
Leonardi F (2022) Performance of  
Impedance Control-Based Strategies  
in Power-Assisted Wheelchairs: A  
Predictive Simulation Study.  
*Front. Neurobot.* 16:805835.  
doi: 10.3389/fnbot.2022.805835

Manual wheelchair propulsion is known to be inefficient and causes upper extremity pain, fatigue, and injury. Power-assisted wheelchairs can mitigate these effects through motors that reduce users' effort and load during propulsion. Among the different control strategies proposed to govern the user-wheelchair interaction, impedance control-based ones appear to be the most natural and effective. It can change the apparent dynamical properties of the wheelchair, particularly mass and friction, and automatically compensate for external disturbances such as terrain conditions. This study investigates the advantages and disadvantages of this control strategy employing predictive simulations of locomotion with power-assisted wheelchairs in different scenarios. The simulations are generated using a biomechanically realistic model of the upper extremities and their interaction with the power-assisted wheelchair by solving an optimal control problem. Investigated scenarios include steady-state locomotion vs. a transient maneuver starting from rest, movement on a ramp vs. a level surface, and different choices of reference model parameters. The results reveal that the investigated impedance control-based strategy can effectively reproduce the reference model and reduce the user's effort, with a more significant effect of inertia in the transient maneuver and of friction in steady-state locomotion. However, the simulations also show that imposing a first-order, linear reference model with constant parameters can produce disadvantageous locomotion patterns, particularly in the recovery phase, leading to unnecessary energy dissipation and consequent increase in energy consumption from the batteries. These observations indicate there is room for improvement, for instance, by exploring energy regeneration in the recovery phase or by switching reference model nature or parameters along the cycle. To the best of our knowledge, this is the first investigation of impedance control-based strategies for power-assisted wheelchairs using predictive simulations and a realistic, nonlinear model of the user-wheelchair system.

**Keywords:** power-assisted wheelchairs, impedance control, optimal control, predictive simulations, assistive technology

## 1. INTRODUCTION

Wheelchair locomotion is common among people with physical disabilities and can help them have a more independent living. However, locomotion with manual, pushrim-propelled wheelchairs is known to have low efficiency and to impose significant and repetitive loads on the upper extremity, often leading to muscle fatigue, pain and injuries (van der Woude et al., 2001).

In order to mitigate these effects, wheelchairs with partial motor assistance are drawing increasing interest, and studies compare the performance of commercially available models in different circumstances (Karmarkar et al., 2008). This type of wheelchair is often referred to as PAPA (Pushrim-Activated Power Assisted Wheelchairs). It has electric motors that assist the person in manually propelling the wheelchair, thus enabling the user to exercise while avoiding excessive muscle effort and upper extremity loads and, consequently, reducing the risk of muscle fatigue and joint injuries (Kloosterman et al., 2012). This type of assistance is important in conditions where large torques are required, such as on ramps or rough terrain (Kloosterman et al., 2012). It can also be helpful on descents where the assistance torque can act as a brake to ensure safer locomotion (Seki et al., 2009).

There are different types of assistance strategies for a PAPA. The simplest are those based on feedforward control laws where the motor torque is directly related to the torque applied by the user on the pushrim. The most elementary version of this type of assistance applies constant torque whenever the pushrim is actuated by the user.

A frequently used feedforward strategy is the generation of an assistance torque proportional to the torque applied by the user (Guillon et al., 2015), but this torque amplification strategy may compromise handling of the wheelchair due to possible differences in the magnitudes of forces applied by the person's right and left arms on the pushrim (Heo et al., 2018). In order to provide an effective shared control system, Cooper et al. (2002) propose a proportional feedforward control during the propulsion phase, a linear decay of assistance over time in the recovery phase, and a regenerative braking in case the maximum speed threshold is achieved.

The literature reports a series of other control strategies for PAPAs that range from reducing the effects of the environment on the dynamics of wheelchairs to the assistance in particular conditions and applications. Lee et al. (2016), for instance, attempt to correct for the effects of gravity on ramps by introducing inclination sensors and requiring additional information such as user's mass. Oonishi et al. (2010), in turn, proposes the combined use of an electromyography-based estimator of user intention and a disturbance torque estimator to define the assistance torque. Assistance strategies are also proposed for special maneuvers such as steps climbing (Seki et al., 2006) and wheelie (Santos et al., 2016).

Among the various control strategies proposed for power-assisted wheelchairs, a promising one is the impedance control as it provides a natural interaction with the user by manipulation of the apparent system properties, such as apparent mass

and friction. In fact, impedance control is a well-established technique to control the relationship between the movement kinematics and the force between robots and humans (Hogan, 1985) and is widely used in situations where the environment influences the controlled dynamic system, such as in exoskeletons (Li et al., 2017). Its application to power-assisted wheelchairs is investigated in different studies (Oh and Hori, 2014; Shieh et al., 2015; Lee et al., 2016).

The implementation of the impedance control strategy often requires the adoption of a reference model for the wheelchair system, which is almost invariably assumed as a linear first-order model composed of a lumped mass and a viscous damping. It is, indeed, a common practice to investigate and design assistance strategies for power-assisted wheelchairs on the basis of such simple mass-damper models (Chénier et al., 2014; Oh and Hori, 2014; Shieh et al., 2015; Lee et al., 2016; Heo et al., 2018). Such first-order models, however, neglect the dynamics associated with the cyclic motion of the arms and the biomechanics of the upper extremity, which may lead to substantial inaccuracies in representing the wheelchair-user system dynamics (Chénier et al., 2014).

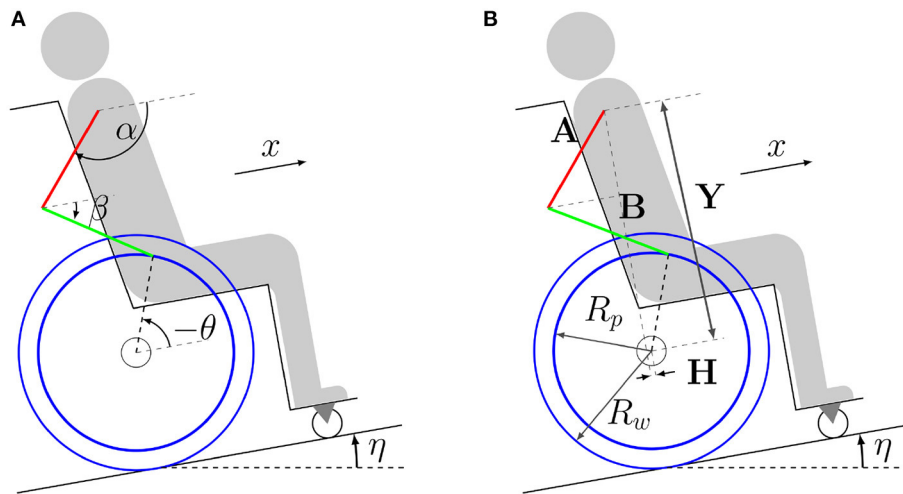
Assessing the performance of impedance control-based strategies in different locomotion conditions, investigating the potentially deleterious effects of using a simple mass-damper model as a reference model, is an important step toward its effective implementation in real power-assisted wheelchairs. Considering this, the main objective of this study is to evaluate, through predictive simulations of wheelchair locomotion at different typical conditions, the performance of assistance based on impedance control and the effects of considering in the control law a first-order dynamics (mass/damper) as the reference model. The proposed simulation framework is based on a musculoskeletal model of the upper extremities and its interaction with the power-assisted wheelchair, and the solution of an optimal control problem. The effects of alterations in the reference model parameters are predicted for steady-state and transient locomotion on a level surface and on a ramp.

## 2. MATERIALS AND METHODS

The approach adopted here is similar to that in Ackermann et al. (2014). A biomechanical model of the upper extremity and its interaction with the wheelchair is used to represent the two phases of the wheelchair locomotion cycle. An impedance control strategy is implemented whose objective is that the system dynamics seen by the user matches a reference, linear, lumped-mass model subject to viscous damping. Different mass and damping combinations are tested to investigate the effects on system performance in terms of muscle and motor effort. Simulations are generated by solving an optimal control problem to predict the performance in four locomotion conditions representing different activities of daily living, steady-state and transient locomotion on level surfaces and ramps.

### 2.1. Wheelchair-User Model

A moving four-bar mechanism is adopted to model the wheelchair-user system (Ackermann et al., 2014). Bilateral



**FIGURE 1 |** Model of the wheelchair-user system composed of four rigid bodies representing arms (red), forearms (green), rear wheels (blue) and the remaining body and wheelchair elements (gray/black). Coordinates are represented in figure (A), where  $\alpha$  is the upper arm angle with respect to the direction of motion,  $\beta$  is the forearm angle with respect to the direction of motion,  $\theta$  is the rear wheel angular displacement,  $x$  is the forward displacement of the shoulder/wheelchair and  $\eta$  is the ramp inclination angle. Lengths are represented in figure (B), where  $Y$  is the relative vertical and  $H$  is the relative horizontal distance between the center of the rear wheels and the shoulder,  $A$  is the upper arm length,  $B$  is the forearm length,  $R_p$  is the pushrim radius, and  $R_w$  is the rear wheel radius.

symmetry is assumed, which is usual in daily wheelchair locomotion, (Goosey-Tolfrey and Kirk, 2003; Soltau et al., 2015). The user model represents an average individual, whose total mass (70.0 kg) and height (1.70 m) are consistent with Brazilian male averages and with ranges reported in Gil-Agudo et al. (2010). The model is formed by four rigid bodies representing arms, forearms, rear wheels, and a fourth rigid body encompassing the remaining segments of the body and elements of the wheelchair, as illustrated in Figure 1.

The shoulder and elbow joints and the wheel axle are considered ideal hinge joints. In the recovery phase, in which the hand is not in contact with the pushrim and undergo repositioning in preparation for the next propulsion phase, the model has three degrees of freedom, and the generalized coordinate vector is

$$q = \begin{bmatrix} \alpha \\ \beta \\ \theta \end{bmatrix}, \quad (1)$$

where  $\alpha$  and  $\beta$  are the angles between forearms and arms concerning the direction of motion, respectively, and  $\theta$  is the angular displacement of the wheelchair's rear wheels, as shown in Figure 1. In the propulsion phase, the contact between the hands and the pushrims is represented by a hinge joint that transforms the mechanical system into a moving four-bar mechanism with a single degree of freedom.

Applying the D'Alembert's principle in a code implemented in MATLAB, we derived the equations of motion in their minimal form for the recovery phase as

$$M(q)\ddot{q} + k(q, \dot{q}) = k_e(q), \quad (2)$$

**TABLE 1 |** Adopted model parameters.

Dimensions	
User's height	1.70 m
Upper arm length ( $A$ )	0.3162 m
Upper arm center of mass location	0.1379 m
Forearm length ( $B$ )	0.3400 m
Forearm center of mass location	0.1693 m
Pushrim radius ( $R_p$ )	0.2570 m
Rear wheel radius ( $R_w$ )	0.2988 m
Rear-wheel/shoulder distance ( $H$ )	0.05 m
Rear-wheel/shoulder distance ( $Y$ )	0.75 m
Inertia properties	
User's mass	70.0 kg
Upper arms mass	3.9200 kg
Upper arms moment of inertia	0.0406 kg m <sup>2</sup>
Forearms mass	3.0800 kg
Forearms moment of inertia	0.0416 kg m <sup>2</sup>
Rear wheels moment of inertia	0.1274 kg m <sup>2</sup>
Combined mass (Wheelchair+user)	72.5200 kg

where  $M$  is the mass matrix,  $k$  is the vector of generalized Coriolis and centrifugal forces and  $k_e$  is the generalized force vector.

Length and inertia parameters are determined for a person 1.70 m in height with a total body mass of 70 kg, based on anthropometric data in Winter (2009), see Table 1. As the simulations do not involve turning, the only resistive force considered was the rolling resistance (Sauret et al., 2012), adopted as 20 N, corresponding to an approximate value reported in van der Woude et al. (2001) for locomotion on a vinyl pavement.

In the propulsion phase, in which a hinge joint is formed between the hands and the pushrims, the generalized coordinates



$\alpha$ ,  $\beta$  and  $\theta$  are linked through the holonomic constraints

$$c(\alpha, \beta, \theta) = \begin{bmatrix} A \cos \alpha + B \cos \beta - R_p \cos \theta - H \\ A \sin \alpha + B \sin \beta - R_p \sin \theta - Y \end{bmatrix} = 0, \quad (3)$$

where  $H$  and  $Y$  are the horizontal and vertical distances between the shoulder and the center of the wheelchair's rear wheels, respectively,  $A$  is the upper arm length,  $B$  is the forearm length and  $R_p$  is the pushrim radius, whose values are adopted as indicated in **Table 1**.

Considering the constraints in Equation (3), the equations of motion in the minimal form for the propulsion phase are obtained from Equation (2) as

$$J^T M J \ddot{\theta} + J^T M \frac{dJ}{dt} \dot{\theta} + J^T k = J^T k_e, \quad (4)$$

where  $J$  is the Jacobian defined as

$$J(\alpha, \beta, \theta) = \frac{\partial q}{\partial \theta}. \quad (5)$$

Using ideal joint torque generators can lead to unrealistic joint torque patterns, such as torque discontinuities between phases, unrealistic torque magnitudes, and torque peaks when the elbow is close to full extension, due to the large mechanical gain in this configuration. For these reasons, it is important to take the physiological, intrinsic musculoskeletal properties into account. Muscle force-length and force-velocity relationships and passive joint torques due to ligaments and connective tissue were adopted from Brown (2018), that reports data obtained for an elite wheelchair basketball athlete. According to this approach, upper extremity joint torques in both, extension and flexion, are functions of elbow and shoulder angles and angular velocities as

$$\tau_i = f_i(a_i, \alpha, \dot{\alpha}, \beta, \dot{\beta}), \quad (6)$$

where  $a_i \in [0, 1]$  represents equivalent, global muscle activations for shoulder extensors ( $i = se$ ), shoulder flexors ( $i = sf$ ), elbow extensors ( $i = ee$ ) and elbow flexors ( $i = ef$ ) that modulate the corresponding active joint torques  $\tau_i$ .

The muscle activation dynamic is modeled, as in He et al. (1991), by a linear, first-order dynamic as

$$\frac{da_i}{dt} = (u_i - a_i) \left( \frac{u_i}{T_a} + \frac{1 - u_i}{T_d} \right), \quad (7)$$

where  $u_i \in [0, 1]$  is the neural excitation corresponding to the muscle activation  $a_i$ ,  $T_a$  is the activation time constant assumed as 20 ms and  $T_d$  is the deactivation time constant assumed as 40 ms. The adopted activation and deactivation time constants are consistent with values reported in the literature, as in Brown (2018).

## 2.2. Impedance Control

The assistance strategy considered is continuous and based on the impedance control, which aims at imposing the dynamic behavior between the force applied by the user and the wheelchair

velocity, i.e., the dynamics seen by the user. The chosen reference dynamics are commonly used in the literature, corresponding to a lumped mass and a resistive damping force. This dynamics is the impedance control reference model, as

$$M_i \frac{dv_r}{dt} + C_i v_r = \frac{\tau_p}{R_w}, \quad (8)$$

where  $M_i$  is the apparent mass,  $C_i$  is the apparent damping coefficient,  $\tau_p$  is the torque applied by the user,  $R_w$  is the wheel radius and  $v_r$  is the reference speed for the control loop, with  $v_r = R_w \omega_r$ .

The nominal parameters of this reference model,  $M_i$  and  $C_i$ , are obtained based on a linear approximation of the four-bar model in **Figure 1**. The parameters that best fit the response of the nonlinear model for a startup simulation on level ground in open loop are identified using the *tfest* MATLAB transfer function estimator.

In order to indirectly impose the apparent impedance, feedback control is employed to control the speed based on the desired speed generated by the reference impedance. The control strategy adopted is illustrated by the block diagram in **Figure 2**, where  $G(s)$  is a PI controller that seeks to impose the reference angular velocity  $\omega_r$  to the output angular velocity  $\omega$ . For this purpose, the controller is designed using the pole and zero cancellation technique, resulting in a closed-loop system that has similar behavior to the first-order system in Equation (8). The time constant of this closed loop was adjusted to 0.02 s so that its dynamics would be negligible compared to the other time constants of the wheelchair-user system dynamics.

The reference angular velocity  $\omega_r$  is produced based on the torque  $\tau_p$  applied by the user to the pushrim and through the first-order reference model that describes the desired mechanical impedance in the sense that, if the speed control error is small, so the relationship between  $\omega$  and  $\tau_p$  is apparently imposed in a similar way to that of the reference impedance.

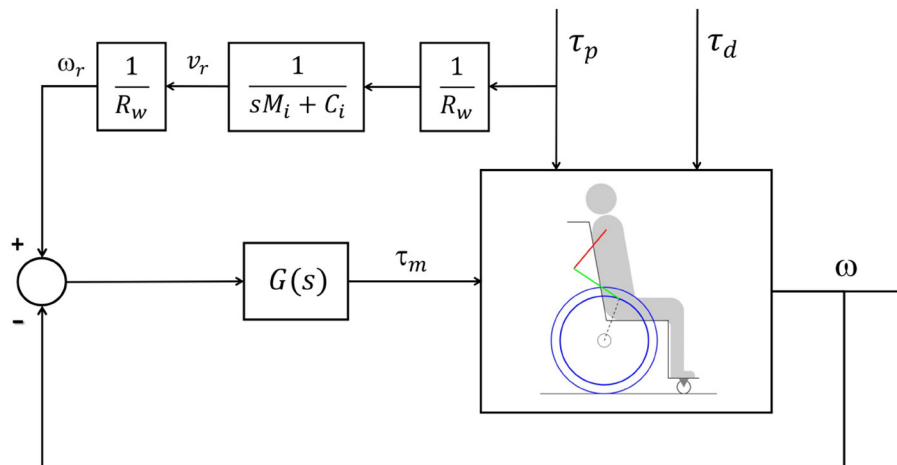
## 2.3. Predictive Simulation Approach

The predictive simulations are generated by solving an optimal control problem, a formulation commonly used in studies on human movement in activities such as walking (Ackermann and van den Bogert, 2010; Sreenivasa et al., 2017), jumping (Porsa et al., 2015), and also wheelchair locomotion (Brown and McPhee, 2020).

The predictive simulations for all conditions and scenarios consisted of searching optimal motion duration  $t_f$  and time series of the controls (equivalent neural excitations) and states (equivalent muscle activations and generalized coordinates and their time derivatives) that minimize a cost function quantifying physiological muscle effort as

$$W_p = \int_0^{t_f} (u_{ee}^2 + u_{ef}^2 + u_{se}^2 + u_{sf}^2) dt, \quad (9)$$

where the subindices *se* refers to the shoulder extensors, *sf* to the shoulder flexors, *ee* to the elbow extensors, and *ef* to the elbow flexors.



**FIGURE 2 |** Block diagram representing the impedance control loop, where the signal  $\tau_p$  is the user torque,  $\tau_d$  is the disturbance torque,  $\tau_m$  is the motor torque,  $v_r$  is the reference rear wheel velocity generated by the reference model,  $\omega_r$  is the reference rear wheel angular velocity, and  $\omega$  is the angular velocity of the wheelchair rear wheels. The transfer function  $G(s)$  represents the velocity controller. The parameter  $R_w$  is the wheel radius,  $M_i$  is the desired apparent mass and  $C_i$  is the desired apparent friction coefficient.

The performance of the control strategy in the different conditions and reference model parameter combinations was assessed in terms of user and motor effort. User effort was quantified by  $W_p$  in Equation (9), which is the cost function minimized to generate the predictive simulations of unassisted and assisted locomotion. The motor effort, in turn, is quantified by

$$W_m = \int_0^{t_f} (\tau_m^2) dt. \quad (10)$$

The constraints of the optimal control problem include the dynamics in Equation (2) for the recovery phases, in Equation (4) for the propulsion phases, and in Equation (7) for the activation dynamics. In the assisted locomotion simulations, in which the control loop in **Figure 2** is active, the corresponding closed-loop dynamics is included as well. Other constraints are: continuity of all states between adjacent propulsion and recovery phases, the imposition of an average speed of 0.9 m/s, and physiological upper and lower bounds on neural excitations ( $u_i \in [0, 1]$ ), muscle activations ( $a_i \in [0, 1]$ ) and generalized coordinates and velocities.

In the *steady state* simulations, periodicity constraints are added on initial and final states of one complete cycle to ensure a periodic motion at a prescribed average speed, with one propulsion phase and one recovery phase. There are no periodicity constraints in the *startup* simulations, the wheelchair starts from rest, with  $\omega(t=0)=0$ , and a prescribed total displacement of 1.6 m is added. The *startup* simulation is composed of five phases in the following sequence: propulsion-recovery-propulsion-recovery-propulsion.

All simulations are performed using the direct collocation method and implemented in MATLAB. The time discretization was performed using the pseudospectral Radau method (Garg et al., 2009) where the derivative of the states are obtained by deriving a Lagrange polynomial. The resulting nonlinear

optimization problem (NLP) is then solved using the IPOPT software (Wächter and Biegler, 2005), using the linear solver *ma57* (HSL, 2013). In the *startup* simulations, 100 collocation points divided in 10 polynomials of order 10 are used in the propulsion phases and 144 collocation points divided in 12 polynomials of order 12 are used in the recovery phases to reduce mesh errors. In the *steady-state* simulations, 5 polynomials of order 20 in each phase are sufficient to minimize mesh errors. The mesh is weighted using a Legendre-Gauss-Lobatto polynomial to further reduce mesh errors, especially in the interface between phases. The first and second derivatives of the constraints and cost function are obtained through an automatic differentiation class using the forward mode written in MATLAB.

## 2.4. Simulations

The transient locomotion, representing the frequent activities of daily living where the wheelchair is accelerated from rest (Koontz et al., 2009), is referred to as *startup* simulation and is characterized by the sequence of phases propulsion-recovery-propulsion-recovery-propulsion, starting from rest, covering a predefined displacement, and at a given average speed. The steady-state locomotion, in turn, is referred to as *steady state*, represents locomotion over longer distances and is generated for one complete, periodic propulsion cycle at a predefined average speed.

The simulations are planned to investigate the effects of imposing a first-order linear reference model in the impedance control strategy and to assess the influence of changing the reference model parameters,  $M_i$  and  $C_i$ , on user effort and energy consumption by the motor. The simulations are performed to cover a range of typical locomotion conditions, *steady state* vs. transient (*startup*), on a level surface vs. on a ramp.

The average speed is constrained to 0.9 m/s in both, *steady state* and *startup* simulations, while in the *startup* simulation a

total displacement of 1.6 m is added as a constraint. For the simulations on a ramp, an inclination of  $\eta = 3^\circ$  is adopted.

First, reference simulations of unassisted locomotion (motors turned off) are generated by solving the optimal control problem in Section 2.3 in all conditions: *steady state* on a level surface and on a ramp, and *startup* on a horizontal plane and on a ramp. The predictive simulations for assisted locomotion, with the impedance control loop in **Figure 2**, are generated using these reference simulations as initial guesses. When the convergence to a local minimum corresponding to clearly unrealistic patterns occurs, identified, for instance, by an unnaturally large push angle with an excessively posterior hand position on the pushrim in the beginning of the propulsion phase, the optimization is rerun with a different initial guess. This new initial guess corresponds to a predictive simulation generated for the same locomotion conditions and closest possible reference model parameters.

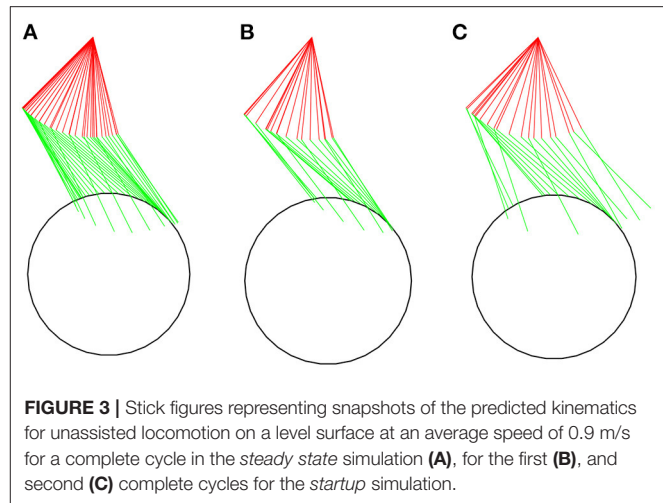
To investigate the impedance controller performance and its impacts on the wheelchair-user interaction we have applied a 50% reduction in the dynamic parameters of the reference model. This reduction represents a significant change in the parameters and therefore in the impedance, but it still keeps the user as the protagonist of the propulsion, who applies the largest part of the torque necessary to characterize the movement. We found through simulation that changes of 50% in the model parameters are sufficient to analyze its effects, while the maximum torque produced by the motor doesn't increase excessively.

In the assisted locomotion simulations, four combinations of the reference model mass and friction parameters are tested: 100%  $M_i$  and 100%  $C_i$  (nominal model,  $M_{100} - C_{100}$ ), 50%  $M_i$  and 100%  $C_i$  ( $M_{50} - C_{100}$ ), 100%  $M_i$  and 50%  $C_i$  ( $M_{100} - C_{50}$ ), and 50%  $M_i$  and 50%  $C_i$  ( $M_{50} - C_{50}$ ). The nominal simulation ( $M_{100} - C_{100}$ ) permits investigating the effects of imposing first-order linear dynamics in the impedance control loop and also to verify the disturbance rejection capability of this approach without changing overall system mass and friction properties. For instance, in locomotion on ramps, it is expected that the impedance control strategy provides the user the sensation of locomotion on a level surface. The other model parameter combinations allow for investigating the effects on locomotion performance of reducing apparent system mass and/or friction by 50%.

In summary, reference simulations are generated for locomotion without assistance, i.e., with the control loop turned off, for the four conditions, *steady state* and *startup* locomotion on a level surface and on a ramp. For each of these four locomotion conditions, four simulations of power-assisted locomotion are generated for the referred combinations of reference model parameters in the impedance control loop. Therefore, the total number of generated predictive simulations amounts to twenty.

### 3. RESULTS

The predicted patterns for the *steady state* simulation at 0.9 m/s (**Figure 3A**) show overall agreement with kinematic, kinetic



and spatiotemporal data reported in the literature. **Tables 2, 3** present a comparison of parameters of the predicted patterns with data reported in Boninger et al. (2002) and Gil-Agudo et al. (2010) for different groups. The predicted cadence of  $1.07 \text{ s}^{-1}$  is close to median values reported in Gil-Agudo et al. (2010). Predicted push time (0.395 s) and recovery time (0.545 s) are close to the reported in Gil-Agudo et al. (2010), leading to a ratio push time/recovery time of 0.73, which is lower than the reported in both papers, indicating a somewhat lower predicted duty cycle. In the case of Boninger et al. (2002), this difference can be attributed to the substantially larger reported push angles compared to the predicted push angle of  $64.8^\circ$ , which is close to the ones reported in Gil-Agudo et al. (2010). The push angle is influenced by factors such as adopted stroke patterns, wheelchair adjusting or trunk mobility, which may explain the differences in the reported push angles. The predicted maximal pushrim tangential force of 38.1 N agrees well with the mean values reported in Boninger et al. (2002). The shoulder maximal flexion (7.6 N.m) and extension moments (3.97 N.m) agree well with the ones reported in Gil-Agudo et al. (2010). For the elbow, the maximal flexion moment (3.72 N.m) shows good agreement, while the predicted maximal extension moment (2.3 N.m) is larger in magnitude than the reported in Gil-Agudo et al. (2010), although not incompatible with expected patterns considering the large overall variability of the data reported in the literature.

The predicted wheelchair speed profile for the reference simulation on a level surface for *steady state* locomotion (solid black line in **Figure 4A**) shows the expected acceleration in the propulsion phase, in which the system kinetic energy increases due to positive work exerted by the hands on the pushrim. In the recovery phase, starting at  $t = 0.395 \text{ s}$ , the center of mass of the whole user-wheelchair system decelerates under the action of the rolling resistance force. However, the wheelchair speed profile does show an acceleration in the first half of the recovery phase, a behavior caused by the dynamic effect associated with the backwards motion of the upper limbs. The same effect occurs in the two recovery phases

**TABLE 2 |** Comparison of kinematic, kinetic and spatiotemporal parameters of the *steady state* simulation at 0.9 m/s to experimental data reported in Gil-Agudo et al. (2010) for locomotion at 3 km/h  $\approx$  0.83 m/s.

	Predicted	Gil-Agudo et al. (2010) median (interquartile range)			
		G1	G2	G3	G4
Speed (m/s)	0.90	0.83	0.83	0.83	0.83
Max rim tangencial force (N)	38.1	-	-	-	-
Cadence (1/s)	1.07	0.9 (0.3)	1.1 (0.4)	1.1 (0.4)	1.2 (0.3)
Push time (s)	0.395	0.6 (0.3)	0.5 (0.1)	0.4 (0.5)	0.4 (0.1)
Recovery time (s)	0.545	0.5 (0.1)	0.5 (0.1)	0.5 (0.2)	0.5 (0.2)
Push/Recovery	0.73	1.3 (0.5)	1.1 (0.4)	0.8 (0.2)	0.8 (0.2)
Push angle (°)	64.8	62.5 (16.1)	58.6 (29.0)	64.5 (21.1)	57.5 (13.8)
Contact angle (°)	-110.1	-108.2 (18.5)	-111.3 (20.6)	-115.7 (17.5)	-110.4 (17.5)
Release angle (°)	-45.3	-51.3 (14.2)	-52.2 (16.1)	-54.0 (16.4)	-48.1 (13.4)
Max shoulder flex mom (N.m)	7.60	10.7 (4.6)	8.0 (3.2)	7.7 (4.8)	6.4 (4.6)
Max shoulder ext mom (N.m)	3.97	3.9 (4.5)	4.8 (2.3)	6.9 (2.5)	4.9 (2.6)
Max elbow flex mom (N.m)	3.72	4.6 (9.9)	4.9 (2.4)	6.0 (1.7)	4.6 (2.0)
Max elbow ext mom (N.m)	2.30	1.6 (1.3)	0.9 (1.0)	0.5 (0.9)	0.6 (0.9)

Data is reported as median (interquartile range). The fifty-one people are grouped by their level of spinal cord injury (SCI): C6 tetraplegia (G1), C7 tetraplegia (G2), high paraplegia (G3), and low paraplegia (G4). "-" represents data not reported in the paper.

**TABLE 3 |** Comparison of kinematic, kinetic and spatiotemporal parameters of the *steady state* simulation at 0.9 m/s to experimental data reported in Boninger et al. (2002) for locomotion at 0.9 m/s.

	Predicted	Boninger et al. (2002) mean (standard deviation)			
		ARC	SC	SLOP	DLOP
Speed (m/s)	0.90	0.9	0.9	0.9	0.9
Max rim tangencial force (N)	38.1	45.8 (22.1)	38.3 (20.6)	47.0 (19.4)	65.8 (26.6)
Cadence (1/s)	1.07	1.13 (0.18)	0.88 (0.08)	1.03 (0.14)	0.81 (0.13)
Push time (s)	0.395	-	-	-	-
Recovery time (s)	0.545	-	-	-	-
Push/Recovery	0.73	1.12 (0.19)	1.21 (0.31)	1.03 (0.28)	0.78 (0.18)
Push angle (°)	64.8	94.4 (24.1)	114.0 (13.7)	91.7 (13.8)	110.0 (13.0)
Contact angle (°)	-110.1	-	-	-	-
Release angle (°)	-45.3	-	-	-	-
Max shoulder flex mom (N.m)	7.60	-	-	-	-
Max shoulder ext mom (N.m)	3.97	-	-	-	-
Max elbow flex mom (N.m)	3.72	-	-	-	-
Max elbow ext mom (N.m)	2.30	-	-	-	-

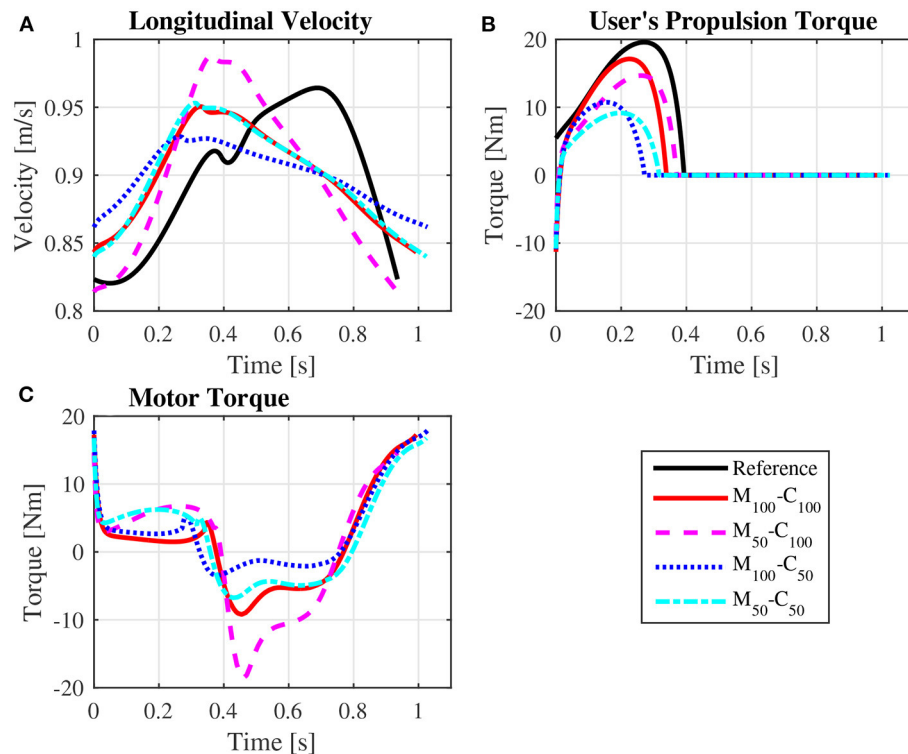
Data is reported as mean (standard deviation). The thirty-eight individuals with paraplegia are grouped according to their selected stroke pattern in the recovery phase: semicircular (SC), SLOP, DLOP, and arcing (ARC). "-" represents data not reported in the paper.

of the unassisted reference *startup* simulation for locomotion on a level surface (Figures 3B,C, and solid black line in Figure 5A).

The predicted joint torque profiles for the reference unassisted locomotion on a level surface (Figure 6 for *steady state* and Figure 7 for *startup*) show that the largest torques are applied by the shoulder in flexion during the propulsion phases, with shoulder flexion activations achieving peaks of about 0.14 in *steady state* (Figure 8A) and 0.55 in *startup* (Figure 9A). The activation profiles (Figures 8, 9) lead to similar joint torque profiles (Figures 6, 7), modulated by the intrinsic

muscle properties. Note, for instance, that the elbow extension torque peaks in Figure 6D, in the end of the propulsion phase ( $t \approx 0.35$  s) and in the beginning of the recovery phase ( $t \approx 0.55$  s), have similar magnitudes, in spite of the different corresponding elbow activation peaks shown in Figure 8D. This difference is due to the effect of the force-velocity relationship, which reduces force generation capacity of the elbow extensor muscles during the concentric contraction at larger rates close to full elbow extension in the end of the propulsion phase, leading to a larger necessary activation to generate the same torque.





**FIGURE 4 |** Predicted wheelchair speed profile (A), bilateral propulsion torque applied by the user (B), and bilateral torque applied by the motors on the rear wheels of the wheelchair (C) for steady state locomotion on a level surface at an average speed of 0.9 m/s for the reference unassisted condition (Reference), and for the assisted locomotion with 100% of reference model parameters  $M_i$  and  $C_i$  ( $M_{100} - C_{100}$ ), reduction of 50% in  $M_i$  ( $M_{50} - C_{100}$ ), reduction of 50% in  $C_i$  ( $M_{100} - C_{50}$ ), and reduction of 50% in  $M_i$  and  $C_i$  ( $M_{50} - C_{50}$ ).

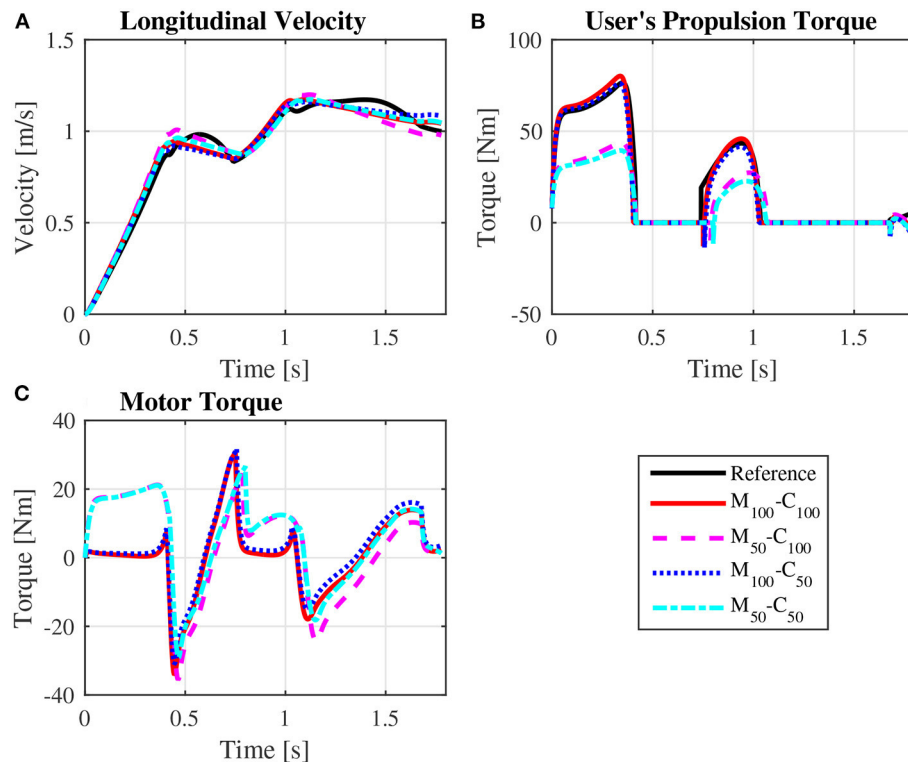
The identification of the first-order linear model used as reference in the impedance control strategy resulted in a dynamic friction parameter of  $C_i = 14.88$  N.s/m and a mass parameter of  $M_i = 92.50$  kg, which is consistent with system overall mass (wheelchair + user).

Note that the typical speed profile in the recovery phase of the unassisted reference locomotion vanishes in the assisted locomotion simulations, which are characterized mostly by a monotonic speed decrease along the recovery phase (Figures 4A, 5A). Since the reference model in the impedance control loop in Figure 2 corresponds to a block of mass  $M_i$  under the effect of a viscous damping  $C_i$ , the reference velocity  $v_r$  decreases exponentially in the recovery phase in which  $\tau_p = 0$ . In this condition, the control loop ends up suppressing the wheelchair acceleration as the upper extremity is moved backwards by applying a negative motor torque  $\tau_m$ . This behavior occurs particularly in the first half of the recovery phase, as clearly shown in Figure 4C (from  $t \approx 0.4$  s to  $t \approx 0.8$  s) and Figure 5C (from  $t \approx 0.4$  s to  $t \approx 0.6$  s and from  $t \approx 1.1$  s to  $t \approx 1.4$  s). This explains to a great extent why motor effort is far from null in the assisted, nominal simulations with 100% of  $M_i$  and 100% of  $C_i$  ( $W_m$  for condition  $M_{100} - C_{100}$  in Table 4).

The results for assisted steady state locomotion on a level surface show that reducing the apparent coefficient of friction

( $M_{100} - C_{50}$  and  $M_{50} - C_{50}$ ) is effective in decreasing user's wheel torque (Figure 4B) as well as shoulder and elbow torques (Figure 6) and the corresponding activations (Figure 8). This explains the reduction in user's effort ( $W_p$ ) shown in Table 4 for these conditions. For example, the maximum shoulder flexion torque changes from approximately 15 N.m to 12 N.m in the  $M_{50} - C_{50}$  condition and to 9 N.m in the  $M_{100} - C_{50}$  condition (Figure 6A). A reduction in apparent mass alone, on the contrary, has a relatively small effect on the user's propulsion torque profile ( $M_{50} - C_{100}$  in Figure 4B). In fact, the  $M_{50} - C_{100}$  condition leads to increases in both user and motor effort (Table 4), reflecting larger shoulder flexion torque and activation compared to the reference unassisted simulation (Figures 6A, 8A), even in the presence of larger motor torque magnitudes (Figure 4C). This shows that an isolated decrease in apparent system mass in the investigated impedance control strategy is detrimental to performance in steady state locomotion on a level surface.

The scenario is different for the assisted startup locomotion on a level surface. The reduction in apparent viscous friction alone ( $M_{100} - C_{50}$ ) has little influence on user propulsion torque profile (Figure 5B), joint torques (Figure 7) and activations (Figure 9) compared to the unassisted condition, leading to similar user's effort  $W_p$  in Table 4.



**FIGURE 5 |** Predicted wheelchair speed profile (A), bilateral propulsion torque applied by the user (B), and bilateral torque applied by the motors on the rear wheels of the wheelchair (C) along the sequence of phases propulsion-recovery-propulsion-recovery-propulsion in the startup locomotion on a level surface at an average speed of 0.9 m/s for the reference unassisted condition (Reference), and for the assisted locomotion with 100% of reference model parameters  $M_i$  and  $C_i$  ( $M_{100} - C_{100}$ ), reduction of 50% in  $M_i$  ( $M_{50} - C_{100}$ ), reduction of 50% in  $C_i$  ( $M_{100} - C_{50}$ ), and reduction of 50% in  $M_i$  and  $C_i$  ( $M_{50} - C_{50}$ ).

The reduction in apparent mass, instead, cuts user propulsion torque by half ( $M_{50} - C_{100}$  and  $M_{50} - C_{50}$  in Figure 5B), substantially decreasing shoulder flexion and elbow extension torques (Figures 7A,D) and the corresponding activations (Figures 9A,D) in the propulsion phases. This is achieved through the assistance provided by a larger motor torque in the propulsion phases (Figure 5C, from  $t = 0$  to  $t \approx 0.4$  s and from  $t \approx 0.8$  s to  $t \approx 1.05$  s).

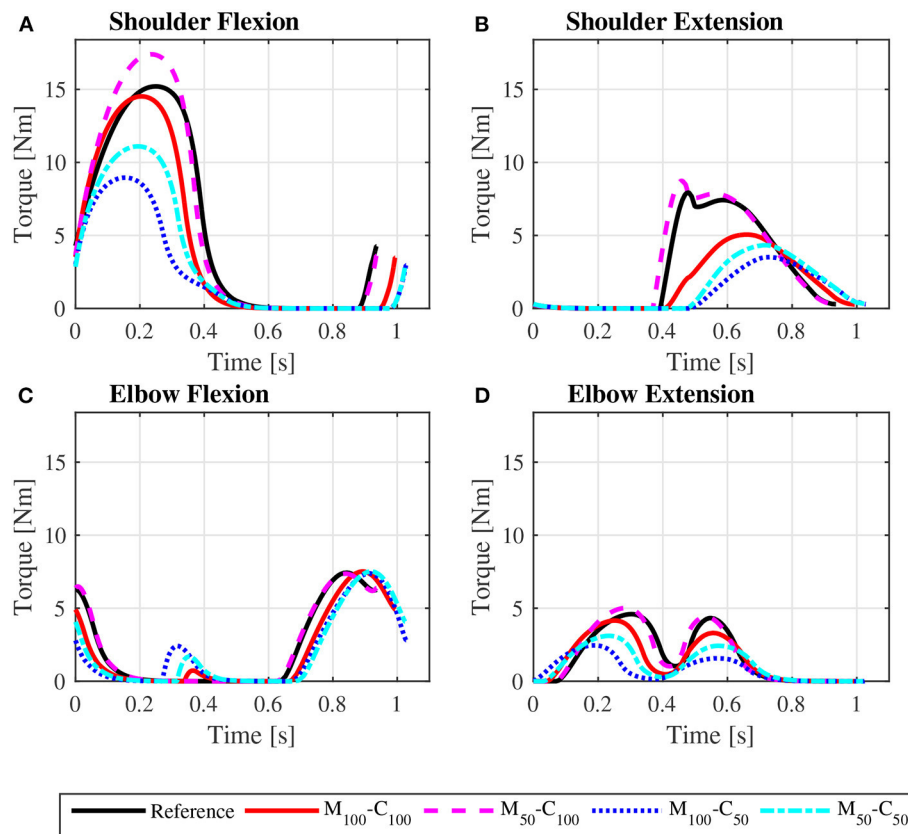
The user propulsion torque profiles for the four reference model parameter combinations in assisted *steady state* locomotion on a 3° ramp, depicted in Figure 10A, are much lower than those for the reference simulation and similar to those predicted for locomotion on a level surface, Figure 4B. The same occurs for the assisted *startup* locomotion, as shown in Figure 11A, compared to results for the reference *startup* locomotion on a level surface in Figure 5B. The predicted muscle activation profiles for shoulder and elbow extensors and flexors for the assisted locomotion on the ramp (Supplementary Figure S4 for *steady state*, Supplementary Figure S7 for *startup*) are similar to those predicted for locomotion on a level surface (Figure 8 for *steady state*, Figure 9 for *startup*). Note that user effort values  $W_p$  reported in Table 4 for the assisted locomotion on a ramp for both, *steady state* and *startup*, are much lower than

those for the unassisted reference simulations of locomotion on the ramp. This compensation of gravity in the assisted locomotion on ramps is ensured by an offset of motor torque profiles in *steady state*, Figure 10B compared to Figure 4C, and in *startup*, Figure 11B compared to Figure 5C. This motor action is associated to a substantial motor effort  $W_m$  (Table 4) and consequent large energy consumption from the batteries.

## 4. DISCUSSION

The predicted patterns for the reference *steady state* locomotion at 0.9 m/s shows overall agreement with data reported in the literature (Boninger et al., 2002; Gil-Agudo et al., 2010), with the isolated observed differences compatible with the typical variability in reported wheelchair propulsion patterns in the literature. This indicates that the employed model and optimal control approach are able to generate realistic wheelchair locomotion patterns.

The results for the assisted locomotion indicate that the studied impedance control strategy can effectively impose the reference dynamics, despite the nonlinear dynamic nature of the wheelchair-user system. This provides a natural way of



**FIGURE 6 |** Predicted bilateral shoulder flexion (A), shoulder extension (B), elbow flexion (C), and elbow extension (D) torque profiles along a complete cycle for steady state locomotion on a level surface at an average speed of 0.9 m/s for the reference unassisted condition (Reference), and for the assisted locomotion with 100% of reference model parameters  $M_i$  and  $C_i$  ( $M_{100} - C_{100}$ ), reduction of 50% in  $M_i$  ( $M_{50} - C_{100}$ ), reduction of 50% in  $C_i$  ( $M_{100} - C_{50}$ ), and reduction of 50% in  $M_i$  and  $C_i$  ( $M_{50} - C_{50}$ ).

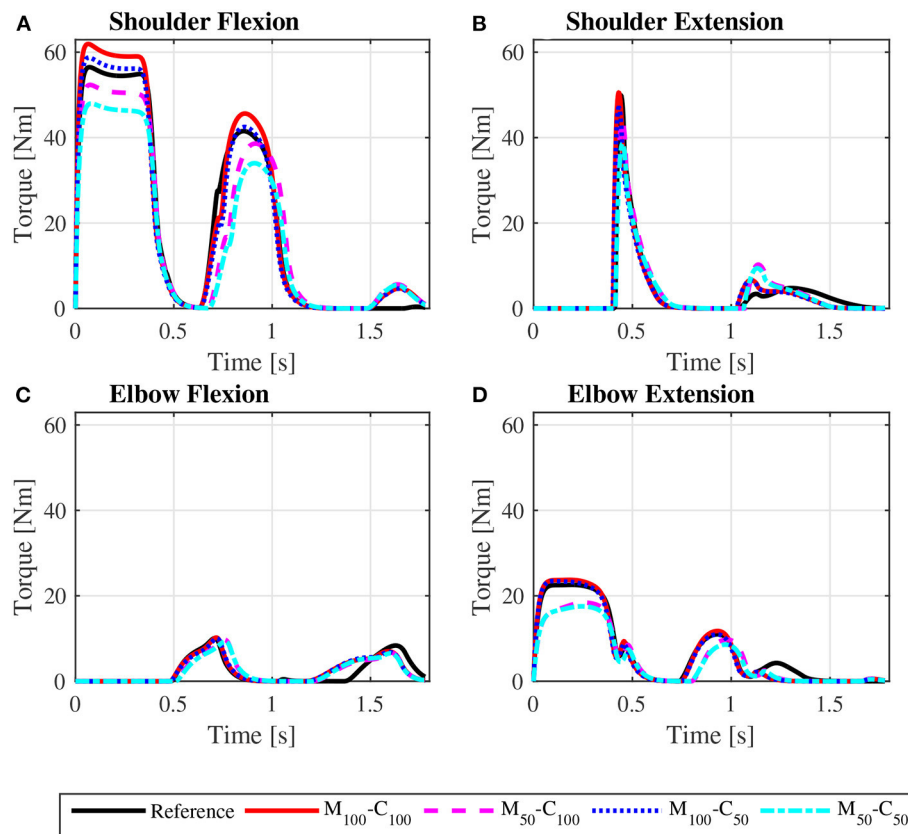
adjusting assistance intensity by manipulation of mass and damping parameters in the reference model and leads to automatic compensation of external disturbances such as the effect of gravity on slopes or changes in rolling resistance force in different pavements or rough terrain. These constitute highly desirable characteristics of the impedance control strategy. In fact, the predicted profiles for locomotion on a 3° ramp show that the impedance control strategy effectively rejects the disturbance due to the weight component in the direction of motion, so that the required user joint torques, muscle activation profiles and muscle effort are similar to those observed during locomotion on a level surface. This effectively gives to the user the impression of propelling the wheelchair on a level surface during upwards locomotion on a ramp.

Despite the benefits of the investigated control strategy, the simulations also reveal that imposing a first-order reference model in the impedance control loop might cause undesired side effects. The commonly used reference model seems adequate for a situation in which a caregiver pulls the wheelchair-user system. However, when the user self-propels the wheelchair, the dynamics of the movement becomes markedly nonlinear,

mainly in the recovery phase when the motion of the arms changes the system dynamics in a way not captured by the first-order impedance control reference model that has the tangential force on the pushrim and the wheelchair wheel angular speed as the only inputs. The result is that the impedance control treats these system nonlinearities as disturbances and tries to reject them. This rejection leads to unnecessary energy dissipation and battery power consumption to produce unnatural movement.

This waste of energy is evident in the predicted nominal simulations with 100% of  $M_i$  and 100% of  $C_i$ . One would expect this parameter configuration would lead to low control effort, as the reference model approximates the dynamics of the original user-wheelchair system. In spite of that, **Table 4** reports large motor effort for the condition  $M_{100} - C_{100}$  during locomotion on a level surface. This effect is associated to a great extent with large motor breaking torques in the first half of the recovery phase to suppress the forward acceleration of the wheelchair as arms are accelerated backwards (**Figures 4C, 5C**).

Different strategies can mitigate these undesired effects. One possibility is to turn off assistance in the recovery



**FIGURE 7 |** Predicted bilateral shoulder flexion (A), shoulder extension (B), elbow flexion (C), and elbow extension (D) torque profiles along the sequence of phases propulsion-recovery-propulsion-recovery-propulsion in the startup locomotion on a level surface at an average speed of 0.9 m/s for the reference unassisted condition (Reference), and for the assisted locomotion with 100% of reference model parameters  $M_i$  and  $C_i$  ( $M_{100} - C_{100}$ ), reduction of 50% in  $M_i$  ( $M_{50} - C_{100}$ ), reduction of 50% in  $C_i$  ( $M_{100} - C_{50}$ ), and reduction of 50% in  $M_i$  and  $C_i$  ( $M_{50} - C_{50}$ ).

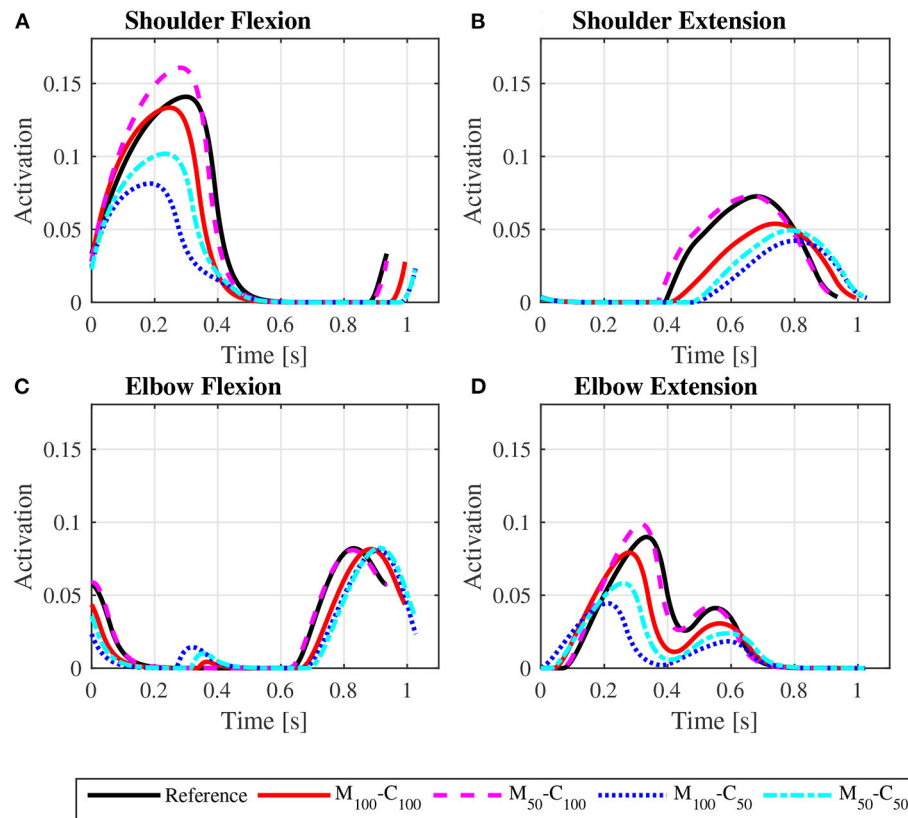
phase or impose different dynamics for each phase. Another possible strategy is to formulate an impedance control with a proportional-derivative control law based solely on the measurement of the wheelchair velocity. This strategy dispenses the measurement of pushrim tangential forces, but, since it does not impose a reference dynamics, it does not compensate for external disturbances such as slopes. A third possible strategy is to use a reference model that can also capture the nonlinear dynamics associated with the swinging of the arms.

The opposing effects of mass and viscous damping parameters on *steady state* vs. *startup* locomotion can be attributed to their different nature. The *startup* locomotion represents transient maneuvers, where inertial forces are more important due to larger accelerations. In *steady state* locomotion, instead, accelerations are lower and average speed is greater, leading to the predominant effect of viscous damping over mass. In daily wheelchair use, which encompasses transient as well as steady-state locomotion, an isolated reduction in  $C_i$  could lead to overall improvement in terms of user effort, but only a concomitant reduction in both apparent parameters, friction and mass, can lead to a substantial user

effort decrease in all investigated conditions, as indicated in **Table 4**. Thus, the reduction in both parameters seems to be the most indicated choice when adjusting assistance intensity level.

The employed model in this study allowed for a realistic investigation of wheelchair propulsion, while ensuring continuity and computational efficiency, important features for solving optimal control problems. The model appropriately represents the two phases of the locomotion cycle, the primary dynamic effects related to the motion of the upper limbs, and the intrinsic muscle properties. Nevertheless, a set of limitations must be mentioned. Adopting a muscle model formulated on the joint level should be sufficient to characterize muscle system capacity in assessing overall system performance, but it does not consider individual muscles, which may be important in studies concerned with joint loads and muscle coordination. Assuming the shoulder joint fixed to the wheelchair dispenses the use of complex and computationally costly trunk models but neglects the possible forward projection of the trunk during propulsion, better representing populations with a lower trunk mobility. A 2D model represents appropriately the upper limb dynamics and its interaction with the power-assisted





**FIGURE 8 |** Predicted shoulder flexion (A), shoulder extension (B), elbow flexion (C) and elbow extension (D) activation profiles along a complete cycle for steady state locomotion on a level surface at an average speed of 0.9 m/s for the reference unassisted condition (Reference), and for the assisted locomotion with 100% of reference model parameters  $M_i$  and  $C_i$  ( $M_{100} - C_{100}$ ), reduction of 50% in  $M_i$  ( $M_{50} - C_{100}$ ), reduction of 50% in  $C_i$  ( $M_{100} - C_{50}$ ), and reduction of 50% in  $M_i$  and  $C_i$  ( $M_{50} - C_{50}$ ).

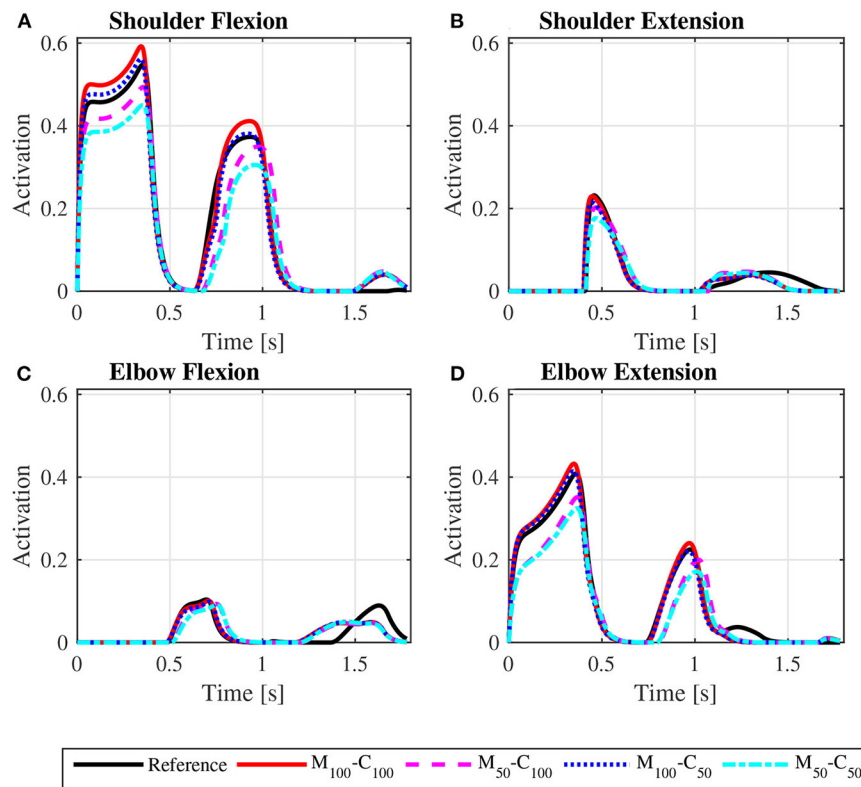
wheelchair as they occur predominantly in the sagittal plane, but do not represent, for instance, the relevant shoulder abduction in the beginning of the propulsion phase. Finally, the adoption of force-length and force-velocity relationships from data obtained by Brown (2018) for an elite wheelchair basketball athlete leads to a model with larger force capacity than the average wheelchair user population, but this should have limited impact on overall predicted patterns as the simulations are submaximal, except for the reference *startup* simulation on a ramp at the relatively large average speed of 0.9 m/s, that reaches a peak shoulder flexion activation of nearly 0.9. These limitations will be addressed in future studies as trunk and upper extremity models become more available and computationally tractable.

## 5. CONCLUSION

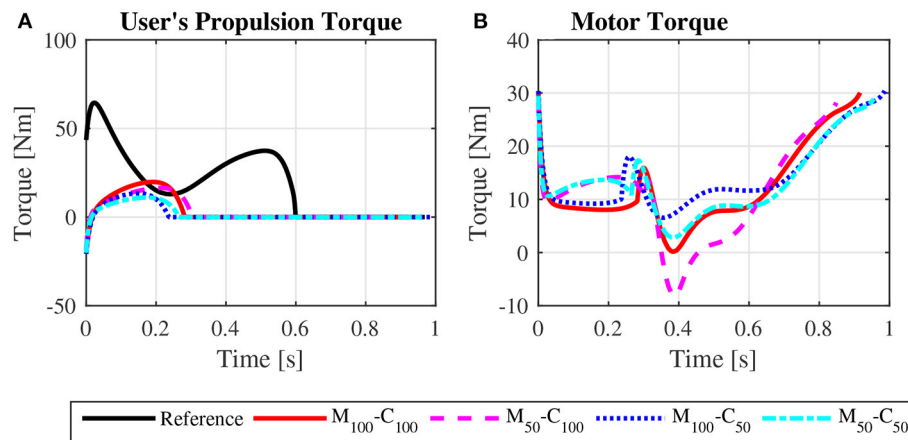
This work investigates the benefits and drawbacks of implementing an impedance control strategy in assisted wheelchair locomotion, adopting a first-order linear mass-damper model as reference dynamics, a recurrent choice in the literature. A realistic physiological model

of the user's musculoskeletal system and its interaction with the power-assisted wheelchair was developed and used in predictive simulations of steady-state locomotion and of starting up from rest, representing common transient maneuvers in activities of daily living. The model allowed for taking the dynamic effects of arm motion, the intrinsic muscle properties, and the varying system dynamics in the propulsion and recovery phases into account.

The results confirm the advantages of the studied impedance control strategy, including automatic compensation of gravity forces in inclined terrains and the possibility of naturally adjusting assistance by manipulation of physical parameters such as mass and damping. An important finding, however, is that assuming a mass-damper model as reference in the impedance control loop leads to unnecessary braking in the recovery phase, since the natural forward motion of the wheelchair as the arms retreat is suppressed by the control loop as a disturbance, leading to waste of energy and performance degradation. Proposed solutions to this behavior include turning off motor assistance in the recovery phase, switching reference models depending on the locomotion phase,



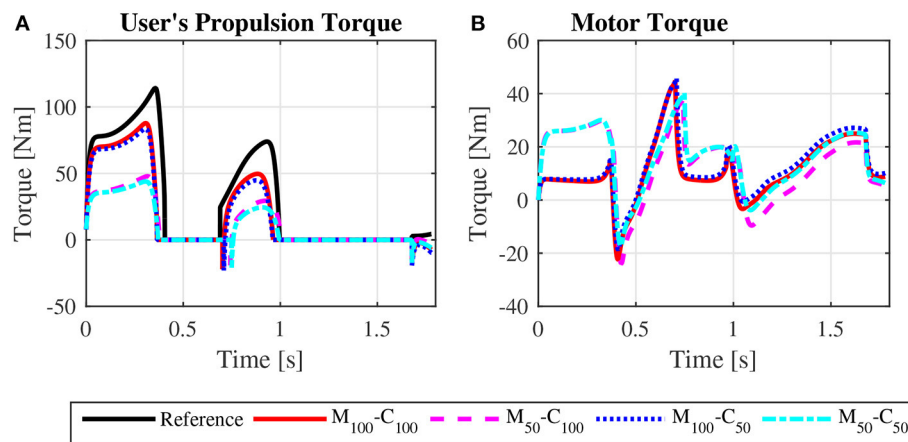
**FIGURE 9** | Predicted shoulder flexion (A), shoulder extension (B), elbow flexion (C), and elbow extension (D) activation profiles along the sequence of phases propulsion-recovery-propulsion-recovery-propulsion in the *startup* locomotion on a level surface at an average speed of 0.9 m/s for the reference unassisted condition (Reference), and for the assisted locomotion with 100% of reference model parameters  $M_i$  and  $C_i$  ( $M_{100} - C_{100}$ ), reduction of 50% in  $M_i$  ( $M_{50} - C_{100}$ ), reduction of 50% in  $C_i$  ( $M_{100} - C_{50}$ ), and reduction of 50% in  $M_i$  and  $C_i$  ( $M_{50} - C_{50}$ ).



**FIGURE 10** | Bilateral propulsion torque applied by the user (A) and bilateral torque applied by the motors on the rear wheels of the wheelchair (B) for *steady state* locomotion on a 3° ramp at an average speed of 0.9 m/s for the reference unassisted condition (Reference), and for the assisted locomotion with 100% of reference model parameters  $M_i$  and  $C_i$  ( $M_{100} - C_{100}$ ), reduction of 50% in  $M_i$  ( $M_{50} - C_{100}$ ), reduction of 50% in  $C_i$  ( $M_{100} - C_{50}$ ), and reduction of 50% in  $M_i$  and  $C_i$  ( $M_{50} - C_{50}$ ).

or incorporating the upper extremity nonlinear dynamics into the impedance control reference model. These strategies will be investigated in future studies using the developed predictive simulation approach.

Regarding the effects of manipulating the reference model parameters, the results reveal that reducing apparent mass effectively decreases user effort in transient maneuvers but is detrimental to performance in steady-state locomotion, where



**FIGURE 11 |** Bilateral propulsion torque applied by the user **(A)** and bilateral torque applied by the motors on the rear wheels of the wheelchair **(B)** for *startup* locomotion on a 3° ramp at an average speed of 0.9 m/s for the reference unassisted condition (Reference), and for the assisted locomotion with 100% of reference model parameters  $M_i$  and  $C_i$  ( $M_{100} - C_{100}$ ), reduction of 50% in  $M_i$  ( $M_{50} - C_{100}$ ), reduction of 50% in  $C_i$  ( $M_{100} - C_{50}$ ), and reduction of 50% in  $M_i$  and  $C_i$  ( $M_{50} - C_{50}$ ).

**TABLE 4 |** Predicted user effort  $W_p$  (Equation 9) and motor effort  $W_m$  (Equation 10) for all simulated conditions.

Condition	$W_p$ [ $10^{-1}$ s]	$W_m$ [ $N^2m^2s$ ]
<b>Level/steady state</b>		
Reference	0.107	-
$M_{100} - C_{100}$	0.079	48.92
$M_{50} - C_{100}$	0.124	76.14
$M_{100} - C_{50}$	0.035	46.46
$M_{50} - C_{50}$	0.051	52.11
<b>Ramp/steady state</b>		
Reference	0.733	-
$M_{100} - C_{100}$	0.164	183.95
$M_{50} - C_{100}$	0.237	155.12
$M_{100} - C_{50}$	0.084	244.66
$M_{50} - C_{50}$	0.116	213.63
<b>Level/startup</b>		
Reference	2.00	-
$M_{100} - C_{100}$	2.22	206.10
$M_{50} - C_{100}$	1.57	380.02
$M_{100} - C_{50}$	1.99	202.57
$M_{50} - C_{50}$	1.30	339.92
<b>Ramp/startup</b>		
Reference	4.39	-
$M_{100} - C_{100}$	2.75	410.77
$M_{50} - C_{100}$	2.05	611.11
$M_{100} - C_{50}$	2.48	477.74
$M_{50} - C_{50}$	1.71	687.29

inertial forces are less important. On the contrary, reducing the damping parameter is advantageous in steady-state locomotion but affects only marginally the performance in transient maneuvers. A concomitant reduction in both parameters, apparent damping and mass, is able to substantially decrease user

effort in all investigated conditions, constituting, therefore, the most indicated strategy for daily wheelchair use.

We expect the reported findings as well as the proposed simulation framework will provide guidance to the development of better control strategies for power-assisted wheelchairs. Future studies will employ more complete biomechanical models of the upper limbs and incorporate braking and locomotion in curves. Experimental studies with a prototype of a power-assisted wheelchair are planned for validation and testing.

## DATA AVAILABILITY STATEMENT

The raw data supporting the conclusions of this article will be made available by the authors, without undue reservation.

## AUTHOR CONTRIBUTIONS

MA developed and implemented the model. FL developed and implemented the control system. VC designed and ran the simulations. All authors have designed the study and elaborated the manuscript.

## FUNDING

This study was partially funded by the Coordenação de Aperfeiçoamento de Pessoal de Nível Superior—Brasil (CAPES)-Finance Code 001.

## SUPPLEMENTARY MATERIAL

The Supplementary Material for this article can be found online at: <https://www.frontiersin.org/articles/10.3389/fnbot.2022.805835/full#supplementary-material>

## REFERENCES

- Ackermann, M., Leonardi, F., Costa, H., and Fleury, A. (2014). "Modeling and optimal control formulation for manual wheelchair locomotion: the influence of mass and slope on performance," in *5th IEEE RAS/EMBS International Conference on Biomedical Robotics and Biomechanics* (São Paulo: IEEE, Institute of Electrical and Electronics Engineers), 1079–1084.
- Ackermann, M., and van den Bogert, A. J. (2010). Optimality principles for model-based prediction of human gait. *J. Biomech.* 43, 1055–1060. doi: 10.1016/j.jbiomech.2009.12.012
- Boninger, M., Souza, A., Cooper, R., Fitzgerald, S., Koontz, A., and Fay, B. (2002). Propulsion patterns and pushrim biomechanics in manual wheelchair propulsion. *Arch. Phys. Med. Rehabil.* 83, 718–723. doi: 10.1053/apmr.2002.32455
- Brown, C. (2018). *Predictive forward dynamic simulation of manual wheelchair propulsion* (Master's thesis). Waterloo, ON.
- Brown, C., and McPhee, J. (2020). Predictive forward dynamic simulation of manual wheelchair propulsion on a rolling dynamometer. *J. Biomech. Eng.* 142, 071008. doi: 10.1115/1.4046298
- Chénier, F., Bigras, P., and Aissaoui, R. (2014). A new dynamic model of the wheelchair propulsion on straight and curvilinear level-ground paths. *Comput. Methods Biomech. Biomed. Engin.* 18, 1031–1043. doi: 10.1080/10255842.2013.869318
- Cooper, R., Corfman, T., Fitzgerald, S., Boninger, M., Spaeth, D., Ammer, W., et al. (2002). Performance assessment of a pushrim-activated power-assisted wheelchair control system. *IEEE Trans. Control Syst. Technol.* 10, 121–126. doi: 10.1109/87.974345
- Garg, D., Patterson, M. A., Francolin, C., Darby, C. L., Huntington, G. T., Hager, W. W., et al. (2009). Direct trajectory optimization and costate estimation of finite-horizon and infinite-horizon optimal control problems using a radau pseudospectral method. *Comput. Optim. Appl.* 49, 335–358. doi: 10.1007/s10589-009-9291-0
- Gil-Agudo, A., Del Ama-Espinosa, A., Pérez-Rizo, E., Pérez-Nombela, S., and Rodríguez-Rodríguez, L. (2010). Upper limb joint kinetics during manual wheelchair propulsion in patients with different levels of spinal cord injury. *J. Biomech.* 43, 2508–2515. doi: 10.1016/j.jbiomech.2010.05.021
- Goosey-Tolfrey, V. L., and Kirk, J. H. (2003). Effect of push frequency and strategy variations on economy and perceived exertion during wheelchair propulsion. *Eur. J. Appl. Physiol.* 90, 154–158. doi: 10.1007/s00421-003-0875-6
- Guillon, B., Van-Hecke, G., Iddir, J., Pellegrini, N., Beghoul, N., Vaugier, I., et al. (2015). Evaluation of 3 pushrim-activated power-assisted wheelchairs in patients with spinal cord injury. *Arch. Phys. Med. Rehabil.* 96, 894–904. doi: 10.1016/j.apmr.2015.01.009
- He, J., Levine, W., and Loeb, G. (1991). Feedback gains for correcting small perturbations to standing posture. *IEEE Trans. Automat. Contr.* 36, 322–332. doi: 10.1109/9.73565
- Heo, Y., pyo Hong, E., hee Chang, Y., Jeong, B., and sung Mun, M. (2018). Experimental comparison of torque balance controllers for power-assisted wheelchair driving. *Measurement* 120, 175–181. doi: 10.1016/j.measurement.2018.02.024
- Hogan, N. (1985). Impedance control: An approach to manipulation: Part II-implementation. *J. Dyn. Syst. Meas. Control.* 107, 8–16. doi: 10.1115/1.3140713
- HSL (2013). *A Collection of Fortran Codes for Large Scale Scientific Computation*. Available monline at: <http://www.hsl.rl.ac.uk> (accessed October 21, 2021).
- Karmarkar, A., Cooper, R. A., yi Liu, H., Connor, S., and Puhlman, J. (2008). Evaluation of pushrim-activated power-assisted wheelchairs using ansi/resna standards. *Arch. Phys. Med. Rehabil.* 89, 1191–1198. doi: 10.1016/j.apmr.2007.10.029
- Kloosterman, M. G., Eising, H., Schaake, L., Buurke, J., and Rietman, J. (2012). Comparison of shoulder load during power-assisted and purely hand-rim wheelchair propulsion. *Clin. Biomech.* 27, 428–435. doi: 10.1016/j.clinbiomech.2011.11.010
- Kloosterman, M. G., Snoek, G. J., van der Woude, L. H., Buurke, J. H., and Rietman, J. S. (2012). A systematic review on the pros and cons of using a pushrim-activated power-assisted wheelchair. *Clin. Rehabil.* 27, 299–313. doi: 10.1177/0269215512456387
- Koontz, A., Roche, B., Collinger, J., Cooper, R., and Boninger, M. (2009). Manual wheelchair propulsion patterns on natural surfaces during start-up propulsion. *Arch. Phys. Med. Rehabil.* 90, 1916–1923. doi: 10.1016/j.apmr.2009.05.022
- Lee, K., Lee, C., Hwang, S., Choi, J., and bong Bang, Y. (2016). Power-assisted wheelchair with gravity and friction compensation. *IEEE Trans. Ind. Electron.* 63, 2203–2211. doi: 10.1109/TIE.2016.2514357
- Li, Z., Huang, Z., He, W., and Su, C.-Y. (2017). Adaptive impedance control for an upper limb robotic exoskeleton using biological signals. *IEEE Trans. Ind. Electron.* 64, 1664–1674. doi: 10.1109/TIE.2016.2538741
- Oh, S., and Hori, Y. (2014). Disturbance attenuation control for power-assist wheelchair operation on slopes. *IEEE Tran. Control Syst. Technol.* 22, 828–837. doi: 10.1109/TCST.2013.2265396
- Oonishi, Y., Oh, S., and Hori, Y. (2010). A new control method for power-assisted wheelchair based on the surface myoelectric signal. *IEEE Trans. Ind. Electron.* 57, 3191–3196. doi: 10.1109/TIE.2010.2051931
- Porsa, S., Lin, Y.-C., and Pandey, M. G. (2015). Direct methods for predicting movement biomechanics based upon optimal control theory with implementation in OpenSim. *Ann. Biomed. Eng.* 44, 2542–2557. doi: 10.1007/s10439-015-1538-6
- Santos, E. G., Leonardi, F., and Ackermann, M. (2016). "Optimal control of the wheelchair wheelie," in *IASTED 2016-The Sixth IASTED International Conference on Modelling, Simulation and Identification* (Campinas), 218–224.
- Sauret, C., Bascou, J., de Saint Remy, N., Pillet, H., Vaslin, P., and Lavaste, F. (2012). Assessment of field rolling resistance of manual wheelchairs. *J. Rehabil. Res. Dev.* 49, 63–74. doi: 10.1682/JRRD.2011.03.0050
- Seki, H., Iijima, T., Minakata, H., and Tadakuma, S. (2006). "Novel step climbing control for power assisted wheelchair based on driving mode switching," in *IECON 2006 - 32nd Annual Conference on IEEE Industrial Electronics* (Paris: IEEE), 3827–3832.
- Seki, H., Ishihara, K., and Tadakuma, S. (2009). Novel regenerative braking control of electric power-assisted wheelchair for safety downhill road driving. *IEEE Trans. Ind. Electron.* 56, 1393–1400. doi: 10.1109/TIE.2009.2014747
- Shieh, M.-Y., Chen, S.-C., Chen, P.-C., and Wu, C.-M. (2015). "Exerted-torque estimation of a power-assisted wheelchair," in *2015 IEEE/SICE International Symposium on System Integration (SII)* (Nagoya: IEEE).
- Soltau, S. L., Slowik, J. S., Requejo, P. S., Mulroy, S. J., and Neptune, R. R. (2015). An investigation of bilateral symmetry during manual wheelchair propulsion. *Front. Bioeng. Biotechnol.* 3:86. doi: 10.3389/fbioe.2015.00086
- Sreenivasa, M., Millard, M., Felis, M., Mombaur, K., and Wolf, S. I. (2017). Optimal control based stiffness identification of an ankle-foot orthosis using a predictive walking model. *Front. Comput. Neurosci.* 11:23. doi: 10.3389/fncom.2017.00023
- van der Woude, L. H., Veeger, H. E., Dallmeijer, A. J., Janssen, T. W., and Rozendaal, L. A. (2001). Biomechanics and physiology in active manual wheelchair propulsion. *Med. Eng. Phys.* 23, 713–733. doi: 10.1016/S1350-4533(01)00083-2
- Wächter, A., and Biegler, L. T. (2005). On the implementation of an interior-point filter line-search algorithm for large-scale nonlinear programming. *Math. Program.* 106, 25–57. doi: 10.1007/s10107-004-0559-y
- Winter, D. A. (2009). *Biomechanics and Motor Control of Human Movement*. Waterloo: John Wiley & Sons, Inc.

**Conflict of Interest:** The authors declare that the research was conducted in the absence of any commercial or financial relationships that could be construed as a potential conflict of interest.

**Publisher's Note:** All claims expressed in this article are solely those of the authors and do not necessarily represent those of their affiliated organizations, or those of the publisher, the editors and the reviewers. Any product that may be evaluated in this article, or claim that may be made by its manufacturer, is not guaranteed or endorsed by the publisher.

Copyright © 2022 Cuerva, Ackermann and Leonardi. This is an open-access article distributed under the terms of the Creative Commons Attribution License (CC BY). The use, distribution or reproduction in other forums is permitted, provided the original author(s) and the copyright owner(s) are credited and that the original publication in this journal is cited, in accordance with accepted academic practice. No use, distribution or reproduction is permitted which does not comply with these terms.





# Safety and Feasibility of a Novel Exoskeleton for Locomotor Rehabilitation of Subjects With Spinal Cord Injury: A Prospective, Multi-Center, and Cross-Over Clinical Trial

## OPEN ACCESS

### Edited by:

Francisco Romero Sánchez,  
University of Extremadura, Spain

### Reviewed by:

Sean Sanford,  
United States Department of Veterans  
Affairs, United States  
Saikat Pal,  
New Jersey Institute of Technology,  
United States

### \*Correspondence:

Jianan Li  
lijianan@carm.org.cn  
Mei Shuai  
shuaim@buaa.edu.cn  
Zishan Jia  
jzs1963@163.com  
Xiaolin Huang  
xiaolin2006@tjh.tjmu.edu.cn  
Yulong Wang  
ylwang66@126.com

<sup>†</sup>These authors have contributed  
equally to this work

**Received:** 04 January 2022

**Accepted:** 16 March 2022

**Published:** 12 May 2022

### Citation:

Chen S, Wang Z, Li Y, Tang J, Wang X,  
Huang L, Fang Z, Xu T, Xu J, Guo F,  
Wang Y, Long J, Wang X, Liu F, Luo J,  
Wang Y, Huang X, Jia Z, Shuai M and  
Li J (2022) Safety and Feasibility of a  
Novel Exoskeleton for Locomotor  
Rehabilitation of Subjects With Spinal  
Cord Injury: A Prospective,  
Multi-Center, and Cross-Over Clinical  
Trial. *Front. Neurobot.* 16:848443.  
doi: 10.3389/fnbot.2022.848443

**Sijing Chen**<sup>1,2†</sup>, **Zhanbin Wang**<sup>3†</sup>, **Yongqiang Li**<sup>1,2</sup>, **Jiashuai Tang**<sup>2</sup>, **Xue Wang**<sup>1,2</sup>,  
**Liping Huang**<sup>4</sup>, **Zhuangwei Fang**<sup>4</sup>, **Tao Xu**<sup>5</sup>, **Jiang Xu**<sup>5</sup>, **Feng Guo**<sup>5</sup>, **Yizhao Wang**<sup>5</sup>,  
**Jianjun Long**<sup>6,7</sup>, **Xiaodong Wang**<sup>6,7</sup>, **Fang Liu**<sup>6,7</sup>, **Jianfeng Luo**<sup>8,9,10</sup>, **Yulong Wang**<sup>6,7\*</sup>,  
**Xiaolin Huang**<sup>5\*</sup>, **Zishan Jia**<sup>4\*</sup>, **Mei Shuai**<sup>11\*</sup> and **Jianan Li**<sup>1,2\*</sup>

<sup>1</sup> Center of Rehabilitation Medicine, The First Affiliated Hospital of Nanjing Medical University, Nanjing, China, <sup>2</sup> Jiangsu Zhongshan Geriatric Rehabilitation Hospital, Nanjing, China, <sup>3</sup> School of Automation Science and Electrical Engineering, Beihang University, Beijing, China, <sup>4</sup> Department of Rehabilitation, The First Medical Center, Chinese PLA General Hospital, Beijing, China, <sup>5</sup> Department of Rehabilitation Medicine, Tongji Hospital, Tongji Medical College, Huazhong University of Science and Technology, Wuhan, China, <sup>6</sup> Department of Rehabilitation, Shenzhen Second People's Hospital, Shenzhen, China, <sup>7</sup> Department of Rehabilitation, The First Affiliated Hospital of Shenzhen University, Shenzhen, China, <sup>8</sup> Department of Biostatistics, School of Public Health, Fudan University, Shanghai, China, <sup>9</sup> NHC Key Laboratory of Health Technology Assessment, Fudan University, Shanghai, China, <sup>10</sup> Key Laboratory of Public Health Safety of Ministry of Education, Fudan University, Shanghai, China, <sup>11</sup> School of Biological Science and Medical Engineering, Beijing Advanced Innovation Centre for Biomedical Engineering, Beihang University, Beijing, China

**Objective:** To evaluate the safety, walking efficiency, physiological cost, don and doff time cost, and user satisfaction of Ai-robot.

**Design:** Prospective, multi-center, and cross-over trial.

**Subjects:** Paraplegic subjects ( $n = 40$ ) with T6–L2 level spinal cord injury.

**Methods:** Subjects who could walk independently using Aiwalker, Ailegs, and hip knee ankle foot orthosis (HKAFO) for 6 min within 30 days of training underwent 10 sets of tests. In each set, they completed three 6-min walk test (6MWT) sessions using the three aids in random order.

**Results:** Skin lesions, pressure sores, and fractures, were the main adverse events, likely due to a lack of experience in using exoskeleton systems. The average 6MWT distances of the Aiwalker, Ailegs, and HKAFO groups were  $134.20 \pm 18.74$ ,  $79.71 \pm 18.06$ , and  $48.31 \pm 19.87$  m, respectively. The average heart rate increases in the Aiwalker ( $4.21 \pm 8.20\%$ ) and Ailegs ( $41.81 \pm 23.47\%$ ) groups were both significantly lower than that in the HKAFO group ( $62.33 \pm 28.32\%$ ) (both  $p < 0.001$ ). The average donning/doffing time costs for Ailegs and Aiwalker were significantly shorter than that of HKAFO (both  $p < 0.001$ ). Satisfaction was higher in the Ailegs and Aiwalker groups (both  $p < 0.001$ ).

**Conclusion:** Subjects with paraplegia below T6 level were able to ambulate safely and efficiently with Ai-robot. The use of Ai-robot should be learned under the guidance of experienced medical personnel.

**Keywords:** exoskeleton, spinal cord injury (SCI), paraplegia, walking aid, rehabilitation, orthosis

## INTRODUCTION

Spinal cord injury (SCI) is a common cause of paralysis. The worldwide annual incidence of SCI varied from 13.0 to 220.0 per million people depending upon the country (Kang et al., 2017). Missing prevalence data for major populations persist and the range of reported global prevalence was between 440 and 526 per million (Fitzharris et al., 2013; Lee et al., 2013; New et al., 2015; Kang et al., 2017). Many people with SCI are confined to a wheelchair for life, causing a heavy burden to society and families. SCI can lead to limb paralysis and many complications such as osteoporosis, fractures, spinal deformities, muscle atrophy, cardiopulmonary dysfunction, obesity, and metabolic disorders, etc. (Castro et al., 1999; Giangregorio and McCartney, 2006; Shah et al., 2006; Liusuwan et al., 2007; Widman et al., 2007; Dudley-Javoroski, 2008; Adriaansen et al., 2012; Mulcahey et al., 2013; Lai et al., 2014; Sezer, 2015; Gee et al., 2019, 2021).

The advent of exoskeletal robotic technology can benefit the spinal cord injury population in three ways: (1) extensive repetitions of walking can help them improve and regain their walking ability, (2) the need for medical manual labor can be reduced, making extensive walking training feasible and even shortening the course of treatment, and (3) complications can be reduced, such as reduced pain, spasticity, osteoporosis and improved cardiorespiratory, lower urinary tract and bowel function (Esquenazi et al., 2012; Kolakowsky-Hayner, 2013; Benson et al., 2015; Stampacchia et al., 2016; Chun et al., 2019; Jang et al., 2019; Alashram et al., 2021; Brinkemper et al., 2021; Shackleton et al., 2021; Williams et al., 2021; Garnier-Villarreal et al., 2022).

Good fixation and support of the trunk during walking is required for subjects with poor upper limb and trunk function, insufficient endurance, or cognitive impairment. However, the existing stationary gait robots are often bulky and some are equipped with a treadmill (Peshkin et al., 2005; Bessler et al., 2020; Alashram et al., 2021; Calabrò et al., 2022). Patients mostly need to be transferred specifically to a dedicated treatment room to use the device, which cannot be used within the patient's ward, resulting in reduced accessibility. There are also devices that attach a robot exoskeleton to a mobile frame suspended in a sling with a high degree of freedom of trunk and pelvis movement. If the user cannot maintain balance with the trunk and lower extremities, the upper extremities are required to effectively hold the frame, which may not be suitable for patients with upper extremity paralysis and cognitive impairment (Bouri et al., 2006; Fukuda et al., 2015). Few exoskeleton robots are currently available to address these problems. For this reason, a new powered exoskeleton called Ai-robot has been developed

(Figures 1B, 2A). It comes in two types, namely, Aiwalker and Ailegs.

Aiwalker is characterized by its small size and ease of mobility, allowing it to be moved directly to any ward or even bedside, and may also be suitable for use at home. The subject can transfer from the wheelchair to Aiwalker in a seated position and then adjust to a standing position after securing the straps. Walking exercises can be performed while suspended or on the real ground while speed and stride length could also be modified as needed. The subject sees the external environment as moving and changing, which enriches the input of visual signals, adds interest to the therapy and helps to improve mood. With the small footprint of the device, the Aiwalker may have a wide range of clinical applications, namely, patients with tetraplegia, cognitive impairment, ataxia, and those who cannot easily leave the ward. It may be suitable for home use for patients in the chronic phase, helping to reduce complications.

The Ailegs does not have a support platform and is suitable for patients with good upper limb and trunk function at the advanced stage of gait training. It requires elbow crutches to maintain balance when using it. The therapist can choose the appropriate type for the patient to provide a tailor-made treatment (Fukuda et al., 2015). Similar to other wearable exoskeletons, subjects can also walk outdoors, turn around, go through small obstacles such as speed bumps and go upstairs and downstairs with the assistance of Ailegs (Lajeunesse et al., 2015; Tefertiller et al., 2018).

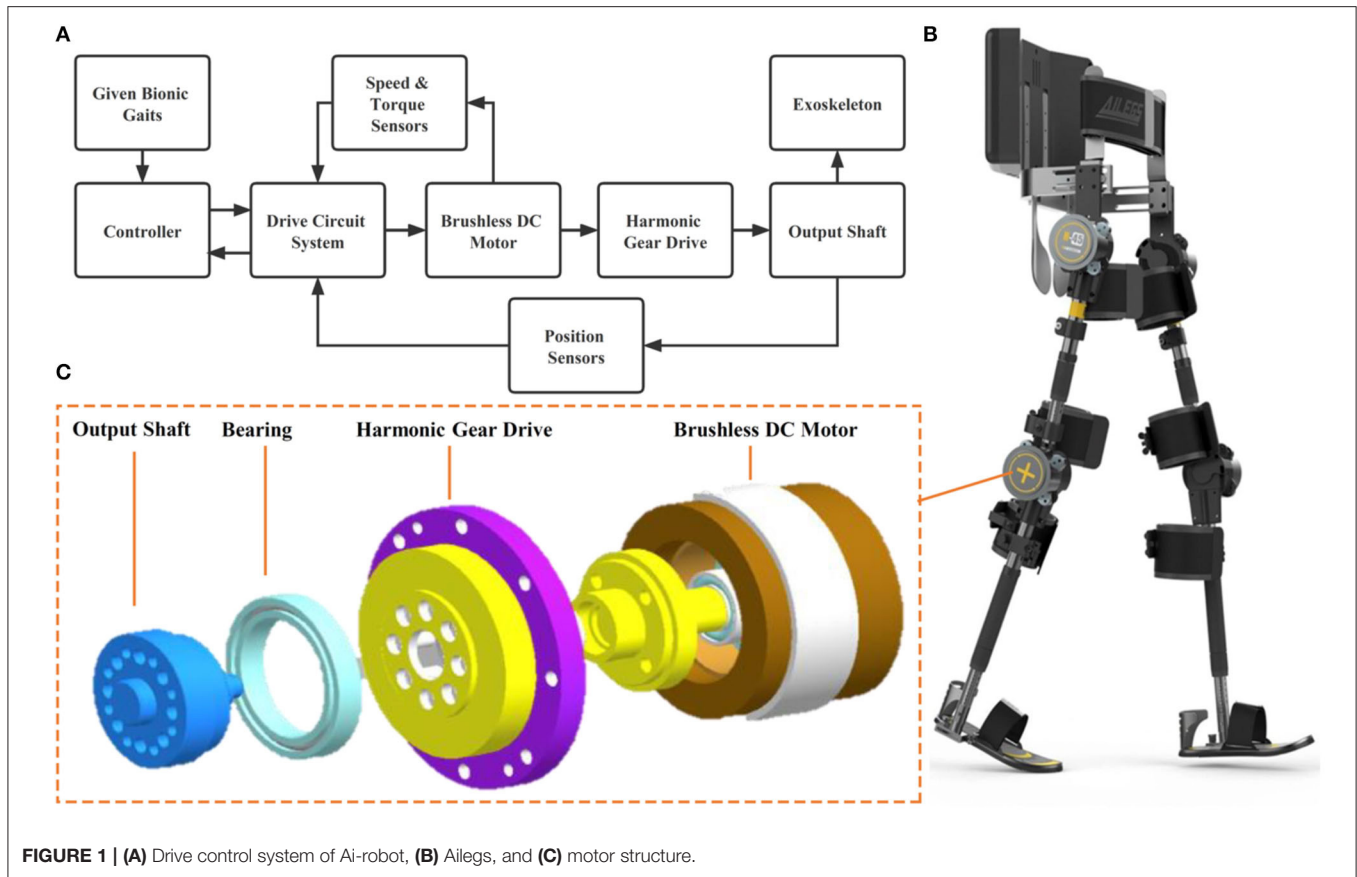
The purpose of this first clinical research of Ai-robot was to evaluate the safety, walking efficiency, physiological cost, don and doff time cost, and user satisfaction.

## MATERIALS AND METHODS

### Design

A prospective, multi-center, cross-over clinical trial was designed to assess the safety and effectiveness of two powered exoskeleton devices used to assist paraplegic subjects in walking by comparing them with a conventional hip knee ankle foot orthosis (HKAFO), based on subject walking ability indicators.

The clinical trial was conducted in four hospitals in eastern, northern, central, and southern China: The First Affiliated Hospital with Nanjing Medical University, Chinese PLA General Hospital, Affiliated Tongji Hospital with Tongji Medical College of Huazhong University of Science and Technology, and Shenzhen Second People's Hospital. The protocol, informed consent, case report form, and other implemented documents were approved by the ethical committee of the First Affiliated Hospital of Nanjing Medical University (No. 2017-MD-069).



**FIGURE 1 | (A)** Drive control system of Ai-robot, **(B)** Ailegs, and **(C)** motor structure.

Registration was recorded at ClinicalTrials.gov (identifier: NCT 03452059).

Each participant was clearly informed of the purpose of the research and the potential benefits and risks of enrolling in the research. Informed consent was obtained from all individual participants included in the study.

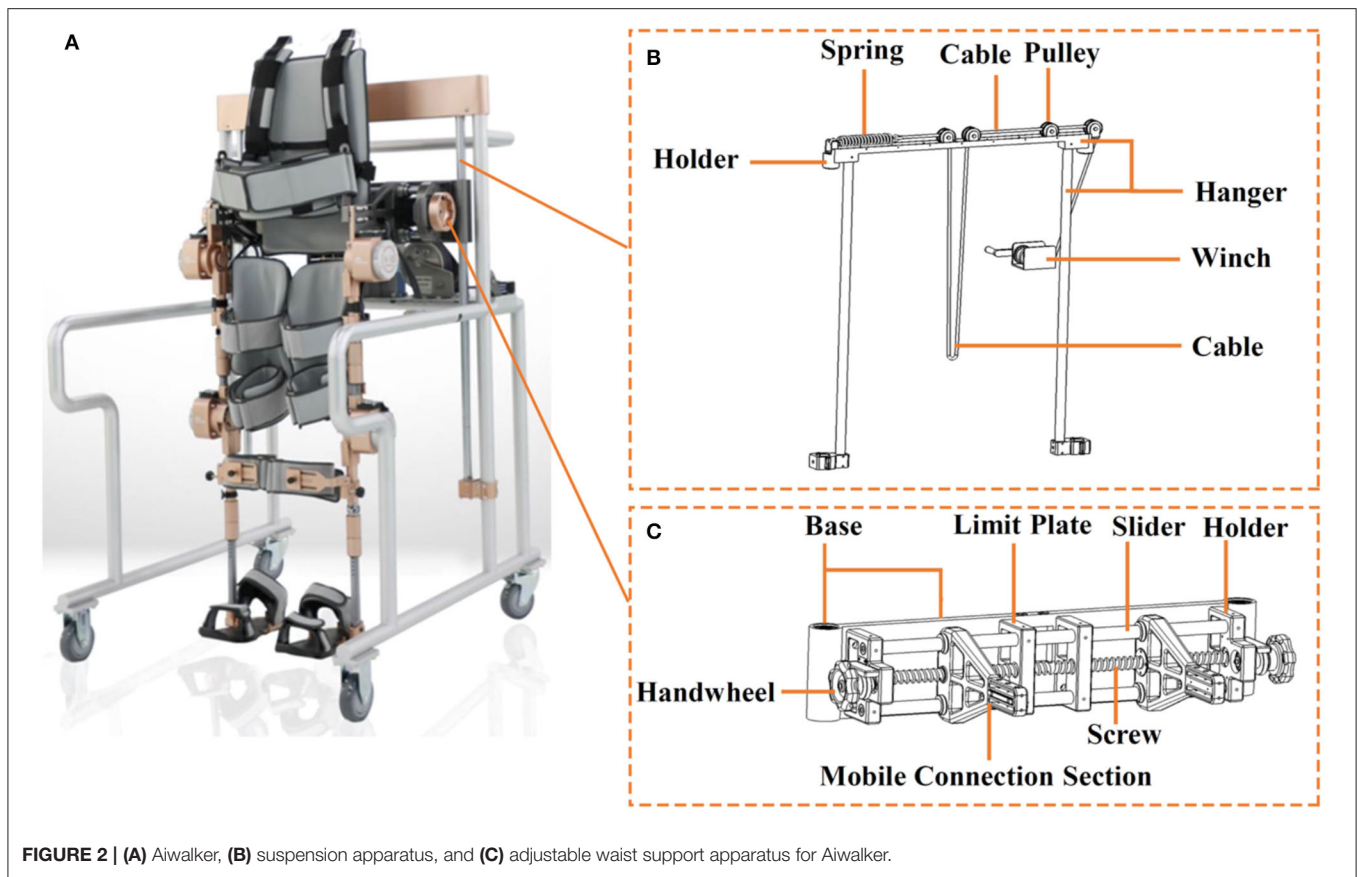
Some subjects had previously walked with an HKAFO, but none had previously walked or stood with a powered exoskeleton walking aid. Subject eligibility criteria were as follows: (1) age 18–60 years, body weight <80 kg, height 1.55–1.85 m; (2) confirmed by MRI/CT, International Standards for Neurological Classification of Spinal Cord Injury (ISNCSCI): A–C (without walking ability), injury level T6–L2; (3) muscle tone (modified Ashworth Scale):  $\leq 2$ ; (4) passive range of motion (ROM) of the bilateral hip and knee joints approximately normal, while the bilateral ankle joint could be maintained in a neutral position; (5) muscle strength of upper limbs and physical strength sufficient to stabilize crutches during assisted walking; (6) muscle strength of upper limbs and physical strength sufficient to transfer independently between a wheelchair and Ailegs/Aiwalker device; (7) able to understand and actively participate in the training program, agreed and signed the informed consent form. Subjects with any of the following criteria were excluded (1) unable to walk due to severe joint ROM limitation; (2) unhealed spinal fractures and unstable clinical condition, consultation with orthopedists or other specialists if not fully confirmed; (3) skin injury or infection

in the robot contact skin area or lower extremities; (4) subject showed poor compliance and was unable to complete the study in accordance with the requirements; (5) severe chronic obstructive pulmonary disease; (6) other contraindications or complications that may affect walking training; (7) severe cognitive or visual impairment; (8) unilateral neglect; (9) pregnant or lactating women; (10) unstable angina, severe arrhythmia, or other heart diseases.

## Devices

### Common Design of Ai-Robot

Ai-robot (Ai-Robotics Technology Co. LTD, Beijing, China) uses a drive control system that provides closed-loop and coordinated motion control of the two hips and two knee motors (**Figure 1C**) simultaneously to achieve bionic gaits. The drive control system includes a controller, a driver (drive circuit system), a brushless DC motor, a harmonic gear drive, an information acquisition unit (relative coding disk and absolute coding disk), and an output shaft (**Figure 1A**). The controller is responsible for outputting the motion gait and coordinating the synchronized and coordinated motion among the four drives, while adjusting the motion parameters of the drives in real-time according to the state information such as the angular speed of the motor shaft and the angular position of the output shaft during the movement of the leg bars (Shuai, 2017). The rotation centers of the hip and knee motors should be on the same horizontal axis as the user's



**FIGURE 2 | (A)** Aiwalker, **(B)** suspension apparatus, and **(C)** adjustable waist support apparatus for Aiwalker.

hip and knee joint rotation centers, respectively. The device is connected to the wearer's limb *via* straps on the waist, thigh, calf, and foot.

Ai-robot provides sufficient power to assist walking without the need for active exertion of the lower limbs. The power is supplied by a 48 V 18,650 lithium battery with 15 Ah max capacity and 20 A max discharge current. The service life of Ai-robot is 8 years. The thigh and calf bars are designed as a retractable structure, with convenient and precise length adjustment for quick adaptation for users of different heights and body shapes (**Figure 3**) (Shuai, 2019).

The angles of the hip and knee joints can also be optimally adjusted to the needs of the user. The maximum angles are hip flexion 33°, hip extension 23° (Aiwalker)/0° (Ailegs), knee flexion 53°, knee extension 0°. The duration of each gait cycle can be adjusted between 2.45 and 5.25 s, as required. Its gait training control strategy is shown in **Figure 1A**, which takes the given bionic gait as the standard gait input to the drive control system, establishes the lower limb dynamics and kinematics model, calculates and controls the motion output, and drives the user's lower limb to perform the movement.

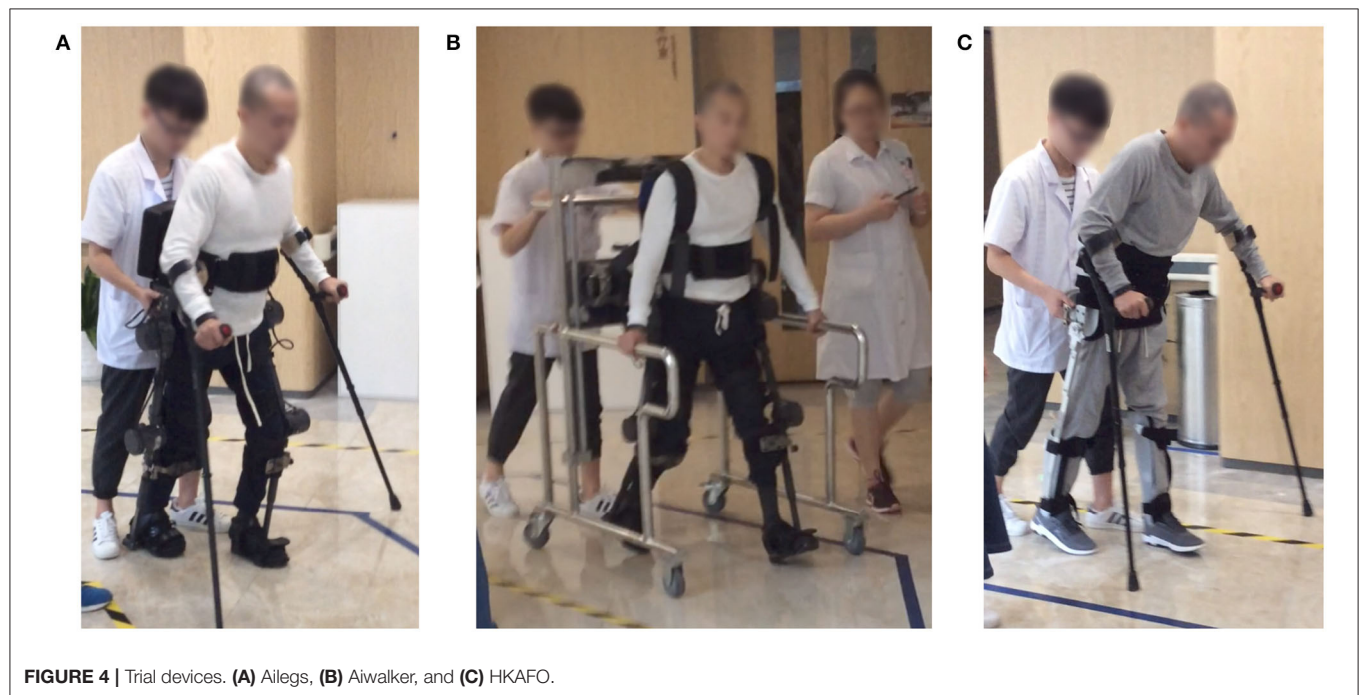
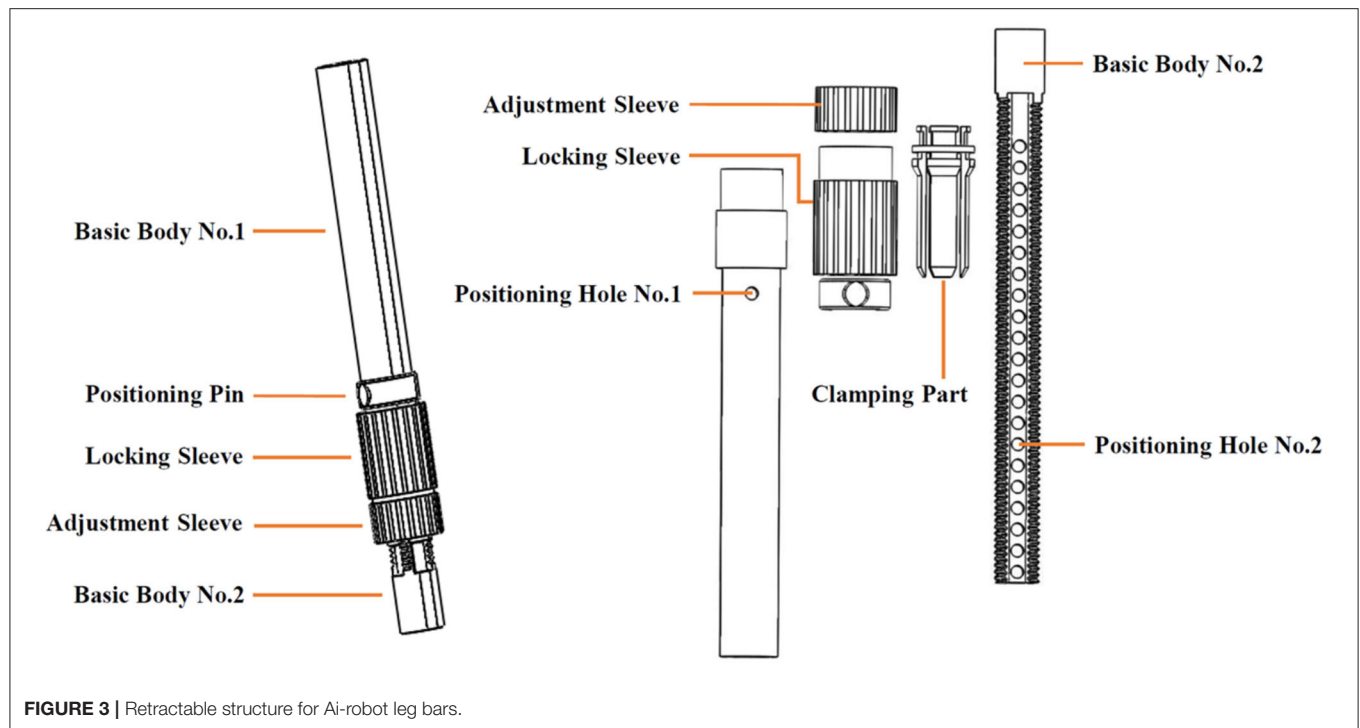
### Type Design of Ai-Robot

Ailegs (frameless type of Ai-robot) weighs 25 kg and is made primarily of titanium alloy, requiring a pair of elbow crutches

or walking aid for balance (**Figure 4A**). The waist structure connecting the lower limb exoskeleton comprises two waist connection frames and an adjustment unit. The waist structure connecting the lower limb exoskeleton comprises two first waist connection frames and an adjustment component unit. Each of the two waist connectors is provided with a sliding section, which is aligned with each other and connected to the adjustment unit. By turning the adjusting unit, the two connectors can be moved closer or further away from each other simultaneously, thus, adjusting the width of the waist structure (**Figure 5**) (Shuai, 2020).

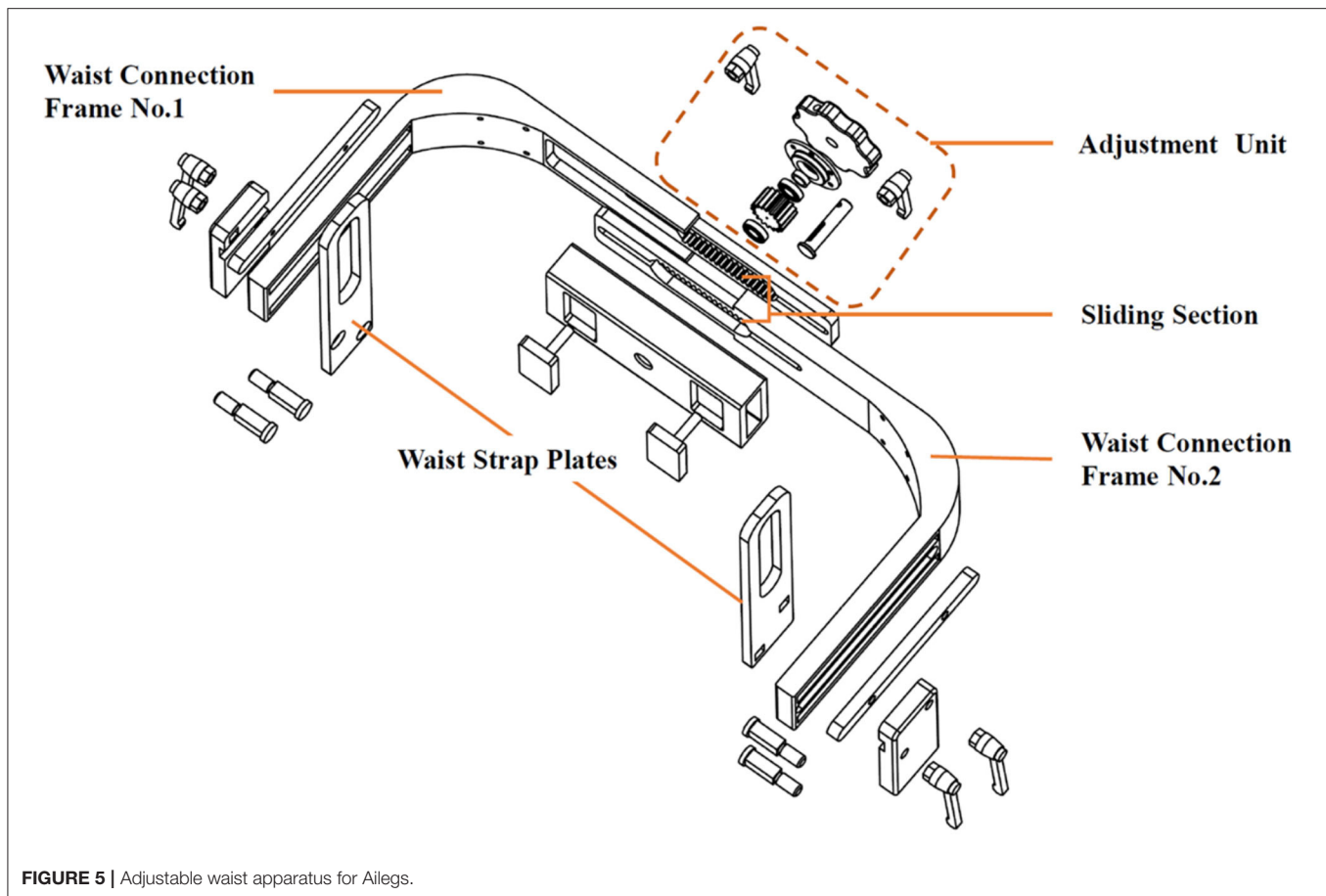
Aiwalker (frame type of Ai-robot) weighs 80 kg and is mainly made of titanium alloy and stainless steel. It consists of a similar structure of Ailegs and a mobile support platform that provides stable trunk support. There are four wheels under the platform to allow easy movement of the device (**Figure 4B**). Its main features are waist fixation, lower limb drive, and true overground ambulation. The waist support device connected to the lower limb exoskeleton has an adjustable distance between the two mobile connection sections, thus being suitable for users with different waist widths (**Figure 2C**) (Shuai, 2018a). The suspension system shown in **Figure 2B** is capable of ensuring up and down movement of the human gravity center in the vertical plane during body weight support training or overground training. The suspension system includes





a suspension frame, pulley, cable, holder, spring, winch, etc. The suspension structure will be locked when the lumbar support device is suspended to a predetermined position. The movement of the user's lower limbs also drives the waist support device

up and down relative to the predetermined position (Shuai, 2018b). Aiwalker is designed to securely and stably fix the user's trunk and pelvis without requiring active effort to maintain standing balance.



**FIGURE 5 |** Adjustable waist apparatus for Ailegs.

## HKAFO

Considering that SCI subjects with T6-L1 do not have the ability to flex the hips, the effect of walking with KAFO will be reduced. Therefore, HKAFO was chosen as a control. A custom-made unpowered HKAFO for each subject was produced by Beijing Sereborn Technology Co. LTD (**Figure 4C**).

## Experiment Protocol

This clinical trial was divided into the screening, trial, and data analysis phases. Since it was the first clinical use of Ai-robot, the therapist followed closely behind the subject during the Ailegs and HKAFO assisted ambulation to ensure safety. When using Aiwalker, the therapist walks behind the device and controls the direction of walking.

### Screening Phase

During the screening phase, in addition to meeting the inclusion and exclusion criteria, subjects were assessed for their proficiency in independent transfer between wheelchair and walking aids, and ability to walk independently with Ailegs (with a pair of elbow crutches) and HKAFO (with a pair of elbow crutches). Only adaptive use was required for Aiwalker because it is a passive walking aid. If the subject was unable to independently walk with any of the three devices continuously for 6 min (due

to lack of physical or trunk strength, postural hypotension, fear, etc.), a screening failure was recorded. The screening period did not exceed 30 days for each individual subject.

In total 49 participants signed informed consent forms, 40 were enrolled, and 9 failed the screening (2 were not exposed to the devices and 7 were unable to achieve the expected level of proficiency with the devices). As shown in **Table 1**, the mean age of the participants was  $38.1 \pm 9.4$  years and injury levels ranged from T6 to L2.

### Trial Phase

After the researchers judged that the subjects had mastered the trial devices, the subjects entered the test phase. The experimental period was 5 days, with one group of tests each half workday, and a total of 10 sets of tests. In each group, subjects were assigned to finish three 6-min walk tests (6MWTs) using Aiwalker, Ailegs, and HKAFO, respectively, in a random order. The circular walkway of a hospital hall (perimeter of  $\geq 100$  m) was set up as a test trail. Test trials were pre-marked on the ground. The 6MWT with each device was conducted at least 30 min apart, and the next test was performed after confirming that the subject's heart rate, blood pressure, and breathing had normalized. Six (15%) of the 40 subjects did not complete all 10 trial sets due to cystoscopy, adverse events, or requests to withdraw from the research.

**TABLE 1 |** Demographic characteristics of participants.

Characteristic	Value
Sex ( <i>n</i> )	Male (31), female (9)
Age (years), mean ± SD	38.1 ± 9.4
Height (cm), mean ± SD	169.8 ± 6.5
Weight (kg), mean ± SD	62.2 ± 7.8
Level of injury ( <i>n</i> )	T6–L2: T10 (15), T12 (8), T9 (5), T8/T11/L1 (3 for each level), and T6/T7/L2 (1 for each level)
Type of injury ( <i>n</i> )	Traumatic (33), Non-traumatic (7)
AIS classification ( <i>n</i> )	A (29), B (4), C (7)
Skin integrity ( <i>n</i> )	Intact (36), Broken but not affect use of the devices (4)
Spasticity in lower limbs ( <i>n</i> )	Yes but not affect use of the devices (10), No (30)
Arrhythmia ( <i>n</i> )	Normal or abnormal without clinical significance (40)
HRrest (beats/minute), mean ± SD	77.6 ± 8.3
Blood Pressure (mmHg), mean ± SD	Systolic (118.0 ± 11.7), Diastolic (74.7 ± 9.1)

AIS, American Spinal Cord Injury Association Impairment Scale; HRrest, heart rate rest.

## Data Collection

### Safety Indicator

#### Adverse Events

The following adverse medical events were monitored and their relationship to the device used analyzed: incidence of falls, skin damage, joint injury, fracture, and other adverse events.

#### Blood Pressure

Blood pressure was measured twice using a calibrated medical electronic blood pressure monitor. The first upper limb blood pressure measurement was taken in a sitting position immediately before the beginning of the walking test. The second blood pressure was taken from the same upper limb in the same position 3 min after the end of the walking test. Subjects removed their walking aids and returned to the wheelchair after blood pressure measurement.

### Validity Indicator

#### Primary Validity Indicator

**Six Minutes Walking Distance.** The 6MWT was used to record the maximum walking distance within 6 min (Tappan et al., 2012). A circular walkway with a circumference  $\geq 100$  m was used as a training and test trail, and the walking path was marked on the ground in advance. Subjects were asked to walk as fast as they could at a comfortable and self-determined speed. There were  $\geq 30$  min between tests, and heart rate, blood pressure, and respiratory rate were also required to return to resting levels before the next test.

**Average Percentage Heart Rate Increase.** A wireless single-channel medical electrocardiogram (ECG) recorder (Wearable ECG Recorder, Nanjing Xijian Information Technology Co., Ltd.,

China) was used to record the channel II ECG before and during the total 6MWT. %HRI was calculated as follows:

$$\%HRI = \frac{HR_{walk} - HR_{before}}{HR_{before}} \times 100$$

where “HRwalk” was the average heart rate determined by ECG between 120 and 330 s of the 6MWT (the steady phase) and “HRbefore” was the heart rate determined by a 1-min ECG recorded just before the start of a test, after sufficient rest, to calculate the average heart rate in the resting state.

### Secondary Validity Indicator

**The Borg rating of Perceived Exertion Scale.** Subjects were evaluated using the Borg RPE scale after each walking test (Heath, 1998). Each participant was assessed 10 times, by self-rating how tired they felt after walking with each of the three devices. RPE scores ranged from 6 to 20, with 6 indicating no effort and no fatigue at all, and 20 indicating maximum effort and exertion.

**Time Cost of Donning and Doffing.** Two dedicated medical staff helped each subject to get into and take off the walking aids without helping transfer. The donning period began at the point the subject was ready to transfer from the wheelchair to the walking aid and ended when they were ready to stand up with the walking aid, including changing shoes for HKAFO. The doffing period was defined as the time from the point the subject was ready to take off the device until transfer back to the wheelchair, including placing the feet back on the pedals.

**Satisfaction Questionnaire.** After each 6MWT, participants were asked to rate their satisfaction levels regarding device comfort, don and doff speeds, and stability during walking. Satisfaction was rated on the following five-point scale: (1) very satisfied, (2) satisfied, (3) fair, (4) dissatisfied, and (5) very dissatisfied. Data for very satisfied and satisfied were used to calculate the percentage of satisfaction.

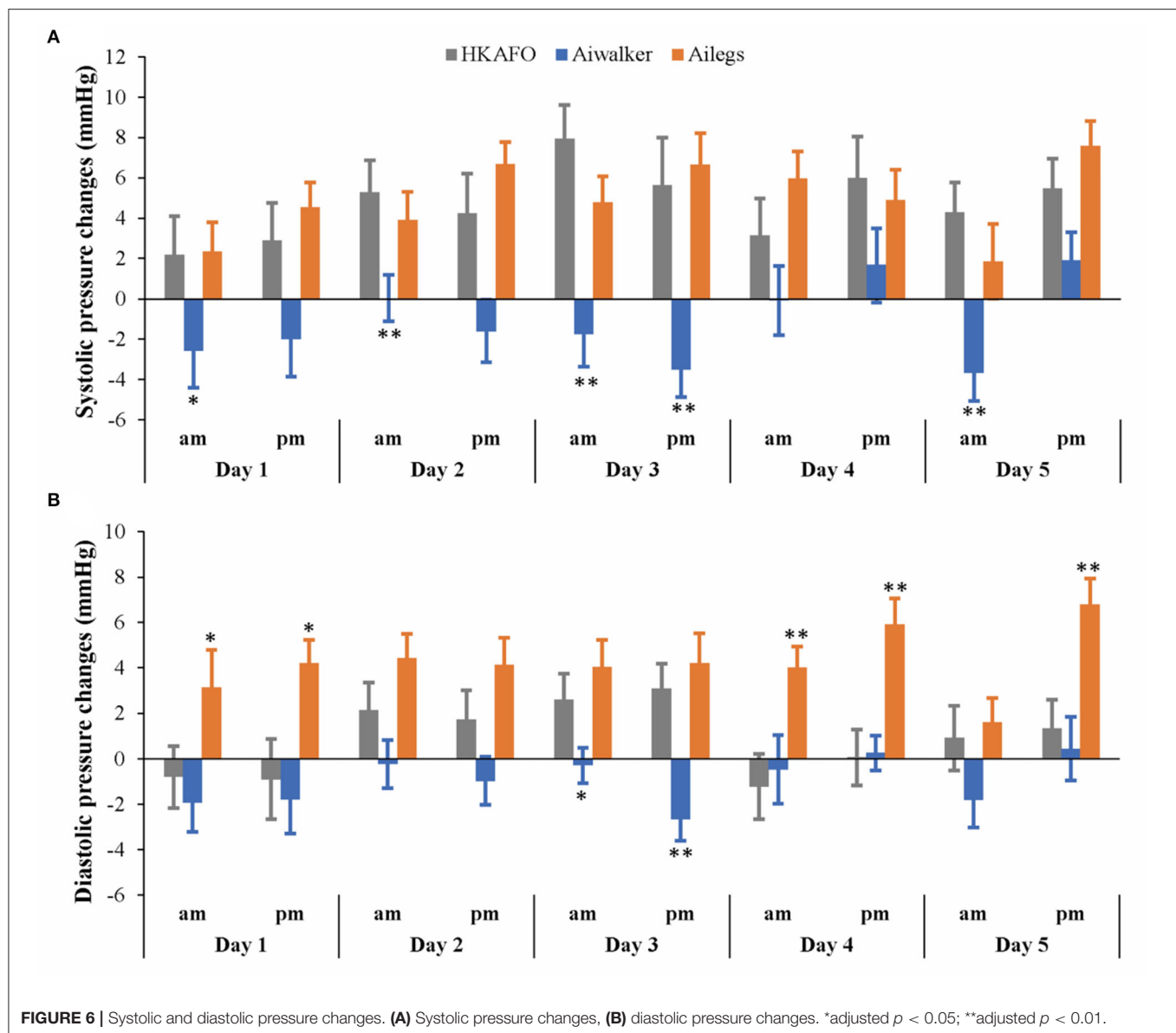
## Statistical Methods

### Statistical Design and Evaluation Methods

The hypotheses of this study were that (1) the 6MWT distance of both Ailegs and Aiwalker group was farther than the HKAFO group and (2) the average %HRI of both Ailegs and Aiwalker group were lower than the HKAFO group. Two primary validity indicators were set in this study. The hypotheses for both indicators need to be valid for the test group (Ailegs and Aiwalker) to be considered superior to the control group (HKAFO).

For the primary validity indicators, 10 consecutive groups of data were collected considering that each study subject was crossed over to the three orthoses. The mixed model considered grouping (Ailegs, Aiwalker, and HKAFO groups), order (ABC/ACB/BCA/BAC/CAB/CBA, 6 in total), time (5 days in the morning and afternoon, 10 time points in total), and the interaction of grouping and time. If the interaction test  $p > 0.1$ , the interaction term was removed and the model was refitted.

The safety analysis will be performed separately for the three groups (Ailegs, Aiwalker, and HKAFO).



## Statistical Analysis

The number of subjects, average, standard deviation, minimum, and maximum were calculated for continuous variables. A number of examples and percentages were used to summarize categorical variables. For continuous variables, differences among the Ailegs, Aiwalker, and HKAFO groups were compared using repeated measured analysis of variance, paired  $t$ -test, or paired sign rank-sum test, according to the data distribution. For categorical variables, differences among the Ailegs, Aiwalker, and HKAFO groups were compared by paired chi-square test. Data were used from the participants who had completed at least one set of walking tests. Differences among the Ailegs, Aiwalker, and HKAFO groups were compared using a mixed model, and the confidence intervals of differences were calculated. Adjusted

$p$ -values of multiple comparisons were performed using the Benjamini-Hochberg procedure to control the false discovery rate (FDR) at 0.05. All the statistical analyses were performed using SAS9.3 (SAS Institute, Cary, NC, USA), and  $p < 0.05$  was considered statistically significant.

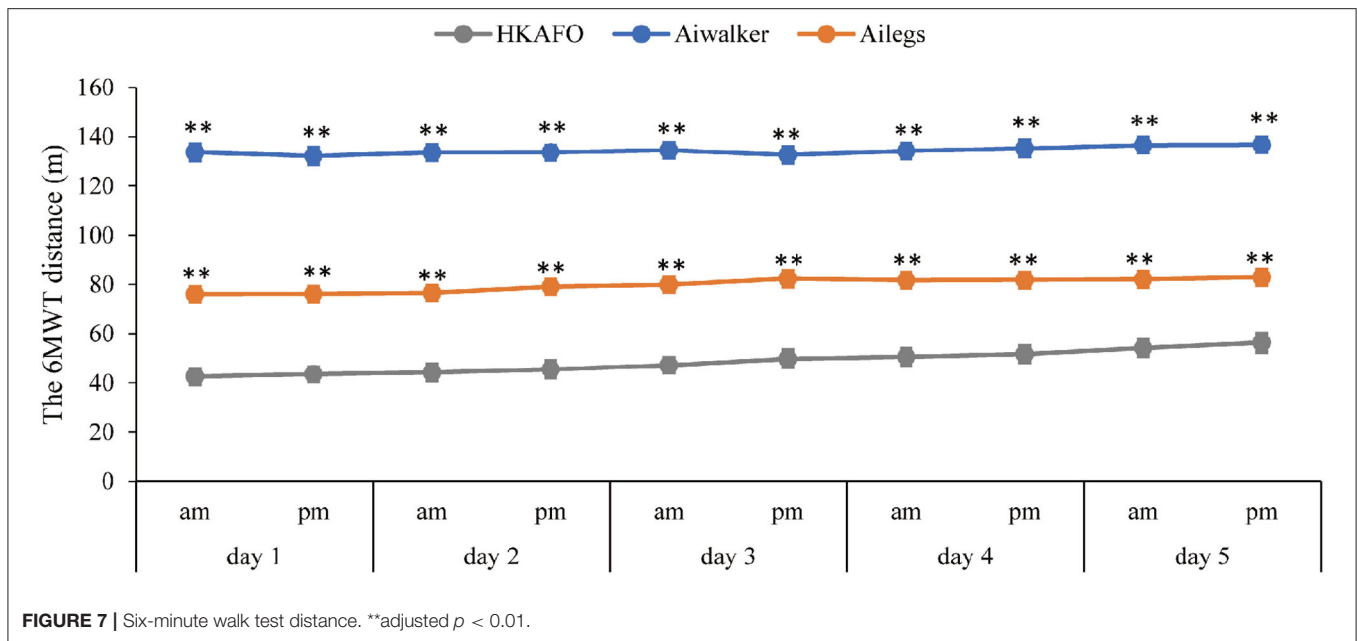
## RESULTS

### Safety Indicator

#### Adverse Events

There were no falls, increased pain, increased muscle tone, fatigue, or cardiovascular episodes. A total of four adverse events determined to be device-related occurred in four different subjects, including two cases of mild skin abrasion (lumbosacral





region and left lumbar region), one case of bilateral heel pressure sores, and one case of calcaneal sinus compression fracture.

### Blood Pressure

As shown in **Figure 6**, systolic blood pressure increased to varying degrees in the Ailegs (mean [SD] 4.89 [8.68] mmHg) and HKAFO (mean [SD] 4.67 [11.41] mmHg) groups after exercise; there was no significant difference between the two groups (Ailegs vs. HKAFO, the difference in LS means:  $-0.22$  [95%CI,  $-1.58$  to  $1.14$ ], adjusted  $p > 0.05$ ,  $n = 40$ ). In the Aiwalker group (mean [SD]  $-1.20$  [9.85] mmHg), systolic blood pressure decreased slightly after exercise in 5 out of 10 tests; the difference with the HKAFO group was significant (Aiwalker vs. HKAFO, the difference in LS means:  $5.87$  [95%CI,  $4.52$ – $7.23$ ], adjusted  $p < 0.001$ ,  $n = 40$ ).

After exercise, diastolic blood pressure in the Ailegs group (mean [SD]  $4.22$  [7.39] mmHg) was slightly higher than that in the HKAFO group (mean [SD]  $0.89$  [8.29] mmHg), and the difference was significant (Ailegs vs. HKAFO, the difference in LS means:  $-3.33$  [95%CI,  $-4.39$  to  $-2.27$ ], adjusted  $p < 0.001$ ,  $n = 40$ ). Diastolic blood pressure decreased in the Aiwalker group (mean [SD]  $-0.97$  [7.25] mmHg) and increased in the HKAFO group during most of the tests, and there was a significant difference between the two groups (Aiwalker vs. HKAFO difference in LS means:  $1.86$  [95%CI,  $0.80$ – $2.92$ ], adjusted  $p < 0.001$ ,  $n = 40$ ).

### Validity Indicator

#### Primary Validity Indicator

##### Six Minutes Walking Distance

As shown in **Figure 7**, the mean (SD) 6MWT distance (m) of subjects in the Ailegs group was significantly farther than those in the HKAFO group (Ailegs  $79.71$  [18.06] vs. HKAFO

$48.31$  [19.87] m difference in LS means:  $30.56$  [95%CI,  $28.42$  to  $32.70$ ], adjusted  $p < 0.001$ ,  $n = 40$ ). Similarly, subjects in the Aiwalker group achieved greater 6MWT distances than those in the HKAFO group (Aiwalker  $134.20$  [18.74] vs. HKAFO  $48.31$  [19.87] m difference in LS means:  $85.26$  [95%CI,  $82.94$ – $87.59$ ], adjusted  $p < 0.001$ ,  $n = 40$ ). The mean (SD) distance for the first 6MWT with HKAFO was  $42.59$  (19.22) m, and that of the tenth 6MWT was  $56.33$  (21.49) m, showing a trend of increasing speed. The mean distance of the first 6MWT using Ailegs was  $76.04$  (17.68) m, and the 10th was  $82.84$  (17.98) m, also showing an improving trend. As the subjects were walking fully passively, the 6MWT distance remained constant over the 10 tests in the Aiwalker group.

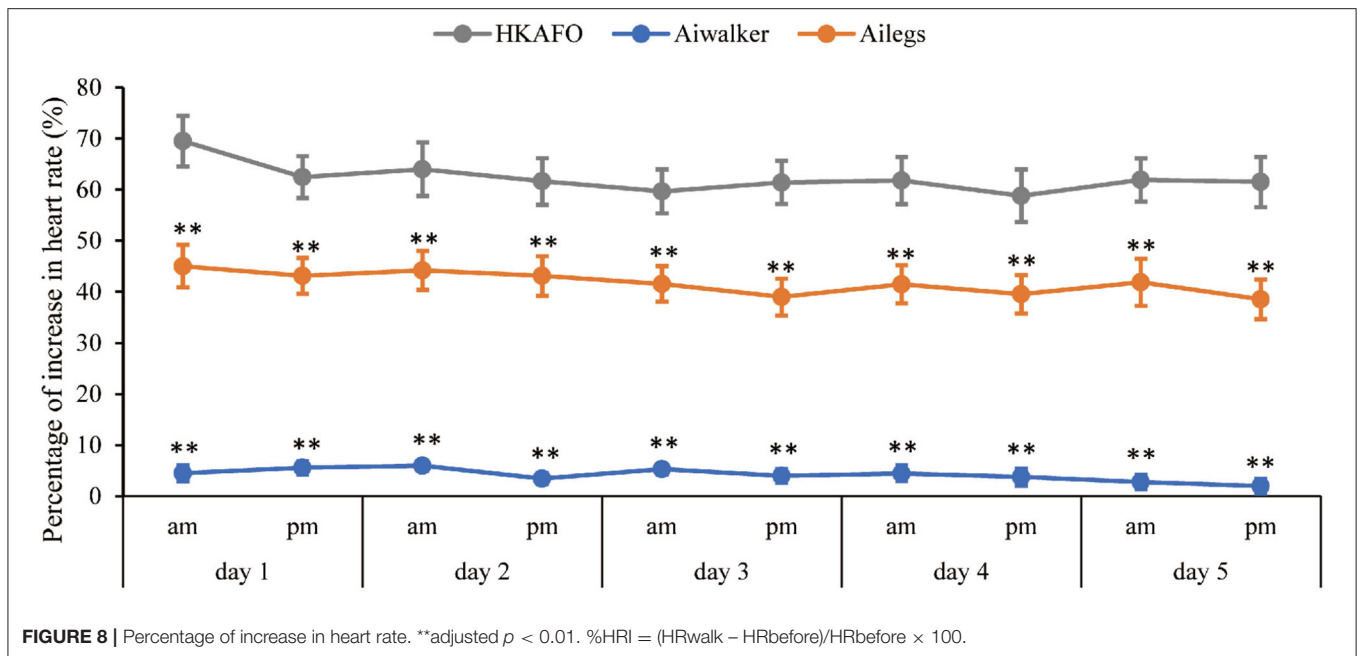
#### Average %HRI

A slightly decreasing trend from test 1 to 10 of the %HRI in Ailegs and HKAFO groups was exhibited (**Figure 8**). The %HRI (mean  $\pm$  SD) of  $4.21 \pm 8.20$  in the Aiwalker group and  $41.81 \pm 23.47$  in the Ailegs group were significantly lower than  $62.33 \pm 28.32$  in the HKAFO group (Aiwalker vs. HKAFO, the difference in LS means:  $-58.7$  [95%CI,  $-61.7$  to  $-55.7$ ], adjusted  $p < 0.001$ ,  $n = 40$ ; Ailegs vs. HKAFO, the difference in LS means:  $-22.2$  [95%CI,  $-25.0$  to  $-19.4$ ], adjusted  $p < 0.001$ ,  $n = 40$ ).

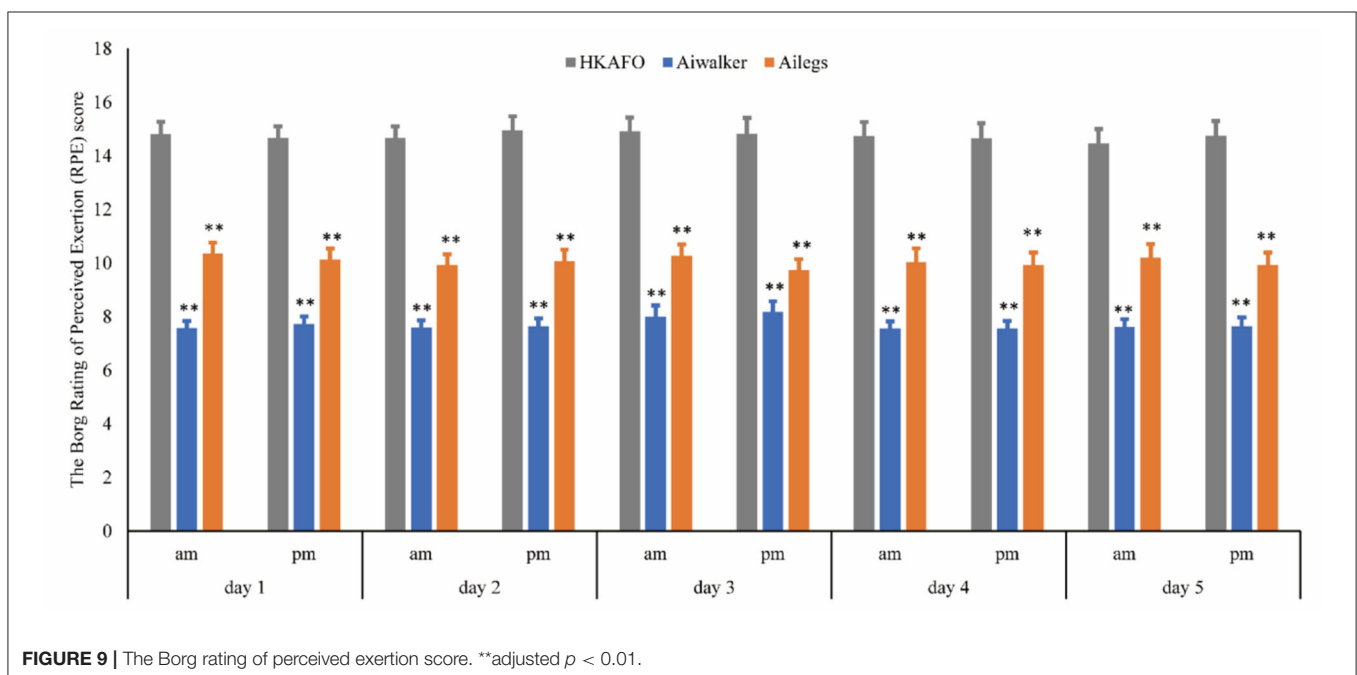
### Secondary Validity Indicator

#### Borg RPE Scale Scores

The RPE scores of subjects were relatively stable, with little variation. The mean (SD) scores were  $10.07$  (2.67),  $7.71$  (1.93), and  $14.74$  (3.17) in the Ailegs, Aiwalker, and HKAFO groups, respectively. The mean RPE scores for the Ailegs and Aiwalker groups were significantly lower than that of the HKAFO group (Ailegs vs. HKAFO, the difference in LS means:  $4.68$  [95%CI,  $4.38$ – $4.99$ ], adjusted  $p < 0.001$ ,  $n = 40$ ; Aiwalker vs. HKAFO,



**FIGURE 8** | Percentage of increase in heart rate. \*\*adjusted  $p < 0.01$ . %HRI =  $(HR_{walk} - HR_{before}) / HR_{before} \times 100$ .



**FIGURE 9** | The Borg rating of perceived exertion score. \*\*adjusted  $p < 0.01$ .

the difference in LS means: 7.03 [95%CI, 6.73–7.33], adjusted  $p < 0.001$ ,  $n = 40$ ; **Figure 9**).

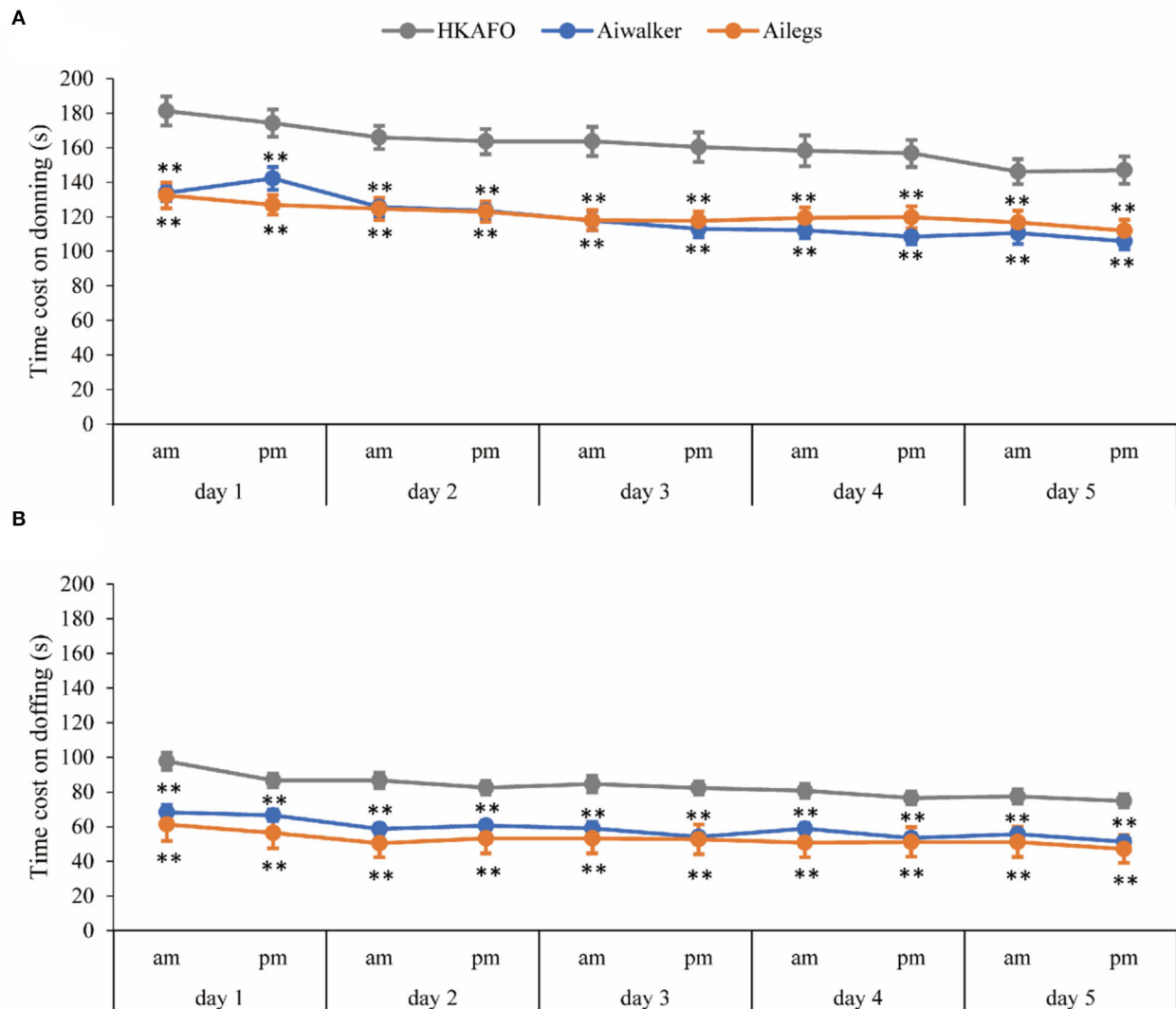
#### Time Cost for Donning and Doffing

The mean time costs for donning and doffing both Ailegs and Aiwalker were significantly shorter than that for HKAFO ( $n = 40$ , adjusted  $p < 0.001$ ). In the 10 sets of tests, the time costs for the three devices all showed a shortening trend, and the doffing time cost was significantly shorter than that of donning. The time costs (mean  $\pm$  SD) for donning were  $121.24 \pm 38.23$  s (Ailegs),

$119.82 \pm 33.99$  s (Aiwalker), and  $162.23 \pm 49.43$  s (HKAFO). The mean time costs for doffing were  $52.84 \pm 21.77$  s (Ailegs),  $58.82 \pm 20.66$  s (Aiwalker), and  $83.28 \pm 26.70$  s (HKAFO) (**Figure 10**).

#### Satisfaction

The results of the survey regarding device comfort, donning/doffing speed, and stability satisfaction all showed similar trends, with little change over the 10 sets of tests. The satisfaction of subjects was higher in both the Ailegs and



**FIGURE 10 |** Time cost of donning and doffing. **(A)** Donning and **(B)** doffing. \*\*adjusted  $p < 0.01$ .

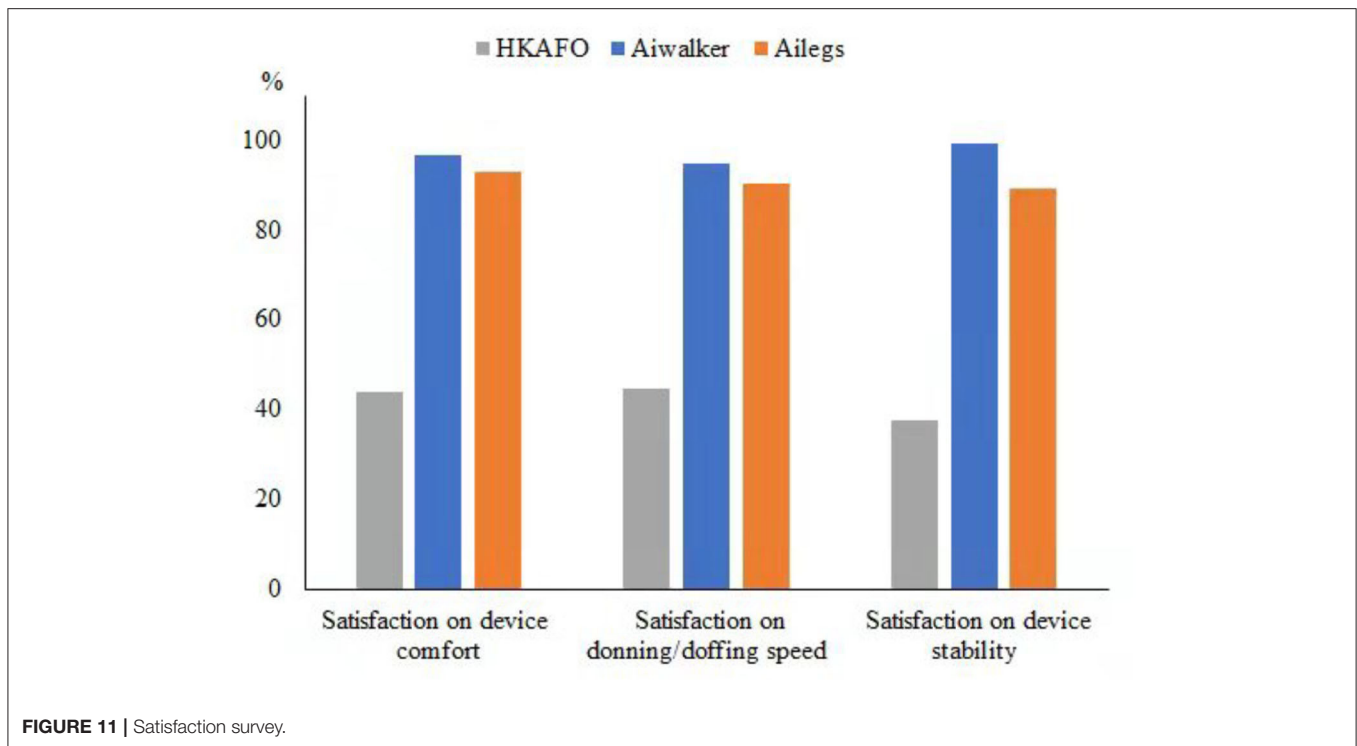
Aiwalker groups than that in the HKAFO group ( $n = 40$ , all adjusted  $p$ -values of the comparisons were  $< 0.001$ ; **Figure 11**).

## DISCUSSION

This study evaluated the safety, walking efficiency, and usability of a newly designed, easily mobile exoskeleton set that can be used in different stages of the disease. The results showed that the Ai-robot's technology is safe, but requires progressive weight-bearing on the lower extremities, with special attention to the skin at the heel and lumbosacral region. The Ai-robot assisted walking was more efficient, less physiological cost, faster in donning and doffing speed, and more satisfying for the user than traditional assistive walking devices.

We did not use ECG data from the entire 6MWT because subjects may be nervous at the beginning of the walk and the heart rate may be affected when they try to adapt to the equipment. Also, as the subjects approach the end of the walk, the heart rate may also be affected by emotion and the preparations of staff for measurements at the end. Therefore, we removed the ECG data from the first 2 min and the last 30 s and used the ECG data from the stable state in the middle segment to calculate heart rates.

A calcaneal sinus compression fracture occurred as a severe adverse event in this study. Due to loss of sensation in both lower extremities, the specific time point at which the injury occurred and the associated instrument could not be determined. After adaptive training using the exoskeleton robots and before training for HKAFO, the subject found that the skin temperature



of their left calf was higher than that of the right calf in the late afternoon. Moreover, the left ankle was clearly bluish with swelling when he was cleaning his body in the evening. Compression fracture of the calcaneus sinus was confirmed by computed tomography. The likely reason may be a lack of experience with exoskeletons. The subject had not received lower limb weight bearing training for the last 4 years. SCI population has different degrees of osteoporosis below the injury level, particularly in the lower femur and the upper tibia. The fracture rate in the SCI population has been reported to be from 1% to 21% of subjects and may increase with time (Giangregorio and McCartney, 2006). The causes of osteoporosis may be related to factors such as nerve damage, loss of muscle loading, reduced mechanical stimulation, and duration of paralysis (Giangregorio and McCartney, 2006; Dudley-Javoroski, 2008; Johnston et al., 2008; Groah et al., 2010). Weight bearing of both legs in the upright position and weight bearing of one leg during walking will greatly increase skeletal stress. The calcaneus sinus has the lowest bone density in the calcaneus, and the occurrence of a compressible fracture could be explained by this mechanism. In this study, the researchers initially did not assess the weight-bearing capacity of the subject's lower extremities, nor did they gradually increase the amount and duration of weight bearing prior to adaptive training using the exoskeleton. The traditional dual-energy x-ray bone density test is performed on the proximal femur and lumbar spine and does not target the areas where spinal cord injuries are most likely to result in decreased bone density. Therefore, after this serious adverse event, two additional inclusion criteria were added: to confirm that the subject had

the ability to bear weight in an upright position and to perform knee and ankle x-rays to confirm whether the bone density was severely reduced. Because of the inevitable decrease in bone density in the spinal cord injury population, the subject's ability to tolerate upright weight bearing is more important from our experience. Both lower limbs could tolerate the full weight-bearing position for at least 30 min before the use of the exoskeleton is suggested from this study.

In this study, there was also a case of pressure sore at the back of the heel. The reason was that the subject walked in shoes for the first time after SCI, and the shoes were new. He had a complete SCI with no lower limb sensory function. The shoe size was small and the material was stiff. While healthy people feel discomfort or pain in the heel when walking, people with SCI do not. The risk of pressure ulcers was reported in a clinical trial of Ekso, an exoskeleton-assisted walking device. The most common sites of skin erythema caused by pressure were the anterior tibia, greater trochanter of the femur, sacral region, abdomen, and dorsum of the feet (Kolakowsky-Hayner, 2013). These findings should serve as a reminder that skin color must be checked very carefully after each use of an exoskeleton device, particularly during the initial stages of use, due to lack of pain sensation.

Similar to the results of other studies, the 6MWT distance after wearing exoskeletons in this study was significantly higher than that when using the traditional non-dynamic orthosis, HKAFO; however, the walking distances in this research were shorter than those recorded in other ones. A meta-analysis by Miller et al. reported a summarized mean 6MWT distance of subjects wearing powered exoskeleton of 98 m (95% CI, 80–117 m) (Miller



et al., 2016). While Arazpour et al. showed that the mean 6MWT distance was  $120 \pm 12.98$  m in the exoskeleton group and  $90.20 \pm 10.63$  m in the HKAFO group (Arazpour et al., 2012). This difference may be related to the duration of learning to use the exoskeleton devices and HKAFO during the screening period. The training period in our study included 4–6 training hours per day but was relatively short (no longer than 1 week), while training periods in other studies ranged widely from 1 to 24 weeks. Most experiments involved 60–120 min of training per session, three times a week (Esquenazi et al., 2012; Zeilig et al., 2012; Fineberg et al., 2013; Kolakowsky-Hayner, 2013; Kressler et al., 2014; Benson et al., 2015; Hartigan et al., 2015; Kozłowski et al., 2015; Yang et al., 2015). If the training period was extended in this research, subject walking distances may have increased. However, the purpose of this study was to verify the safety and feasibility of an exoskeleton walking aid, not the subject's improvement in walking speed and function.

Similar to other studies, this study also used mean %HRI to evaluate the physiological cost during walking (Arazpour et al., 2012). The physiological cost of walking with exoskeleton devices was lower than that with HKAFO, due to their power assist function. Walking distance with the exoskeleton was longer than that with HKAFO, further indicating that walking with an exoskeleton device consumed less energy. In a randomized controlled research, the physiological cost index was reported ~50% lower with a powered exoskeleton relative to HKAFO (Arazpour et al., 2012). The RPE scores for the walking aids used in this study were also consistent with the results of other studies, with the exoskeleton group scoring 9–11 and the HKAFO group 14–15 (Arazpour et al., 2012; Kolakowsky-Hayner, 2013; Kressler et al., 2014).

Although subjects did not show obvious changes in systolic and diastolic blood pressure before and after walking with Aiwalker and Ailegs, they did tend to have a slight decrease in systolic and diastolic blood pressure after Aiwalker use. Most of the subjects also stated that Aiwalker gave them a very stable and safe feeling and that they could relax and enjoy walking, which may explain the slight decrease in blood pressure. Research indicated a slight increase in blood pressure after walking with Rewalk, a comparable exoskeleton device, relative to before walking. The mean pre-training blood pressure was 121/77 (SD = 1.43/7.4) mmHg, while the mean post-training blood pressure was 129/83 (SD = 4.09/7.4) mmHg. Faulkner et al. conducted a pilot study on walking training assisted by an Ekso exoskeleton robot for the SCI population (Faulkner et al., 2019). The results showed that arterial wave reflection could be improved by a mean reduction of 9% and the training led to favorable changes in mean arterial pressure and central diastolic blood pressure, with mean decreases of 5 and 7 mmHg, respectively. These data suggest that exoskeleton robot-assisted walking training may be beneficial to the vascular health of subjects with SCI; this warrants further study.

The exoskeleton robotics industry is developing rapidly worldwide. Both Ailegs and Aiwalker were able to facilitate subjects walking on the real ground with a human-like gait. However, currently, Ai-robot cannot be controlled by the user to start, stop, sit down, stand up, etc. Further research is needed

on (1) user control of the exoskeleton device, (2) personalized assistance provided by Ai-robot, and (3) the frequency and duration of training with Ai-robot, including gait speed and angle settings for each joint.

## CONCLUSION

Subjects with paraplegia (below T6 level) were able to walk safely and efficiently using the powered exoskeleton devices, Ailegs and Aiwalker, for overground ambulation with lower physiological cost. Satisfaction with Ailegs and Aiwalker was better than that with the traditional walking aid, HKAFO. The use of Ai-robot should be learned under the guidance of experienced medical personnel. The soft tissue compression at the strapping area and heel area needs to be checked after using the device. Subjects with SCI who have not recently trained to stand or walk will need to be weight-adapted before considering the use of an exoskeleton robot.

## DATA AVAILABILITY STATEMENT

The raw data supporting the conclusions of this article will be made available by the authors, without undue reservation.

## ETHICS STATEMENT

The studies involving human participants were reviewed and approved by the Ethical Committee of the First Affiliated Hospital of Nanjing Medical University (No. 2017-MD-069). The patients/participants provided their written informed consent to participate in this study. Written informed consent was obtained from the individual(s) for the publication of any potentially identifiable images or data included in this article.

## AUTHOR CONTRIBUTIONS

SC and ZW: manuscript writing. SC, YL, JT, XuW, LH, ZF, TX, JX, FG, YiW, JLo, XiW, and FL: subject recruitment and data collection. JLu and SC: data analysis. ZW and MS: design of the exoskeleton device. JLi, ZJ, XH, and YuW: study design and study supervision. All authors have read and approved the submitted version.

## FUNDING

This study was supported by Beijing Ai-Robotics Technology Co., Ltd, Beijing, China.

## ACKNOWLEDGMENTS

The authors would thank all the subjects who participated in the research, especially those who experienced adverse events, for their dedication, and the first subject who provided many valuable comments on the details of the research. Also, would also like to thank all the staff at Links Medical Scientific Co., Ltd. (Guangzhou, China) and Linkstart Med-Tech Company (Beijing,

China) for their great support in the application, coordination, data recording, and collation of the experiment. Furthermore, the authors are highly grateful to their colleagues for their extensive help with subject recruitment, screening and enrollment, and data collation.

## REFERENCES

- Adriaansen, J. J. E., van Asbeck, F. W. A., Lindeman, E., van der Woude, L. H. V., de Groot, S., and Post, M. W. M. (2012). Secondary health conditions in persons with a spinal cord injury for at least 10 years: design of a comprehensive long-term cross-sectional study. *Disabil. Rehabil.* 35, 1104–1110. doi: 10.3109/09638288.2012.712196
- Alashram, A. R., Annino, G., and Padua, E. (2021). Robot-assisted gait training in inspaniduals with spinal cord injury: a systematic review for the clinical effectiveness of Lokomat. *J. Clin. Neurosci.* 91, 260–269. doi: 10.1016/j.jocn.2021.07.019
- Arazpour, M., Bani, M. A., Hutchins, S. W., and Jones, R. K. (2012). The physiological cost index of walking with mechanical and powered gait orthosis in patients with spinal cord injury. *Spinal Cord* 51, 356–359. doi: 10.1038/sc.2012.162
- Benson, I., Hart, K., Tussler, D., and van Middendorp, J. J. (2015). Lower-limb exoskeletons for inspaniduals with chronic spinal cord injury: findings from a feasibility study. *Clin. Rehabil.* 30, 73–84. doi: 10.1177/0269215515575166
- Bessler, J., Prange-Lasonder, G. B., Schulte, R. V., Schaake, L., Prinsen, E. C., and Buurke, J. H. (2020). Occurrence and type of adverse events during the use of stationary gait robots—a systematic literature review. *Front. Robot. AI* 7:557606. doi: 10.3389/frobt.2020.557606
- Bouri, M., Stauffer, Y., Schmitt, C., Allemand, Y., Gnemmi, S., Clavel, R., et al. (2006). “The WalkTrainer: a robotic system for walking rehabilitation,” in 2006 *IEEE International Conference on Robotics and Biomimetics* (Kunming: IEEE).
- Brinkemper, A., Aach, M., Grasmücke, D., Jettkant, B., Rosteijs, T., Dudda, M., et al. (2021). Improved physiological gait in acute and chronic SCI patients after training with wearable cyborg hybrid assistive limb. *Front. Neurobot.* 15:723206. doi: 10.3389/fnbot.2021.723206
- Calabrò, R. S., Billeri, L., Ciappina, F., Balletta, T., Porcari, B., Cannavò, A., et al. (2022). Toward improving functional recovery in spinal cord injury using robotics: a pilot study focusing on ankle rehabilitation. *Expert Rev. Med. Devices* 19, 1–13. doi: 10.1080/17434440.2021.1894125
- Castro, M. J., Apple, D. F., Staron, R. S., Campos, G. E. R., and Dudley, G. A. (1999). Influence of complete spinal cord injury on skeletal muscle within 6 mo of injury. *J. Appl. Physiol.* 86, 350–358. doi: 10.1152/jappl.1999.86.1.350
- Chun, A., Asselin, P. K., Knezevic, S., Kornfeld, S., Bauman, W. A., Korsten, M. A., et al. (2019). Changes in bowel function following exoskeletal-assisted walking in persons with spinal cord injury: an observational pilot study. *Spinal Cord* 58, 459–466. doi: 10.1038/s41393-019-0392-z
- Dudley-Javoroski, S. (2008). Muscle and bone plasticity after spinal cord injury: Review of adaptations to disuse and to electrical muscle stimulation. *J. Rehabil. Res. Dev.* 45, 283–296. doi: 10.1682/JRRD.2007.02.0031
- Esquenazi, A., Talaty, M., Packel, A., and Saulino, M. (2012). The ReWalk powered exoskeleton to restore ambulatory function to inspaniduals with thoracic-level motor-complete spinal cord injury. *Am. J. Phys. Med. Rehabil.* 91, 911–921. doi: 10.1097/PHM.0b013e318269d9a3
- Faulkner, J., Martinelli, L., Cook, K., Stoner, L., Ryan-Stewart, H., Paine, E., et al. (2019). Effects of robotic-assisted gait training on the central vascular health of inspaniduals with spinal cord injury: a pilot study. *J. Spinal Cord Med.* 44, 299–305. doi: 10.1080/10790268.2019.1656849
- Fineberg, D. B., Asselin, P., Harel, N. Y., Agranova-Breyter, I., Kornfeld, S. D., Bauman, W. A., et al. (2013). Vertical ground reaction force-based analysis of powered exoskeleton-assisted walking in persons with motor-complete paraplegia. *J. Spinal Cord Med.* 36, 313–321. doi: 10.1179/2045772313Y.0000000126
- Fitzharris, M., Cripps, R. A., and Lee, B. B. (2013). Estimating the global incidence of traumatic spinal cord injury. *Spinal Cord* 52, 117–122. doi: 10.1038/sc.2013.135
- Fukuda, H., Morishita, T., Ogata, T., Saita, K., Hyakutake, K., Watanabe, J., et al. (2015). Tailor-made rehabilitation approach using multiple types of hybrid assistive limb robots for acute stroke patients: a pilot study. *Assist. Technol.* 28, 53–56. doi: 10.1080/10400435.2015.1080768
- Garnier-Villarreal, M., Pinto, D., Mummidisetty, C. K., Jayaraman, A., Tefertiller, C., Charlifue, S., et al. (2022). Predicting duration of outpatient physical therapy episodes for inspaniduals with spinal cord injury based on locomotor training strategy. *Arch. Phys. Med. Rehabil.* 103, 665–675. doi: 10.1016/j.apmr.2021.07.815
- Gee, C. M., Eves, N. D., Sheel, A. W., and West, C. R. (2021). How does cervical spinal cord injury impact the cardiopulmonary response to exercise? *Respir. Physiol. Neurobiol.* 293:103714. doi: 10.1016/j.resp.2021.103714
- Gee, C. M., Williams, A. M., Sheel, A. W., Eves, N. D., and West, C. R. (2019). Respiratory muscle training in athletes with cervical spinal cord injury: effects on cardiopulmonary function and exercise capacity. *J. Physiol.* 597, 3673–3685. doi: 10.1113/JP277943
- Giangregorio, L., and McCartney, N. (2006). Bone loss and muscle atrophy in spinal cord injury: epidemiology, fracture prediction, and rehabilitation strategies. *J. Spinal Cord Med.* 29, 489–500. doi: 10.1080/10790268.2006.11753898
- Groah, S. L., Lichy, A. M., Libin, A. V., and Ljungberg, I. (2010). Intensive electrical stimulation attenuates femoral bone loss in acute spinal cord injury. *PM R* 2, 1080–1087. doi: 10.1016/j.pmrj.2010.08.003
- Hartigan, C., Kandilakis, C., Dalley, S., Clausen, M., Wilson, E., Morrison, S., et al. (2015). Mobility outcomes following five training sessions with a powered exoskeleton. *Top Spinal Cord Inj. Rehabil.* 21, 93–99. doi: 10.1310/sci2102-93
- Heath, E. M. (1998). Borg's perceived exertion and pain scales. *Med. Sci. Sport Exer.* 30:1461. doi: 10.1249/00005768-199809000-00018
- Jang, Y.-C., Park, H.-K., Han, J.-Y., Choi, I. S., and Song, M.-K. (2019). Cardiopulmonary function after robotic exoskeleton-assisted over-ground walking training of a patient with an incomplete spinal cord injury. *Medicine* 98:e18286. doi: 10.1097/MD.00000000000018286
- Johnston, T. E., Smith, B. T., Oladeji, O., Betz, R. R., and Lauer, R. T. (2008). Outcomes of a home cycling program using functional electrical stimulation or passive motion for children with spinal cord injury: a case series. *J. Spinal Cord Med.* 31, 215–221. doi: 10.1080/10790268.2008.11760715
- Kang, Y., Ding, H., Zhou, H., Wei, Z., Liu, L., Pan, D., et al. (2017). Epidemiology of worldwide spinal cord injury: a literature review. *J. Neurorestoratol.* 6, 1–9. doi: 10.2147/JN.S143236
- Kolakowsky-Hayner, S. A. (2013). Safety and feasibility of using the Ekso™ bionic exoskeleton to aid ambulation after spinal cord injury. *J. Spine* S4, 1–8. doi: 10.4172/2165-7939.S4-003
- Kozlowski, A., Bryce, T., and Dijkers, M. (2015). Time and effort required by persons with spinal cord injury to learn to use a powered exoskeleton for assisted walking. *Top Spinal Cord Inj. Rehabil.* 21, 110–121. doi: 10.1310/sci2102-110
- Kressler, J., Thomas, C. K., Field-Fote, E. C., Sanchez, J., Widerström-Noga, E., Cilien, D. C., et al. (2014). Understanding therapeutic benefits of overground bionic ambulation: exploratory case series in persons with chronic, complete spinal cord injury. *Arch. Phys. Med. Rehabil.* 95, 1878–1887.e4. doi: 10.1016/j.apmr.2014.04.026
- Lai, Y.-J., Lin, C.-L., Chang, Y.-J., Lin, M.-C., Lee, S.-T., Sung, F.-C., et al. (2014). Spinal cord injury increases the risk of Type 2 diabetes: a population-based cohort study. *Spine J.* 14, 1957–1964. doi: 10.1016/j.spinee.2013.12.011
- Lajeunesse, V., Vincent, C., Routhier, F., Careau, E., and Michaud, F. (2015). Exoskeletons' design and usefulness evidence according to a systematic review of lower limb exoskeletons used for functional mobility by people with spinal cord injury. *Disabil. Rehabil. Assist. Technol.* 11, 535–547. doi: 10.3109/17483107.2015.1080766

## SUPPLEMENTARY MATERIAL

The Supplementary Material for this article can be found online at: <https://www.frontiersin.org/articles/10.3389/fnbot.2022.848443/full#supplementary-material>

- Lee, B. B., Cripps, R. A., Fitzharris, M., and Wing, P. C. (2013). The global map for traumatic spinal cord injury epidemiology: update 2011 global incidence rate. *Spinal Cord* 52, 110–116. doi: 10.1038/sc.2012.158
- Liusuwan, R. A., Widman, L. M., Abresch, R. T., Styne, D. M., and McDonald, C. M. (2007). Body composition and resting energy expenditure in patients aged 11 to 21 years with spinal cord dysfunction compared to controls: comparisons and relationships among the groups. *J. Spinal Cord Med.* 30, S105–S111. doi: 10.1080/10790268.2007.11754613
- Miller, L., Zimmermann, A., and Herbert, W. (2016). Clinical effectiveness and safety of powered exoskeleton-assisted walking in patients with spinal cord injury: systematic review with meta-analysis. *Med. Devices (Auckl)* 9, 455–466. doi: 10.2147/MDE.RS103102
- Mulcahey, M. J., Gaughan, J., Betz, R., Samdani, A., Barakat, N., and Hunter, L. (2013). Neuromuscular scoliosis in children with spinal cord injury. *Top Spinal Cord Inj. Rehabil.* 19, 96–103. doi: 10.1310/sci1902-96
- New, P. W., Baxter, D., Farry, A., and Noonan, V. K. (2015). Estimating the incidence and prevalence of traumatic spinal cord injury in Australia. *Arch. Phys. Med. Rehabil.* 96, 76–83. doi: 10.1016/j.apmr.2014.08.013
- Peshkin, M., Brown, D. A., Santos-Munne, J. J., Makhlin, A., Lewis, E., Colgate, J. E., et al. (2005). “KineAssist: a robotic overground gait and balance training device,” in *9th International Conference on Rehabilitation Robotics* (Chicago, IL: IEEE).
- Sezer, N. (2015). Chronic complications of spinal cord injury. *World J. Orthop.* 6:24. doi: 10.5312/wjo.v6.i1.24
- Shackleton, C., Evans, R., West, S., Derman, W., and Albertus, Y. (2021). Robotic walking to mitigate bone mineral density decline and adverse body composition in inspaniduals with incomplete spinal cord injury. *Am. J. Phys. Med. Rehabil.* doi: 10.1097/PHM.0000000000001937. [Epub ahead of print].
- Shah, P. K., Stevens, J. E., Gregory, C. M., Pathare, N. C., Jayaraman, A., Bickel, S. C., et al. (2006). Lower-extremity muscle cross-sectional area after incomplete spinal cord injury. *Arch. Phys. Med. Rehabil.* 87, 772–778. doi: 10.1016/j.apmr.2006.02.028
- Shuai, M. (2017). *Drive Control System and the Exoskeleton Robot That Uses It*. CN Patent No 206, 764, 764 U. Beijing: China National Intellectual Property Administration.
- Shuai, M. (2018a). *Adjustable Waist Support Apparatus and the Exoskeleton Robot That Uses It*. CN Patent No 108, 143, 593 A. Beijing: China National Intellectual Property Administration.
- Shuai, M. (2018b). *Suspension Apparatus and the Exoskeleton Robot That Uses It*. CN Patent No 108, 143, 584 A. Beijing: China National Intellectual Property Administration.
- Shuai, M. (2019). *Retractable Structure and The Exoskeleton Robot That Uses It*. CN Patent No 109, 431, 752 A. Beijing: China National Intellectual Property Administration.
- Shuai, M. (2020). *Adjustable Waist Apparatus and the Exoskeleton Robot That Uses It*. CN Patent No 111, 434, 323 A. Beijing: China National Intellectual Property Administration.
- Stampacchia, G., Rustici, A., Bigazzi, S., Gerini, A., Tombini, T., and Mazzoleni, S. (2016). Walking with a powered robotic exoskeleton: subjective experience, spasticity and pain in spinal cord injured persons. *NeuroRehabilitation* 39, 277–283. doi: 10.3233/NRE-161358
- Tappan, R., Raad, J., and Moore, J. (2012). Measurement characteristics and clinical utility of the 6-minute walk test among inspaniduals with spinal cord injury. *Arch. Phys. Med. Rehabil.* 93, 1675–1676. doi: 10.1016/j.apmr.2012.07.005
- Tefertiller, C., Hays, K., Jones, J., Jayaraman, A., Hartigan, C., Bushnik, T., et al. (2018). Initial outcomes from a multicenter study utilizing the indego powered exoskeleton in spinal cord injury. *Top Spinal Cord Inj. Rehabil.* 24, 78–85. doi: 10.1310/sci17-00014
- Widman, L. M., Abresch, R. T., Styne, D. M., and McDonald, C. M. (2007). Aerobic fitness and upper extremity strength in patients aged 11 to 21 years with spinal cord dysfunction as compared to ideal weight and overweight controls. *J. Spinal Cord Med.* 30, S88–S96. doi: 10.1080/10790268.2007.11754611
- Williams, A., Deegan, E., Walter, M., Stothers, L., and Lam, T. (2021). Exoskeleton gait training to improve lower urinary tract function in people with motor-complete spinal cord injury: a randomized pilot trial. *J. Rehabil. Med.* 53:jrm00222. doi: 10.2340/16501977-2864
- Yang, A., Asselin, P., Knezevic, S., Kornfeld, S., and Spungen, A. (2015). Assessment of in-hospital walking velocity and level of assistance in a powered exoskeleton in persons with spinal cord injury. *Top Spinal Cord Inj. Rehabil.* 21, 100–109. doi: 10.1310/sci2102-100
- Zeilig, G., Weingarden, H., Zwickler, M., Dudkiewicz, I., Bloch, A., and Esquenazi, A. (2012). Safety and tolerance of the ReWalkTM exoskeleton suit for ambulation by people with complete spinal cord injury: a pilot study. *J. Spinal Cord Med.* 35, 96–101. doi: 10.1179/2045772312Y.0000000003

**Conflict of Interest:** ZW and MS were employed by Beijing Ai-Robotics Technology Co., Ltd.

The remaining authors declare that the research was conducted in the absence of any commercial or financial relationships that could be construed as a potential conflict of interest.

**Publisher's Note:** All claims expressed in this article are solely those of the authors and do not necessarily represent those of their affiliated organizations, or those of the publisher, the editors and the reviewers. Any product that may be evaluated in this article, or claim that may be made by its manufacturer, is not guaranteed or endorsed by the publisher.

Copyright © 2022 Chen, Wang, Li, Tang, Wang, Huang, Fang, Xu, Xu, Guo, Wang, Long, Wang, Liu, Luo, Wang, Huang, Jia, Shuai and Li. This is an open-access article distributed under the terms of the Creative Commons Attribution License (CC BY). The use, distribution or reproduction in other forums is permitted, provided the original author(s) and the copyright owner(s) are credited and that the original publication in this journal is cited, in accordance with accepted academic practice. No use, distribution or reproduction is permitted which does not comply with these terms.



# sEMG-Based Gesture Classifier for a Rehabilitation Glove

Dorin Copaci\*, Janeth Arias, Marcos Gómez-Tomé, Luis Moreno and Dolores Blanco

Department of Systems Engineering and Automation, Carlos III University of Madrid, Madrid, Spain

Human hand gesture recognition from surface electromyography (sEMG) signals is one of the main paradigms for prosthetic and rehabilitation device control. The accuracy of gesture recognition is correlated with the control mechanism. In this work, a new classifier based on the Bayesian neural network, pattern recognition networks, and layer recurrent network is presented. The online results obtained with this architecture represent a promising solution for hand gesture recognition (98.7% accuracy) in sEMG signal classification. For real time classification performance with rehabilitation devices, a new simple and efficient interface is developed in which users can re-train the classification algorithm with their own sEMG gesture data in a few minutes while enables shape memory alloy-based rehabilitation device connection and control. The position of reference for the rehabilitation device is generated by the algorithm based on the classifier, which is capable of detecting user movement intention in real time. The main aim of this study is to prove that the device control algorithm is adapted to the characteristics and necessities of the user through the proposed classifier with high accuracy in hand gesture recognition.

## OPEN ACCESS

### Edited by:

Luciano Luperini Menegaldo,  
Federal University of Rio de Janeiro,  
Brazil

### Reviewed by:

Jiahao Chen,  
Institute of Automation (CAS), China  
Yingwei Zhang,  
Institute of Computing Technology  
(CAS), China  
Denis Delisle Rodriguez,  
Federal University of Espirito Santo,  
Brazil

### \*Correspondence:

Dorin Copaci  
dcopaci@ing.uc3m.es

**Received:** 30 July 2021

**Accepted:** 15 April 2022

**Published:** 30 May 2022

### Citation:

Copaci D, Arias J, Gómez-Tomé M,  
Moreno L and Blanco D (2022)  
sEMG-Based Gesture Classifier for a  
Rehabilitation Glove.  
Front. Neurobot. 16:750482.  
doi: 10.3389/fnbot.2022.750482

**Keywords:** sEMG, gestures recognition, neural networks, hand rehabilitation, shape memory alloy

## 1. INTRODUCTION

As a result of complex human evolution, the hand is one of the most versatile parts of our body (Craig and Taylor, 1955). As well as giving us the ability to perform several tasks during our daily life, it is also one of the key factors that differentiates humans from other species. Its 27 degrees of freedom provide a mechanism able to manipulate nearly every kind of object.

According to different studies, a system placed in the brain takes the responsibility of hand control (Hirzinger et al., 1998; Biagiotti et al., 2003; Yue et al., 2017). The control system structure is complex and difficult to understand, which hinders the motor function recovery process after a stroke, disease, or disorder.

With the aim to improve the rehabilitation techniques applied to the human hand, several robotic solutions have been proposed over the past 20 years. The main benefit of robotic rehabilitation is that it allows an active interaction between the patient and the rehabilitation system, which is essential in the recovery process (Londoa et al., 2017).

Taking into consideration the interaction between the user and the rehabilitation system, rehabilitation procedures can be classified into two groups:

- Physical interaction (PI): physical contact between the rehabilitation system and the user is needed in order to apply several forces to the patient during the task performance;
- Emotional interaction (EI): the system encourages the user during the process in the absence of physical contact.



PI rehabilitation using robotic systems requires direct physical contact between the robot and patient during the rehabilitation process. External forces provided by the robot help or hinder patient movement. Usually, the first steps of the rehabilitation process are completed with robotic assistance, while in the last stages, the user receives robotic opposition during the rehabilitation tasks.

For instance, Pyk et al. (2008) proposed PITS, a glove-based robotic system with different position sensing devices. In the same way, the NJIT-RAVR structure is a ring gimbal with six degrees of freedom for hand rehabilitation (Qiu et al., 2009). Both systems perform similarly. A glove covers the hand of the patient which, depending on the system, gives more or less freedom to the user. For example, more freedom is given by PITS as its glove is not linked to any structure, whereas the NJIT-RAVR glove is placed in a ring gimbal with a limited number of degrees of freedom. Also, virtual reality is used for displaying several interactive tasks in the systems. Patients must perform the task in contact with the robotic system which has a haptic master able to capture hand movements and translate them into the computer space. The complexity level of the task displayed is adapted to each patient recovery phase.

Several advantages such as creating a safer environment with nearly zero risk of injury, motivating the patient with different interactive exercises, automation of the rehabilitation process, adaptation of the device to different rehabilitation stages, and quantifying the rehabilitation process making it objective are characteristic of PI rehabilitation robotic devices.

EI rehabilitation focuses on different tasks completed in collaboration with a robotic system using one of these three methods: (1) imitation: robot movements are followed by the user, (2) motivation: robot-user interaction using sounds or visual effects encourages the user during the process, and (3) imitation and motivation: combination of (1) and (2) (Maciejasz et al., 2014). In this context, systems such as CosmoBot (Wood et al., 2009) or Ursus (Calderita et al., 2014) are prominent. The process is simple: the robot performs an action that must be followed by the user. At the same time, the system monitors the progress and status of the patient during the recovery process.

Recently, several studies have proposed the use of electroencephalogram (Zhang et al., 2021, 2022) or electromyography (Ahsan et al., 2011; Asif et al., 2020; Pamungkas and Simatupang, 2020) sensors in order to control robotic rehabilitation procedures, because they are able to detect the patient's intention of motion. Electromyography sensors measure the electrical signals originated in the muscles for quantifying its activity. Information such as the activity performed by the muscle or the effort needed to perform the activity could be obtained by surface electromyography (sEMG) analysis.

Specifically, the type of hand gesture performed by a person could be identified using electromyography sensors (Binh et al., 2005; Alsheakhali et al., 2011; Khan and Ibraheem, 2012). sEMG data captured by electromyography sensors contain features that could be extracted in order to train different neural network architectures. Neural networks are used to predict the type of

hand gesture executed by the user. For example, Ahsan et al. (2011) used a back-propagation algorithm to train a network architecture for hand gesture classification using sEMG reaching an 88.4% average success rate of identification. Asif et al. (2020) achieved a 92% average classification accuracy for the same issue using a convolutional neural network architecture. Another possibility presented by Pamungkas and Simatupang (2020) is the use of Bayesian neural network architecture for sEMG classification, which was able to reach a 90.61% average accuracy. All of these architectures could be combined in order to obtain higher accuracy rates (He et al., 2018; Asif et al., 2020).

Hand gesture recognition using sEMG is useful not only for rehabilitation issues (knowing the type of gesture is helpful for the patient during the rehabilitation tasks and allows them to correct the application of movement opposition), but also for building artificial hands or robotic structures with the ability to imitate human motions.

Another rehabilitation system which combines physical contact with robotic devices and sEMG detection is AMADEO (Londoa et al., 2017), a platform with five end-effectors where the five fingers can be placed. Several exercises are displayed in a screen while, at the same time, sEMG signals are recorded. sEMG features are used to help the patient during the activity and to evaluate the rehabilitation process.

Although several works address the topic of sEMG signals for hand gesture identification, few works use these identified gestures for hand rehabilitation devices and they usually focus on the mixed gesture identification between the wrist movements and the hand gesture. In this paper, we propose to identify six hand gestures using only finger movements, which will be implemented in a high-level control algorithm for hand rehabilitation with an exo-glove.

Specifically, this study is focused on the implementation of a PI rehabilitation system combined with an sEMG recognition architecture for hand gesture identification. The goal is to evaluate new classifier structures for sEMG recognition. A novel hand gesture classifier for sEMG based on a neural network architecture (a combination between the Bayesian neural network, pattern recognition networks, and layer recurrent network) is developed, which enables the generation of the position of reference for PI rehabilitation devices according to the specific patient movement intention. Results from this study will ultimately provide insights on the feasibility of the neural networks' structures proposed for hand gesture recognition.

Compared to other state-of-the-art solutions, our approach's contribution is:

- The development of a novel neural network architecture based on the Bayesian neural network, pattern recognition networks, and layer recurrent network with 98.7% accuracy for hand gesture recognition.
- The generation of a new algorithm to calculate the position reference for the rehabilitation device according to the user intention of movement.
- Previous contributions could be used in real time. They were tested in a hand rehabilitation device actuated by shape memory alloy (SMA) and developed by our research group.

- A new user-friendly interface was developed for personalized sEMG acquisition, neural network training and verification, and control of the rehabilitation device.

This paper contains five sections. Section 2 presents the methodology with a description of the sEMG data acquisition and processing method, neural network architectures used for gesture classification, and the rehabilitation system: actuator characteristics and design, rehabilitation device, and the high-level control algorithm. Preliminary experimental results are covered in Section 3. Section 4 presents the discussion and Section 5 proposes the conclusions and future works.

## 2. MATERIALS AND METHODS

### 2.1. Experimental Protocol

A gesture recognition algorithm is proposed with an individual calibration of the neural networks carried out simultaneously, with the objective of using this information in rehabilitation glove control. For this reason, the experimental protocol consists of:

- The sEMG signal acquisition for a new database consisted of 250 samples per each proposed gesture. One sample represents a 300 ms sEMG signal. In total, 1,500 samples were stored.
- The features were extracted from the sEMG windows (this was done during the acquisition process);
- The features for the 1,500 samples were used in the neural network architecture training and offline evaluation process.
- A total of 100 new samples per gesture (in total 600 samples) were acquired and in this case, storing of the output of the proposed classifier architecture and the user gesture occurred at the same time. With this information the confusion matrix was built to evaluate the proposed architecture in the online evaluation process.
- On the last step, the gesture recognition algorithm was connected with the glove rehabilitation device, and the data from sEMG, gesture, tendon positions, and reference were stored.

### 2.2. Proposed Hand Gesture Identification

sEMG data are used for hand gesture identification. Considering the hand movement on daily activities and the consecrated hand rehabilitation movements, six hand gestures are proposed for the identification:

- Relax, lack of user movement;
- Gripper (pinch), tap the thumb with the index finger;
- Thumb up, thumb extension;
- Grip, replication of object holding;
- Fist, close the hand;
- Open hand, finger extension;

The proposed classifier must be able to identify these gestures regardless of the user's hand: left or right, and based on this, must generate the reference for the rehabilitation glove. Right hand gestures are shown in **Figure 1**.

sEMG data are collected using the Thalmic Labs Myo Gesture Control Armband (Huitzil-Velasco et al., 2017). The armband features eight sEMG sensors with a stream rate of 200 Hz.

According to Merletti and Parker (2004), Konrad (2005) almost all of the EMG signal power is located between 10 and 250 Hz, and considering the Nyquist-Shannon sampling theorem, the amplifier device band will need to be set to 500 Hz or higher. In this case, a part of the signal will be lost, the armband frequency being limited to 200 Hz. sEMG sensors are placed over the forearm giving information of the activity of the arm muscle groups responsible for hand and wrist movements. As a non-invasive method, the accuracy of the sEMG acquisition process depends on well-known factors such as electrode position, skin factors, ambient noises, and movement noises.

Also, it is usually good practice to rectify sEMG a priori only considering its absolute value. Note that this change can affect other characteristics, like the frequency which will be doubled.

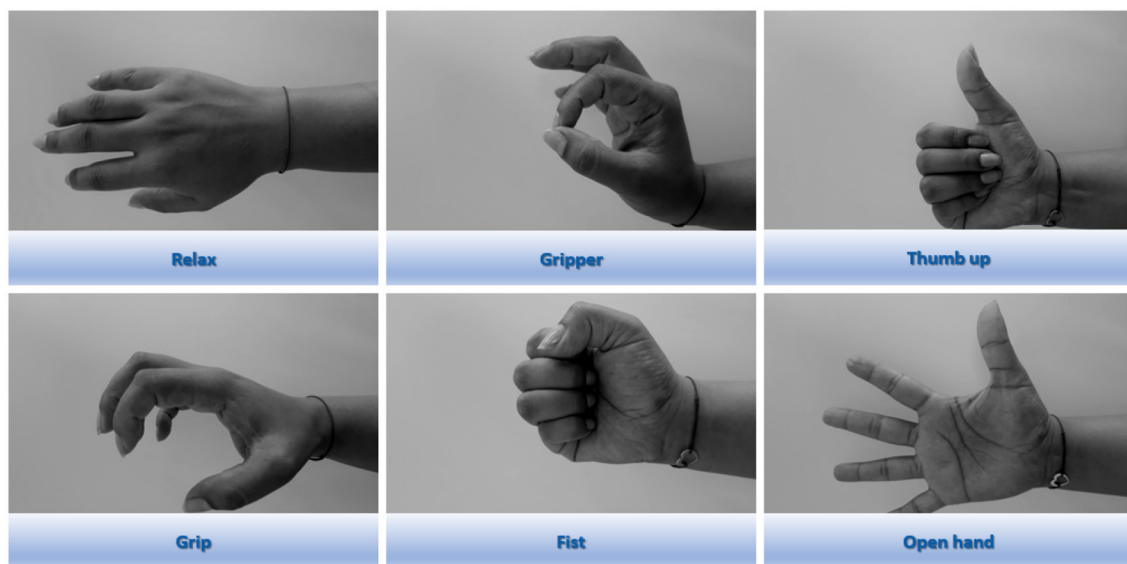
Another interesting process is sEMG filtering. It is a good technique for noise reduction as unwanted harmonics are removed. Several studies use upper cutoff frequency filters (around 500 Hz). In general, notch filters with lower cutoff frequencies between 10 and 500 Hz are common, although it depends on the study and the limb analyzed. Butterworth architecture filters are the most common. Balbinot and Favieiro (2013) used a 60 Hz notch filter to remove the noise characteristic of the power line (in Europe it would have been 50 Hz).

Another possibility is to normalize the sEMG amplitude as it prevents noise variations with no influence on the classification (Konrad, 2005).

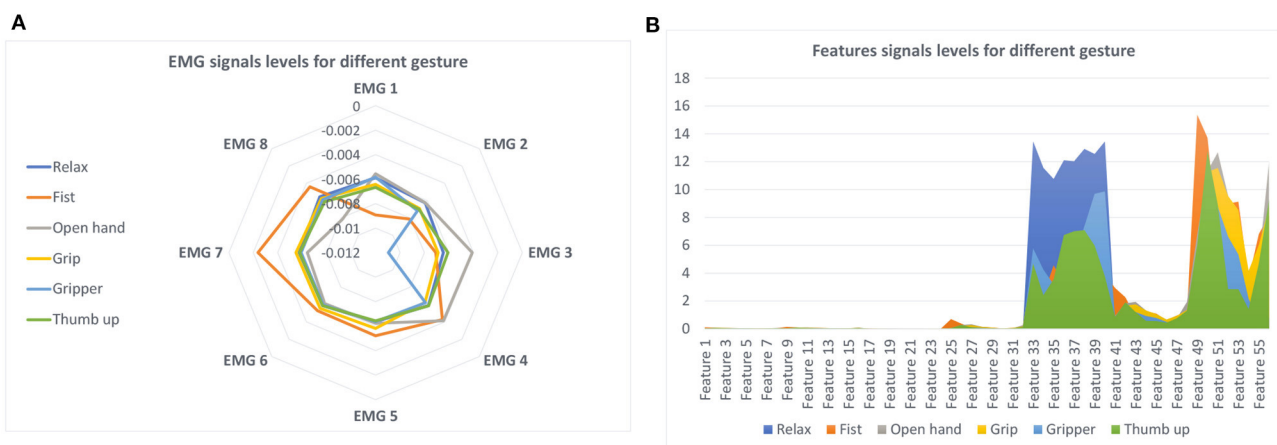
After these previous steps: rectification, filtering, and normalization, sEMG can be more easily interpreted and classified. In this work only the rectification process was implemented because the signals were filtered and normalized by the Myo SDK (Tomaszewski, 2016).

The sEMG level for each gesture is presented in **Figure 2A**. After the feature extraction process (**Figure 2B**), an average of 1,000 samples from one of each electrode is acquired for each proposed gesture. The fist gesture can be easily distinguished from the open hand gesture, however, other gestures like the gripper and thumb up gestures are more similar. Moreover, when the average of several signals is plotted on the graph (**Figure 2A**), a certain signal segment for a short time can negatively influence the classification.

Results demonstrate that sEMG signal segmentation and feature extraction are needed. There are two main techniques for signal segmentation: adjacent segmentation and overlapping segmentation. The adjacent segmentation technique was selected. In this approach, sEMG data are split into adjacent windows. According to Oskoei and Hu (2007), a real-time classification is considered when the length of the segment lasts less than 300 ms, but the longer the segment, the more accurate the classification of the gesture. For this reason, segments were fragmented into windows with a fixed length of 300 ms. In each window, seven time-domain features were calculated: (1) mean average value (MAV), (2) root mean square (RMS), (3) variance (VAR), (4) signal strength indicator (SSI), (5) zero-crossing (ZC), (6) wavelet transform (WL), and (7) side scatter (SSC). These represent 56 values extracted from each window. Values 1–8 represent the first feature MAV for each electrode (8 electrodes), from 9 to 16 represent the second feature RMS for each electrode,



**FIGURE 1** | Hand gestures performed during sEMG signal recording.

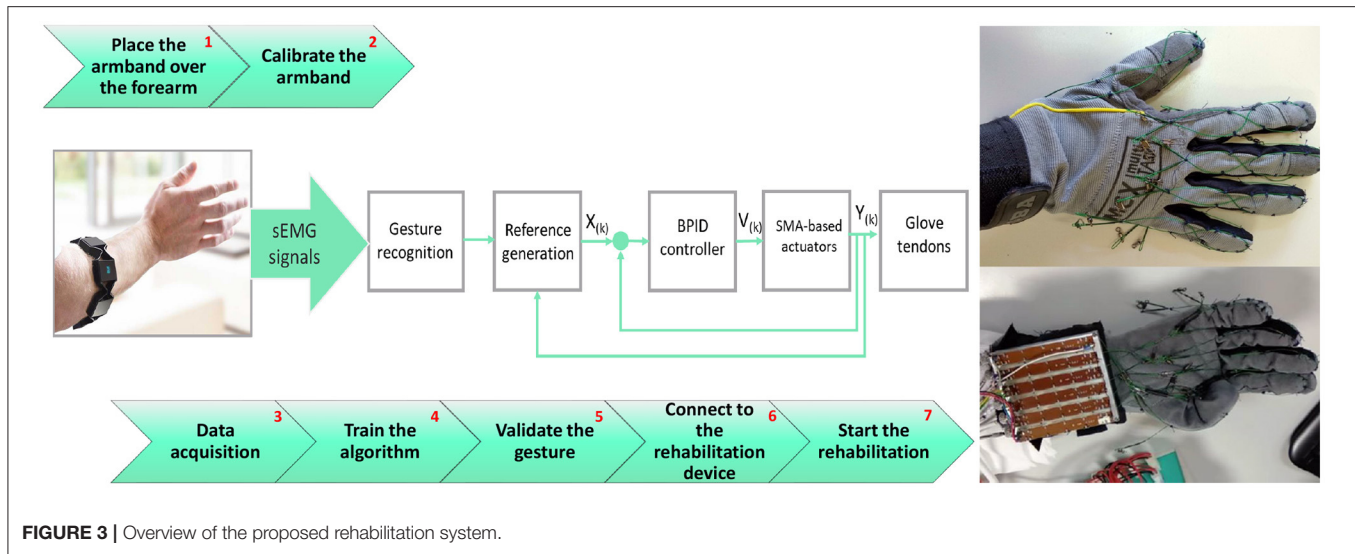


**FIGURE 2** | Gesture according with the sEMG signal and features: **(A)** sEMG signals; **(B)** signals features.

and so on. Previous studies used these features for classification (Phinyomark et al., 2012; Phinyomark and Scheme, 2018; Barioulet al., 2019; Wu et al., 2020; Khushaba et al., 2022).

Features from 100 segments for each gesture were extracted where the mean value is represented in **Figure 2B**. Although the first features do not seem to be relevant, the last features showed notable differences in the gesture recognition. Similarly to sEMG, noticeable differences could be observed when observing the fist and hand open gestures; but the gripper and thumb up gestures could be easily confused.

These characteristics will be used as an input for the proposed classifier for gesture recognition. An overview of the proposed rehabilitation system can be seen in **Figure 3**. After a minimal set-up consisting in placing the armband over a forearm and its calibration (steps 1 and 2 from **Figure 3**), the data acquisition process, training the network architecture, and the validation of gesture recognition are necessary (steps 3, 4, and 5). The process continues with the control algorithm which generates the tendon references according to the gesture recognition and ends with glove rehabilitation device connection, and then the rehabilitation therapy can begin (steps 6 and 7).



## 2.3. Classifier Architecture

During the classification process, each hand gesture presented in Section 2.2 was related with static position information given by the sEMG features. The proposed classifier in this work is based on three sub-architectures: a Bayesian neural network (BNN) in parallel with an artificial neural network (ANN) in which the results are connected in series with a layer recurrent network (LRN). The final gesture classification is the result of the LRN. The proposed architecture can be seen in **Figure 4**. Each supervised architecture was configured and trained as follow:

- **ANN:** A feedforward network with the ability to classify different inputs according to target classes. The target data for pattern recognition networks consist of arrays of all zero values except for a 1 in element  $i$ , where  $i$  is the class it represents. In this case, there is a 56-feature input array whose target is represented by a 6-element vector, each one for a specific gesture recognition. The proposed architecture contains two layers; the first hidden layer of eight neurons and the output layer with six neurons corresponding to the six gestures. Weights and bias parameters of the neurons were adjusted using the scaled conjugate gradient (Hestenes and Stiefel, 1952) and its performance was evaluated with cross-entropy. Like BNN, ANN was trained with 250 samples but in this case the data were divided into 70% for training, 15% for testing, and another 15% for validation. The data for validation and testing were not used during the training process.
- **BNN:** A probabilistic classifier based on the naive Bayes assumption (predictors are independent of one another within each class) (Martinez-Arroyo and Sucar, 2006). The network, built with the classification learner app in Matlab 2020b (The MathWorks, Inc., 2021), uses a kernel distribution because the Gaussian distribution often results in error due to the non-Gaussian distribution of the sEMG features. For offline training, 250 samples were used from each hand motion and a five-fold cross validation was employed during the training

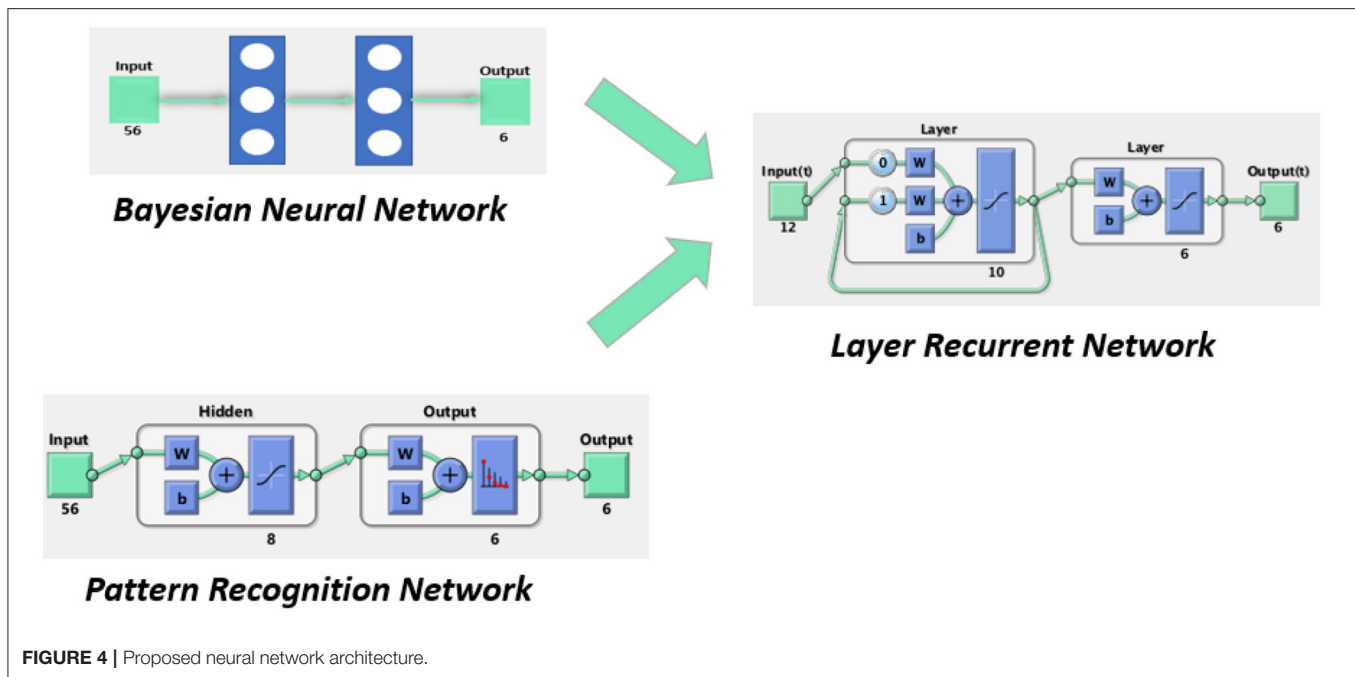
process: each set of five samples was divided into four samples for training and one sample for validation.

- **LRN:** This architecture presents two layers: a hidden layer with 10 neurons that receive information from the past by taking into account the previous results for future predictions and a output layer with 6 neurons; a vector of 6 positions, one for each gesture. LRN input results from the output of the first two networks combined in a 12-element array. LRN remembers a past sample structure by using a feedforward network, being capable of analyzing sequential data structures, such as consecutive hand gestures. LRN is trained using 250 samples using the Levenberg-Marquardt algorithm (Levenberg, 1944) while its performance is tested with mean squared error. LRN receives 12 inputs obtained from 6 inputs of the BNN prediction over these 250 samples and another 6 inputs produced by ANN over the same 250 samples. Similarly with the ANN training process, the data were divided into 70% for training, 15% for testing, and another 15% for validation.

## 2.4. User Interface

Though the armband device must be placed in a certain position on the forearm, the possibility that the electrodes are placed over the same muscle fiber in two different rehabilitation sessions is very low. For this reason, a new personalized dataset was created before each rehabilitation session from the user sEMG (forearm muscles sEMG) data. During this process, features are extracted from each sEMG segment and a file with the name of the motion and the number of the sample is stored in a folder called Dataset. Each sample contains a  $56 \times 1$  double array, from the seven features for each sEMG segment. For building the neural network architecture,  $56 \times 600$  feature samples were collected for each motion, resulting in a database with  $56 \times 3600$  samples. Depending on each supervised architecture, the whole dataset is split randomly into 70% for neural network training, 15% for validation, and another 15% for tests for the ANN and LRN, and using the five-fold cross validation for BNN.





To automate and speed up this process, a user interface is developed in Matlab 2020b (The MatWorks, Inc., 2021) as an intuitive way of following the seven steps detailed in the pipeline in **Figure 5**. The interface is shown in **Figure 5**.

After the armband is placed, the user is asked to perform each gesture in order to create the personalized database. After that, the button—network training—automatically trains the Bayesian classifier. For gesture validation, the switch button is turned on and the lamp of the recognized gesture is colored green while the other lamps are red. The bottom switch buttons are used to connect the rehabilitation device and start the therapy.

## 2.5. Rehabilitation System

Restoring the hand function after spinal cord injury (SCI), cerebral vascular accident (CVA), or different musculoskeletal disorders represents a challenging issue. Rehabilitation gives the user the possibility to recover the ability to perform daily life tasks. Recently, several exoskeleton devices have been proposed for hand rehabilitation over the last years, but most of them focused on soft and low-cost designs, offering a passive rehabilitation without taking into account user movement intention. The rehabilitation device used in this paper is an SMA-actuated glove. It is a wearable device, with low weight and noiseless performance due to the actuators' characteristics.

### 2.5.1. SMA-Based Actuator

SMA is an alloy, commonly Ni-Ti, which has the property to deform when it is cold and recover its pre-deformed shape ("memory") when heated. This process takes place between the two transformation phases: martensite at low temperature and austenite at high temperature. To achieve the necessary transformation temperature, electrical energy is transformed into thermal energy thanks to the Joule effect. Due to the

shape memory effect (SME), thermal energy is transformed in mechanical work. The SMA-based actuator used in the proposed rehabilitation device is based on Copaci et al. (2019a), and it is composed by:

- Bowden cable: a metallic spiral covered with a nylon sheath. It has the property of SMA wire force transmission, achieving the flexibility property. Also, it helps in wire heat dissipation in the cooling stage.
- Polytetrafluoroethylene (PTFE) tube. The isolator is placed between the SMA wire and Bowden cable and is able to resist more than 250°C. It is considered as a solid lubricant because it decreases the friction in the SMA wire.
- SMA wire. Flexinol wire from the Dynalloy company was used (DYNALLOY, Inc., 2020). With a diameter of 0.51 mm, it applies a force of approximately 34.91 N. The wire activation temperature is 90°C where an ~4% displacement of the wire length is reached.

According to the necessary finger tendon displacement (~8 cm), 2 m of SMA wire is needed. Due to the actuator flexibility, it can take on the human body shape and can possibly be used to guide the user.

### 2.5.2. Glove Rehabilitation Device

The rehabilitation glove is presented in **Figure 3**. A strong but comfortable mobility glove is used to withstand the strength of the cables (tendons) without tearing and, at the same time, allowing natural movements to the fingers. Twelve tendons were guided/routed over the glove to generate the flexion/extension movement in each finger contraction (five tendons for extension and another five for flexion) and another two to help in the thumb opposition movement.

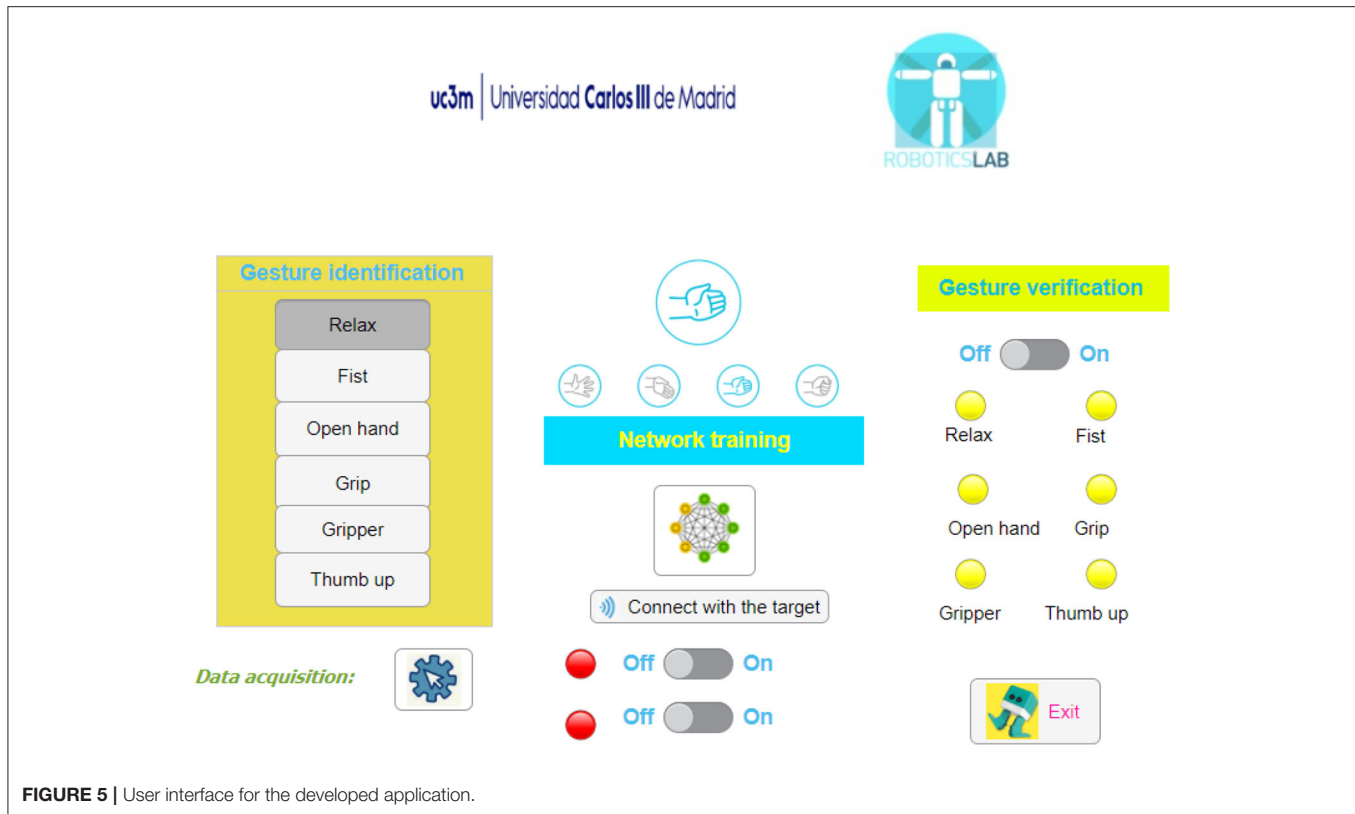


FIGURE 5 | User interface for the developed application.

Glove tendons are connected with SMA-based actuators through a sensor box composed of six rails where a small cylindrical piece, which connects the SMA wire with the tendons, could be moved when the actuator is enabled. The same piece is connected to a Bourns PTA Potentiometer, PTA6043-2015DPB103 which is able to measure each tendon displacement.

In addition to the six position sensors, we used electronic hardware of the glove rehabilitation device including a microcontroller and a power circuit essential in controlling the SMA-based actuators as feedback for the controller loop.

The electronic power circuit for SMA wires is based on MOSFET transistors which can be activated by pulse width modulation (PWM) generated by the controller. MOSFET transistors open and close the circuit with a power supply for actuators. The control hardware architecture can manage six different actuators; in this case each actuator was an SMA wire. The whole architecture has been developed by our research group.

The controller board is based on the STM32F407 Discovery kit (STM, 2021), from STMicroelectronics, which is programmed using Matlab/Simulink® (Caballero et al., 2016). The board manages signals from the sensors, executes the control actuator algorithm, and generates the required PWM signals. The low-level control used for this device is based on a bilinear proportional integral derivative (BPID) controller, developed by the research group presented in Villoslada et al. (2015), Copaci et al. (2019b).

The identified hand gesture together with the sensors positions signals from the rehabilitation device and generates six reference signals building a representation of the user's movement intention for each finger (two references for the thumb). In this way, an active reference is generated involving the patient undergoing rehabilitation therapy, leading to a faster recovery.

## 2.6. Reference Generation

According to the rehabilitation device structure, these six references are duplicated with the opposite ones to provide the inputs for the low-level control algorithm (six references for the flexion actuators and six references for the extension actuators) for the antagonistic movement. However, the current device only presents a boxed sensor and it can only be tested in one of the movements, for example the flexion movement.

The entry algorithm from the sEMG data is captured by the glove tendon movements as can be seen schematically in **Figure 3**.  $X_{(k)}$  represents the reference generated by the high-level algorithm,  $V_{(k)}$  represents the control signal (PWM generated by the microcontroller for the electronic power circuit), and  $Y_{(k)}$  represents the position of the actuator signals from the position sensors.

The reference generation block from **Figure 3** receives the recognized gesture as input, a six-number array from 0 to 1, where each number represents the probability of being the gesture performed. The maximum value of the array represents the gesture predicted. Apart from the gesture array, a six-position

array is generated. In this case, the position represents the maximum actuator reference reached according to the gesture. Using this six-position array, the actual actuator positions, the actual reference positions, and two adjustable increments (six references in real time for the actuators) are generated. Increments are used to change the reference speed and the finger movement speed. A higher increment is required to move from the current reference to the current position of the actuator, and a slower one is required to generate a smoother reference when we are close to the current position (used when the reference wants to be followed, during the gesture performance).

### 3. RESULTS

#### 3.1. Offline Classifier Results

The three architectures presented in Section 2.3 were offline-evaluated with a database with 1,500 samples (250 features for each gesture). The results obtained with each architecture are detailed here.

For the ANN architecture, the samples were split into three groups: 70, 15, and 15% for training, validation, and testing, where the validation and test data were not used in network training. After the network training, the confusion matrix of each group was determined as shown in **Figure 6**.

In **Figure 6**, the diagonal cells (in blue) correspond to observations/gestures that are correctly classified. The off-diagonal cells correspond to incorrectly classified observations. In the validation and test confusion matrix, as can be observed, the gesture recognition is 99.1%, where the predicted percentage or output corresponds to the rows and the target class corresponds to the columns. The last row represents the normalized row which summarizes the percentages of correctly and incorrectly classified observations for each true class. The last column, a normalized-column summary, displays the percentages of correctly and incorrectly classified observations for each predicted class. For example, in the confusion matrix test (**Figure 6**), one fist gesture was classified as a grip gesture. In this case, the predicted fist gestures were classified correctly with 100% accuracy (last column, first row) but the predicted grip gestures were classified correctly with only 97.7% accuracy (last column, second row). In the last row, first column, 96.9%, of the fist gestures were correctly classified for the true fist class.

The kernel naive Bayes classifier achieved 99.2% accuracy. The confusion matrix is presented in **Figure 7A** where five samples from the pinch gesture were classified as an open hand gesture, five samples for the relax gesture were confused with the thumb up gesture, and one sample of the grip and thumb up gestures were classified as the relax gesture. **Figure 7B** presents the parallel coordinate prediction where each sample is represented (correct classified—continuous line and incorrect classified—dotted line).

With the results of the two architectures and the output target, the LRN architecture was trained. Similar with the ANN case, the data were split into three groups before the network training. The best validation performance was obtained after 57 epochs of training, with a value of 0.00144.

#### 3.2. Online Classifier Results

For online validation, with the trained architectures, a new dataset was stored containing the outputs of each architecture and target gesture. According to these data, the confusion matrix of each architecture was built. Only 100 samples of the training database were used for the final three-network architecture testing. The ANN and BNN classifier responses are represented in the confusion arrays in **Figure 8**.

According to the results presented in **Figure 8B**, gesture classification with BNN is more accurate with a 97.0% hit rate compared with the ANN architecture which had a 93.3 % hit rate (**Figure 8A**). Although the BNN architecture presents better results in general, the ANN architecture for a specific gesture presents a good classification, for example the classification results of the pinch gesture. To reduce gesture confusion, a combination of both architectures was proposed using another neural network, LRN, which also takes into account the past classification gesture. The online results of this LRN architecture can be seen in **Figure 9**.

Results presented in **Figure 9** show that the proposed hand gestures can be classified with a precision of 98.7%. The three-neural network architecture increases the final hit rate in comparison with previous BNN or ANN approaches. The neural network was tested with different users obtaining a percentage between 92 and 99%.

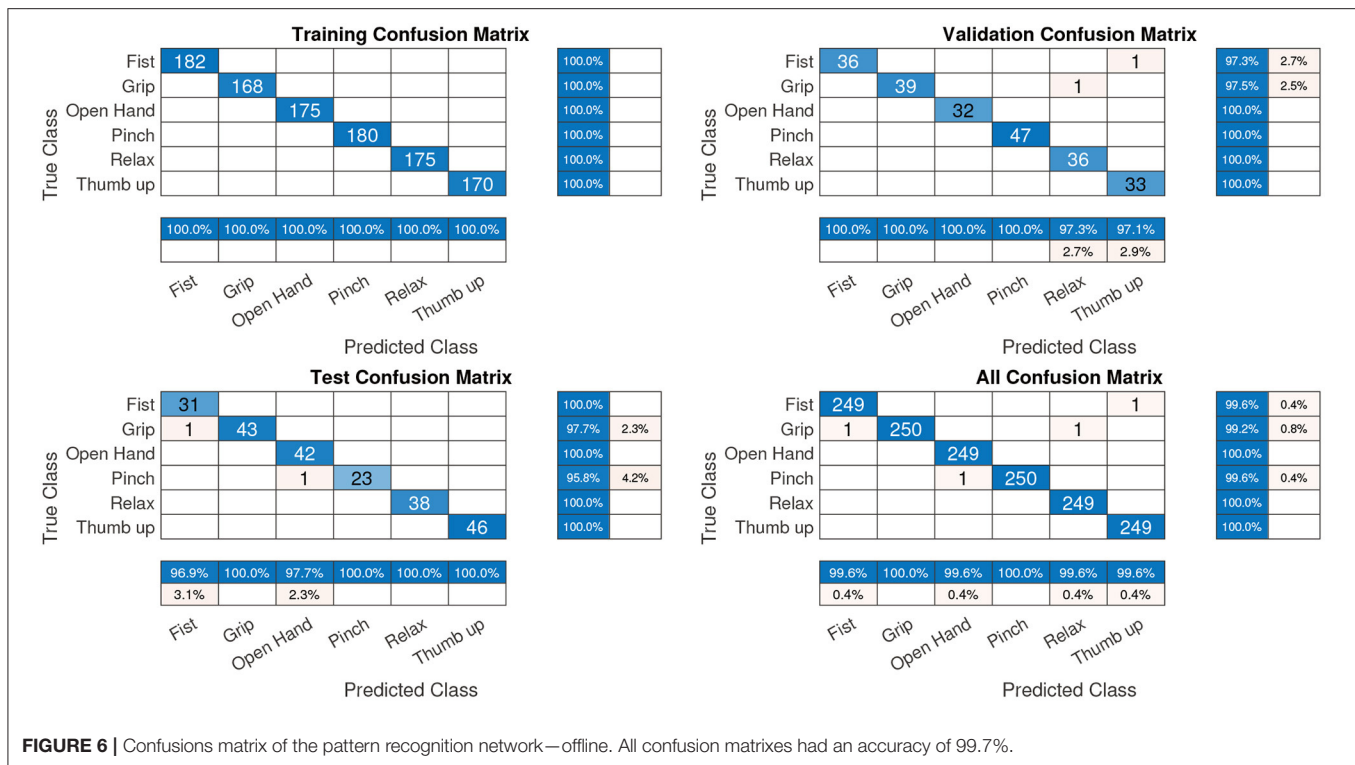
The whole hand gesture classification process takes approximately 0.12 s while sEMG window segmentation lasts 0.3 s meaning the whole classification process takes less than 0.5 s. Time consumption depends on the computer components measuring the times. We utilized an Intel (R) CORE (TM) i7-5500U CPU @ 2.40 GHz and 16 GB RAM in Windows 10 64bits. A specific database for a new user and all neural network training with 100 samples for each gesture (in an automated way with the interface) requires 3–5 min, depending on each user experience.

#### 3.3. Gesture Recognition and Reference Generation

Gesture recognition and reference generation evaluation according to the user's movement intention are performed using a new healthy subject who has not tested the Myo Armband with this algorithm before. The rehabilitation device is placed in a test bench over the forearm, below the elbow, and the process starts with data acquisition. Overall, 100 samples were recorded in the database for each gesture. Neural networks were trained with these data. Finally, the user must perform some gestures to test the gesture recognition system. The system is connected to the rehabilitation device.

Some gestures are recorded for 40 s. sEMG data from eight sensors are presented in **Figure 10**. Signals are related to:

- from  $t = 0$  s to  $t = 4.5$  s, the hand is relaxed. Actuators are off and there is free movement of the hand.
- from  $t = 4.5$  s to  $t = 10.25$  s, the fist gesture is performed. The actuator step reference intention (movement intention represented in **Figure 11**) for each finger is 60 mm, presenting all the fingers in a flexion movement for closing the hand.



**FIGURE 6 |** Confusions matrix of the pattern recognition network—offline. All confusion matrixes had an accuracy of 99.7%.

The reference intention is not the final reference which is the actuator input. The input reference to the actuators is composed by the intention reference helped by the increments.

- from  $t = 10.25$  s to  $t = 16.76$  s, the hand open gesture is presented. In this case, the finger intention reference is 0 mm, so the rehabilitation device structure, which only presents actuators for flexion, is left to free the hand and is opened by the user.
- from  $t = 16.76$  s to  $t = 20.18$  s, the gripper gesture is shown, in which the thumb flexion, thumb opposition, index finger, and middle finger have a step reference intention of 40 mm while the last two fingers (ring and pinky) have a reference intention of 60 mm to simulate the gripper gesture position.
- from  $t = 20.18$  s to  $t = 29.97$  s, the user performs the grip gesture. All the actuators have a step reference intention of 40 mm.
- from  $t = 29.97$  s to  $t = 35.46$  s, the thumb up gesture is found. The thumb flexion and the opposition actuators have a step reference intention of 0 mm while the rest of the fingers have a step reference intention of 60 mm.
- from  $t = 35.46$  s to  $t = 40$  s, the hand relaxed gesture finishes the test.

Neural networks can clearly identify each hand motion achieving accuracy in each gesture recognition. According to **Figure 11**, gestures are clearly identified except for a little instability at  $t = 22$  s. Also, the transition between gestures could be identified as a different gesture. For example, at  $t = 35$  s, the user switches from the thumb up gesture to the relax gesture, but in this transition, a grip gesture was identified.

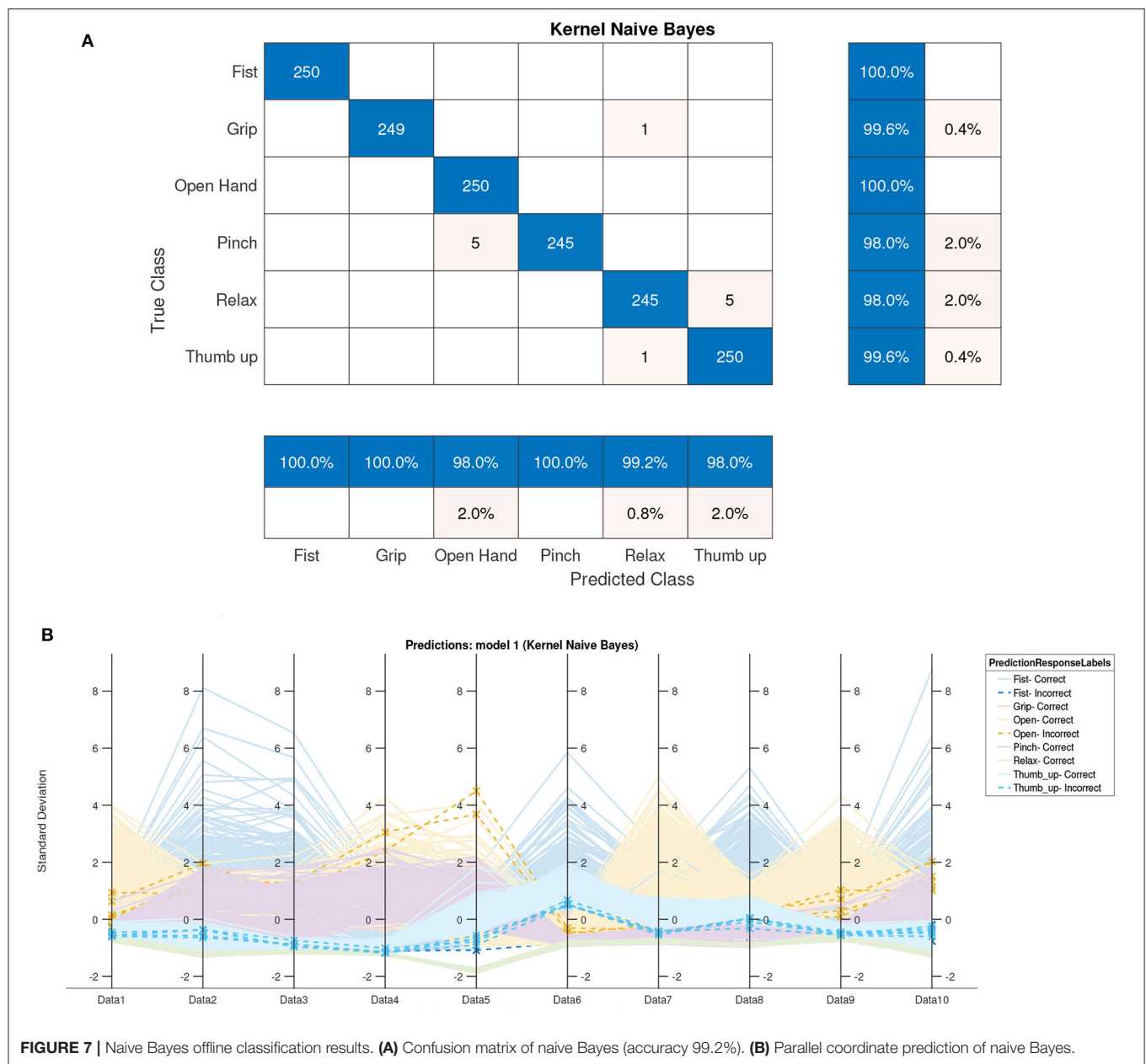
According to the movement intention (black signal in **Figure 11**), the actuator reference (red signal) is generated. The movement velocity (the slope) could be modified thanks to the increments which can be personalized. The green signal represents the actuator position, which is related to the finger position. For example, the error between the reference and the actuator position between  $t = 11$  to  $t = 17$  s is due to the actuator behavior (the SMA-based actuator needs to be cold to expand).

## 4. ANALYSIS AND DISCUSSION

The proposed classifier achieved 98.7% precision with the gesture classification, which is a promising result. In this work, according to the final application (generating the rehabilitation glove reference) only finger movements were considered due to the fact that the rehabilitation device did not permit wrist movement.

It is difficult to compare the state-of-the-art methods with our data acquisition and network training method. In this work the process consists in acquiring data (600 samples), training the proposed architecture, and after that, starting the rehabilitation therapy. This personalizes the classifier for a specific user. This approach has the disadvantage that the user spends 3-5 min acquiring the data and training the classifier but offers good accuracy in gesture classification. If the classifier is not retrained for a new user, the accuracy of the classifier decreases depending on different characteristics: how the armband is collocated, muscles route, and so on. The literature does not personalize this process using a dataset which contains samples from different subjects. With this point of view, they do not spend time in the training process with the user as the neural network is already



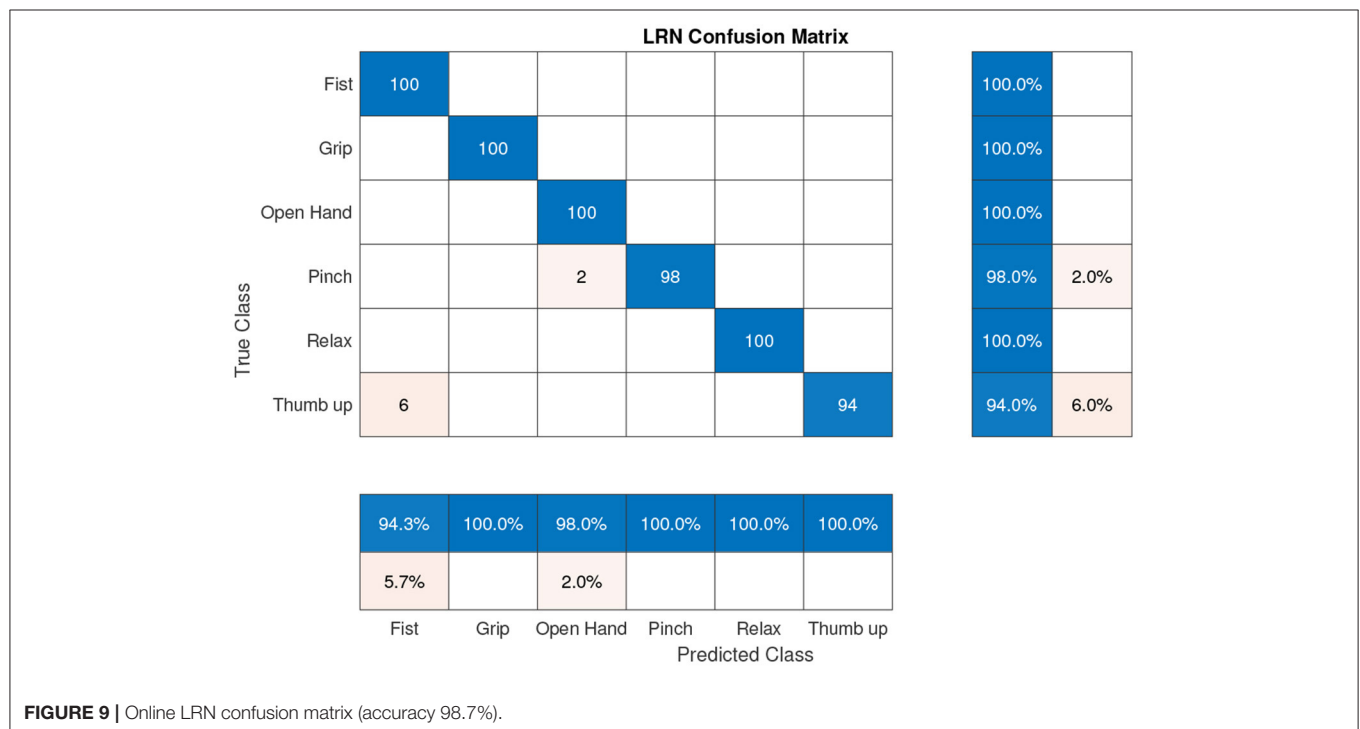
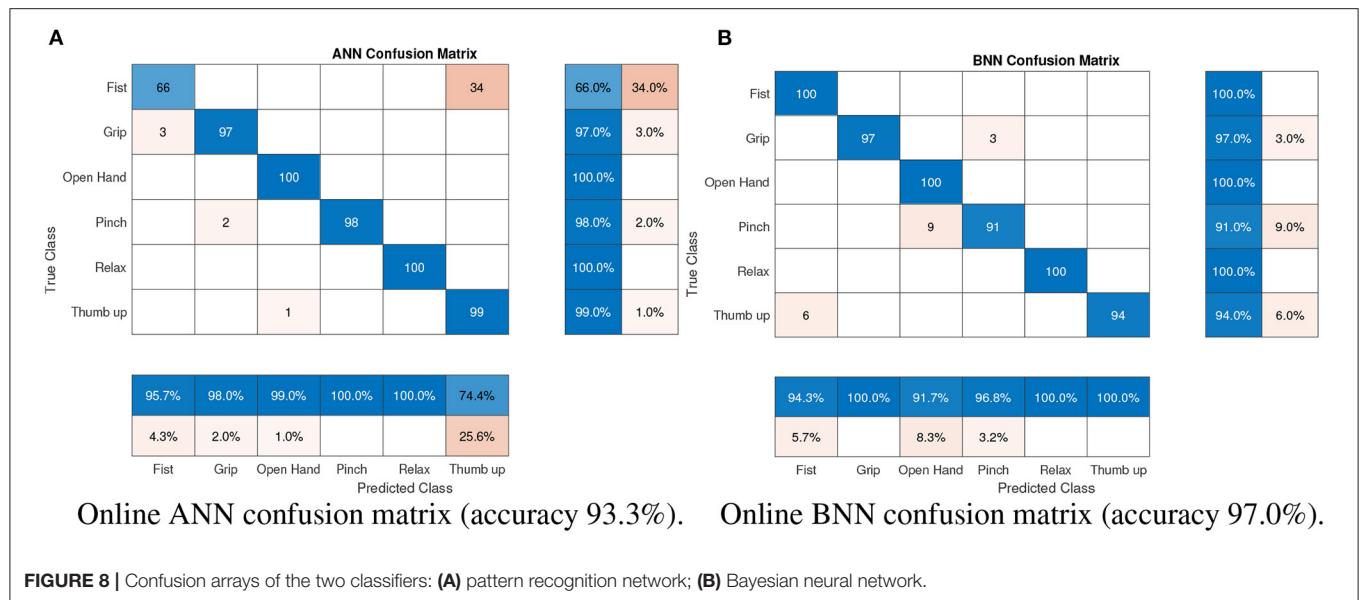


trained, which is more comfortable for the user. In contrast, the classification results are poorer.

Compared with the literature (although gestures are different), using the same device with feedforward neural networks, 90.1% accuracy is achieved for the fist, wave-in, wave-out, open, and pinch gestures by the system proposed by Benalcazar et al. (2018). In our case, with the six gestures (relax, fist, grip, gripper, open hand, and thumb up), the feedforward (pattern recognition network) method achieved 93.3% accuracy online. In Ahsan et al. (2011), they built a feedforward network with one hidden layer (10 neurons with tangsig activation function) and one output layer (4 neurons with purelin activation function) for left, right,

up, and down gestures, presenting 89.2% precision. Likewise, the architecture proposed by Ahsan et al. (2011) was replicated and has been tested with our dataset achieving 93.8% accuracy. Asif et al. (2020) developed a convolutional neural network tested in real time with 18 subjects for close hand, flex hand, extend hand, and fine grip gestures, reaching  $83.7 \pm 13.5\%$ ,  $71.2 \pm 20.2\%$ ,  $82.6 \pm 13.9\%$ , and  $74.6 \pm 15\%$  hit rates, respectively. This last case could not be replicated as they used a deep learning architecture.

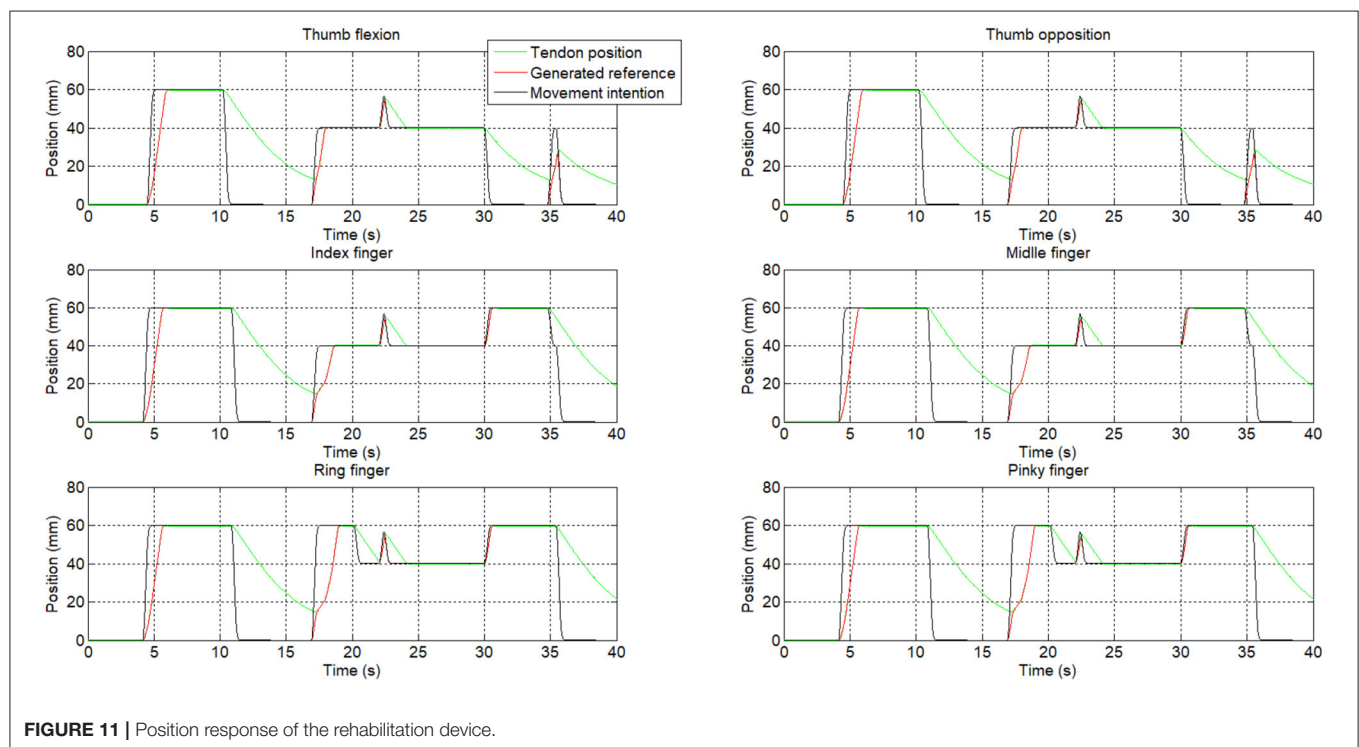
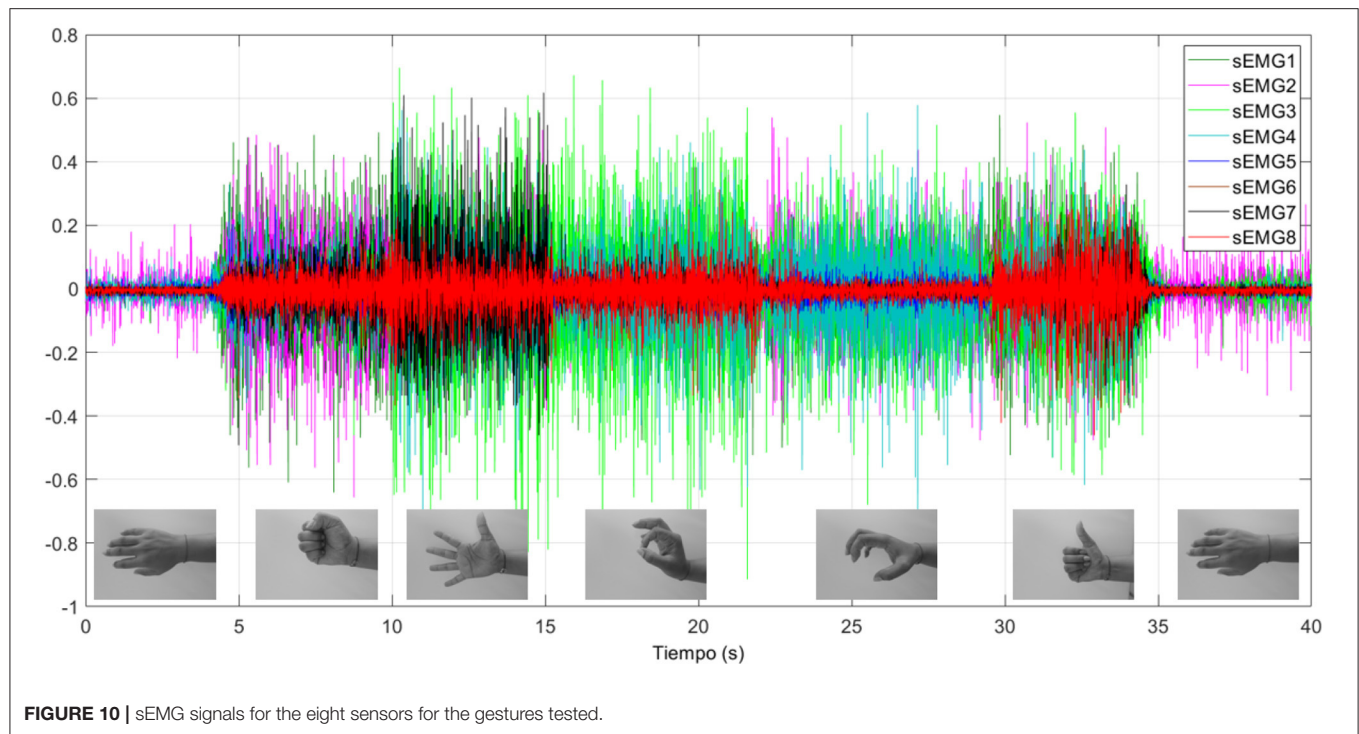
A well-known database, NinaPro Database 5 (Pizzolato et al., 2017), was used to test this architecture. The sEMG features of this dataset were acquired with two Myo Armbands, in total 16 channels. For this test only the first 8 channels corresponding



to the first Myo armband were selected for more similarity with this work. The presented results were obtained with only one Myo armband. Before the test, the data were segmented, and from each segment the 56 features were extracted. In parallel, the target gesture was stored to be used for supervised training. This database consists of 13 gestures, for this reason the proposed architecture was modified according to this at 13 outputs. In this case the accuracy result for the 13 gesture classification was 58.5%. The confusion matrix of this dataset can be seen in **Figure 12**. The biggest confusion was between the gestures

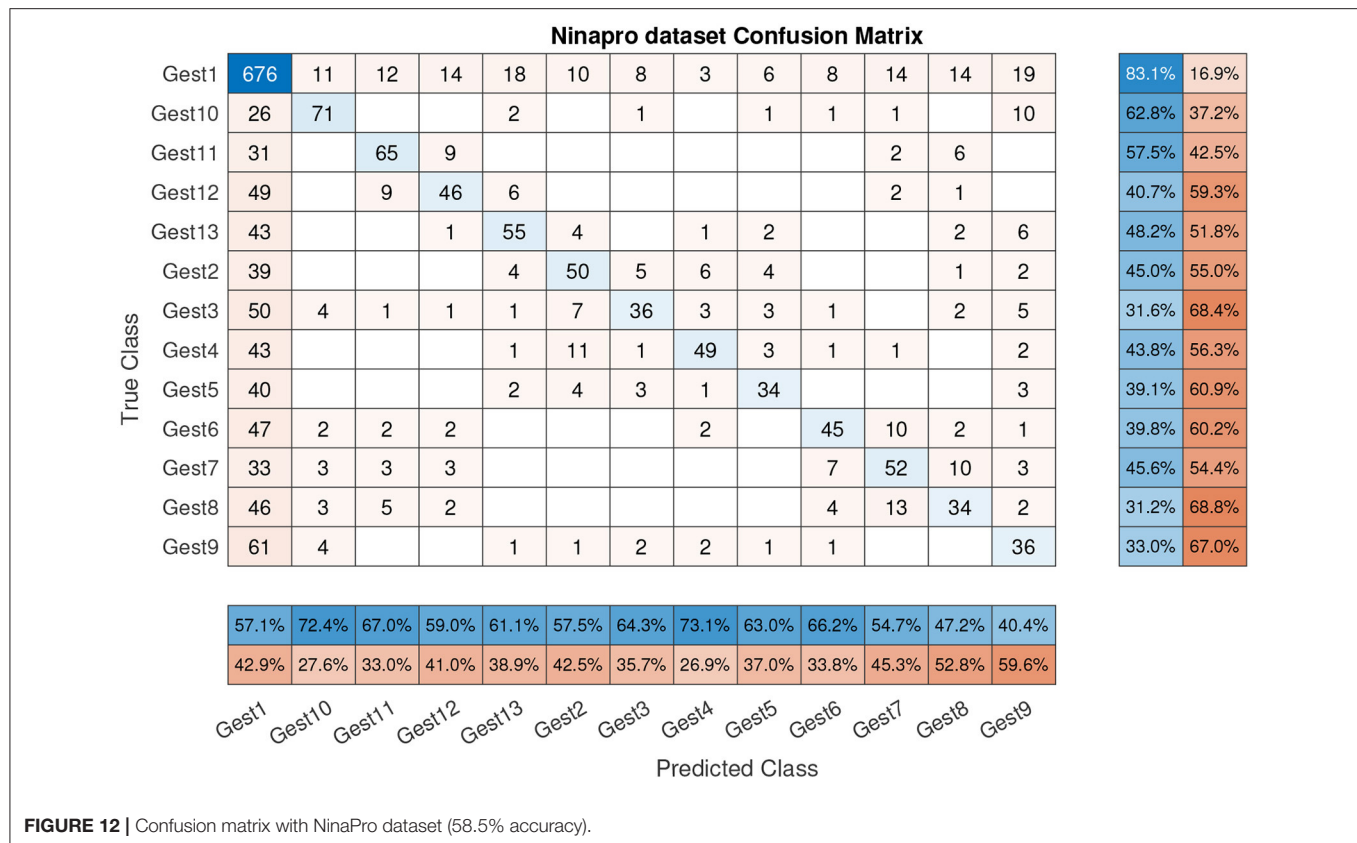
(gesture 2 to gesture 13) and the relaxed gesture. This can be influenced by the target gesture data (a scalar value) which were created for each 300 ms segment (60 samples). This target data were set with the stimulus value from the dataset, the value of the sample  $n = 31$ . In our case, when the database is created for a new user, we store each gesture separately in parallel assigning the target value.

Similar research with the NinaPro database obtained an accuracy between 42.47 and 68.98% (Côté-Allard et al., 2019) using deep learning algorithms. In this case, only one Myo



armband was used and the sEMG signal was split into 260 ms segments, observing that the classifier accuracy grew with the training repetition. In another work, the accuracy of the classifier was between 81.9 and 90.1% (Wei et al., 2019), the better score was obtained with the multi-view convolutional neural network using both Myo armbands (16 channels)

and a maximum of 83.9% using only one Myo armband. Accordingly, to these previous studies, the channel number influences the classifier accuracy; more information presents better results. Also, the deep learning algorithms present good results, but the necessary time to train these algorithms was not presented.



To better understand all processes during neural network training, a dataset with 56 features  $\times$  600 samples was used for statistical analysis. Performance of the proposed neural network (output vector of each gesture) was compared statistically using a one-way analysis of variance (ANOVA), in Matlab 2020b. Results were declared statistically significant if they were associated with  $p < 0.05$ .

The precision, recall, and f-score of the LRN confusion matrix presented in **Figure 9** were calculated obtaining a score of 0.99 for precision, 1 for recall, and an F1 score of 0.994.

The proposed classifier presents 98.7% accuracy, but this value can be influenced by the user characteristics and also by the hardware and the method with which the signals were stored. Combining different neural networks presents promising results for gesture recognition, with a reasonable time to acquire new data and retrain neural network architectures. According to the results obtained with the NinaPro dataset, the deep learning architecture presents 25.4% better results (a better result with similar hardware of 83.9%). In our case, the proposed architecture can be easily retrained with a personalized user database (100 samples /gesture), where this number of samples can be a limitation for the deep learning architectures. Also, future works will include a test with different users where the sEMG signal can be altered and where personalized classifiers can be a good approach for a good classification.

A limitation of the proposed method is constraining the user to acquire the data and retrain the algorithm at the beginning of therapy for good results.

## 5. CONCLUSIONS

Neural networks are a promising alternative to identify hand gestures depending on the sEMG signals. The proposed architecture - composed by the probabilistic, Bayesian, and temporal networks - offers a good accuracy for hand gesture identification, with a hit rate precision of 98.7%, higher than the previous results mentioned in the literature. Nevertheless, state-of-the-art papers use different gestures which use different muscle groups, so comparison between results is not representative.

This work studied different architectures of shallow and deep neural networks and the best result was reached when combining a probabilistic network in parallel with a Bayesian network and whose results fed a temporal network. To automatically train these architectures, an application was developed which enables sEMG data acquisition for the Myo Armband for a specific user and trains the network's architecture in less than 5 min, guaranteeing a personalized good classification of gestures in real time. Indeed, the application allows the connection with a hand rehabilitation device. Opposite from other solutions, the interface proposed accurately achieved the hand gesture identification (six gestures created only by finger movement), generating reference for the rehabilitation device and a direct connection with it.

According to the hand gesture recognition, a high-level algorithm was developed to generate the necessary reference for the rehabilitation device of the actuators (thumb flexion,



thumb opposition, index, middle, ring, and pinky fingers). This algorithm generates the reference according to the user's intention of movement, motivating them to participate in the rehabilitation therapy. In this way, rehabilitation therapy is more effective.

In the future, the rehabilitation device presented in this paper may be improved by adding the extension actuators and connecting the movement of the actuators with each finger position. The proposed algorithm was tested only on a few healthy subjects and more tests need to be applied. Also, the algorithm needs to be tested and validated by different subjects with neural and muscle disorders.

## DATA AVAILABILITY STATEMENT

The original contributions presented in the study are included in the article/**Supplementary Material**, further inquiries can be directed to the corresponding author/s.

## ETHICS STATEMENT

The studies involving human participants were reviewed and approved by the Research Ethics Committee of the Universidad Rey Juan Carlos Madrid, with the internal register number 26/12. Written informed consent to participate in this study was provided by the participants.

## REFERENCES

- Ahsan, M. R., Ibrahimy, M. I., and Khalifa, O. O. (2011). "Electromyography (EMG) signal based hand gesture recognition using artificial neural network (ANN)," in *2011 4th International Conference on Mechatronics* (Kuala Lumpur), 1–6. doi: 10.1109/ICOM.2011.5937135
- Alsheekhali, M., Skaik, A., Aldahdouh, M., and Alhelou, M. (2011). "Hand gesture recognition system," in *Information & Communication Systems*, ed W. Mardni (Ibriid: Faculty of Computer & Information Technology Jordan University of Science & Technology).
- Asif, A. R., Waris, A., Gilani, S. O., Jamil, M., Ashraf, H., Shafique, M., et al. (2020). Performance evaluation of convolutional neural network for hand gesture recognition using EMG. *Sensors* 20, 1642. doi: 10.3390/s20061642
- Balbinot, A., and Favieiro, G. (2013). A neuro-fuzzy system for characterization of arm movements. *Sensors* 13, 2613–2630. doi: 10.3390/s130202613
- Barioul, R., Fakhfakh, S., Derbel, H., and Kanoun, O. (2019). "Evaluation of EMG signal time domain features for hand gesture distinction," in *2019 16th International Multi-Conference on Systems, Signals Devices (SSD)* (Istanbul), 489–493. doi: 10.1109/SSD.2019.8893277
- Benalcazar, M. E., Anchundia, C. E., Zea, J. A., Zambrano, P., Jaramillo, A. G., and Segura, M. (2018). "Real-time hand gesture recognition based on artificial feed-forward neural networks and EMG," in *2018 26th European Signal Processing Conference (EUSIPCO)* (Rome), 1492–1496. doi: 10.23919/EUSIPCO.2018.8553126
- Biagiotti, L., Lotti, F., Melchiorri, C., and Vassura, G. (2003). *How far is the human hand? a review on anthropomorphic robotic end-effectors*. Available online at: <https://citeseerx.ist.psu.edu/viewdoc/summary?doi=10.1.1.104.7899>
- Binh, N. D., Shuichi, E., and Ejima, T. (2005). "Real-time hand tracking and gesture recognition system," in *Proceedings of International Conference on Graphics, Vision and Image Processing (GVIP-05)* (Cairo), 362–368. Available online at: <https://citeseerx.ist.psu.edu/viewdoc/summary?doi=10.1.1.87.9769>

## AUTHOR CONTRIBUTIONS

DB and LM oversaw project administration and funding acquisition. MG-T developed the neural network architectures and carried out the experiments. DC collaborated on experiments and supervised the research. JA developed the application and the high-level algorithm for the rehabilitation device. DC, MG-T, and DB wrote the manuscript. All authors read and approved the final manuscript.

## FUNDING

For this research, we received funding from the Sistema robótico para propiciar la marcha en niños pequeños con Parálisis Cerebral under Grant PID2019-105110RB-C32/AEI/10.13039/501100011033, Spanish research project; from RoboCity2030-DIH-CM, Madrid Robotics Digital Innovation Hub, S2018/NMT-4331, funded by Programas de Actividades I&D en la Comunidad de Madrid; and co-funding from Structural Funds of the EU.

## SUPPLEMENTARY MATERIAL

The Supplementary Material for this article can be found online at: <https://www.frontiersin.org/articles/10.3389/fnbot.2022.750482/full#supplementary-material>

- Caballero, A. F., Copaci, D. S., Pecina, Á. V., Rojas, D. B., and Lorente, L. M. (2016). Sistema avanzado de protipado rápido para control en la educación en ingeniería para grupos multidisciplinares. *Revista Iberoamericana de Automática e Informática Industrial* 13, 350–362. doi: 10.1016/j.riai.2016.05.004
- Calderita, L. V., Manso, L. J., Bustos, P., Suárez-Mejías, C., Fernández, F., and Bandera, A. (2014). Therapist: towards an autonomous socially interactive robot for motor and neurorehabilitation therapies for children. *JMIR Rehabil. Assist. Technol.* 1, e1. doi: 10.2196/rehab.3151
- Copaci, D., Blanco, D., and Moreno, L. E. (2019a). Flexible shape-memory alloy-based actuator: mechanical design optimization according to application. *Actuators* 8, 63. doi: 10.3390/act8030063
- Copaci, D., Martin, F., Moreno, L., and Blanco, D. (2019b). SMA based elbow exoskeleton for rehabilitation therapy and patient evaluation. *IEEE Access* 7, 31473–31484. doi: 10.1109/ACCESS.2019.2902939
- Côté-Allard, U., Fall, C. L., Drouin, A., Campeau-Lecours, A., Gosselin, C., Glette, K., et al. (2019). Deep learning for electromyographic hand gesture signal classification using transfer learning. *IEEE Trans. Neural Syst. Rehabil. Eng.* 27, 760–771. doi: 10.1109/TNSRE.2019.2896269
- Craig, L., and Taylor, R. J. S. (1955). The anatomy and mechanics of the human hand. *Artif. Limbs* 2, 22–35.
- DYNALLOY, Inc. (2020). *Technical Characteristics of FLEXINOL*.
- He, Y., Fukuda, O., Bu, N., Okumura, H., and Yamaguchi, N. (2018). "Surface EMG pattern recognition using long short-term memory combined with multilayer perceptron," in *2018 40th Annual International Conference of the IEEE Engineering in Medicine and Biology Society (EMBC)* (Honolulu, HI: IEEE), 5636–5639. doi: 10.1109/EMBC.2018.8513595
- Hestenes, M. R., and Stiefel, E. (1952). Methods of conjugate gradients for solving linear systems. *J. Res.* 6, 49. doi: 10.6028/jres.049.044
- Hirzinger, G., Butterfaß, J. K., Knoch, S., and Liu, H. (1998). "DLR's multisensory articulated hand," in *Experimental Robotics V*, eds A. Casals and A. T. Almeida (Berlin; Heidelberg: Springer), 47–55. doi: 10.1007/BFb0112949

- Huitzil-Velasco, I., Pajaro-Cruz, J. O., and Ramírez-Alfaro, I. D. (2017). Test of a myo armband. *Revista de Ciencias Ambientales y Recursos Naturales* 3, 48–56. Available online at: [https://www.econforan.org/spain/researchjournals/Ciencias\\_Ambientales\\_y\\_Recursos\\_Naturales/vol3num10/Revista\\_de\\_Ciencias\\_Ambientales\\_y\\_Recursos\\_Naturales\\_V3\\_N10.pdf#page=55](https://www.econforan.org/spain/researchjournals/Ciencias_Ambientales_y_Recursos_Naturales/vol3num10/Revista_de_Ciencias_Ambientales_y_Recursos_Naturales_V3_N10.pdf#page=55)
- Khan, R. Z., and Ibraheem, N. A. (2012). Hand gesture recognition: a literature review. *Int. J. Artif. Intell. Appl.* 3, 161. doi: 10.5121/ijaia.2012.3412
- Khushaba, R. N., Al-Timemy, H. A., Samuel, O. W., and Scheme, E. J. (2022). “Myoelectric control with fixed convolution-based time-domain feature extraction: exploring the spatio-temporal interaction,” in *IEEE Transactions on Human-Machine Systems* (IEEE), 1–10. doi: 10.1109/THMS.2022.3146053
- Konrad, P. (2005). *The ABC of EMG: A Practical Introduction to Kinesiological Electromyography*. New York, NY: Noraxon. p. 30–35.1, 30–35. Available online at: <http://www.noraxon.com/wp-content/uploads/2014/12/ABC-EMG-ISBN.pdf>
- Levenberg, K. (1944). A method for the solution of certain non-linear problems in least squares. *Q. Appl. Math.* 2, 164–168. doi: 10.1090/qam/10666
- Londoa, J. A. A., Bravo, E. C., and Garcia, J. F. C. (2017). Aplicación de tecnologías de rehabilitación robótica en niños con lesión del miembro superior. *Revista de la Universidad Industrial de Santander Salud* 49, 103–114. doi: 10.18273/revsal.v49n1-2017010
- Maciejasz, P., Eschweiler, J., Gerlach-Hahn, K., Jansen-Troy, A., and Leonhardt, S. (2014). A survey on robotic devices for upper limb rehabilitation. *J. Neuroeng. Rehabil.* 3, 1–11. doi: 10.1186/1743-0003-11-3
- Martínez-Arroyo, M., and Sucar, L. (2006). “Learning an optimal naive bayes classifier,” in *18th International Conference on Pattern Recognition (ICPR'06)* (Hong Kong), 1236–1239. doi: 10.1109/ICPR.2006.748
- Merletti, R., and Parker, P. J. (2004). *Electromyography: Physiology, Engineering, and Non-invasive Applications*, Vol. 11. Hoboken, NJ: John Wiley & Sons. doi: 10.1002/0471678384
- Oskoei, M. A., and Hu, H. (2007). Myoelectric control systems—a survey. *Biomed. Signal Process. Control* 2, 275–294. doi: 10.1016/j.bspc.2007.07.009
- Pamungkas, D. S., and Simatupang, I. (2020). “Comparison EMG pattern recognition using bayes and NN methods,” in *2020 3rd International Conference on Mechanical, Electronics, Computer, and Industrial Technology (MECnIT)* (Medan), 1–4. doi: 10.1109/MECnIT48290.2020.9166666
- Phinyomark, A., Phukpattaranont, P., and Limsakul, C. (2012). Feature reduction and selection for EMG signal classification. *Expert Syst. Appl.* 39, 7420–7431. doi: 10.1016/j.eswa.2012.01.102
- Phinyomark, A., and Scheme, E. (2018). “An investigation of temporally inspired time domain features for electromyographic pattern recognition,” in *2018 40th Annual International Conference of the IEEE Engineering in Medicine and Biology Society (EMBC)* (Honolulu, HI: IEEE), 5236–5240. doi: 10.1109/EMBC.2018.8513427
- Pizzolatto, S., Tagliapietra, L., Cognolato, M., Reggiani, M., Müller, H., and Atzori, M. (2017). Comparison of six electromyography acquisition setups on hand movement classification tasks. *PLoS ONE* 12, e0186132. doi: 10.1371/journal.pone.0186132
- Pyk, P., Wille, D., Chevrier, E., Hauser, Y., Holper, L., Fatton, I., et al. (2008). “A paediatric interactive therapy system for arm and hand rehabilitation,” in *2008 Virtual Rehabilitation, IWVR* (Vancouver, BC: IEEE), 127–132. doi: 10.1109/ICVR.2008.4625148
- Qiu, Q., Ramirez, D. A., Saleh, S., Fluet, G. G., Parikh, H. D., Kelly, D., et al. (2009). The New Jersey Institute of Technology Robot-assisted virtual rehabilitation (NJIT-RAVR) system for children with cerebral palsy: a feasibility study. *J. Neuroeng. Rehabil.* 1, 6–40. doi: 10.1186/1743-0003-6-40
- STM (2021). *Control BOARD STM32f407*. Geneva: Plan-les-Ouates. Available online at: <https://www.st.com/en/evaluation-tools/stm32f4discovery.html>
- The MathWorks, Inc. (2021). *Statistics and Machine Learning Toolbox User's Guide*. Natick, MA: The MathWorks, Inc. Available online at: [https://mathworks.com/](https://mathworks.com/Tomaszewski, M. (2016). Myo SDK MATLAB MEX Wrapper. Available online at: https://github.com/mark-toma/MyoMex)
- Tomaszewski, M. (2016). *Myo SDK MATLAB MEX Wrapper*. Available online at: <https://github.com/mark-toma/MyoMex>
- Villoslada, Á., Escudero, N., Martín, F., Flores, A., Rivera, C., Collado, M., et al. (2015). Position control of a shape memory alloy actuator using a four-term bilinear pid controller. *Sens. Actuat. A Phys.* 236, 257–272. doi: 10.1016/j.sna.2015.10.006
- Wei, W., Dai, Q., Wong, Y., Hu, Y., Kankanhalli, M., and Geng, W. (2019). Surface-electromyography-based gesture recognition by multi-view deep learning. *IEEE Trans. Biomed. Eng.* 66, 2964–2973. doi: 10.1109/TBME.2019.2899222
- Wood, K. A., Lathan, C. E., and Kaufman, K. R. (2009). Development of an interactive upper extremity gestural robotic feedback system: from bench to reality. *Annu. Int. Conf. IEEE Eng. Med. Biol. Soc.* 2009, 5973–5976. doi: 10.1109/IEMBS.2009.5333523
- Wu, C., Yan, Y., Cao, Q., Fei, F., Yang, D., Lu, X., et al. (2020). sEMG measurement position and feature optimization strategy for gesture recognition based on ANOVA and neural networks. *IEEE Access* 8, 56290–56299. doi: 10.1109/ACCESS.2020.2982405
- Yue, Z., Xue, Z., and Wang, J. (2017). Hand rehabilitation robotics on poststroke motor recovery. *Behav. Neurol.* 2017, 1–35. doi: 10.1155/2017/3908135
- Zhang, Z., Chen, G., and Chen, S. (2022). “A support vector neural network for P300 EEG signal classification,” in *IEEE Transactions on Artificial Intelligence*, Vol. 3 (IEEE), 309–321. doi: 10.1109/TAI.2021.3105493
- Zhang, Z., Chen, G., and Yang, S. (2021). “Ensemble support vector recurrent neural network for brain signal detection,” in *IEEE Transactions on Neural Networks and Learning Systems* (IEEE), 1–11. doi: 10.1109/TNNLS.2021.3083710

**Conflict of Interest:** The authors declare that the research was conducted in the absence of any commercial or financial relationships that could be construed as a potential conflict of interest.

**Publisher's Note:** All claims expressed in this article are solely those of the authors and do not necessarily represent those of their affiliated organizations, or those of the publisher, the editors and the reviewers. Any product that may be evaluated in this article, or claim that may be made by its manufacturer, is not guaranteed or endorsed by the publisher.

Copyright © 2022 Copaci, Arias, Gómez-Tomé, Moreno and Blanco. This is an open-access article distributed under the terms of the Creative Commons Attribution License (CC BY). The use, distribution or reproduction in other forums is permitted, provided the original author(s) and the copyright owner(s) are credited and that the original publication in this journal is cited, in accordance with accepted academic practice. No use, distribution or reproduction is permitted which does not comply with these terms.

# Advantages of publishing in Frontiers



## OPEN ACCESS

Articles are free to read  
for greatest visibility  
and readership



## FAST PUBLICATION

Around 90 days  
from submission  
to decision



## HIGH QUALITY PEER-REVIEW

Rigorous, collaborative,  
and constructive  
peer-review



## TRANSPARENT PEER-REVIEW

Editors and reviewers  
acknowledged by name  
on published articles

## Frontiers

Avenue du Tribunal-Fédéral 34  
1005 Lausanne | Switzerland

**Visit us:** [www.frontiersin.org](http://www.frontiersin.org)

**Contact us:** [frontiersin.org/about/contact](http://frontiersin.org/about/contact)



## REPRODUCIBILITY OF RESEARCH

Support open data  
and methods to enhance  
research reproducibility



## DIGITAL PUBLISHING

Articles designed  
for optimal readership  
across devices



## FOLLOW US

@frontiersin



## IMPACT METRICS

Advanced article metrics  
track visibility across  
digital media



## EXTENSIVE PROMOTION

Marketing  
and promotion  
of impactful research



## LOOP RESEARCH NETWORK

Our network  
increases your  
article's readership